

# Northumbria Research Link

Citation: Chille, Chiara (2021) Er:YAG laser interactions with natural and synthetic varnishes for paintings. Doctoral thesis, Northumbria University.

This version was downloaded from Northumbria Research Link:  
<http://nrl.northumbria.ac.uk/id/eprint/46051/>

Northumbria University has developed Northumbria Research Link (NRL) to enable users to access the University's research output. Copyright © and moral rights for items on NRL are retained by the individual author(s) and/or other copyright owners. Single copies of full items can be reproduced, displayed or performed, and given to third parties in any format or medium for personal research or study, educational, or not-for-profit purposes without prior permission or charge, provided the authors, title and full bibliographic details are given, as well as a hyperlink and/or URL to the original metadata page. The content must not be changed in any way. Full items must not be sold commercially in any format or medium without formal permission of the copyright holder. The full policy is available online: <http://nrl.northumbria.ac.uk/policies.html>



**Northumbria  
University**  
NEWCASTLE



**UniversityLibrary**

# Northumbria Research Link

Citation: Chille, Chiara (2021) Er:YAG laser interactions with natural and synthetic varnishes for paintings. Doctoral thesis, Northumbria University.

This version was downloaded from Northumbria Research Link:  
<http://nrl.northumbria.ac.uk/id/eprint/46051/>

Northumbria University has developed Northumbria Research Link (NRL) to enable users to access the University's research output. Copyright © and moral rights for items on NRL are retained by the individual author(s) and/or other copyright owners. Single copies of full items can be reproduced, displayed or performed, and given to third parties in any format or medium for personal research or study, educational, or not-for-profit purposes without prior permission or charge, provided the authors, title and full bibliographic details are given, as well as a hyperlink and/or URL to the original metadata page. The content must not be changed in any way. Full items must not be sold commercially in any format or medium without formal permission of the copyright holder. The full policy is available online: <http://nrl.northumbria.ac.uk/policies.html>

**Er:YAG LASER INTERACTIONS  
WITH NATURAL AND  
SYNTHETIC VARNISHES FOR  
PAINTINGS**

**CHIARA CHILLÈ**

**PhD**

**2021**

**Er:YAG LASER INTERACTIONS  
WITH NATURAL AND  
SYNTHETIC VARNISHES FOR  
PAINTINGS**

CHIARA CHILLÈ

A thesis submitted in partial fulfilment  
of the requirements of the  
University of Northumbria at Newcastle  
for the degree of  
Doctor of Philosophy

Research undertaken in the  
Faculty of Arts, Design & Social  
Sciences

January 2021



## Abstract

This PhD study aims to deepen the comprehension of the Er:YAG (2940 nm) laser-induced physicochemical effects on aged varnishes by a systematic examination of the side effects caused by the temperature rise in the irradiated surfaces, the heat propagation in the bulk and examines if the laser beam could reach the underlying layer during the laser-material interaction. It also focused on whether Er:YAG lasers can be used to safely thin varnishes applied to works of art, therefore, enhancing the use of laser as an alternative to traditional cleaning methods for paintings. A series of dammar, Ketone N, MS2A, and Paraloid B67 varnish mock-ups on glass slides were light and hydrothermally aged for a comprehensive study. Artists and conservators commonly used these resins in paintings of the late nineteenth and twentieth centuries. Changes in temperature upon laser irradiation were determined by i) recording live thermal imaging with an IR thermal camera and ii) obtaining the optical properties of the varnishes to estimate the absorption coefficients and the temperature increases. A mathematical model and a two-dimensional simulation of the laser heat diffusion through each irradiated varnish supported the second approach. They also provided an additional possibility to study the heat propagation in the bulk of the irradiated varnishes. It was found that, in this case, the IR thermal camera was unable to provide accurate maximum peak temperature data. Nonetheless, the pre-wetted varnishes using an aqueous solution showed  $\Delta T_{\text{mean}}$  values higher than on the dry varnishes due to the superheating of the aqueous film on the surface (Nahen and Vogel, 2002). Transmission Infrared Spectroscopy and Differential Scanning Calorimetry determined the absorption coefficients and the specific heat capacities of films. The mathematical model and the 2D simulations showed that the maximum temperature was obtained using a short pulse duration (VSP) mode, and the heat distribution was less than the one obtained with a long pulse duration (SP) mode. The temperature at the interface between the coating films and the substrate remained at room temperature, thereby protecting the underlying paint surface. Transmission studies were carried out on the aged varnishes in real-time upon laser irradiation, showing that the energy transmitted upon a single laser pulse in VSP and SP modes increased almost linearly with fluence. By pre-wetting the varnishes' surface with an aqueous solution, the

laser energy propagation into the selected varnishes was reduced because of the maximum absorption coefficient of water at the Er:YAG laser wavelength (Shori *et al.*, 2001). Since Paraloid B67 does not contain O-H groups in its chemical structure, the transmission infrared spectroscopy showed almost all the Er:YAG laser radiation passed through the film, reaching the underlying layer. Chemical changes were monitored with Attenuated Total Reflection/Fourier Transform Infra-Red Spectroscopy. This analysis registered a reduction of hydroxides and carbonyls relative to hydrocarbon bonds compared to the films before irradiation. The decrease in hydroxides confirmed that the dominating mechanism of Er:YAG laser is directly related to the maximum absorption of the 2940 nm laser wavelength from the hydroxides in the irradiated surface. The resulted laser spots were observed with Scanning Electron Microscopy. A comparison between dry and pre-wetted irradiation revealed morphological differences between the dry irradiated surfaces and the pre-wetted ones with less marked laser spots in the latter. After the tests, an Er:YAG laser was used to thin an aged varnish on a nineteenth-century oil painting. Dry and pre-wetted laser tests were conducted using single and multiple laser scans. The efficacy of the cleaning procedure was evaluated using stereomicroscopy and colourimetry, and spectral clusterisation maps derived from multispectral imaging (MSI). MSI data, used herein for the first time, were particularly useful in evaluating and monitoring the laser effects to the surface. Fourier Transform Infra-Red Spectroscopy and Pyrolysis Gas Chromatography/Mass Spectrometry analysis indicated that the varnish resin was dammar. The collected resin fragments were analysed by FT-IR. The results showed that the resin did not degrade even at the highest level of fluence employed, thereby allowing a subsequent analytical evaluation.



# Table of Contents

	Page
<b>Abstract</b> .....	<b>I</b>
<b>Table of Contents</b> .....	<b>III</b>
<b>List of Figures</b> .....	<b>IX</b>
<b>List of Tables</b> .....	<b>XXXVIII</b>
<b>List of Abbreviations</b> .....	<b>XLV</b>
<b>Acknowledgments</b> .....	<b>XLIX</b>
<b>Author's declaration</b> .....	<b>LI</b>
<b>CHAPTER 1 Introduction</b> .....	<b>1</b>
1.1 Background and motivation .....	<b>1</b>
1.2 Rationale .....	<b>4</b>
1.3 Aims and objectives .....	<b>6</b>
1.4 Thesis structure .....	<b>8</b>
<b>CHAPTER 2 Literature Review</b> .....	<b>11</b>
2.1 Introduction .....	<b>12</b>
2.2 LITERATURE REVIEW I: On Varnishes .....	<b>14</b>
2.2.1 Brief history of varnishes .....	<b>16</b>
2.2.1.1 Natural soft resins .....	<b>18</b>
2.2.1.2 Synthetic resins .....	<b>19</b>
2.3 LITERATURE REVIEW II: On the cleaning of paintings - varnish removal .....	<b>23</b>
2.3.1 Wet and Dry cleaning methodologies .....	<b>26</b>
2.3.1.1 Wet cleaning .....	<b>27</b>
2.3.1.2 Dry cleaning .....	<b>29</b>
2.4 LITERATURE REVIEW III: On the laser cleaning treatments for cultural heritage .....	<b>30</b>
2.4.1 Brief history of the use of laser in paintings conservation .....	<b>31</b>
2.5 Summary of the Literature Review Findings on the use of laser to treat varnishes .....	<b>59</b>



## **CHAPTER 4 Er:YAG Laser Tests (Part I): A study on the heat distribution**

.....	<b>113</b>
4.1 Lasers systems .....	<b>114</b>
4.1.1 Mechanism of laser cleaning and its interaction with the materials .....	<b>116</b>
4.1.2 Laser-material interaction: Thermal effects .....	<b>118</b>
4.1.2.1 Radiation heat transfer .....	<b>119</b>
4.1.2.2 Heat conduction and convection .....	<b>120</b>
4.1.3 Erbium-doped:Yttrium-Aluminium-Garnet (Er:YAG) laser ....	<b>122</b>
4.1.3.1 Liquid-assisted laser-material interaction .....	<b>125</b>
4.1.4 Thermal studies of Er:YAG laser .....	<b>128</b>
4.2 Material and methods .....	<b>131</b>
4.2.1 Er:YAG laser .....	<b>131</b>
4.2.2 Optical properties varnishes .....	<b>132</b>
4.2.2.1 Transmission FT-IR .....	<b>132</b>
4.2.2.2 Mid-IR integrating sphere measurement .....	<b>132</b>
4.2.3 Transmission study .....	<b>133</b>
4.2.4 Heat distribution on the coatings upon laser irradiation .....	<b>135</b>
4.2.4.1 IR thermal camera recordings .....	<b>135</b>
4.2.4.2 Modelling of the heat distribution upon laser irradiation .....	<b>138</b>
4.2.4.2.1 Mathematical computation of the temperature rise .....	<b>139</b>
4.2.4.2.2 2 Dimensional Simulation model .....	<b>144</b>
4.3 Results and Discussion .....	<b>150</b>
4.3.1 % Transmission, % Reflectance and Absorption coefficient ....	<b>150</b>
4.3.2 Transmission study .....	<b>152</b>
4.3.3 Heat distribution on the coatings upon laser irradiation .....	<b>158</b>
4.3.3.1 Thermal camera recordings .....	<b>158</b>
4.3.3.2 Heat distribution modelling .....	<b>162</b>
4.3.3.2.1 Computation of the temperature rise .....	<b>163</b>
4.3.3.2.2 Transient temperature profiles of varnishes regarded as semi-infinite solids .....	<b>166</b>
4.3.3.2.3 2 Dimensional Simulation model .....	<b>182</b>

4.4	Conclusion .....	191
<b>CHAPTER 5 Er:YAG Laser Tests (Part II): Microscopies and Spectroscopic investigations .....</b>		
<b>194</b>		
5.1	An introduction on the use of Er:YAG laser in Conservation .....	195
5.2	Material and methods .....	198
5.2.1	Er:YAG laser .....	198
5.2.2	Microscopies .....	198
5.2.3	Attenuated Total Reflection/Fourier Transform Infrared Spectroscopy (ATR/FT-IR) .....	199
5.3	Results and Discussion .....	200
5.3.1	Laser tests on dammar, Ketone N, MS2A and Paraloid B67 films and laser-induced morphological modifications .....	200
5.3.1.1	Single Er:YAG laser tests on dammar and ketone resin films .....	201
5.3.1.2	3-Pulse tests on dammar and ketone resin films .....	215
5.3.2	ATR/FT-IR .....	228
5.4	Conclusion .....	234
<b>CHAPTER 6 An analytical evaluation of Er:YAG laser cleaning tests on a nineteenth century varnished painting .....</b>		
<b>236</b>		
6.1	Introduction .....	237
6.2	Material and methods .....	238
6.2.1	Attenuated Total reflection / Fourier Transform - Infra-Red spectroscopy (ATR/FT-IR) .....	238
6.2.2	Pyrolysis-TMAH-Gas Chromatography/Mass spectroscopy (Py-TMAH-GC/MS) .....	239
6.2.3	Laser cleaning tests .....	240
6.2.4	Technical photography .....	244
6.2.5	Stereomicroscopy .....	244
6.2.6	Colourimetry .....	245
6.2.7	Multispectral imaging .....	246
6.3	Results and discussion .....	248
6.3.1	Varnish Characterisation .....	248
6.3.2	Er:YAG laser tests .....	251

6.3.3	Colourimetric measurements .....	257
6.3.4	Multispectral imaging .....	263
6.3.5	Further spectroscopic evaluation .....	271
6.4	Conclusion .....	275
 <b>CHAPTER 7 Conclusions &amp; Future Prospects .....</b>		<b>276</b>
7.1	Conclusions .....	276
6.1.1	Summary of Contributions .....	277
7.2	Future Prospects .....	284
7.3	Summary the overarching findings of the thesis .....	284
 <b>LIST OF REFERENCES .....</b>		<b>289</b>
 <b>APPENDICES .....</b>		<b>354</b>
<b>Appendix A Varnishes Data .....</b>		<b>354</b>
A1)	Stylus Profilometry .....	355
A.1.1	Dammar .....	355
A.1.2	Ketone N .....	356
A.1.3	MS2A .....	357
A.1.4	Paraloid B67 .....	358
A2)	Colourimetry .....	359
A3)	Differential Scanning Calorimetry (DSC) analysis .....	361
 <b>Appendix B Er:YAG laser tests &amp; Experimental results .....</b>		<b>363</b>
B1)	Transmission FT-IR spectra .....	364
B2)	Mid-IR integrating sphere measurement .....	366
B3)	Fotona Fidelis Er:YAG lasers system specifications .....	368
B4)	FLIR T620bx IR thermal camera .....	369
B5)	FLIR with K type thermocouple .....	370
B6)	FLIR thermal camera: thermal data acquired on the uncoated glass slide . .....	372
B7)	Transient temperature profiles of varnishes regarded as semi-infinite solids .....	373

B7.1 Dammar – VSP mode ( $\tau_L \approx 100 \mu\text{s}$ ) .....	373
B7.2 Dammar – SP mode ( $\tau_L \approx 300 \mu\text{s}$ ) .....	376
B7.3 Ketone N – VSP mode ( $\tau_L \approx 100 \mu\text{s}$ ) .....	379
B7.4 Ketone N – SP mode ( $\tau_L \approx 300 \mu\text{s}$ ) .....	384
B7.5 MS2A – VSP mode ( $\tau_L \approx 100 \mu\text{s}$ ) .....	389
B7.6 MS2A – SP mode ( $\tau_L \approx 300 \mu\text{s}$ ) .....	394
B8) An example of FlexPDE script for the 2D simulation .....	399
B9) 2D Simulations .....	401
B9.1 Dammar – VSP mode ( $\tau_L \approx 100 \mu\text{s}$ ) .....	401
B9.2 Dammar – SP mode ( $\tau_L \approx 300 \mu\text{s}$ ) .....	403
B9.3 Ketone N – VSP mode ( $\tau_L \approx 100 \mu\text{s}$ ) .....	405
B9.4 Ketone N – SP mode ( $\tau_L \approx 300 \mu\text{s}$ ) .....	409
B9.5 MS2A – VSP mode ( $\tau_L \approx 100 \mu\text{s}$ ) .....	413
B9.6 MS2A – SP mode ( $\tau_L \approx 300 \mu\text{s}$ ) .....	417
B10) Varnish parameters .....	421
B10.1 Dammar .....	421
B10.2 Ketone N .....	421
B10.3 MS2A .....	422
B10.4 Paraloid B67 .....	422
<b>Appendix C Er:YAG laser cleaning tests on a nineteenth century varnished painting .....</b>	<b>423</b>
C1) Py-TMAH-GC/MS acquired from the nineteenth century varnished painting .....	424
C2) Er:YAG laser tests .....	426
C3) ATR/FT-IR .....	448



# List of Figures

<b>Figure 2.1</b> – The picture shows a graphical illustration of the structure of an easel painting. Figure adapted from Ocon and Findley .....	<b>13</b>
<b>Figure 2.2</b> – Classification of material usually employed as coatings on paint surfaces (Matteini, Mazzeo and Moles, 2017, p. 167) .....	<b>17</b>
<b>Figure 2.3</b> – Teas chart showing the solubility parameters of neutral organic solvents customarily used in the conservation field (Figure adapted from Baglioni and Chelazzi, 2013, p. 188) .....	<b>28</b>
<b>Figure 3.1</b> – Triterpenoid molecular structures present in dammar (Figure adapted from Theodorakopoulos, 2005, p. 82) .....	<b>70</b>
<b>Figure 3.2</b> – Chemical structure of n-butyl methacrylate commercially known as Paraloid B67 .....	<b>73</b>
<b>Figure 3.3</b> – Chemical structure of cyclohexanone (A); methyl cyclohexanone (B); structure of ketone resins as suggested by de la Rie and Shedrinsky (1989) where n is equal to 3 and 5; (C) and structure of ketone resins published by Mills and White (1999, p. 138) (D) .....	<b>75</b>
<b>Figure 3.4</b> – Probable structure of MS2A as suggested by Routledge (2000) . .....	<b>76</b>
<b>Figure 3.5</b> – Varnishes selected for the research. (A) dammar resin in xylene; (B) Ketone N in Stoddard solvent; (C) Paraloid B67 in xylene and (D) MS2A in Stoddard solvent .....	<b>80</b>
<b>Figure 3.6</b> – Elcometer 3540 film applicator used to cast dammar, Ketone N, MS2A and Paraloid B67 on glass slides .....	<b>81</b>
<b>Figure 3.7</b> – The absorption spectrum of a glass slide used for this research on which it has been specified the Er:YAG laser absorption .....	<b>81</b>
<b>Figure 3.8</b> – The spectrum produced by the Window-Q filter (Figure adapted from Q-Lab Corporation, 2014) .....	<b>82</b>

<b>Figure 3.9</b> – Accelerated aged (left) and unaged (right) varnish films selected for this research (from top to bottom Ketone N, MS2A, Paraloid B67 and dammar) .....	<b>83</b>
<b>Figure 3.10</b> – Schematic representation of the methodology employed to acquire the colourimetric values. (A-B) The border of a clean glass slide was drawn on an A4 white paper and (C) six measurements were acquired inside that area, each of them shifted horizontally along the centre of the selected area. Then, (D) the clean glass slide was put again onto the drawn area, and five colourimetric readings were acquired. Finally, two unaged and two aged glass-coated varnish samples were placed onto the drawn area, and three measurements were taken along the centre of the samples .....	<b>87</b>
<b>Figure 3.11</b> – Stylus profilometry on the air-resin film interfaces, showing the surface morphology of the varnishes (A: dammar; B: Ketone N; C: MS2A and D: Paraloid B67) on glass slide substrates after the accelerated ageing process .....	<b>93</b>
<b>Figure 3.12</b> – 2 µL droplet of DI-W+TW20 was deposited on the surface of each aged varnish. Dammar resin shows no static contact angle due to the highly cracked surface, which resulted in the diffusion of DI-W+TW20 within the cracks of the film. The contact angle ( $\theta$ ) of the aged Ketone N ( $32.4^\circ \pm 2.9^\circ$ ), MS2A ( $41.6^\circ \pm 6.3^\circ$ ) and Paraloid B67 ( $45.4^\circ \pm 0.8^\circ$ ) varnishes is below $90^\circ$ indicating that all these varnishes are hydrophilic. The most hydrophilic film is the aged Ketone N varnish which has the smallest contact angle .....	<b>95</b>
<b>Figure 3.13</b> – Brightness, $L^*$ , of the unaged and aged varnishes in SCI (A) and SCE (B) modes. The dammar varnish appears to be the most affected after the ageing with a darkening of the surface detectable as a significant decrease in brightness. The most stable varnish is the Paraloid B67 .....	<b>97</b>
<b>Figure 3.14</b> – Chromaticity coordinates ( $a^*$ and $b^*$ ) of the varnishes before and after ageing. All the varnishes show a toning towards yellow-green values .....	<b>98</b>

<b>Figure 3.15</b> – Total colour variation $\Delta E$ for all the varnishes. The dashed line at $\Delta E=1$ specifies the threshold at which the eye can detect visible differences .....	<b>98</b>
<b>Figure 3.16</b> – Thermogravimetric curves (solid lines) of the varnish selected for this research and their corresponding first derivative DrTGA curves (dashed lines) .....	<b>100</b>
<b>Figure 3.17</b> – Glass transition temperature ( $T_g$ ) of the unaged resins obtained by DSC analysis. The solid lines indicate the first heating and the dashed lines the second heating .....	<b>103</b>
<b>Figure 3.18</b> – ATR/FT-IR spectra of dammar, Ketone N, MS2A and Paraloid B67 varnish films in the wavenumber ranges of 3800-2500 and 1900-750 $\text{cm}^{-1}$ . The arrows show the modifications of the main vibrational groups produced by the ageing .....	<b>107</b>
<b>Figure 4.1</b> – Laser used in the conservation field (Figure is from Marczak <i>et al.</i> , 2008) .....	<b>114</b>
<b>Figure 4.2</b> – Laser Pulse Parameters (Inspired by an original image published in ThorLabs website) .....	<b>115</b>
<b>Figure 4.3</b> – Comparison between PNF and VSP technologies (Inspired by an original image published in Lukač, Sult and Sult, 2007) .....	<b>122</b>
<b>Figure 4.4</b> – VSP free-running Er:YAG laser pulse shape for different laser pulse duration (Fotona laser) (Figure is from Lukač, Primc and Pirnat, 2012) .....	<b>123</b>
<b>Figure 4.5</b> – (A) ‘Top hat’ beam profile handpiece, (B) Gaussian beam profile handpiece (Figure is from Lukač, Sult and Sult, 2007) and (C) Fotona R11 handpiece (see <a href="http://www.fotona.com">www.fotona.com</a> - Fotona) .....	<b>123</b>
<b>Figure 4.6</b> – The absorption coefficient of water. The Er:YAG laser has the highest absorption coefficient in water (Inspired by an original image published in Olivi and Olivi, 2010) .....	<b>124</b>
<b>Figure 4.7</b> – This images are reproduced by (A) Dynamics of the interaction of water film upon a single Er:YAG laser irradiation at 2 $\text{J}/\text{cm}^2$ , beam diameter of 8 mm and $\tau_L$ of 200 $\mu\text{s}$ . The time-resolved images, acquired in bright-field, show	

that after the beginning of the laser pulse, at about 100  $\mu\text{s}$ , the material ejection begins in the areas of the highest energy density and spreads over the entire beam cross-section after about 180  $\mu\text{s}$ . (B) Images in the dark-field, using the same laser device and employing the above mentioned parameters. After 40  $\mu\text{s}$ , Apitz (2006, pp. 77–79) described a clear formation of vapour, which falls after about 300  $\mu\text{s}$ . The light stripe in front of the cloud indicates a zone of high vapour density ..... 126

**Figure 4.8** – Fotona Fidelis<sup>XS</sup> ..... 131

**Figure 4.9** – Experimental set-up for the transmission study tests ..... 134

**Figure 4.10** – Experimental set-up for the thermal camera recording tests (A) and a detail of an irradiated dammar varnish applied onto a glass slide during the laser irradiation secured to a support placed at 10 cm from the working desk (B) ..... 136

**Figure 4.11** – The thermal camera records a series of frames in which the energy radiated from the varnish surfaces upon Er:YAG irradiation is shown as a form of the surface signal. By manually selecting the area influenced by the laser irradiation (A), the device translated the radiated surface signal to the temperature values by defining an internal conversion equation (B). Thus, by selecting the desired maximum temperature (C), the data were extracted in comma-separated values (CSV) file and exported in a data analysis software (e.g., Excel) (D) ..... 137

**Figure 4.12** – FLIR T620bx thermal camera. A1: Thermograph of the maximum temperature variation recorded (44.2 °C) including TR, which at the time of acquisition was 24 °C, as recorded on VSP dry dammar (one pulse at 2 J/cm<sup>2</sup>) in real-time. On the top side: (A) the thermal image (thermogram) of the dammar varnish surface while receiving a single laser pulse; (B) the thermogram after 67 ms; (C) the thermogram after 0.56 s; (D) the thermogram after 8 s ..... 138

**Figure 4.13** – Graphical representation of direct and conduction heating on varnishes (Inspired by an original image published in Siano *et al.*, 2000) ..  
..... 141

<b>Figure 4.14</b> – The 3D-geometry of the modelled <b>dammar</b> film applied on a glass slide with the dimension of each layer analysed (optical penetration depth $[\delta]$ + varnish film) .....	<b>144</b>
<b>Figure 4.15</b> – The 3D-geometry of the modelled <b>Ketone N</b> film applied on a glass slide with the dimension of each layer analysed (optical penetration depth $[\delta]$ + varnish film) .....	<b>145</b>
<b>Figure 4.16</b> – The 3D-geometry of the modelled <b>MS2A</b> film applied on a glass slide with the dimension of each layer analysed (optical penetration depth $[\delta]$ + varnish film) .....	<b>145</b>
<b>Figure 4.17</b> – Graphical representation of the geometry created to run the 2D simulation. A sub-domain has been created in which it is assumed that part of the laser photon energy is absorbed into the bulk of the <b>dammar</b> varnish film .....	<b>147</b>
<b>Figure 4.18</b> – Graphical representation of the geometry created to run the 2D simulation. A sub-domain has been created in which it is assumed that part of the laser photon energy is absorbed within the bulk of the <b>Ketone N</b> varnish film .....	<b>147</b>
<b>Figure 4.19</b> – Graphical representation of the geometry created to run the 2D simulation. A sub-domain has been created in which it is assumed that part of the laser photon energy is absorbed into the bulk of the <b>MS2A</b> varnish film .....	<b>148</b>
<b>Figure 4.20</b> – The average single-pulse laser transmitted energies ( $E_{trans}$ ) as a function of fluence. $E_{trans}$ values were experimentally measured by placing a Pyroelectric Detector behind the dry and pre-wetted varnishes .....	<b>154</b>
<b>Figure 4.21</b> – $E_{trans}/E_{inc}$ versus the chosen range of fluences in VSP and SP modes upon a single laser pulse for dammar, Ketone N and MS2A .....	<b>154</b>
<b>Figure 4.22</b> – The dependence of the thermal diffusion length ( $l_{th}$ ) of the varnishes as a function of laser pulse duration $\tau_L$ for the Fotona Fidelis <sup>XS</sup> Er:YAG laser. VSP mode: $\tau_L \approx 100 \mu s$ ; SP mode: $\tau_L \approx 300 \mu s$ ; LP mode $\tau_L \approx 600 \mu s$ ; VLP mode $\tau_L \approx 1000 \mu s$ .....	<b>162</b>

**Figure 4.23** – Representation of the heat-wave propagation inside the **dammar** film, in VSP mode, at different times [100  $\mu\text{s}$  (gray), 200  $\mu\text{s}$  (pink), 400  $\mu\text{s}$  (cyan), 800  $\mu\text{s}$  (brow) and 1 ms (magenta)] as a function of depth (A and C) and the temperature rise evolution at various depth [0 (black), 5  $\mu\text{m}$  (red), 10  $\mu\text{m}$  (blue), 20  $\mu\text{m}$  (green), 33.21  $\mu\text{m}$  (purple)] as a function of time (B and D). The laser beam diameter was set at  $\varnothing = 4$  mm. Temperature is given relative to room temperature (25  $^{\circ}\text{C}$ ) ..... 172

**Figure 4.24** – Representation of the heat-wave propagation inside the **dammar** film, in SP mode, at different times [300  $\mu\text{s}$  (gray), 600  $\mu\text{s}$  (pink), 1.2 ms (cyan), 2.4 ms (brow) and 3 ms (magenta)] as a function of depth (A and C) and the temperature rise evolution at various depth [0 (black), 5  $\mu\text{m}$  (red), 10  $\mu\text{m}$  (blue), 20  $\mu\text{m}$  (green), 33.21  $\mu\text{m}$  (purple)] as a function of time (B and D). The laser beam diameter was set at  $\varnothing = 4$  mm. Temperature is given relative to room temperature (25  $^{\circ}\text{C}$ ) ..... 173

**Figure 4.25** – Representation of the heat-wave propagation inside the **Ketone N** film, in VSP mode, at different times [100  $\mu\text{s}$  (gray), 200  $\mu\text{s}$  (pink), 400  $\mu\text{s}$  (cyan), 800  $\mu\text{s}$  (brow) and 1 ms (magenta)] as a function of depth (A and C) and the temperature rise evolution at various depth [0 (black), 2  $\mu\text{m}$  (red), 4  $\mu\text{m}$  (blue), 6  $\mu\text{m}$  (green), 7.16  $\mu\text{m}$  (purple)] as a function of time (B and D). The laser beam diameter was set at  $\varnothing = 4$  mm. Temperature is given relative to room temperature (25  $^{\circ}\text{C}$ ) ..... 174

**Figure 4.26** – Representation of the heat-wave propagation inside the **Ketone N** film, in SP mode, at different times [300  $\mu\text{s}$  (gray), 600  $\mu\text{s}$  (pink), 1.2 ms (cyan), 2.4 ms (brow) and 3 ms (magenta)] as a function of depth (A and C) and the temperature rise evolution at various depth [0 (black), 5  $\mu\text{m}$  (red), 10  $\mu\text{m}$  (blue), 20  $\mu\text{m}$  (green), 33.21  $\mu\text{m}$  (purple)] as a function of time (B and D). The laser beam diameter was set at  $\varnothing = 4$  mm. Temperature is given relative to room temperature (25  $^{\circ}\text{C}$ ) ..... 176

**Figure 4.27** – Representation of the heat-wave propagation inside the **MS2A** film, in VSP mode, at different times [100  $\mu\text{s}$  (gray), 200  $\mu\text{s}$  (pink), 400  $\mu\text{s}$  (cyan), 800  $\mu\text{s}$  (brow) and 1 ms (magenta)] as a function of depth (A and C) and the temperature rise evolution at various depth [0 (black), 5  $\mu\text{m}$  (red), 10  $\mu\text{m}$  (blue),

15  $\mu\text{m}$  (green), 18.92  $\mu\text{m}$  (purple)] as a function of time (B and D). The laser beam diameter was set at  $\varnothing = 4$  mm. Temperature is given relative to room temperature (25  $^{\circ}\text{C}$ ) ..... 178

**Figure 4.28** – Representation of the heat-wave propagation inside the **MS2A** film, in SP mode, at different times [300  $\mu\text{s}$  (gray), 600  $\mu\text{s}$  (pink), 1.2 ms (cyan), 2.4 ms (brow) and 3 ms (magenta)] as a function of depth (A and C) and the temperature rise evolution at various depth [0 (black), 5  $\mu\text{m}$  (red), 10  $\mu\text{m}$  (blue), 15  $\mu\text{m}$  (green), 18.92  $\mu\text{m}$  (purple)] as a function of time (B and D). The laser beam diameter was set at  $\varnothing = 4$  mm. Temperature is given relative to room temperature (25  $^{\circ}\text{C}$ ) ..... 180

**Figure 4.29** – 2D simulation of the Er:YAG laser-based heat diffusion inside the **dammar** film in VSP mode ( $\tau_L \approx 100$   $\mu\text{s}$ ) and temperature distribution by cross-section of varnish film + glass slide. Fluences of 0.5  $\text{J}/\text{cm}^2$ , and thermal conductivity (k) between 0.21  $\text{W}/\text{m}\cdot\text{K}$  and 0.021  $\text{W}/\text{m}\cdot\text{K}$ . The beam diameter was set at  $\varnothing = 4$ mm. The laser absorption zone represents the area in which the laser wavelength penetrates into the dammar film ( $\delta$ ) before releasing 63% of its energy ..... 186

**Figure 4.30** – 2D simulation of the Er:YAG laser-based heat diffusion inside the **dammar** film in SP mode ( $\tau_L \approx 300$   $\mu\text{s}$ ) and temperature distribution by cross-section of varnish film + glass slide. Fluences of 2.4  $\text{J}/\text{cm}^2$ , and thermal conductivity (k) between 0.21  $\text{W}/\text{m}\cdot\text{K}$  and 0.021  $\text{W}/\text{m}\cdot\text{K}$ . The beam diameter was set at  $\varnothing = 4$ mm. The laser absorption zone represents the area in which the laser wavelength penetrates into the dammar film ( $\delta$ ) before releasing 63% of its energy ..... 186

**Figure 4.31** – 2D simulation of the heat diffusion inside the **Ketone N** film in VSP mode ( $\tau_L \approx 100$   $\mu\text{s}$ ) and temperature distribution by cross-section of varnish film + glass slide. Fluences of 0.5  $\text{J}/\text{cm}^2$  and thermal conductivity (k) of 0.22  $\text{W}/\text{m}\cdot\text{K}$ . One simulation was run using the %R from the FTIR (\*) the other using the %R from the Fresnel equation (\*\*). The beam diameter was set at  $\varnothing = 4$ mm. The laser absorption zone represents the area in which the laser wavelength penetrates into the Ketone N film ( $\delta$ ) before releasing 63% of its energy ... ..... 187

**Figure 4.32** – 2D simulation of the heat diffusion inside the **Ketone N** film in VSP mode ( $\tau_L \approx 100 \mu\text{s}$ ) and temperature distribution by cross-section of varnish film + glass slide. Fluences of  $0.5 \text{ J/cm}^2$  and thermal conductivity ( $k$ ) of  $0.022 \text{ W/m}\cdot\text{K}$ . One simulation was run using the %R from the FTIR (\*) the other using the %R from the Fresnel equation (\*\*). The beam diameter was set at  $\varnothing = 4\text{mm}$ . The laser absorption zone represents the area in which the laser wavelength penetrates into the Ketone N film ( $\delta$ ) before releasing 63% of its energy ...  
 ..... 187

**Figure 4.33** – 2D simulation of the heat diffusion inside the **Ketone N** film in SP mode ( $\tau_L \approx 300 \mu\text{s}$ ) and temperature distribution by cross-section of varnish film + glass slide. Fluences of  $0.5 \text{ J/cm}^2$  and thermal conductivity ( $k$ ) of  $0.22 \text{ W/m}\cdot\text{K}$ . One simulation was run using the %R from the FTIR (\*) the other using the %R from the Fresnel equation (\*\*). The beam diameter was set at  $\varnothing = 4\text{mm}$ . The laser absorption zone represents the area in which the laser wavelength penetrates into the Ketone N film ( $\delta$ ) before releasing 63% of its energy ...  
 ..... 188

**Figure 4.34** – 2D simulation of the heat diffusion inside the **Ketone N** film in SP mode ( $\tau_L \approx 300 \mu\text{s}$ ) and temperature distribution by cross-section of varnish film + glass slide. Fluences of  $0.5 \text{ J/cm}^2$  and thermal conductivity ( $k$ ) of  $0.022 \text{ W/m}\cdot\text{K}$ . One simulation was run using the %R from the FTIR (\*) the other using the %R from the Fresnel equation (\*\*). The beam diameter was set at  $\varnothing = 4\text{mm}$ . The laser absorption zone represents the area in which the laser wavelength penetrates into the Ketone N film ( $\delta$ ) before releasing 63% of its energy ...  
 ..... 188

**Figure 4.35** – 2D simulation of the heat diffusion inside the **MS2A** film in VSP mode ( $\tau_L \approx 100 \mu\text{s}$ ) and temperature distribution by cross-section of varnish film + glass slide. Fluences of  $0.5 \text{ J/cm}^2$  and thermal conductivity ( $k$ ) of  $0.19 \text{ W/m}\cdot\text{K}$ . One simulation was run using the %R from the FTIR (\*) the other using the %R from the Fresnel equation (\*\*). The beam diameter was set at  $\varnothing = 4\text{mm}$ . The laser absorption zone represents the area in which the laser wavelength penetrates into the MS2A film ( $\delta$ ) before releasing 63% of its energy .....  
 ..... 189

**Figure 4.36** – 2D simulation of the heat diffusion inside the **MS2A** film in VSP mode ( $\tau_L \approx 100 \mu\text{s}$ ) and temperature distribution by cross-section of varnish film + glass slide. Fluences of  $0.5 \text{ J/cm}^2$  and thermal conductivity ( $k$ ) of  $0.019 \text{ W/m}\cdot\text{K}$ . One simulation was run using the %R from the FTIR (\*) the other using the %R from the Fresnel equation (\*\*). The beam diameter was set at  $\varnothing = 4\text{mm}$ . The laser absorption zone represents the area in which the laser wavelength penetrates into the MS2A film ( $\delta$ ) before releasing 63% of its energy ..... **189**

**Figure 4.37** – 2D simulation of the heat diffusion inside the **MS2A** film in SP mode ( $\tau_L \approx 300 \mu\text{s}$ ) and temperature distribution by cross-section of varnish film + glass slide. Fluences of  $0.5 \text{ J/cm}^2$  and thermal conductivity ( $k$ ) of  $0.19 \text{ W/m}\cdot\text{K}$ . One simulation was run using the %R from the FTIR (\*) the other using the %R from the Fresnel equation (\*\*). The beam diameter was set at  $\varnothing = 4\text{mm}$ . The laser absorption zone represents the area in which the laser wavelength penetrates into the MS2A film ( $\delta$ ) before releasing 63% of its energy ..... **190**

**Figure 4.38** – 2D simulation of the heat diffusion inside the **MS2A** film in SP mode ( $\tau_L \approx 300 \mu\text{s}$ ) and temperature distribution by cross-section of varnish film + glass slide. Fluences of  $0.5 \text{ J/cm}^2$  and thermal conductivity ( $k$ ) of  $0.019 \text{ W/m}\cdot\text{K}$ . One simulation was run using the %R from the FTIR (\*) the other using the %R from the Fresnel equation (\*\*). The beam diameter was set at  $\varnothing = 4\text{mm}$ . The laser absorption zone represents the area in which the laser wavelength penetrates into the MS2A film ( $\delta$ ) before releasing 63% of its energy ..... **190**

**Figure 5.1** – Graphical representation of the Er:YAG laser irradiation of a dry surface: (A) if the coating contains O-H groups, the laser wavelength is strongly adsorbed by the hydroxyl groups in the unwanted layer. (B) The laser irradiation leads to heating, rapid expansion and ejection of fragments from the irradiated material. (C) The photo-thermal disaggregation causes the formation of a whitish appearance created by the light scattering. (D) The use of solvents allows to carry on with the thinning of the coating surface ..... **196**

**Figure 5.2** – Graphical representation of the Er:YAG laser irradiation pre-wetting the surface: (A) if the coating do not have enough O-H groups, the surface can be wetted with an OH-containing liquid. (B) The laser irradiation leads to liquid-phase expulsion, rapid expansion and ejection of liquid droplets and fragments

from the irradiated material. (C) The photo-thermal disaggregation causes the formation of a whitish appearance created by the light scattering. (D) The use of solvents allows the continuation of the thinning of the coating surface ..... 196

**Figure 5.3** – Image taken with Dino-Lite microscope of the dammar varnish surface after ageing ..... 200

**Figure 5.4** – Image taken with Dino-Lite microscope of the Paraloid B67 varnish surface after ageing ..... 200

**Figure 5.5** – Image taken with Dino-Lite microscope of the Ketone N varnish surface after ageing ..... 200

**Figure 5.6** – Image taken with Dino-Lite microscope of the MS2A varnish surface after ageing ..... 200

**Figure 5.7** – Stereophotographs of dry irradiated dammar in VSP (A1–A3) and SP (B1–B3) modes. Spot diameter at  $\varnothing = 4\text{mm}$ , pulse repetition rate 2Hz and spots generated by fluences of  $0.6\text{ J/cm}^2$  (A1 and B1),  $1.6\text{ J/cm}^2$  (A2 and B2) and  $2.5\text{ J/cm}^2$  (A3 and B3) ..... 201

**Figure 5.8** – Brightfield Optical Microscopy (OM) micrographs the dry irradiated Paraloid B67 in VSP mode ( $\tau_L \approx 100\ \mu\text{s}$ ). Spot diameter at  $\varnothing = 4\text{ mm}$ , pulse repetition rate 2Hz and fluences of  $1\text{ J/cm}^2$  (A) and  $2.5\text{ J/cm}^2$  (B). No laser spots are visible in the areas irradiated with the Er:YAG laser ..... 201

**Figure 5.9** – Low vacuum BSE-SEM micrographs of the VSP single pulse dry test areas on aged **dammar films**. A and A1:  $0.6\text{ J/cm}^2$ ; B and B1:  $1.6\text{ J/cm}^2$ ; C and C1:  $2.5\text{ J/cm}^2$ . Spot diameter at  $\varnothing = 4\text{mm}$ , pulse repetition rate 2Hz. The micro-craquelure inside the laser spots is not a result of irradiation and was observed prior to irradiation and outside the spots. In VSP, the spot diameter is increased by  $0.63\text{ mm}$  at  $1.6\text{ J/cm}^2$  compared to the spot at  $0.6\text{ J/cm}^2$  and then by  $0.22\text{ mm}$  more at  $2.5\text{ J/cm}^2$  ..... 203

**Figure 5.10** – Low vacuum BSE-SEM micrographs of the SP single pulse dry test areas on aged **dammar films**. A and A1:  $0.6\text{ J/cm}^2$ ; B and B1:  $1.6\text{ J/cm}^2$ ; C and C1:  $2.5\text{ J/cm}^2$ . The micro-craquelure inside the laser spots is not a result of irradiation and was observed prior to irradiation and outside the spots. In SP, the

spot diameter at 1.6 J/cm<sup>2</sup> is 0.54 mm larger compared to the spot at 0.6 J/cm<sup>2</sup> and by a further 0.17 mm at 2.5 J/cm<sup>2</sup> ..... 204

**Figure 5.11** – Low vacuum BSE-SEM micrographs of the DI-W+TW20 pre-wet single pulse laser irradiated test areas in VSP mode on aged **dammar film**. A and A1: 0.6 J/cm<sup>2</sup>; B and B1: 1.6 J/cm<sup>2</sup>; C and C1: 2.5 J/cm<sup>2</sup>. The micro-craquelure inside the laser spots is not a result of irradiation and was observed prior to irradiation and outside the spots. In VSP, the spot diameter is increased by 0.37 mm at 1.6 J/cm<sup>2</sup> compared to the spot at 0.6 J/cm<sup>2</sup> and then by 0.14 mm at 2.5 J/cm<sup>2</sup> ..... 205

**Figure 5.12** – Low vacuum BSE-SEM micrographs of the DI-W+TW20 pre-wet single pulse laser irradiated test areas in SP mode on aged **dammar films**. A and A1: 0.6 J/cm<sup>2</sup>; B and B1: 1.6 J/cm<sup>2</sup>; C and C1: 2.5 J/cm<sup>2</sup>. The micro-craquelure inside the laser spots is not a result of irradiation and was observed prior to irradiation and outside the spots. In SP, the spot diameter at 1.6 J/cm<sup>2</sup> is 0.26 mm larger compared to the spot at 0.6 J/cm<sup>2</sup> and by a further 0.17 mm at 2.5 J/cm<sup>2</sup> ..... 206

**Figure 5.13** – Low vacuum BSE-SEM micrographs of the VSP single pulse dry test areas on aged **Ketone N films**. A: 0.6 J/cm<sup>2</sup>; B and B1: 1.6 J/cm<sup>2</sup>; C and C1: 2.5 J/cm<sup>2</sup>. Spot diameter at Ø = 4mm, pulse repetition rate 2Hz. The micro-craquelure inside the laser spots (A and B) is a result of laser-material interaction. In VSP, the spot diameter is increased by 0.26 mm at 2.5 J/cm<sup>2</sup> compared to the spot at 1.6 J/cm<sup>2</sup> ..... 208

**Figure 5.14** – Low vacuum BSE-SEM micrographs of the SP single pulse dry test areas on aged **Ketone N films**. A: 0.6 J/cm<sup>2</sup>; B and B1: 1.6 J/cm<sup>2</sup>; C and C1: 2.5 J/cm<sup>2</sup>. Spot diameter at Ø = 4mm, pulse repetition rate 2Hz. The view field in micrograph A is 2.49 mm. The micro-craquelure inside the laser spots is a result of irradiation. In SP, the spot diameter at 1.6 J/cm<sup>2</sup> is 0.42 mm smaller compared to the spot at 2.5 J/cm<sup>2</sup> ..... 209

**Figure 5.15** – Low vacuum BSE-SEM micrographs of the DI-W+TW20 pre-wet single pulse laser irradiated test areas in VSP mode on aged **Ketone N films**. A: 0.6 J/cm<sup>2</sup>; B and B1: 2.5 J/cm<sup>2</sup>. Spot diameter at Ø = 4mm, pulse repetition rate 2Hz. The view field in micrographs A and B is 2.49 mm. The craquelure inside

the laser spots is an intensification of the pre-existing cracking on the aged coatings not a result of irradiation and it was observed prior to irradiation and outside the spots ..... 210

**Figure 5.16** – Low vacuum BSE-SEM micrographs of the DI-W+TW20 pre-wet single pulse laser irradiated test areas in SP mode on aged **Ketone N films**. A: 1.6 J/cm<sup>2</sup>; B and B1: 2.5 J/cm<sup>2</sup>. The view field in micrographs A and B is 2.49 mm. The craquelure inside the laser spots is an intensification of the pre-existing cracking on the aged coatings not a result of irradiation and it was observed prior to irradiation and outside the spots ..... 211

**Figure 5.17** – Low vacuum BSE-SEM micrographs of the VSP single pulse dry test areas on aged **MS2A films**. A and A1: 0.6 J/ cm<sup>2</sup>; B and B1: 1.6 J/cm<sup>2</sup>; C and C1: 2.5 J/cm<sup>2</sup>. Spot diameter at Ø = 4mm, pulse repetition rate 2Hz. The micro-craquelure inside the laser spots is partially a result of irradiation and partially an intensification of the pre-existing cracking on the aged coatings (B, B1, C and C1). Lift-off phenomena have been observed on the dry MS2A sample irradiated at 0.6 J/cm<sup>2</sup> (A, A1). In VSP, the spot diameter is increased by 0.17 mm at 1.6 J/cm<sup>2</sup> compared to the spot at 0.6 J/cm<sup>2</sup>, and the difference in diameter remains unchanged at 2.5 J/cm<sup>2</sup> ..... 212

**Figure 5.18** – Low vacuum BSE-SEM micrographs of the SP single pulse dry test areas on aged **MS2A films**. A and A1: 0.6 J/ cm<sup>2</sup>; B and B1: 1.6 J/cm<sup>2</sup>; C and C1: 2.5 J/cm<sup>2</sup>. Spot diameter at Ø = 4mm, pulse repetition rate 2Hz. The micro-craquelure inside the laser spots is partially a result of irradiation (B, B1) and partially an intensification of the pre-existing cracking on the aged coatings (C, C1). Lift-off phenomena have been observed on the dry MS2A sample irradiated at 0.6 J/cm<sup>2</sup> (A, A1). In SP, the spot diameter at 2.5 J/cm<sup>2</sup> is 0.17 mm larger compared to the spots at 0.6 and 1.6 J/cm<sup>2</sup> ..... 213

**Figure 5.19** – Low vacuum BSE-SEM micrographs of the DI-W+TW20 pre-wet single pulse laser irradiated test areas in VSP mode on aged **MS2A films**. A: 0.6 J/cm<sup>2</sup>; B and B1: 1.6 J/cm<sup>2</sup>; C and C1: 2.5 J/cm<sup>2</sup>. The view field in micrograph A is 2.49 mm. The craquelure inside the laser spots is an intensification of the pre-existing cracking on the aged coatings not a result of irradiation and it was observed prior to irradiation and outside the spots. In VSP, the spot diameter at 1.6 J/cm<sup>2</sup> is 0.19 mm smaller compared to the spot at 2.5 J/cm<sup>2</sup> ..... 214

**Figure 5.20** – Low vacuum BSE-SEM micrographs of the DI-W+TW20 pre-wet single pulse laser irradiated test areas in SP mode on aged **MS2A films**. A and A1: 1.6 J/cm<sup>2</sup>; B and B1: 2.5 J/cm<sup>2</sup>. The craquelure inside the laser spots is an intensification of the pre-existing cracking on the aged coatings not a result of irradiation and it was observed prior to irradiation and outside the spots ....  
 ..... 215

**Figure 5.21** – Low vacuum BSE-SEM micrographs of the VSP dry test areas on aged **dammar films** after 3 consecutive laser pulses. A and A1: 0.6 J/cm<sup>2</sup>; B and B1: 1.6 J/cm<sup>2</sup>; C and C1: 2.5 J/cm<sup>2</sup>. Spot diameter at Ø = 4mm, pulse repetition rate 2Hz. The micro-craquelure inside the laser spots at fluences above 1.5 J/cm<sup>2</sup> is a result of the laser irradiation. In VSP, the spot diameter is increased by 0.49 mm at 1.6 J/cm<sup>2</sup> compared to the spot at 0.6 J/cm<sup>2</sup> and then by 0.29 mm more at 2.5 J/cm<sup>2</sup> ..... 216

**Figure 5.22** – Low vacuum BSE-SEM micrographs of the SP dry test areas on aged **dammar films** after 3 consecutive laser pulses. A and A1: 0.6 J/cm<sup>2</sup>; B and B1: 1.6 J/cm<sup>2</sup>; C and C1: 2.5 J/cm<sup>2</sup>. Spot diameter at Ø = 4mm, pulse repetition rate 2Hz. The micro-craquelure inside the laser spots at fluences above 1.5 J/cm<sup>2</sup> is a result of the laser irradiation. In SP, the spot diameter is increased by 0.65 mm at 1.6 J/cm<sup>2</sup> compared to the spot at 0.6 J/cm<sup>2</sup> and then by 0.13 mm more at 2.5 J/cm<sup>2</sup> ..... 217

**Figure 5.23** – Low vacuum BSE-SEM micrographs of the DI-W+TW20 pre-wet laser irradiated test areas in VSP mode on aged **dammar film** after 3 consecutive laser pulses. A and A1: 0.6 J/cm<sup>2</sup>; B and B1: 1.6 J/cm<sup>2</sup>; C and C1: 2.5 J/cm<sup>2</sup>. The craquelure inside the laser spots at fluences above 1.5 J/cm<sup>2</sup> is a result of the laser irradiation. The consecutive irradiations (three pulses at 2 Hz) have caused at 2.5 J/cm<sup>2</sup> a partial removal or shrinkage of the dammar film (C). In VSP, the spot diameter is increased by 0.23 mm at 1.6 J/cm<sup>2</sup> compared to the spot at 0.6 J/cm<sup>2</sup> and then by 0.35 mm at 2.5 J/cm<sup>2</sup> ..... 218

**Figure 5.24** – Low vacuum BSE-SEM micrographs of the DI-W+TW20 pre-wet laser irradiated test areas in SP mode on aged **dammar film** after 3 consecutive laser pulses. A and A1: 0.6 J/cm<sup>2</sup>; B and B1: 1.6 J/cm<sup>2</sup>; C and C1: 2.5 J/cm<sup>2</sup>. The craquelure inside the laser spots at fluences above 1.5 J/cm<sup>2</sup> is a result of the laser irradiation. The consecutive irradiations (three pulses at 2 Hz) have caused

at 2.5 J/cm<sup>2</sup> a partial removal or shrinkage of the dammar film (C). In SP, the spot diameter is increased by 0.65 mm at 1.6 J/cm<sup>2</sup> compared to the spot at 0.6 J/cm<sup>2</sup> and then it remains unchanged at 2.5 J/cm<sup>2</sup> ..... 219

**Figure 5.25** – Low vacuum BSE-SEM micrographs of the VSP dry test areas on aged **Ketone N films** after 3 consecutive laser pulses. A: 0.6 J/ cm<sup>2</sup>; B and B1: 1.6 J/cm<sup>2</sup>; C and C1: 2.5 J/cm<sup>2</sup>. Spot diameter at Ø = 4mm, pulse repetition rate 2Hz. The micro-craquelure inside the laser spots at 0.6 J/cm<sup>2</sup> is a result of laser-material interaction. In VSP, the spot diameter is increased by 0.19 mm at 2.5 J/cm<sup>2</sup> compared to the spot at 1.6 J/cm<sup>2</sup>. At 0.6 J/cm<sup>2</sup>, it proved impossible to detect the external ring of the laser spot ..... 220

**Figure 5.26** – Low vacuum BSE-SEM micrographs of the SP dry test areas on aged **Ketone N films** after 3 consecutive laser pulses. A and A1: 0.6 J/ cm<sup>2</sup>; B and B1: 1.6 J/cm<sup>2</sup>; C and C1: 2.5 J/cm<sup>2</sup>. Spot diameter at Ø = 4mm, pulse repetition rate 2Hz. The view field in micrograph A is 2.49 mm. In SP, the spot diameter is increased by 0.25 mm at 2.5 J/cm<sup>2</sup> compared to the spot at 1.6 J/cm<sup>2</sup>. At 0.6 J/cm<sup>2</sup>, it proved impossible to detect the external ring of the laser spot ..... 221

**Figure 5.27** – Low vacuum BSE-SEM micrographs of the DI-W+TW20 pre-wet laser irradiated test areas in VSP mode on aged **Ketone N film** after 3 consecutive laser pulses. A: 0.6 J/cm<sup>2</sup>; B and B1: 1.6 J/cm<sup>2</sup>; C and C1: 2.5 J/cm<sup>2</sup>. The view field in micrograph A is 2.49 mm. The craquelure inside the laser spots is an intensification of the pre-existing cracking on the aged coatings not a result of irradiation and it was observed prior to irradiation and outside the spots ..... 222

**Figure 5.28** – Low vacuum BSE-SEM micrographs of the DI-W+TW20 pre-wet laser irradiated test areas in SP mode on aged **Ketone N film** after 3 consecutive laser pulses. A and A1: 1.6 J/cm<sup>2</sup>; B and B1: 2.5 J/cm<sup>2</sup>. The craquelure inside the laser spots is an intensification of the pre-existing cracking on the aged coatings not a result of irradiation and it was observed prior to irradiation and outside the spots ..... 223

**Figure 5.29** – Low vacuum BSE-SEM micrographs of the VSP dry test areas on aged **MS2A films** after 3 consecutive laser pulses. A and A1: 0.6 J/ cm<sup>2</sup>; B and B1: 1.6 J/cm<sup>2</sup>; C and C1: 2.5 J/cm<sup>2</sup>. Spot diameter at Ø = 4mm, pulse repetition

rate 2Hz. The micro-craquelure inside the laser spots is a result of irradiation and lift-off phenomena have been observed on the dry MS2A sample irradiated at 0.6 J/cm<sup>2</sup> (A, A1). In VSP, the spot diameter is increased by 0.32 mm at 1.6 J/cm<sup>2</sup> compared to the spot at 0.6 J/cm<sup>2</sup> and then by 0.29 mm more at 2.5 J/cm<sup>2</sup> ..... 224

**Figure 5.30** – Low vacuum BSE-SEM micrographs of the SP dry test areas on aged **MS2A films** after 3 consecutive laser pulses. A and A1: 0.6 J/cm<sup>2</sup>; B and B1: 1.6 J/cm<sup>2</sup>; C and C1: 2.5 J/cm<sup>2</sup>. Spot diameter at Ø = 4mm, pulse repetition rate 2Hz. The micro-craquelure inside the laser spots is partially a result of irradiation (B, B1) and partially an intensification of the pre-existing cracking on the aged coatings (C, C1). Lift-off phenomena have been observed on the dry MS2A sample irradiated at 0.6 J/cm<sup>2</sup> (A, A1). In VSP, the spot diameter is increased by 0.32 mm at 1.6 J/cm<sup>2</sup> compared to the spot at 0.6 J/cm<sup>2</sup> and then by 0.16 mm more at 2.5 J/cm<sup>2</sup> ..... 225

**Figure 5.31** – Low vacuum BSE-SEM micrographs of the DI-W+TW20 pre-wet laser irradiated test areas in VSP mode on aged **MS2A film** after 3 consecutive laser pulses. A and A1: 0.6 J/cm<sup>2</sup>; B and B1: 1.6 J/cm<sup>2</sup>; C and C1: 2.5 J/cm<sup>2</sup>. The craquelure inside the laser spots (A and B) is an intensification of the pre-existing cracking on the aged coatings probably not a result of irradiation. Lift-off phenomena have been observed on the MS2A sample irradiated at 0.6 J/cm<sup>2</sup>. The consecutive irradiations (three pulses at 2 Hz) have caused at 2.5 J/cm<sup>2</sup> a partial removal of the MS2A film (C, C1). In VSP, the spot diameter is increased by 0.33 mm at 1.6 J/cm<sup>2</sup> compared to the spot at 0.6 J/cm<sup>2</sup> and then by 0.14 mm at 2.5 J/cm<sup>2</sup> ..... 226

**Figure 5.32** – Low vacuum BSE-SEM micrographs of the DI-W+TW20 pre-wet laser irradiated test areas in SP mode on aged **MS2A film** after 3 consecutive laser pulses. A and A1: 0.6 J/cm<sup>2</sup>; B and B1: 1.6 J/cm<sup>2</sup>; C and C1: 2.5 J/cm<sup>2</sup>. The craquelure inside the laser spots (A and B) is an intensification of the pre-existing cracking on the aged coatings probably not a result of irradiation. The consecutive irradiations (three pulses at 2 Hz) have caused at 1.5 J/cm<sup>2</sup> a partial shrinkage and warpage of the top layer of the MS2A film (B). In SP, the spot diameter is increased by 0.49 mm at 1.6 J/cm<sup>2</sup> compared to the spot at 0.6 J/cm<sup>2</sup> and then by 0.14 mm at 2.5 J/cm<sup>2</sup> ..... 227

**Figure 5.33** – Ratios of the integrated areas of the –OH/CH and the –C=O/CH bands as acquired by ATR/FT-IR vs fluence of the dry irradiated **dammar films** in VSP ( $\tau_L \approx 100 \mu\text{s}$ ) and SP ( $\tau_L \approx 300 \mu\text{s}$ ) modes after five consecutive laser pulses at 5Hz. The horizontal lines define the corresponding ratios of the dammar films before (dark green solid line) and after ageing (light green solid line). Dotted lines correspond to the experimental error (standard deviation)

..... 231

**Figure 5.34** – Ratios of the integrated areas of the –OH/CH and the –C=O/CH bands as acquired by ATR/ FTIR vs fluence of the DI-W+TW20 pre-wetted irradiated **dammar films** in VSP ( $\tau_L \approx 100 \mu\text{s}$ ) and SP ( $\tau_L \approx 300 \mu\text{s}$ ) modes after five consecutive laser pulses at 5Hz. The horizontal lines define the corresponding ratios of the dammar films before (dark green solid line) and after ageing (light green solid line). Dotted lines correspond to the experimental error (standard deviation)

..... 231

**Figure 5.35** – Ratios of the integrated areas of the –OH/CH and the –C=O/CH bands as acquired by ATR/FT-IR vs fluence of the dry irradiated **Ketone N films** in VSP ( $\tau_L \approx 100 \mu\text{s}$ ) and SP ( $\tau_L \approx 300 \mu\text{s}$ ) modes after five consecutive laser pulses at 5Hz. The horizontal lines define the corresponding ratios of the Ketone N films before (dark green solid line) and after ageing (light green solid line). Dotted lines correspond to the experimental error (standard deviation) .....

232

**Figure 5.36** – Ratios of the integrated areas of the –OH/CH and the –C=O/CH bands as acquired by ATR/ FTIR vs fluence of the DI-W+TW20 pre-wetted irradiated **Ketone N films** in VSP ( $\tau_L \approx 100 \mu\text{s}$ ) and SP ( $\tau_L \approx 300 \mu\text{s}$ ) modes after five consecutive laser pulses at 5Hz. The horizontal lines define the corresponding ratios of the Ketone N films before (dark green solid line) and after ageing (light green solid line). Dotted lines correspond to the experimental error (standard deviation)

232

**Figure 5.37** – Ratios of the integrated areas of the OH/CH and the C = O/CH bands as acquired by ATR/FT-IR vs fluence of the dry irradiated **MS2A films** in VSP ( $\tau_L \approx 100 \mu\text{s}$ ) and SP ( $\tau_L \approx 300 \mu\text{s}$ ) modes after five consecutive laser pulses at 5Hz. The horizontal lines define the corresponding ratios of the MS2A films

before (dark green solid line) and after ageing (light green solid line). Dotted lines correspond to the experimental error (standard deviation) .....	233
<b>Figure 5.38</b> – Ratios of the integrated areas of the OH/CH and the C = O/CH bands as acquired by ATR/ FTIR vs fluence of the DI-W+TW20 pre-wetted irradiated MS2A films in VSP ( $\tau_L \approx 100 \mu\text{s}$ ) and SP ( $\tau_L \approx 300 \mu\text{s}$ ) modes after five consecutive laser pulses at 5Hz. The horizontal lines define the corresponding ratios of the MS2A films before (dark green solid line) and after ageing (light green solid line). Dotted lines correspond to the experimental error (standard deviation) .....	233
<b>Figure 6.1</b> – The nineteenth century oil painting “Hunting Scene” (95 × 54 cm) belonging to the collection of paintings of the Department of Arts at Northumbria University (Newcastle upon Tyne) .....	237
<b>Figure 6.2</b> – Data collected by fixing the R11 handpiece at three different working distances (WD): 2, 5 and 10 cm from a photosensitive black paper substrate and three output laser energies: 35, 106 and 170 mJ as set in a Fotona XS Dynamis laser unit. The nominated fluences: 0.5, 1.5 and 2.4 J/cm <sup>2</sup> , and the beam diameter at 3 mm were set and shown in the laser unit display. The repetition rate was set at 5Hz to allow a single pulse to hit the paper substrate using a shutter. The spatial laser beam profiles mapped directly on the photosensitive paper (A) and demonstrate that at 5 cm WD and 106 mJ, the 1.5 J/cm <sup>2</sup> actual and nominated fluence coincides, as shown when fluence versus WD is plotted (B). Further information is provided in Chapter 5 .....	241
<b>Figure 6.3</b> – Detail of one test (one scan, 2.1 J/cm <sup>2</sup> ). At top left the dry irradiated area is shown, followed by other irradiated areas pre-wetted with the following solutions: deionised water (DI-W), 1% v/v Tween20 in DI-W, 50% v/v Industrial Methylated Spirit (IMS) in DI-W, 50% v/v IMS in White Spirit (WS) and pure White Spirit. All the laser irradiated areas were 15x15 mm .....	242
<b>Figure 6.4</b> – XpeCAM X01 camera (XpectralTEK) .....	246
<b>Figure 6.5</b> – ATR/FT-IR spectra of the triterpenoid varnish sampled on the nineteenth century painting by scalpel. The control dammar resin spectrum is shown in the inlet .....	248

- Figure 6.6** – The Py-TMAH-GC/MS chromatograph that indicates that the varnish of the painting is dammar. The MS spectra are shown in Appendix C ..... **249**
- Figure 6.7** – The nineteenth century oil painting “Hunting Scene” (95 × 54 cm) with the Er:YAG laser test areas (A); Laser cleaning in progress (B) - also published in Chillè, Papadakis and Theodorakopoulos (2020) ..... **251**
- Figure 6.8** – UV induced fluorescence of resin fragments collected on glass coverslips at different fluences ..... **253**
- Figure 6.9** – Micrographs of the dry irradiated test areas with a satisfactory outcome. A: One laser scanned area at nominated fluence 2 J/cm<sup>2</sup> and B: two laser scanned area at nominated fluence 0.7 J/cm<sup>2</sup>; I) visible light (VL); II) UV induced fluorescence; III) VL stereomicrograph. All the laser irradiated areas studied were 15x15 mm ..... **253**
- Figure 6.10** – Micrographs of the dry irradiated test areas where the brown hue was visually detected. A: One laser scanned area at nominated fluence 2.1 J/cm<sup>2</sup> and B: two laser scanned area at nominated fluence 1 J/cm<sup>2</sup>; I) visible light (VL); II) UV induced fluorescence; III) VL stereomicrograph. All the laser irradiated areas studied were 15x15 mm ..... **254**
- Figure 6.11** – Micrographs of the DI-W + TW20 prewetted irradiated test areas with a satisfactory outcome. A: One laser scanned area at nominated fluence 2.4 J/cm<sup>2</sup>, B: two laser scanned area at nominated fluence 2.3 J/cm<sup>2</sup> and C: three laser scanned area at nominated fluence 2.1 J/cm<sup>2</sup>; I) visible light (VL); II) UV induced fluorescence; III) VL stereomicrograph. All the laser irradiated areas studied were 15 × 15 mm ..... **255**
- Figure 6.12** - Micrographs of the 50% IMS+WS prewetted irradiated test areas. A: One laser scanned area at nominated fluence 2 J/cm<sup>2</sup>, B: two laser scanned area at nominated fluence 1 J/cm<sup>2</sup> and C: three laser scanned area at nominated fluence 1 J/cm<sup>2</sup>; I) visible light (VL); II) UV induced fluorescence; III) VL stereomicrograph. All the laser irradiated areas studied were 15 × 15 mm .  
..... **256**
- Figure 6.13** – UV induced fluorescence of resin fragments collected on glass coverslips upon dry (A) and pre-wet (B) laser irradiation at 1.5 J/cm<sup>2</sup>. The glass coverslips were 15 × 15 mm ..... **257**

- Figure 6.14** – Gloss related impact due to laser-irradiation ( $\Delta$ GRF) as a function of nominated fluences. A good correlation of this factor with the disruption of the varnish at these fluences as visually assessed for the dry irradiation tests is observed. In the case of the wet irradiation tests this correlation is less representative, perhaps due to the significantly less material that escaped the irradiated varnish ..... **258**
- Figure 6.15** – Gloss related impact due to laser-irradiation ( $\Delta$ GRF) as a function of nominated fluences. A good correlation between the dry irradiated areas and the same areas irradiated with WS ..... **259**
- Figure 6.16** – The registered and calibrated spectral images of the Er:YAG laser scans at  $1.55 \text{ J/cm}^2$  ranging from 360 - 650 nm. The data used are the first and the third  $15 \times 15 \text{ mm}$  spots in the first line of each spectral image, corresponding to the dry and pre-wetted tests. Spectral clustering has been carried out inside the spots on the first 11 spectral images in the 360-550 nm range. As shown the interference of the reflectance from the underlying paint layer to the data recorded in the clusterisation maps was negligible. Even at longer wavelengths up to 650 nm the background contribution was negligible ..... **263**
- Figure 6.17** – Multispectral Imaging clusterisation maps of one (A) and two (B) laser scanned areas at nominated fluence  $1.5 \text{ J/cm}^2$ . The sequence of the cleaning test areas is the same as in Figure 6.3. All the laser irradiated areas shown are  $15 \times 15 \text{ mm}$  ..... **264**
- Figure 6.18** – Ratios of average reflectance spectra of red and green clusters, representing reflectance differences due to remaining varnish thickness as reported elsewhere (Papadakis *et al.*, 2011; Zacharopoulos *et al.*, 2018) .... **265**
- Figure 6.19** – A % clustered reflection monitored by the spectral imaging clusterisation maps as a function of fluence for the two laser scan applications in the dry and pre-wet tests. The gradual reduction of the varnish from the early stage (green line) to the deeper thinning (red line) was captured by spectral imaging. The black line corresponds to the remaining varnish within the irradiated spots ..... **266**

- Figure 6.20** – A % clustered reflection monitored by the spectral imaging clusterisation maps as a function of fluence for a single laser scan application in the dry and pre-wet tests using WS ..... 266
- Figure 6.21** – ATR/FT-IR spectra of the resin fragments collected on the glass coverslips, acquired at nominated fluence 1.5 and 2.1 J/cm<sup>2</sup> and of the untreated varnish (control). ATR/FTIR spectra of: the dry irradiated area after two laser scans (A); and the pre-wetted area after three laser scans (B). The spectra show the gradual reduction in intensity of the C=O stretching group by increasing fluence. Baseline points ranging from 3700 to 3100, 3100-2700, and 1900-1550 cm<sup>-1</sup> ..... 272
- Figure 6.22** – Ratios of the integrated areas of the –OH/CH and the –C=O/CH bands as acquired by ATR/FT-IR vs fluence of the dry irradiated varnish films collected on the coverslips in VSP ( $\tau_L \approx 100 \mu s$ ) mode. The horizontal lines define the corresponding ratios of the varnish samples that have been not irradiated (dark green solid line). The dotted lines correspond with the area of the standard deviation ..... 273
- Figure 6.23** – Ratios of the integrated areas of the –OH/CH and the –C=O/CH bands as acquired by ATR/ FTIR vs fluence of the DI-W+TW20 pre-wetted irradiated varnish films collected on the coverslips in VSP ( $\tau_L \approx 100 \mu s$ ) mode. The horizontal lines define the corresponding ratios of the varnish samples that have been not irradiated (dark green solid line). The dotted lines correspond with the area of the standard deviation ..... 273
- Figure 6.24** – Ratios of the integrated areas of the –OH/CH and the –C=O/CH bands as acquired by ATR/ FTIR vs fluence of the White Spirit (WS) pre-wetted irradiated varnish films collected on the coverslips in VSP ( $\tau_L \approx 100 \mu s$ ) mode. The horizontal lines define the corresponding ratios of the varnish samples that have been not irradiated (dark green solid line). The dotted lines correspond with the area of the standard deviation ..... 274
- Figure 6.25** – Ratios of the integrated areas of the –OH/CH and the –C=O/CH bands as acquired by ATR/ FTIR vs fluence of the IMS+WS pre-wetted irradiated varnish films collected on the coverslips in VSP ( $\tau_L \approx 100 \mu s$ ) mode. The horizontal lines define the corresponding ratios of the varnish samples that

have been not irradiated (dark green solid line). The dotted lines correspond with the area of the standard deviation ..... 274

---

<b>Figure A1</b> – Specific heat capacity ( $C_p$ ) ( $J/g \cdot ^\circ C$ ) vs temperature ( $^\circ C$ ) obtained from DSC (LAB SYS-DSC 8500 Perkin Elmer) for all the raw unaged resins. The $C_p$ values and the temperature are listed in Table 3.9 (see section 3.5.7) .....	<b>361</b>
<b>Figure A2</b> – DSC curve (LAB SYS-DSC 8500 Perkin Elmer) of raw unaged dammar, Ketone N, MS2A and Paraloid B67 resins .....	<b>362</b>
<b>Figure B1</b> – Transmission spectra of dammar film .....	<b>364</b>
<b>Figure B2</b> – Transmission spectra of Ketone N film .....	<b>364</b>
<b>Figure B3</b> – Transmission spectra of MS2A film .....	<b>365</b>
<b>Figure B4</b> – Transmission spectra of Paraloid B67 film .....	<b>365</b>
<b>Figure B5</b> – Reflectance spectra of the aged dammar varnish .....	<b>366</b>
<b>Figure B6</b> – Reflectance spectra of the aged Ketone N varnish .....	<b>366</b>
<b>Figure B7</b> – Reflectance spectra of the aged MS2A varnish .....	<b>367</b>
<b>Figure B8</b> – Reflectance spectra of the aged Paraloid B67 varnish .....	<b>367</b>
<b>Figure B9</b> – FLIR T620bx IR thermal camera .....	<b>369</b>
<b>Figure B10</b> – Experimental set-up using the FLIR T620bx IR thermal camera, a point type K thermocouple and a thermoelectric solid-state Heat/Cool plate to check the reliability of the thermal camera in pre-set temperature values ...	<b>370</b>
<b>Figure B11</b> – Visual and IR images showing the recorded temperature registered by the thermal camera during the tests .....	<b>370</b>
<b>Figure B12</b> – Representation of the heat-wave propagation inside the <b>dammar film</b> , in VSP mode, at different times as a function of depth (A and C) and the temperature rise evolution at various depth as a function of time (B and D) .....	<b>373</b>
<b>Figure B13</b> – Representation of the heat-wave propagation inside the <b>dammar film</b> , in SP mode, at different times as a function of depth (A and C) and the	

temperature rise evolution at various depth as a function of time (B and D)	376
.....	
<b>Figure B14</b> – Representation of the heat-wave propagation inside the <b>Ketone N film</b> , in VSP mode, at different times as a function of depth (A and C) and the temperature rise evolution at various depth as a function of time (B and D)	379
.....	
<b>Figure B15</b> – Representation of the heat-wave propagation inside the <b>Ketone N film</b> , in SP mode, at different times as a function of depth (A and C) and the temperature rise evolution at various depth as a function of time (B and D)	384
.....	
<b>Figure B16</b> – Representation of the heat-wave propagation inside the <b>MS2A film</b> , in VSP mode, at different times as a function of depth (A and C) and the temperature rise evolution at various depth as a function of time (B and D)	389
.....	
<b>Figure B17</b> - Representation of the heat-wave propagation inside the <b>MS2A film</b> , in SP mode, at different times as a function of depth (A and C) and the temperature rise evolution at various depth as a function of time (B and D)	394
.....	
<b>Figure B18</b> – 2D simulation of the heat diffusion inside the dammar film in VSP mode and temperature distribution by cross-section of varnish film + glass slide. Fluences of 1 J/cm <sup>2</sup> , and thermal conductivity (k) between 0.21W/m·K and 0.021W/m·K	401
.....	
<b>Figure B19</b> – 2D simulation of the heat diffusion inside the dammar film in VSP mode and temperature distribution by cross-section of varnish film + glass slide. Fluences of 1.5 J/cm <sup>2</sup> , and thermal conductivity (k) between 0.21W/m·K and 0.021W/m·K	401
.....	
<b>Figure B20</b> – 2D simulation of the heat diffusion inside the dammar film in VSP mode and temperature distribution by cross-section of varnish film + glass slide. Fluences of 2.1 J/cm <sup>2</sup> , and thermal conductivity (k) between 0.21W/m·K and 0.021W/m·K	402
.....	

<b>Figure B21</b> – 2D simulation of the heat diffusion inside the dammar film in VSP mode and temperature distribution by cross-section of varnish film + glass slide. Fluences of 2.4 J/cm <sup>2</sup> , and thermal conductivity (k) between 0.21W/m·K and 0.021W/m·K .....	<b>402</b>
<b>Figure B22</b> – 2D simulation of the heat diffusion inside the dammar film in SP mode and temperature distribution by cross-section of varnish film + glass slide. Fluences of 1 J/cm <sup>2</sup> , and thermal conductivity (k) between 0.21W/m·K and 0.021W/m·K .....	<b>403</b>
<b>Figure B23</b> – 2D simulation of the heat diffusion inside the dammar film in SP mode and temperature distribution by cross-section of varnish film + glass slide. Fluences of 1.5 J/cm <sup>2</sup> , and thermal conductivity (k) between 0.21W/m·K and 0.021W/m·K .....	<b>403</b>
<b>Figure B24</b> – 2D simulation of the heat diffusion inside the dammar film in SP mode and temperature distribution by cross-section of varnish film + glass slide. Fluences of 2.1 J/cm <sup>2</sup> , and thermal conductivity (k) between 0.21W/m·K and 0.021W/m·K .....	<b>404</b>
<b>Figure B25</b> – 2D simulation of the heat diffusion inside the dammar film in SP mode and temperature distribution by cross-section of varnish film + glass slide. Fluences of 2.4 J/cm <sup>2</sup> , and thermal conductivity (k) between 0.21W/m·K and 0.021W/m·K .....	<b>404</b>
<b>Figure B26</b> – 2D simulation of the heat diffusion inside the Ketone N film in VSP mode and temperature distribution by cross-section of varnish film + glass slide. Fluences of 1 J/cm <sup>2</sup> and thermal conductivity (k) of 0.22 W/m·K .....	<b>405</b>
<b>Figure B27</b> – 2D simulation of the heat diffusion inside the Ketone N film in VSP mode and temperature distribution by cross-section of varnish film + glass slide. Fluences of 1 J/cm <sup>2</sup> and thermal conductivity (k) of 0.022 W/m·K .....	<b>405</b>
<b>Figure B28</b> – 2D simulation of the heat diffusion inside the Ketone N film in VSP mode and temperature distribution by cross-section of varnish film + glass slide. Fluences of 1.5 J/cm <sup>2</sup> and thermal conductivity (k) of 0.22 W/m·K .....	<b>406</b>

- Figure B29** – 2D simulation of the heat diffusion inside the Ketone N film in VSP mode and temperature distribution by cross-section of varnish film + glass slide. Fluences of 1.5 J/cm<sup>2</sup> and thermal conductivity (k) of 0.022 W/m·K ..... **406**
- Figure B30** – 2D simulation of the heat diffusion inside the Ketone N film in VSP mode and temperature distribution by cross-section of varnish film + glass slide. Fluences of 2.1 J/cm<sup>2</sup> and thermal conductivity (k) of 0.22 W/m·K ..... **407**
- Figure B31** – 2D simulation of the heat diffusion inside the Ketone N film in VSP mode and temperature distribution by cross-section of varnish film + glass slide. Fluences of 2.1 J/cm<sup>2</sup> and thermal conductivity (k) of 0.022 W/m·K ..... **407**
- Figure B32** – 2D simulation of the heat diffusion inside the Ketone N film in VSP mode and temperature distribution by cross-section of varnish film + glass slide. Fluences of 2.4 J/cm<sup>2</sup> and thermal conductivity (k) of 0.22 W/m·K ..... **408**
- Figure B33** – 2D simulation of the heat diffusion inside the Ketone N film in VSP mode and temperature distribution by cross-section of varnish film + glass slide. Fluences of 2.4 J/cm<sup>2</sup> and thermal conductivity (k) of 0.022 W/m·K ..... **408**
- Figure B34** – 2D simulation of the heat diffusion inside the Ketone N film in SP mode and temperature distribution by cross-section of varnish film + glass slide. Fluences of 1 J/cm<sup>2</sup> and thermal conductivity (k) of 0.22 W/m·K ..... **409**
- Figure B35** – 2D simulation of the heat diffusion inside the Ketone N film in SP mode and temperature distribution by cross-section of varnish film + glass slide. Fluences of 1 J/cm<sup>2</sup> and thermal conductivity (k) of 0.022 W/m·K ..... **409**
- Figure B36** – 2D simulation of the heat diffusion inside the Ketone N film in SP mode and temperature distribution by cross-section of varnish film + glass slide. Fluences of 1.5 J/cm<sup>2</sup> and thermal conductivity (k) of 0.22 W/m·K ..... **410**
- Figure B37** – 2D simulation of the heat diffusion inside the Ketone N film in SP mode and temperature distribution by cross-section of varnish film + glass slide. Fluences of 1.5 J/cm<sup>2</sup> and thermal conductivity (k) of 0.022 W/m·K ..... **410**
- Figure B38** – 2D simulation of the heat diffusion inside the Ketone N film in SP mode and temperature distribution by cross-section of varnish film + glass slide. Fluences of 2.1 J/cm<sup>2</sup> and thermal conductivity (k) of 0.22 W/m·K ..... **411**

- Figure B39** – 2D simulation of the heat diffusion inside the Ketone N film in SP mode and temperature distribution by cross-section of varnish film + glass slide. Fluences of 2.1 J/cm<sup>2</sup> and thermal conductivity (k) of 0.022 W/m·K ..... **411**
- Figure B40** – 2D simulation of the heat diffusion inside the Ketone N film in SP mode and temperature distribution by cross-section of varnish film + glass slide. Fluences of 2.4 J/cm<sup>2</sup> and thermal conductivity (k) of 0.22 W/m·K ..... **412**
- Figure B41** – 2D simulation of the heat diffusion inside the Ketone N film in SP mode and temperature distribution by cross-section of varnish film + glass slide. Fluences of 2.4 J/cm<sup>2</sup> and thermal conductivity (k) of 0.022 W/m·K ..... **412**
- Figure B42** – 2D simulation of the heat diffusion inside the MS2A film in VSP mode and temperature distribution by cross-section of varnish film + glass slide. Fluences of 1 J/cm<sup>2</sup> and thermal conductivity (k) of 0.19 W/m·K ..... **413**
- Figure B43** – 2D simulation of the heat diffusion inside the MS2A film in VSP mode and temperature distribution by cross-section of varnish film + glass slide. Fluences of 1 J/cm<sup>2</sup> and thermal conductivity (k) of 0.019 W/m·K ..... **413**
- Figure B44** – 2D simulation of the heat diffusion inside the MS2A film in VSP mode and temperature distribution by cross-section of varnish film + glass slide. Fluences of 1.5 J/cm<sup>2</sup> and thermal conductivity (k) of 0.19 W/m·K ..... **414**
- Figure B45** – 2D simulation of the heat diffusion inside the MS2A film in VSP mode and temperature distribution by cross-section of varnish film + glass slide. Fluences of 1.5 J/cm<sup>2</sup> and thermal conductivity (k) of 0.019 W/m·K ..... **414**
- Figure B46** – 2D simulation of the heat diffusion inside the MS2A film in VSP mode and temperature distribution by cross-section of varnish film + glass slide. Fluences of 2.1 J/cm<sup>2</sup> and thermal conductivity (k) of 0.19 W/m·K ..... **415**
- Figure B47** – 2D simulation of the heat diffusion inside the MS2A film in VSP mode and temperature distribution by cross-section of varnish film + glass slide. Fluences of 2.1 J/cm<sup>2</sup> and thermal conductivity (k) of 0.019 W/m·K ..... **415**
- Figure B48** – 2D simulation of the heat diffusion inside the MS2A film in VSP mode and temperature distribution by cross-section of varnish film + glass slide. Fluences of 2.4 J/cm<sup>2</sup> and thermal conductivity (k) of 0.19 W/m·K ..... **416**

<b>Figure B49</b> – 2D simulation of the heat diffusion inside the MS2A film in VSP mode and temperature distribution by cross-section of varnish film + glass slide. Fluences of 2.4 J/cm <sup>2</sup> and thermal conductivity (k) of 0.019 W/m·K .....	<b>416</b>
<b>Figure B50</b> – 2D simulation of the heat diffusion inside the MS2A film in SP mode and temperature distribution by cross-section of varnish film + glass slide. Fluences of 1 J/cm <sup>2</sup> and thermal conductivity (k) of 0.19 W/m·K .....	<b>417</b>
<b>Figure B51</b> – 2D simulation of the heat diffusion inside the MS2A film in SP mode and temperature distribution by cross-section of varnish film + glass slide. Fluences of 1 J/cm <sup>2</sup> and thermal conductivity (k) of 0.019 W/m·K .....	<b>417</b>
<b>Figure B52</b> – 2D simulation of the heat diffusion inside the MS2A film in SP mode and temperature distribution by cross-section of varnish film + glass slide. Fluences of 1.5 J/cm <sup>2</sup> and thermal conductivity (k) of 0.19 W/m·K .....	<b>418</b>
<b>Figure B53</b> – 2D simulation of the heat diffusion inside the MS2A film in SP mode and temperature distribution by cross-section of varnish film + glass slide. Fluences of 1.5 J/cm <sup>2</sup> and thermal conductivity (k) of 0.019 W/m·K .....	<b>418</b>
<b>Figure B54</b> – 2D simulation of the heat diffusion inside the MS2A film in SP mode and temperature distribution by cross-section of varnish film + glass slide. Fluences of 2.1 J/cm <sup>2</sup> and thermal conductivity (k) of 0.19 W/m·K .....	<b>419</b>
<b>Figure B55</b> – 2D simulation of the heat diffusion inside the MS2A film in SP mode and temperature distribution by cross-section of varnish film + glass slide. Fluences of 2.1 J/cm <sup>2</sup> and thermal conductivity (k) of 0.019 W/m·K .....	<b>419</b>
<b>Figure B56</b> – 2D simulation of the heat diffusion inside the MS2A film in SP mode and temperature distribution by cross-section of varnish film + glass slide. Fluences of 2.4 J/cm <sup>2</sup> and thermal conductivity (k) of 0.19 W/m·K .....	<b>420</b>
<b>Figure B57</b> – 2D simulation of the heat diffusion inside the MS2A film in SP mode and temperature distribution by cross-section of varnish film + glass slide. Fluences of 2.4 J/cm <sup>2</sup> and thermal conductivity (k) of 0.019 W/m·K .....	<b>420</b>
<b>Figure C1</b> – Py-TMAH-GC/MS of the varnish painting at 45.3 min. Characteristic m/z 109, 205 and 424 due to methylated dammaradienone and its derivatisation products .....	<b>424</b>

<b>Figure C2</b> – Py-TMAH-GC/MS of the varnish painting at 46.3 min. Characteristic m/z 109, 207 and 426 due to methylated dammaradienol and its derivatisation products .....	<b>424</b>
<b>Figure C3</b> – Py-TMAH-GC/MS of the varnish painting at 49.5 min. Characteristic m/z 109, 454 and 472 due to methylated dammarenolic acid and its derivatisation products .....	<b>424</b>
<b>Figure C4</b> – Py-TMAH-GC/MS of the varnish painting at 53 min. Characteristic m/z 133, 189, 203, 262, 408, and 468 due to methylated oleanonic acid and its derivatisation products .....	<b>424</b>
<b>Figure C5</b> – Py-TMAH-GC/MS of the varnish painting at 54 min. Characteristic m/z 109, 205, 424 and 442 due to methylated hydroxydammarenone (3-oxo-dammara-20,24-diene) and its derivatisation products .....	<b>425</b>
<b>Figure C6</b> – Py-TMAH-GC/MS of the varnish painting at 55.5 min. Characteristic m/z 189, 203, 232 and 409 due to methylated oleanonic aldehyde and its derivatisation products .....	<b>425</b>
<b>Figure C7</b> – Py-TMAH-GC/MS of the varnish painting at 55.6 min. Characteristic m/z 133, 203, 262, 409 and 468 due to methylated ursonic acid and its derivatisation products .....	<b>425</b>
<b>Figure C8</b> – Py-TMAH-GC/MS of the varnish painting at 56.4 min. Characteristic m/z 133, 189, 203, 232, 409 and 438 due to methylated ursonic aldehyde and its derivatization products .....	<b>425</b>
<b>Figure C9</b> – UV induced fluorescence micrographs of the irradiated test areas (A, B, C) and Multispectral Imaging clusterisation maps (B1 and C1) of one (A), two (B and B1) and three (C and C1) laser scanned areas at ‘ <i>nominated fluence</i> ’ 0.6 J/cm <sup>2</sup> .....	<b>426</b>
<b>Figure C10</b> – UV induced fluorescence micrographs of the irradiated test areas (A, B, C) and Multispectral Imaging clusterisation maps (B1 and C1) of one (A), two (B and B1) and three (C and C1) laser scanned areas at ‘ <i>nominated fluence</i> ’ 0.7 J/cm <sup>2</sup> .....	<b>429</b>
<b>Figure C11</b> – UV induced fluorescence micrographs of the irradiated test areas (A, B, C) and Multispectral Imaging clusterisation maps (B1 and C1) of one (A),	

two (B and B1) and three (C and C1) laser scanned areas at ‘ <i>nominated fluence</i> ’ 1 J/cm <sup>2</sup> .....	432
<b>Figure C12</b> – UV induced fluorescence micrographs of the irradiated test areas (A, B, C) and Multispectral Imaging clusterisation maps (A1 and C1) of one (A and A1), two (B and B1) and three (C and C1) laser scanned areas at ‘ <i>nominated fluence</i> ’ 1.5 J/cm <sup>2</sup> .....	435
<b>Figure C13</b> – UV induced fluorescence micrographs of the irradiated test areas (A, B, C) and Multispectral Imaging clusterisation maps (A1 and C1) of one (A and A1), two (B and B1) and three (C and C1) laser scanned areas at ‘ <i>nominated fluence</i> ’ 2 J/cm <sup>2</sup> .....	438
<b>Figure C14</b> – UV induced fluorescence micrographs of the irradiated test areas (A, B, C) and Multispectral Imaging clusterisation maps (A1 and C1) of one (A and A1), two (B and B1) and three (C and C1) laser scanned areas at ‘ <i>nominated fluence</i> ’ 2.1 J/cm <sup>2</sup> .....	441
<b>Figure C15</b> – UV induced fluorescence micrographs of the irradiated test areas (A, B) and Multispectral Imaging clusterisation maps (A1 and B1) of one (A and A1) and two (B and B1) laser scanned areas at ‘ <i>nominated fluence</i> ’ 2.3 J/cm <sup>2</sup> .....	444
<b>Figure C16</b> – UV induced fluorescence micrographs of the irradiated test areas (A, B) and Multispectral Imaging clusterisation maps (A1 and B1) of one (A and A1) and two (B and B1) laser scanned areas at ‘ <i>nominated fluence</i> ’ 2.4 J/cm <sup>2</sup> .....	446
<b>Figure C17</b> – Ratios of the integrated areas of the –OH/CH and the –C=O/CH bands as acquired by ATR/FT-IR vs fluence of the dry irradiated varnish films collected on the coverslips in VSP ( $\tau_L \approx 100 \mu s$ ) mode .....	448
<b>Figure C18</b> – Ratios of the integrated areas of the –OH/CH and the –C=O/CH bands as acquired by ATR/ FTIR vs fluence of the White Spirit (WS) pre-wetted irradiated varnish films collected on the coverslips in VSP ( $\tau_L \approx 100 \mu s$ ) mode .....	448

- Figure C19** – Ratios of the integrated areas of the –OH/CH and the –C=O/CH bands as acquired by ATR/ FTIR vs fluence of the DI-W pre-wetted irradiated varnish films collected on the coverslips in VSP ( $\tau_L \approx 100 \mu\text{s}$ ) mode ..... **449**
- Figure C20** – Ratios of the integrated areas of the –OH/CH and the –C=O/CH bands as acquired by ATR/ FTIR vs fluence of the DI-W+TW20 pre-wetted irradiated varnish films collected on the coverslips in VSP ( $\tau_L \approx 100 \mu\text{s}$ ) mode ..... **449**
- Figure C21** – Ratios of the integrated areas of the –OH/CH and the –C=O/CH bands as acquired by ATR/ FTIR vs fluence of the IMS+DI-W pre-wetted irradiated varnish films collected on the coverslips in VSP ( $\tau_L \approx 100 \mu\text{s}$ ) mode ..... **450**
- Figure C22** – Ratios of the integrated areas of the –OH/CH and the –C=O/CH bands as acquired by ATR/ FTIR vs fluence of the IMS+WS pre-wetted irradiated varnish films collected on the coverslips in VSP ( $\tau_L \approx 100 \mu\text{s}$ ) mode ..... **450**



## List of Tables

<b>Table 3.1</b> – List of the selected varnishes together with the solvents used for their preparation and the varnish solution concentration in weight % .....	<b>80</b>
<b>Table 3.2</b> – List of the selected varnishes with the weight used to carry out the DSC analysis with the Shimadzu DSC-50 thermal analyser .....	<b>89</b>
<b>Table 3.3</b> – List of the selected varnishes and sapphire reference together with the weight used to carry out the DSC analysis with the LAB SYS-DSC 8500 Perkin Elmer .....	<b>90</b>
<b>Table 3.4</b> – Mean thickness and standard deviation ( $\sigma$ ) values of the aged varnish samples .....	<b>93</b>
<b>Table 3.5</b> – Mean contact angle and standard deviation ( $\sigma$ ) values obtained using one 2 $\mu$ L droplet of DI-W+TW20 solution deposited on the surface of each aged varnish film. Values were obtained by fitting the image data with the ImageJ contact angle plugin .....	<b>94</b>
<b>Table 3.6</b> – Density of the powder unaged raw resins .....	<b>96</b>
<b>Table 3.7</b> – Data obtained from the thermogravimetric analysis (TGA) for the unaged resins .....	<b>99</b>
<b>Table 3.8</b> – Glass transition data of the selected unaged raw resins obtained by DSC analysis. The start ( $T_i$ ) and end ( $T_f$ ) points of the regression lines and the Tg points of the raw resins are demonstrated .....	<b>104</b>
<b>Table 3.9</b> – Specific heat capacities ( $C_p$ ) of the unaged raw resins between 20-210 $^{\circ}$ C obtained by DSC .....	<b>105</b>
<b>Table 3.10</b> – Wavenumber values ( $\text{cm}^{-1}$ ) corresponding to the maxima of the IR absorbance bands identified in the aged mock-ups studied and their assignment .....	<b>110</b>

<b>Table 4.1</b> – Dissociation energies of the most common single and double bonds of organic molecules (1 eV=1.6x10 <sup>-19</sup> J) (Cooper, 1998, p. 41; Ciofini, 2014, p. 41) .....	<b>117</b>
<b>Table 4.2</b> – Parameters required to define the thermal modelling of all the varnishes selected during Er:YAG laser treatment. The thermal diffusivity (D)* was taken from Fotakis <i>et al.</i> (2007, p. 36) .....	<b>143</b>
<b>Table 4.3</b> – % reflection, % transmission, absorption coefficient ( $\alpha$ ) and optical penetration depth ( $\delta$ ) required to define the thermal modelling of varnish films .....	<b>151</b>
<b>Table 4.4</b> – % reflection obtained using the Fresnel eq. (Eq. 4.21) .....	<b>152</b>
<b>Table 4.5</b> – The Er:YAG laser energy ( $E_{inc}$ ) measured using the QE25ELP-H-MB-DO Pyroelectric Detector for each fluence employed for this study .....	<b>152</b>
<b>Table 4.6</b> – %Transmission (%T) of an uncoated glass slide for each fluence employed for this study .....	<b>152</b>
<b>Table 4.7</b> – The transmission profile of the <b>dammar film</b> for a single-pulse laser has been determined by using the % transmission (%T) as a function of the fluence employed in this study .....	<b>156</b>
<b>Table 4.8</b> – The transmission profile of the <b>Ketone N film</b> for a single-pulse laser has been determined by using the % transmission (%T) as a function of the fluence employed in this study .....	<b>156</b>
<b>Table 4.9</b> – The transmission profile of the <b>MS2A film</b> for a single-pulse laser has been determined by using the % transmission (%T) as a function of the fluence employed in this study .....	<b>157</b>
<b>Table 4.10</b> – The transmission profile of the <b>Paraloid B67 film</b> for a single-pulse laser has been determined by using the % transmission (%T) as a function of the fluence employed in this study .....	<b>157</b>
<b>Table 4.11</b> – Maximum effect of temperature variation recorded by using the FLIR thermal camera and the mean maximum heat impact ( $\Delta T_{mean}$ ) on dry and pre-wet <b>dammar varnish</b> , according to Eq. 4.11. In bold are highlighted the temperature at which the thermal camera reached its maximum acquisition temperature value (160 °C) and the * indicates a plateau in the heat	

measurements. The beam was delivered perpendicularly to the varnish surface with a 20 cm working distance, emissivity ( $\epsilon$ ) of the varnish of 0.93 and laser  $\varnothing$  of 3 mm ..... 159

**Table 4.12** – Maximum effect of temperature variation recorded by using the FLIR thermal camera and the mean maximum heat impact ( $\Delta T_{\text{mean}}$ ) on dry and pre-wet **Ketone N varnish**, according to Eq. 4.11. In bold are highlighted the temperature at which the thermal camera reached its maximum acquisition temperature value (160 °C) and the \* indicates a plateau in the heat measurements. The beam was delivered perpendicularly to the varnish surface with a 20 cm working distance, emissivity ( $\epsilon$ ) of the varnish of 0.93 and laser  $\varnothing$  of 3 mm ..... 160

**Table 4.13** – Maximum effect of temperature variation recorded by using the FLIR thermal camera and the mean maximum heat impact ( $\Delta T_{\text{mean}}$ ) on dry and pre-wet **MS2A varnish**, according to Eq. 4.11. In bold are highlighted the temperature at which the thermal camera reached its maximum acquisition temperature value (160 °C). The beam was delivered perpendicularly to the varnish surface with a 20 cm working distance, emissivity ( $\epsilon$ ) of the varnish of 0.93 and laser  $\varnothing$  of 3 mm ..... 160

**Table 4.14** – Maximum effect of temperature variation recorded by using the FLIR thermal camera and the mean maximum heat impact ( $\Delta T_{\text{mean}}$ ) on dry and pre-wet **Paraloid B67 varnish**, according to Eq. 4.11. The \* indicates a plateau in the heat measurements. The beam was delivered perpendicularly to the varnish surface with a 20 cm working distance, emissivity ( $\epsilon$ ) of the varnish of 0.93 and laser  $\varnothing$  of 3 mm ..... 161

**Table 4.15** – Thermal conductivity (k) varnishes ..... 162

**Table 4.16** – Estimated temperature ( $z = l_{\text{th}}$ ) using Eq. 4.13 of the heat distribution inside the **dammar** layer following an Er:YAG laser pulse at VSP ( $\tau_L \approx 100 \mu\text{s}$ ) and SP ( $\tau_L \approx 300 \mu\text{s}$ ) modes ..... 164

**Table 4.17** – Estimated temperature ( $z = l_{\text{th}}$ ) using Eq. 4.13 of the heat distribution inside the **Ketone N** layer following an Er:YAG laser pulse at VSP ( $\tau_L \approx 100 \mu\text{s}$ ) and SP ( $\tau_L \approx 300 \mu\text{s}$ ) modes ..... 164

<b>Table 4.18</b> – Estimated temperature ( $z = l_{th}$ ) using Eq. 4.13 of the heat distribution inside the <b>MS2A</b> layer following an Er:YAG laser pulse at VSP ( $\tau_L \approx 100 \mu s$ ) and SP ( $\tau_L \approx 300 \mu s$ ) modes .....	<b>165</b>
<b>Table 4.19</b> – Estimated temperature ( $z = l_{th}$ ) using Eq. 4.13 of the heat distribution inside the <b>Paraloid B67</b> layer following an Er:YAG laser pulse at VSP ( $\tau_L \approx 100 \mu s$ ) and SP ( $\tau_L \approx 300 \mu s$ ) modes .....	<b>165</b>
<b>Table 4.20</b> – Estimates of the surface power densities ( $F_0$ ) absorbed by the vanishes at $z = 0$ .....	<b>166</b>
<b>Table 4.21</b> – Estimated temperature rise using Eq. 4.17 on <b>dammar film</b> following an Er:YAG laser pulse at VSP ( $\approx 100 \mu s$ ) and SP ( $\approx 300 \mu s$ ) modes. Temperature is given relative to room temperature ( $25 \text{ }^\circ\text{C}$ ) .....	<b>170</b>
<b>Table 4.22</b> – Estimated temperature rise using Eq. 4.17 on <b>Ketone N film</b> following an Er:YAG laser pulse at VSP ( $\approx 100 \mu s$ ) and SP ( $\approx 300 \mu s$ ) modes. (*) $\Delta T$ ( $^\circ\text{C}$ ) has been determined by using the %R from the FTIR data. However, (**) $\Delta T$ ( $^\circ\text{C}$ ) has been obtained using the %R from the Fresnel equation (Eq. 4.21). Temperature is given relative to room temperature ( $25 \text{ }^\circ\text{C}$ ) .....	<b>170</b>
<b>Table 4.23</b> – Estimated temperature rise using Eq. 4.17 on <b>MS2A film</b> following an Er:YAG laser pulse at VSP ( $\approx 100 \mu s$ ) and SP ( $\approx 300 \mu s$ ) modes. (*) $\Delta T$ ( $^\circ\text{C}$ ) has been determined by using the %R from the FTIR data. However, (**) $\Delta T$ ( $^\circ\text{C}$ ) has been obtained using the %R from the Fresnel equation (Eq. 4.21). Temperature is given relative to room temperature ( $25 \text{ }^\circ\text{C}$ ) .....	<b>171</b>
<b>Table 4.24</b> – Thermal diffusion time ( $t_{th}$ ) calculated for dammar, Ketone N and MS2A and compared with the laser pulse duration in VSP and SP modes . .....	<b>185</b>
<b>Table 6.1</b> – Cremonesi-Wolbers tests of solubility .....	<b>243</b>
<b>Table 6.2</b> – Wavenumbers corresponding to the maxima of the IR absorbance bands of the control dammar and the painting varnish (Theodorakopoulos <i>et al.</i> , 2007; Ciofini <i>et al.</i> , 2016; Invernizzi <i>et al.</i> , 2018) .....	<b>248</b>
<b>Table 6.3</b> – Molecules recorded via Py-TMAH-GC/MS. The data are in line with findings published elsewhere (van der Doelen <i>et al.</i> , 1998; Colombini <i>et al.</i> ,	

2000; Watts and de la Rie, 2002; Theodorakopoulos <i>et al.</i> , 2007; Dietemann <i>et al.</i> , 2009; Bonaduce <i>et al.</i> , 2016) .....	250
<b>Table 6.4</b> – The table provides the $L_{SCI_{mean}}^*$ and $L_{SCE_{mean}}^*$ and the GRF data before and after laser irradiation and the $\Delta GRF$ values. Standard deviations ( $\sigma$ ) of all data are provided. Data in bold represent the least efficient visually assessed outcome. Underlined data represent an acceptable level of irradiation of the varnish with no identification of brown hue of the laser scanned area .....	260
<b>Table 6.5</b> – Multispectral Imaging (MSI) Clusterisation Analysis data of the Er:YAG laser irradiated areas. Green % corresponds to a gradual reduction of the early stage varnish thinning. Red % coincides with gradual deeper irradiation of the varnish layer. The Black % corresponds to the remaining varnish within the irradiated spots .....	268
<hr/>	
<b>Table A1</b> – The thicknesses of dammar varnish casted on glass slides were acquired using Vision64 application software .....	355
<b>Table A1</b> – The thicknesses of the Ketone N casted on glass slides were acquired using Vision64 application software .....	356
<b>Table A2</b> – The thicknesses of the MS2A casted on glass slides were acquired using Vision64 application software .....	357
<b>Table A3</b> - The thicknesses of the Paraloid B67 casted on glass slides were acquired using Vision64 application software .....	358
<b>Table A5</b> – White paper and Glass slide + white paper colourimetric results .	359
<b>Table A6</b> – Colorimetric coordinates ( $L^*$ , $a^*$ and $b^*$ ) before and after ageing .....	359
<b>Table A7</b> – Colorimetric measurements of the resins selected for this research in SCI and SCE modes .....	360
<b>Table B1</b> – Fotona laser specifications .....	368
<b>Table B2</b> – FLIR thermal camera specifications .....	369
<b>Table B3</b> – Temperature data acquired using a Type K thermocouple and IR thermal camera vs. temperature from the Hot Plate .....	371

<b>Table B4</b> - Maximum effect of temperature variation recorded by using the FLIR thermal camera and the mean maximum heat impact ( $\Delta T_{\text{mean}}$ ) on a dry glass slide, according to Eq. 4.11 .....	<b>372</b>
<b>Table B5</b> – Parametric table for the dammar resin required to define the thermal modelling of varnish film .....	<b>421</b>
<b>Table B6</b> – Parametric table for the Ketone N resin required to define the thermal modelling of varnish film .....	<b>421</b>
<b>Table B7</b> – Parametric table for the MS2A resin required to define the thermal modelling of varnish film .....	<b>422</b>
<b>Table B8</b> – Parametric table for the Paraloid B67 resin required to define the thermal modelling of varnish film .....	<b>422</b>
<b>Table C1</b> – The table provides the $L_{SCI_{\text{mean}}}^*$ and $L_{SCE_{\text{mean}}}^*$ and the GRF data before and after laser irradiation $0.6 \text{ J/cm}^2$ and the $\Delta\text{GRF}$ values .....	<b>427</b>
<b>Table C2</b> – Multispectral Imaging (MSI) Clusterisation Analysis data of the Er:YAG laser irradiated areas $0.6 \text{ J/cm}^2$ .....	<b>428</b>
<b>Table C3</b> – The table provides the $L_{SCI_{\text{mean}}}^*$ and $L_{SCE_{\text{mean}}}^*$ and the GRF data before and after laser irradiation $0.7 \text{ J/cm}^2$ and the $\Delta\text{GRF}$ values .....	<b>430</b>
<b>Table C4</b> – Multispectral Imaging (MSI) Clusterisation Analysis data of the Er:YAG laser irradiated areas $0.7 \text{ J/cm}^2$ .....	<b>431</b>
<b>Table C5</b> - The table provides the $L_{SCI_{\text{mean}}}^*$ and $L_{SCE_{\text{mean}}}^*$ and the GRF data before and after laser irradiation at $1 \text{ J/cm}^2$ and the $\Delta\text{GRF}$ values .....	<b>433</b>
<b>Table C6</b> – Multispectral Imaging (MSI) Clusterisation Analysis data of the Er:YAG laser irradiated areas at $1 \text{ J/cm}^2$ .....	<b>434</b>
<b>Table C7</b> – The table provides the $L_{SCI_{\text{mean}}}^*$ and $L_{SCE_{\text{mean}}}^*$ and the GRF data before and after laser irradiation at $1.5 \text{ J/cm}^2$ and the $\Delta\text{GRF}$ values .....	<b>436</b>
<b>Table C8</b> – Multispectral Imaging (MSI) Clusterisation Analysis data of the Er:YAG laser irradiated areas at $1.5 \text{ J/cm}^2$ .....	<b>437</b>
<b>Table C9</b> – The table provides the $L_{SCI_{\text{mean}}}^*$ and $L_{SCE_{\text{mean}}}^*$ and the GRF data before and after laser irradiation at $2 \text{ J/cm}^2$ and the $\Delta\text{GRF}$ values .....	<b>439</b>

**Table C10** – Multispectral Imaging (MSI) Clusterisation Analysis data of the Er:YAG laser irradiated areas at 2 J/cm<sup>2</sup> ..... **440**

**Table C11** – The table provides the  $L_{SCI_{mean}}^*$  and  $L_{SCE_{mean}}^*$  and the GRF data before and after laser irradiation at 2.1 J/cm<sup>2</sup> and the  $\Delta$ GRF values ..... **442**

**Table C12** - Multispectral Imaging (MSI) Clusterisation Analysis data of the Er:YAG laser irradiated areas at 2.1 J/cm<sup>2</sup> ..... **443**

**Table C13** – The table provides the  $L_{SCI_{mean}}^*$  and  $L_{SCE_{mean}}^*$  and the GRF data before and after laser irradiation at 2.3 J/cm<sup>2</sup> and the  $\Delta$ GRF values ..... **445**

**Table C14** – Multispectral Imaging (MSI) Clusterisation Analysis data of the Er:YAG laser irradiated areas at 2.3 J/cm<sup>2</sup> ..... **445**

**Table C15** – The table provides the  $L_{SCI_{mean}}^*$  and  $L_{SCE_{mean}}^*$  and the GRF data before and after laser irradiation at 2.4 J/cm<sup>2</sup> and the  $\Delta$ GRF values ..... **447**

**Table C16** – Multispectral Imaging (MSI) Clusterisation Analysis data of the Er:YAG laser irradiated areas at 2.4 J/cm<sup>2</sup> ..... **447**



# Nomenclature and Abbreviations

## Acronym Lasers:

ArF	<i>Argon fluoride laser excimer laser (193 nm)</i>
KrF	<i>Krypton fluoride excimer laser (248 nm)</i>
XeCl	<i>Xenon chloride excimer laser (308 nm)</i>
Ruby laser	Ruby laser (695 nm)
Ti:Al <sub>2</sub> O <sub>3</sub>	<i>Ti:sapphire laser (795 nm)</i> Second harmonic ( $2\omega$ ) = 398 nm
Nd: YAG	<i>Neodymium-doped Yttrium Aluminium Garnet lasers</i> Fundamental wavelength ( $\omega$ ) = 1064 nm Second harmonic ( $2\omega$ ) = 532 nm Third harmonic ( $3\omega$ ) = 355 nm Fourth harmonic ( $4\omega$ ) = 266 nm Fifth harmonic ( $5\omega$ ) = 213 nm
Er: YAG	<i>Erbium-doped Yttrium Aluminium Garnet laser (2940 nm)</i>

## Acronym Analyses:

AFM	Atomic Force Microscopy
BSE-SEM	Back-Scatter Electron Scanning Electron Microscopy
OCT	Confocal Optical Coherence Tomography
DSC	Differential Scanning Calorimetry
DTA	Differential Thermal Analysis
DTMS	Direct Temperature Resolved Mass Spectrometry
EDS	Energy Dispersive X-Ray Spectroscopy
EDX	Energy Dispersive X-ray Spectroscopy
ESEM	Environmental Scanning Electron Microscopy
FTR	Fourier transform Raman
FT-IR	Fourier Transformed Infrared Spectrometry
GC/MS	Gas-chromatography Mass-spectrometry
LDI-MS	Laser Desorption and Ionisation MS
LIBS	Laser-Induced Breakdown Spectroscopy

LIF	Laser-Induced Fluorescence Spectroscopy
MALDI-ToF-MS	Matrix Assisted Laser Desorption-Ionisation (time-of-flight)
MSI	Multispectral Imaging
NIR	Near-Infrared Spectroscopy
NMR	Nuclear Magnetic Resonance spectroscopy
OM	Optical Microscopy
Py-GC/MS	Pyrolysis-GC/MS
SEM	Scanning Electron Microscopy
SEC	Size Exclusion Chromatography
SD-OCT	Spectral-Domain Confocal Optical Coherence Tomography
TGA	Thermogravimetric analysis
TMA	Thermomechanical Analysis
TD-OCT	Time-domain Confocal Optical Coherence Tomography
TR-LIFS	Time-Resolved Laser Induced Fluorescence Spectroscopy
TEM	Transmission Electron Microscopy
UV-Vis	Ultraviolet-visible spectrophotometry
VIS-FORS	Visible Fibre Optics Reflectance Spectroscopy
XRD	X-ray Diffraction Spectroscopy
XRF	X-ray Fluorescence Spectroscopy
XPS	X-ray Photoelectron Spectroscopy

### **Acronym wetting agents**

DI-W	Deionised water
DI-W+TW20	Deionised water with 1% (v/v) surfactant (Tween 20)
DIW+TW20	Distilled water with 2% (v/v) surfactant (Tween 20)
DIW-ETH	Distilled water + ethanol mixture (1:1, v/v)
IMS+DI-W	Industrial Methylated Spirit + Deionised water
IMS+WS	Industrial Methylated Spirit + White Spirit
WS	White Spirit

## Acronym Variables

%T	% transmission
$T_{\text{surr}}$	Absolute surrounding temperature
$F_0$	Absorbed laser power density ( $\text{W}/\text{m}^2$ )
$\alpha$	Absorption coefficient ( $\text{cm}^{-1}$ )
H	Convection heat transfer coefficient ( $\text{W}/\text{m}^2\cdot\text{K}$ )
$\rho$	Density ( $\text{kg}/\text{m}^3$ )
z	Distance from the front surface of the sample along the z-axis
$\varepsilon$	Emissivity of the surface
F	Fluence ( $\text{J}/\text{cm}^2$ )
$T_g$	Glass transition temperature ( $^{\circ}\text{C}$ )
q	Heat generation ( $\text{W}/\text{m}^3$ )
$E_{\text{inc}}$	Incident laser energy (mJ)
$T_i$	Initial temperature throughout the solid ( $^{\circ}\text{C}$ )
A	Laser beam Area ( $\text{cm}^2$ )
$\varnothing$	Laser beam diameter (mm)
$E_{\text{transglas}}$	Laser light passing through the uncoated glass slide (mJ)
$P_{\text{tot}}$	Laser total power (W)
$T_{\text{max}}$	Maximum average effect of the temperature recorded on the irradiated varnish surface using the IR thermal camera ( $^{\circ}\text{C}$ )
$\Delta T_{\text{mean}}$	Mean maximum temperature due to the heat impact ( $^{\circ}\text{C}$ )
$\delta$	Optical penetration depth ( $\mu\text{m}$ )
$P_{\text{avg}}$	Peak Average (W)
$P_{\text{peak}}$	Peak Power (W)
%R	Percentage of diffuse reflection
$\tau_L$	Pulse duration ( $\mu\text{s}$ )
E	Pulse Energy (J)
PPR	Pulse Repetition Rate (Hz)
r	Radius of the laser beam (mm)
$T_R$ or $T_i$	Room temperature ( $^{\circ}\text{C}$ )

$C_p$	Specific heat capacity (J/Kg·°C)
$\sigma$	Stefan-Boltzmann constant (W/m <sup>2</sup> ·K <sup>4</sup> )
$T_s$	Surface temperature (°C)
$T$	Temperature (°C)
$\Delta T$	Temperature distribution (°C)
$\Delta T_{(z)}$	Temperature distribution along the z-axis (°C)
$T_\infty$	Temperature of the fluid (°C)
$k$	Thermal conductivity (W/m·K)
$t_{th}$	Thermal diffusion time (sec)
$D$	Thermal diffusivity (m <sup>2</sup> /s)
$l_{th}$	Thermal-diffusion length (μm)
$t$	Time (s)
$E_{trans}$	Transmitted energy (mJ)



# Acknowledgements

There have been many people who have helped and supported me throughout my PhD studies. First and foremost, I would like to express my gratitude to my principal supervisor Dr *Charis Theodorakopoulos* who accepted me as a postgraduate student at Northumbria University and for his continued support, guidance, patience, and writing-up process of my PhD. The RDF scheme at Northumbria University supported this project.

In particular, I would like to thank *Ed Teppo* (founder and president of former Enterprise Big Sky Laser Technologies) and his wife *Anne Teppo* for their generosity, total willingness, support, encouragement, interesting food for thought, and because they were always available for valuable advice. I also wish to thank Ed Teppo for lending the Er:YAG laser to the Northumbria University Art Conservation Laboratory and for the laser spots analysis and transmission study carried out during a very interesting week spent in Montana (US State).

I would like to express my gratitude to Dr *Marianne Odlyha* for the DSC and TGA analyses performed at the Birkbeck, University of London, and her guidance, support throughout this research project, and all the time she dedicated to my work.

I am also thankful to Dr *Juri Agresti*, whose help was essential with the mathematical computation of the temperature rise and the time he dedicated to my work. I also wish to thank Dr *Iacopo Osticioli* and Dr *Daniele Ciofini* for their advice and valuable suggestions.

I am grateful to Dr *Fernando Sala*, who helped me with the two-dimensional simulation. There is no way I would ever have done it without his help. Many thanks to you, brother-in-law, for everything.

I acknowledge Dr *Qiang Wu*'s contribution to this research for giving me access to the thermal camera and Dr *Yufeng Wu*.

Also special thanks to XpectralTEK LDA for providing the XpeCAM X01 multispectral imaging system and the software tools used for the study, thanking, in particular, Dr *Vassilis Papadakis* for his valuable help.

I thank the PerkinElmer's London office's technical personnel for allowing me to use the mid-IR integrating sphere and their assistance.

I would like to express my appreciation to Prof. Dr *Giuseppe Lazzara* for the density analysis carried out at University of Palermo; Dr *Nicasio Geraldini* and Dr *Bethany Orme* for the assistance on the use of the analysis of the contact angle at Northumbria University; Dr *Kate Nicholson* and *William Carswell* for the DSC analysis at Durham University; Prof. Dr *Justin Perry* for giving me access to the gas chromatography-mass spectrometry (GC-MS) equipment, *Karen Haggerty* for providing guidance on the use of the Pyrolysis-GC/MS analysis and *Gordon Forrest*; Dr *Anson Hancock* for his assistance and advice on using the thermal camera; Dr *Francesca Alberghina* for the assistance on the colourimetry; Dr *Pietro Maiello* for providing guidance on the use of SEM and his technical assistance during my work; *Ana Flynn*, painting conservation Officer at Tyne & Wear Archives & Museums, for her encouragement, support, advice and valuable suggestions; and at the same time *Nicola Grimaldi*, Senior Lecturer for the Master's Degree in Conservation of Fine Art at Northumbria University.

Huge gratitude also to my friends and colleagues *Panos Galatis*, *Sofia Pascal*, *Valentina Risdonne*, *Vanessa Johnson* *Giorgia Marucci* and *Massimiliano Papini* for all their encouragement and support. In particular, I would like to thank *Valentina*, and her boyfriend *Manuel*, for her readiness to listen, invaluable ideas, valuable help in writing and most of all for letting me stay in her house for a couple of months.

I would like to thank my best friend *Benedetta Cotza*, without whom my Newcastle experience would not have been the same, for being in my life and for being my best friend through all ups and downs. You are the best bestie ever!

Finally, I would like to thank *Josephine Garrett* for her time spent proofreading and her friendship, support and kindness.

Last but not least, I would never have been able to begin this journey or end it without my parents and sister's unconditional love, support, and patience. They were always there to encourage me and my choices. Having parents and a sister like you by my side makes me what I am today.



## Declaration

I declare that the work contained in this thesis has not been submitted for any other award and that it is all my own work. I also confirm that this work fully acknowledges opinions, ideas and contributions from the work of others.

Any ethical clearance for the research presented in this thesis has been approved. Approval has been sought and granted by the University Ethics Committee on 09/2017.

I declare that the Word Count of this Thesis is 79,823 words.

Name: *Chiara Chillè*

Signature:

Date: 27/01/2021



# CHAPTER 1 INTRODUCTION

This initial chapter covers the background and motivation of this PhD research, the issues connected to the use of Er:YAG laser in the conservation field and the possibility of using this laser system for the thinning degraded varnishes of coatings which were used during the twentieth century. The research aim and objectives, scope, and novelty of this work are also presented, along with a summary of the structure of this thesis.

## 1.1 Background and motivation

In western European paintings, varnishes are commonly applied to canvas to improve aesthetic properties as well as to protect the paint layer(s) (Cennini, 1960).

As described by Étienne Gilson, a French philosopher, “There are two ways for a painting to perish, the one is for it to be restored; the other is for it not to be restored” (Gilson, 1959, p. 484). Soil particulates from the environment may overtime accumulate on the surfaces of paintings, contributing to trigger deterioration processes. In the same way, degradation due to the ageing of coatings applied onto the paint layer(s) has a detrimental effect on the readability and appearance of paintings surface (Feller and Curran, 1975; Wolbers, Sterman and Stavroudis, 1990; Phenix, 2013; Tempest *et al.*, 2013; van den Berg *et al.*, 2014; Steyn *et al.*, 2017; Tsang and Erhardt, 2018; Baij *et al.*, 2020). The question of whether or not to clean a surface, but also the level of cleaning continues to be open to discussion in the conservation field. This does not mean that the varnish layer(s) needs to be removed. Generally, surface cleaning involves the removal of accumulated dirt from painted surfaces but also the cleaning of aged varnished paint substrates (Baglioni and Chelazzi, 2013). In laser treatment applications of varnished paintings, thinning of varnishes rather than their complete removal leads to the optimal and safe cleaning. It is well known that both ageing, and degradation processes can compromise the chemical and physical properties of these varnish layers, making the cleaning procedure challenging. In fact, an inappropriate approach could lead to a faster deterioration of the original characteristics of the paint layer(s) underneath. For this reason, surface cleaning can be considered as

one of the most critical, highly sensitive and complex procedures in conservation (Cremonesi and Signorini, 2012; Baglioni and Chelazzi, 2013).

The need for a well-designed cleaning methodology has made conservators recognise the importance of identifying controllable and selective cleaning procedures in order to preserve the underlying original layers. In this respect, the use of lasers in the conservation field has increased significantly, because of their ability to remove in a selective way any unwanted material applied onto the original layer(s) as well as aged and discoloured varnish layers.

The word laser is an abbreviation for *Light Amplification by Stimulated Emission of Radiation*, and this definition was proposed for the first time by Schawlow and Townes (1958). Only pulsed lasers can be used for the cleaning of cultural objects (Siano, 2008). The rationale for using lasers in removing coatings takes into account the following: the use of the laser ensures a good control during the coating thinning process; it minimises the risks of possible substrate damage caused by the exclusive liquid-based conservation cleaning using free solvent admixtures, mechanical means or residue leaving agents; it reduces health-related risks of other procedures for the operator; it is environmentally sustainable; and it cuts the cost of labour reducing the treatment time (Coutouly *et al.*, 2009).

This study will concentrate on the use of the Er:YAG lasers. In recent years the application of mid-infrared wavelengths (Er:YAG laser [2940 nm]) has successfully been introduced as an alternative to traditional cleaning methodology on easel paintings (De Cruz, Hauger and Wolbarsht, 1999).

Since works of art are multi-component systems and multi-layered structures, the interaction of their organic and inorganic constituents with laser beam(s) and the subsequent removal mechanism of particular unwanted materials (e.g. coatings and overpaintings) is complex (De Cruz *et al.*, 2014). Thus, the application of lasers for the removal of coatings from works of art is a challenging process due to the high sensitivity of the materials constituting these surfaces. The highly selective absorption of the 2940 nm Er:YAG laser wavelength by hydroxyl groups, which constitute several materials of cultural heritage objects (e.g. varnishes, pigments and binders), can lead to diverse photo-thermal and mechanical effects on the

surface of coated artworks (De Cruz *et al.*, 2014; Pereira-Pardo and Korenberg, 2018). Using Er:YAG lasers, the laser-material interaction is carried out through thermal (melting and vaporization) effects. Paint layers and coatings have a non-negligible absorption in the mid-infrared region, which leads to vibrational and electronic excitations of these constituents (De Cruz *et al.*, 2014) without chemical bond dissociation. The energy absorbed by vibrational modes is thus thermally dissipated increasing the temperature of the surface coating irradiated and leading to the thinning of the targeted material (De Cruz *et al.*, 2014). In order to maximise the 2940 nm beam absorption at the surface, it is a common practice to pre-wet the area with aqueous or OH-containing solutions. By doing so, an effective and gradual thinning can be obtained. In fact, the auxiliary wetting agents applied as a thin layer film increase the absorption of the Er:YAG radiation and thus reduce the penetration of the laser beam into the surface with a limited increase of temperature (Andreotti *et al.*, 2016). In general, the ideal approach for the treatment of coated surfaces with the use of an Er:YAG laser is to thin the targeted layers first instead of attempting their complete removal. This process can be obtained by setting the laser parameters such as fluence, pulse width, repetition rate and beam size in accordance with the chemical compositions of the materials in substrates.

Nonetheless, the major issues of the use of Er:YAG lasers, for the irradiated materials, relate to the temperature rise to the surface and the heat propagation in the bulk (De Cruz *et al.*, 2014). In fact, during laser-material interaction, part of the laser energy is reflected, part is absorbed, and the remaining energy is transmitted to the underlying layers (Fotakis *et al.*, 2006; Siano, 2008; Madhukar, Mullick and Nath, 2013). Moreover, the thermal energy delivered by the laser beam onto the surface is influenced by the selected laser parameters and by the optical and physicochemical characteristics of the irradiated materials (Mayboudi, 2008).

The side effects of the heat impact on materials have been studied mainly for Nd:YAG (1064nm) lasers on inorganic materials, mock-ups and painted surfaces (Siano, 2008; Siano *et al.*, 2012; Ciofini, 2014). However, only two studies have been published on the effect of the surface temperature increase during Er:YAG lasers irradiations. De Cruz *et al.* (2014) have shown that a thermocouple-monitored temperature increase remained low when wetting agents were used upon Er:YAG irradiation on artefacts, such as a panel painting, a bronze coin and a

Roman urn. Felici *et al.* (2019) presented a different approach in order to quantify the local thermal effects upon Er:YAG laser irradiation. The authors monitored in real-time the heat impact using an IR thermal camera on ‘frescoes’ mock-ups coated using organic and synthetic consolidants.

Therefore, the side effect caused by thermal heating must be further investigated in order to avoid procedures that may affect the physical and chemical stability of artworks.

## 1.2 Rationale

The use of IR lasers in the industrial field can be considered as an established system for material processing such as metals and semiconductors, as well as there is an extensive scientific base that supports the use of Er:YAG lasers for clinical and surgical applications, which is related to the amount of water in skin (ca. 70% water) and hydroxyapatite making the Er:YAG lasers the most efficient wavelength for processing soft and hard tissues (e.g. Partovi *et al.*, 1987; Lukač *et al.*, 2010; Vogel and Venugopalan, 2010; Diaci and Gaspirc, 2012; Yaneva *et al.*, 2016). To date the use of Er:YAG lasers in the conservation field has not yet been established and the physicochemical mechanisms have not yet been thoroughly investigated, although promising publications have demonstrate the potential for Er:YAG laser irradiation in the controlled removal of unwanted materials applied onto the surface of cultural objects (e.g., De Cruz, Wolbarsht and Hauger, 2000; Andreotti *et al.*, 2007, 2016; Striova *et al.*, 2011; De Cruz *et al.*, 2014; Pereira-Pardo and Korenberg, 2018; Lopez *et al.*, 2019; Alabone and Carvajal, 2020; Pereira-Pardo, Melita and Korenberg, 2020; Teppo, 2020; Boonrat, Dickinson and Cooper, 2020; Brunetto, Bono and Frezzato, 2020; Hellen, 2020).

Therefore this work aims to provide a systematic study of the Er:YAG laser interaction with aged varnishes. The research main contribution is to investigate and increase the knowledge of Er:YAG laser-induced effects in order to provide less invasive and more selective methods for the conservation of varnished paintings.

As a rule of thumb, the understanding of both the physical principles governing the laser-material interaction and the physicochemical properties of the

materials are the two crucial aspects in designing specific tests and understanding the interaction of the Er:YAG lasers on coatings. Such studies aim to represent a step forward regarding the conservation treatments with Er:YAG lasers.

Therefore, in order to shed some light on the interaction mechanisms of the Er:YAG laser with different coatings, four different artificially aged varnishes are investigated. These varnishes are as follows:

- a natural triterpenoid varnish (dammar) which deteriorates mainly due to an increase in oxidation (de la Rie, 1988; Zumbühl *et al.*, 1998; van der Doelen, 1999; Dietemann, 2003; Scalarone *et al.*, 2003) and the presence of degradation gradients formed by a reduction of the oxidised compounds as a function of depth (Theodorakopoulos, 2005; Theodorakopoulos, Boon and Zafirooulos, 2009);
- three synthetic resins: i) an acrylate polymer (Paraloid B67), which showed cross-linking processes (Feller, 1976) due to a severe UV exposure (Chiantore and Lazzari, 2001) becoming insoluble (Colombini and Modugno, 2009, p. 343), and ii) two Ketone resins (Ketone N and MS2A) which proved to be chemically unstable having a general tendency of yellowing and cracking or becoming difficult to remove after time (Berns and de la Rie, 2003; Maines and de la Rie, 2005; Gheno, 2017, p. 22).

These resins have been selected because they have been commonly employed by artists and conservators in modern and contemporary paintings. Very little information is available regarding the properties of these varnishes, such as heat capacity, thermal conductivity and diffusivity and percentage of transmission of the laser beam through the materials. Therefore, at first, it is necessary to characterise the coatings which will be laser irradiated with the fabrication of a series of mock-ups. Therefore, these artificially aged systems will be subjected to a systematic investigation and the parameters needed for interpreting later the laser-induced effects will be acquired and processed.

A major task in this approach is to investigate interactions between the Er:YAG laser light and coatings. Based on the state-of-the-art regarding the laser cleaning techniques using UV lasers and Nd:YAG lasers, and following the already published work on the use of the Er:YAG lasers, it is essential to understand the

interaction between the laser beam and the varnish layers during the laser irradiations and to assess the deterioration risks during the laser irradiation procedure. A special focus has been given to the study of temperature changes upon irradiation. Two procedures have been performed to achieve this aim: i) recordings of live thermal imaging by employing an IR thermal camera, and ii) the determination of the varnish optical properties, which allowed to estimate the linear absorption coefficient and the temperature rise associated to the laser irradiation. The second procedure was supported by a 2-dimensional simulation of the laser-based heat diffusion inside each varnish employed for this research. Transmission study and Fourier Transform Infrared (FT-IR) spectroscopy captured increased energy transmissions through varnish films, as well as registering a reduction of hydroxides and carbon–hydrogen bonding as a function of fluence, respectively.

Finally, based on these analytical results carried out on laboratory mock-ups, the Er:YAG laser was used to thin a triterpenoid varnish on a canvas painting. The “Hunting Scene”, which was dated as over 100 years old, belongs to the collection of paintings of the Department of Arts at Northumbria University (Newcastle upon Tyne).

### **1.3 Aims and objectives**

Exploiting the potentialities of the laser cleaning methodologies, this thesis aims to establish an understanding of the laser-induced effects, the side effects of the temperature rise onto the surface of selected irradiated varnishes and the heatwave propagation in the bulk of varnishes by increasing the fluence values. Transmission energies throughout varnish films necessitate investigation in order to understand if the high-powered laser action could reach the underlying layer(s). Moreover, the physicochemical interaction between the Er:YAG laser and the selected varnishes (a triterpenoid resin, Ketone Resins, and an Acrylic polymer) had to be evaluated to provide the evidence to how these films react upon laser irradiation.

Thus, questions arise such as: whether the Er:YAG laser pulses induces side effects caused by the temperature rise onto the surface and the heat propagation in the bulk; whether physicochemical modifications are increasing upon the laser

irradiation; whether the high-powered laser pulses could reach the underlying layer while removing surface layers; whether Er:YAG lasers can be used to safely thin varnishes applied to works of art

In order to achieve the aims of this research, the following objectives will be addressed:

- a) The completion of a comprehensive literature review on the history of varnish formulations commonly used by conservators in the twentieth century and a brief description of the ageing processes for three classes of coatings (Triterpenoid resin, Ketone Resin, Acrylic polymer). This provides a basis for a good basis of the understanding of the demands made by artists, and later conservators, to overcome the problem related to the ageing mechanisms of natural varnishes and the introduction of synthetic varnishes.
- b) The characterisation of morphological and physicochemical modifications of the selected varnishes after ageing and to measure the changing in mass as a function of temperature and time prior to the laser tests. Stylus profilometry, static contact angle, gas pycnometry, colourimetry, thermogravimetric analysis (TGA), differential scanning calorimetry (DSC) and attenuated total reflection/Fourier transform infrared spectroscopy (ATR/FT-IR) will allow the determination of the optical and chemical varnishes properties, their characteristic decomposition patterns, the specific heat at a constant pressure ( $C_p$ ) and the monitoring of the artificial ageing processes.
- c) The completion of a comprehensive literature review starting from the standard cleaning methodologies used nowadays by conservators, which range from wet to dry cleaning methodologies, followed by an overview of the origins and circumstances framing the gradual increased in the use of UV and IR lasers to thin or remove varnish coatings from painted surfaces. This includes tracking the gradual transition of the Er:YAG lasers from their use in clinical and surgical applications to the conservation field.
- d) The investigation and the interpretation of laser-induced effects on the varnish mock-ups upon Er:YAG laser irradiation. For this purpose, in

order to describe the temperature changes upon irradiation two procedures are employed, i) an IR thermal camera will be used to monitor in real-time the heat impact on the dry and pre-wet varnish surfaces; ii) the varnishes parameters (such as specific heat capacity [ $C_p$ ], density, thermal diffusivity, thermal conductivity, absorption coefficient and optical penetration depth) will be mathematically processed and simulations of the heat distribution in the bulk of the resins in combination with the Er:YAG laser characteristics will be generated.

- e) The real-time monitoring of the transmitted energy of the Er:YAG laser beam as it propagates through aged varnishes.
- f) The assessment of laser-material interactions using Scanning Electron Microscopy (SEM).
- g) The investigation of the laser irradiation at different fluences using a semi-quantitative analysis with ATR/FT-IR.
- h) The evaluation of the Er:YAG laser efficacy to safely thin a varnish on a real case of study (a varnished modern oil painting).

#### 1.4 Thesis structure

This Introduction chapter provided the project background, motivation, aims and objectives, research questions, research novelty and originality, research scope as well as the importance of the project to the conservation field. The following thesis chapter outline is as follows:

**Chapter 2: Literature Review.** This chapter presents a discussion regarding the innovations in the industrial production of materials for artists and the history of varnish formulations commonly used by artists and conservators in the twentieth century. Thus, the chapter continues by discussing the standard cleaning methodologies used nowadays by conservators, ranging from wet to dry-cleaning methodologies. Lastly, the state-of-the-art of the laser techniques used to thin or remove coatings from easel paintings, with an excursus of the most relevant papers published and organised in a chronological order.

**Chapter 3: Natural and Synthetic Varnishes: Preparation and Characterisation.** This chapter starts with a short review of the different chemical structures of the triterpenoid, ketone resin and acrylic varnishes investigated in this

research and their ageing processes. Therefore, the dammar, Ketone N, MS2A, and Paraloid B67 selected for this research and applied onto glass slides were photo- and hydrothermally aged. This methodology aimed at providing suitable mock-ups for the optimisation of the Er:YAG laser tests. Morphological and physicochemical modifications have been investigated using stylus profilometry, static contact angle, gas pycnometry for the definition of the density, colourimetry, thermogravimetric analysis (TGA), differential scanning calorimetry (DSC) and attenuated total reflection/Fourier transform infrared spectroscopy (ATR/FT-IR).

**Chapter 4: Er:YAG laser tests (Part I): A study on the heat distribution and Spectroscopic investigations.** This chapter is essentially centred on the systematic assessment of the laser-induced modifications upon Er:YAG laser irradiation onto the aged coating films. The first half of this chapter starts with the state-of-the-art of the laser systems commonly employed in the conservation field, the characterisation of the laser parameters, and the explanation of the mechanisms involved in the laser-material interactions. This first part ends with the presentation of the Fotona Er:YAG laser source, the state-of-the-art of the liquid-assisted laser-material interaction within clinical and surgical fields and finally, the use of Er:YAG laser methodologies in the Conservation Field with a special focus on the published thermal studies in the same area. Therefore, due to the photo-thermal process associated with the use of IR lasers two procedures have been used to examine the temperature rise at the surface and the heat propagation in bulk of the aged coatings, i) recording of live thermal imaging by using an IR thermal camera for the dry and pre-wet irradiated films, and ii) a mathematical computation and 2D simulations of the temperature rise only on the dry varnishes. FT-IR experimentally has determined the absorption coefficient of the films. Transmission studies have captured increased energy transmissions through the aged coatings. This specific analysis monitors the transmission of the Er:YAG laser light online during the irradiation of the aged varnish surface layers and aims to identify the transmitted energy that may interact with the underlying layers. The transmitted energy of laser light passing through the varnish films are particularly noteworthy in light of the fact that in the infrared portion of the electromagnetic spectrum varnishes are highly transmissive materials.

**Chapter 5: Er:YAG laser tests (Part II): Microscopies and Spectroscopic investigations.** The chapter presents a spectroscopic investigation using ATR-FTIR analysis straight on the laser treated surfaces, registering a reduction of hydroxides and carbon-hydrogen bonding as a function of fluence. An overview of laser spots will be carried out with Scanning Electron Microscopy (SEM). Dry irradiation or distilled water + a non-ionic surfactant (Tween 20) (DI-W+TW20) have been chosen based on their different thermal and physicochemical interaction during the laser-material interaction.

**Chapter 6: An analytical evaluation of Er:YAG laser cleaning tests on a nineteenth century varnished painting.** This highlights the approach carried out using an Er:YAG laser to safely thin a varnish on a nineteenth century oil painting. Spectral clusterisation maps of Multispectral Imaging (MSI) data of the irradiated surface have supported the evaluation of the procedure. Further evaluation has been performed by stereomicroscopy and colourimetry. FT-IR and Pyrolysis Gas Chromatography/Mass Spectrometry (Py-GC/MS) analysis have indicated that the varnish resin was dammar. ATR/FT-IR has allowed analysing the collected resin fragments.

**Chapter 7: Conclusions and Recommendations.** This chapter lists the essential conclusions that have emerged from the evaluation of the Er:YAG laser interaction with the aged mock-ups and the results deriving from the use of the Er:YAG laser on a real case study. This information can offer suggestions and insights for future work that will allow more informed conservation treatments with Er:YAG lasers.

## CHAPTER 2 LITERATURE REVIEW

*“The traditional materials and techniques of painting, as well as the corresponding and traditional restoration method, will be tested in respect of ageing, reversibility and other basic demands, in order to find an answer to the question of how far traditional art production and the corresponding restoration methods are applicable to modern art. At the same time, it should be examined to see how traditional restoration techniques could be applied to contemporary object in order to avoid new unreliable methods and material.”*

— Dr. Althöfer (1985)<sup>1</sup>

*“There are times when I can clearly see a possible – and desirable – alliance between art and science, when the chemist and physicist will be able to take their place beside you and enlighten you.”*

— Luis Pasteur (March 6, 1865)<sup>2</sup>

*The thinning or the removal of discoloured old varnishes from paintings is one the most critical, highly sensitive and complex procedures in the conservation and restoration field, and it represents the main focus of this research.*

*The period between the end of the nineteenth century and the beginning of the twentieth century was a time of innovation in the industrial production of materials for artists. The main reason for this innovation, which led to the introduction of new varnish formulations, was the willingness to overcome the degradation processes connected with the use of natural resins. Therefore, synthetic resins such as Ketone N, MS2A, Paraloid B67 were launched on the market and extensively used throughout the mid-twentieth century.*

*Nowadays, the necessity of a well-designed cleaning methodology has made conservators realise the necessity to identify a cleaning procedure as respectful as*

---

1 (Althöfer and Schinzel, 1985; Pavić, 2014).

2 (Ruhemann, 1968).

*possible in preserving the underlying original layers of easel paintings when they remove any previous coating.*

*Therefore, this chapter starts with a description of what varnish actually is and a brief history of modern varnish formulations partially addressing **objective a** of this thesis. The cleaning methodology used by conservators divided into chemical and physical cleaning will be summarised. Lastly, the state-of-the-art of the laser techniques used on the thinning or the removal of unwanted materials will be introduced focusing specifically on the laser interaction with varnish films and an excursus of the most relevant papers published and organised in a chronological order, partially addressing **objective c**. A comprehensive overview of the published research on laser cleaning is summarised. All the resins are listed, and the lasers employed together with the fluence threshold parameters determined for a safe varnish irradiation are reported.*

## 2.1 Introduction

**B**efore embarking on the research in the treatment of paintings, it is crucial to understand the paintings anatomy and standard technical terms. What is a painting and how it is composed has been exhaustively explained in several publications (Armenini, 1587; Cennini, 1960; Gettens and Stout, 1966; Ruhemann, 1968; Mayer, 1991; Nicolaus, 1999; Carlyle, 2001; Bomford, Dunkerton and Wyld, 2009; Stoner and Rushfield, 2012; Bonino, 2016; Stols-Witlox, 2017). The following is a short extract from *The Care of Picture* by George L. Stout in which he fully explained the structure of paintings (Figure 2.1) (Stout, 1948; Ruhemann, 1968, pp. 99–102):

“The most common supports [...] are wood, fabric, and paper. The use of ground brings more complex type of picture construction [...]. The ground is a smooth, flat coating put over the support. [...] Many materials have been used for the purpose: gypsum, chalk, China clay and white pigments. [...] In a structural sense there is no difference between a ground and a paint. The different terms merely indicate different functions or uses in the construction of a picture. Ground is a smooth, even coat the purpose of which is largely mechanical. The paint, [...] contains the drawing and development of the pictorial idea.

Whatever the material is ground or paint, it is usually composed of two very different substrates – the pigments and the binding materials. [...] The number of materials used for medium in Europe has been greater probably than the Far East. Egg yolk and egg white, [...] and drying oils have been added to the more ancient glues and waxes. Oils as a binding medium may have come into use in the early Middle Ages. [...] The kind of picture familiar as an oil painting in the Western world is regularly coated with films-forming substances or mixtures referred to a varnish. The word ‘varnish’ is ordinarily related to those film materials that are made of resins or of mixture oil and resins”.

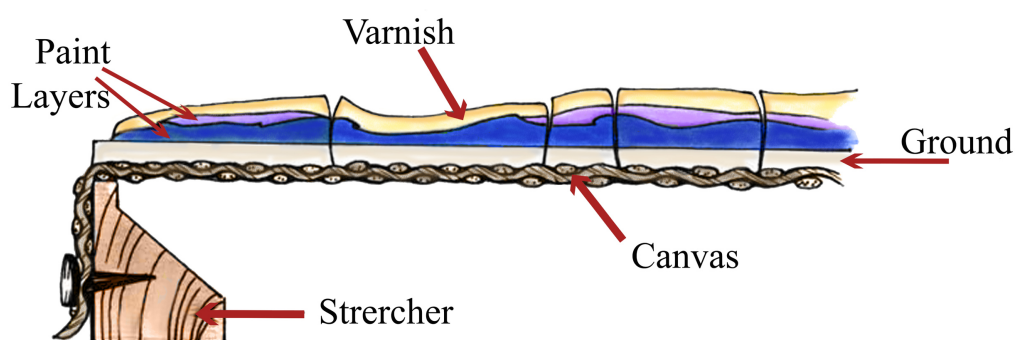


Figure 2.1 – The picture shows a graphical illustration of the structure of an easel painting. Figure adapted from Ocon and Findley.

Since the nineteenth century, chemists, physicists, and conservators started researching systematically in the conservation field (Ruhemann, 1968, p. 117). There is no doubt that the research in the history of painting techniques should be considered a multidisciplinary area of study, which requires extensive research in the field of art history and technique, science, and conservation (Wallert, Hermens and Peek, 1995). Art conservators work within a wide range of materials, chemical composition of which is to be considered particularly broad and diversified. Pure single materials can form art objects or, more frequently, are made up of combination of blended materials. To preserve these unique pieces of art, conservators must follow strict ethical frameworks and high professional standards, in order to deliver such high standards, they need to collaborate extensively with conservation scientists to develop new methodologies for the conservation of these cultural assets (van den Berg *et al.*, 2014).

The period between the end of the nineteenth century and the beginning of the twentieth century was a time of innovation in the industrial production of materials for artists, architects, and designers (Kokkori *et al.*, 2017). This research focuses on one of the most crucial issues in the conservation of paintings in recent times: the possibility to use an Erbium-doped Yttrium Aluminium Garnet (Er:YAG) laser to (2940 nm) thin natural and synthetic varnishes applied to paintings.

## 2.2 LITERATURE REVIEW I: On Varnishes

“Varnish is a powerful liquid”, wrote Cennino Cennini in *Il Libro dell’Arte* (Cennini, 1960) and in sixteenth-century Giovanni Battista Armenini in his treatise explicitly stated that (Armenini, 1820):

“There are then the varnishes, whose effect is to enliven and draw out the colours and preserve their beauty for a very long time. Varnish has the power to bring out all the minute details in a work, making them appear very clear”.

The varnish film has the capacity to change the appearance of easel paintings (imparting gloss and matte aspect) and also provide a degree of protection against mechanical and atmospheric stress (Nicolaus, 1999, p. 310; Stoner and Rushfield, 2012, p. 252). Varnishes can be classified, depending on the solvent used to dissolve them, into two main groups: i) oil varnishes, obtained by dissolving a tree resin or fossil resin in hot linseed, poppy or walnut oils and ii) spirit varnishes, which are obtained by dissolving tree resins or resinous materials in solvents like alcohol or turpentine (Maclaren and Werner, 1950; Stoner and Rushfield, 2012, p. 252). Oil varnishes dry without the need for solvent evaporation. This class of varnish forms a hard film not easily solubilised. Spirit varnishes, conversely, dry by solvent evaporation and their solubility is closely related to the solvent used during their preparation (Maclaren and Werner, 1950). In this research, only modern varnishes, which belong to spirit varnishes, would be taken into consideration.

The ideal qualities of the best final varnish film for paintings were outlined in 1930 during the *Conference on the Examination and Conservation of Works of*

*Art*, held under the auspices of the International Museums Office in Rome. A committee of about 15 well-known conservators/restorers was convened under the chairmanship of Professor W. G. Constable (Ruhemann, 1968, p. 272). The identified qualities of the films were: i) transparency and colourlessness; ii) applicability in thin coating layers using brush or spray (convenient degree of viscosity); iii) maintaining elasticity and cohesiveness during normal environmental changes; iv) efficient wetting and filling the pores of the paint sufficiently (appropriate ‘wetting power’); v) capability to dry over a period that prevents dust from setting and adhering on the surface, retaining the elasticity of the paint film; vi) durability and resilience avoiding the formation of ‘blooming’, cracking, wrinkling etc.; vii) ease of removability (no ‘cross-link’ with the paint layer); viii) bringing out the full depth and transparency of the colour underneath without being excessively ‘brilliant’; ix) providing protection of the painting from atmospheric impurities, as well as offering protection against moisture acting as a ‘barrier’; x) protecting the paint surface from direct touch and minor scratches (Stout and Cross, 1937; Ruhemann, 1968, pp. 270–271). That Conference revealed that no ideal picture varnishes existed at that exact time, and a precise methodology was adopted to overcome the issue related to the varnishing process and the coatings to use (Ruhemann, 1968, p. 272). Those recommendations were subsequently made to all museums by the International Museum Office, as the best solution in that moment (League of Nations, 1933; Ruhemann, 1968, p. 272).

In broad terms, the varnish is a solution of resins in organic solvents that, when applied over a solid surface, dries to a transparent film giving to the paint surface various characteristics, such as different degrees of glossiness, hardness and flexibility, depending on the physicochemical properties of the incorporated resins (Maclaren and Werner, 1950; Mayer, 1991, p. 214; Nicolaus, 1999, p. 310). Its function is also to saturate the paint layer and create a uniform reflective surface (Kirsh and Levenson, 2002, p. 216). Varnishes prevent direct deposition of dirt on paint surfaces (Farr *et al.*, 1987; Watson and Burnstock, 2013), protect artworks from fingerprint, scratches, environmental pollution (Motherwell and O’Hara, 1965, p. 237) and to protect the paint layers by deflecting ultraviolet (UV) rays. The UV parts of light can trigger specific alterations and yellowing on the varnish film (Chiantore and Rava, 2012, p. 144). Furthermore, depending on the environment in

which the paintings are stored, other alterations can be triggered like grey discolouration, craquelure formation and crazing (Nicolaus, 1999, p. 310). Additionally, the refractive indices of the varnish and the paint play a substantial role in the appearance of paintings (de la Rie, 1987, p. 1).

### 2.2.1 *Brief history of varnishes*

A very early form of varnish was the use of pure oil brushed into the dry surface of paintings (Eastlake, 1869; Ruhemann, 1968, p. 271; Stoner and Rushfield, 2012, p. 253). Later, between the twelfth and sixteenth centuries, publications started reporting the use of varnishes composed of sandarac, amber or copal resins and dissolved in hot oil. These specific formulations, known as oil-varnishes, dried by oxidative cross-linking of the oil and pretty quickly showed the side-effect of darkening with time and became insoluble in strong solvents (Stoner and Rushfield, 2012, p. 252)<sup>3</sup>. Since then, another class of coating has been mentioned which is considered as ‘spirit varnish’ dissolved in volatile solvents such as alcohol (spirits of wine), naphtha (petroleum distillate) and essential oils derived from turpentine or spike lavender (Stoner and Rushfield, 2012, p. 252). This type of varnish was easier to make and apply as a thin film, compared to the older formulations. However, it was reported that spirit varnishes produced brittle and fragile coatings, restricting their use to pictures and objects nor frequently subjected to handling or surface cleaning (Thomson, 1957; Ruhemann, 1968, p. 272).

In the early sixteenth century, a new class of varnish began to be used by artists and by the seventeenth century, spirit varnishes were in regular use in both Northern and Southern Europe (Stoner and Rushfield, 2012, p. 257). This new kind of varnish was composed of ‘soft resins’, which exude naturally from trees, such as mastic, and dissolved in naphtha or distilled turpentine. Like the oil-varnishes, soft resin varnishes eventually yellowed with age. Still, unlike the oil-varnishes, soft resins varnishes were ‘easily removable’ using organic solvents that were commonly employed in conservation cleaning treatments. This concept was later invalidated due to the impossibility to solubilise these varnishes in comparatively

---

<sup>3</sup> For additional discussion of oil varnishes, see (Carlyle, 2001).

mild solvents (Ruhemann, 1968, p. 272). Nonetheless, it took over several hundred years to drastically change the artist materials (Ruhemann, 1968, p. 272).

In the twentieth century, natural resins, were eventually side-lined by the commercialisation of synthetically produced polyacrylic, polyvinyl and polycyclohexanone-based resins (Nicolaus, 1999, p. 315).

In general, modern resins varnishes can be classified into two major categories: the first group of natural soft resins, and the second group of synthetic resins. The latter have been used since the 1930s by conservators as finishing varnishes (Feller, Jones and Stolow, 1985, p. 3; Mayer, 1991; Nicolaus, 1999, p. 315).

A scheme of the frequently used film-forming materials in paint applications is presented below (Figure 2.2).

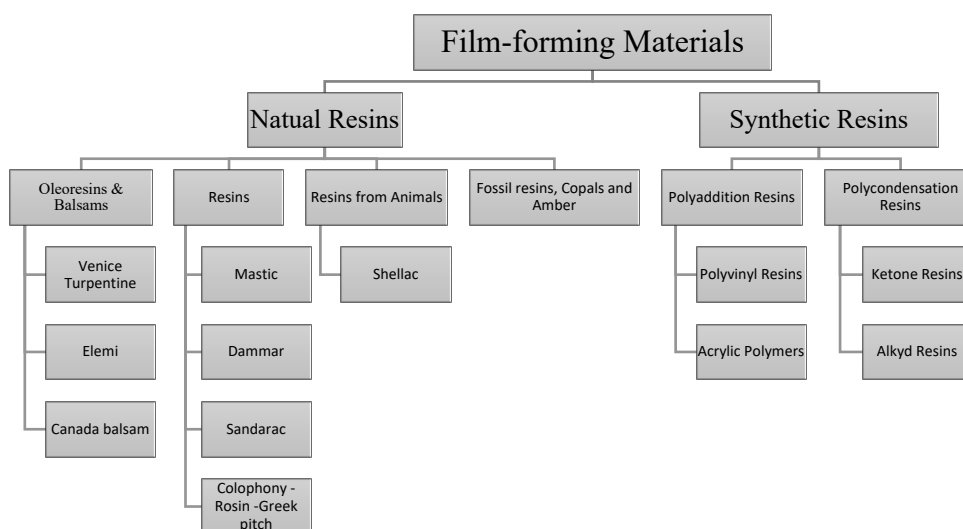


Figure 2.2 – Classification of material usually employed as coatings on paint surfaces (Matteini, Mazzeo and Moles, 2016, p. 167)

### 2.2.1.1 Natural soft resins

Dammar resin, belonging to the group of natural soft resins (Feller, 1958)<sup>4</sup>, has a similar chemical composition to mastic resin, and became widely used as a picture varnish during the nineteenth century (Ruhemann, 1968, p. 272). F. Lucanus (1832), a German apothecary, first described the use and the properties of dammar in one of his paper in 1829 “Dammar resin – concerning the properties, chemical behaviour, and technical application” (Feller and Whitmore, 2002, p. 27). This apothecary was the first to use dammar varnish on European easel paintings (Nicolaus, 1999, p. 315). This resin is obtained from the trunk of a specific family of trees (*Dipterocarpaceae*) (Feller, 1958; Gettens and Stout, 1966, pp. 16, 51; Mayer, 1991, p. 221). The dry secretion appeared in the European market in transparent, brittle, odourless pieces (Gettens and Stout, 1966, p. 16) and it was commonly dissolved in turpentine oil or petroleum fractions (Feller, 1958; Mayer, 1991, p. 221; Nicolaus, 1999, p. 315). According to Mayer (1991, pp. 221–222), in order to prepare dammar varnishes, ethanol should not be used, because it does not lead to complete solubilisation of the resin. Gettens and Stout (1966) described the dammar film as colourlessness. Its simple and obvious application made this varnish resin very popular among artists, thereby acknowledging dammar as one of the best varnishes for pictures (Toch, 1934; Thomson, 1957; Gettens and Stout, 1966, p. 16).

Since the nineteenth century, it has been possible to perceive a change in both techniques and materials commonly used for paintings (e.g., varnishes and finishing surface appearance). Technical innovation and industrialisation broadened the materials available to artists (Neher, 1936; Feller and Whitmore, 2002, p. 27). According to Ruhemann (1931, 1968, p. 277), in the nineteenth, and after, at the beginning of the twentieth century, varnishes were mainly applied by using brushes or by dabbing the surface with clothes brushes while the coating film was getting sticky. In this way, by brushing it was possible to obtain an even and glossy or by using clothes a semi-glossy finishing. The application of varnishes by

---

<sup>4</sup> According to Feller, the term ‘hard’ is usually used for resins which have to be thermally processed (Feller, 1958).

using spray guns came along when the art industry was able to use availability of electric compressors (Ruhemann, 1931, 1968, p. 277).

During the second half of the twentieth century, conservators realised that traditional soft-resin varnishes did not last indefinitely (Chiantore and Rava, 2012, p. 150; Hackney, 2013). Indeed, after a few decades, these varnishes yellowed and became brittle, losing their most important characteristic: their transparency (Hackney, 2013). The most significant factor for the degradation of natural varnishes and their yellowing was found to be related to the absorption of the UV wavelengths in the ambient light (Feller, 1958, 1994; Feller and Curran, 1975; Chiantore and Rava, 2012, p. 143). Thomson (1957) stressed in his research that the exposure of the coating films to the UV light could trigger the same problem. Therefore, art conservators, mainly in the USA, started to experiment in the use of synthetic resins (Nicolaus, 1999, pp. 312, 318).

#### 2.2.1.2 *Synthetic resins*

The introduction of these new synthetic materials revolutionised the range of available material commonly employed by artists and art conservators (later). Eventually, artists manufacturers and distributors started replacing natural resins, which had been standard as essential ingredients of varnishes, with products of considerably varied compositions (Mayer, 1991, pp. 232–234). The aim, in the use of these new group of materials, was to reproduce the same optical effect achieved through the application of natural varnishes as finishing layers but to avoid the drawback recognised in use on natural resin varnishes. Additionally, art conservators could dissolve and readily remove these new coatings with non-polar solvents or solvents with low polarity even after long-term exposures and observed better stability of these varnishes even under substantial environmental fluctuations (Nicolaus, 1999, p. 318). Nonetheless, these new synthetic resins were less efficient in filtering the UV rays of daylight and fluorescent light when compared with natural resins (Gettens and Stout, 1966, p. 67; Ruhemann, 1968, p. 274). Early in the exploration of the synthetic resins, it became clear that these new varnishes also had limitations (Nicolaus, 1999, p. 312). Even though they could form a more stable coatings, questions arose concerning their negative aspects (Bradford, 1996), which were identifiable in their: i) possible long-term non-removability as a result of

crosslinking of their molecules; ii) loss of elasticity that would make them very brittle and easily detachable from the paint layer; iii) unfavourable glass transition temperature ( $T_g$ ) leading to hard dried varnish films at room temperature, or remaining soft and sticky leading to films prone to trap airborne volatile particles, soils and dust (Nicolaus, 1999, p. 312).

In 1928, the first synthetic polymer to be mentioned as a potential picture varnish in the conservation literature was the *poly(vinyl acetate)* (PVAc) (Gettens, 1935; Mayer, 1991, p. 232; Nicolaus, 1999, p. 319; Chiantore and Rava, 2012, p. 150). During the International Council of Museum in Rome in 1930, G. Stout (former Head of the Laboratories of the Fogg Museum in Harvard and then Director of the Isabella Stewart Gardner Museum in Boston) described the properties of PVAc<sup>5</sup>, and in 1937 he suggested to use this resin as a varnish for paintings (Stout and Cross, 1937). According to Feller (1961), PVAc proved to be stable, with no formation of crosslinking in both natural and accelerated light aged samples of paintings, and remained in excellent condition, retaining its original solubility in organic solvents mixtures (Feller, 1961). However, this polymer showed to have various drawbacks. It did not provide sufficient colour saturation (Chiantore and Rava, 2012, p. 150), and it was soluble only in ‘strong’ organic solvents like toluene, which solubilises paint layers too (Ruhemann, 1968, p. 274). Furthermore, the  $T_g$  (31.4 °C – [Sato and Okaya, 1992]) of the PVAc was as low as the room temperature range (Nicolaus, 1999, p. 319), leading to the formation of soft and sticky coating layers and a rapid darkening in the appearance of the artwork (Chiantore and Rava, 2012, p. 150).

As early as 1843, Redtenbacher (1843) described the preparation of a new acidic substance obtained by the chemical oxidation of acrolein with air. Redtenbacher named this substance acrylic acid (Neher, 1936). But, only in the early 1940s, this new film-forming material started to be used as a material for picture varnish. Otto Röhm of Darmstadt, chemist and entrepreneur, was one of the first who focused his interest in the identification and industrial development of

---

<sup>5</sup> As reported by Ruhemann (1968, p. 274), George Stout showed to the participants of the international conference a material that looked like glass, and he stated: “*This is probably the varnish of the future*”.

acrylic acid derivatives, commercially known as Acryloids (Röhm, 1901; Neher, 1936). He was co-founder, and long-term co-owner and director of Röhm & Haas (The Corporate Archives of Evonik) where the production of acrylic esters began. Polymers of iso-butyl methacrylate (PiBMA) (Lucite 45 also known as Elvacite 2045) and n-butyl methacrylate (PnBMA) (Lucite 44 also known as Elvacite 2044) were the first two coatings introduced to the art market (Feller, Jones and Stolow, 1985; Chiantore and Rava, 2012, p. 150). Initial testing began in the early 1930s at the Fogg Art Museum, Harvard University (Nicolaus, 1999, p. 319). PiBMA and PnBMA varnishes had a high molecular weight and they could be dissolved in hydrocarbon solvents (the latter considered more compatible with the underlying paint layers) (Chiantore and Rava, 2012, p. 150) and showed: i) resistance to yellowing, ii) solubility in hydrocarbon solvents and iii) flexibility. In particular, iBMA coatings had a significantly high  $T_g$  (53 °C – [Geng *et al.*, 2017]) which prevented dirt particles from retaining on their surface (Horie, 2010). However, it was soon evident that these varnishes turned into partially insoluble materials a few years after application, thus raising the problem of their removal (Nicolaus, 1999, p. 319; Chiantore and Rava, 2012, p. 150). Studies revealed that the insolubility of these materials was due to the formation of crosslinks under intense UV light exposure in museum, whilst their transparency was almost unchanged (Thomson, 1957). This finding was in part responsible for the cessation of the use of methacrylate varnishes at the National Gallery in London (Thomson, 1961). At the end of the 1960s, a poly-isobutyl methacrylate (PiBMA) homopolymer (Paraloid B67 also known as Acryloid in the United States) with a lower viscosity grade was gradually replaced as a final varnish (Feller, 1972). Paraloid B67 was recommended as the final varnish, despite its instability (Nicolaus, 1999, p. 319).

In the 1950s, the viscosity of solutions in which varnishes were prepared was identified as a crucial factor (Chiantore and Rava, 2012, p. 150). The use of varnishes with low molecular weight (LMW) and low viscosity seemed to be an excellent alternative to the use of natural resins due to their comparable molecular weight distribution (Berns and de la Rie, 2003c; Maines and de la Rie, 2005; Gheno, 2017). Furthermore, LMW varnishes could improve the saturation of the paint colours, since these resins could create smooth films over rough paint surfaces (de la Rie, 1987; Berns and de la Rie, 2003b; Berns and de la Rie, 2003c). Werner

(Werner, 1952) and Thomson (Thomson, 1957) were among those involved in developing a new class of resins known as ketone resins which were used as a coating film for art conservation (Nicolaus, 1999, p. 320) since the 1960s (Nicolaus, 1999, p. 319). The ketone resins included the AW-2, a *polycyclohexanone* resin patented in Germany in 1930 (Bradford, 1996), produced by BASF in 1950 and manufactured until 1967. AW-2 is a condensation product of cyclohexanone and methyl cyclohexanone (de la Rie and Shedrinsky, 1989). From studies published by Thomson (1957), the AW-2 resin yellowed but to a lesser degree than natural varnishes. Also, AW-2 films tended to turn matte in some areas due to the formation of micro-wrinkling (Brommelle, 1956; Ruhemann, 1968, p. 275). Therefore, Howards Ltd, a chemical manufacturers near London, launched on the market a more stable form of ketone resin, named MS2A (Ruhemann, 1968, p. 275). MS2A was officially introduced in 1961 and it is composed of *cyclohexanone* and *methylcyclohexanone* (Routledge, 2000; Doménech-Carbó *et al.*, 2008).

The MS2A resin at the time of its launch on the market was considered to be the most promising resin for varnishing (Ruhemann, 1968, p. 276). It was regarded as a very similar resin to dammar for its varnishing and handling properties. Moreover, MS2A varnishes darkened slower than mastic and dammar varnishes (Ruhemann, 1968, p. 276). In 1967, BASF discontinued AW-2 and replaced the latter with Ketone Resin N (de la Rie and Shedrinsky, 1989), a homopolymer formed from the condensation of *cyclohexanone* only (Mills and White, 1999, pp. 118–119). Ketone Resin N was discontinued by BASF in 1982 and replaced by Laropal K80, a condensation product from *cyclohexanone* (de la Rie and Shedrinsky, 1989). Nonetheless, the first long-term tests manifested that poly-cyclohexanone resin was highly susceptible to light-induced oxidation (Bradford, 1996), becoming hard and inelastic over time. Due to the oxidation process, poly-cyclohexanone resins showed the formation of a yellow hue, although to a lesser extent than natural resins (Masschelein-Kleiner, 1984; Nicolaus, 1999, p. 320). Additionally, as time passed, art conservators became aware that with the ageing, these coating films would often lose their elasticity becoming detached from the paint surface by merely applying slight pressure on it. This varnish could also be chipped away with the use of a scalpel (Masschelein-Kleiner, 1984; Nicolaus, 1999, p. 320).

Lastly, in 1990, in the United States, two new class of varnishes were introduced into the market. One of them, is a hydrogenated hydrocarbon (HHC) resin entirely free of double bond or reactive functional group, commercially known as Regalrez. The other, manufactured by BASF, is a condensation product of urea and aliphatic aldehydes, formaldehyde and iso-butyraldehyde, commercially known as Laropal A81 (de la Rie and Shedrinsky, 1989; Piena, 2001; Chiantore and Rava, 2012, p. 152; Farmakalidis *et al.*, 2016; Gheno, 2017).

### **2.3 LITERATURE REVIEW II: On the cleaning of paintings - varnish removal**

Cleaning of paintings has been thoroughly examined and endlessly debated over the years (Stoner and Rushfield, 2012, p. 742). The practice of removing the discoloured varnish layer dates from at least the seventeenth century (Kirsh and Levenson, 2002, p. 214). In 1968, Ruhemann in his book *The cleaning of Paintings* reported the concern of Huyghe (Curator of Paintings and Drawings at the Louvre) and Brandi (Head of the Istituto Centrale del Restauro in Rome) about the cleaning procedure carried out on paintings, remarking that “What has been removed cannot be replaced; what has been left can be removed later” (Ruhemann, 1968, p. 80). Moreover, Philippot (Director of the International Centre for the Study of the preservation and the Restoration of Cultural Property – ICCROM – in Rome) reminded that (Bomford and Leonard, 2004, p. 392):

“No restoration could ever hope to re-establish the original state of a painting. It can only reveal the present state of the original materials. Even if restoration could determine the original state, it would still be impossible to abolish the second historicity of the work, the span of time it has crossed to appear before us”.

The cleaning procedure is considered the most critical, challenging and delicate operation for art conservators among all the standard procedures in the conservation of paintings (Ruhemann, 1968, p. 170; Nicolaus, 1999, p. 356; Chiantore and Rava, 2012, p. 122). The stereotypical cleaning practice is related to the possibility of not only removing accumulated grime but also the thin or removing of any non-original materials from the surface of paintings artworks (Stoner and Rushfield, 2012, pp. 768, 789; Mecklenburg, Charola and Koestler,

2013, p. 7; Watson and Burnstock, 2013) following the ancient Latin motto “*similia similibus solvuntur*” (like dissolves like) (Baglioni and Chelazzi, 2013, p. 182). Varnish removal is considered an irreversible process, which could lead to the risk of permanently modifying the cultural object (Ruhemann, 1968, p. 182; Chiantore and Rava, 2012, p. 122) or distort the artist’s intention (Maclaren and Werner, 1950). Thus, it must be performed after the complete and absolute knowledge of the technical history of the painting and the theoretical framework that defines which materials should be removed and their motivation (Ruhemann, 1968, p. 182; Chiantore and Rava, 2012, p. 122).

In his book Ruhemann divided varnish removal into three different stages: i) removal of surface dirt; ii) complete removal of varnish and iii) removal of retouching; (Ruhemann, 1968, pp. 189–206), only the first two points will be taken into account in this study. Surface cleaning could easily facilitate the ‘reading’ of paintings. Darkening may be attributable to the accumulation of soot and dust on the top side of the varnish film and easily distinguished on the light part of the paintings. Furthermore, according to Ruhemann “it is always imperative to remove the surface dirt before attempting the actual varnish removal” (Ruhemann, 1968, p. 190), this is well known in the conservation field, and Ruhemann himself stresses this point.

The second point focused on the complete removal of the varnish films. The risks associated with the use of solvents, during the process of varnish removal, were identified for the first time in the middle of the nineteenth century (Horsin-Déon, 1852; Nicolaus, 1999, p. 312). In 1968, Ruhemann suggested the use of ‘strong’ solvents, such as alcohol, acetone diluted in turpentine or in petroleum solvent such as white spirit, to solubilise aged varnishes (Ruhemann, 1968, p. 190), which were no longer removable with the use of ‘gentle’ (nonpolar) solvents, such as turpentine or white spirit (Nicolaus, 1999, p. 312). Furthermore, he emphasised the impossibility of providing ‘safe’ solvent mixtures or methodologies as a general rule for paintings, stressing the concept that “Every case is different, and often different areas in the same painting react differently” (Ruhemann, 1968, p. 190). Ruhemann acknowledges that AW-2 and MS2 synthetic varnishes could dissolve in white spirit; instead, by using alcohol and acetone, only weak effects were detected. Furthermore, Ruhemann pointed out that some paintings from the later

eighteenth, early nineteenth century, and most of the modern ones were painted with mixtures of soft resins (whose chemical composition was the same as modern varnishes). These similarities in chemical composition led to making the paint layers easily dissolvable during the cleaning procedure (Ruhemann, 1968, p. 191). Later in the 1980s when the issue of cleaning paintings continued to arise debates among conservators, Gerry Hedley (paintings conservator and lecturer at the Courtauld Institute), in his published lectures '*On Humanism, Aesthetics and the Cleaning of Paintings*' (Stoner and Rushfield, 2012, p. 743), proposed three different approaches to the problem of cleaning paintings, divided as 'complete', 'partial' and 'selective' cleaning (Bomford and Leonard, 2004, p. 413). i) The 'complete' cleaning intended to remove the varnish film from the paint layers entirely. As reported by Hedley, this approach was generally used by the National Gallery of London, but it was also used in North America and Ruhemann was one of the most influential conservators in favour of this decision (Bomford and Leonard, 2004, p. 414). The 'partial' cleaning aimed to uniformly thin the varnish so that the lowest layers of the original varnish would remain on the surface of the painting. This approach was used, according to the author, mainly in Europe and widely used at the Louvre Museum in Paris (Bergeon, 1968). The third and last approach was the 'selective' cleaning. This typology of cleaning consisted of a differential removal of the varnish coating in order to create a 'pictorial cleaning' and achieve a visual balance on the painting. This cleaning was used in Europe as well as at the Metropolitan Museum of Fine Art of New York (Bomford and Leonard, 2004, p. 414).

Since the second half of the twentieth century, research has been carried out to determine whether varnishes could be safely removed from painted surfaces (Stoner and Rushfield, 2012, p. 370). Several studies on the removal of varnishes applied to paintings, however, provided evidence to be an extremely complex process, due to the deep penetration of varnish films into the underlying paint layers (Chiantore and Rava, 2012, p. 149; Watson and Burnstock, 2013). Already in 1902, Pettenkofer (a chemist specialised in medical chemistry was asked to review the cleaning and restoration of paintings at the Alte Pinakothek in Munich) pointed out that resin varnishes did not merely remain on top of a paint film. Instead, they penetrated into the paint layers, complicating the cleaning process (Pettenkofer,

1902; Bomford and Leonard, 2004, p. 339). In 1999 the concept of reversibility started to be critically reviewed, culminating in its full confutation during an International Congress held at the British Museum titled ‘*Reversibility: does it exist?*’ (Oddy, 1999; Oddy and Carroll, 1999).

Furthermore, some of the practical problems for varnish removal on paintings could arise due to the similarity in solubilities of the materials used to create the original artwork with those used by art conservators. Cleaning practices, in fact, frequently requires the use of materials which exploit definite differences in chemistry, age, or arrangements inside the materials (Stoner and Rushfield, 2012, p. 768). With regard to treatment on modern and contemporary paintings, cleaning can be considered a complicated procedure due to the selective sensitivity reaction of the paint layer to solvents cleaning reagents and mechanical methods (Feller, Jones and Stolow, 1985; Watson and Burnstock, 2013).

### 2.3.1 *Wet and Dry cleaning methodologies*

The removal of discoloured varnish layers is often referred to by the common term ‘cleaning’ in the UK and USA, whereas the terms ‘varnish removal’, ‘reduction’ or ‘de-varnishing’ have been commonly used in France and Italy, etc. In general, the cleaning of paintings involves the removal of contaminated layers or a discoloured varnish from the surface of an oil-and-pigment film(s) (Stoner and Rushfield, 2012, p. 517). Over the long term, the stability of the resins used for picture varnishes has been found to significantly disturbed by light absorption, favouring chemical reactions that could be controlled or inhibited (Baglioni and Chelazzi, 2013, p. 99). This change is due to photo-oxidation induced reactions, visibly acknowledged with an increase in yellow hue of the varnishes (Chiantore and Rava, 2012, p. 150; Stoner and Rushfield, 2012, p. 789). The thinning or the complete removal of the photo-oxidised, darkened and yellowed varnishes by skilled conservators is required to preserve the appearance of paintings and to allow a better understanding of the original colours of the paint layers (Baglioni and Chelazzi, 2013, p. 99). Several studies have been published, and new materials and systems have been developed to achieve more controllable and selective cleaning (Baglioni and Chelazzi, 2013, p. 122). The cleaning procedure can be classified into two main categories: wet and dry cleaning (Chiantore and Rava, 2012, p. 123;

Baglioni and Chelazzi, 2013, p. 126). More specifically, the paint layer surface could be treated by means of solvents or aqueous mixtures (wet cleaning) and mechanical tools (dry cleaning) (Nicolaus, 1999, p. 351). The concepts of ‘controllability’ and ‘selectivity’ can be considered critical points in all the cleaning procedures. Overall, they should leave no residual material behind on the surface (Stoner and Rushfield, 2012, pp. 768, 769).

### 2.3.1.1 Wet cleaning

Since antiquity ‘Surface cleaning’ has been practised to reduce or remove accumulated soils on paint surfaces (Stoner and Rushfield, 2012, p. 501) as well as solvents and blends were employed to swell and dissolve deteriorated varnishes to facilitate their removal (Stoner and Rushfield, 2012, p. 789). The use of various solvents can result in significant chemical and physical modifications into the underlying paints, causing undesired effects of varnish dissolution, paint swelling, solvent diffusion, leaching and chemical reactions within the paint layers (Baglioni and Chelazzi, 2013, p. 126; Baij *et al.*, 2020). The decision in using neat solvents or solvent blends and the correct application time is crucial in the process of varnish removal (Baglioni and Chelazzi, 2013, p. 126; Baij *et al.*, 2020) and it is fundamental to determine the most suitable solvent which allows solubilisation of the varnish without altering the paint layers underneath (Baglioni and Chelazzi, 2013, p. 126). In order to predict the interaction of the varnish film upon the application of a liquid solvent, the most commonly used approach is the one proposed by Hansen (1967, 2007). According to Hansen, the solubility parameter of a solvent could be considered the sum of three contributions: dispersion ( $\delta_d$ ), polarity ( $\delta_p$ ) and hydrogen bonding ( $\delta_h$ ) (Hansen, 1967, 2007; Hansen and Beerbower, 1971; Hansen and Just, 2001). From Hansen’s parameters, it is possible to derive the reduced solubility parameters due to hydrogen bonds ( $f_h$ ), to polar forces ( $f_p$ ), and to dispersion forces ( $f_d$ ). The Hansen’s parameters formed the basis for the Teas chart (Teas, 1968). These parameters are calculated as the percentage of the different forces that contribute to the overall interaction between the solvent molecules and their sum total is 100 ( $f_d + f_p + f_h = 100$ ) (Horie, 2010; Baglioni and Chelazzi, 2013, p. 188; Baij *et al.*, 2020). In the Teas chart the percentage of the Hansen parameters are plotted on a single planar graph. Thus, each solvent and

solvent blends can be univocally identified by numerical parameters and

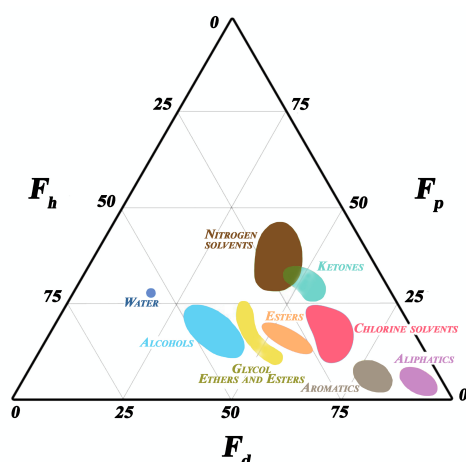


Figure 2.3 – Teas chart showing the solubility parameters of neutral organic solvents customarily used in the conservation field (Figure adapted from Baglioni and Chelazzi, 2013, p. 188).

graphically represented in a triangular diagram (Figure 2.3) (Teas, 1968; Coladonato and Scarpitti, 2005; Horie, 2010; Bajj *et al.*, 2020). The same is true for different substances that need to be removed. Following the idea that like dissolves like, the more similar these parameters are, the more the substances are mutually soluble (Masschelein-Kleiner, 1994; Talarico and Coladonato, 1997; Cremonesi and Signorini, 2012, pp. 171–172; Baglioni and Chelazzi, 2013, p. 188; Phenix, 2013; Fink, 2017;

Fuster-López *et al.*, 2017).

Since the 1990s, a new approach to the varnish removal on paintings as marked its entrance among the methodologies routinely adopted by conservators. The use of aqueous methods responded to the practical concerns of art professionals regarding the drawbacks in the use of solvent solutions and their retention in the art materials. This alternative cleaning approach has ensured the possibility of reducing toxicity, targeting certain soils, controlling the cleaning processes, and providing more safety for the underlying paint film. Wolders was one of the first pioneers to carry out research in this field (Wolbers, Sterman and Stavroudis, 1990; Byrne, 1991; Wolbers, 2000, p. 1; Baglioni and Chelazzi, 2013, p. 769). In his book ‘*Cleaning painted surfaces, aqueous Methods*’, referring to the cleaning of varnish surfaces, he reported that “water-based or water-containing preparations can and do form an impressive array of tools for the conservators” (Wolbers, 2000, p. 1). The use of water as an agent, combined with various additives, allows the thinning or the removal of varnish films. More specifically, water alone as a polar solvent (high hydrogen bonding and dipolar aspects) owns an intrinsic solvent power towards ionic compounds like salts, as well as film-forming materials like proteinaceous materials (e.g. animal glue) and polysaccharide substances (e.g. vegetable gums) (Cremonesi, 2011, p. 1; Baglioni and Chelazzi, 2013, p. 770). If the use of neat

water does not achieve its solubilisation power, conservators can modify the chemistry and behaviour of the water giving to it new ‘properties’ thereby increasing the number of materials that can be treated. Specifically, weak acids, bases and salts, chelating agents, surfactants and enzymes can be added. For additional discussion see Wolbers (2000), Cremonesi (2011, pp. 5–7), Cremonesi and Signorini (2012, pp. 30–41), Baglioni and Chelazzi (2013, pp. 770–780) and Baij *et al.* (2020).

### 2.3.1.2 Dry cleaning

In the nineteenth century, Lucanus (1832) was the first to speak about the use of mastic powder for the mechanical removal of the varnish layer(s). Pressure was applied with the fingers, using circular movements, making the mastic powder act like sandpaper on the painting surface (Nicolaus, 1999, p. 368). Of course, this specific technique must not be included among the standard methods employed nowadays by art conservators to clean varnished paintings. A different approach for the removal of unwanted materials, such as deteriorated varnishes, overpaints and fillings, is carried out using scalpels. This risky procedure is carried out either on layers previously swollen with solvents or directly on the dry layer with the scalpel using stereomicroscopes and goggles. During the international conference “*New Insights into the Cleaning of Paintings*”, which was held at the Universidad Politecnica de Valencia in Spain, Daudin-Schotte and co-authors (2013) presented the results of the use of dry-cleaning materials on sensitive surfaces. As reported by the authors, the dry surface cleaning could be carried out by using a broad range of materials such as sponges, erasers, malleable materials, and microfiber cloths. Nonetheless, not enough evidence had been published on the nature and potentially detrimental effects of the use of these materials on the surface of paintings (Wehlte, 1971; Schorbach, 2009; Daudin-Schotte *et al.*, 2013). Therefore, a project carried out by the Cultural Heritage Agency of the Netherlands and some institutions in the UK aimed to achieve a better understanding of the properties of dry cleaning (RCE 2006-2009 dry cleaning research project) (Learner *et al.*, 2007; Morrison *et al.*, 2007). Based on the conclusions obtained from this research project, a gradual test approach was presented in order to use these malleable materials in the safest way possible (Daudin-Schotte *et al.*, 2013).

Among the dry-cleaning approaches, laser cleaning has become the newest tool in the conservation of easel paintings, encouraging applications due to its controllability and selectivity in the removal of unwanted materials.

#### **2.4 LITERATURE REVIEW III: On the laser cleaning treatments for cultural heritage**

Along with established systems and methodologies (e.g. the use of organic solvents, aqueous solutions with surfactants, chelating agents, enzymes, weak and strong acids and bases, etc.) (Feller, Jones and Stolow, 1985; Wolbers, 2000; Phenix and Sutherland, 2001; Cremonesi and Signorini, 2012), there has been a steady increase in studies focusing on the application of lasers in the cultural heritage.

The use of lasers in the conservation of cultural heritage was proposed for the first time by Asmus and co-workers (1973) while examining the possibilities of in situ holographic interferometry of a Venetian marble statue ‘*Madonna con Bambino*’ by Nino Pisano using a pulsed ruby laser (690 nm). Asmus and co-authors (Asmus *et al.*, 1973; Lazzarini, Marchesini and Asmus, 1973; Asmus, Seracini and Zetler, 1976) discovered that the dark incrustations on stone artefacts were easily detached, bringing about no evident damage on the underlying stone and exposing the patina of the marble. Moreover, Asmus and co-workers explored the possibility of using the ruby laser for cleaning of stained glass, frescoes, leather, and other materials (Asmus, 1975; Asmus, Westlake and Newton, 1975; Vitkus and Asmus, 1976). During the late ‘70s, Asmus and Lazzarini also investigated the use of pulsed *Neodymium-doped Yttrium Aluminium Garnet* (Nd: YAG) lasers (1060 nm) showing promising results and stressing the fact that the laser tools are by no means a ‘*completely universal system*’. The suitability of a certain type of laser for a certain object, considering the appropriate wavelength and pulse durations, is a case-by-case basis scenario (Lazzarini and Asmus, 1973; Lazzarini, Marchesini and Asmus, 1973; Asmus, Murphy and Munk, 1974). During the ‘80s, the technological advancement of lasers spiked significantly even though their price was still unaffordable for the conservation field. The situation changed in the 1990s. As reported by Teppo and Calcagno (1995) affordable Nd:YAG laser systems became available in Europe, which raised the interest of art conservators.

Moreover, the establishment of the international conference called Lasers in the Conservation of Artworks (LACONA) (Kautek *et al.*, 1997), held for the first time in Heraklion, Greece (1995), represented an essential step for debates on the use of the laser in the conservation field (Siano, 2008, p. 3; Teppo, 2020). In particular, the LACONA conference aims to investigate the laser cleaning processes on various materials of cultural objects (e.g., stones, metals, paintings, paper, parchment, etc.) and evaluate the laser-material interactions. The first LACONA conference had a significant impact on bringing the art conservation community closer to the new laser technology. Applicazioni Laser per il Restauro (APLAR) is a more recent international conference established alongside the aforementioned. The APLAR conference, which took place for the first time in Vicenza in 2007, has been wholly dedicated to the application of laser techniques in the conservation field under a more practical point of view.

Several research groups, including that at the *Laboratoire de Recherche de Monuments Historiques* in France, the Foundation of Research and Technology – Hellas (FORTH), in Greece, both the *Conservation Centre* at National Museums Liverpool, and the University of Loughborough in the U.K., Opificio delle Pietre Dure (OPD), Istituto Centrale per la Conservazione ed il Restauro (ISCR) and Conservation and Restoration Centre La Venaria Reale in Italy, led fundamental research on the use of the laser for the treatment of marble sculpture, limestone, terracotta, wood, metal, and other materials (Verges-Belmin, Pichot and Oriol, 1993; Cooper, Emmony and Larson, 1995; Cooper and Larson, 1996; Verges-Belmin, 1997; Siano, 2008).

#### 2.4.1 Brief history of the use of laser in paintings conservation

In general, only pulsed lasers are employed in the cleaning of artworks and historical objects (Siano, 2008). The use of lasers for the cleaning of painted artworks is a demanding approach due to the high sensitivity of paint layers to lasers of different wavelengths (Scholten *et al.*, 2000, 2005; Striber, Jovanović and Jovanović, 2017). In fact, the laser beam interaction with the surface of the paintings constituent materials may result in irreversible unwanted changes (Castillejo *et al.*, 2003). Despite several promising publications with a systematic

investigation on the effects of the laser's interaction on pigments, binders and coatings, the laser technology was not accepted by many conservators, and it was not considered among the day-to-day conventional conservation treatments (Scholten *et al.*, 2000; Striber, Jovanović and Jovanović, 2017).

During the late 1980s, the Foundation of Research and Technology – Hellas (FORTH), in Greece, led a research project on the cleaning of painted works of art. A procedure using short-pulsed *krypton fluoride* (KrF) excimer laser (248 nm) was developed to clean paintings (Hontzopoulos, Fotakis and Doulgeridis, 1993). Nevertheless, this laser system proved to be expensive, immobile and therefore not convenient to be commercialised, making the system inaccessible (Scholten *et al.*, 2000; Scholten and Schipper, 2001; Striber, Jovanović and Jovanović, 2017). The 213 nm and 355 nm Nd:YAG lasers have given significant results for the use of this lasers to paintings' conservation (Scholten *et al.*, 2000; Hildenhausen and Dickmann, 2003; Siano *et al.*, 2012; Ciofini *et al.*, 2016; Striber, Jovanović and Jovanović, 2017). The first people who used a pulsed *Erbium-doped Yttrium Aluminium Garnet* (Er:YAG) laser (2940 nm) for the irradiation of painted surfaces were Adele de Cruz and co-workers (De Cruz, Hauger and Wolbarsht, 1999; De Cruz, Wolbarsht and Hauger, 2000a, 2000b; Andreotti, 2007). They developed a method to treat painted surfaces which were previously considered to be untreatable. Regardless of evidence reported during international conferences and workshops in the use of the Er:YAG laser (De Cruz, Hauger and Wolbarsht, 1999; De Cruz, Wolbarsht and Hauger, 2000a, 2000b; Andreotti, *et al.*, 2007; Pereira-Pardo and Korenberg, 2018; Teppo, 2020) there were two patents (Wolbarsht and De Cruz, 1999; De Cruz and Wolbarsht, 2006) that limited the access to this technology and delayed the progress in the investigation of the interaction of Er:YAG lasers with paintings (Teppo, 2020). Subsequent licensing agreements, obtained in 2013 and 2014 and the expiry of the patents improved access to this laser technology, with the launching onto the market of three new Er:YAG lasers available from the companies El.En. (Light Brush 2), Lynton Laser (Compact Phoenix) and Fotona (Fidelis, Dualis, Dynamis) (Teppo, 2020). A Fotona Fidelis<sup>XS</sup> Er:YAG laser was made available at the Conservation Science Laboratory at Northumbria University in 2016 and was employed for the research described in this thesis.

---

Below is a brief history of the scientific and practical advancements in the use of lasers as new cleaning tools for paintings and their constituent material(s), presented in a chronological order.

The first paper reporting the prospect of using lasers for the cleaning of easel paintings is an unpublished report dated 1981 from the Canadian Conservation Institute (Carlyle, 1981). The report described pilot tests using a XeCl excimer laser and a TE-290 laser to remove dirt and aged discoloured varnishes from paintings.

In 1993, a study was published reporting preliminary work on the use of nanosecond excimer lasers for the removal of unwanted layers from the surface of easel paintings. **Hontzopoulos *et al.* (1993)** advanced the idea to use UV laser light as a tool to induce ablation of aged varnishes on painted works of art, with the possibility to remove overpainting. In addition, they explored the possibility of online monitoring of art objects during laser ablation with digital image processing and reflectography. The authors proposed a study to identify the optimal laser parameters for the cleaning procedure due to the direct dependence of the selected laser parameters with the physicochemical characteristics of the materials composing art objects (Hontzopoulos, Fotakis and Doulgeridis, 1993). In the same year, **Morgan (1993)** published a paper referring that excimer lasers had been satisfactorily employed for the cleaning of fourteenth century icons.

**Fotakis and co-workers (1995)** published preliminary experimental results carried out at the FORTH. This paper described the prospect in the use of a KrF laser (248 nm and 15 ns pulse duration [ $\tau_L$ ]) to clean the varnish surface and to facilitate overpainting removal as well as to monitor the removal of the material. Thick layers between 20 to 300  $\mu\text{m}$  were removed using the KrF excimer laser. Excimer lasers provided a selective laser ablation process and allowed to leave, a protective thin varnish layer on the irradiated painted area (Zafropoulos and Fotakis, 1998).

In October 1995, the first edition of the international conference LACONA, held at FORTH, **Zergioti *et al.* (1997)** in collaboration with conservators from the National Gallery in Athens, demonstrated their results of paintings treated with excimer lasers. Laser-Induced Breakdown Spectroscopy (LIBS) and reflectography

analysis provided online monitoring of the laser interaction with the matter. Thus, the authors guaranteed the safety of the original artwork materials during the laser cleaning procedure (Zergioti *et al.*, 1997).

In 1998, **Cooper (1998)** published the first book exclusively dedicated to laser cleaning of artworks with a chapter entirely dedicated to laser in the conservation of painted artwork (Zafiropulos and Fotakis, 1998). **Zafiropulos and Fotakis** emphasised the importance of maintaining a thin layer of aged varnish onto the painted surface to prevent the excess of UV photons from interacting with the underlying paint layer(s). The authors (1998) referred that the possible penetration of UV photons could result in devastating effects, like medium ablation, pigment desorption and paint discolouration.

Between 1999 and 2001, research institutes, industrial and conservation companies from Germany, Greece, Ireland, the Netherlands, Portugal and Spain collaborate on an EU project “*Advanced workstation for controlled laser cleaning of artworks*” (ENV4-CT98-0787) with the aim to study laser cleaning of paintings using excimer lasers (Scholten *et al.*, 2000). Engineers and laser specialists at FORTH successfully exploited the prospects of a prototype excimer laser set-up to selectively ablate aged varnishes or to remove overpaints from old paintings (Fotakis *et al.*, 1997; Zergioti *et al.*, 1997). Furthermore, researchers at FORTH established a method to monitor the laser cleaning procedure with Laser-induced Breakdown Spectroscopy (LIBS) which was operated for online monitoring of the laser irradiation procedure (Anglos *et al.*, 1996).

At that time, **De Cruz and Trokel** presented some preliminary tests using a prototype Er:YAG (2940 nm) laser source (De Cruz *et al.* 1999 referred to an unpublished report). In 1999, De Cruz and co-workers (1999), demonstrated that it was possible, using an Er:YAG (2940 nm) laser, to remove unwanted materials from paintings when solvent applications were unable to accomplish that problem (Teppo, 2020). A pulsed Er:YAG laser (model *Conservator 2940*)<sup>6</sup> was provided by Schwartz Electro-Optics (SEO) of Orlando, FL (De Cruz, Hauger and

---

6 The Er:YAG laser had a 1 mm beam diameter delivered through a hollow glass waveguide, a minimum fluence of 1.3 J/cm<sup>2</sup> and emitting pulses of approximately 250 μs, each consisting of a train of about ten 1-2 μs micro pulses (Teppo, 2020).

Wolbarsht, 1999). According to the authors, the portable Er:YAG laser could safely and effectively remove encrustations from paint surfaces without altering the original material (De Cruz, Hauger and Wolbarsht, 1999). The portable Conservator 2940 system was tested on a late-fourteenth century tempera painting on wood ‘*Praying Madonna*’ of unknown artist with water gilding. The entire artwork was covered with a thick shellac varnish layer and particles of various salts. As described by **De Cruz *et al.* (2000a)**, half of the painting was irradiated with a single laser pass with energy of 10 mJ and repetition rate of 10 Hz. The authors established that the absorbing properties of the material, which needed to be removed, did not necessitate to be pre-wetted with containing OH-groups due to the presence of animal glue (‘*colletta*’) as consolidants, which is particularly rich in hydroxyl groups. In fact, the dominating mechanism of Er:YAG laser cleaning is directly related to the maximum absorption of the 2940 nm laser wavelength from the hydroxides in the irradiated surface. Furthermore, De Cruz and co-authors (De Cruz, Wolbarsht and Hauger, 2000a) found that after laser irradiation the shellac varnish layer could be removed with a swab loaded in ethanol. In the same year, De Cruz *et al.* (2000a) submitted a paper to the international conference LACONA III, reporting that heat diffusion on the laser-irradiated area could be minimised when the surface is pre-wetted with small amounts of water or OH-rich solvents. Moreover, the authors described that for all the tests, a microscope coverslip was placed on the painting to prevent the ejected materials from clogging the output port of the laser beam. Laser cleaning tests were performed on a seventeenth century Italian oil on canvas from the circle of Guido Reni, ‘*Beatrice Cenci*’. In order to carry out the laser cleaning tests, the paint surface, covered with a synthetic resin, was pre-wetted with isopropyl alcohol prior to irradiation with a single Er:YAG laser pass at 12 mJ (De Cruz, Wolbarsht and Hauger, 2000a).

During the same LACONA III conference, **Athanassiou and co-authors (2000)** presented their findings on the effects of a KrF excimer laser (248 nm,  $\tau_L$  20 ns) on common inorganic pigments that are found in paintings. The pigments Athanassiou *et al.* (2000) examined were: yellow ochre, raw sienna, cadmium yellow and chrome yellow. This research aimed to study the discolouration of these pigments into linseed oil upon the UV laser irradiation. Only raw sienna and yellow ochre darken appreciably. The authors of the paper reported that the X-ray

diffraction (XRD) analysis revealed the nature of the pigment's discolouration. It was due to the thermally generated release of water molecules from the pigments' crystal lattice. Furthermore, Raman and laser-induced fluorescence spectroscopy (LIF) showed that linseed oil or its impurities could also be responsible for the discoloration of the pigments embedded in linseed oil (Athanassiou *et al.*, 2000). **Sansonetti and Realini (2000)** examined the laser interaction with inorganic pigments using a Q-switched (QS) Nd:YAG laser (1064 nm, 10 ns, 60 Hz). The inorganic pigments were red ochre, yellow ochre, chromium green, ultramarine blue, black bone and white gypsum and they were dispersed in two binders (linseed oil and gypsum) and applied onto wood panels. These pigments were characterised using XRD and Fourier Transformed Infrared Spectrometry (FT-IR). Colourimetric, stereomicroscopy and X-ray photoelectron spectroscopy (XPS) investigation were carried out prior to Nd:YAG laser irradiation. The specimens were irradiated an increasing fluence values between 0.1 to 3 J/cm<sup>2</sup>. Regarding the oil specimen, the authors observed that the use of 0.1 J/cm<sup>2</sup> could be considered a satisfactory threshold value, leaving the underlying layer well conserved (Sansonetti and Realini, 2000).

In 2001 in Paris (LACONA IV), **Bracco, Colombini and co-authors** (Bracco *et al.*, 2001, 2003; Colombini *et al.*, 2003) presented two interconnected researches using the Conservator 2940 Er:YAG laser, with 1 mm<sup>2</sup> beam, for the breakdown of mock-ups samples made of natural resin and oil-resin varnishes, synthetic varnishes/fixatives/adhesives, artificial patinas and overpaint<sup>7</sup>. Tests were also performed on real paintings. Glass coverslips were placed on the mock-ups and painting surfaces, before laser irradiation, to collect the extracted material, introducing so a micro-destructive sampling technique to carry out further analytical investigations (Colombini *et al.*, 2003). Both research teams aimed to

---

<sup>7</sup> The laboratory models were prepared on ceramic plates, covered with a ground layer of gypsum/animal glue and painted with yellow ochre/egg tempera. Subsequently, the authors coated these mock-ups using various top-layers: natural resins (mastic or dammar varnishes); oil-resin mixtures (linseed oil/sandarac varnishes); synthetic resin (Paraloid B72); over-painting (burnt umber in linseed oil); and artificial patina (animal glue) and aged the samples by exposure to UV radiation for 45 days (Bracco *et al.*, 2001, 2003).

evaluate Er:YAG laser cleaning with various pulse energies<sup>8</sup> and wetting agents<sup>9</sup> (ranging from highly polar to a-polar solutions) to observe the efficiency and selectivity of the Er:YAG laser. The authors planned a set of diagnostic controls to consider the impacts of the laser irradiation on the surface, involving chromatic, morphological, optical and chemical analyses such as colourimetry, optical microscopy (OM), back-scatter electron scanning electron microscopy (BSE-SEM), gas-chromatography mass-spectrometry (GC/MS) and FT-IR spectroscopy. These studies indicated that Er:YAG laser can sufficiently thin unwanted materials, especially in combination with chemical and mechanical cleaning methods (Bracco *et al.*, 2001, 2003; Colombini *et al.*, 2003). The authors concluded that by irradiating at laser energies lower than 20 mJ, at 15 pulses/s (pulses per second - pps) and wetting with distilled water-ethanol mixture (DIW-ETH), there was no degradation of the organic material collected on the glass coverslips allowing, in the case of the real paintings, the subsequent analysis and characterisation of binders and varnishes (Bracco *et al.*, 2003; Colombini *et al.*, 2003). GC/MS analysis detected a decrease in the content of oleic acid in the irradiated oil-resin and pure-resin varnish containing samples. The authors correlated this finding with a laser-induced modification of the oleic acid in di-carboxylic acid and epoxy by-products. There was no substantial modification in the composition of the resin acids, although, a slight decrease in the number of hydroxyl groups on the condensate material on the coverslips was identified. GC/MS spectra of samples coated with an ethyl methacrylate/methyl acrylate copolymer (Paraloid B72) had a weak signal and the authors suggested that this was due to the minimal quantity of this coating collected on the coverslips compared to the other materials tested. FT-IR analysis did not detect modifications in the irradiated Paraloid B72 coatings either. However, a minimal change in the content of specific polar substances, in

---

8 According to the information reported in the articles P. Bracco *et al.* and M.P. Colombini *et al.* (2003), the authors used: i) a single laser scan at energies of 4, 10, 12, 13, 13.5, 15, 20, 30, 45 mJ; ii) five consecutive laser scans on the same area at a fixed energy of 10, 13, 20 mJ; and iii) a single laser scan prewetting the surface (see footnote 9) and applying laser energies at 10, 12, 13, 15, 45 mJ.

9 The wetting agents employed by Bracco and co-authors were: distilled water with 2% surfactant (Tween 20) (DIW+TW20), distilled water-ethanol mixture (1:1, v/v) (DIW-ETH), and White Spirit (WS) with 15% diethylene glycol (Bracco *et al.*, 2001, 2003).

particular as slight wavenumber shift of the ester absorption bands at 1650-1700  $\text{cm}^{-1}$  before and after laser irradiation was reported (Bracco *et al.*, 2001, 2003; Colombini *et al.*, 2003). In LACONA IV, the partners of the EU project “*Advanced workstation for controlled laser cleaning of artworks*” (ENV4-CT98-0787) (1998) presented two papers (Castillejo *et al.*, 2003; Teule *et al.*, 2003) on the application of KrF excimer laser on painted samples and their progress. **Teule and co-workers (2003)** carried out a systematic study on the laser-irradiation effects on tempera paint mock-ups. The gradual thinning of varnish layers without altering the underlying paint layers was determined. The varnish selected for this study were: dammar, Mastic, Ketone N and shellac (Teule *et al.*, 2003). The optimal fluence level for the controlled thinning of the varnish layer was found to be 0.40 – 0.48  $\text{J}/\text{cm}^2$  and the cleaning process was monitored using LIBS. The authors showed that the excimer laser light was mainly confined into the irradiated surface and that the laser-induced oxidation of the binding medium was only detected in the area close to the surface. For this study colourimetry, spectroscopy<sup>10</sup>, mass spectrometry<sup>11</sup> and profilometry together with thermographic and UV transmission measurements were performed. Transmission recordings quantified the amount of UV radiation that was transmitted through the irradiated varnish and absorbed by the underlying paint layer. MS data on the KrF excimer laser ablated egg tempera binding medium suggested that deterioration of the medium might have developed a long term effect and the authors suggested that further investigations should be carried out on this particular issue (Teule *et al.*, 2003). Moreover, **Castillejo and co-authors (2003)**, presented their findings on the physical and chemical alterations of unvarnished egg tempera paints upon KrF laser irradiation. To characterise and quantify possible modifications, profilometry, colourimetry, LIF, LIBS, Fourier transform Raman (FTR) and FT-IR, direct temperature resolved mass spectrometry (DTMS) and Laser Desorption and Ionization Time of Flight Mass Spectrometry (LDI-TOF) were employed. The authors showed that organic paint systems, based on alizarin,

---

10 The spectroscopic techniques reported in the article are: LIF, LIBS, Fourier transform Raman (FT-Raman) and FT-IR (Teule *et al.*, 2003).

11 The mass spectrometric techniques listed in Teule *et al.* (2003) were: direct temperature resolved mass spectrometry (DTMS), laser desorption and ionisation MS (LDI-MS) and matrix assisted laser desorption-ionisation (time-of-flight) (MALDI-ToF-MS).

indigo and phenothiazine dyes, remained stable upon KrF laser irradiation. Conversely, azurite, lead white, lead chromate, Naples yellow, sienna and zinc white pigments showed diverse degrees of discolouration. In particular, two modifications depending on the actual paint/pigment composition were reported. These were a change of oxidation state of the pigments or to formation of a thin layer of charred particles formed by laser intervention in the organic material (Castillejo *et al.*, 2003; Teule *et al.*, 2003). **Theodorakopoulos and Zafiropulos (2003)**, presented KrF excimer nanosecond laser ( $\tau_L$  25 ns) cleaning tests on three nineteenth century Byzantine icons covered with aged natural varnishes of various thicknesses. This study showed for the first time that aged varnishes can be sufficiently thinned and removed in a controlled way due to the existence of a gradual depth-dependent degradation of the resinous films (Theodorakopoulos and Zafiropulos, 2003). Thus, by gradually removing layers from the surface towards the bulk of the aged varnish with the laser, the degrees of the resin crosslinking and oxidation decreased. In LACONA V in 2003 in Germany, **Theodorakopoulos and co-authors (2005)**, presented findings of KrF excimer laser ablation of two accelerated aged triterpenoid (TTP), mastic and dammar, varnish films. The authors presented further evidence based on direct temperature mass spectrometry (DTMS) that confirmed the previous findings and established the formation of oxidative gradients across the depth profiles of aged TTP varnishes, which are useful to develop a wide number of applications including laser ablation, thinning, step-by-step solubilisation, optical and spectroscopic studies. This work established that by adjusting the fluence and the number of pulses of excimer lasers to the gradual reduction of the oxygenated and aged by-products across the varnish depth profiles, it is possible to reach a layer within the same varnish at which the composition of remaining film has not been affected by ageing (Theodorakopoulos, 2005; Theodorakopoulos *et al.*, 2005; Theodorakopoulos and Zafiropulos, 2009; Theodorakopoulos, Boon and Zafiropulos, 2009). **Hildenhagen and Dickmann (2003)** discussed the release of a new generation of Nd:YAG lasers that offered a new tool in the field of laser cleaning in cultural heritage. The new laser system (Type SAGA 220/10), with emission at 532 nm ( $2\omega$  - second harmonic), 355 nm ( $3\omega$  - third harmonic) and 266 nm ( $4\omega$  - fourth harmonic) wavelengths, took place alongside the already known Nd:YAG laser in its fundamental wavelength 1064 nm ( $\omega$ ). The new Nd:YAG laser was tested on sandstone artefacts covered with

black encrustation, varnish layer on a piece of wooden furniture, a painting frame with synthetic colours, a gilded iron organ and a Russian icon covered with black candle smoke, with promising results. As regards the removal of old varnish coatings (no chemical characterisation is provided in the paper), the authors highlighted different outcomes depending on the wavelengths employed. At 1064 nm, it was possible to remove the coating using a fluence of 1.3 J/cm<sup>2</sup> but with damage to the underlying wood structure. At 532 nm and fluence of 1.2 J/cm<sup>2</sup>, no impact to the paint layer was reported in the article with the formation of discolouration of the underlying material. At 266 nm, a sufficient cleaning result was not achieved. The best cleaning results for this range of wavelengths were shown at 355 nm (Hildenhagen and Dickmann, 2003). **Pouli *et al.* (2003)** presented a study on the discolouration effect induced on various pigments with a Q-switched Nd:YAG laser at 1064 nm ( $\tau_L$  30 ns, 5 Hz) following previous studies that had been presented in LACONA III (Pouli and Emmony, 2000). These studies were focused on lead, ferrous and copper powder pigments in linseed oil coated on limestone plates. Discolouration (darkening) was characterised by employing spectroscopic and surface analysis such as transmission electron microscopy (TEM) and XPS. Their findings showed that upon laser irradiation pigment decomposition was favoured while thin layers and/or globules of the metals remain on the surface. According to the authors, oxidation of the laser-induced products could reverse this discoloration (Pouli *et al.*, 2003). The authors suggested that further investigations should be carried out on this particular issue. **Chappé and co-authors (2003)** presented a paper on the chemical and physical interactions of 11 pure pigments that were irradiated at 1064, 532, 355 and 266 nm using a Nd:YAG laser. Colourimetry, differential thermal analysis (DTA), XRD and energy dispersive X-ray (EDX) spectroscopy were employed. The 11 powder pigments used for the study presented were: Lead White, Zinc White, Brown Ochre, Naples Yellow, Vermilion, Red Lead, Madder Lake, Oxide of Chromium, Malachite, Cobalt Blue and Ultramarine. The authors concluded that the best results were obtained using the Nd:YAG laser in its fundamental wavelength (1064 nm). However, at 355 nm discolouration were induced by laser oxidation, reduction or phase change in the irradiated pigments (Chappé *et al.*, 2003).

In 2003 at LACONA V, **Schnell and co-workers (2005)** presented findings on the ‘blackening effects’ of 45 different pigments and their possible modification upon QS Nd:YAG laser (1064 nm) irradiation. The authors also studied the laser-material interaction on three different binders (linseed oil, casein and gum Arabic organic) used for the painting of sandstone samples. Colourimetry was carried out to document the discolouration of all the irradiated pigments. It was shown that QS Nd:YAG lasers are suitable for the cleaning of polychrome surfaces, with some limitations in the fluence values according to the characteristics of specific pigments. However, they showed that Nd:YAG lasers must be avoided on paints containing zinc white, titanium white and cinnabar pigments. The authors provided evidence that discolouration is induced by chemical decomposition reactions, phase changes or physical effects such as melting of pigment particles. Also they showed that paint binders were less sensitive to laser irradiation, some Nd:YAG laser-related decomposition of the linseed oil was detected by nuclear magnetic resonance (NMR) spectroscopy (Schnell, Goretzki and Kaps, 2005). **Madden and co-worker (2005)** presented extended research following results from LACONA IV (Scheerer, Abraham and Madden, 2003) on the interaction of lasers and adhesives, consolidants, and coatings generally used in conservation. Two nanosecond lasers were used: a QS Nd:YAG laser at 1064, 532, and 355 nm and a KrF excimer (248 nm). The latter laser was operated at 255 mJ/cm<sup>2</sup>, 10 Hz for 30 seconds. The authors showed that it is important to characterise the composition of the substrate materials prior to laser irradiation. The acrylic resins were resistant to all the laser wavelengths except 248 nm, which made the resins soft and tacky. **McGlinchey and co-authors (2005)** showed preliminary findings on the practical use of Nd:YAG (1064 nm) and KrF lasers as a possible means to remove the overpaint<sup>12</sup> from Ad Reinhardt’s series of paintings known as ‘Black Square’ (1960’s), in which traditional conservation methods had not been satisfactory. The authors proposed the development of a protocol to allow conservators to obtain a uniform surface appearance upon irradiation. To characterise the effect of laser irradiation on the exposed painted surface, the authors carried out visual

---

12 According to what is reported by the authors, the over-painting was characterised by various layers of acrylic emulsion plus an intermediate layer between the latter and the underlying paint layer (McGlinchey *et al.*, 2005).

examinations together with LIBS, Near-infrared (NIR) spectroscopy, UV imaging, FT-IR, X-ray fluorescence (XRF) spectroscopy, and Energy Dispersive X-Ray Spectroscopy (EDS) coupled with SEM analysis. McGlinchey and co-authors (2005), reported that overpaints did not dissociate, but, they blistered and separated from oil paint substrates, which made them readily removable with tweezers after irradiation. The dissimilarity in heat capacity between the high organic content in the overpaint and the low organic content in the original artwork helped in the separation of the two layers. After these preliminary findings carried out on specimen, they tested a nanosecond KrF laser and performed elemental monitoring with LIBS and SEM on cross-sections. The authors concluded that overpaints on the Ad Reinhardt's paintings can be sufficiently removed with a KrF laser. In 2006, during the International symposium organised by the Getty Conservation Institute, Tate, and the National Gallery of Art in London, a similar study, focusing on the cleaning of Ad Reinhardt's paintings was presented by **Stringari and co-authors (2007)**. Scholten et al. (2005) presented results of treatments using the commercially developed workstation that incorporated a KrF excimer laser and LIBS (Anglos *et al.*, 1996; Teule *et al.*, 2003). The authors reported that the UV excimer laser proved to be a valuable tool for fire-damaged paintings.

In LACONA VI in Vienna, **Andreotti and co-authors (2007)** presented research on the use of an Er:YAG laser following two previous papers that had been presented in LACONA IV by Bracco and Colombini (Bracco *et al.*, 2003; Colombini *et al.*, 2003). Laser tests were carried out on an extensive series of mock-ups subdivided by coatings<sup>13</sup>, overpaints<sup>14</sup>, conservation materials<sup>15</sup> and uncoated tempera/oil surfaces. Some tests were performed on real old paintings. The laser

---

13 The coatings were: oil-resin and natural resin varnishes prepared in 1999 and published in Bracco *et al.*, 2003 and Colombini *et al.*, 2003. Apart from these, the authors tested also shellac, mastic alone and with walnut oil mixture varnish, ketone and vinylic resin and boiled linseed oil varnish (Andreotti, *et al.*, 2007).

14 The over-painting selected were: burnt umber casein, Naples yellow-linseed oil, Naples yellow casein, burnt umber-linseed oil on gypsum/rabbit glue (Andreotti, *et al.*, 2007).

15 The restoration materials were: EVA based resin and acrylic resin such as BMA and EA/MMA (Andreotti, *et al.*, 2007).

tests were planned to proceed with increased energies (between 3 and 200 mJ) directly on the surface and after pre-wetting with DIW+TW20, DIW-ETH, and WS with 15% diethylene glycol that had been previously tested for Er:YAG laser cleaning treatments (Bracco *et al.*, 2001, 2003; Colombini *et al.*, 2003). The Er:YAG laser beam diameter was set at 1 mm, and pulse repetition rate at 15 Hz. The same set of diagnostics controls and the methodology carried out, previously listed in Bracco *et al.* (2001, 2003) and Colombini *et al.* (2003) were also used for this research. The authors reported that below the energy threshold, that is unique for each material, no chromatic alteration had been observed upon Er:YAG laser irradiation for the majority of the materials tested. However, yellow ochre, mineral iron-based blue, and Naples yellow in casein were discoloured. FT-IR and GC/MS analyses showed that irradiation under the threshold limits resulted in no significant variation in the chemical composition of the materials tested (Andreotti, *et al.*, 2007). The authors reported that the laser cleaning tests performed on a seventeenth century oil painting on canvas and a fifteenth century panel tempera painting exhibited results quite similar to traditional cleaning methods. **Pouli and co-authors (2007)** reported findings on the use of ultrafast UV *xenon chloride* (XeCl) excimer laser (308 nm) and nanosecond KrF excimer laser for the cleaning of varnished polychrome artworks. The authors carried out comparative studies on the ablation rate and threshold of femto- and nanosecond laser pulses on dammar and mastic varnish samples applied to quartz glass slides. Nanosecond KrF excimer lasers ( $\tau_L$  10 ns) at fluences between 4 and 500 mJ/cm<sup>2</sup> were selected for the ablation of dammar and mastic films. Irradiation at 500 fs and fluences between 0.05 and 0.75 mJ/cm<sup>2</sup> resulted in minimal photochemical modifications on the irradiated coating samples. Femtosecond pulses ensured higher etching resolutions and edge precision without noticing the formation of melting. By using ultrashort lasers, the authors were able to provide a highly precise treatment almost independent to the optical properties (i.e., absorptivity) of the substrate ablated. Later, in 2009 a paper by **Pouli and co-author (2009)** aimed to identify the optimal parameters for the laser cleaning of wall paintings surfaces, treated with acrylic, vinyl, epoxy polymers commercially known as Elvacite, Laropal and Paraloid B72. Mock-ups were created ad hoc casting the resins on quartz disks. The authors were interested in characterising a plausible morphological modification in the remaining coating after laser ablation. The same lasers were employed to study the effects of different

pulse durations. Femtosecond laser pulses resulted in reduced morphological alterations in comparison to ns pulse duration. **Morais and co-workers (2007)** aimed to characterise the KrF excimer laser interaction with inorganic pigments<sup>16</sup> on egg tempera and dammar, mastic and shellac varnishes. To detect morphological modifications, mechanical profilometry, colourimetry and SEM analysis were carried out. XRD and FTR were performed on the irradiated pigments and UV/VIS spectroscopy onto the varnished samples to monitor their transparency in the visible regions of the electromagnetic spectrum. Upon laser ablation yellow ochre, malachite and red lead showed various levels of discolouration and therefore paints with these pigments are not suitable for direct laser cleaning as also reported elsewhere (Chappé *et al.*, 2003). According to Morais *et al.* (2007), varnish systems did not present discolouration, and the laser irradiation allowed the removal of varnish films in a controllable way. The authors suggested undertaking post-ageing procedures to investigate possible long-term effects on the ablated surfaces (Morais *et al.*, 2007).

In LACONA VII, Madrid 2007, **Camaiti *et al.* (2008)** presented findings on the pattern of azurite and malachite pigments exposed to a pulsed, free-running, Er:YAG laser. Pure pigments, mock-ups and fragments of wall painting were irradiated with the ER:YAG laser to detect their fluence thresholds. With means of colourimetry, OM and  $\mu$ -Raman and GC/MS, the authors showed that, pure malachite was more sensitive than azurite upon laser irradiation. Both pigments presented partial darkening due to the formation of cupric oxide (CuO) when the surface was not prewetted. Prewetting the surface, no colour alterations were detected even at laser fluences between 7 and 10 J/cm<sup>2</sup> (Camaiti *et al.*, 2008). **Marczak and co-authors (2008)** reported results on the laser cleaning process on several art materials. Only those related to coated polychrome surfaces are presented in detail herein. An ancient Roman fresco fragment, that was

---

16 The inorganic pigments chosen by the authors were barium sulphate, yellow ochre, lapis-lazuli, malachite, white lead, red lead, Prussian blue and cobalt green (Morais *et al.*, 2007).

consolidated with different adhesives<sup>17</sup>, was tested by employing a UV KrF excimer laser. Paraloid B72 was one of the consolidants used for this test. The encrustations on the fresco surface without any consolidants were removed using fluences between 20 J/cm<sup>2</sup> (thick layers) and 0.5-0.3 J/cm<sup>2</sup> (thin layer). The authors reported that Paraloid B72 was thinned by using fluences up to 2 J/cm<sup>2</sup>. Discolouration occurred when cinnabar or Yellow ochre were detected on the tests. The first pigment excluded the use of KrF laser since it blackens irreversibly, and the second pigment became brown. Pre-wetting of the surface with distilled water improved the cleaning process. The cleaning irradiation was also repeated with an Nd:YAG laser, 1064 nm at 0.6 J/cm<sup>2</sup>. The author referred that all the pigments were more sensitive to Nd:YAG laser irradiation when compared to the results using the KrF excimer laser and Paraloid B72 did not show any laser-material interactions upon Nd:YAG laser irradiation (Marczak *et al.*, 2008).

In LACONA VIII Romania 2009, **Kogou and co-authors (2011)** presented findings on the irradiation of model samples coated with Paraloid B72 with UV pulsed lasers (193 nm up to 355 nm, in ns, pico- and femto-second pulse duration)<sup>18</sup>. The study was focused on the absorptivity of Paraloid B72 film at the laser wavelengths as well as on the role of pulse durations in the ablation process. The authors concluded that no removal of the Paraloid film was observed. Moreover, severe alterations, such as melting and discolouration, to the underlying surfaces, were described after irradiation at 355 nm. Excellent results and safe cleaning irradiation were reported after ns irradiation at 193 nm and fs irradiation at 248 nm. Well definite laser spots with minimal effect on the surrounding surfaces were obtained by employing the lasers at 193 and 248 nm. **Striova and co-workers**

---

17 The consolidants reported by (Marczak *et al.*, 2008) are a aqueous silica dispersion with 30% of silica nanoparticles (Syton X30), an acrylic dispersion resin in water (Primal WS24) and a copolymer of ethyl methacrylate and methyl acrylate (Paraloid B72).

18 The lasers employed by the authors were an argon fluoride laser (ArF) excimer laser (Lambda physik complex 110,  $\lambda$  193 nm and  $\tau_L$  25 ns), a KrF Excimer dye system (Laser lab Göttingen,  $\lambda$  248 and  $\tau_L$  500 fs), a KrF Excimer (Lambda physik complex 110,  $\lambda$  248 nm,  $\tau_L$  25 ns), a QS Nd:YAG (EKSPLA, SL312,  $\lambda$  355 nm and  $\tau_L$  150 ps) and a QS Nd:YAG laser (Spectron, SL805,  $\lambda$  355 nm and  $\tau_L$  10 ns).

(2011b) presented a pilot research using free-running Er:YAG laser<sup>19</sup> to remove organic materials, such as linseed oil, ‘*beverone*’,<sup>20</sup> and Paraloid B72, previously applied to the surfaces of mock-ups of ‘*a fresco*’ mural paintings. Except for the case of Paraloid B72, the organic materials selected absorbed the 2940 nm Er:YAG laser wavelength. In the case of Paraloid B72 the use of hydroxylated wetting agents was necessary to keep the absorption on the irradiated surface and prevent transmission, and thereby protect, the underlying layer. The fresco’s colours chosen by the authors were St. John’s white and yellow ochre pigments. Irradiation was carried out on the dry surface, and later after wetting the surface with water or isopropyl alcohol. The irradiated surfaces were cleared with rolling cotton swabs loaded in the same wetting agents. Glass sliders were used as reported previously (De Cruz, Wolbarsht and Hauger, 2000a; Bracco *et al.*, 2001, 2003; Colombini *et al.*, 2003). Irradiation of the non-wetted surface did not achieve the removal of Paraloid B72 film due to the absence of hydroxyl groups in the structure of the resin. However, pre-wetting with isopropanol and using a fluence of 0.6 J/cm<sup>2</sup> enabled a sufficient removal. Colourimetry, OM, and  $\mu$ -Raman spectroscopy were employed to determine the most suitable fluence parameters for the materials investigated. In dry irradiation conditions, damage thresholds of St. John’s white and yellow ochre pigment were found at 15.2 and 2.5 J/cm<sup>2</sup>, respectively. Irradiation of the non-wetted surface showed comparable damage thresholds for both pigments. Er:YAG laser irradiation at 0.6 and 1.3 J/cm<sup>2</sup> with isopropanol allowed the authors to achieve a gradual removal of the oil layer. At a fluence of 0.6 J/cm<sup>2</sup> efficient removal of the ‘*beverone*’ was obtained prewetting the surface with water (Striova *et al.*, 2011b).

Meanwhile, in the “*New Insights into the Cleaning of Paintings*” conference in 2010 held at the Universidad Politécnica de Valencia, **De Cesare and co-workers (2013)** presented work on the removal of overpaints on a twentieth century

---

19 High Power Erbium CrystaLase – Mona Laser, 2940 nm,  $\tau_L$  300  $\mu$ s (consisting of a train of 1-2  $\mu$ s micro-pulses), spot diameter 1 mm and repetition rate of 10 Hz.

20 As reported by Conti (2007), ‘*beverone*’ was a mixture of organic substances, which could also include eggs and vinegar as well as the glue and oil mentioned by De Mayerne, made up to the personal recipe of the restorer, which seems to have been used both as a brightening agent on frescos.

painting using an innovative laser methodology. Painting mock-ups were created and later laser-irradiated with the purpose of not compromising the underlying layers. The samples were blends of six different binders<sup>21</sup> (commercial tube formulations) with titanium white, representing the first layer of the mock-ups. Above the first layer, a second layer was applied made by commercial tube formulations containing either ultramarine blue or phthalocyanine blue. The lasers employed ranged from the KrF Excimer laser ( $\tau_L$  30 ns) to near-infrared Nd:YAG laser (532 and 1064 nm,  $\tau_L$  10 ns). OM,  $\mu$ -FTIR, and  $\mu$ -Raman spectroscopy were employed to monitor the efficacy of the laser to homogeneously remove the overpainted layers and LIF analysis to check the laser cleaning process (De Cesare *et al.*, 2013). The authors reported good results using the 248 and 355 nm lasers with effective and safe removal of the overpainted layers. At 532 nm, no impact to the overpainted layers was reported. At 1064 nm, laser irradiations were found to be particularly aggressive, showing photomechanical effects visible as cracks around the laser spots.  $\mu$ -FT-IR and  $\mu$ -Raman spectroscopy revealed residues of the showed the presence of alteration phases responsible for the colour changes. The authors concluded that IR laser-irradiation of titanium white could possibly have triggered the discolouration phenomena and the degradation of the organic medium.

In 2011, **Oujja and co-authors (2011)** evaluated the use of diverse UV lasers for the removal of shellac varnish from egg-yolk based tempera paints samples. Two cleaning strategies were employed for this research: fs pulsed 398 and 265 nm lasers and a ns pulsed 213 nm laser. The effect upon laser-treated varnished tempera samples was carried out with colourimetry, OM, and LIF. The fs laser pulses changed the morphology of the shellac varnish surfaces leading the degradation of the underlying paint layers. More efficient removal of the shellac varnish was obtained by using the ns pulses of the highly absorbed 213 nm laser without a chemical or physical modification of the underlying tempera (Oujja *et al.*, 2011).

---

21 The binders listed by the authors were acrylic emulsion resin (for artists), vinyl emulsion resin (for artists), acrylic in solvent, oil- modified alkyd (for artists), oil- modified alkyd (household), and alkyd with nitrocellulose (for artists) (De Cesare *et al.*, 2013).

In 2011, **Castelli *et al.* (2011)** reported work on the ‘Triptych of Badia in Rofeno’ by Ambrogio Lorenzetti at Museo di Asciano and documented the successful removal of old overpaints and an dark aged varnish (no detail are provided) from sensitive paint substrates with an Er:YAG laser.

In the same year, LACONA IX conference was organised in London and **Kane and co-workers (2013)**, reported a study on the removal of a polyurethane coating as well as Paraloid B72, polyvinyl butyral (PVB) and gelatine consolidants that had been originally applied to protect the fragile pigmentations on traditional Australian aboriginal paintings with plant- and animal-based binders. A nanosecond KrF excimer laser<sup>22</sup> with an attenuator to reduce the energy output of the laser and a nanosecond Nd:YAG laser<sup>23</sup> running in the second harmonic were employed. As regards the Paraloid B72 resin, the authors observed no ablative removal or vaporisation of the coating with either the KrF or Nd:YAG lasers. At the shorter wavelength of the KrF excimer laser, the beam caused discolouration effects on the underlying layer before the removal of the Paraloid B72 resin. In contrast, Nd:YAG laser (single pulse with fluences ranging between 200 mJ/cm<sup>2</sup> and 1 J/cm<sup>2</sup>) enabled delamination mechanism that made it possible to remove the Paraloid B72 resin with a scalpel (Kane *et al.*, 2013).

In 2012, a review on the progress of laser cleaning in the conservation of cultural heritage (Siano *et al.*, 2012) was published. This work was focused on the use of QS (6 ns) and long Q-switch (LQS) (120 ns) Nd:YAG lasers. The tests aimed to recreate discoloured varnishes and to simulate optical, thermal, and mechanical characteristics encountered in real case scenarios and to carry out comparative evaluations. Thick dammar and mastic varnish samples were doped with carbon black, resulting in an optical penetration depth of 147 µm. Ablation thresholds were

---

22 KrF excimer GSI Lumonics Pulsemaster PM848 laser, 248 nm and  $\tau_L$  8 ns (Kane *et al.*, 2013).

23 Nd:YAG Continuum Surelite I-10 laser, 532 nm and  $\tau_L$  5 ns (Kane *et al.*, 2013).

precisely characterised via colourimetry, microstratigraphy and microscopy investigations. The threshold obtained on the samples without pre-wetting was around 0.6 and 0.8 J/cm<sup>2</sup> with the QS and LQS Nd:YAG lasers respectively (Siano *et al.*, 2012).

In 2013, ‘*Dipinti mobili. Applicazioni sperimentali di sistemi laser per la pulitura*’ were published by Nardini Editore summarising the findings of the TemArt project (POR-CReO/FESR 2007-2013) (Patti and Siano, 2015). The study aimed to evaluate the efficacy of QS and LQS Nd:YAG lasers<sup>24</sup> to thin varnished layers (Hilling and Nakahara, 2005; Siano *et al.*, 2011; Ciofini, 2014). Moreover, a KrF excimer laser<sup>25</sup> was tested due to its well-known thinning possibilities (Theodorakopoulos and Zafirooulos, 2005; Bordalo *et al.*, 2006; Morais *et al.*, 2007). Thin shellac, mastic and dammar varnishes on both specimens and real paintings were laser irradiated. The irradiated areas were observed under visible, raking and UV light and OM. Environmental scanning electron microscopy (ESEM)-EDS, FT-IR and XRF analysis were employed to study the efficacy of laser cleaning in removing the unwanted materials. The choice to test several lasers offered a comparison of the condition of the irradiated materials at different wavelengths. The authors concluded that KrF lasers facilitate a noticeable thinning of varnish films. A more superficial interaction was detected with double QS pulses (LQS<sub>2</sub>) Nd:YAG laser when compared to a single QS pulse (LQS<sub>1</sub>). Moreover, a thermal action followed by micro-ablative effects was observed. The second harmonic of the QS Nd:YAG laser (532 nm) were not applicable to easel paintings due to the chromatic shades of the goggles’ lenses which did not allow the conservators to detect variations of the surface colour. Regardless, the 532 nm laser showed promising results in the cleaning of polychrome coated surfaces. The second stage of the research focused on the use of lasers in real paintings housed at

---

24 The lasers listed in the research were: a long q-switch (LQS) Nd:YAG (EOS 1000 – by El.En., 1064 nm with single QS pulses at  $\tau_L$  120 ns [LQS<sub>1</sub>] and double QS pulses at  $\tau_L$  120 ns for each pulse and a time interval between pulses of 40  $\mu$ s [LQS<sub>2</sub>]) and a QS Nd:YAG (CRF 400 – by Quantel, 532 nm and  $\tau_L$  10-30 ns) (Patti and Siano, 2015).

25 The KrF excimer laser was a Complex 102 – by Lamda Physik, 248 nm and  $\tau_L$  30-40 ns (Patti and Siano, 2015).

Fortezza da Basso in the laboratory of Opificio delle Pietre Dure in Florence. On a thirteenth century painting ‘Virgin and Child’, the authors tested the Nd:YAG laser<sup>26</sup> in LQS<sub>1</sub> and LQS<sub>2</sub> modes and in Short free-running (SFR) mode ( $\tau_L$  40  $\mu$ s). In this case the laser cleaning tests were carried out with the use of wetting agents. The Nd:YAG laser tests in LQS<sub>1</sub> and LQS<sub>2</sub> modes showed the same drawbacks already discussed above. The SFR Nd:YAG laser facilitated the controlled and selective thinning of the original varnishes which were prewetted with an aqueous solution of non-ionic surfactant, Tween 20. The authors reported no photothermal and photomechanical interaction during the laser irradiation (Patti and Siano, 2015).

At LACONA X, Sharjah (Egypt) 2014, **Siano and co-workers (2015)** reported the first validation study to remove oil-based overpaints from easel paintings with a LQS Nd:YAG laser. The laser was employed on the verso of a signed Giacomo Balla’s easel painting. Cleaning of the painting had been previously attempted using organic solvents, but the results were unsatisfactory. Thorough characterisation of the original pigments (lithopone, titanium white, cadmium yellow, green copper carbonate, chrome yellow and zinc yellow) and overpaints (artificial ultramarine blue, cobalt blue, zinc oxide, alizarin, chromium oxide green) also was carried out by the authors using different analysis Raman and FT-IR spectroscopy, along with stratigraphic examination combined with OM and ESEM-EDX analysis. Then, the overpaints were removed by the laser with fluences ranging from 0.5 to 0.7 J/cm<sup>2</sup>. The laser-material interactions presented spallation effects in areas with whitish overpaint layers. Moreover, during the laser cleaning tests, laser self-termination was observed. The authors concluded that the oil-based overpaints removal using an Nd:YAG laser was driven by a superposition of phase change, including glass transition of the binders, melting of wax impurities, vaporisation of solvent residues, and photoacoustic generation. Glass transition and melting led to physical changes within the irradiated volume, while the photoacoustic generation provided the mechanical action needed for the overpaints removal (Siano *et al.*, 2015). **Striova and co-authors (2015)** reported findings on

---

26 The 1064 nm Nd:YAG laser reported by the authors was a Combo by El.En. (Patti and Siano, 2015).

the use of an Er:YAG laser ( $\tau_L$  40–150  $\mu$ s) to remove naturally and accelerated aged shellac varnishes from mural painting samples. Colourimetry, micro profilometry and time-domain confocal optical coherence tomography (TD-OCT) were employed for the characterisation of the laser thinning procedure. FT-IR in reflectance mode was performed to determine possible chemical modification upon laser irradiation. A progressive increase in the fluence values was adopted to detect the removal threshold of the varnish film. Laser irradiation on the surface was carried out both prior to and post-wetting with water or isopropanol. The effectiveness of the removal process was monitored by detecting the condensed material on microscope glass cover-slides applied on the sample surface prior to the irradiation, similarly to Bracco *et al.* (2001, 2003) and Colombini *et al.* (2003). There was no varnish removal upon dry irradiation up to a fluence of 2.6 J/cm<sup>2</sup>. In agreement with an earlier report (Striova *et al.*, 2011a, 2011b), isopropanol was considered the most suitable solvent achieving satisfactory results at 1.9 J/cm<sup>2</sup> (Striova *et al.*, 2015).

Meanwhile in 2014, during the 5<sup>th</sup> APLAR conference held at the Vatican museums in Rome, **Giardina and co-workers (2017)** presented their work on a laser cleaning method that successfully assisted the removal of natural resins applied on two Lorenzo Lotto's easel paintings. Prior to the laser cleaning, the painting surface had been examined under visible, UV and IR light,  $\mu$ -FTIR and Pyrolysis-GC/MS (Py-GC/MS). Analysis showed that the coating resin was an oil varnish. Chemical cleaning tests using solvent-gels showed unsatisfactory results. Therefore, laser cleaning tests were carried out as a possible alternative. Two different lasers were compared. A SFR Nd:YAG laser ( $\tau_L$  50-130  $\mu$ s) and a QS Nd:YAG laser ( $\tau_L$  8-10 ns). A selection of Laponite RD at pH 11, Carbopol Ultrez 21 at pH 4 and Agar at pH 7 gels and glass, Perspex and a photographic blue filters were employed to shield the laser beam energy reaching the pictorial surface and therefore ensuring a gradual thinning of the unwanted material. The QS Nd:YAG laser (with energy values between 60 mJ at 10Hz and 85 mJ at 15 Hz) together with the Agar gel obtained the best results (Giardina *et al.*, 2017). **De Cesare and co-authors (2017)** discussed the feasibility of the removal of varnish and retouching from vinyl-acrylic emulsion paints and the possibility to selective clean these

surfaces by employing different lasers that are commercially available, including: QS ( $\tau_L$  6-8 ns), LQS ( $\tau_L$  100 ns) Nd:YAG lasers and a free running Er:YAG laser. Spereomicroscopy and OM, together with SEM-EDS, colourimetry,  $\mu$ -Raman and FT-IR analyses were performed to assess the procedure. An acrylic Surfing by Lefranc et Bourgeois (L&B) and hydrocarbon Regalrez 1094 synthetic resins and a palette of 11 Maimari vinyl colours were applied on a cloth-lined board. In most of the cases, irradiation with either the Nd:YAG or the Er:YAG lasers was harmful to the underlying paint substrates. Irradiation with one pulse of LQS Nd:YAG laser at  $4.5 \text{ J/cm}^2$  had acceptable results on green oxide, brown and black colours. However, on the carbon black acceptable results had been achieved at  $0.058 \text{ J/cm}^2$  (De Cesare, Izurlo and Biocca, 2017). No changes in the chemical structure and composition of the varnishes and binders had been reported after laser irradiation using both lasers. The SEM-EDS analysis showed the presence of Calcium Carbonate ( $\text{CaCO}_3$ ) used as a dispersion additive in the acrylic paint media (Mayer, 1991, p. 184; Izzo, 2011).

In 2016, at LACONA XI in Poland, **Striber *et al.* (2017)** discussed the use of a 355 nm QS Nd:YAG laser<sup>27</sup> on an twentieth century painting on canvas and nineteenth century icon. As regard the twentieth century painting, the final varnish could not be removed with organic solvents due to the high sensitivity to solvents of brown, ochre, red, green earthy pigments. Therefore, laser cleaning was tested. Based on the results of solubility tests, the authors suggested that varnish the painting was made of a natural resin (the chemical characterization of the varnish film is not provided in the article) (Striber, Jovanović and Jovanović, 2017). The high absorption coefficient of varnish at the laser wavelength assured that the underlying paint layer was protected. The laser was operated at  $80 \text{ mJ/cm}^2$  and the cleaning process was stopped by the authors when the ablated area satisfied the aesthetic aspect. No morphological surface variations after laser irradiation was detected by OM (Striber, Jovanović and Jovanović, 2017). **Ciofini and co-authors**

---

<sup>27</sup> The 355 nm Nd:YAG laser reported by the authors was a Thunder Art system with  $\tau_L$  10 ns (Striber, Jovanović and Jovanović, 2017).

(2016a) assessed the chemical and physical modifications induced by UV laser ablation of natural and accelerated aged mastic, mastic-oil, dammar and bleached shellac coatings using E-SEM,  $\mu$ -Raman and LIF, which was part of his PhD thesis (Ciofini, 2014). The varnishes were irradiated at 266 nm ( $4\omega$ ) and 213 nm ( $5\omega$ ) with a QS Nd:YAG laser. UV-Vis absorption spectroscopy was employed to quantify the linear absorption coefficients at the laser wavelength. The quality of the ablation process significantly depended on the laser irradiation wavelength, as well as on the chemical composition of varnish, and its degree of polymerisation, as it was already determined elsewhere (Theodorakopoulos *et al.*, 2007). Irradiation of the samples on coated quartz and canvas substrates with the 213 nm laser beam exhibited controllable thinning of the ablated coatings, which according to Ciofini and co-workers made this laser promising for practical cleaning treatments on easel paintings. The importance of using a highly absorbed laser wavelength to remove unwanted materials from cultural objects was highlighted (Ciofini *et al.*, 2016a). Subsequently, as reported in the LACONA XII book of abstracts, Paris in 2018, **Ciofini and co-authors (2018)** reported further results on the thinning of dammar, mastic, colophony and sandarac films using an Nd:YAG laser at 266 and 213 nm and a KrF excimer laser. The resin films were applied onto photosensitive substrates and irradiated with nano-, pico- and femto-second pulses of these lasers. The 213 nm laser was the best choice for the safety of the underlying paint layer. The same set of methods and analysis as in (Ciofini *et al.*, 2016a) were used to assess physicochemical modifications after laser ablation (Ciofini *et al.*, 2018). According to the authors, any thermal or mechanical side effects are observed employing QS Nd:YAG 213 nm laser on oxidised varnish layers. Furthermore, 213 nm Nd:YAG laser did not show any spectral variations through LIF and Raman measurements (Ciofini *et al.*, 2018).

In 2016, the conservation of a fourteenth century panel painting by Lluís Borrassà with a 250  $\mu$ s Er:YAG laser as an alternative method to the traditional solvent mixture and gels cleaning was reported (Andreotti *et al.*, 2016). The condensated material collected upon Er:YAG laser irradiation on glass coverslips were used for GC/MS and FT-IR analyses, as reported previously (Bracco *et al.*, 2001, 2003; Colombini *et al.*, 2003; Andreotti, *et al.*, 2007; Camaiti *et al.*, 2008; Striova *et al.*, 2011a). The painting was covered with a thick discoloured varnish.

At first, the varnish film was thinned with solvent gels. FT-IR and GC/MS helped to characterise the main constituents of the film remained on the paint substrate, which was composed of polysaccharide, proteinaceous and resinous materials. The Er:YAG laser was used at fluences ranging between 1.7 and 3.2 J/cm<sup>2</sup> depending the area irradiated and pre-wetted with hydroxide-rich solvents, following published recommendations (De Cruz, Wolbarsht and Hauger, 2000a, 2000b; Bracco *et al.*, 2001, 2003; Andreotti, *et al.*, 2007; Striova *et al.*, 2015).

In 2017, at APLAR 6 conference, in Florence, **Brunetto and co-workers (2019)** reported findings on the combination of the use of lasers and well established cleaning treatments for the removal of unwanted materials on three polyptych by Hieronymus Bosch belonging to the Gallerie dell'Accademia Museum in Venice. Two different lasers were employed for this study: a LQS (120 ns) and SFR (60-120 µs) Nd:YAG laser and an Er:YAG laser in Very Short Pulse mode (150-200 µs) and Short mode (300 µs). The areas cleaned using the lasers as well as the constituent materials on the polyptychs were studied using cross-sections, macro- and micro-photography, UV fluorescence, XRF, FT-IR and Raman spectroscopy (Brunetto *et al.*, 2019). The original paint layer was covered by a grey non-original layer of proteinaceous substance that was almost entirely transformed into calcium oxalate as detected by FT-IR spectroscopy. The LQS Nd:YAG laser was tested at 0.15 and 0.25 J/cm<sup>2</sup>, using a filter to cut 75% of the laser beam energy. The laser irradiation left a grey-yellow layer on the painting surface. The latter was removed by the authors using a White Spirit and isopropanol blend thickened in a stearic emulsion ('*pappina fiorentina*'). Due to the presence of white lead in the underlying paint layer, the use of the SFR Nd:YAG laser with the long pulse duration at fluences between 1 and 1.9 J/cm<sup>2</sup> was selected. Lastly, the Er:YAG laser at 0.7 J/cm<sup>2</sup> in Short mode (300 µs) was tested. The surface was prewetted with a 50% (v/v) white spirit and isopropyl alcohol blend, and the paint layer was covered with a glass coverslip, following published recommendations (De Cruz, Wolbarsht and Hauger, 2000a, 2000b; Bracco *et al.*, 2001, 2003; Andreotti, *et al.*, 2007; Striova *et al.*, 2015).

In 2018, **Pereira-Pardo and Korenberg (2018)** published a relevant review of state of the art in the use of the Er:YAG laser for the cleaning of paintings, stone, textiles, paper and plastics. The authors summarised all the research findings published as well as the characteristics and cleaning mechanisms of Er:YAG lasers. The major achievements using the Er:YAG laser in art conservation were recapped as the successful removal of resins from different substrates; the determination of the damage threshold of some potentially sensitive pigments and the optimisation of the methodology to remove overpainting; the measurement of the removal depth per laser pass by OCT and micro-profilometry; investigating the effect of the wetting agents; finding optimal cleaning strategies using the Er:YAG laser in combination with other methods on a case-by-case basis. The authors stated that Er:YAG laser are not used as a standalone appliance and they can generate excellent results when used in combination with conventional cleaning methods.

**Lopez and co-authors (2019)** compared two lasers for the removal of an urea-aldehyde resin (Laropal A81): an Er:YAG laser<sup>28</sup> and a Nd:YAG laser<sup>29</sup> working at 266 nm (4 $\omega$ ). Samples were prepared on a photosensitive substrate (red lead embedded in oil paint) where the Laropal A81 was applied as a final varnish. The interaction of the lasers on the surface of the samples was monitored with OM, Spectral-Domain (SD) OCT and UV-induced fluorescence and time-resolved laser induced fluorescence spectroscopy (TR-LIFS). The Er:YAG laser used by Lopez and co-workers (2019) has a non-collimated handpiece with a laser beam which diverges from the irradiated surface changing its diameter by coming closer to or moving away from the surface. Therefore, the fluence changes by varying the distance between the output and the surface. Hence, before running the lasers test on the mock-ups, the authors had to define and identify the different fluences suitable for the laser tests. Therefore, they had to create a setup, firing the laser onto a photosensitive paper and changing the distance between the laser output and the

---

28 According the authors a Light Brush II Er:YAG laser by El.En was used in Very Short (VS) pulse mode  $\tau_L$  150  $\mu$ s (Lopez *et al.*, 2019).

29 A Quantel CFR 266 nm Nd:YAG laser with a  $\tau_L$  5 ns laser pulse duration was used by Lopez *et al.* (2019).

paper surface. The Er:YAG laser irradiation on the surface was carried out both prior to and post-wetting with water+Tween20 solution, following published recommendations (De Cruz, Wolbarsht and Hauger, 2000a, 2000b; Bracco *et al.*, 2001, 2003; Andreotti, *et al.*, 2007; Striova *et al.*, 2015; Andreotti *et al.*, 2016). The samples were irradiated dry with a single laser pulse and a pulse duration of 150  $\mu$ s, and the optimum fluences ranged between 1.5 and 5.5 J/cm<sup>2</sup>. The authors removed the varnish with no visible alteration of the underlying paint layer by pre-wetting firing at 5 J/cm<sup>2</sup> (Lopez *et al.*, 2019). The second set of tests was performed using a 4  $\omega$  Nd:YAG laser. The inhomogeneous intensity of the laser beam profile was solved using a beam shaping through mask imaging. This led to a decrease in the energy output. The fluence parameters employed in this case were between 250 and 650 mJ/cm<sup>2</sup>. The authors reported good results using the 266 nm Nd:YAG laser and the 2940 nm Er:YAG laser allowing no detectable photo-induced modifications of either the remaining varnish or the underlying painting layer. Moreover, **Lopez and co-authors (Lopez *et al.*, 2019)** in APLAR 7 reported further results on the varnish removal using two nanosecond UV Nd:YAG lasers at 266 nm and 213 nm and a microsecond Er:YAG laser. SD-OCT and OM were employed for the characterisation of the lasers thinning procedure, while colourimetry and time-resolved UV-induced luminescence assessed the possible photo-induced modifications of the remaining coating.

In 2019, **Cappelloni and co-authors (2019)**, at the APLAR 7 conference, reported preliminary laser cleaning tests a Gothic panel painting belonging to the Galleria degli Uffizi in Florence. FT-IR spectroscopy revealed the presence of calcium oxalates, chalk, calcium carbonate and silicates on the paint surface. As reported in the book of abstracts, the Er:YAG laser was used to thin a thick layer applied on the azurite blue paints. In the light blue background, made of azurite with a thin layer of lapis lazuli in animal glue binder, the authors decided to use a 532 nm Nd:YAG laser, due to the high reflectivity of azurite at that laser wavelength. The cleaning process was evaluated with macro- and micro-photography, OM and Raman spectroscopy (Cappelloni *et al.*, 2019).

In February 2020, a special issue was published in the Journal of the Institute of Conservation (ICON) on the use of Er:YAG lasers in conservation of

cultural heritage. According to the Editors the time had come “*when [the use of] Er:YAG [lasers] is becoming more accepted for treatment in the US and UK, and on a variety of materials’ and although more established in Italy ‘there too it seems to be increasing in its applications for treatment’*”(Kemp, 2020). Several institutions and research teams, both in the UK and in Italy, collaborated in the publication of this special issue. **Pereira-Pardo and co-authors (2020)** reviewed the results in the Er:YAG laser cleaning research on historical samples, unregistered objects and mock-ups present in the collection of the British Museum. Er:YAG laser treatment on polychrome coated surfaces are summarised. The techniques employed were SEM-EDS, multispectral imaging (MSI), FT-IR, Raman spectroscopy, visible fibre optics reflectance spectroscopy (VIS-FORS) and Py-GC/MS (Pereira-Pardo, Melita and Korenberg, 2020). A Byzantine fresco, massively restored and extensively overpainted, appeared to be covered with a glossy and discoloured protective coating. FT-IR and Py-GC/MS showed that the coating was shellac, and the overpaintings were an alkyd resin and the acrylic paint. Dry cleaning with sponges or water, acetone and industrial methylated spirits (IMS) solutions had been, unsuccessfully, tested for the removal of the old restoration materials. Therefore, in these areas, the surface was directed irradiated with an Er:YAG laser<sup>30</sup>. The shellac was removed by pre-wetting the surface with isopropanol and using fluences between 1.4 and 1.6 J/cm<sup>2</sup>. Thus, the surface was cleaned by removing the residue mechanically or swabbing with isopropanol. Overpaints were removed upon dry irradiation at 1.4-2.4 J/cm<sup>2</sup> followed by surface cleansing with isopropanol. Red ochre and carbon black pigments were identified in the fresco with Raman spectroscopy. A series of tests were performed to determine the lowest fluence at which changes in the irradiated material could be visually observed and named by the authors as alteration threshold fluence (ATF). The ATF of these pigments was detected on samples prepared ad hoc. This procedure enabled the authors to establish safe working parameters for the subsequent cleaning procedure. ATF values for the dry irradiation of red ochre was 2.9-3.1 J/cm<sup>2</sup> and 2.2-2.3 J/cm<sup>2</sup> using isopropanol or water as pre-wetting agents. ATF values for the dry irradiation

---

30 As reported by the authors a Fidelis XS Er:YAG laser by Fotona was used in Very Short Pulse (VSP) mode  $\tau_L$  100  $\mu$ s (Pereira-Pardo, Melita and Korenberg, 2020).

of carbon black was  $1.5 \text{ J/cm}^2$  (Pereira-Pardo, Melita and Korenberg, 2020). **Brunetto and co-workers (2020)** performed a study for the use of an Er:YAG laser<sup>31</sup> in combination with different solvent mixtures for the cleaning of a Jacopo Tintoretto's oil painting on canvas 'St. Martial in Glory with the Saints Peter and Paul' (Brunetto, Bono and Frezzato, 2020). Microstratigraphic analysis, Reflectance Transformation Imaging (RTI), 3D Microprofilometry, OM, ESEM-EDS,  $\mu$ -FT-IR were employed to study the condition of the painting, the artist techniques, and to evaluate the laser cleaning treatments. The varnish film was made of two superimposed varnish layers, the first one, close to the original paint layer, consisted in a thick layer of terpene resin (25 – 50  $\mu\text{m}$ ) on which there was an unidentified resinous substance (5 – 10  $\mu\text{m}$ ). The Er:YAG laser was used to break and weaken the varnish, before its final removal with Wolbers–Cremonesi solvent mixtures (Teas, 1968; Wolbers, 2000; Cremonesi and Signorini, 2012, pp. 82–87; Phenix, 2013). The fluences ranged from 0.38 to  $0.55 \text{ J/cm}^2$  (pulse duration 150  $\mu\text{s}$ ) and from 0.32 to  $0.65 \text{ J/cm}^2$  (pulse duration 250-300  $\mu\text{s}$ ). Cleaning was both directly on the dry surface and after pre-wetting with water. The cleaning procedure was finalised using a macro-emulsion, which was then removed with a swab and rinsed with a isooctane – acetone solution (Brunetto, Bono and Frezzato, 2020). **Hellen (2020)**, carried out Er:YAG laser<sup>32</sup> cleaning tests on a disposable nineteenth century oil painting with dry laser exposures followed by solvent removal of the remaining varnishes. FT-IR characterised the varnishes as natural resins. A 5 Hz repetition rate and fluences between 0.6 and  $1 \text{ J/cm}^2$  were utilised. The author reported that laser irritation was followed by removal of the disaggregated varnish film using cotton swabs loaded with propan-2-ol with isooctane solvent mixtures at different ratios. The authors concluded that the Er:YAG laser cleaning method successfully assisted the removal of the natural varnish (Hellen, 2020). Part of your thesis was also represented in this special edition (Chillè *et al.*, 2020), and the data published are discussed in chapters 4 and 5.

---

31 According the authors a Light Brush II Er:YAG laser by El.En was used in Very Short (VS) pulse mode  $\tau_L$  150  $\mu\text{s}$  and Short pulse mode  $\tau_L$  250-300  $\mu\text{s}$  (Brunetto, Bono and Frezzato, 2020).

32 As reported by the authors a Fotona XS Dynamis Er:YAG laser was used, no reference is provided by the author for the laser pulse durations selected (Hellen, 2020).

## 2.5 Summary of the Literature Review Findings on the use of laser to treat varnishes

Material irradiated	Substrate	Lasers employed	Laser conditions			Analysis	References
			Pulse duration ( $\tau$ )	Fluence or Energy	Mode Conditions		
Acryloid B-67	Glass slides	QS Nd:YAG laser ( $\lambda$ 1064, 532, and 355nm) (Coherent Infinity)	3 ns	No interaction	Dry	Visual observations	(Madden <i>et al.</i> , 2005)
Acryloid B-72	Glass slides	QS Nd:YAG laser ( $\lambda$ 1064, 532, and 355nm) (Coherent Infinity)	3 ns	No interaction	Dry	Visual observations	(Madden <i>et al.</i> , 2005)
Dammar	Quartz plates and canvas	QS Nd: YAG laser ( $\lambda$ 213 nm) (Lotis II, LS-2147)	15 ns	$60 \pm 2$ mJ/cm <sup>2</sup>	Dry	E-SEM, $\mu$ -Raman, UV-Vis absorption spectroscopy and LIF	(Ciofini, 2014; Ciofini <i>et al.</i> , 2016a)
Dammar	Quartz glass slide	KrF laser ( $\lambda$ 248 nm) (Lamda Physic®)	25 ns	0.6 J/cm <sup>2</sup>	Dry	DTMS	(Theodorakopoulos <i>et al.</i> , 2005)
Dammar	Glass slides	KrF laser ( $\lambda$ 248 nm) (Lambda Physic LPX 240i)	14 ns	0.41 – 0.75 J/cm <sup>2</sup>	Dry	UV/VIS spectroscopy	(Morais <i>et al.</i> , 2007)
Dammar	Glass slides	KrF laser ( $\lambda$ 248 nm) (Lambda Physic LPX 240i)	14 ns	0.41 – 0.75 J/cm <sup>2</sup>	Dry	UV/VIS spectroscopy	(Morais <i>et al.</i> , 2007)
Dammar	Glass slides	QS Nd:YAG laser ( $\lambda$ 355 nm) (Coherent Infinity)	3 ns	0.3 J/cm <sup>2</sup>	Dry	Visual observations	(Madden <i>et al.</i> , 2005)

Material irradiated	Substrate	Lasers employed	Laser conditions			Analysis	References
			Pulse duration ( $\tau$ )	Fluence or Energy	Mode Conditions		
Dammar and Mastic	Quartz plates	XeCl laser ( $\lambda$ 248 nm)	500 fs	0.05 and 0.75 mJ/cm <sup>2</sup>	Dry	LIF	(Pouli <i>et al.</i> , 2007)
Dammar and Mastic	Quartz plates	KrF laser ( $\lambda$ 248 nm) (Braggstar 200, TUI Laser)	10 ns	4 and 500 mJ/cm <sup>2</sup>	Dry	LIF	(Pouli <i>et al.</i> , 2007)
Dammar and Mastic	Gypsum and rabbit glue on wooden panel	QS Nd:YAG laser ( $\lambda$ 1064 nm)	6 ns	0.6 J/cm <sup>2</sup>	Dry	CIELAB, OM	(Siano <i>et al.</i> , 2012)
Dammar and Mastic	Gypsum and rabbit glue on wooden panel	LQS1 Nd:YAG laser ( $\lambda$ 1064 nm)	120 ns	0.8 J/cm <sup>2</sup>	Dry	CIELAB, OM	(Siano <i>et al.</i> , 2012)
Heterogeneous coating: terpene resin + unidentified resinous coating	Oil painting on canvas	Er:YAG laser ( $\lambda$ 2940 nm) (El.En LightBrush2)	~150 $\mu$ s	0.38 to 0.55 J/cm <sup>2</sup>	Dry	RTI, 3D Microprofilometry, OM, ESEM-EDX, $\mu$ -FT-IR	(Brunetto, Bono and Frezzato, 2020)
Heterogeneous overpainting: animal glue, drying oil, saccharide material, natural resin, paraffin	Egg tempera	Er:YAG laser ( $\lambda$ 2940 nm) (MonaLaser)	250 ms	1.7 – 3.2 J/cm <sup>2</sup>	Isopropyl alcohol, Ethanol/water + white spirits, isopropyl alcohol/water,	Cross section, OM, SEM-EDX, FT-IR, GC-MS and Py/GC-MS	(Andreotti <i>et al.</i> , 2016)
Ketone-N	Test samples on Melinex and wooden panels	KrF laser ( $\lambda$ 248 nm)	25 ns	0.40 – 0.48 J/cm <sup>2</sup>	Dry	LIF, LIBS, FT-Raman, FT-IR, DTMS, LDI-MS, MALDI-ToF-MS	(Teule <i>et al.</i> , 2003)

Material irradiated	Substrate	Lasers employed	Laser conditions			Analysis	References
			Pulse duration ( $\tau$ )	Fluence or Energy	Mode Conditions		
<b>Ketone and vinylic resin</b>	Laboratory tempera or oil paint models	Er:YAG (2940 nm) <i>CrystaLase 2940 and Light Scalpel</i> ©	250, 300–350 $\mu$ s	1.0–1.7 J/cm <sup>2</sup>	OH liquid	CIELAB, OM, $\mu$ -Profilometry, BSE SEM, PY-GC-MS and GC-MS, FT-IR	(Andreotti <i>et al.</i> , 2007)
<b>Laropal A81</b>	Red lead oil pigment	Nd: YAG laser ( $\lambda$ 266 nm) (Quantel CFR)	10 ns	250 - 650 mJ/cm <sup>2</sup>	Dry	OM, OCT and UV-induced fluorescence and TR-LIFS	(Lopez <i>et al.</i> , 2019)
<b>Laropal A81</b>	Red lead oil pigment	Er:YAG laser ( $\lambda$ 2940 nm) (El.En LightBrush2)	~150 $\mu$ s	5 J/cm <sup>2</sup> ,	water + Tween20	OM, OCT and UV-induced fluorescence and TR-LIFS	(Lopez <i>et al.</i> , 2019)
<b>Laropal@A81</b>	Red lead oil pigment	Er:YAG laser ( $\lambda$ 2940 nm) (El.En LightBrush2)	~150 $\mu$ s	1.5 – 5.5 J/cm <sup>2</sup> ,	Dry	OM, SD-OCT and UV-induced fluorescence and TR-LIFS	(Lopez <i>et al.</i> , 2019)
<b>Mastic</b>	Quartz plates and canvas	QS Nd: YAG laser ( $\lambda$ 213 nm) (Lotis II, LS-2147)	15 ns	70 $\pm$ 2 mJ/cm <sup>2</sup>	Dry	E-SEM, $\mu$ -Raman, UV-Vis absorption spectroscopy and LIF	(Ciofini, 2014; Ciofini <i>et al.</i> , 2016)
<b>Mastic</b>	Quartz glass slide	KrF laser ( $\lambda$ 248 nm) (Lamda Physic®)	25 ns	0.45 J/cm <sup>2</sup>	Dry	DTMS	(Theodorakopoulos <i>et al.</i> , 2005)

Material irradiated	Substrate	Lasers employed	Laser conditions			Analysis	References
			Pulse duration ( $\tau$ )	Fluence or Energy	Mode Conditions		
Mastic	Glass slides	KrF laser ( $\lambda$ 248 nm) (Lambda Physic LPX 240i)	14 ns	0.36 – 0.73 J/cm <sup>2</sup>	Dry	UV/VIS spectroscopy	(Morais <i>et al.</i> , 2007)
Mastic and oil varnish	Laboratory tempera or oil paint models	Er:YAG (2940 nm) <i>Crystalase 2940 and Light Scalpel</i> ©	250, 300–350 $\mu$ s	1.0–1.7 J/cm <sup>2</sup>	OH liquid	CIELAB, OM, $\mu$ -Profilometry, BSE SEM, PY-GC-MS and GC-MS, FT-IR	(Andreotti <i>et al.</i> , 2007)
Natural resins (dammar, mastic)	Test samples on Melinex and wooden panels	KrF laser ( $\lambda$ 248 nm)	25 ns	0.40 – 0.48 J/cm <sup>2</sup>	Dry	LIF, LIBS, FT-Raman, FT-IR, DTMS, LDI-MS, MALDI-ToF-MS	(Teule <i>et al.</i> , 2003)
Natural resins (dammar, Mastic, Shellac)	Paintings (oil on board)	QS Nd:YAG laser ( $\lambda$ 532 nm) (CRF 400 – Quantel)	10-30 ns	83 mJ/cm <sup>2</sup> - 440 mJ/cm <sup>2</sup>	---	Visible, raking and UV light, OM, ESEM-EDS, FT-IR and XRF	(Patti and Siano, 2015)
Natural resins (dammar, Mastic, Shellac)	Egg tempera	Er:YAG (2940 nm) <i>(Conservator 2940</i> ®)	250 $\mu$ s	1.3–1.5 J/cm <sup>2</sup>	Dry	CIELAB, OM, $\mu$ -Profilometry, BSE SEM, PY-GC-MS and GC-MS, FT-IR	(Bracco <i>et al.</i> , 2003)
Natural resin (?)	Painting	QS Nd:YAG laser ( $\lambda$ 355 nm) (Thunder art system)	10 ns	80 mJ/cm <sup>2</sup>	Dry	multispectral analysis and OM	(Striber, Jovanović and Jovanović, 2017)
Natural resin (?)	Painting	SFR Nd:YAG laser ( $\lambda$ 1064 nm) (Combo – El.En)	40 $\mu$ s	402 - 886 mJ/cm <sup>2</sup>	2% (v/v) of Tween 20 in demineralised water	Visible, raking and UV light, OM, ESEM-EDS, FT-IR and XRF	(Patti and Siano, 2015)

Material irradiated	Substrate	Lasers employed	Laser conditions			Analysis	References
			Pulse duration ( $\tau$ )	Fluence or Energy	Mode Conditions		
Natural resin (?)	Oil painting on board	Er:YAG laser ( $\lambda$ 2940 nm) (Fotona XS Dynamis)	?	0.6 and 1 J/cm <sup>2</sup>	Dry	VIS and UV light, DinoLite microscope, FT-IR	(Hellen, 2020)
Oil varnishes	Painting	QS Nd:YAG laser ( $\lambda$ 1064 nm) (Art Light Laser Lambda Scientifica S.p.A.)	8 – 10 ns	60 mJ at 10Hz 85 mJ at 15 Hz	Agar gel (pH 6-7)	Visible, UV and IR light, $\mu$ -FTIR and Py-GCMS	(Giardina <i>et al.</i> , 2017)
Paraloid B72	Quartz plates	ArF laser ( $\lambda$ 193 nm) (Lambda Physik 100)	25 ns	1.25 J/cm <sup>2</sup>	Dry	OM	(Kogou <i>et al.</i> , 2011)
Paraloid B72	Fresco	KrF laser ( $\lambda$ 248 nm)	---	2 J/cm <sup>2</sup>	Dry	---	(Marczak <i>et al.</i> , 2008)
Paraloid B72	Quartz plates	KrF laser ( $\lambda$ 248 nm) (Laser lab Göttingen)	500 fs	2.1 J/cm <sup>2</sup>	Dry	OM	(Kogou <i>et al.</i> , 2011)
Paraloid B72	Aboriginal bark paintings with plant- and animal-based binders	Nd:YAG laser ( $\lambda$ 532 nm) (Continuum Surelite I-10)	5 ns	200 mJ/cm <sup>2</sup> - 1 J/cm <sup>2</sup>	Dry	----	(Kane <i>et al.</i> , 2013)
Paraloid B72	'a fresco' mural sample	Er:YAG (2940 nm) (High Power Erbium CrystaLase – Mona Laser)	300 $\mu$ s	0.6 J/cm <sup>2</sup>	Acetone/isopropanol (1:1 v/v)	CIELAB, OM, $\mu$ -Raman	(Striova <i>et al.</i> , 2011a)

Material irradiated	Substrate	Lasers employed	Laser conditions			Analysis	References
			Pulse duration ( $\tau$ )	Fluence or Energy	Mode Conditions		
<b>Paraloid B72 and Laropal K80</b>	Quartz plates	XeCl laser ( $\lambda$ 248 nm)	500 fs	0.08–0.7 J/cm <sup>2</sup>	Dry	OM and SEM	(Pouli <i>et al.</i> , 2009)
<b>Paraloid B72 and Laropal K80</b>	Quartz plates	KrF laser ( $\lambda$ 248 nm) (Lambda Physik LPX 200)	30 ns	0.6–2 J/cm <sup>2</sup>	Dry	OM and SEM	(Pouli <i>et al.</i> , 2009)
<b>Regalrez 1094</b>	Cloth-lined board with 11 Maimari vinyl colours	LQS Nd:YAG laser ( $\lambda$ 1064 nm)	100 ns	0.058 J/cm <sup>2</sup>	Dry	Stereomicroscopy OM, SEM-EDS, CIELAB, $\mu$ -Raman and FT-IR	(De Cesare, Izurlo and Biocca, 2017)
<b>Shellac</b>	Tempera paints samples	UV laser ( $\lambda$ 213 nm)	15 ns	0.14 J/cm <sup>2</sup>	Dry	CIELAB, OM, LIF	(Oujja <i>et al.</i> , 2011)
<b>Shellac</b>	Quartz plates and canvas	QS Nd: YAG laser ( $\lambda$ 213 nm) (Lotis II, LS-2147)	15 ns	85 $\pm$ 2 mJ/cm <sup>2</sup>	Dry	E-SEM, $\mu$ -Raman, UV-Vis absorption spectroscopy and LIF	(Ciofini, 2014; Ciofini <i>et al.</i> , 2016)
<b>Shellac</b>	Test samples on Melinex and wooden panels	KrF laser ( $\lambda$ 248 nm)	25 ns	0.40 – 0.48 J/cm <sup>2</sup>	Dry	LIF, LIBS, FT-Raman, FT-IR, DTMS, LDI-MS, MALDI-ToF-MS	(Teule <i>et al.</i> , 2003)
<b>Shellac</b>	Glass slides	KrF laser ( $\lambda$ 248 nm) (Lambda Physik LPX 240i)	14 ns	0.48 – 0.86 J/cm <sup>2</sup>	Dry	UV/VIS spectroscopy	(Morais <i>et al.</i> , 2007)

Material irradiated	Substrate	Lasers employed	Laser conditions			Analysis	References
			Pulse duration ( $\tau$ )	Fluence or Energy	Mode Conditions		
Shellac	Glass slides	KrF laser ( $\lambda$ 248 nm) (Lambda Physic LPX 240i)	14 ns	0.48 – 0.86 J/cm <sup>2</sup>	Dry	UV/VIS spectroscopy	(Morais <i>et al.</i> , 2007)
Shellac	Tempera paints samples	UV laser ( $\lambda$ 265 nm)	260 fs	0.85 J/cm <sup>2</sup>	Dry	CIELAB, OM, LIF	(Oujja <i>et al.</i> , 2011)
Shellac	Glass slides	QS Nd:YAG laser ( $\lambda$ 355 nm) (Coherent Infinity)	3 ns	0.3 J/cm <sup>2</sup>	Dry	Visual observations	(Madden <i>et al.</i> , 2005)
Shellac	Tempera paints samples	UV laser ( $\lambda$ 398 nm)	150 fs	0.96 J/cm <sup>2</sup>	Dry	CIELAB, OM, LIF	(Oujja <i>et al.</i> , 2011)
Shellac	Glass slides	QS Nd:YAG laser ( $\lambda$ 532 nm) (Coherent Infinity)	3 ns	0.2–2 J/cm <sup>2</sup>	Dry	Visual observations	(Madden <i>et al.</i> , 2005)
Shellac	Glass slides	QS Nd:YAG laser ( $\lambda$ 1064 nm) (Coherent Infinity)	3 ns	1 – 3 J/cm <sup>2</sup>	Dry	Visual observations	(Madden <i>et al.</i> , 2005)
Shellac	14 <sup>th</sup> century tempera painting	Er:YAG (2940 nm) ( <i>Conservator 2940</i> ®)	250 $\mu$ s	1.3 J/cm <sup>2</sup>	Dry	---	(De Cruz, Wolbarsht and Hauger, 2000a; De Cruz, Wolbarsht. and Hauger, 2000b)
Shellac	Laboratory tempera or oil paint models	Er:YAG (2940 nm) ( <i>Crystalase 2940 and Light Scalpel</i> ©)	250, 300–350 $\mu$ s	1.0–1.7 J/cm <sup>2</sup>	OH liquid	CIELAB, OM, $\mu$ -Profilometry, BSE SEM, PY-GC-MS and GC-MS, FT-IR	(Andreotti <i>et al.</i> , 2007)
Shellac	Mural painting samples	Er:YAG (2940 nm) ( <i>LightBrush</i> , El.En.)	~150 $\mu$ s	1.9 J/cm <sup>2</sup>	Isopropanol	CIELAB, micro profilometry, OCT	(Striova <i>et al.</i> , 2015)

Material irradiated	Substrate	Lasers employed	Laser conditions			Analysis	References
			Pulse duration ( $\tau$ )	Fluence or Energy	Mode Conditions		
Shellac	'a fresco' mural painting	Er:YAG laser ( $\lambda$ 2940 nm) (Fotona)	~100 $\mu$ s	1.4 – 1.6 J/cm <sup>2</sup>	Isopropanol	FT-IR, Py-GC/MS, Raman spectroscopy	(Pereira-Pardo, Melita and Korenberg, 2020)
Synthetic resin (N.A.)	17 <sup>th</sup> century oil on canvas painting	Er:YAG (2940 nm) ( <i>Conservator 2940</i> ®)	250 $\mu$ s	1.5 J/cm <sup>2</sup>	Isopropyl alcohol	---	(De Cruz, Wolbarsht and Hauger, 2000a; De Cruz, Wolbarsht. and Hauger, 2000b)
Varnish (?)	Paintings	KrF laser ( $\lambda$ 248 nm)	15 ns *	---	Dry	LIBS, reflectography analysis	(Hontzopoulos, Fotakis and Doulgeridis, 1993; Fotakis, Hontzopoulos and Zergioti, 1995; Anglos <i>et al.</i> , 1996; Fotakis <i>et al.</i> , 1997; Zergioti <i>et al.</i> , 1997; *Zafirooulos and Fotakis, 1998)

# CHAPTER 3      NATURAL AND SYNTHETIC VARNISHES: Preparation and Characterisation

*“The more we learn about the material structure of paintings through technical study, the more we appreciate their true complexity”.*

— Zuccari (2003)<sup>1</sup>

*“Varnishes are the most vulnerable part of a pictures. The large surface to volume ratio of this thin layers of organic materials, maximizes their exposure to the deteriorating effect of environment.”*

— René de la Rie (1988)<sup>2</sup>

*This chapter provide a brief review based on the up-to-date knowledge of the chemical characteristics of a triterpenoid resin (Dammar), two ketone resins (Ketone N and MS2A), and an acrylic polymer (Paraloid B67) addressing so the **objective a**. Dammar, Ketone N, MS2A, and Paraloid B67 films have been applied on glass slides by using a film applicator and received 170.6 klux·hrs irradiation dose in a xenon-arc fadeometer (310-800 nm) followed by hydrothermal ageing (30 days in 40% RH and 40 °C). The morphological and physicochemical modifications of the varnishes were investigated using stylus profilometry, static contact angle, gas pycnometry, colourimetry, thermogravimetric analysis (TGA), differential scanning calorimetry (DSC) and attenuated total reflection/Fourier transform infrared spectroscopy (ATR/FT-IR), addressing **objective b**. The analytical findings provided physicochemical features of the resinous substrates which were useful for the subsequent Er:YAG laser interaction studies.*

---

1 (Zuccari, 2003)

2 (de la Rie, 1988b)

### 3.1 Introduction

In conservation, it is fully acknowledged that original materials from artworks present distinctive chemical and physical features that make them unique if compared to specimens created in laboratories for research. Nonetheless, the systematic acquisition of data from mock-ups, which represent original degraded materials, can verify the effectiveness of the research due to the knowledge of the preparation technique employed in creating the mock-ups, the chemical and physical composition of the materials used, and their distribution in various substrates. Moreover, tests carried out on samples allow the researcher to control and trace the results obtained and, in doing so, making this tests repeatable (Giovagnoli, 2009).

As previously described in section 2.3, the surface cleaning of easel paintings can be considered one the most critical, highly sensitive and complex procedures in conservation of fine arts (Cremonesi and Signorini, 2012). The substances added to the works of arts that need to be thinned or removed can be categorised as: i) layers such as original varnishes with possible degradation products, or ii) layers applied later upon conservation, such as other varnishes, overpaints, adhesives, and consolidants. These materials degrade as a result of interaction with light, air and pollution, which leads to modifications in their chemical and physical properties (Giovagnoli, 2009).

### 3.2 Degradation of the varnishes

Modern spirit varnishes, commonly used by artists or applied by conservators, are made of natural or synthetic resins. These resins are commonly dissolved in suitable solvents and upon evaporation after their application generate varnish films (Massa and Scicolone, 2004). After their application on the surface of art objects, resin varnishes start interacting with the surrounding environment.

Degradation is defined as the “act or process of simplifying or breaking down a molecule into smaller parts, either naturally or artificially” (*Oxford English Dictionary*, 1995), leading to a deterioration of the constituent materials of cultural objects (Bovey and Winslow, 1979). Light, oxygen, heat, humidity and pollutants can trigger inhomogeneous degradation processes with the formation of oxidation

products at the surface of the varnish films (Feller and Curran, 1975; Wolbers, Serman and Stavroudis, 1990; Phenix, 2013; Tempest *et al.*, 2013; van den Berg *et al.*, 2014; Steyn *et al.*, 2017; Tsang and Erhardt, 2018; Baij *et al.*, 2020). In general, during ageing, all varnishes degrade through oxidation, auto-oxidation and crosslinking processes, catalysed by the direct absorption of UV-radiation (Theodorakopoulos and Zafiropulos, 2003) and these changes can be detected over long periods (Ghenou, 2017)

### 3.2.1 *Natural triterpenoid resin: Dammar*

Natural Terpenic Resins are exudate from various plants (Feller, 2002). They are blends of volatile and non-volatile terpenoid and phenolic secondary compounds usually secreted by specific areas of the plants (Colombini and Modugno, 2009, p. 12). Natural terpenic resins derive from the reaction of isoprene units (the chemical building block of natural resins). Depending on the number of molecules linked together, they can be divided into four different chemical classes: monoterpenes (two units of isoprene), sesquiterpenes (three units of isoprene), diterpenes (four units of isoprene) and triterpenes (six units of isoprene) (Mills and White, 1999, p. 95; Massa and Scicolone, 2004; Ciofini, 2014, p. 6). Dammar is a triterpenoid (TTP) resin containing a volatile fraction, a fraction of mono- and a fraction of sesquiterpenoids, and a high-molecular weight fraction (van der Doelen *et al.*, 1998; van der Doelen, 1999; Dietemann *et al.*, 2000; Dietemann, 2003; Theodorakopoulos, 2005; Bonaduce *et al.*, 2016).

Natural resins are primarily composed of mixtures of simple<sup>3</sup>, long and short-chain hydrocarbon molecules<sup>4</sup> as well as more complex polymers (Matteini, Mazzeo and Moles, 2016, p. 170). As reported by Colombini and co-authors (2009, p. 17), dammar resin is characterised by tetracyclic triterpenoids of the dammarane

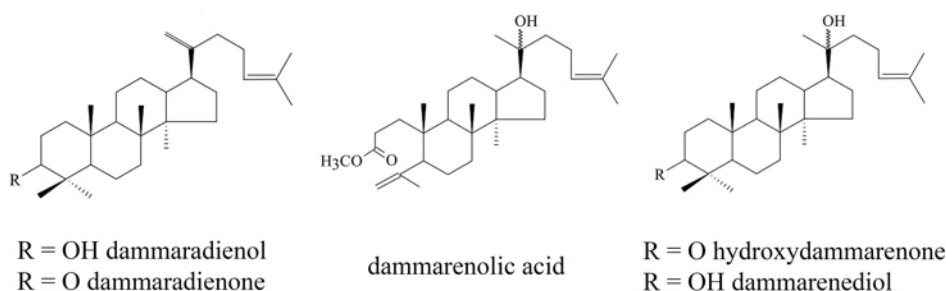
---

3 Simple molecules can be classified as aromatic acids composed by short unsaturated aliphatic hydrocarbons chains (not always detected in all the natural resins), essential oils such as terpenic hydrocarbons and their alcoholic and ether derivatives; resins acids with complex terpenic, cyclic and polycyclic structures, whose presence changes depending on the natural resin (Matteini, Mazzeo and Moles, 2016, p. 170).

4 Long hydrocarbon molecules (e.g. Essential oils and resins acids) tend to create high molecular weight compounds via oxidative reactions, changing the fundamental properties of the resins (Matteini, Mazzeo and Moles, 2016, p. 170).

series and contains minor amounts of pentacyclic triterpenoids of the series of oleanane, ursane, and hopane (Figure 3.1). Furthermore, dammar resin contains a polymeric fraction called polycadinene<sup>5</sup> or  $\beta$ -resene (Van Aarssen *et al.*, 1990; Colombini and Modugno, 2009, p. 17). However, dammar is regarded as a low molecular weight natural resin with a number-average molecular weight  $\bar{M}$  of 418 (de la Rie, 1989; de la Rie *et al.*, 2010; Theodorakopoulos and Boon, 2011)

### Dammarane Skeleton Molecules



### Oleanane and Ursonic Molecules

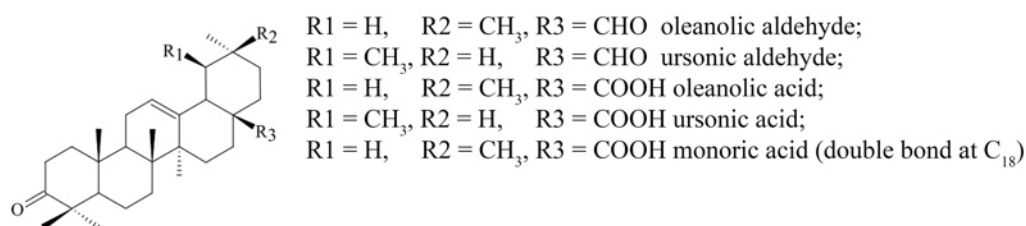


Figure 3.1 – Triterpenoid molecular structures present in dammar (Figure adapted from Theodorakopoulos, 2005, p. 82)

Over time, extensive molecular studies have carried out for characterisation of fresh and aged dammar resin films (Mills, 1956; Arigoni *et al.*, 1960; Brewis and Halsall, 1961; Cerny, Vystrcil and Huneck, 1963; Brewis *et al.*, 1970; Harrison *et al.*, 1971; Mills and White, 1977; Feller, Jones and Stolow, 1985; de la Rie, 1988a, 1988b; de la Rie, 1989; Larson, Shin and Zink, 1991; van der Doelen, 1999; van der Doelen and Boon, 2000; Dietemann *et al.*, 2000; Feller and Whitmore, 2002; Scalarone *et al.*, 2005; Theodorakopoulos *et al.*, 2005; Buder, 2008; Theodorakopoulos, Boon and Zafirooulos, 2009; Nevin *et al.*, 2009; Dietemann *et al.*, 2009; Horie, 2010, p. 253; Filippidis *et al.*, 2014; Bonaduce *et al.*, 2016; Ciofini *et al.*, 2016b; Invernizzi *et al.*, 2018). In particular, photochemical and thermal

<sup>5</sup> Polycadinene derives from the polymerised sesquiterpenoid cadinene. Dammar resin contains a small amount of this polymeric fraction (Van Aarssen *et al.*, 1990).

degradation studies have been performed with the use of Ultraviolet-visible (UV-Vis), IR and UV fluorescence spectrophotometry (de la Rie, 1982, 1988a; Theodorakopoulos *et al.*, 2007), FT-IR and  $\mu$ -Raman spectroscopies (Vandenabeele *et al.*, 2000; Theodorakopoulos *et al.*, 2007; Nevin *et al.*, 2009; Azémard, Vieillescazes and Ménager, 2014) and chromatographic and mass spectrometric techniques (van der Doelen *et al.*, 1998; Zumbühl *et al.*, 1998; Zumbühl, Knochenmuss and Wülfert, 1998; van den Berg *et al.*, 2000; Dietemann *et al.*, 2001; Watts and de la Rie, 2002; Theodorakopoulos, Boon and Zafirooulos, 2009).

In principle, the ageing process of dammar resin is triggered mainly by an oxidative process, and the degradation can be attributed to autoxidative radical chain reactions (de la Rie, 1988a; van der Doelen, 1999; Theodorakopoulos, 2005, p. 83; Colombini and Modugno, 2009, p. 133). In particular, three different main mechanisms have been identified: i) light-induced auto-oxidation of functional groups within the resin film, which results in the addition of oxygen-containing functional groups to the original triterpenoid hydrocarbon backbones (up to six oxygen atoms per molecule [Horie, 2010, p. 253]) and therefore a change in solubility<sup>6</sup>; ii) radical polymerisation (cross-linking and condensation mechanisms) generating higher molecular weight (MW) components and iii) yellow chromophores such as unsaturated quinones (de la Rie, 1988a; Dietemann, 2003, pp. 24–25; Theodorakopoulos, 2005, pp. 83–84; Ciofini, 2014, pp. 9–10). As described by Dietemann (2003), in the dark conditions delayed kinetics of self-formations of radicals were identified. Radical chain reactions are due to the absorption of UV light having sufficient energy to break C-C and C-H bonds in the polymer chain at 375 and 420 kJ/mol, respectively (Gheno, 2017, p. 15). The energy to initiate these reactions can also come from thermal energy (Ciofini, 2014), which can lead to thermal rearrangements in the chemical structure of the dammar resin and the formation of the high MW materials (van der Doelen and Boon, 2000; Horie, 2010, p. 253). The degradation of natural resins inevitably leads to a reduction in solubility of old varnishes, together with problems of yellowing, darkening, and brittleness (Colombini and Modugno, 2009, p. 342). Moreover,

---

<sup>6</sup> The change in solubility results in an increase in the polarity of solvents needed for the dissolution of a dammar film (Horie, 2010, p. 253).

Theodorakopoulos and co-workers (Theodorakopoulos and Zafiropoulos, 2003; Theodorakopoulos *et al.*, 2005, 2007; Theodorakopoulos and Boon, 2011) assessed the presence of an exponential gradient in oxidation and crosslinking across the film thicknesses of aged TTP resins which can be considered directly related with an equivalent gradient in the solubility within the same varnish layer. The changes in the physicochemical properties of the natural varnishes deteriorate the appearance of works of art and lead conservation treatments for the removal or thinning of aged varnishes.

### 3.2.2 Synthetic resins: Ketone N, MS2A and Paraloid B67

Synthetic polymers (such as polyvinyl, acrylic, and ketonic) are materials that almost entirely replaced the use of traditional paint varnishes, such as mastic, dammar, and sandarac (Matteini, Mazzeo and Moles, 2016). Only thermoplastic resins are used in solvent-type varnishes (Feller, Jones and Stolow, 1985, p. 125). These resins can be dissolved in organic solvents and they can create transparent and colourless films (Gettens and Stout, 1966, p. 66; Massa and Scicolone, 2004; Colombini and Modugno, 2009, p. 26).

In general, the convenience in the use of synthetic resins, when compared to the natural ones, is that they are made up of single small molecular species (monomers), which form larger macromolecules upon polymerisation. This characteristic enabled researchers to readily study their degradation properties easily (Mills and White, 1999, p. 129; Horie, 2010, p. 15; Lawman, 2011, pp. 10–11) and ensure the production of more stable coatings after their application on works of arts.

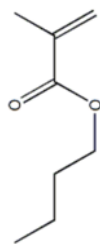


Figure 3.2 – Chemical structure of n-butyl methacrylate commercially known as Paraloid B67.

**Paraloid B67** (Figure 3.2) is an acrylate polymer (poly-isobutyl methacrylate homopolymer<sup>7</sup> - PiBMA) with a high MW structure. The polymer chain length of B67 is relatively long, resulting in a higher number-average molecular weight ( $\bar{M} \sim 5831$ ) compared to the dammar ( $\bar{M} \sim 418$ ) (de la Rie, 1989; de la Rie *et al.*, 2010). Paraloid B67 was used as a finishing varnish/coating (Feller, 1972; Nicolaus, 1999). The high MW and low refractive index<sup>8</sup> (de la

Rie, 1989) made the B67 less satisfactory from the point of view of the final appearance achieved onto the painting's surface, when compared to low MW natural resins, owing to differences in gloss and penetration of porous paint (Gettens and Stout, 1966, p. 3; Feller, Jones and Stolow, 1985, p. 139; Mills and White, 1999, p. 133)<sup>9</sup>. Therefore, B67 was regarded as a less satisfactory varnish. Moreover, B67 cross-links severely (Feller, 1976), in particular under intense UV exposure (Lazzari and Chiantore, 2000; Chiantore and Lazzari, 2001) becoming insoluble (Colombini and Modugno, 2009, p. 343; Horie, 2010). The stability of this polymer, as shown by Chiantore and Lazzari (2000, 2001), appeared strongly reduced by the presence of relatively longer esters in alkyl side groups. The oxidation of B67 was described by the authors as favoured by hydrogen atoms on the tertiary carbon of the isobutyl groups. Moreover, Chiantore and Lazzari (2000, 2001) proved that the presence of butyl ester groups in the polymer chain could trigger fast and extensive cross-linking reactions accompanied with the fragmentation of the polymer and the consequent weight loss of the overall polymeric chain (Favaro *et al.*, 2006).

Furthermore, Gordienko and Dmitriev (1996) reported that the first step of ageing of B67 could involve the thermal decomposition of easy alterable structures formed during the synthesis of the polymer. Conversely, for more extended ageing,

---

7 B67 is obtained by the reaction of n-butanol and methacrylic acid (Learner, 2004, p. 7)

8 The refractive index of Paraloid B67 is 1.48 as reported by Feller, Jones and Stolow (1985, p. 142)

9 For the description of appearance of paintings varnishes please refer to Feller, Jones and Stolow (1985, p. 139) and Berns and de la Rie (2002).

the oxidative decomposition of the side groups could be favoured (Gheno, 2017, p. 17).

Several studies have been carried out to characterise the structural and molecular changes which occurred under artificial ageing using UV-Vis, FT-IR Spectroscopy and by Size Exclusion Chromatography (SEC) (Kashiwagi, Hirata and Brown, 1985; Melo *et al.*, 1999; Chiantore, Trossarelli and Lazzari, 2000; Lazzari and Chiantore, 2000; Chiantore and Lazzari, 2001; Learner, 2004; Favaro *et al.*, 2006; Lawman, 2011, pp. 10–11; Gheno, 2017, pp. 17–18)

**Ketone resins** (particularly cyclohexanone and its methyl-substituted derivatives - [Mills and White, 1999, p. 137]) were the first low MW synthetic resins to be used as finishing varnishes (Nicolaus, 1999, p. 320). Variations of ketone resins, that were first seen on the market in the 1950s, were well received because of their similarities to natural TTP varnishes, such as dammar and mastic (Mills and White, 1999, p. 137; Horie, 2010, p. 183). Due to their excellent optical characteristics<sup>10</sup>, including a low MW and a relatively high refractive index<sup>11</sup> (de la Rie and Shedrinsky, 1989; Berns and de la Rie, 2003a, 2003b, 2003c), ketone resins have often replaced traditional natural varnishes. As aforementioned, the latter proved to be chemically unstable having general tendency of yellowing, cracking and less soluble over time (Berns and de la Rie, 2003a, 2003b, 2003c; Maines and de la Rie, 2005; Gheno, 2017, p. 22). Moreover, the cross-linking reactions do not have a significant influence in the solubility features of these resins. This peculiarity was considered to be an important point in the use of low MW resins in the conservation field (Colombini and Modugno, 2009, p. 345).

Ketone resins are made by heating cyclohexanone<sup>12</sup> (C<sub>6</sub>H<sub>10</sub>O) and/or methyl cyclohexanone at high pressure with formaldehyde in presence of NaOH as catalyst (Hill, 1948; Mestdagh *et al.*, 1992; Horie, 2010, p. 183; Appala Naidu and Dinda, 2015). Ketone resin is an oligomer made of small number of monomers per

---

10 The number-average molecular weight of MS2A ( $\bar{M}_n \sim 482$ ) is similar to the one of dammar ( $\bar{M} \sim 418$ ) (de la Rie *et al.*, 2010).

11 The refractive index of MS2A and Ketone N is respectively 1.52 and 1.53 as reported by Berns and de la Rie (2002)

12 Cyclohexanone is formed by six carbon cyclic molecule with a ketone functional group (Appala Naidu and Dinda, 2015).

molecule (de la Rie and Shedrinsky, 1989) rather than a polymer (Figure 3.3). Commercial Ketone resin products AW2 (by BASF, Germany) and MS2 (by Howards, UK) are condensation products of cyclohexanone and a mixture of all the isomers of the methylcyclohexane (the methyl group can be ortho, meta and para to the carbonyl group) (Mills and White, 1999, p. 138), while Ketone N was a product of the condensation of cyclohexanone only (de la Rie and Shedrinsky, 1989).

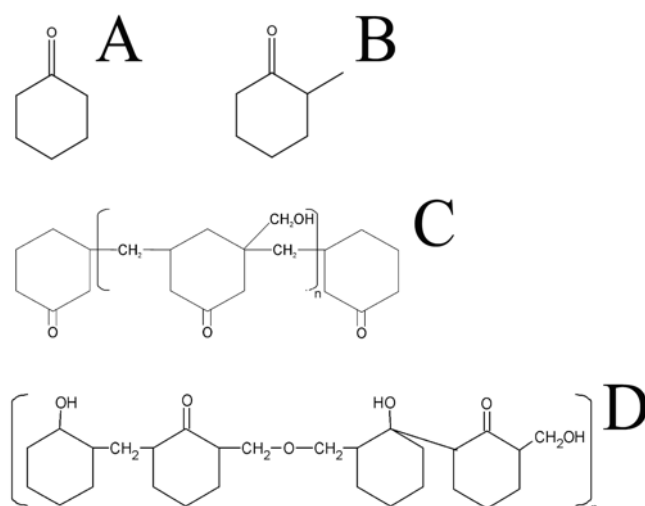


Figure 3.3 – Chemical structure of cyclohexanone (A); methyl cyclohexanone (B); structure of ketone resins as suggested by de la Rie and Shedrinsky (1989) where n is equal to 3 and 5; (C) and structure of ketone resins published by Mills and White (1999, p. 138) (D).

In 1963, the MS2A was released on the market. The resin was produced from MS2, and it was obtained by reduction with sodium borohydride in presence of methanol (Mills and White, 1999, p. 138; Appala Naidu and Dinda, 2015). The probable chemical structure of MS2A resin is presented in Figure 3.4, as reported by Routledge (2000) on a report on the history of the development of ketonic resins.

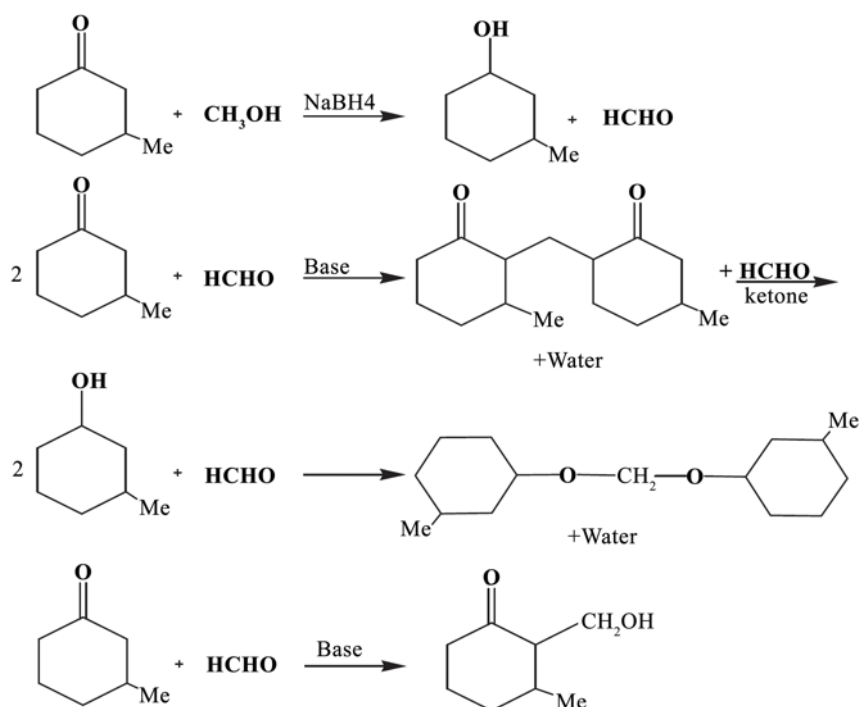


Figure 3.4 – Probable structure of MS2A as suggested by Routledge (2000)

Thus, if on the one hand the MS2A was more photochemically stable to light-induced oxidation than the material containing ketone groups, on the other hand, the resin resulted to be more brittle because of the increased hydrogen bonding (Colombini and Modugno, 2009, p. 345; Horie, 2010, p. 183).

The degradation of Ketone varnishes was studied and characterised mainly by de la Rie and Shedrinsky (1989). Brittleness was considered one of the main drawbacks of this type of resins, particularly for picture varnish applications. They showed that autoxidation reactions are mostly responsible for the degradation of ketone resins. In particular, ketone groups and C-C double bonds are the most vulnerable sites to autoxidation (de la Rie and Shedrinsky, 1989). Hydrogen atoms attached to tertiary carbon atoms can easily produce alkyl radicals. The latter can, therefore, react with oxygen to produce peroxy radicals (de la Rie and Shedrinsky, 1989). Ketone groups are prone to scission reactions leading to free radicals when exposed to UV light (Norrish Type I and II reactions) (de la Rie and Shedrinsky, 1989). The authors defined Norrish Type I and II scission reactions of carbonyl groups as the important process in the degradation of ketone resin films (de la Rie and Shedrinsky, 1989). Accelerated ageing of ketone resin films, carried out under UV and air exposure, lead to the development of UV-absorbing chromophores (de

la Rie and Shedrinsky, 1989), as well as the formation of oxidation and crosslinking, which are responsible for the slight yellow hue and reduced solubility of the resins to moderately polar solvents (Routledge, 2000). Doménech-Carbó and co-authors (2008, 2009) confirmed in their research all the previous published findings. Indeed these researchers established that ketone resins are more sensitive to photoageing, with the development of significant changes in the chemical structure of the coating films. The characteristic yellowing of the resins, already observed by de la Rie and Shedrinsky (1989) is associated with the autoxidation of ketone groups and the formation of carboxylic fractions as well as the formation of unsaturated chromophores (Doménech-Carbó *et al.*, 2008, 2009). Bonaduce and co-workers (2013) reported this side effect on MS2A, confirming that the presence of carbon-carbon double bonds and small amounts of unreduced carbonyl groups can make the resin sensitive to light ageing and subject to radical reactions, with the consequence of cross-linking and oxidation. Several types of research have been carried out to characterise these products and their structural changes after ageing using Optical and electron microscopy techniques, atomic force microscopy (AFM), UV-Vis spectrophotometry, FT-IR, Py-GC-MS and a combination of the last two instrumental techniques (Hill, 1948; Lank, 1972; Feller and Curran, 1975; de la Rie and Shedrinsky, 1989; Mestdagh *et al.*, 1992; Routledge, 2000; Berns and de la Rie, 2002; Doménech-Carbó *et al.*, 2008, 2009; Bonaduce *et al.*, 2013; Uttaravalli, 2018).

### 3.3 Justification of Methodology

The following methodology was designed to determine the representative varnishes to be used for the Er:YAG laser interaction study. Four varnishes based on a triterpenoid resin (Dammar), two Ketone resins (Ketone N and MS2A), and an Acrylic polymer (Paraloid B67)<sup>13</sup> – that were commonly used by artists and conservators during the twentieth century in the West – and applied on painted surfaces were selected. In order to create representative mock-ups, it was necessary to reproduce the effects of time through controlled and reproducible accelerated

---

<sup>13</sup> This polymer is known in Europe with the trade name of *Paraloid* and in the USA with the trade name of *Acryloid*.

ageing, even though such processes lead to mere approximations of the conditions of naturally aged materials (Gheno, 2017). Herein, the accelerated ageing process has been conducted in a xenon-arc light ageing chamber and a microclimatic chamber with temperature and humidity controls (Doménech-Carbó *et al.*, 2008). Once the ageing process was completed, as described by Theodorakopoulos (2005, p. 78), to overcome the problem of discolouration (yellowing) (de la Rie, 1987, 1988a, 1988b; Feller, 1994; van der Doelen, van den Berg and Boon, 1998; Dietemann, 2003) the aged varnishes mock-ups were kept 30 days in the dark prior to the laser irradiation (Theodorakopoulos, 2005; Ciofini, 2014).

A polyethylene glycol sorbitan monolaurate surfactant non-ionic surfactant (Tween 20) in deionised water (DI-W+TW20) was selected in this study. The use a surfactant was mainly motivated by the necessity to decrease the surface tension of the deionised water, increasing the wettability of the varnish surfaces in sight of the tests using an Er:YAG laser. Moreover, according to the literature (Bracco *et al.*, 2001; Andreotti *et al.*, 2007), the use of deionised water combined with Tween 20 appeared to provide the best results when applied as a pre-wet agent on the area to be irradiated using an Er:YAG laser.

Stylus profilometry, static contact angle and colourimetry analyses allowed to monitor the morphological modification triggered by the ageing processes on the varnish films. ATR/FT-IR spectroscopy, which was carried out before and after ageing, was employed to evaluate the ageing effects of the aged resin films (Theodorakopoulos *et al.*, 2005, 2007; Nevin *et al.*, 2009; Prati *et al.*, 2011). A gas pycnometer was used to measure the density of the resins (Donato and Lazzara, 2012). Thermogravimetric analysis (TGA) and differential scanning calorimetry (DSC) were carried out to provide the fundamental thermal properties (Gallagher, 2002; Li and Stoliarov, 2013; Majewsky *et al.*, 2016; Alonso Ipina *et al.*, 2018) of the resins, including the kinetics of thermo-oxidative degradation (TGA) (Fügleri, 2014) and the specific heat capacity ( $C_p$ ) using the ASTM standard E1269 (2011) (DSC). DSC analysis has been scarcely used in the conservation field, even though dedicated scientific literature is gradually increasing (Odlyha, 1988, 1991; Odlyha and Burmester, 1988; Schilling, 1989; Odlyha and Scott, 1994; Prati, Chiavari and Cam, 2001). In general, not considering Thermomechanical Analysis (TMA) and Dynamic Mechanical Analysis (DMA) which are commonly employed to study the

properties of thin films, Rasi *et al.* (2018) reported that the use of films is quite limited since the ratio of signal to noise depends on the sample's mass, and for films, the sample mass is normally one order of magnitude smaller than the mass of the sample used in DSC and TGA studies. Therefore herein, the samples were used in a fine powder form. Moreover, it was decided to run DSC, TGA, and gas pycnometry on the unaged raw resins to study the starting point of thermophysical and kinetic behaviour of these varnish resins. As reported in the literature, the ageing process can cause the modification of the polymer structure at the molecular, macromolecular, and morphological level (Verdu, 1994). The DSC, TGA and gas pycnometry results defined the thermodynamic properties for each varnish employed and supported the study of Er:YAG laser-material interactions.

### 3.4 Material and methods

#### 3.4.1 Preparation of natural and synthetic varnishes

After detailed research, four coatings were chosen for their different physicochemical characteristics. Dammar, Ketone N, MS2A and Paraloid B67 (Figure 3.5) were grinded resins and placed into a gauze bag and dissolved in their suitable solvent (Table 3.1).

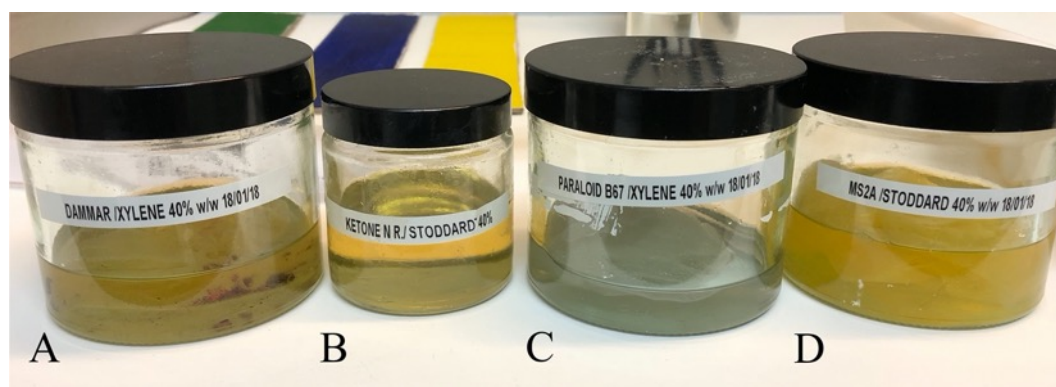


Figure 3.5 – Varnishes selected for the research. (A) dammar resin in xylene; (B) Ketone N in Stoddard solvent; (C) Paraloid B67 in xylene and (D) MS2A in Stoddard solvent.

Table 3.1 – List of the selected varnishes together with the solvents used for their preparation and the varnish solution concentration in weight %.

Product	Chemical composition	Solvent	Wt % concentration
Dammar (Kremer Pigmente)	Triterpenoid resin	xylene (Sigma Aldrich)	40/60
Ketone Resin N (Archive material)	condensation of cyclohexanone only	stoddard solvent (Fisher Scientific)	40/60
MS2A (Kremer Pigmente)	chemically reduced polycyclohexanone resin	stoddard solvent (Fisher Scientific)	40/60
Paraloid B67 (Kremer Pigmente)	Isobutyl methacrylate polymer (PiBMA)	xylene (Sigma Aldrich)	40/60

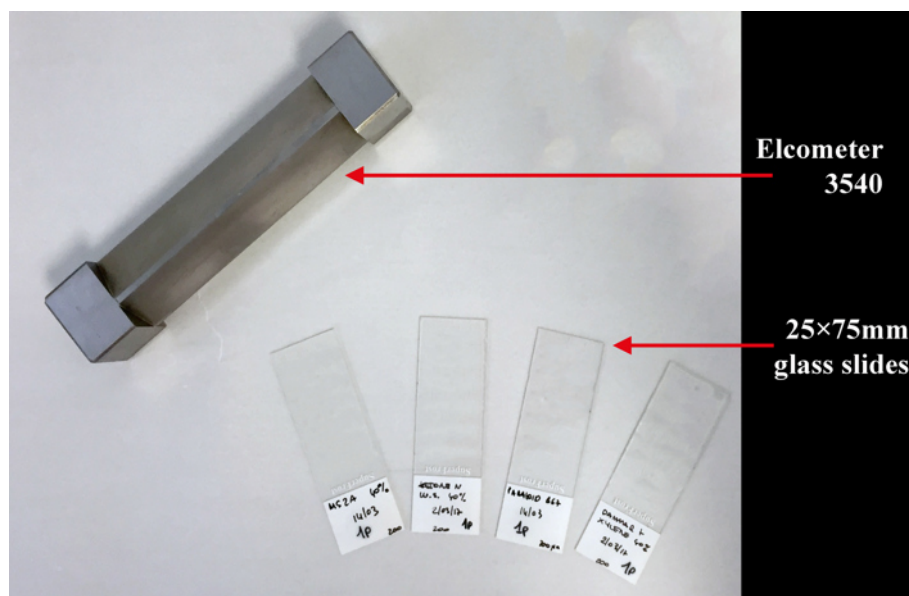


Figure 3.6 – Elcometer 3540 film applicator used to cast dammar, Ketone N, MS2A and Paraloid B67 on glass slides.

200  $\mu\text{m}$  wet varnish film were casted on 25x75 mm glass slides (CLS294875X25 Sigma Aldrich) with a four-sided film applicator (Elcometer 3540) (Figure 3.6). The fabricated varnishes were specially formulated to be thick enough to enable a better investigation of the laser-material interaction.

Glass slides, having a low absorption at the Er:YAG laser wavelength (2940 nm), of about 0.07 (Figure 3.7), were used as supports of the varnishes. Prior to varnish casting, all the glass slides had been cleaned using deionised water, acetone, ethanol and then dried. The resulting samples dried at room temperature for a month and were kept in the dark.

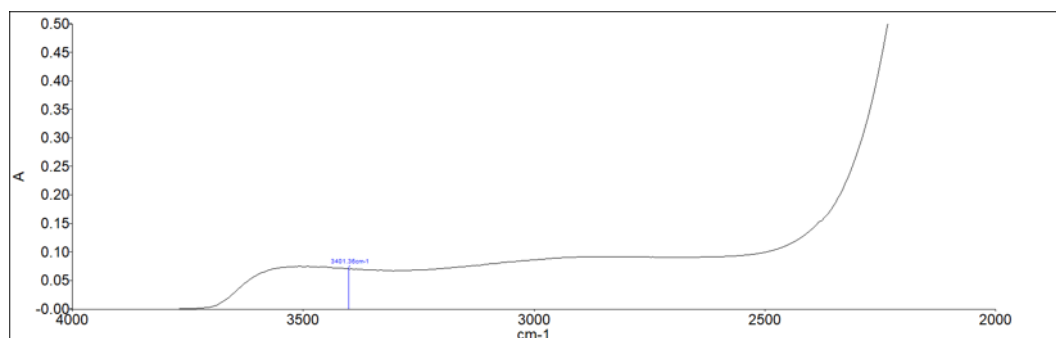


Figure 3.7 – The absorption spectrum of a glass slide used for this research on which it has been specified the Er:YAG laser absorption.

### 3.4.2 Accelerated ageing

After curing, all the samples were exposed to accelerated photo-ageing treatment in a Q-Sun Xe-1-Bc chamber with a single 1800 W (X-1800) Xenon-arc lamp equipped with a Window-Q filter, which has a nominal cut-on of 310 nm to simulate daylight in a museum environment which has passed through the windows. The reciprocity principle helped calculate the length of time required for the accelerated light ageing. According to Saunders (1995) “reciprocity assumes that each photon of light has an equal potential to cause damage, it is worth describing the probable mechanism of light-induced damage”. Power to the arc lamp was controlled to maintain an irradiance at 420 nm of 1.1 W/m<sup>2</sup>/nm (Figure 3.8), the temperature was kept constant at 25 °C and the samples were exposed continuously to light for an overall time of 181 hours.

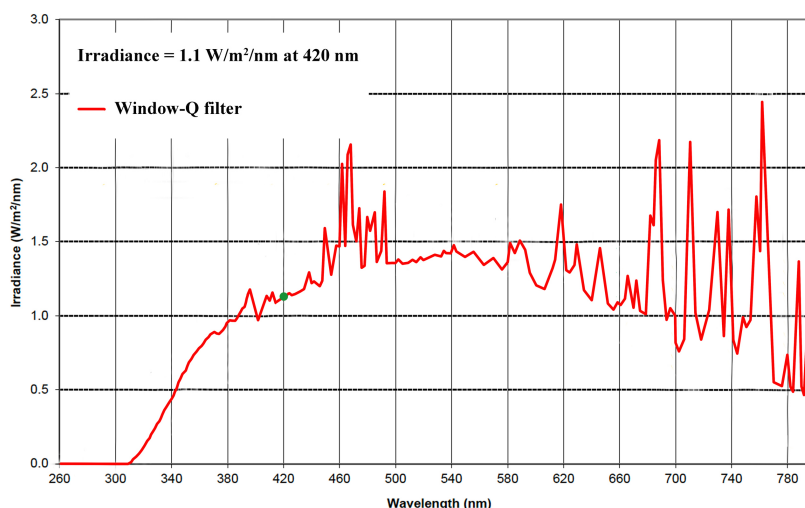


Figure 3.8 – The spectrum produced by the Window-Q filter (Figure adapted from Q-Lab Corporation, 2014)

The dried varnish films received a dose of 170.6 klux·h, corresponding to 53 museum years assuming reciprocity, based on 200 lux illuminations for 8 h per day (Thomson, 1986).

After photo-oxidative ageing, the samples were subjected to accelerated hydrothermal ageing. Taking into account the ageing procedure described by Doménech-Carbó *et al.* (2008), the temperature was set at 40 °C ( $\pm 2^\circ\text{C}$ ), and the samples were kept at relative humidity (RH) of 40 % ( $\pm 2\%$ ) for 30 days in a Marcia Scientific MGF8401 oven. The temperature set for hydrothermal ageing experiment was selected in accordance to the glass transition temperatures ( $T_g$ ) of each varnish

(Table 3.8), as above this point, the properties of resins change (Horie, 2010, pp. 23–27).

Subsequently, all the mock-ups were kept in darkness storage area for 30 days before further experiments were carried out (Figure 3.9).



Figure 3.9 – Accelerated aged (left) and unaged (right) varnish films selected for this research (from top to bottom Ketone N, MS2A, Paraloid B67 and dammar).

### 3.4.3 *Stylus Profilometry*

A Bruker Dektak XT™2D stylus profiler was employed to determine the thickness of the accelerated aged varnish films. A 12.5 µm radius tip was loaded onto the surfaces of the samples to be measured with a force of 10 mg. A standard linear scan of the surface at constant velocity was run with a ‘hills & valley’ profile and acquisition of 40 s with a resolution of 2.076 µm/pt. The height variation of the aged varnish surfaces and step heights were collected and analysed using the Vision64 software.

An average of six measurements was carried out for each varnish film. The surface roughness profiles of the varnishes were recorded on the upper, middle, and lower part of the films. The edges of the varnishes applied on glass slides were etched down to the glass substrate with a stainless-steel scalpel blade No10, removing minor quantities of the varnish layer. Having etched at two points along

the films, the measurement started and finished on the flat surface of the glass slide, which was considered as the zero point.

#### 3.4.4 *Static Contact Angle*

Contact angle measurements provide one of the most rapid methods to investigate the surface modification on resin films before and after accelerating ageing (Ploeger, Musso and Chiantore, 2009; Farmakalidis *et al.*, 2016).

A Drop Shape Analyzer (Krüss DSA 30, Hamburg, Germany), using the sessile drop method (Shang *et al.*, 2008; Saulick, Lourenço and Baudet, 2017), was employed to determine the surface properties of all the varnishes that had been chosen for the research. The High-definition images of the droplet cross-sectional profile were recorded using the Krüss DSA Advance software.

The static contact angle measurements were carried out using a 2  $\mu$ L droplet of 1% (v/v) of non-ionic surfactant (Tween 20) in deionised water (DI-W+TW20). Static contact angle has been carried out to characterise the wetting affinity of the DI-W+TW20 when applied to the surface of aged varnish films.

Drops were deposited randomly on the aged varnish surfaces cast on glass slides using a TE needle (27 Gauge Dispensing Tip – TE727150 Tip 1.5 Inch Long by Adhesive Dispensing Ltd). Particular attention was paid to place the solvent drops on the surfaces of the aged varnish films in areas where no visible surface defects were detected. A volume of 2  $\mu$ L was selected because it allowed the drop to be released on the surface rather than adhere to the surface of the needle. Four droplets were released in different parts of the aged varnish films and recorded with the Krüss own software.

The images acquired with the Krüss DSA Advance software were, therefore, processed with ImageJ free software (Rasband, 2009) using the contact angle plugin (Brugnara, 2006). For each measurement, the first two points defined the baseline (contact between the droplet and the solid surface). Thus, three more points, along with the drop profile, were selected, connecting the left and right three-phase points of the drop. The program, therefore, fitted the profile of the drop and the drop-edge tangent to calculate the left and right theta angles (Williams *et al.*, 2010; Buahom, 2018; Gates, 2018, p. 11).

#### 3.4.5 Density of the varnishes

Gas pycnometry is based on the Boyle–Mariotte law of the volume–pressure relationship (Geary, 1943) and it has been employed to quantify the volume of unaged porous varnishes. This technique was chosen because it does not possess the limitations of other testing methods (Tamari, 2004), such as the floating (suspension) method, the buoyancy method and the density gradient methods (Frick, Stern and Muralidharan, 2019). As reported by Donato and Lazzara (2012), in this technique, the primary approximation in the evaluation of the material volume is the non-ideal gas behaviour and its absorption within the sample. Helium can be used a displacement medium as already demonstrated in the literature (Weber and Bastick, 1968; Tamari, 2004; Donato and Lazzara, 2012; Gao and Masiello, 2017), and it can be considered an ideal and non-absorbing gas at a 37 °C and pressure less than 0.5 MPa.

An Accupyc 1330 Micromeritics gas pycnometer, which used 99.995% of pure helium, was employed to quantify the pure internal volume of the varnishes by measuring the pressure change of helium in a calibrated volume. Prior to the sample analysis, the volume of the sample chamber and the expansion chamber were calibrated using small non-porous steel spheres standards with known volume and weight (purchased from Micromeritics,  $V_{\text{cal}} = 6.371684 \text{ cm}^3$ ) (Gao and Masiello, 2017). The spheres standards were used at 25°C. All the unaged resin varnishes were ground to fine powder using an agate mortar. Before each density measurement, the varnishes were kept in a desiccator for two hours under vacuum. The desiccant used was calcium chloride ( $\text{CaCl}_2$ ). The powder specimens were sealed in the instrument compartment, which has a cell of 10 cm<sup>3</sup> size and the pure helium was introduced into the sample chamber. All the experiments were performed by using the cell with a 75% filling ratio, and the measurements were carried out on the same day.

#### 3.4.6 Colourimetry

Colourimetric measurements were carried out with a Konica Minolta portable Spectrophotometer CM 2600-D covering a 360 – 740 nm spectral range at a spectral resolution of 10 nm. The diameter spot was set at 3 mm, using a Target

Mask CM-A147. The data were acquired with CM-S 100w Spectra Magic™ NX software.

The spectrophotometer has an integrated sphere geometry (coated with a highly reflective white layer) with a specular port that can be open or closed allowing the acquisition of parameters in Specular Component Included (SCI)<sup>14</sup> and Specular Component Excluded (SCE)<sup>15</sup> modes (Figure 3.3.10). In the CIELAB colour space, the parameter L\*, a\* and b\*, in SCI (in which the light trap is closed) and SCE mode (in which the light trap is open) were acquired for each sample (Kun, Huimin and Shangzhong, 2014).

The total colour variation  $\Delta E$  for each measurement has been calculated as an Euclidean distance between two points in the colour space (Schanda, 2007, p. 87).  $\Delta E$  was obtained following the colour parameters adopted by the CIEL\*a\*b\* 1976 (Commission Internationale de l'Éclairage), the BS EN 15886 standard<sup>16</sup> and by applying the formula:

$$\Delta E = \sqrt{(L^*)^2 + (a^*)^2 + (b^*)^2} \quad (\text{Eq. 3.1})$$

where L\* (lightness) ranges between 100 (brightest white) and 0 (darkest black) and a\* and b\* (chromaticity coordinates) represent the green (-a\*) and red (+a\*) component and the blue (-b\*) and yellow (+b\*) component, respectively (Schanda, 2007, p. 86).  $\Delta L$ ,  $\Delta a$  and  $\Delta b$  values are related to the difference between the aged samples and the equivalent unaged ones ( $\Delta L = L_1^* - L_0^*$ ;  $\Delta a = a_1^* - a_0^*$ ;  $\Delta b =$

---

14 “SCI mode includes both the specular and diffused reflected light” as reported on the website of Konica Minolta (Konica Minolta). When the port is closed, the specular component of the light reflected by the surface is included in the measurement. The only portion of light lost from the source is the one which was absorbed by the sample (Kun, Huimin and Shangzhong, 2014; Sanderson, 2015).

15 “SCE mode excludes specular reflected light. Using this mode, a glossy surface will typically measure darker than a matt surface of the same colour” as reported on the website of Konica Minolta (Konica Minolta). When the port is open, the aperture in the integrating sphere allows excluding the specular reflectance from the final measurement (Kun, Huimin and Shangzhong, 2014; Sanderson, 2015). In SCE mode a glossy surface returns values closer to zero (darker) than a matte surface of the same colour (Mouw, 2018).

16 Conservation of cultural property. Test methods. Colour measurement of surfaces (BS EN 15886:2010).

$b_1^* - b_0^*$ ) (Schanda, 2007, p. 87; BS EN 15886:2010, 2010; Ciofini, 2014, p. 57; Raimondi *et al.*, 2015; Gheno, 2017, p. 30).

The colourimetric values have been determined in three-steps (Figure 3.10): i) the border of a clean glass slide was drawn on an A4 white paper (Figure 3.10 B and Appendix A), and six measurements were acquired inside that perimeter, each of them shifted horizontally along the centre of the selected area (Figure 3.10 C and Appendix A). Thus, ii) a clean glass slide (the same used for the preparation of the mock-ups) was put onto the drawn area, and five colourimetric readings were acquired (Figure 3.10 D and Appendix A). Finally, iii) two unaged and two aged varnish samples applied onto glass slides were placed onto the drawn perimeter. For each varnish film, three measurements were taken along the centre of the casted glass slides. A total of six readings were averaged to obtain one data point. This procedure created a comparable statistical error by determining mean and standard deviation values.

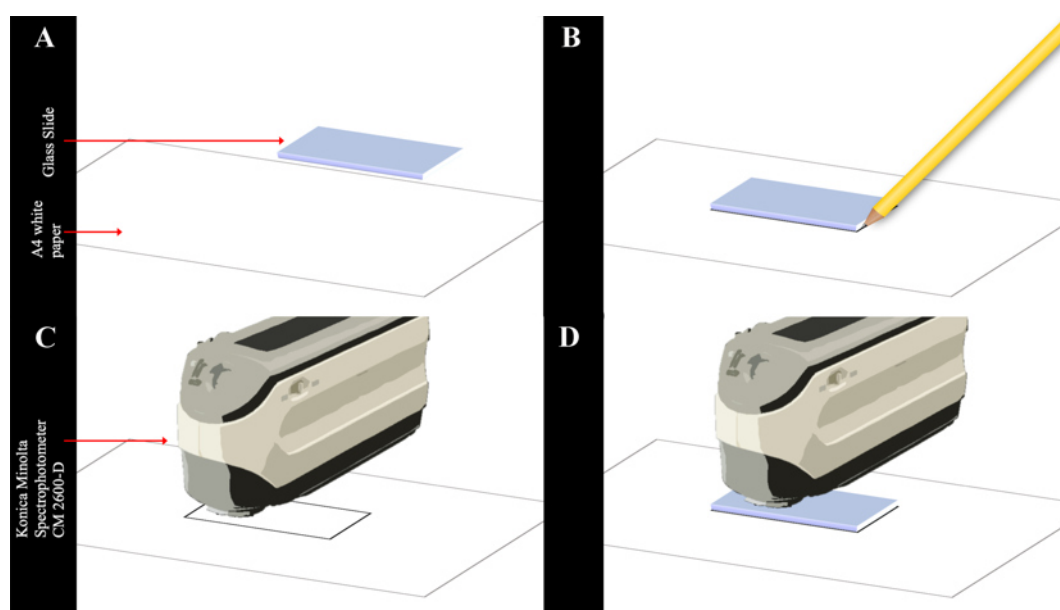


Figure 3.10 – Schematic representation of the methodology employed to acquire the colourimetric values. (A-B) The border of a clean glass slide was drawn on an A4 white paper and (C) six measurements were acquired inside that area, each of them shifted horizontally along the centre of the selected area. Then, (D) the clean glass slide was put again onto the drawn area, and five colourimetric readings were acquired. Finally, two unaged and two aged glass-coated varnish samples were placed onto the drawn area, and three measurements were taken along the centre of the samples.

### 3.4.7 Thermogravimetric analysis (TGA)

Thermal analysis technique which allows to measure mass of samples as a function of temperature and time is known as thermogravimetry (TGA) (Wunderlich, 2005, p. 79; Gaisford, Kett and Haines, 2016). The TGA analysis was carried out in order to study thermal degradation accompanied by oxidation of materials commonly employed in artistic fields during the twentieth century (Prati, Chiavari and Cam, 2001; Al-Dharrab and Shinawi, 2016; Jain, Mehra and Ranade, 2016; Gheno, 2017, p. 31).

A Shimadzu TGA-50 thermogravimetric analyser with TA60 software was employed to record the dynamics of the weight loss of the raw resins with increase in temperature at a programmed the heating rate and selected purge gas and flow rate. Prior to performing the analysis on the raw resins, a baseline was recorded using the empty platinum crucible (Shimadzu 201-53843 Platinum Macro Cell, diameter  $6 \times 5$  mm). This process allowed the acquisition of the background later to be subtracted from the TGA curves of the raw resins and so to correct for buoyancy effects. Each sample was measured twice. The purge gas was oxygen with rate flow maintained at 50 mL/min, in the range temperature from 25 to 800 °C at a heating rate of 10°C/min.

As previously described in section 3.4.5, in order to carry out this analysis, all the raw resins were ground to powder using an agate mortar.

The thermogravimetric analysis was performed by heating the samples (c. 2.5 mg) from 25 to 800 °C at a heating rate of 10 °C/min in oxygen purge gas. TGA curves were recorded and the associated first derivative (DrTGA) curves were calculated using the TA60 software (Al-Dharrab and Shinawi, 2016; Jain, Mehra and Ranade, 2016; Gheno, 2017, p. 31).

### 3.4.8 Differential Scanning Calorimetry (DSC) analysis

#### 3.4.8.1 Determination of Glass transition temperature ( $T_g$ )

The thermal behaviour of the raw resins was analysed by means of DSC in order to determine the glass transition temperatures ( $T_g$ ) of the coatings (D’Orazio *et al.*, 2001; Farmakalidis *et al.*, 2016), following ASTM E1356-08 (2014). The glass transition ( $T_g$ ) is manifested as a step-change in specific heat capacity (ASTM

E1356-08, 2014). In general, the  $T_g$  of a polymer describes the temperature at which amorphous polymers change from hard to soft (Horie, 2010), therefore, a polymer with a low value of  $T_g$  could lead to the possibility of imbedding dust and remaining sticky. However, a polymer with a high value of  $T_g$  could turn out to be too stiff, leading to the formation of cracking consequently not following the natural movement of the underlying paint layers. The vast majority of the resins commonly used in the conservation field have a  $T_g$  of about room temperature (Horie, 2010, p. 23).

The DSC curves of the raw resins have been obtained using a Shimadzu DSC-50 calorimeter (Shimadzu, Kyoto, Japan) and the data have been processed with the TA60 software. A purge nitrogen gas at a rate flow of 50 mL/min was used. The raw resins were ground to powder using an agate mortar (Table 3.2).

Table 3.2 – List of the selected varnishes with the weight used to carry out the DSC analysis with the Shimadzu DSC-50 thermal analyser.

Product	Sample Weight (mg)
Dammar	16.5
Ketone N	14.7
MS2A	15
Paraloid B67	14.7

The samples were placed in open aluminium crucibles, and the measurements were taken with indium as reference. In particular, the Heat/Cool/Heat experiments was carried out initially i) heating the samples from 25 to 200 °C (first heating cycle), then ii) cooling the system to 25 °C, and finally iii) heating it up to 200 °C (second heating cycle). Both the heating and cooling rates were kept at 10 °C/min for all cycles. The controlled heat evolution, also during the cooling rate, was recorded as a function of temperature and time. The thermal history is essential in understanding how a material behaves<sup>17</sup>. Heat-cooling-heat cycles procedure is deemed to be standard practise when dealing with polymers. In general, the first heating cycle shows the influence of physical ageing reactions. It removes volatiles

---

<sup>17</sup> Heat History is the last thermal excursion the material has experienced. In polymers, heat history is erasable by heating the material slightly above the melting temperature and then cooling (annealing) material from its melt temperature to room temperature. This process is used to study the effects of structural ordering within the material (PerkinElmer).

and the thermal history of the samples (e.g., removal of relaxation effects), imposing a standard heat history on the materials and producing a better thermal contact between the sample and the sample pan (Schilling, 1989). The second heating reveals the influence of the molecular arrangement and allows the comparing of the varnishes (Opeña and Jägers, 2013). The second heating was used in this research to obtain the glass transition temperature ( $T_g$ ) for each varnish.

#### 3.4.8.2 Determination of Specific heat at constant pressure ( $C_p$ )

A Double-furnace LAB SYS-DSC 8500 by Perkin Elmer was employed to determine the specific heat capacity at a constant pressure ( $C_p$ ) of all the raw resins, as described elsewhere (Morîntale *et al.*, 2013). The specific heat capacity ( $C_p$ ) is the ability of the material to store thermal energy. It is defined as the amount of heat energy required to raise the temperature of a mass unit of a substance by one degree at a constant pressure (Wunderlich, 2005, p. 82; Çengel, Ghajar and Kanoglu, 2014, p. 7). To the best of the author’s knowledge, in the conservation field there is a lack for estimating the heat capacity of solid organic materials at constant pressure.

For the analysis, a nitrogen purge gas at a rate flow of 20 mL/min was employed. DSC measurements were performed on raw resins, ground to powder using an agate mortar. A more significant amount of samples compared to the samples required for the TGA analysis was necessary to determine the  $C_p$  and the  $T_g$  of the resins (see section 3.3.8). The weights of the samples and synthetic sapphire disk used to carry out the DSC analysis are reported in Table 3.3.

Table 3.3 – List of the selected varnishes and sapphire reference together with the weight used to carry out the DSC analysis with the LAB SYS-DSC 8500 Perkin Elmer.

Product	Sample Weight (mg)
Sapphire	27.9
Dammar	14.1
Ketone N	11.8
MS2A	10.3
Paraloid B67	12.5

A synthetic sapphire ( $\alpha$ -aluminum oxide; alumina) disk is commonly used as a reference to calibrate the DSC analysis because its  $C_p$  is similar to the  $C_p$  of polymers and organic materials (Slough and Hesse, 2007). Sapphire  $C_p$  values

range from about 0.9 J/g·°C at 100 °C to about 1.02 J/g·°C at 200 °C (ASTM E 1269-11, 2011).

A total of three measurements were taken for a three-point calibration run (Cowie, McEwen and Pedram, 1983) following the Standard ASTM E 1269-11, 2011: the first measurement using the empty specimen holder (blank) which gave the baseline (DSC pans were standard pans 02190041 by Perkin Elmer); the second measurement with the sapphire disks; and the third measurement performed with each samples. An isothermal scan was programmed, starting by keeping the internal temperature at 0 °C for 5 min and then going from 0 °C to 220 °C at a heating rate of 10°C/min and completing the programme keeping the temperature at 220 °C for 5 min. Perkin Elmer Pyris™ software was used during the acquisition of the isothermal thermograms, to perform shifting and sloping of the data and for the post-processing of the data. Since DSC measurement is at constant pressure, heat flow is equivalent to enthalpy changes as  $(dq/dt)_p = dH/dt$  (Finn, 1993; Arvanitoyannis, 2016, p. 25) where  $dH/dt$  is the heat flow (HF) measured in mW or equivalently to mJ/s. The software provided the corrected heat flow for the sapphire ( $HF_{ref}$ ), and the heat flow of each varnish ( $HF_{varnish}$ ). The corrected heat flows were determined by subtracting the heat flow of the blank from each of the two heat flows (reference and samples) previously analysed<sup>18</sup>. The corrected heat flow can be either positive or negative (Arvanitoyannis, 2016, p. 25). The  $C_p$  curves of the varnish samples were calculated using the known heat capacity of the sapphire ( $C_{p,ref}$ ) and its weight ( $W_{ref}$ ) together with the weight of the samples ( $W_{varnish}$ ), following the formula:

$$C_{p, varnish} = C_{p, ref} \frac{HF_{varnish}}{HF_{ref}} \frac{W_{ref}}{W_{varnish}} \quad (\text{Eq. 3.2})$$

(Höhne, Hemminger and Flammersheim, 1996, p. 119; Santos *et al.*, 2005; Gomez, Glatzmaier and Mehos, 2012).

Therefore, the  $C_{p, mean}$  was calculated by averaging all the  $C_p$  data acquired between the corresponding value obtained at room temperature (RT) and the  $C_p$  data obtained at the highest temperature of 210 °C.

---

<sup>18</sup> The heat flow difference between the analysed sample and the selected reference is obtained as  $\Delta dH/dt = (dH/dt)_{sample} - (dH/dt)_{blank}$  (Arvanitoyannis, 2016, p. 25).

3.4.9 Attenuated Total Reflection/Fourier Transform Infrared Spectroscopy (ATR/FT-IR)

Attenuated Total Reflection/Fourier Transform Infrared (ATR/FTIR) Spectroscopy was carried out on a Perkin Elmer bench spectrometer coupled with a FTIR microscope (Perkin Elmer Spotlight 400N FT-NIR Imaging System) and aimed to evaluate and detect any possible chemical modification of the coated varnishes before and after accelerated ageing. The spectrometer was equipped with a Universal Attenuated Total Reflection (UATR) single polarisation accessory using a pure diamond ATR unit. This allows the acquisition of a spectrum of just a few superficial microns (normally 1-2  $\mu\text{m}$ ) of the material analysed (Learner, 2004, p. 37).

The glass-coated varnishes were placed directly onto the diamond window of the ATR unit and pressed (up to pressure gauge of 100). The wave-number range was set from 4000 to 380  $\text{cm}^{-1}$  and the spectra were acquired over 16 scans at 4  $\text{cm}^{-1}$  resolution. The background was automatically subtracted. The ATR/FT-IR spectra were processed with Perkin Elmer Spectrum™ 10 software suite. The integrated areas of the peaks corresponding to hydroxide (2700–3700  $\text{cm}^{-1}$ ), C–H (2850–3000  $\text{cm}^{-1}$ ) and carbonyl (1500–1900  $\text{cm}^{-1}$ ) stretching vibrations were determined. The baseline points were ranged at 3700 – 3100, 3100 – 2700 and 1900 – 1550  $\text{cm}^{-1}$ , as indicated elsewhere (Ciofini, 2014, p. 58).

### 3.5 Results and Discussion

#### 3.5.1 *Stylus Profilometry*

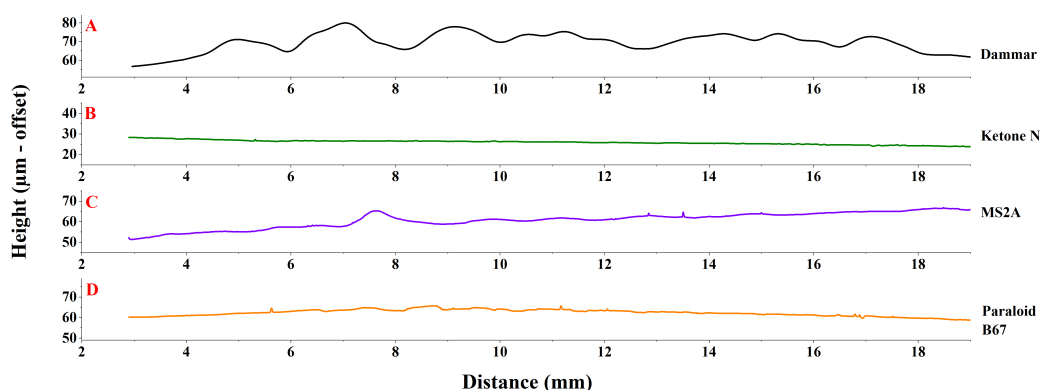


Figure 3.11 – Stylus profilometry on the air-resin film interfaces, showing the surface morphology of the varnishes (A: dammar; B: Ketone N; C: MS2A and D: Paraloid B67) on glass slide substrates after the accelerated ageing process.

Profilometry traces of the glass-coated aged varnishes were obtained with a stylus profilometer (Poon and Bhushan, 1995; de la Rie *et al.*, 2010). The traces are shown in Figure 3.11. Height data show smooth surfaces for Ketone N and Paraloid B67 varnish films. The MS2A films were less smooth than the previous two varnishes, and they became extremely brittle after the ageing. However, dammar indicates larger-scale roughness also in this case due to the ageing process.

The thickness of each varnish was measured (Appendix A) and the mean data are presented in Table 3.4.

Table 3.4 – Mean thickness and standard deviation ( $\sigma$ ) values of the aged varnish samples.

Product	Thickness varnish film ( $\mu\text{m}$ ) $\pm$ $\sigma$
Dammar	82.3 $\pm$ 13.2
Ketone N	28.2 $\pm$ 7.5
MS2A	58.8 $\pm$ 11.7
Paraloid B67	51.3 $\pm$ 12.6

#### 3.5.2 *Static Contact Angle*

In order to interpret the static contact angle data acquired on the aged varnish films depositing a droplet of DI-W+TW20, a series of assumptions have been made:

- A homogeneous chemical modification occurred on the surface of the varnish films applied on the glass slides after ageing;

- No swelling of the aged varnish surface happened during the experimental depositing of a drop of DI-W+TW20;
- No change in the roughness of the varnish films was produced during the analysis, and the potential loss of volatile oxidation products was considered negligible regarding the surface roughness of the coatings.

These assumptions facilitated the interpretation of the contact angle data, and the results of all measurements are summarised in Table 3.5.

When a droplet of liquid is free to adjust its shape, it adopts a spherical shape since a sphere has the smallest surface area with minimum free energy that a fluid is able to assume in order to reduce its surface tension (Shirtcliffe *et al.*, 2010). The DI-W+TW20 droplets highlighted a non-spherical shape because the *polyethylene glycol sorbitan monolaurate* surfactant (Tween 20) reduced the surface tension of the water, thereby enabling adhesion forces with the substrate to become larger than the cohesion forces within the droplet of the solution (Wolbers, 2000; Cremonesi and Signorini, 2012).

Table 3.5 – Mean contact angle and standard deviation ( $\sigma$ ) values obtained using one 2  $\mu$ L droplet of DI-W+TW20 solution deposited on the surface of each aged varnish film. Values were obtained by fitting the image data with the ImageJ contact angle plugin.

		Static Contact Angle of a drop of DI-W+TW20	
		Angle Left (L) $\pm \sigma$	Angle Right (R) $\pm \sigma$
Product on which was deposited a drop of DI-W+TW20	Dammar	----	-----
	Ketone N	32.4° $\pm$ 2.9°	32.4° $\pm$ 2°
	MS2A	41.6° $\pm$ 6.3°	40° $\pm$ 6.5°
	Paraloid B67	45.4° $\pm$ 0.8°	43.7° $\pm$ 3°

The varnishes show a contact angle ( $\theta$ ) below 90°, which is typical of hydrophilic substrates (Ploeger, Musso and Chiantore, 2009; Lamour *et al.*, 2010; Shirtcliffe *et al.*, 2010; Baglioni and Chelazzi, 2013). The smallest contact angle obtained depositing DI-W+TW20 on the surface of the aged varnish films has been observed on the Ketone N varnish (32.4°  $\pm$  2.9°) and the highest on Paraloid B67 varnish (45.4°  $\pm$  0.8°) (Table 3.5). The affinity of DI-W+TW20 solution droplets with the surface of Ketone N varnish film is caused by the presence of a higher

proportion of reactive oxygenated species on the film, making Ketone N the most hydrophilic varnish among the varnishes tested herein. Dammar film shows a non-contact angle due to the highly cracked surface which derives from the ageing process, causing the diffusion of the DI-W+TW20 solution droplet within the film (Figure 3.12).

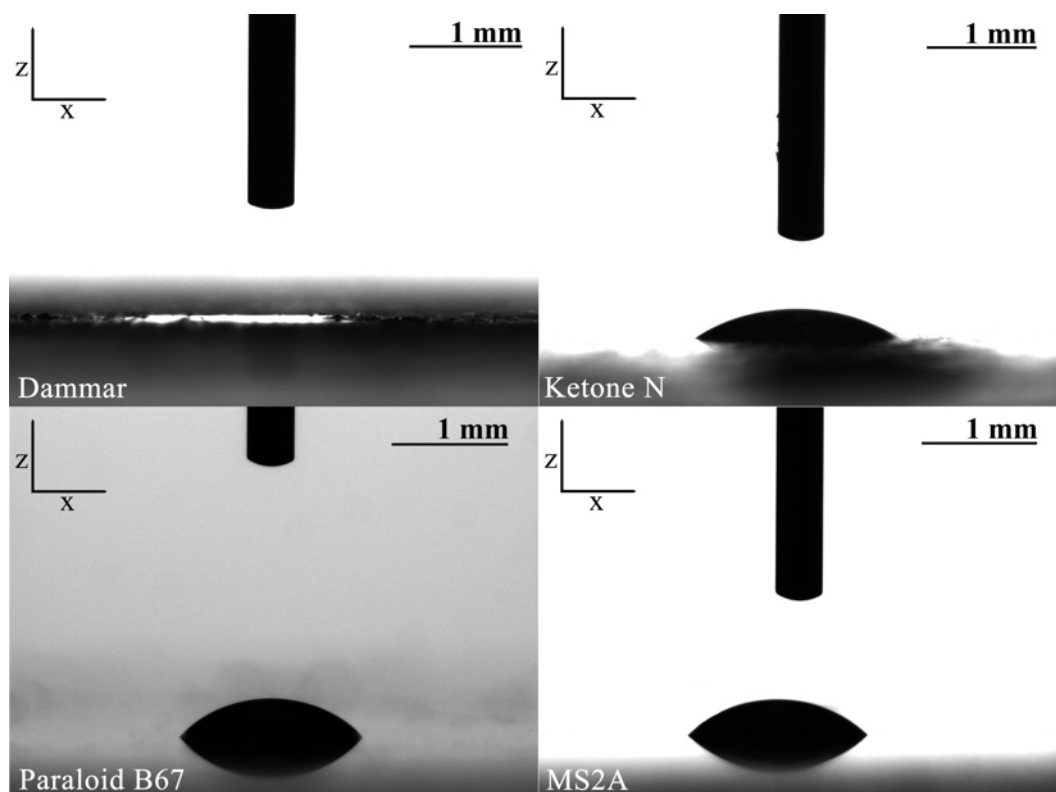


Figure 3.12 – 2  $\mu\text{L}$  droplet of DI-W+TW20 was deposited on the surface of each aged varnish. Dammar resin shows no static contact angle due to the highly cracked surface, which resulted in the diffusion of DI-W+TW20 within the cracks of the film. The contact angle ( $\theta$ ) of the aged Ketone N ( $32.4^\circ \pm 2.9^\circ$ ), MS2A ( $41.6^\circ \pm 6.3^\circ$ ) and Paraloid B67 ( $45.4^\circ \pm 0.8^\circ$ ) varnishes is below  $90^\circ$  indicating that all these varnishes are hydrophilic. The most hydrophilic film is the aged Ketone N varnish which has the smallest contact angle.

### 3.5.3 Density

The density values for all the varnishes selected for this study have been experimentally determined by using the helium pycnometer. The densities have been reported in Table 3.6.

Table 3.6 – Density of the powder unaged raw resins.

Product	Density (g/cm <sup>3</sup> )
Dammar	1.2
Ketone N	1.1
MS2A	1.1
Paraloid B67	1.0

The data experimentally determined are in line with the literature values (Routledge, 2000; Knapp and Halloran, 2006; Ciofini, 2014, p. 115; Appala Naidu and Dinda, 2015; Uttaravalli, 2018, p. 22). Even though the raw resins have different molecular weights (see section 3.2.2), the densities data acquired are very close to each other.

#### 3.5.4 *Colourimetry*

One of the main problems in polymer degradation is their colour change variation (Favaro *et al.*, 2006). Colour change ( $\Delta E$ ), calculated using Eq. 3.1, allows only to determine the total colour variation and therefore, chromaticity coordinates ( $a^*$  and  $b^*$ ) and lightness ( $L^*$ ) are reported herein to define the colour variation before and after ageing.

As presented in Figure 3.13 and Appendix A, the ageing resulted in a darkening of the film surfaces with a decrease  $L^*$  values both in SCI and SCE modes. Paraloid B67 varnish shows the lowest reduction in brightness ( $L^*$ ) after ageing, with an  $L^*_{SCI}$  value of 93.1 and  $L^*_{SCE}$  value of 89.6. Conversely, the varnish that shows the highest change in brightness is dammar varnish with  $L^*_{SCI}$  value after ageing of 88.1 and  $L^*_{SCE}$  value of 85.3. Since the SCE mode excludes the specular component of the light reflected from the surface (Kun, Huimin and Shangzhong, 2014), it enables the study of change in the surface of the varnish samples after ageing. Thus, the  $L^*_{SCE}$  value of the dammar samples correlates and confirms the findings, including the increased roughness, of the stylus profilometry (section 3.5.1) and the non-existent static contact angle (section 3.5.2).

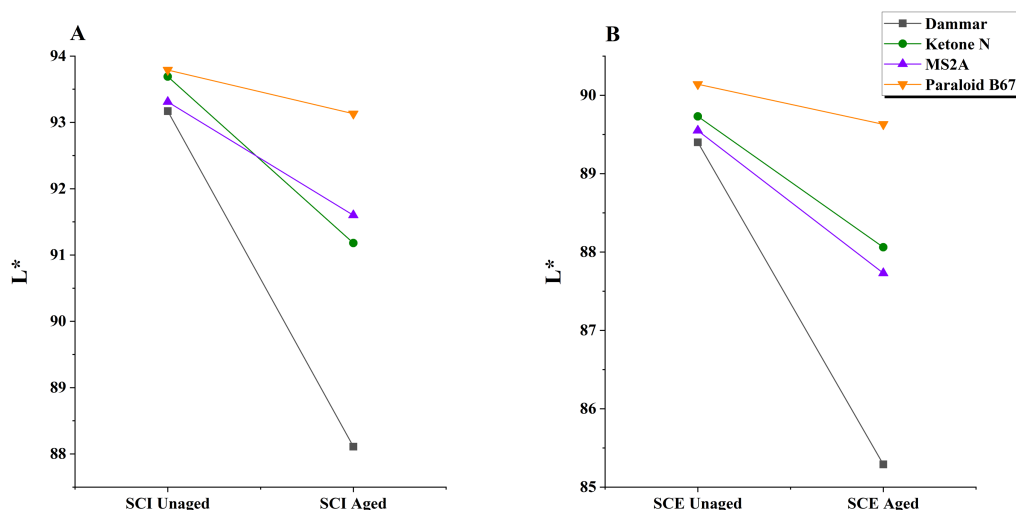


Figure 3.13 – Brightness,  $L^*$ , of the unaged and aged varnishes in SCI (A) and SCE (B) modes. The dammar varnish appears to be the most affected after the ageing with a darkening of the surface detectable as a significant decrease in brightness. The most stable varnish is the Paraloid B67.

Herein, the colourimetric coordinates ( $a^*$  and  $b^*$ ) are presented only in SCI mode. The decision to show only the data in that mode is because in SCI mode the colourimetric coordinates ( $a^*$  and  $b^*$ ) are not affected by gloss and texture but capture the true colour of the measured materials (Kun, Huimin and Shangzhong, 2014). As showed in Figure 3.14, the main colour changes for dammar, Ketone N and MS2A varnishes are attributable to a substantial shift towards a yellow-green shade (see also Appendix A), indicating the formation of unsaturated ketones that are formed upon autoxidation and absorb in the blue (400– 490 nm) (de la Rie, 1988a, 1988b; van der Doelen, van den Berg and Boon, 1998; van der Doelen, 1999; Dietemann, 2003; Theodorakopoulos, 2005; Theodorakopoulos *et al.*, 2007; Ciofini *et al.*, 2016b). The colourimetric data confirms the behaviour of the dammar to undergo ageing processes, which lead to yellowed products (Figure 3.14), as reported in the literature (de la Rie, 1987, 1988a, 1988b; Feller, 1994; van der Doelen, van den Berg and Boon, 1998; Dietemann, 2003; Theodorakopoulos, 2005; Dietemann *et al.*, 2009; Theodorakopoulos and Boon, 2011).

Likewise the slight yellow hue exhibited by the aged ketone resins (Ketone N and MS2A) (Figure 3.14), with readings towards  $-a^*$  and  $+b^*$ , is related to the formation of chromophores (de la Rie and Shedrinsky, 1989; Doménech-Carbó *et al.*, 2008). A different behaviour has been detected for Paraloid B67 which shows

an only slight modification in both  $a^*$  (green-red) and  $b^*$ (blue-yellow) values (Figure 3.14).

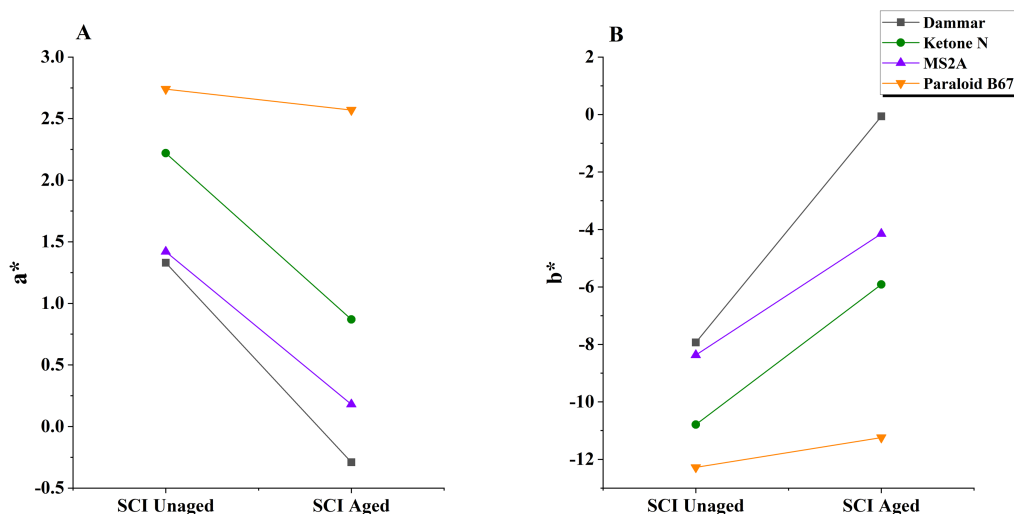


Figure 3.14 – Chromaticity coordinates ( $a^*$  and  $b^*$ ) of the varnishes before and after ageing. All the varnishes show a toning towards yellow-green values.

The overall colour change ( $\Delta E$ ) values are presented in Figure 3.15 (see also Appendix A). As reported in the European Standard EN15886, if  $\Delta E$  values are below 1.5, no colour change can be visually detected to the naked eye (BS EN 15886:2010, 2010; Micheli *et al.*, 2016).

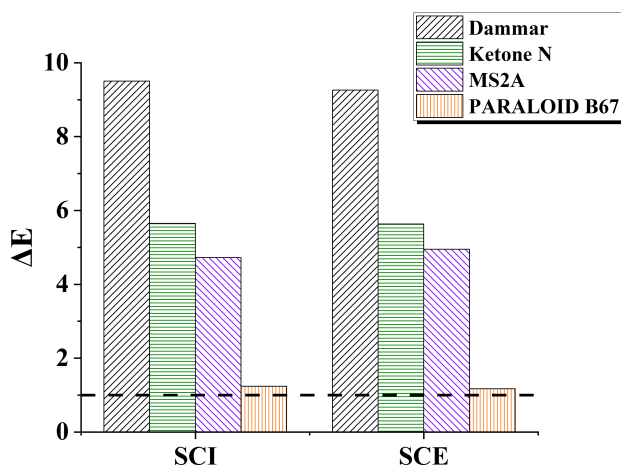


Figure 3.15 – Total colour variation  $\Delta E$  for all the varnishes. The dashed line at  $\Delta E=1$  specifies the threshold at which the eye can detect visible differences.

The aged varnish films with the highest  $\Delta E$  value is dammar with  $\Delta E_{SCI}$  9.5 and  $\Delta E_{SCE}$  9.3. Similarly, Ketone N ( $\Delta E_{SCI}$  and  $\Delta E_{SCE}$  of 5.6) and MS2A ( $\Delta E_{SCI}$  4.7 and  $\Delta E_{SCE}$  4.9) have shown high  $\Delta E$  values proving to be sensitive to the ageing procedure selected for this study. Conversely, Paraloid B67, with a value of  $\Delta E_{SCI}$  and  $\Delta E_{SCE}$  of 1.2,

results to be the most stable aged film.

### 3.5.5 *Thermogravimetric analysis (TGA)*

The thermal stability of the raw resins has been studied using the thermogravimetric analysis (TGA) under oxygen atmosphere (the purge rate of gas was 50 mL/min). The results are shown in Figure 3.16 and the key data collected from TGA curves are given in Table 3.7. The thermal analysis curve provides evidence of the percentage weight loss of each resin (TGA % and the corresponding first derivative DrTGA) as a function of temperature increase and the use the first derivative allowed to define the start and end temperatures of the degradation processes.

Table 3.7 – Data obtained from the thermogravimetric analysis (TGA) for the unaged resins.

Product	Degradation Steps (°C)	Weight Loss (wt %)
Dammar	199-349	49.8
	349-526	45.9
Ketone N	105-243	19.2
	243-344	25.7
	344-540	53.4
MS2A	94-255	20.7
	255-359	25.1
	359-521	51.7
Paraloid B67	184-382	99.5

The thermal decomposition of raw dammar resin shows that two reaction stages occur during oxidative degradation with a gradual loss of weight of the resin (Figure 3.16). The first degradation step starts at about 199 °C and the second transition starts at 349 °C (Table 3.7). They represent the thermal decomposition associated with a weight loss of 50 % for the first transition and 46 % for the second transition. The first transition is may be ascribed to the degradation of aromatic sesquiterpenoids compounds (Van Aarssen *et al.*, 1990; van Aarssen, de Leeuw and Horsfield, 1991) and volatile triterpenoids molecules (de la Rie, 1989; van der Doelen *et al.*, 1998; Theodorakopoulos, 2005, p. 82). The second transition represents the more thermally stable part of the resin because it needs higher temperature to be degraded and is related to the polymeric fraction, consisting of C45-hydrocarbons (Van Aarssen *et al.*, 1990; van Aarssen, de Leeuw and Horsfield, 1991; Theodorakopoulos and Boon, 2011). The complete decomposition of the raw dammar resin, corresponding to 100% weight loss, ends at about 521 °C (Table 3.7).

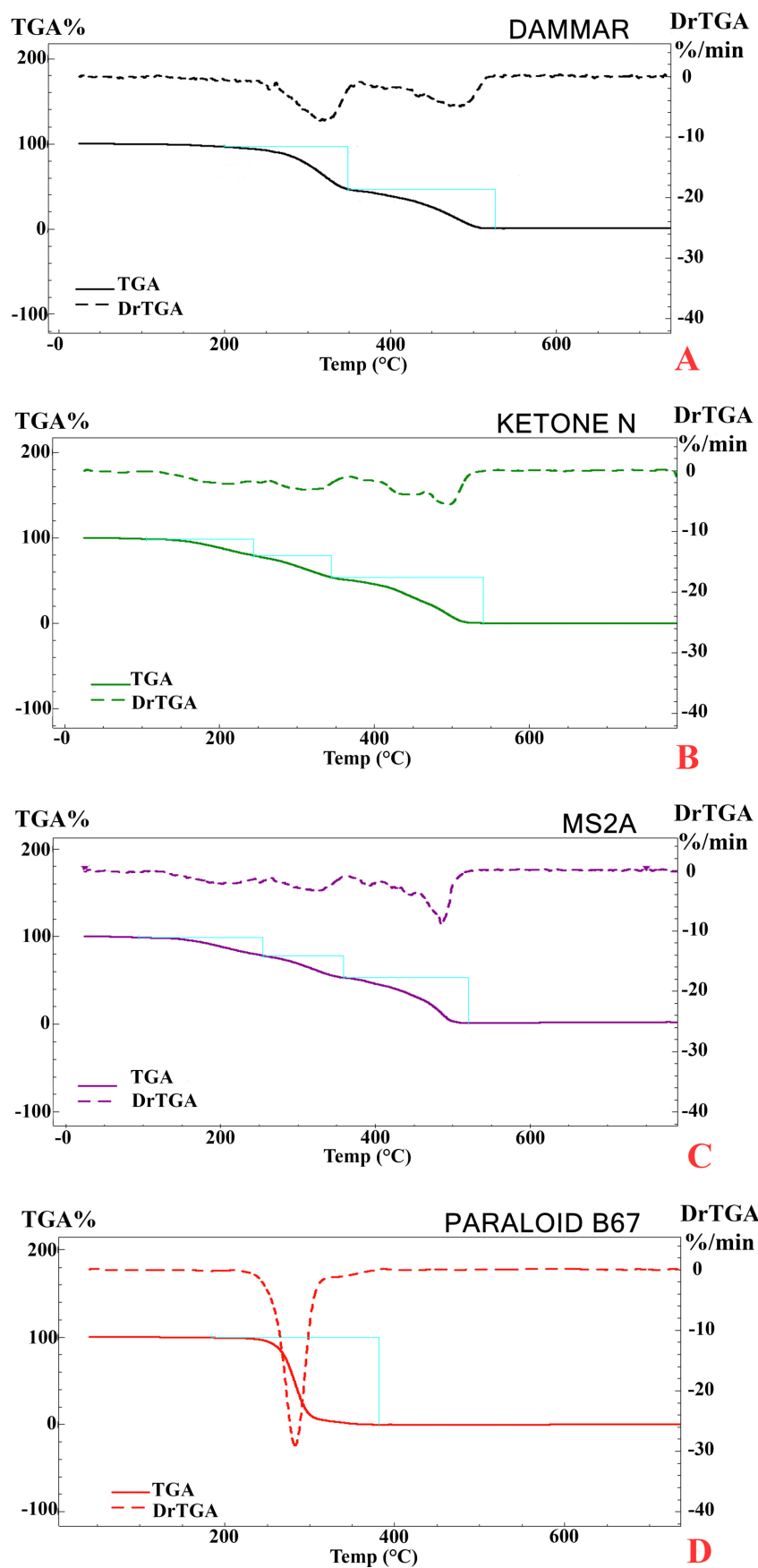


Figure 3.16 – Thermogravimetric curves (solid lines) of the varnish selected for this research and their corresponding first derivative DrTGA curves (dashed lines).

The thermogravimetric curve (i.e., TGA curve) of Ketone N and MS2A resins show that three distinct transitions have occurred during the oxidative degradation of the resins with a similar trend (Figure 3.16). For Ketone N, the first transition starts at approximately 105 °C with a weight loss of 19.2 % (Table 3.7). The second transition appears at about 243 °C, with a weight loss of 26 %. The third transition appears around 344 °C with a weight loss of 53.4 % and is composed of a peak with a series of shoulders. The wider curve shape of the third transition, which represents the more thermally stable part of the resin and its actual decomposition, could be explained by the oxidative degradation of the higher MW fractions in the polymeric chain (Odlyha, 1995; Cohen *et al.*, 2000). The thermal decomposition of Ketone N ends at around 540 °C (Table 3.7). The MS2A raw resin is similar to the Ketone N as demonstrated by the three transitions in its TGA curve (Figure 3.16). The first transition starts at 94 °C with a weight loss of 21 %, most probably caused by volatile monomers lost in evaporation (Bonaduce *et al.*, 2013) (Table 3.7). The second transition appears 254 °C with a weight loss of 25 %. As previously described with Ketone N resin, the MS2A third transition starts at 359 °C with a more defined peak compared to the Ketone N resin and with a series of small shoulders. This final stage leads to a weight loss of 52 % and the complete decomposition of the resin ends at about 521 °C (Table 3.7). The wider curve shape of the third transition may be ascribed to the oxidative degradation of the high MW fractions of the polymer (Odlyha, 1995; Cohen *et al.*, 2000). To the best of the author's knowledge, although three transitions between c.100 and 540 °C are clearly observed in the TGA curves of the Ketone N and MS2A resins (Figure 3.16), further investigation is required to correlate the detected weight loss to specific compositions corresponding to these transitions. For that purpose, additional TGA studies also in nitrogen atmosphere are required, and TG-MS studies should be carried out. As the changes appear clearly related to the thermal reaction, they are reported here and summarised in Table 3.7.

The thermogravimetric curve of Paraloid B67 shows that only one transition occurs during degradation. This stage starts at 184 °C and ends at 382 °C with a peak temperature of 283 °C and a weight loss of 99.5 %. The sharp peak of the DrTGA curve indicates that a rapid loss in weight occurs in Paraloid B67. The isobutyl methacrylate homopolymer undergoes a complete degradation process,

which is a typical characteristic of all polymethacrylates (Irwin, 1979; Learner, 2004, p. 39).

### 3.5.6 *Glass transition temperature ( $T_g$ )*

The glass transition ( $T_g$ ) is a second-order transition, therefore resulting in constant enthalpy of the system and a change in heat capacity  $C_p$ . The  $T_g$  is defined as the temperature at which a material changes from a solid ‘glassy’ state to a softer ‘rubbery’ state (Schilling, 1989). It is essential to take into account that the  $T_g$  values of the polymers given in the literature cannot be directly compared (Schilling, 1989; Horie, 2010, p. 25) unless it is certain that the methodology employed as well as the characteristics of the sample analysed are identical (Nielsen and Landel, 1993). In particular, values may vary depending on whether the measurements are made on bulk powdered form of resin or from prepared films on slides etc.

The thermoanalytical curves of all the resins acquired by DSC analysis are shown in Figure 3.17. In these curves, the  $T_g$  appears as an inverse ‘S’ and occurs within a temperature range. What happens is an endothermic shift in the baseline as a result of the change in heat capacity and it is a phenomenon of molecular relaxation (Wellen, Canedo and Rabello, 2011). The starting point and the ending point of this transition give the regression line, obtained by drawing two tangent lines where the inflexion point of the slope starts and ends (Schilling, 1989). Table 3.8 lists the temperatures at which the regression lines start ( $T_i$ ) and end ( $T_f$ ) and the midpoint temperature, which is commonly referred to as the  $T_g$  of the material (Schilling, 1989).

The first heating cycle of the raw dammar resin (Figure 3.17 A) shows an enthalpy relaxation peak (downward endothermic peak [Laidler, 1996]), which occurs at about 73 °C, related to the reorientation of the polymer chain, followed by a broad exothermic curve related to the curing and crystallisation of the resin (150 °C) in the high molecular mass degradation region (Prati, Chiavari and Cam, 2001; Wellen, Canedo and Rabello, 2011; Gaisford, Kett and Haines, 2016). The relaxation peak is not present in the second heating curve, allowing to define the peak as a relaxation peak and not as a melting peak which is reproducible upon reheating (Schilling, 1989). The  $T_g$  of the raw dammar resin is 58.3 °C.

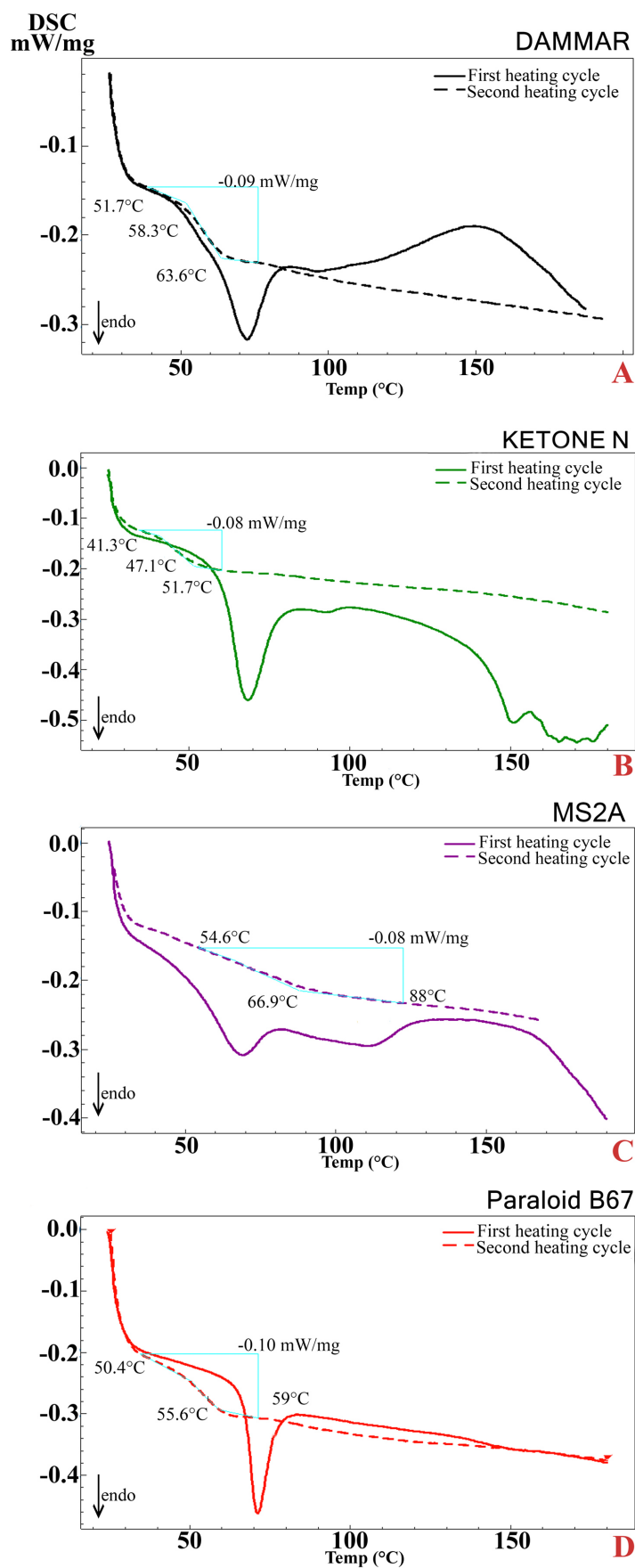


Figure 3.17 – Glass transition temperature ( $T_g$ ) of the unaged resins obtained by DSC analysis. The solid lines indicate the first heating and the dashed lines the second heating.

The thermoanalytical first heating curve of the raw Ketone N resin presents an enthalpy relaxation peak (Schilling, 1989) and a small shoulder which appears at around 68 °C. Similarly to dammar resin, the relaxation peak is not present in the second heating curve of Ketone N resin. The  $T_g$  obtained during the second heating cycle is 47 °C. The raw MS2A resin shows that the first heating cycle is composed of a double process, identified by two endothermic peaks. The first peak is an enthalpy relaxation peak caused by a reorientation of the polymer chain (Schilling, 1989). This is followed by a smaller peak which could be probably caused by losses due to the evaporation of volatile compounds, resulting in the shift of the  $T_g$  value towards a higher temperature.

The first heating cycle of the raw Paraloid B67 resin shows a sharp enthalpy relaxation peak at about 71 °C, and a  $T_g$  value on the second heating curve at 56 °C.

Moreover, considering the first heating curve, dammar, ketone N, and MS2A resins show a melting process followed by degradation, resulting in an endothermic peak which starts from about 150 °C. However, in Paraloid B67, which is an amorphous polymer, the same process is not visible.

Since the  $T_g$  values determined by DSC analysis are values dependent on the methodology of acquisition, the data in Table 3.8 should be treated as relative rather than as absolute.

Table 3.8 – Glass transition data of the selected unaged raw resins obtained by DSC analysis. The start ( $T_i$ ) and end ( $T_f$ ) points of the regression lines and the  $T_g$  points of the raw resins are demonstrated.

Product	Second Heating Cycle		
	$T_i$ (°C)	$T_f$ (°C)	$T_g$ (°C)
Dammar	51.7	63.6	58.3
Ketone N	41.3	51.7	47.1
MS2A	54.6	88	66.9
Paraloid B67	50.4	59	55.6

### 3.5.7 Specific heat capacity at constant pressure ( $C_p$ )

The heat capacity is one of the basic thermophysical and thermodynamic properties that characterises a material (Benson, 1976; Koutchoukali, Haloui and Koutchoukali, 2013). The  $C_p$  of the resins was obtained from the DSC curves in

the temperature range spanning from 20 °C to 210 °C, as shown in Table 3.9 (see also Appendix A). The experimental data show that the specific heat capacity of dammar and MS2A do not differ significantly presenting similar  $C_{p\text{mean}}$  values of 1.75 J/g·°C and 1.73 J/g·°C, respectively. However, the highest specific heat capacities were recorded for the Ketone N with at 1.98 J/g·°C and Paraloid B67 at 2.05 J/g·°C. These results show that the  $C_p$  values can be considered dependent on the molecular weight of the varnishes (Benson, 1976; Koutchoukali, Haloui and Koutchoukali, 2013). Correlations between  $C_p$  and temperature of each resin has been employed for the mathematical thermal modelling and a 2D simulation presented in Chapter 4.

Table 3.9 – Specific heat capacities ( $C_p$ ) of the unaged raw resins between 20-210 °C obtained by DSC.

Temperature (°C)	$C_p$ (J/g·°C)			
	Dammar	Ketone N	MS2A	Paraloid B67
20	1.33	1.12	1.26	1.46
30	1.36	1.10	1.30	1.48
40	1.40	1.13	1.41	1.51
50	1.58	1.33	1.75	1.56
60	2.24	3.05	2.3	1.74
70	2.27	1.85	1.88	2.02
80	1.81	1.66	1.66	1.87
90	1.75	1.45	1.60	1.90
100	1.68	1.40	1.51	1.93
110	1.59	1.37	1.47	1.96
120	1.51	1.39	1.42	1.98
130	1.43	1.49	1.37	2.04
140	1.39	2.21	1.30	2.09
150	1.47	2.43	1.25	2.10
160	1.70	2.70	1.38	2.15
170	1.85	2.94	1.96	2.23
180	1.89	3.00	2.12	2.34
190	1.92	2.84	2.29	2.53
200	2.10	2.59	2.34	2.47
210	2.18	2.40	2.48	2.59

### 3.5.8 ATR/FT-IR

Figure 3.18 shows the ATR/FT-IR absorption spectra of the dammar, Ketone N, MS2A and Paraloid B67 films. The figure shows the chemical modifications induced by the accelerated ageing on the films prepared as described in section 3.3.1 and subsequently applied onto glass slides.

The characteristic absorbed bands of the varnish films and their frequency assignments are summarised at the end of the section in Table 3.10. The ART/FTIR spectra of the analysed varnish films, before and after ageing, are characterised by the same band frequencies, with differences in their absorbance intensity.

The interpretation of the absorbance bands of dammar resin was performed according to De la Rie (1988a, 1988b), Theodorakopoulos *et al.* (2007), Dietemann *et al.* (2009), Nevin *et al.* (2009), Ciofini (2014), Invernizzi *et al.* (2018). ATR/FT-IR analysis has confirmed that changes in the composition of dammar films had occurred as a result of the accelerated ageing. In particular, the varnish films exhibit a substantial increase in absorbance at the O–H group stretching vibration frequency at 3700–3000  $\text{cm}^{-1}$  and a broadening of the corresponding peak owing to the accumulation of oxidation products. Dammar shows a significant absorbance increase at 1706  $\text{cm}^{-1}$  which is associated with the carbonyl (C=O) stretching vibration of the of aldehydes, ketones, and carboxylic acids. The increase in the intensity of the carbonyl stretching vibration at about 1706  $\text{cm}^{-1}$  can be associated with the oxidation process induced by the ageing processes (Theodorakopoulos *et al.*, 2007). The presence of carbon-carbon double bonds in the cycling ring structure produces a weak band at about 1634  $\text{cm}^{-1}$ . As reported by Ciofini (2014), the slightly broadening of the carbon-carbon double bond (C=C) vibration is only weakly affected by ageing. A significant increase of the absorbance intensity is also observed in the fingerprint region (1300–700  $\text{cm}^{-1}$ ). The peak at 890  $\text{cm}^{-1}$  indicates CH out-of-plane bending of the exomethylene groups.

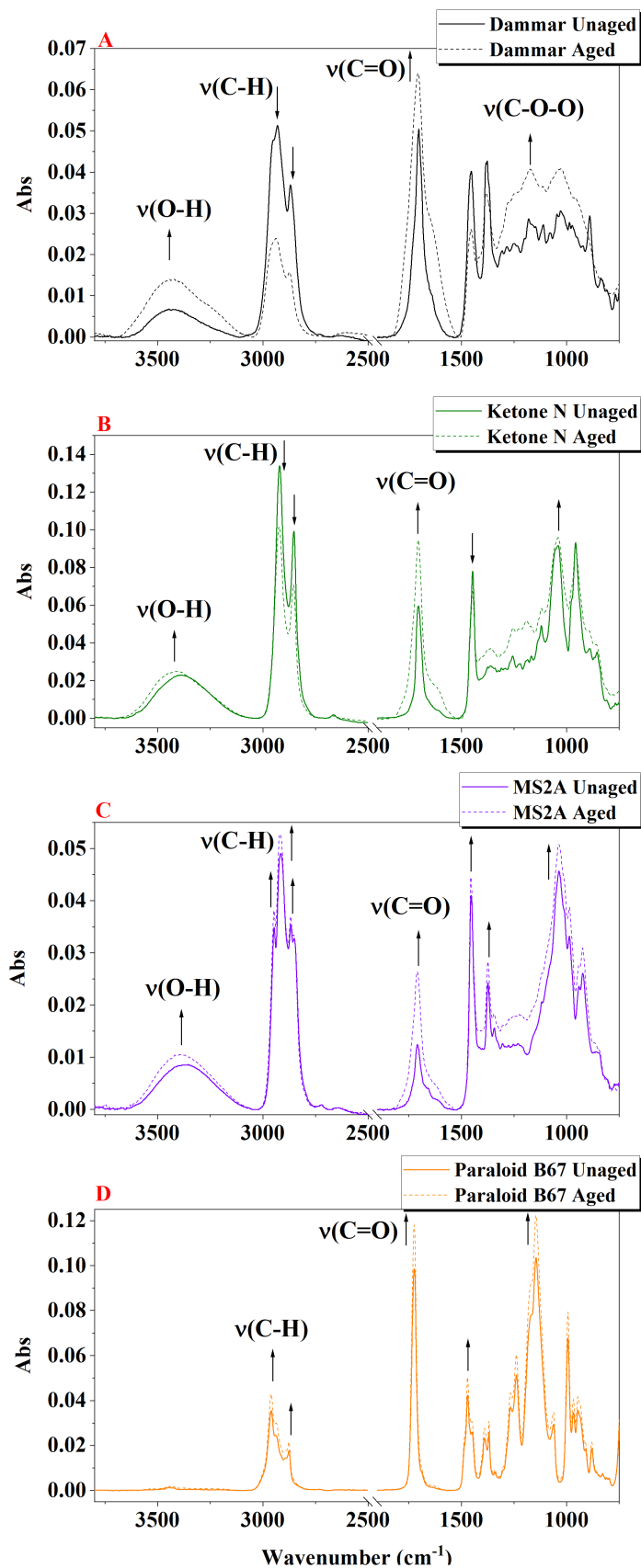


Figure 3.18 – ATR/FT-IR spectra of dammar, Ketone N, MS2A and Paraloid B67 varnish films in the wavenumber ranges of 3800-2500 and 1900-750 cm<sup>-1</sup>. The arrows show the modifications of the main vibrational groups produced by the ageing.

On the contrary, there is a decrease of the C–H stretching modes of methyl  $\nu(\text{CH}_3)$  and methylene  $\nu(\text{CH}_2)$  groups at  $2931\text{ cm}^{-1}$  and  $2869\text{ cm}^{-1}$ , respectively. This modification makes it possible to identify structural changes of the hydrocarbon skeleton in the dammar film under the accelerated ageing carried out for this research. The reduction of the methyl and methylene absorbance at  $1453\text{--}1450\text{ cm}^{-1}$  compared to the methyl absorbance at  $1377\text{ cm}^{-1}$  detects the structural degradation of the dammar films, implying a decrease of the CH bending vibration modes of methylene species (Theodorakopoulos, 2005).

As shown in Figure 3.18 and reported in Table 3.10, the ATR/FT-IR spectra of the Ketone N and MS2A films were interpreted according to de la Rie and Shedrinsky (1989), Doménech-Carbó *et al.* (2008) and Farmakalidis *et al.* (2016). The spectra of both MS2A and Ketone N films are dominated by characteristic bands corresponding to the hydrocarbon skeleton, hydroxyl and ketone groups. Both Ketone N and MS2A show a slight increase in absorbance at  $3400\text{--}3250\text{ cm}^{-1}$ , which has been ascribed to the stretching vibration of associated OH groups. The aged Ketone N film, additionally, exhibits a slight band shift from  $3381$  to  $3425\text{ cm}^{-1}$ . As with the dammar film, after the ageing, the FTIR spectra for both Ketone N and MS2A are dominated by an evident intense band at  $1714\text{--}1692\text{ cm}^{-1}$  corresponding to the stretching vibration of  $\text{--C=O}$  groups, which is associated to cyclic ketones. The shoulder at  $1631\text{ cm}^{-1}$  in both resins is due to  $\alpha$ - or  $\beta$ -unsaturated aliphatic ketones. As reported by Doménech-Carbó *et al.* (2008),  $\alpha$ - or  $\beta$ -unsaturated aliphatic ketones are responsible for the yellowing of ketone resins. This observation is in line with the colourimetric readings (Figure 3.4.4). The acquired aged MS2A spectra exhibit an increase in the absorption at  $2919$  and  $2865\text{ cm}^{-1}$ , which are due to asymmetric stretching vibration of  $\text{CH}_3/\text{CH}_2$  groups and symmetric stretching vibration of  $\text{CH}_3$  groups from the hydrocarbon skeleton, respectively. Moreover, the third band at  $2946\text{ cm}^{-1}$  has been associated by Doménech-Carbó *et al.* (2008) to the  $\text{--CH}_3$  asymmetric stretching vibration of the hydrocarbon skeleton. Conversely, the acquired aged Ketone N spectra display a decrease in the absorption at  $2852\text{ cm}^{-1}$ , which is due to the symmetric stretching vibration of  $\text{CH}_3$  group from the hydrocarbon skeleton (Doménech-Carbó *et al.*, 2008). The fingerprint region contains bands associated with carbonyl, hydroxyl and ether groups. Both ketone resins exhibit a moderate band at  $1446$  and  $1455$

$\text{cm}^{-1}$ , each of which is ascribed to the symmetric bending vibration of  $-\text{CH}_2$  groups. The aged MS2A varnish film exhibits an increase in the absorption at  $1374 \text{ cm}^{-1}$ , which are ascribed to the symmetric bending vibration of  $-\text{CH}_3$  groups. This confirms the chemical structure of the MS2A resin made up of cyclohexanone and methylcyclohexane. However, the weak peak in Ketone N confirms that the resin is a homopolymer composed only of cyclohexanone (Doménech-Carbó *et al.*, 2008). The band at about  $957 \text{ cm}^{-1}$  can also be related to the cyclohexane ring vibrations (Farmakalidis *et al.*, 2016).

Considering the light-ageing dose at which the Paraloid B67 was exposed, the interpretation of the absorbance bands of the unaged and aged glass-coated varnishes were performed according to Lazzari and Chiantore (2000), Chiantore and Lazzari (2001), Favaro *et al.* (2006), Doménech-Carbó *et al.* (2006) and Learner (2004, p. 81). The ageing of the PiBMA (Paraloid B67) films reveals slight variations in the infrared spectra before and after ageing. The increase of absorption at  $1724 \text{ cm}^{-1}$  corresponds to the symmetric carbonyl ( $\text{C}=\text{O}$ ) stretching vibration from ester groups (Doménech-Carbó *et al.*, 2006). After ageing, the resin shows a weak absorption at about  $1640 \text{ cm}^{-1}$ , which has been associated with the stretching of the carbon-carbon double bond ( $\text{C}=\text{C}$ ) vibration of terminal double bonds as introduced elsewhere (Chiantore and Lazzari, 2001; Favaro *et al.*, 2006). As reported by Learner (2004, p. 81), the doublet at  $1392$  and  $1370 \text{ cm}^{-1}$ , corresponding to the symmetric C-H methyl group bending, can be considered characteristic of the Paraloid B67.

Table 3.10 – Wavenumber values ( $\text{cm}^{-1}$ ) corresponding to the maxima of the IR absorbance bands identified in the aged mock-ups studied and their assignment.

Dammar	Ketone N	MS2A	Paraloid B67	Band assignment of the aged resins
3444	3425	3392	3452	$\nu(\text{O-H})$
			2960	$\nu(\text{O-H})$
		2946		$\nu(\text{CH}_3)$
2931	2920	2919	2927	$\nu(\text{CH}_3)$
2869	2852	2865	2876	$\nu_{\text{as}}(\text{CH}_3/\text{CH}_2)$
1706	1706	1710	1724	$\nu(\text{C=O})$ (aldehydes, ketones and carboxylic acids)
			1640	
1634	1631	1631		$\nu(\text{C=C})$ of cis $-\text{C}=\text{C}-$ $\nu(\text{C=O})$ associated with $\alpha$ - or $\beta$ -unsaturated aliphatic ketones
			1471	
1453	1446	1455		$\delta(\text{CH}_3/\text{CH}_2)$
			1392	
1377	1375	1374	1370	$\delta(\text{CH}_3)$
			1269	
1244	1255	1225	1239	$\nu(\text{C-C})$ , $\delta(\text{C-H})$ , $\delta(\text{C-O-O})$
1174	1191		1183	$\delta(\text{C-H})$ in ring, $\nu(\text{C-O})$ in esters, $\nu(\text{C-C})$ in alkanes
	1120		1147	
			1062	
1026	1039	1038		$\delta(-\text{C}-(\text{C=O})-\text{C}-)$ in cyclic ketone $\delta(\text{C-H})$ in ring, $\nu(\text{C-O})$
		986	993	
			967	
	957			cyclohexane ring vibration
		924	946	
890			880	C-H out-of-plane deformation, (one only H attached to ring)
				C-H out-of-plane deformation, (two adjacent H attached to ring)
	852	854	755	

### 3.6 Conclusions

This chapter provided a brief review based on the up-to-date knowledge of the chemical characteristics of a triterpenoid resin (Dammar), two ketone resins (Ketone N and MS2A), and an acrylic polymer (Paraloid B67) addressing so the **objective a**.

The resins and varnishes were studied by stylus profilometry, static contact angle, gas pycnometry, colourimetry, TGA, DSC and ATR/FT-IR. Analysis enabled a representative characterisation in term of morphology and chemical composition of all the varnishes after accelerated ageing. Physicochemical studies with gas pycnometry, DSC analyses and TGA were carried out on the raw resins prior to the ageing. These studies addressed **objective b**.

ATR/FT-IR analysis successfully provided chemical information on the chemical composition of the unaged and aged varnish films. In particular, the aged Paraloid B67 varnish films showed good stability from structural degradation when compared to all the other varnish films. Moreover, the varnish films remained completely transparent even after the ageing process and no variations were visually detected. Paraloid B67 presented higher stability compared to dammar, Ketone N and MS2A, marking specific differences in the behaviour of the resins when subjected to oxidative degradation, as demonstrated by TGA analysis.

After ageing, dammar films were found to be less stable compared to the other resins. The aged varnishes showed a significant colour change towards a yellow hue. Disruption and highly cracked surfaces with larger-scale roughness were detected when employing a stylus profilometer, and a non-contact angle was obtained by depositing a droplet of the DI-W+TW20 solution. ATR/FT-IR analysis monitored a substantial increase in absorbance at the O–H group stretching vibration frequency at 3700-3000  $\text{cm}^{-1}$  and a broadening of the corresponding peak owing to the accumulation of oxidation products. Moreover, the oxidation process induced by the ageing were identified by an increase in absorbance at 1706  $\text{cm}^{-1}$  together with the broadening of the carbon-carbon double bond (C=C) vibration at about 1634  $\text{cm}^{-1}$ .

Ketone N films was the most hydrophilic resin among the varnishes examined with the smallest static contact angle ( $32.4^\circ \pm 2.9^\circ$ ). TGA and DSC demonstrated that the raw ketone resins (Ketone N and MS2A) were found to be less thermally

stable than dammar and Paraloid B67 resins. The oxidative degradation processes of the ketone resins started at the lowest operating temperature of 105°C (Ketone N) and 94°C (MS2A). Due to the lack of previous studies, despite changes can be clearly observed in the TGA analysis, further investigation is needed to empirically correlate the weight loss of the raw Ketone N and MS2A resins to oxidative mechanisms. ATR/FT-IR spectra of the aged ketone films exhibited a shoulder at 1631  $\text{cm}^{-1}$  which is associated with  $\alpha$ - or  $\beta$ - unsaturated aliphatic ketones responsible for the yellowing of ketone resins (de la Rie and Shedrinsky, 1989; Doménech-Carbó *et al.*, 2008). This observation was supported by the colourimetry data.

Although the accelerated ageing carried out on these coatings cannot be compared to the physicochemical processes of natural ageing, these findings are useful in the evaluation of the condition of each the varnish film. The sum of the results can be considered as a starting point for interpreting the laser-induced effects on the mock-ups upon Er:YAG laser irradiation. These data could also provide a valuable advantage for the conservation field.

## CHAPTER 4 Er:YAG LASER TESTS (Part I): A study on the heat distribution

*“The laser was invented in 1960 and was soon dubbed a solution looking for a problem. So new was the tool that our thinking had not caught up with the possibilities. Today the story is distinctly different.”*

— William M. Steen<sup>1</sup>

*Exploiting the potentialities offered by laser cleaning methodologies, this chapter aims to investigate and deepen the knowledge of the Variable Square Pulse Er:YAG laser. The objectives addressed are: **objective c** on the literature review of the Er:YAG laser, **objective d** on the investigation of the laser induced effects on the irradiated varnished and **objective e** on the transmission of the laser beam through the irradiated varnish films. The chapter starts with the state-of-the-art of the laser systems commonly employed in the conservation field, the characterisation of the laser parameters, and the explanation of the mechanisms involved in the laser-material interactions. The presentation of the Er:YAG laser source and the state-of-the-art of the liquid-assisted laser-material interaction in the clinical and surgical fields follows. The introductory part of the chapter ends with the characteristics of the Fotona laser employed for this thesis and the published thermal studies in the conservation field.*

*This introduction is essential in order to link the established scientific knowledge of the Er:YAG lasers in the clinical and surgical applications with the research presented herein for art conservation. The temperature changes upon irradiation have been determined: i) via real time monitoring with an IR thermal camera and ii) with a mathematical computation of the temperature rise associated with the laser irradiation. Moreover, a model of the thermal diffusion in the irradiated bulk of the coatings has been also generated. Fourier Transform Infrared (FT-IR) spectroscopy has been employed to determine the absorption*

---

<sup>1</sup> (Steen and Mazumder, 2010, p. 51)

coefficient of each coating at the laser wavelength. Transmission studies captured increased energy transmissions through varnish films.

#### 4.1 Lasers systems

The word laser is an abbreviation for *Light Amplification by Stimulated Emission of Radiation*, and this definition was proposed the first time by Schawlow and Townes (1958). The unique properties of lasers, such as a high degree of space and time coherence, intensity, monochromaticity, and directionality have favoured their application in different fields, starting from industrial and medical, and only recently in the conservation field (Schawlow, 1965; Kautek *et al.*, 1997; Cooper, 1998; Dickmann, Fotakis and Asmus, 2005; Fotakis *et al.*, 2006; Nimmrichter, Kautek and Schreiner, 2007; Castillejo *et al.*, 2008; Siano, 2008; Radvan *et al.*, 2011)

In general, the emission of a laser can be continuous (continuous wave [CW]) or pulsed, but it is only the latter class of lasers that are used for the cleaning of cultural objects (Siano, 2008).

The lasers, which are currently available on the market, are capable of emitting at different wavelengths (Fotakis *et al.*, 2006, p. 3) and those which are shown in Figure 4.1 are the ones commonly used in the conservation field.

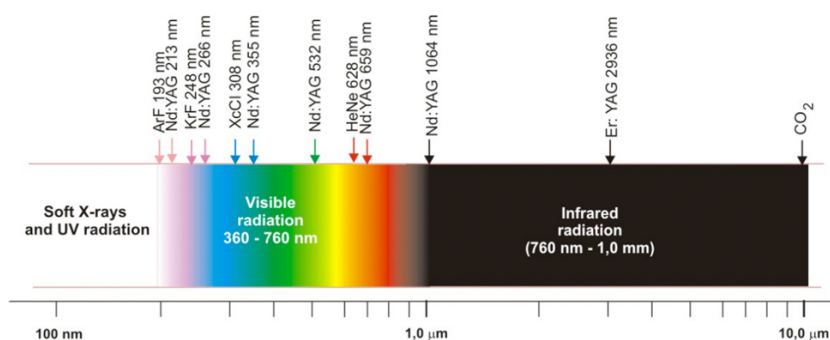


Figure 4.1 – Laser used in the conservation field (Figure is from Marczak *et al.*, 2008).

As defined by Bäuerle (2011, p. 549) “the term laser cleaning denotes the removal of particulates or thin extended contamination layers from solid surfaces”, if the pulsed-laser interaction is related to the heating of the surface, this interaction can be named as ‘*dry laser cleaning*’. However, if the evaporation of thin liquid film assists the pulsed-laser interaction, the interaction is known as ‘*steam laser cleaning*’ (Bäuerle, 2011, p. 549).

The thinning or the removal of unwanted materials from a target surface must take into consideration the selection of appropriate laser parameters, including: wavelength, peak power, fluence, pulse duration and repetition rate, and laser spot size (Asmus, 1986; Larson, 1994; Fotakis, 1995; Fotakis, Hontzopoulos and Zergioti, 1995; Teppo and Calcagno, 1995; Mazumder *et al.*, 1996, p. 797; Watkins, 1997; Cooper, 1998; Fotakis *et al.*, 2006, p. 5; Bäuerle, 2011, p. 4) (Figure 4.2).

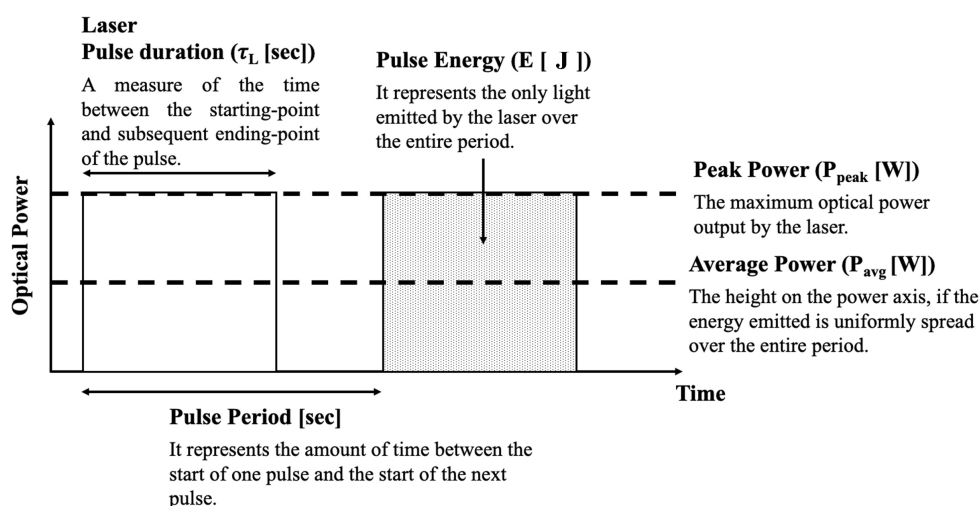


Figure 4.2 – Laser Pulse Parameters (Inspired by an original image published in ThorLabs website)<sup>2</sup>

Fluence is usually expressed in  $J/cm^2$  and describes the energy delivered per unit of area (Cooper, 1998, p. 59), and it is calculated as follows:

$$Fluence (F) = \frac{Laser\ pulse\ energy (E)}{Laser\ beam\ area (A)} = \left[ \frac{J}{cm^2} \right] \quad (Eq. 4.1)$$

The fluence controls the intensity of the laser-material interaction in the irradiated material at surface level (Bäuerle, 2011). Fluence parameter is directly proportional to the laser energy and inversely proportional to the laser beam area (Lukač, Sult and Sult, 2007).

In pulsed lasers, the number of pulses per second or frequency of pulses is known as Pulse Repetition Rate (PRR). The PRR is given by equation 4.2:

<sup>2</sup> The image was inspired by an original image published in ThorLabs website [https://www.thorlabs.com/images/tabimages/Laser\\_Pulses\\_Power\\_Energy\\_Equations.pdf](https://www.thorlabs.com/images/tabimages/Laser_Pulses_Power_Energy_Equations.pdf) (Accessed: 20 December 2020).

$$PRR = \frac{1}{\text{Pulse period}} = [\text{Hz}] \quad (\text{Eq. 4.2})$$

During the laser-material interaction the target material properties are also essential. These properties are: absorption coefficient, heat capacity, thermal conductivity and diffusivity, density, and percentage of transmission of the laser beam through the material (Kogelnik and Li, 1966; Ready, 1971b; Hecht, 1986; Fotakis *et al.*, 2006, p. 5).

From a conservation point of view, leaving a thin layer of varnish on the surface of an art object allows the conservator to control the cleaning process (Zafiropulos and Fotakis, 1997; Theodorakopoulos and Zafiropulos, 2009). In order to accomplish this aim, laser parameters must be appropriately selected and optimised case by case to monitor the cleaning procedure. Therefore, it is essential to understand the process of laser-material interaction.

#### 4.1.1 Mechanism of laser cleaning and its interaction with the materials

Lasers are considered an ideal tool for surface treatment (Razab *et al.*, 2018). Laser cleaning is a physical process in which a laser beam interacts with a solid target without any contact (Mazumder *et al.*, 1996). For this reason, the use of lasers can be considered a non-contact technique (Dickmann, Fotakis and Asmus, 2005), allowing in the field of art conservation, conservators/restorers to lower or in many cases to avoid the use of chemical and mechanical interaction with the surface of artistic objects.

This interaction is based on the physicochemical properties of the target substrate, and the laser parameters (Cooper, 1998, p. 40; Bäuerle, 2011, p. 4).

The energy of an incident laser beam can be partially absorbed by the material, partially scattered producing attenuation and special distribution phenomena, and partially transmitted (Fotakis *et al.*, 2006, pp. 4–5, 25; Siano, 2008).

In general,

$$T + A + R = 1 \quad (\text{Eq. 4.3})$$

where T is the transmittance, A is the absorbance and R is the reflectance with values ranging between 0 to 1 (or between 0 to 100 %).

The wavelength of the laser defines the energy absorption in the material (Mayboudi, 2008, p. 20). In general, when the affinity between the laser wavelength and a target material is high, the greater the quantity of light energy absorbed and the higher the selectivity of the action of laser is. However, if the laser-matter affinity is low, most of the laser light energy will be reflected or transmitted through the irradiated material (Olivi and Olivi, 2010, p. 52).

The spatial distribution of the absorbed laser energy in the substrate can lead to two processes (Hahn, Lippert and Wokaun, 1999; Sato and Nishio, 2001; Serafetinides *et al.*, 2001; Fotakis *et al.*, 2006, p. 25; Cheng *et al.*, 2013):

- 1) **Photo-thermal interaction**, in which the photons do not have enough energy for bond dissociation, causing heat increase inside the material. This process induces a rapid temperature rise in the bulk material, which may lead to the thermal decomposition of the target material. If the vibrational energy attains a particular fluence threshold, the chemical bonds in the irradiated substrate (e.g., a polymer) may be broken (Leme *et al.*, 2012), resulting in a phenomenon known as photo-fragmentation (Pham *et al.*, 2003);
- 2) **Photo-chemical interaction** where the photons have enough energy to trigger photolysis and photodissociation (Bäuerle, 2011).

Generally, photo-chemical processes are predominant in the ultraviolet (UV) region (Mazumder *et al.*, 1996, p. 121), while the photo-thermal process occurs in the infrared (IR) region of the electromagnetic spectrum (Caverhill, 2001, p. 13).

The energies required to dissociate the most common single and double bonds of organic molecules are presented in the table below (Table 4.1):

Table 4.1 – Dissociation energies of the most common single and double bonds of organic molecules (1 eV=1.6x10<sup>-19</sup> J) (Cooper, 1998, p. 41; Ciofini, 2014, p. 41)

Type of covalent bonds	Bond energy (eV)
C-C	3.6
C-O	3.7
C-H	4.2
O-H	4.8
C=C	6.4

The degree of laser-induced thermal and chemical impact is determined by the spatial distribution of the absorbed laser energy into the irradiated substrate. This spatial energy distribution undergoes a typical exponential attenuation following the Beer-Lambert law (Bernath, 2016, p. 21) along the optical axis ( $z$ ):

$$I_{(z)} = I_0 e^{-\alpha z} \quad (\text{Eq. 4.4})$$

where  $I$  is the intensity of the beam that reaches the surface,  $I_0$  is the intensity of the light that is transmitted and  $\alpha$  is the effective **absorption coefficient**. The latter is a parameter that defines how far into a material the laser beam energy can penetrate before it is absorbed (Mazumder *et al.*, 1996, p. 194; Apitz, 2006, p. 14; Mayboudi, 2008, p. 32; Honsberg and Bowden, 2013). The **optical penetration depth** ( $\delta = 1/\alpha$ ) is inversely proportional to the absorption coefficient, and it is defined as the depth at which the laser beam energy falls to  $1/e$  (about 37%) of its initial value at the surface of the sample (Apitz, 2006, p. 14; Mayboudi, 2008, p. 32). When absorption is dominant over reflection, the Beer-Lambert law can be applied to determine the optical penetration depth from the absorption coefficient (Vogel and Venugopalan, 2003b).

Therefore, once the laser beam energy penetrates the material, it is exponentially reduced by absorption according to the Beer-Lambert law and converted into heat. In general, the higher the absorption coefficient, the shorter the laser radiation penetrates into the bulk of an irradiated material (Teppo, 2020). The laser-induced direct heating occurs not only at the surface of the material irradiated, but it is also volumetrically distributed (Teppo, 2020), leading to a local increase in temperature which thus spreads within the material according to the thermodynamics laws of heat transmission (Mazumder *et al.*, 1996, p. 176; Mayboudi, 2008, p. 8). Both the optical and thermal properties of the irradiated material influence the laser-induced temperature profile (Bäuerle, 2011, p. 256).

#### 4.1.2 Laser-material interaction: Thermal effects

In the last decade, especially in the industrial, clinical and surgical fields numerous studies have been published on the direct calculation and mathematical simulation of temperature rise upon IR laser irradiation.

In order to establish heat increase during the laser-matter interaction, many methods have been developed, including the use of thermocouples (Hibst and Keller, 1996; Venugopalan, Nishioka and Mikić, 1996; Armengol, Jean and Marion, 2000; Fried, Ragadio and Champion, 2001; Cavalcanti, Lage-Marques and Rode, 2003; Attrill *et al.*, 2004; Contente *et al.*, 2012; Yaneva *et al.*, 2016) and thermal cameras (Walsh and Deutsch, 1991; Maldague, 2002; Dąbrowski *et al.*, 2006; Perhavec and Diaci, 2009; Perhavec *et al.*, 2009; Lukač *et al.*, 2010; Elhadj, Matthews and Yang, 2012; Usamentiaga *et al.*, 2014; Boccardi *et al.*, 2015). Nevertheless, as reported by Mayboudi (2008, p. 46), in the case of direct measurements of temperature in polymers, some studies have suggested that the use of thermocouples embedded into the analysed material could lead to misleading data due to two factors: i) the wire of thermocouples can directly absorb the laser energy and ii) the errors introduced by the high thermal conductivity of the wires (conduction errors) (Yoder, 2000; Becker and Potente, 2002).

Mathematical simulations (also using the Monte Carlo simulations) have also allowed researchers to model light propagation into multi-layer materials and therefore calculating the distribution of the absorbed light and generated heat during lasers irradiation (Zuerlein *et al.*, 1998; Bityurin *et al.*, 2003; Lippert and Dickinson, 2003; Yao, Chen and Zhang, 2005; Mayboudi, 2008; Marín, 2010; Nath, Gupta and Benny, 2012; Weber *et al.*, 2014; Barvinschi and Bunoiu, 2017).

-----

The following sections give a summarised background theory related to radiation heat transfer and Fourier's law of heat conduction.

#### 4.1.2.1 Radiation heat transfer

Radiation can be defined as the energy emitted by a material in the form of electromagnetic waves (or photons) (Çengel, Ghajar and Kanoglu, 2014, p. 27). For heat transfer studies, it is essential to take into consideration the thermal radiation, which is the form of radiation emitted by bodies due to their temperatures (Çengel, Ghajar and Kanoglu, 2014, p. 27). The magnitude of the energy radiated, and the spectral distribution are representative of the emitting body's surface (Mayboudi, 2008, p. 66). All materials at a temperature above zero emit thermal radiation. The

radiation flux emitted from the surface of an object, which is below the radiation emitted by a blackbody, is described by the Stefan-Boltzmann law:

$$Q_{rad} = \varepsilon \sigma A_s (T_s^4 - T_{surr}^4) \quad [W] \quad (\text{Eq. 4.5})$$

where  $\varepsilon$  is the emissivity of the surface,  $A_s$  is the surface area,  $\sigma$  is the Stefan-Boltzmann constant ( $5.670 \times 10^{-8} \text{ W/m}^2 \cdot \text{K}^4$ ) and  $T_{surr}$  is the absolute surrounding temperature (Mayboudi, 2008, p. 67; Çengel, Ghajar and Kanoglu, 2014, p. 29). The value of emissivity is in the range  $0 \leq \varepsilon \leq 1$ . For a blackbody, the surface emits radiation at its maximum rate ( $\varepsilon = 1$ ). However, for a real surface, the emitted energy is below that of the ideal surface ( $\varepsilon < 1$ ) (Çengel, Ghajar and Kanoglu, 2014, p. 28).

The emissivity value of the varnishes used in this research will be used in section 4.3.3.1 for the thermal studies using an IR thermal camera.

#### 4.1.2.2 Heat conduction and convection

The conduction of heat in solids is a well-defined phenomenon and occurs due to the vibrations of molecules within a medium and a temperature difference through the latter (Çengel, Ghajar and Kanoglu, 2014, p. 18). Fourier established the partial differential equation governing the heat conduction, known as the Fourier's law of heat conduction (Fourier, 1952), in which he concluded that "the heat flux resulting from thermal conduction is proportional to the magnitude of the temperature gradient, opposite to it in sign" and inversely proportional to the thickness of the object (Çengel, Ghajar and Kanoglu, 2014, p. 18). Fourier's law of heat conduction for one-dimensional plane substrate, in the x-direction, can be written as:

$$q_z = -k \frac{dT}{dz} \quad (\text{Eq. 4.6})$$

where  $q$  is the heat flow per unit of area,  $k$  ( $\text{W/m} \cdot \text{K}$ ) is the thermal conductivity<sup>3</sup> along the z-direction,  $dT/dz$  is the temperature gradient in the z-direction and  $T$  is the temperature distribution (Çengel, Ghajar and Kanoglu, 2014, p. 71). When a

---

<sup>3</sup> The **thermal conductivity** ( $k$ ) is a measure which determines the ability of a material to conduct heat. It is defined as the rate of heat transfer through a unit of thickness of the object per unit area per unit temperature difference (Çengel, Ghajar and Kanoglu, 2014, p. 19).

substrate is subjected to unsteady-state heating or cooling, the one-dimensional transient heat conduction equation can be solved by Fourier's second law, in which the thermal conductivity can be considered to remain constant (Marín, 2010; Steen and Mazumder, 2010, p. 255; Çengel, Ghajar and Kanoglu, 2014, p. 74).

In general, heat conduction equation describes the temperature distribution inside a medium, based on the energy conservation law. This law considers the rate of the heat generated within the material, the capacity of the material to store the heat, and the rate of thermal conduction to the boundaries (Mayboudi, 2008, p. 64).

A mathematical solution of the linear heat conduction equation for temperature variation during the heating and cooling cycles after an IR laser pulse irradiation will be presented in sections 4.2.4.2 and 4.3.3.2. Moreover, to obtain a more accurate computation, a two-dimensional simulation of the laser-based heat diffusion inside the varnishes will be presented in section 4.2.4.2.2 and carried out in sections 4.3.3.2.3.

The heat transfer through a solid is always via conduction, but both conduction or convection can transfer heat through a liquid or a gas. This propagation of temperature is expressed by Newton's law of cooling as

$$Q_{\text{conv}} = H A_s (T_s - T_{\infty}) \quad (\text{Eq. 4.7})$$

where  $H$  is the convection heat transfer coefficient ( $\text{W}/\text{m}^2\cdot\text{K}$ ),  $A_s$  is the area of the surface ( $\text{m}^2$ ),  $T_s$  is the surface temperature ( $^{\circ}\text{C}$ ), and  $T_{\infty}$  is the temperature of the fluid ( $^{\circ}\text{C}$ ) (Çengel, Ghajar and Kanoglu, 2014, pp. 378–379). According to the later source (2014, p. 379) the convection heat transfer coefficient  $h$  “can be defined as the rate of heat transfer between a solid surface and a fluid per unit of surface area and per unit of temperature difference”. The heat flow can be considered as natural or forced. In the first case, the flow is caused by buoyancy effect due to temperature differences in the fluid (Mayboudi, 2008, p. 65). In the second case, a fluid is forced to flow over a surface due to an external means (e.g., fan) (Çengel, Ghajar and Kanoglu, 2014, p. 383). The convection heat transfer coefficient will be used in section 4.2.4.2.2.

#### 4.1.3 Erbium-doped:Yttrium-Aluminium-Garnet (Er:YAG) laser

Er:YAG is the acronym for *erbium-doped:yttrium-aluminium-garnet* (Er:Y<sub>3</sub>Al<sub>5</sub>O<sub>12</sub>), and uses a solid-state crystal doped with erbium ions (Er<sup>3+</sup>) as active materials (Diaci and Gaspirc, 2012) and operated in pulsed mode.

The Er:YAG laser (2940 nm) irradiation mechanisms have been extensively researched and documented for clinical and surgical applications. The laser-tissue interaction has been mainly focused on the laser ablation on biological tissues, enamel and dentin (Forrer *et al.*, 1993; Fried *et al.*, 1996, 1998; Hibst and Keller, 1996; Lukač, Marincek and Grad, 2004; Bachmann *et al.*, 2005; Bader and Krejci, 2006; Lukač *et al.*, 2007; Lukač, Sult and Sult, 2007; Gutknecht, 2008; Perhavec and Diaci, 2009; Olivi and Olivi, 2010; Gutknecht *et al.*, 2011; Diaci and Gaspirc, 2012; Kuščer and Diaci, 2013; Zgavec and Stopajnik, 2014; Pich *et al.*, 2015). Unfortunately, the same cannot be said for the conservation field, where this laser seems to be the least established, and the physicochemical mechanisms have not yet been thoroughly investigated.

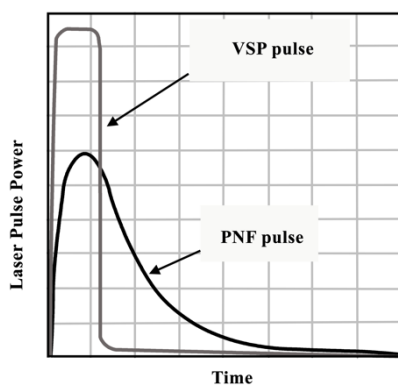


Figure 4.3 – Comparison between PNF and VSP technologies (Inspired by an original image published in Lukač, Sult and Sult, 2007)

All the Er:YAG lasers available nowadays in the marketplace are optically pumped with flashlamps<sup>4</sup> (Koechner, 1976, pp. 288–300). The important difference in the type of technology used to energise the flashlamps is its pulses shapes (Lukač, Marincek and Grad, 2004). In the conventional configuration, known as PFN (Pulse Forming Network) the pulses are bell-shaped. In contrast, in the VSP (Variable Square Pulse)<sup>5</sup>, the pulses are almost square-shaped and of variable pulse duration (Nemeš, Lukač and Možina, 2012) (Figure 4.3). An essential difference between the two typologies of pulses is that for VSP pulses, the average laser power and the

4 For the description of flashlamp please refer to Demtröder, 2006; Nemeš, Lukač and Možina (2012)

5 VSP-Variable Square Technology is a proprietary technology of Fotona d.d. (See [www.fotona.com](http://www.fotona.com) - Fotona).

peak power can be considered alike. The same cannot be said for the PFN pulses. VSP technology is used in Er:YAG lasers commercialised by Fotona (Diaci and Gaspirc, 2012).

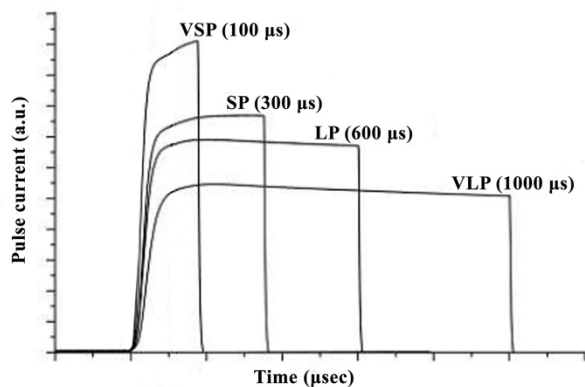


Figure 4.4 – VSP free-running Er:YAG laser pulse shape for different laser pulse duration (Fotona laser) (Figure is from Lukač, Primc and Pirnat, 2012)

An additional asset of the VSP technology is that it enables the user to easily control the laser pulse duration ( $\tau_L$ ) (Diaci and Gaspirc, 2012), as shown in Figure 4.4. The VSP free-running Er:YAG single laser pulse durations are: Very Short Pulse (VSP mode:  $\approx 100 \mu\text{s}$ ); Short Pulse (SP mode:  $\approx 300 \mu\text{s}$ ), Long Pulse (LP mode:  $\approx 600 \mu\text{s}$ ) and

Very Long Pulse (VLP mode:  $\approx 1000 \mu\text{s}$ ) (Lukač, Sult and Sult, 2007; Nemeš, Lukač and Možina, 2012). VSP technology has the advantage of allowing the system to form a controlled train of micro pulses within the aforementioned large pulses therefore giving each pulse an already known pulse width (Diaci and Gaspirc, 2012).

Moreover, the same company developed a special ‘*top-hat*’ beam profile handpiece known as Fotona R11 or R04 (Figure 4.5). As reported by Lukač et al. (2007), this ‘*top-hat*’ beam profile was created for clinical and surgical applications to ensure a homogeneous beam profile, overcoming the issues related to standard laser handpieces with Gaussian profile and energy distribution with a conical shape.

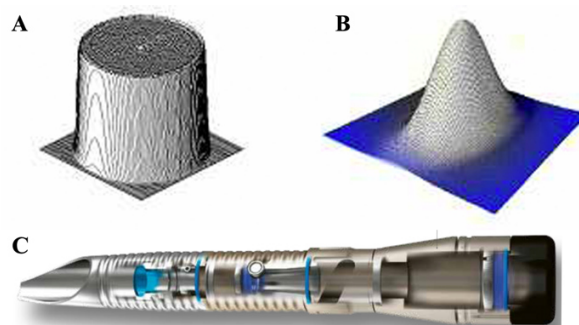


Figure 4.5 – (A) ‘Top hat’ beam profile handpiece, (B) Gaussian beam profile handpiece (Figure is from Lukač, Sult and Sult, 2007) and (C) Fotona R11 handpiece (see [www.fotona.com](http://www.fotona.com) - Fotona).

The removal of materials with an infrared free-running Er:YAG lasers (2940 nm) is based on the selective excitation of OH- or NH-containing molecules present in the substrate (De Cruz, Hauger and Wolbarsht, 1999). The photon energy at the Er:YAG laser wavelength is of about 0.42 eV. Such energy is not high enough to trigger O-H bond dissociation, which requires energy from 3.4 to 4.5 eV/molecule (De Cruz, Hauger and Wolbarsht, 1999; Ciofini, 2014) (see Table 4.1.1). The same applies to multi-photon effects. This laser-material interaction, which might provide the necessary dissociation energy, does not occur because of the irrelevant irradiance attained by laser irradiation (De Cruz, Hauger and Wolbarsht, 1999).

The Er:YAG laser energy is in fact only able to excite bond vibrational stretching modes of the organic molecules (De Cruz, Hauger and Wolbarsht, 1999;

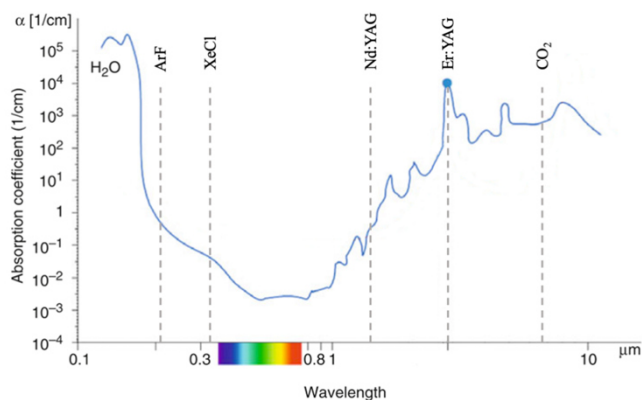


Figure 4.6 – The absorption coefficient of water. The Er:YAG laser has the highest absorption coefficient in water (Inspired by an original image published in Olivi and Olivi, 2010)

De Cruz, Wolbarsht and Hauger, 2000a, 2000b) (Figure 4.6). It is possible to say that, when the Er:YAG laser interacts with the material, the laser energy is transferred to the OH molecules which start to vibrate, causing a local rise in temperature. This laser-matter interaction

results in explosive vaporisation, photo-thermal disaggregation and micro-distillation of the irradiated material (De Cruz, Hauger and Wolbarsht, 1999; De Cruz, Wolbarsht and Hauger, 2000a, 2000b; De Cruz *et al.*, 2014). Therefore, it can be said that the number of hydroxide-containing molecules and the physical properties of the materials combine to determine the pattern of energy deposition into the material treated (Teppo, 2020).

The absorption properties of water are of particular importance for the IR laser interaction with the material (Apitz, 2006, p. 15). The OH bond, whether in water or other polar solutions, participates in the process of the erbium laser

irradiation as it is the primary target chromophore (De Cruz, Wolbarsht and Hauger, 2000a, 2000b; Nahen and Vogel, 2002; Teppo, 2020).

As reported by Shori et al. (2001), at the Er:YAG laser emitted wavelength of 2940 nm, the absorption coefficient of water is  $\approx 13.300 \text{ cm}^{-1}$  matching precisely the maximal absorption in water. This is about 15 times higher than the absorption of a CO<sub>2</sub> laser and 20,000 times than that of an Nd:YAG laser (Walsh and Cummings, 1994; Bader and Krejci, 2006). Nonetheless, Cummings and Walsh (1993) described that upon Er:YAG laser irradiation, the absorption coefficient of water changed from  $\sim 13\,000 \text{ cm}^{-1}$  to  $< 1000 \text{ cm}^{-1}$  due to the increase of irradiation at high fluences.

As a rule of thumb, to estimate the temperature distribution upon Er:YAG laser irradiation, one must take into consideration the distribution into the irradiated material of molecules containing hydroxy or amide groups (De Cruz, Wolbarsht and Hauger, 2000a, 2000b; Diaci and Gaspirc, 2012; Chillè *et al.*, 2020; Teppo, 2020), as well as the laser pulse duration ( $\tau_L$ ). This parameter defines the exposure time of the selected energy delivered to the target material (Farkas, Hoopman and Kenkel, 2013). If the laser beam energy is delivered within a very short period of time, the laser energy has little time to spread into the irradiated volume, limiting heat diffusion within the material (Diaci and Gaspirc, 2012).

#### 4.1.3.1 Liquid-assisted laser-material interaction

Forrer et al. (1993, 1994) reported the energy density value ( $W_v$ ) of 2.7 kJ/cm<sup>3</sup> and a threshold fluence of 1 J/cm<sup>2</sup> as the parameters needed for the evaporation of a pure water film upon an Er:YAG laser pulse irradiation. Using those two parameters, the authors were able to calculate the approximate depth ( $h$ ) of the heated layer at the fluence threshold ( $h = F/W_v = 3.7 \text{ }\mu\text{m}$ ). According to Forrer et al. (1993), the  $h$  value demonstrated the effect of heat conduction since the mathematically obtained  $h$  is about five times larger than the optical penetration depth of the Er:YAG laser radiation in water. Similarly, Teppo (2020), reported that the Er:YAG laser heating could be controlled within a thin surface layer of water, allowing the vaporisation of 4  $\mu\text{m}$  thickness of a water film when it is exposed to a single Er:YAG laser pulse with a fluence of 1 J/cm<sup>2</sup>. Furthermore, Zapka et al.

(1991) and Tam et al. (1992) showed that by using an Er:YAG laser, the optical penetration depth in pure water is approximately 1  $\mu\text{m}$  (Forrer *et al.*, 1994; Frank *et al.*, 2008) allowing, as reported by Diaci et al. (2012), to create a vapour bubble with a diameter much larger than 1000  $\mu\text{m}$ . This applies when the heating rate is fast enough, and the deposited energy is significant (Forrer *et al.*, 1993; Vogel and Venugopalan, 2003a, 2003b; Frank *et al.*, 2008).

In this framework, Apitz (2006, pp. 77–79), carried out a series of tests on the temporal evolution of the ablation plume upon free-running Er:YAG laser irradiation on several substrates, such as gelatine, skin, and water. Herein are reported only the findings relating to laser interaction with water. The short-term photography analysis carried out by Apitz (2006, pp. 57) allowed the author to gain a comprehensive overview of the complex and fast laser-material interaction upon Er:YAG irradiation.

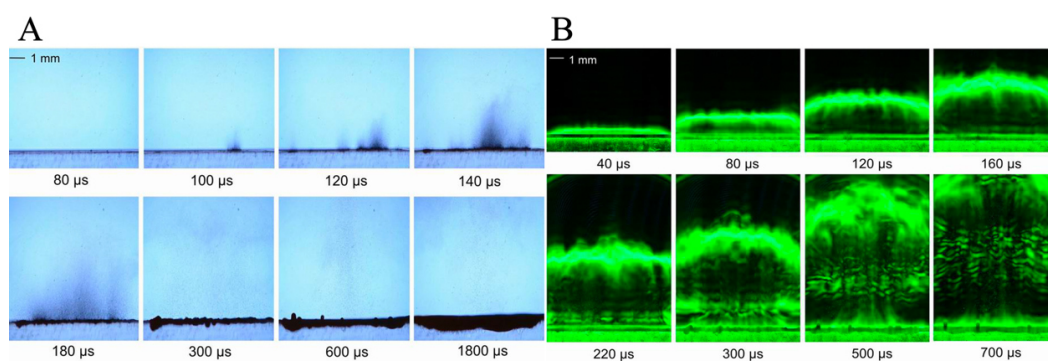


Figure 4.7 – This images are reproduced by Apitz (2006). (A) Dynamics of the interaction of water film upon a single Er:YAG laser irradiation at 2  $\text{J}/\text{cm}^2$ , beam diameter of 8 mm and  $\tau_L$  of 200  $\mu\text{s}$ . The time-resolved images, acquired in bright-field, show that after the beginning of the laser pulse, at about 100  $\mu\text{s}$ , the material ejection begins in the areas of the highest energy density and spreads over the entire beam cross-section after about 180  $\mu\text{s}$ . (B) Images in the dark field, using the same laser device and employing the above-mentioned parameters. After 40  $\mu\text{s}$ , Apitz (2006, pp. 77–79) described a clear formation of vapour, which falls after about 300  $\mu\text{s}$ . The light stripe in front of the cloud indicates a zone of high vapour density.

As reported in Apitz (2006), Figure 4.7 shows a free-running Er:YAG irradiation ( $\tau_L$  of 200  $\mu\text{s}$ ) at a fluence of 2.0  $\text{J}/\text{cm}^2$  and delivered onto 10 mm thickness of water, which was placed in a cuvette, using a laser beam diameter of 8 mm. The time-resolved images in Figure 4.7 (A) were acquired in bright-field. The ejection of water droplets starts after 100  $\mu\text{s}$  (areas of the highest laser intensity) and only after 180  $\mu\text{s}$  does it spread over the entire laser-irradiated area (Figure 4.7 [A]). According to the author, the recoil pressure of the ablation causes a dent in

the surface appearing as a clear black stripe below the water surface with a depth of about 1 mm after 1800  $\mu$ s. The darkfield image (Figure 4.7 [B]) exhibits a strong vapour formation not visible in the bright field method. The presence of droplet ejection indicates an explosive ablation process.

The ejection of water droplets upon free-running Er:YAG laser irradiation is due to superheating of water, leading to a phase explosion followed by the ejection of the irradiated material in the form of water droplets (Forrer *et al.*, 1993; Nahen and Vogel, 2002; Vogel and Venugopalan, 2003a; Apitz and Vogel, 2005; Apitz, 2006, p. 97). As reported by Nahen and Vogel (2002), this phase explosion is characterised by a rapid transition of the superheated metastable liquid into a system containing two separate phases of gas and liquid in equilibrium states (Miotello and Kelly, 1995; Debenedetti, 1996). This transition takes place when the temperature of the water reaches the spinodal limit<sup>6</sup> ( $\approx 305$  °C, at the atmospheric pressure of 9.2 MPa - Apitz, 2006, p. 99), thus generating homogenous nucleation (Vogel, Apitz and Venugopalan, 2007). This phase explosion, under atmospheric conditions, leads to an impressive pressure rise and a shock wave due to the expansion of the vapour phase (Vogel and Venugopalan, 2010, p. 562). The water droplets, which have been created during the phase expansion, are accelerated by the expanding vapour and ejected from the irradiated surface at high velocity (Nahen and Vogel, 2002; Apitz, 2006, p. 97). Therefore, the ‘*popping*’ noise, which the user hears upon Er:YAG laser irradiation, is generated by the photo-vaporization of some water droplets due to a finite amount of absorptive losses of the laser beam during the laser-material interaction (Freiberg and Cozean, 2002).

Previous studies have demonstrated the formation of channel propagation in free liquid water layer followed by the liquid explosion and the transfer of recoil momentum to the irradiated material below the zone of absorption (Forrer *et al.*, 1993, 1994). The mathematical model, also based on Bernoulli’s equation for flowing fluids (Arakeri, 2000), was carried out assuming that the laser beam had a stationary intensity, its incident beam interacted on a free water surface and that it was instantaneously absorbed into the water layer without any loss due to heat

---

<sup>6</sup> For the definition of spinodal and the description of the phase diagrams, please refer to: Martyniuk, 1978; Vogel and Venugopalan, 2003a, 2003b, 2010; Apitz, 2006; Vogel, Apitz and Venugopalan, 2007.

conduction or the light scattering in the surrounding irradiated material. The authors associated the laser effect on the material irradiated to a ‘plunger’ in which the cold material not involved in heat propagation is pushed sideways under the action of pressure. As reported by Ferrer et al. (1994), the laser intensity for the formation of channel propagation “has to be high enough ( $\sim 12 \text{ kW/cm}^2$ ) to produce a pressure inside the channel which balances both the restoring force of the surface tension and the pressure loss caused by heat conduction to and condensation at the inner surface”. Ferrer *et al.* (1993, 1994) were able to demonstrate that the Er:YAG laser could ablate biological tissues through a water layer allowing the achievement of an important practical advantage, the using of water as a cooling reservoir therefore lowering the induced thermal damage.

In fact, the distinctive characteristic of the use of an Er:YAG laser, when a liquid is applied onto the surface, is the confinement of the laser-material interaction within the liquid. Moreover, the laser irradiation in a wet environment is accompanied by bubble formation and much stronger mechanical effects than observed in a gaseous environment (Vogel and Venugopalan, 2003b, 2010, p. 598). It can be said that, because of the highly selective absorption of the 2940 nm Er:YAG laser for hydroxyl groups, steam laser cleaning restricts the peak temperature to the top surface of the liquid rather than at the substrate–liquid interface (Steen and Mazumder, 2010, p. 432), therefore avoiding substrate absorption (Bäuerle, 2011, p. 558) reducing the heat diffusion to the surface underneath (Fotakis *et al.*, 2006, p. 195).

#### 4.1.4 Thermal studies of Er:YAG laser

The major issues of the use of Er:YAG lasers, for the irradiated materials in the conservation field, relate to the temperature rise on the surface and the heat propagation in the bulk (De Cruz *et al.*, 2014). The side effects of the heat impact on materials have been studied mainly for Q-switched Nd:YAG (1064 nm) lasers on inorganic materials, mock-ups and painted surfaces (Siano, 2008; Siano *et al.*, 2012; Ciofini, 2014).

In 2014, a paper by De Cruz and co-authors (2014) was published aiming to address the problem of temperature rise on the material upon Er:YAG laser irradiation (MonaLaser - LLC., Orlando, FL, USA). A customised device was

developed to perform the tests. Type T thermocouples were placed below the irradiated area, and they were used to measure the temperature of the treated surface upon laser irradiation. The authors carried out the tests firstly on graphite as a reference material due to its good absorption at infrared wavelength. The data obtained on the PVA glue/graphite reference revealed a linear trend between the temperature increase upon laser irradiation and the average irradiation power, despite the use of various combinations of pulse repetition rate and laser intensity. The authors reported in the article that a good reproducibility of the results was achieved. The decision to use graphite was essential for the comprehension of laser energy absorption. Subsequently, the same procedure was performed on various samples representative of materials commonly present in art objects with different levels of conductivity and thermal diffusivity (regrettably no data of the thermal diffusivity are provided in the article). The results obtained by De Cruz *et al.* (2014) showed that the increase in surface temperature on irradiated egg and siccative oil was equal to  $\Delta T = 53^{\circ}\text{C}$ , at fluence of  $0.2 \text{ J/cm}^2$  and a repetition rate of 7.5 PPS. This temperature was rightly considered by the authors unsuitable for the constituents of the underlying paint layer. However, prewetting the samples with isopropanol and irradiating the surface with the same laser parameter, the temperature recorded by the thermocouples was much lower with  $\Delta T = 15^{\circ}\text{C}$  (De Cruz *et al.*, 2014).

During the Aplar 6 conference held in Florence in 2017, Felici *et al.* (2019) presented a different approach in order to quantify the local thermal effects upon Er:YAG laser irradiation. The study was carried out on ‘a fresco’ mock-ups (10x10 cm and thickness of 2.5 cm) created specifically for the study, the authors applied organic and synthetic consolidants commonly employed by conservators, such as shellac and polyvinyl acetate (PVA). To these two formulations, Felici *et al.* added a small quantity of carbon black (no data of the amount of pigment is provided in the article) to simulate the ageing process and the inclusion of soot particles.

Two classes of lasers were employed: i) a QS ( $\tau_L 15 \text{ ns}$ ) and SFR ( $\tau_L 50 - 110 \mu\text{s}$ ) Nd:YAG laser (EOS QS by El.En. SpA, 1064 nm) and ii) an Er:YAG laser (Light Brush 2 by El.En. SpA, 2940 nm) in Short mode ( $\tau_L 250 \mu\text{s}$ ). The handpiece of each laser was fixed onto a support placed at 2 cm from the surface of the samples. The heat impact was monitored in real-time by employing an IR thermal

camera (InfReC R300SR by Nippon Avio Co.LTD) which captured 60 frame-per-second and the use of a digital microscope (Dino-Lite®) made it possible to compare the modification of the irradiated material after the interaction of both the selected lasers. The longer pulse duration of the Er:YAG laser compared to the QS and SFR Nd:YAG laser resulted in a modification of the irradiated area showing a brown hue due to burn damages of the pigment/binder. Based on the information supplied by the authors, the use of the IR thermal camera allowed to acquire the time (about 20 sec for both the lasers) required by the target material to get back to room temperature after laser irradiation. Felici *et al.* (2019) were able to acquire the maximum temperature achieved on the areas selected and involved in the lasers' irradiation by using an interpolation algorithm which operated on the temperatures in each pixel. The highest temperature recorded using the Er:YAG laser was 250 °C at a fluence of 2.5 J/cm<sup>2</sup>.

## 4.2 Material and methods

### 4.2.1 Er:YAG laser

A Fotona Fidelis<sup>XS</sup> VSP Er:YAG laser (Figure 4.8) and a Fotona XS Dynamis Er:YAG laser (2940 nm) were employed for this study.



Figure 4.8 – Fotona Fidelis<sup>XS</sup>

The lasers were run in VSP mode (laser pulse duration  $\tau_L \approx 100 \mu\text{s}$ ) and SP mode ( $\tau_L \approx 300 \mu\text{s}$ ).

The Er:YAG lasers were equipped with an articulated mirror arm and were operated in the free-running mode. The beam was delivered perpendicularly to the varnish film surfaces by a straight collimated full-beam titanium handpiece (R11). The optical arm was fixed and mounted on top of the samples at a 20 cm working distance between the handpiece end and the samples surface. The samples were fixed on a support placed at 10 cm from the working desk.

Depending on the tests, the beam diameter was set at 3 and 4 mm, both in the handpiece and in the laser displays, and the pulse repetition rate at 2 and 5 Hz. The laser irradiation tests were carried out in fluences, as shown in the laser's unit displays and single laser pulses, ranging between 0.5 and 2.5 J/cm<sup>2</sup> (depending on the laser unit selected), were fired onto dry and pre-wetted varnish sample surfaces. For the water-assisted tests, an mixture of 1% (v/v) of a non-ionic surfactant (Tween20 — Sigma Aldrich) in 50 mL of deionised water (DI-W+TW20) (Cremonesi and Signorini, 2012) was applied with a cotton swab, firstly drained on a blotting paper, and rolled onto the surface three times. Tween20 was employed in these tests to decrease the surface tension of the deionised water and therefore increase the surface wettability. The varnish surfaces were pre-wetted at the beginning of each laser scan.

#### 4.2.2 Optical properties varnishes

As reported by Zuerlein *et al.* (1998), direct FTIR measurements of dental tissues allowed the authors to calculate the absorption coefficient at the Er:YAG laser wavelength. The same approach has been carried out in this research in order to obtain the absorption coefficient of the aged varnish films (dammar, Ketone N, MS2A and Paraloid B67) applied on glass slides.

##### 4.2.2.1 *Transmission FT-IR*

FTIR transmission spectra of the varnishes were obtained using the same bench spectrometer as described in Chapter 3 (section 3.4.9). The working wavenumber range was from 4000 to 2000  $\text{cm}^{-1}$ , and the spectra were over 16 scans at 4  $\text{cm}^{-1}$  resolution.

A transmission spectrum was recorded on an uncoated glass slide. The transmission spectrum of the glass was subtracted from the spectra of the aged films on glass slides to obtain the percentage transmission component (% T) of the resins at the Er:YAG laser wavelength (2940 nm) (Zuerlein *et al.*, 1998).

Therefore, in order to calculate the absorption coefficient ( $\alpha$ ), the Beer-Lambert law was used. The absorption is governed by the Beer-Lambert law equation in which the absorption (A) is obtained as (Dash, 2011, p. 369):

$$A = 2 - \log_{10}(\%T) \quad (\text{Eq. 4.8})$$

Knowing the thickness (d) of the varnish films applied on the glass slides, and assuming that the energy, which is not transmitted or reflected, is completely absorbed by the material, the absorption coefficient ( $\alpha$ ) was calculated as:

$$\alpha = \frac{\ln\left(\frac{100}{\%T}\right)}{d} \quad (\text{Eq. 4.9})$$

##### 4.2.2.2 *Mid-IR integrating sphere measurement*

To derive the reflectance of the varnishes at the laser wavelength (2940 nm), the Perkin Elmer Frontier, Spectrum 400TM FT-IR was equipped with a PIKE IntegratIR™ sphere.

The reflective gold-coated sphere (Lambertian scatterer for high-performance measurements [Schanda, 2007, p. 48]) with a diameter of 76.2 mm was equipped with a two-sample port ( $\varnothing = 20$  mm). A flipper mirror allowed to direct the light illumination onto the sample or onto the reference surface. With the mirror pointing up towards the sample port, the angle between the incident IR beam on the sample surface and the surface normal was  $12^\circ$ . The background was collected by flipping the inner mirror towards a reference point towards the gold dome. Uncoated and coated slides were placed on the top port, and reflectance spectra were acquired by putting a golden backing on the glass slides. The working wave-number range was from  $4000$  to  $2000\text{ cm}^{-1}$  and the spectra were recorded at 32 scans and  $8\text{ cm}^{-1}$  resolution. In order to obtain the reflectance of the aged varnishes at the laser wavelength (Siano *et al.*, 2000), the same process already described in Chapter 3 (section 3.4.9) was carried out.

#### 4.2.3 Transmission study

Transmission study was carried out to monitor the transmitted energy of the laser beam passing through the aged resins samples applied on glass slides by increasing fluences.

A picture of the configuration employed for the transmission studies is presented in Figure 4.9. On a Nexus optical table, a QE25ELP-H-MB-DO Pyroelectric Detector was placed under and very close to the plane of each of the varnish films analysed to record transmission upon laser irradiation. A Fotona XS Dynamis Er:YAG laser was used to carry out the experiments and the laser beam was set with a spot diameter at  $\varnothing = 4$  mm.

The incident laser energy ( $E_{\text{inc}}$ ) was first measured at the Fotona XS Dynamis output. The PC-Gentec-EO software confirmed that the laser output energy was stable.

The glass slide transmission was measured and acquired at each fluence employed for this study. Owing to partial laser beam light dissipation due to reflection and scattering, the laser light passing through the uncoated glass slide ( $E_{\text{transglass}}$ ) did not coincide with the  $E_{\text{inc}}$ .

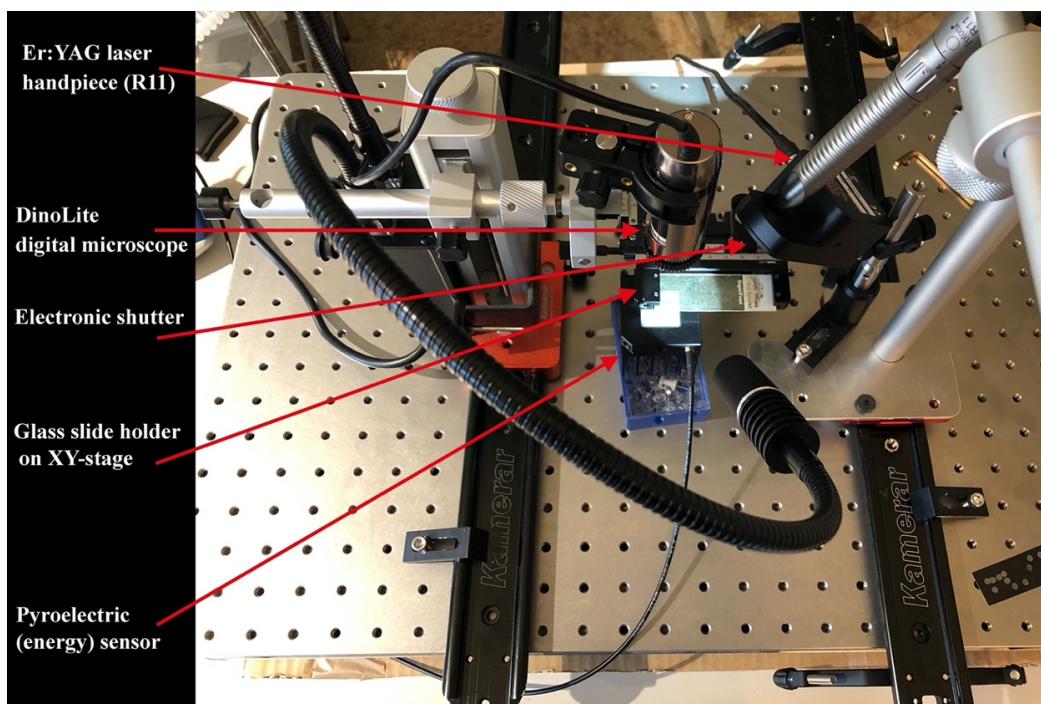


Figure 4.9 – Experimental set-up for the transmission study tests.

The varnish samples were then installed and positioned on an XY-stage. The transmitted energy ( $E_{trans}$ ) was recorded and averaged on at least five points. The samples were tested using a single shot shuttered exposure per site in dry and pre-wet modes, the calculated fluence values of 0.5, 1, 1.5, 2.1 and 2.4 J/cm<sup>2</sup> in VSP and SP modes, 4 mm laser beam diameter and 5Hz pulse repetition rate. For the pre-wetting procedure, the samples were wetted with cotton swabs. The latter loaded with DI-W+TW20 were firstly drained on a blotting paper before the swabs were rolled three times on the varnish films. The area was after immediately irradiated with the Er:YAG laser. Considering practicalities and previous trials (Bracco *et al.*, 2003; Chillè, Papadakis and Theodorakopoulos, 2020) the varnish surfaces were pre-wetted at the beginning of each laser scan.

Therefore, the overall % transmission was then obtained as:

$$\%T = (E_{trans}/E_{inc}) \cdot 100 \quad (\text{Eq. 4.10})$$

Moreover, for each varnish selected for this study, the slopes of transmission were then determined by plotting  $E_{trans}/E_{inc}$  as a function of the chosen fluences (Pettit *et al.*, 1994; Theodorakopoulos, 2005; Fotakis *et al.*, 2006, p. 237; Dash, 2011, p. 369).

#### 4.2.4 Heat distribution on the coatings upon laser irradiation

##### 4.2.4.1 IR thermal camera recordings

Thermal imaging has been employed to record the thermal impact at the laser beam incidence onto the surface of the irradiated varnishes. A Fotona Fidelis<sup>XS</sup> VSP Er:YAG laser has been used for this study. The laser was run in VSP and SP modes, at first on the dry surface and then using DI-W+TW20. The laser beam diameter ( $\varnothing$ ) was set at 3 mm spot size, to facilitate more effective use of the aged coatings and, therefore, increase the acquisition areas.

The average effect of the temperature variation on the surface was monitored using a FLIR T620bx IR thermal camera, which captures 30 frames-per-second<sup>7</sup> with an IR resolution of 640×480 pixels. The thermal camera was set with a varnish flat emissivity value ( $\epsilon$ ) of 0.93, which was selected from the internal materials list of the IR camera<sup>8</sup>.

In appendix B the tests performed are presented using K type thermocouple and the heat impact recordings on an uncoated glass slide. These two preliminary tests had been carried out to validate the thermal imaging study, which were later performed for each varnish film selected for this study.

The IR thermal camera was fixed at 45° and focussed on the irradiated spot area. The samples were secure to a support placed at 10 cm from the working desk, to avoid possible reflectance from the worktop. The beam was delivered perpendicularly to the varnish surface with a 20 cm working distance between the end of the handpiece and the sample surface (Figure 4.10).

---

<sup>7</sup> The frame rate represents the rate at which the IR detector of the thermal camera creates images. However, the thermal time constant defines how fast the IR detector responds to fast changes in the incoming radiation. For the IR camera used in this research, the thermal time constant of the bolometer, ranges between 7 and 12 ms values ([https://flir.custhelp.com/app/answers/detail/a\\_id/236/related/1](https://flir.custhelp.com/app/answers/detail/a_id/236/related/1)) (Accessed: 20 December 2020).

<sup>8</sup> The emissivity value for the varnish films has also been compared with the reference values published by ThermoWorks. Please see the ‘*Infrared Emissivity Table*’: [https://www.thermoworks.com/emissivity\\_table](https://www.thermoworks.com/emissivity_table) (Accessed: 20 December 2020).

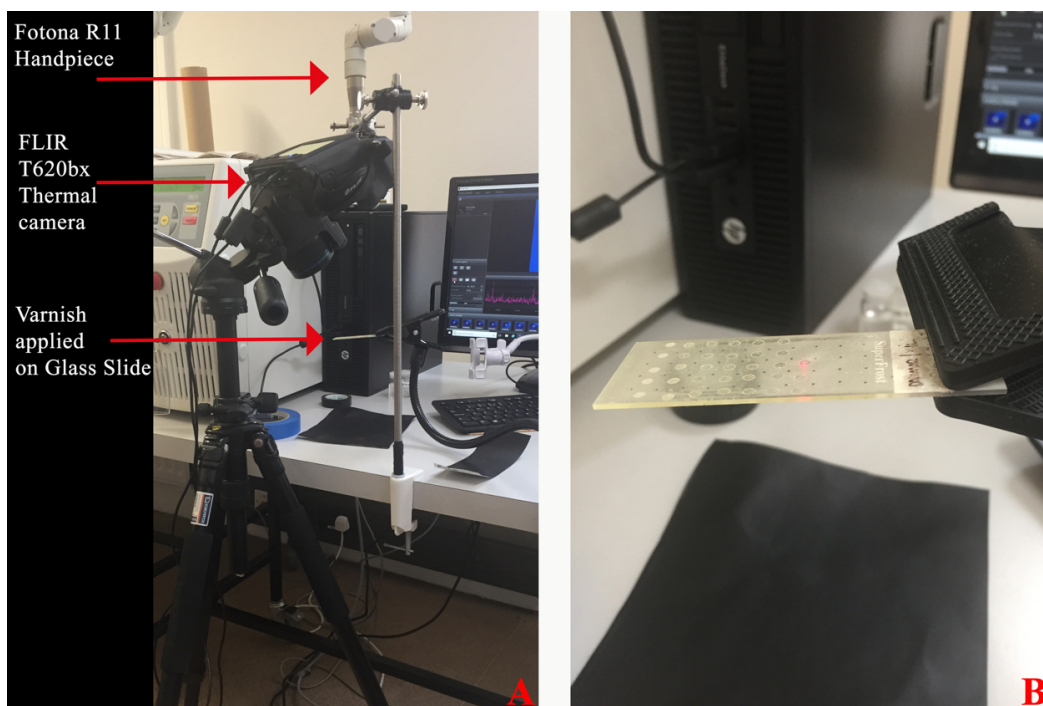


Figure 4.10 – Experimental set-up for the thermal camera recording tests (A) and a detail of an irradiated dammar varnish applied onto a glass slide during the laser irradiation secured to a support placed at 10 cm from the working desk (B).

To avoid irregularities in the recordings with the IR thermal camera, the first few pulses were masked with a ceramic plate in front of the handpiece and the pulse repetition was set at 2 Hz to facilitate manual counting of pulses. This set-up made it possible to observe the temperature rise on the front surface of the varnish films applied onto glass slides using the FLIR thermal camera.

For consistency, all sample acquisition commenced approximately 20 sec before laser irradiation in order to record thermal images of the varnishes at room temperature ( $T_R$ ) and ended as soon as  $T_R$  was reached after the one-pulse laser impact.

The laser–sample interaction data were recorded in real-time with FLIR System Tools+ software. As presented in Figure 4.11 (below), temperature measurements have been obtained from the video images by defining the laser spot areas where the data were to be collected.

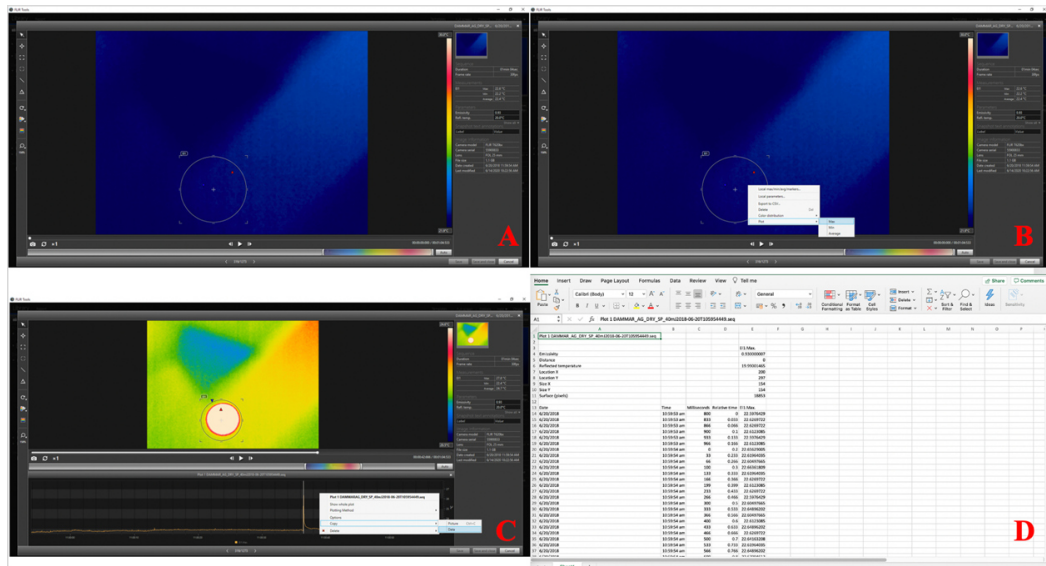


Figure 4.11 – The thermal camera records a series of frames in which the energy radiated from the varnish surfaces upon Er:YAG irradiation is shown as a form of the surface signal. By manually selecting the area influenced by the laser irradiation (A), the device translated the radiated surface signal to the temperature values by defining an internal conversion equation (B). Thus, by selecting the desired maximum temperature (C), the data were extracted in comma-separated values (CSV) file and exported in a data analysis software (e.g., Excel) (D).

The mean maximum temperature due to the heat impact,  $\Delta T_{\text{mean}}$ , was determined as:

$$\Delta T_{\text{mean}} = T_{\text{max}} - T_R \quad (\text{Eq. 4.11})$$

where  $T_{\text{max}}$  was the maximum average effect of the temperature recorded on the irradiated varnish surfaces, and  $T_R$  was the room temperature accurately measured on acquisition.

The single laser pulse test was repeated six times on different areas for each varnish film to exclude possible cumulative effects on the surface. Between consecutive recordings, the irradiated films were left to cool down at room temperature (Figure 4.12). The temperature increments studied for the irradiated films were average values of six consecutive recordings. The data were acquired on the same day to ensure that both  $T_R$  and relative humidity (RH) were constant and noted down each time prior to starting the thermal studies.

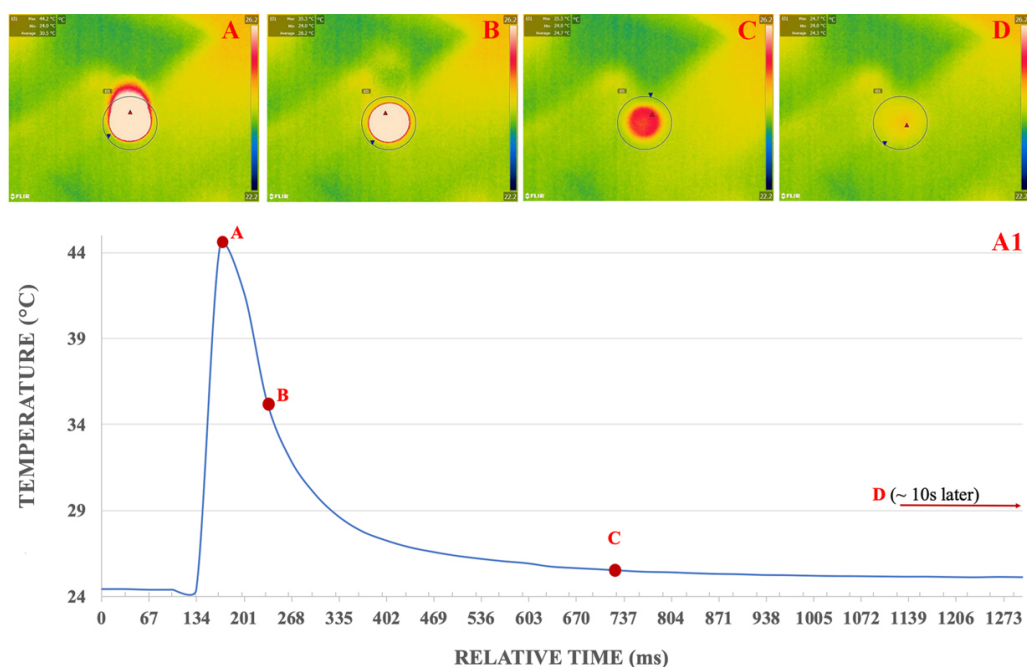


Figure 4.12 – FLIR T620bx thermal camera. A1: Thermograph of the maximum temperature variation recorded (44.2 °C) including TR, which at the time of acquisition was 24 °C, as recorded on VSP dry dammar (one pulse at 2 J/cm<sup>2</sup>) in real-time. On the top side: (A) the thermal image (thermogram) of the dammar varnish surface while receiving a single laser pulse; (B) the thermogram after 67 ms; (C) the thermogram after 0.56 s; (D) the thermogram after 8 s.

#### 4.2.4.2 Modelling of the heat distribution upon laser irradiation

Specific heat capacities ( $C_p$ ) (J/kg·K), a temperature-dependent thermophysical property of the material, presented in Chapter 3, have been determined by carrying out DSC analysis (Table 3.3.6) for each class of unaged raw resin. The absorption coefficient ( $\alpha$ ) was obtained as described in section 4.2.2.1 (Eq. 4.9). The percentage of laser transmission (%T), and the percentage of diffuse reflection (%R) are those in Table 4.3.1.

In this study, the thermal model has been developed under the following assumptions:

- 1) The laser beam profile has been considered as homogeneous in the time average of a pulse and with a uniform intensity distribution over the circular area on the irradiated surface (Mayboudi, 2008, p. 156; Siano, 2008, p. 10);

- 2) Scattering of the laser beam has been considered negligible (Mayboudi, 2008, p. 50);
- 3) Since the laser parameters are fixed, the temperature distribution is dependent on the absorption coefficient ( $\alpha$ ) within the irradiated target area and the transport of heat out of this zone (Bäuerle, 2011, p. 19);
- 4) For simplicity, it has been assumed that  $\alpha$  is constant over the overall thickness of the varnishes applied on glass slides (Fotakis *et al.*, 2006, p. 237);
- 5) All the varnishes have been considered uniform and isotropic (Mayboudi, 2008; Bäuerle, 2011, p. 19);
- 6) Considering all the coatings isotropic, their thermal conductivity ( $k$ ) (W/m·K) is direction-independent (Mayboudi, 2008, p. 139);
- 7) For all the varnishes, thermal diffusivity ( $D$ ) ( $m^2/s$ ), given by  $D = k/\rho \cdot C_p$  (where  $\rho$  is the density [ $kg/m^3$ ]) (Marín, 2010; Çengel, Ghajar and Kanoglu, 2014)<sup>9</sup>, has been taken from Fotakis *et al.* (2007, p. 36), in which for organic substrates  $D$  ranges between  $10^{-3}$  to  $10^{-4}$   $cm^2/s$ .

#### 4.2.4.2.1 Mathematical computation of the temperature rise

A presentation of the modelling of the laser thermal interaction (one Er:YAG laser pulse) with the dry irradiated varnishes is presented below.

In the case of pulsed laser irradiation, when a definite amount of temperature is accomplished at the surface is the requirement, a connection between the laser power density and the selected pulse duration ( $\tau_L$ ) should be looked for (Mazumder *et al.*, 1996, p. 194). The laser spot size determines the power density, which is an important parameter in defining the laser-material interaction. For long pulse duration (e.g., laser pulse  $> 10^{-5}$  sec), the transverse thermal conduction becomes important. The transverse thermal gradients are higher for a small laser spot size, and heat is conducted out of the focal area more rapidly (Ready, 1978, p. 345). With fixed laser parameters, the extent of the bulk distribution within the irradiated zone depends on: i) the substrate absorptivity at the laser wavelength (Fotakis *et al.*,

---

<sup>9</sup> The thermal diffusivity represents the rate at which the temperature diffuses through a material (Marín, 2010; Çengel, Ghajar and Kanoglu, 2014).

2006, p. 199), which plays a distinctive role because it controls the heat input directly onto the targeted samples (being itself a function of surface temperature) (Mazumder *et al.*, 1996, p. 194), and ii) the transport of this said heat out of this zone (Bäuerle, 2011, p. 19).

It is generally stated that, a body whose surface is heated by a laser pulse (with a constant heat flux) can be treated as a semi-infinite solid (Mazumder *et al.*, 1996, p. 194). In this idealised body, the heat transfer occurs merely in the direction normal to the surface (z-direction) as long as the following conditions are fulfilled: i) constant thermophysical properties, ii) no internal heat generation and iii) uniform initial temperature ( $T_i$ ) throughout the solid. In a semi-infinite geometry, the depth of the body is larger ( $z \rightarrow \infty$ ) than the depth at which the heat can penetrate. This can be represented mathematically as a boundary condition as  $T(z \rightarrow \infty, t) = T_i$  (Çengel, Ghajar and Kanoglu, 2014, p. 260).

The one-dimensional heat conduction equation can be solved the following assumption (Incropera and DeWitt, 1996; Mazumder *et al.*, 1996, p. 194; Majaron *et al.*, 1998; Mayboudi, 2008, p. 200; Siano, 2008; Marín, 2010; Nath, Gupta and Benny, 2012):

- radius of the laser beam ( $r$ )<sup>10</sup> at the surface is significantly bigger than both thermal-diffusion length ( $l_{th}$ ) and the optical penetration depth ( $\delta$ ).  
 $r \gg l_{th}$  and  $r \gg \delta \Rightarrow$  **one-dimensional heat conduction;**
- the thickness of the varnish films is significantly bigger than thermal-diffusion length ( $l_{th}$ )  $\Rightarrow$  **semi-infinite solid;**
- $k$  and  $D$  are taken as constants.

The **thermal diffusion length** ( $l_{th}$ ) provides the distance over which temperature changes propagate in the z-direction by diffusion in time  $\tau_L$  (Bird, Stewart and Lightfoot, 1960, p. 780; Siano *et al.*, 2000; Siano, Pini and Salimbeni, 2000; Brown and Arnold, 2010) and it is given by:

$$l_{th} = 2\sqrt{D\tau_L} \quad (\text{Eq. 4.12})$$

---

<sup>10</sup> Laser spot diameter at  $\varnothing = 4$  mm.

Therefore, the longer the pulse duration, and the larger the thermal diffusivity of the irradiated material, the deeper and faster the heat distribution is expected to spread away from the surface (Figure 4.13) (Partovi *et al.*, 1987).

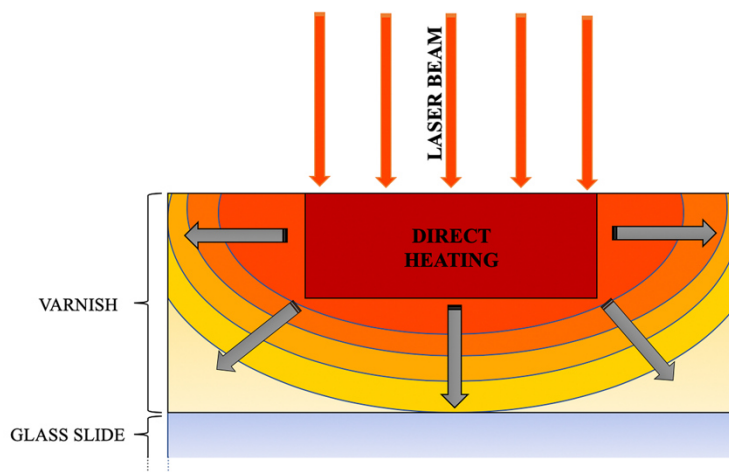


Figure 4.13 – Graphical representation of direct and conduction heating on varnishes (Inspired by an original image published in Siano *et al.*, 2000).

Considering all the varnishes selected for this research, both optical penetration depth ( $\delta$ ) and thermal-diffusion length ( $l_{th}$ ) are considered significantly shorter than the radius of the laser beam employed in this study. Therefore, a single-pulse Er:YAG laser can therefore be treated in one axial dimension with no heat production within the material (Zuerlein *et al.*, 1998).

The temperature distribution can be approximately estimated by using the equation (Siano *et al.*, 2000; Fotakis *et al.*, 2006, p. 35):

$$\Delta T_{(z)} = \frac{\alpha F e^{-z/\delta}}{\rho C_p} \quad (\text{Eq. 4.13})$$

where F is the fluence (J/cm<sup>2</sup>).

In order to attempt a more precise approach to the thermal issues upon Er:YAG laser irradiation, it is possible to assert that the temperature profiles inside the irradiated varnish volume, as a function of time (t) and depth (z) are based on the 1-D heat conduction equation from Fourier's second law (Mazumder *et al.*, 1996, p. 797; Siano, 2008, p. 10; Marín, 2010; Nath, Gupta and Benny, 2012)

$$\frac{\partial^2 T(z, t)}{\partial z^2} = \frac{1}{D} \frac{\partial T(z, t)}{\partial t} \quad 0 \leq z \leq \infty \quad (\text{Eq. 4.14})$$

The absorbed laser power density is defined as (Steen and Mazumder, 2010, p. 257):

$$F_0 = \frac{P_{tot}(1 - R)}{A} \quad (\text{Eq. 4.15})$$

where  $P_{tot}$  is the laser power,  $R$  is the reflectivity of the varnishes and  $A$  is the area of the laser beam. Because of the reflection, the irradiance of the laser beam interacting with the surface change by a factor  $(1 - R)$  (Ready, 1971a, p. 67).

In general, mathematical models can be divided into *surface models* (Carslaw and Jaeger, 1959; D’Couto and Babu, 1994; Arnold, Luk’yanchuk and Bitiyurin, 1998; Siano *et al.*, 2003, 2012; Siano, 2008; Steen and Mazumder, 2010; Bäuerle, 2011) and *volume models* (Carslaw and Jaeger, 1959; Ready, 1971a; Cain *et al.*, 1992; Steen and Mazumder, 2010). In *surface models*, the computation considers laser-material interactions as a surface process with the heat absorption located at the surface of the material. Commonly, this is the model selected to study the heat wave propagation and the laser ablation of metals. However, the *volume models*, the laser-material interaction process occurs within the bulk of the irradiated material. Therefore, obtaining the determined optical properties of varnishes examined, the volume models have been selected for this study.

Considering the laser impact on the selected varnish films, which have different thicknesses (Table 4.2), and assuming that the thermal properties of the varnishes are independent of temperature and the beam energy is absorbed at the surface with an absorption coefficient  $\alpha$ , the following can be stated. In addition to the above conditions if a constant energy flux ( $F_0$ ) is supplied to a semi-infinite body instantaneously at time  $t = 0$  at the end of the laser pulse, a rise followed by a drop in temperature,  $T$ , results in conduction of heat into the material (Steen and Mazumder, 2010). The energy lost from the surface through radiation or convection are assumed to be negligible (Ready, 1971a, p. 70). As reported by Steen and Mazumder (2010) this mathematical model can be employed to approximate the extent of the conduction process and used when the heat flow is in one direction. The boundary conditions are written as follows:

$$\text{At } z = 0 \quad \frac{\partial T}{\partial z} = 0 \quad (\text{Eq. 4.16})$$

for  $T(z > 0, t = 0) = T_i$

Therefore, the solution of Eq. 4.14, with  $F_0 = \text{const}$  for  $t \geq 0$ , can be solved as proposed by Carslaw and Jaeger (1959, p. 80), and later repropoed by Ready (1971a, p. 72), as:

$$\begin{aligned} \Delta T_{(z,t)} = & \left(\frac{2F_0}{k}\right) \sqrt{Dt} \operatorname{ierfc} \left[ \frac{z}{2\sqrt{Dt}} \right] - \left(\frac{F_0}{\alpha k}\right) e^{-\alpha z} \\ & + \left(\frac{F_0}{2\alpha k}\right) e^{(\alpha^2 Dt - \alpha z)} \operatorname{erfc} \left[ \alpha\sqrt{Dt} - \frac{z}{2\sqrt{Dt}} \right] \\ & + \left(\frac{F_0}{2\alpha k}\right) e^{(\alpha^2 Dt + \alpha z)} \operatorname{erfc} \left[ \alpha\sqrt{Dt} + \frac{z}{2\sqrt{Dt}} \right] \end{aligned} \quad (\text{Eq. 4.17})$$

where *erfc* and *ierfc* correspond to the ‘complementary error function and its integral’ (Carslaw and Jaeger, 1959; Ready, 1971a; Marín, 2010; Comini and Cortella, 2013).

Eq. 4.17 determines the temperature at depths  $z$  of the order of  $1/\alpha$  (Ready, 1971a, p. 72), where  $\alpha$  is the absorption coefficient. Moreover, it can provide profiles in depth and time for the temperature rise produced by the pulsed laser. After the end of the laser pulse ( $\tau_L$ ) the irradiated varnishes will cool (cooling cycle). Therefore, the temperature for  $t > \tau_L$  can be conveniently obtained by Duhamel’s theorem (Carslaw and Jaeger, 1959, p. 30), and using Heaviside step function.

In order to carry out the numeric computation, Wolfram Mathematica 12 software (version 12.1.1) was used.

Table 4.2 – Parameters required to define the thermal modelling of all the varnishes selected during Er:YAG laser treatment. The thermal diffusivity (D)\* was taken from Fotakis *et al.* (2007, p. 36)

Product	Average thickness varnish films untreated ( $\mu\text{m}$ ) $\pm \sigma$	$\rho$ (kg/m <sup>3</sup> ) at RT	$C_{p\text{mean}}$ (J/kg·K)	$D^*$ (m <sup>2</sup> /s)	$k$ (W/m·K)		
Dammar	82.3 $\pm$ 15.2	1180	1750	10 <sup>-7</sup>	10 <sup>-8</sup>	0.21	0.021
Ketone N	28.2 $\pm$ 7.5	1100	1980	10 <sup>-7</sup>	10 <sup>-8</sup>	0.22	0.022
MS2A	58.8 $\pm$ 11.7	1090	1730	10 <sup>-7</sup>	10 <sup>-8</sup>	0.19	0.019
Paraloid B67	51.3 $\pm$ 12.6	1040	2050	10 <sup>-7</sup>	10 <sup>-8</sup>	0.21	0.021

#### 4.2.4.2.2 2 Dimensional Simulation model

The model simulation has provided an additional possibility to study the heat propagation in the bulk of the irradiated varnishes. FlexPDE Multi-Physics Finite Element Solution Environment for Partial Differential Equations software (version 5.0.7) was used to carry out the simulation.

To perform the transient thermal model simulation, the software required the following information: i) the mock-ups geometry, with the dimension of each layer analysed (optical penetration depth [ $\delta$ ] + varnish film + glass slide), was developed using FreeCAD (version 0.18) (Figures 4.14-16); ii) the varnishes properties; iii) boundary conditions; iiiii) time step, and iiiiii) laser pulse characteristics.

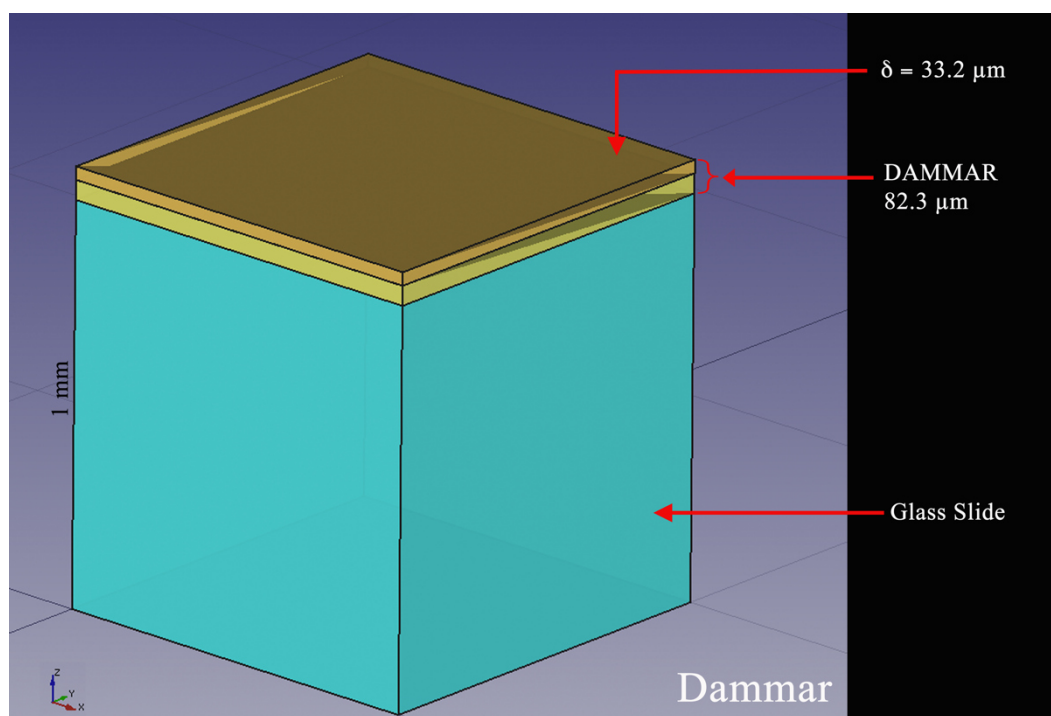


Figure 4.14 – The 3D-geometry of the modelled **dammar** film applied on a glass slide with the dimension of each layer analysed (optical penetration depth [ $\delta$ ] + varnish film).

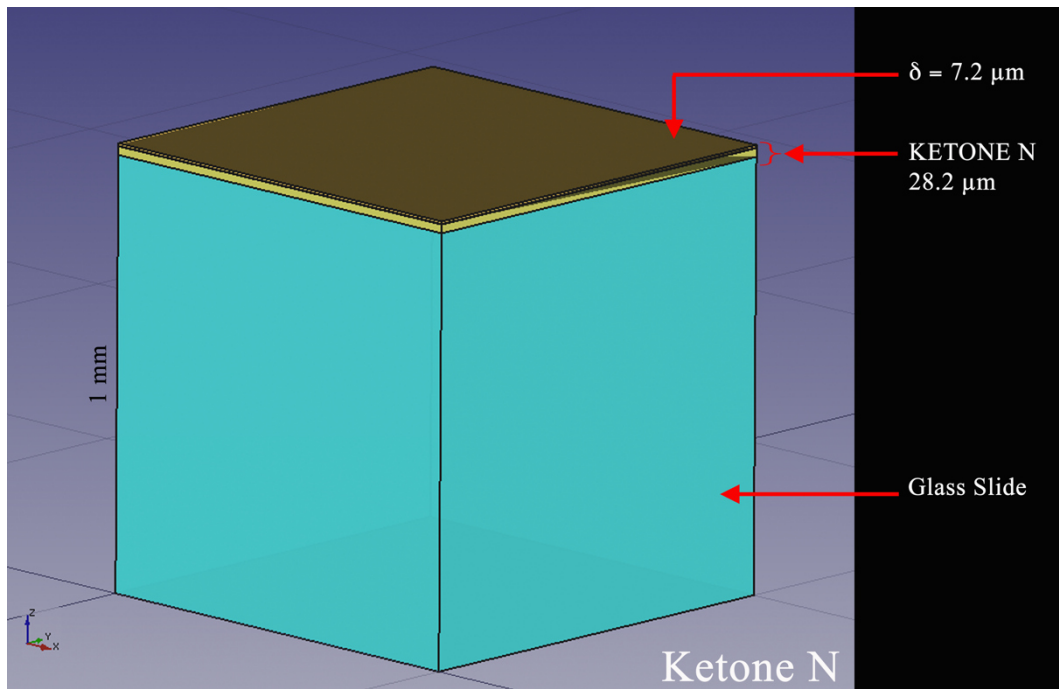


Figure 4.15– The 3D-geometry of the modelled **Ketone N** film applied on a glass slide with the dimension of each layer analysed (optical penetration depth [ $\delta$ ] + varnish film).

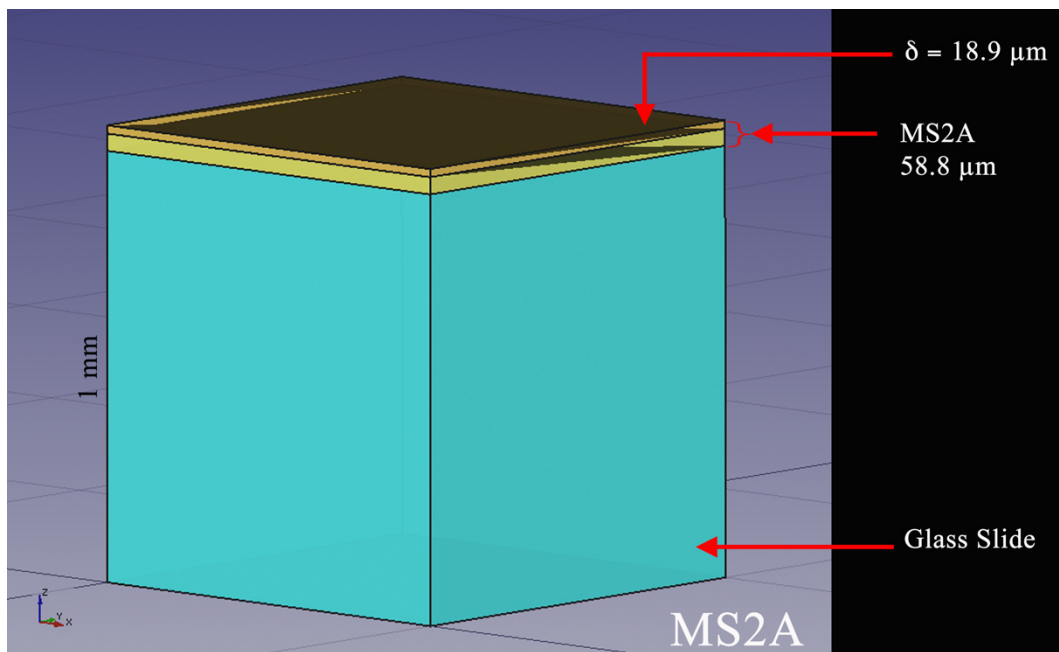


Figure 4.16 – The 3D-geometry of the modelled **MS2A** film applied on a glass slide with the dimension of each layer analysed (optical penetration depth [ $\delta$ ] + varnish film).

Therefore, to simulate the physical phenomena related to the absorption and the propagation of the heat generated by a single pulsed Er:YAG laser onto the dry varnishes, the following simplifications have been made:

- (a) The laser beam was considered to have a cylindrical shape and a uniform power flux distribution;
- (b) Given the geometric feature of the laser beam and its small dimensions compared to the thicknesses of all the varnishes and the glass slides (1 mm) (Figures 4.14-16), the domain of the simulation was considered to be axially symmetric (Figures 4.2.17-19);
- (c) Given the derived optical properties of all the varnishes, the simulation was set as if the entire laser energy had not been entirely absorbed at the surface of the varnish layers. In fact, according to the Beer–Lambert Law, the intensity of the laser light through a material is exponentially reduced by the absorption within the first layer of the material (see section 4.1.1) (Barvinschi and Bunoiu, 2017). For this reason, in writing the 2Dimensional simulation, a sub-domain was created for each varnish in which it was assumed that part of the laser photon energy would be absorbed within the bulk of the varnish films. This subdomain was named as “*laser absorption zone*”. This absorption would lead to a local increment in temperature changing into thermal energy, spreading within each varnish bulk according to the thermodynamics laws of heat transmission. The optical penetration depth ( $\delta = 1/\alpha$ ) of each varnish for the laser-absorbing part derived from Eq. 4.9;

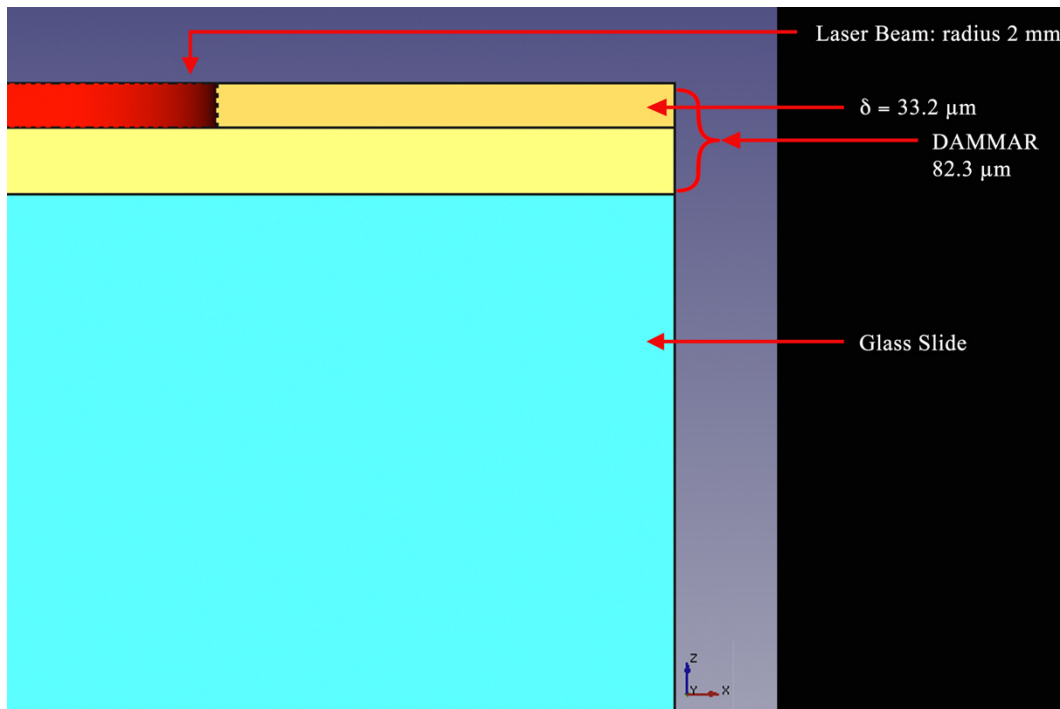


Figure 4.17 – Graphical representation of the geometry created to run the 2D simulation. A sub-domain has been created in which it is assumed that part of the laser photon energy is absorbed into the bulk of the **dammar** varnish film.

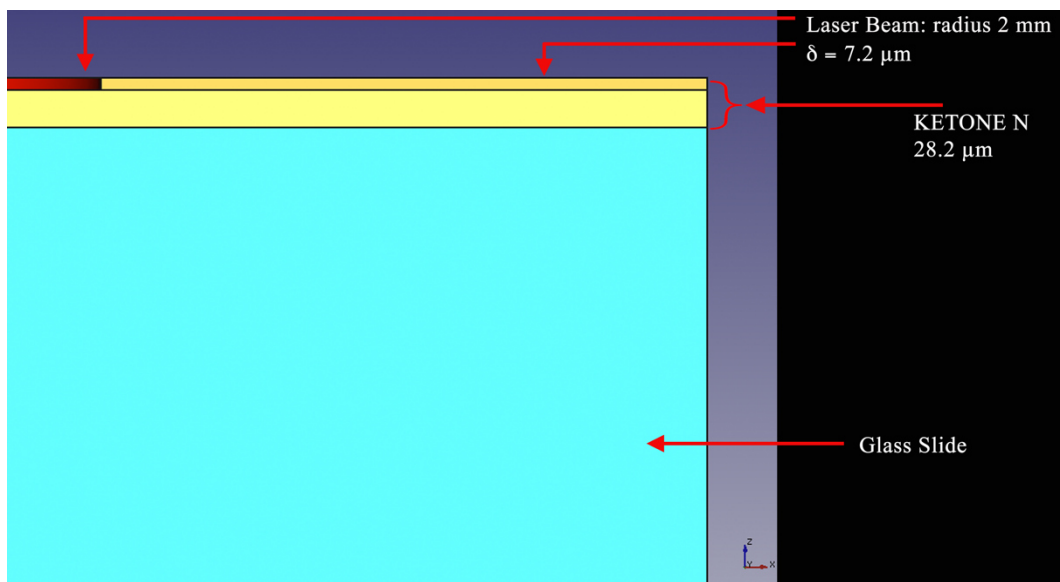


Figure 4.18 – Graphical representation of the geometry created to run the 2D simulation. A sub-domain has been created in which it is assumed that part of the laser photon energy is absorbed within the bulk of the **Ketone N** varnish film.

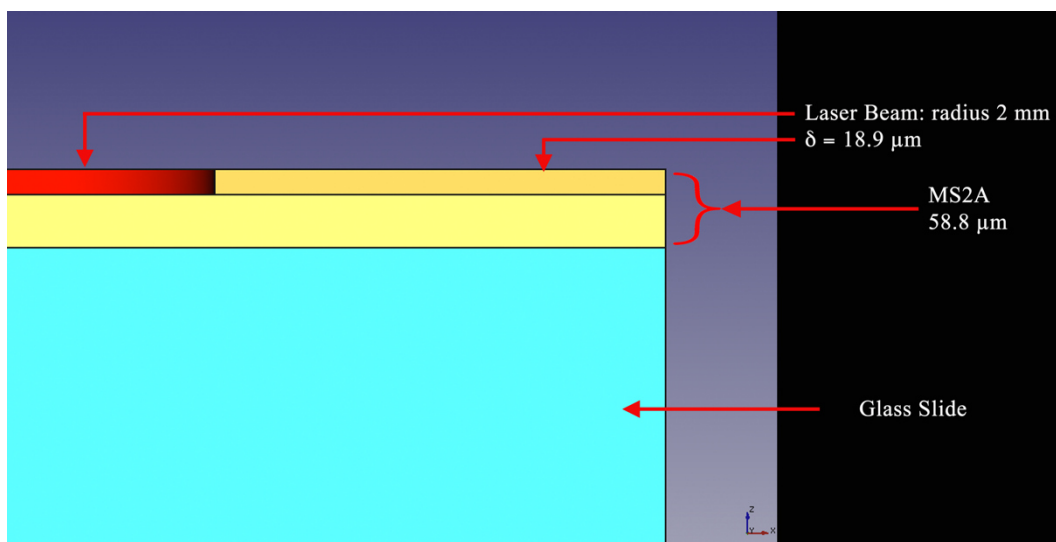


Figure 4.19 – Graphical representation of the geometry created to run the 2D simulation. A sub-domain has been created in which it is assumed that part of the laser photon energy is absorbed into the bulk of the **MS2A** varnish film.

- (d) In the calculation, the laser pulse was taken into account as a step function value;
- (e) The varnishes were considered to have a uniform refractive index with no refraction or reflection occurring when the laser light passes from one area to the other (Ataie-Fashtami *et al.*, 2011).
- (f) The mock-up geometries were assumed to transfer heat by convection to the surrounding environment according to Newton’s law of cooling (section 4.1.2.2). As reported in the literature (Incropera *et al.*, 2007, p. 238; Mayboudi, 2008, p. 149), the free convection of  $H = 5 \text{ W/m}^2\text{K}$  have been applied to the model (Appendix B).
- (g) The simulations were made considering a time step progression of  $1\mu\text{s}$  for each step, while the domain discretisation subdivided the model into:

Product	Nodes	Cells
Dammar	10884	2956
Ketone N	31283	8546
MS2A	19293	5257

- (h) The simulation test started  $50 \mu\text{s}$  before the release of the laser pulse at different pulse duration modes and the model simulated a  $10 \mu\text{s}$  time interval of laser-material interaction with a stationary laser beam.
- (i) The complete simulation-tests duration took into consideration a total time of  $10 \tau_L$  in VSP and SP modes.

The transient temperature distribution generated during the laser-material interaction was determined based on the differential conduction equation (Nikulari and Mordike, 1989, p. 171; Misra *et al.*, 2011; Acherjee *et al.*, 2012; Endo and Walter, 2018, p. 274):

$$\rho * C_p * \frac{\partial T}{\partial z} = \vec{\nabla}(k\vec{\nabla}T) + q \quad (\text{Eq. 4.18})$$

where  $\nabla$  is the gradient operator and  $q$  is the rate of heat generated per unit of volume (Misra *et al.*, 2011; Acherjee *et al.*, 2012). This was reported in the simulation as:

$$\text{div}(k*\text{grad}[Temp]) + \text{Source} = \text{rho}*C_p*dt(\text{temp}) \quad (\text{Eq. 4.19})$$

where  $k$  is the thermal conductivity,  $Temp$  is the temperature,  $\rho$  is the density ( $\text{kg}/\text{m}^3$ ), and  $Source$  was obtained as  $\text{beamsource}*(1-\text{Trans-Refl})$  (all values are in SI). The amplitude of the heat distribution, which is controlled by the density of the delivered power to the medium ( $\text{W}/\text{m}^3$ ), obtained was:

$$\text{PowerVolDensity} = \text{Energysource} / (\text{LaserPulse} * V\text{beam}) \quad (\text{Eq. 4.20})$$

The equation 4.18 has been solved considering the initial environmental temperature as  $T = 25 \text{ }^\circ\text{C}$ .

### 4.3 Results and Discussion

#### 4.3.1 % Transmission, % Reflectance and Absorption coefficient

The FT-IR analysis has enabled to obtain the % transmittance (%T) at the Er:YAG laser wavelength ( $3401.36\text{ cm}^{-1}$ ) for each varnish selected for this research. As a rule, a value of 0% transmittance indicates that the coating has absorbed all of the radiation. The same spectrometer bench, this time equipped with the integrated sphere, enabled to acquire the % Reflectance at the laser wavelength. Both the %T and %R data are summarised in Table 4.3 and the spectra are presented in Appendix B.

Based on the %T and the thickness of the varnish films, the Eq. 4.9 was used to calculate the absorption coefficient mathematically. Part of the irradiated beam was possibly dissipated within the glass-resin interface. This is implied by the %T and %R data, as presented in table 4.3.1. The same table shows the values calculated for the absorption coefficients ( $\alpha$ ) and the optical penetration depths ( $\delta$ ) of all the films at the investigated wavelength. As reported by Ciofini (2014, p. 114), the optical penetration depths thus obtained may not be considered the same as the ones measured through the varnish layer upon laser irradiation (non-linear condition). Nonetheless, these data can be used as a good approximation for the estimation of the heating distribution on the coatings upon Er:YAG laser irradiation. Thus, for the thicknesses of the films studied, it is possible to observe that dammar, Ketone N and MS2A films absorb at the Er:YAG laser wavelength. However, because Paraloid B67 does not have O-H groups in its chemical structure (see Figure 3.2), the coating presents a mathematically calculated optical penetration depth ( $\delta$ ) superior to the thickness of the whole varnish film. This condition results in the Er:YAG laser radiation passing through the coating film and interacting with the underlying layer. All observations indicate that the PiBMA Paraloid B67 does not interact with the Er:YAG laser, as already discussed by (Striova *et al.*, 2011a). The data provided in Table 4.3 show an optical penetration depth ( $\delta$ ) of the Paraloid B67 film that is almost ten times larger than that of dammar, Ketone N and MS2A varnishes. Considering both 0% R and 90.2% T data, an interaction with the glass substrate of the Paraloid B67 sample must be taken into account. This would leave a minimal % of absorbance, which would dissipate within the PiBMA film.

Table 4.3 – % reflection, % transmission, absorption coefficient ( $\alpha$ ) and optical penetration depth ( $\delta$ ) required to define the thermal modelling of varnish films.

Product	%R <sub>mean</sub> ± $\sigma$	%T <sub>mean</sub> ± $\sigma$	Absorption Coefficient ( $\alpha$ ) (cm <sup>-1</sup> )	Optical penetration depth ( $\mu$ m)
Dammar	15.14 ± 0.6	8.39 ± 2.3	301.07	33.21
Ketone N	14.06 ± 4.1*	1.94 ± 1.4	1396.10	7.16
MS2A	15.45 ± 0.1*	4.46 ± 1.1	528.65	18.92
Paraloid B67	0 ± 0	90.19 ± 0.6	20.12	497.14

The reflectance spectra for MS2A and Ketone N, however, showed to be unsuitable to obtaining the %R values since the signals for both the coated films at the laser wavelength were saturated. This is due to the fact that in mid-IR, diffuse reflectance is very weak (Khoshhesab, 2012). From the spectral line shapes presented in Appendix B, it can be assumed that the possible %R values for both coatings are smaller than the ones showed in the Table 4.3.

Therefore, the reflectance parameters for those resins have been obtained using the Fresnel equations (Lvovsky, 2013). As reported by Berns and de la Rie (2003c), the reflection of a light incident on a surface depends on the angle of illumination. In this case, assuming there is perfectly smooth surface for both the coatings, the specular reflectance at normal incidence was estimated by using the following equation (Brown and Arnold, 2010; Hebert, 2013):

$$R = \left( \frac{n_t - n_i}{n_t + n_i} \right)^2 \quad (\text{Eq. 4.21})$$

where  $n_i$  is the refractive index of air (= 1.003) at the Er:YAG laser wavelength (Mathar, 2007), and  $n_t$  is the refractive indices of the resins. Berns and de la Rie (2003c) reported in their studies a refractive index of 1.529 for the Ketone N resin and 1.518 for MS2A, respectively. Saito *et al.* (1995) investigated the properties of polymers in the mid-infrared, highlighting the fact that in the mid-infrared region the changing in the refractive index of polymers is only of the order of  $10^{-2}$  (Wang *et al.*, 1998). Therefore, the changing in the refractive indices at the laser wavelength has been considered negligible if compared to the ones presented in literature and thus, they were used to re-calculate the %R for Ketone N and MS2A (Table 4.4).

Table 4.4 – % reflection obtained using the Fresnel eq. (Eq. 4.21).

Product	%R
Ketone N	4.32
MS2A	4.17

#### 4.3.2 *Transmission study*

In this section laser-material interaction will be studied on the basis of laser-induced transmission through the coatings applied on glass slides because the principal aim for successful laser cleaning is the protection of the underlying layers.

Single laser pulses were delivered to different areas on the varnished surfaces to avoid cumulative desiccation.

First, the incident laser beam energy ( $E_{inc}$ ) was measured directly at the front of the laser handpiece with a pyroelectric detector. The recordings are presented in table 4.5. The laser irradiation tests were performed in fluences, as shown in the laser unit display.

Table 4.5 – The Er:YAG laser energy ( $E_{inc}$ ) measured using the QE25ELP-H-MB-DO Pyroelectric Detector for each fluence employed for this study.

Fluence ( $J/cm^2$ )	0.5	1	1.5	2	2.4
Laser Energy Measured ( $E_{inc}$ ) (mJ)	61	126.9	195.3	262.9	299.3

Therefore, the % transmission of the uncoated glass slide was calculated. The laser light transmittance data on a glass slide are shown in Table 4.6.

Table 4.6 – % Transmission (%T) of an uncoated glass slide for each fluence employed for this study.

Fluence ( $J/cm^2$ )	0.5	1	1.5	2	2.4
Glass transmission (%T)	79.7	77.3	76.2	76.2	76.5

The transmitted energy of laser light passing through the uncoated glass slide ( $E_{transglass}$ ) did not overlap with the average energy acquired by the laser beam passing through the varnish film ( $E_{trans}$ ), due to partial dissipation caused by reflections and scattering. The transmitted energy passing through the uncoated glass slide has been taken into account for the determination of the calculated transmission for each fabricated film. All fluences, as derived from the recorded  $E_{inc}$  (Table 4.5) and the spot area, are consistent with the readings in the laser unit display except for reading at 2  $J/cm^2$  that generated a measured fluence of 2.1  $J/cm^2$ .

It is important to point out that the Er:YAG laser wavelength (2940 nm) is in the transmission range of various compounds commonly present on the surfaces of art objects, and varnishes are highly transmissive materials because they are considered as semi-transparent materials (Siano *et al.*, 2012; Ciofini, 2014).

Prior to the experiment, the thickness of the films was determined (Chapter 3, section 3.5.1). Based on the assumption that Beer's law gives the transmission signal as  $T_L = \exp(-\alpha d)$ , where  $\alpha$  is the absorption coefficient and  $d$  is the varnish film thickness (Pettit *et al.*, 1994), and considering the different thicknesses of the varnishes obtained after the curing of the wet coatings onto the glass slides, the transmission study herein has been focused exclusively on the first transmission signal received by the pyroelectric detector. The transmitted energies ( $E_{\text{trans}}$ ) were acquired upon the release of a single Er:YAG laser pulse onto the aged varnish films and  $E_{\text{trans}}$  in Figure 4.20 is plotted as a function of laser fluence. In contrast to laser transmission observations using UV-pulsed (excimer) lasers, where transmission signals were recorded after several pulses delivered on the same varnish areas (Theodorakopoulos, 2005, p. 210),  $E_{\text{trans}}$  is herein recorded from the first pulse for all the tested varnishes. This is expected due to the weaker absorption of the 2940 nm photons of the Er:YAG lasers from the organic resin compounds when compared to the much stronger absorption of the UV laser photons of similar varnishes (Theodorakopoulos, 2005, p. 210).

As demonstrated in Figure 4.20, the  $E_{\text{trans}}$  readings of the dry and the DI-W+TW20 pre-wetted irradiated varnish surfaces highlight an almost comparable evolution, which show an increasing transmission with increasing laser pulse fluences. The dammar film has shown to have the highest  $E_{\text{trans}}$  values both in dry and pre-wet surfaces with DI-W+TW20, in VSP and SP modes. However, the dry Ketone N presents the lowest  $E_{\text{trans}}$  values in VSP and SP modes. This makes the use of Er:YAG laser safer in the presence of a Ketone N even without pre-wetting the surface (Figure 4.20).  $E_{\text{trans}}$  trends decrease when surfaces are prewetted of all the varnishes tested. In this case, Ketone N and MS2A have similar trends with comparable  $E_{\text{trans}}$ , although, in SP mode, the MS2A presents the lowest transmitted energies. Both the synthetic varnishes absorb most of the laser beam energy, thereby lowering the amount of energy interacting with the underlying paint layer.

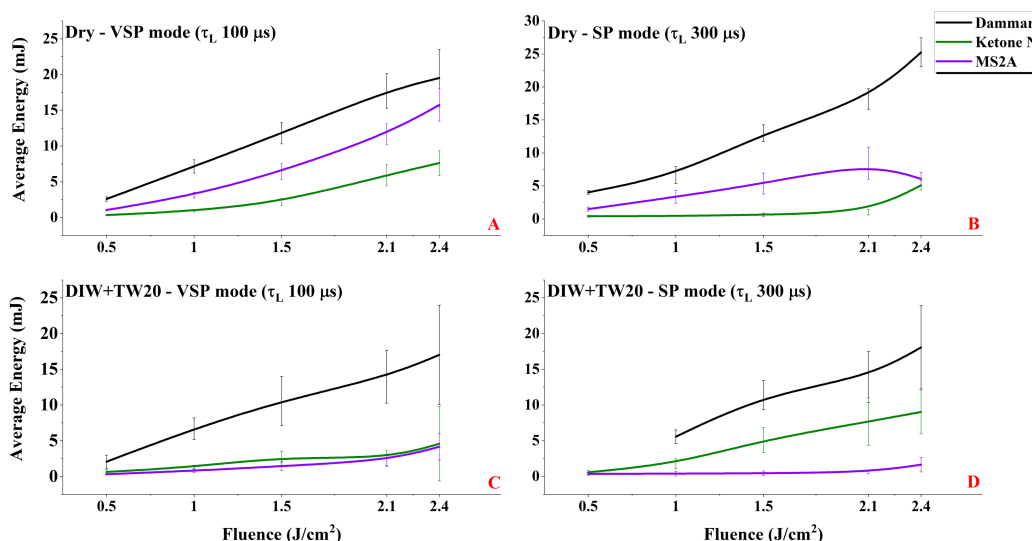


Figure 4.20 – The average single-pulse laser transmitted energies ( $E_{trans}$ ) as a function of fluence.  $E_{trans}$  values were experimentally measured by placing a Pyroelectric Detector behind the dry and pre-wetted varnishes.

This is also demonstrated in Figure 4.21, which shows the dependence of transmission,  $E_{trans}/E_{inc}$ , on fluence in VSP and SP modes.

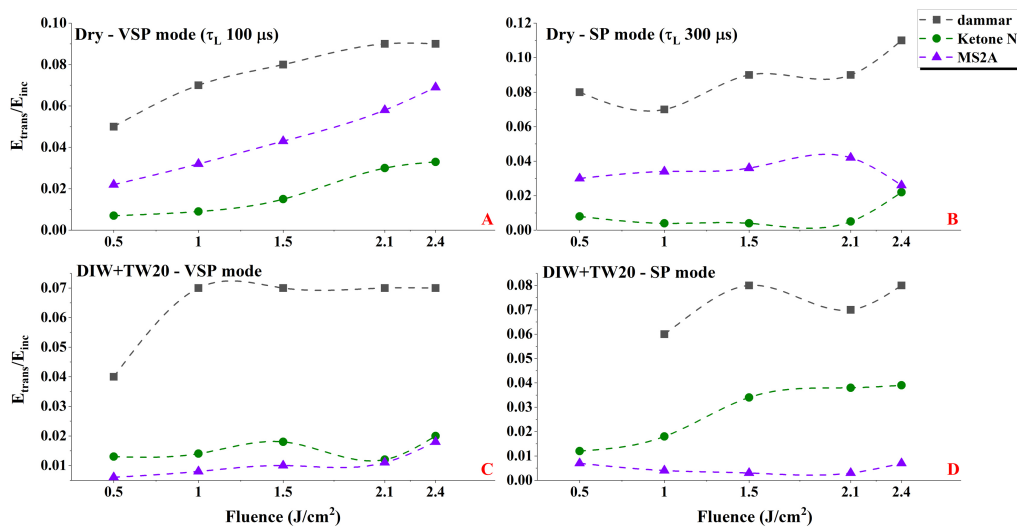


Figure 4.21 –  $E_{trans}/E_{inc}$  versus the chosen range of fluences in VSP and SP modes upon a single laser pulse for dammar, Ketone N and MS2A.

Tables 4.7-10 summarise the calculated % transmission (%T) for each varnish upon a single laser pulse for the chosen range of fluences. The % transmission data acquired herein using the pyroelectric detector at fluences between 1.5 and 2.1 J/cm² can be compared to the FTIR transmission data (Table 4.3).

In all, it is observed that the transmitted laser energy increases with fluence. Transmission of the laser wavelength throughout the coatings is in fact highly

dependent on the degree of absorption of the laser wavelength and the degree of electronic excitations in the irradiated surface (Luk'yanchuk *et al.*, 1993).

The %T values through the dry dammar surface are slightly higher than the one acquired from the DI-W+TW20 pre-wetted surface (Table 4.7). This difference is particularly accentuated for the MS2A with a %T decrease using DI-W+TW20 of about 75% transmission in VSP mode and 84% transmission in SP mode (Table 4.9). For both dammar and MS2A, the application of DI-W+TW20 results in reduced beam penetration into the coatings. On the other hands, in the case of pre-wetting the Ketone N surface, the %T values increase compared to the same transmission data acquired for the dry irradiated areas. In order to explain this inconsistency, the Ketone N and MS2A solubility properties were compared. The polymer solubility charts published by Horie (2010, p. 379) were used, but no differences were found between the solubility properties of Ketone N and MS2A. Further investigation is required to correlate the detected increase in %T values prewetting the Ketone N surface. Nonetheless, this difference in %T could be connected to a modification to the varnish film's optical properties combined with the application of the wetting agent and the thickness of the Ketone N varnish which is thinner than that of the other ones.

Based on the information supplied by the data in Tables 4.7-9, it is possible to observe when used dry, dammar film has the highest calculated %T value (by subtracting the %T glass component) of 11.03 in SP mode, at the highest fluence of 2.4 J/cm<sup>2</sup>.

Table 4.7 – The transmission profile of the **dammar film** for a single-pulse laser has been determined by using the % transmission (%T) as a function of the fluence employed in this study.

<b>Dammar</b>		
<b>Fluence (J/cm<sup>2</sup>)</b>	<b>%T in VSP mode – Dry</b>	<b>%T in SP mode – Dry</b>
<b>0.5</b>	5.3	8.3
<b>1</b>	7.3	6.7
<b>1.5</b>	7.9	8.7
<b>2.1</b>	8.8	9.1
<b>2.4</b>	8.5	11
	<b>%T in VSP mode – DI-W+TW20</b>	<b>%T in SP mode – DI-W+TW20</b>
<b>0.5</b>	4.2	---
<b>1</b>	6.8	5.7
<b>1.5</b>	7.1	7.6
<b>2.1</b>	7	6.9
<b>2.4</b>	7.4	7.9

Table 4.8 – The transmission profile of the **Ketone N film** for a single-pulse laser has been determined by using the % transmission (%T) as a function of the fluence employed in this study.

<b>Ketone N</b>		
<b>Fluence (J/cm<sup>2</sup>)</b>	<b>%T in VSP mode – Dry</b>	<b>%T in SP mode – Dry</b>
<b>0.5</b>	0.7	0.8
<b>1</b>	0.9	0.4
<b>1.5</b>	1.5	0.4
<b>2.1</b>	2.9	0.5
<b>2.4</b>	3.3	2.2
	<b>%T in VSP mode – DI-W+TW20</b>	<b>%T in SP mode – DI-W+TW20</b>
<b>0.5</b>	1.3	1.2
<b>1</b>	1.4	1.8
<b>1.5</b>	1.8	3.4
<b>2.1</b>	1.2	3.8
<b>2.4</b>	2	3.9

Table 4.9 – The transmission profile of the **MS2A film** for a single-pulse laser has been determined by using the % transmission (%T) as a function of the fluence employed in this study.

<b>MS2A</b>		
<b>Fluence (J/cm<sup>2</sup>)</b>	<b>%T in VSP mode – Dry</b>	<b>%T in SP mode – Dry</b>
<b>0.5</b>	2.2	3.1
<b>1</b>	3.2	3.4
<b>1.5</b>	4.3	3.6
<b>2.1</b>	5.7	4.1
<b>2.4</b>	6.7	2.6
	<b>%T in VSP mode – DI-W+TW20</b>	<b>%T in SP mode – DI-W+TW20</b>
<b>0.5</b>	0.7	0.7
<b>1</b>	0.8	0.4
<b>1.5</b>	1	0.3
<b>2.1</b>	1.1	0.3
<b>2.4</b>	1.8	0.7

The % transmission data of the dry irradiated Paraloid B67 surface verified once more that the coating is almost transparent at the Er:YAG laser’s wavelength (Table 4.10). The calculated %T value of the dry irradiated surface is 86% in VSP mode at 0.5 J/cm<sup>2</sup>, decreasing to 40.2% when the varnish was prewetted.

Table 4.10 – The transmission profile of the **Paraloid B67 film** for a single-pulse laser has been determined by using the % transmission (%T) as a function of the fluence employed in this study.

<b>Paraloid B67</b>		
<b>Fluence (J/cm<sup>2</sup>)</b>	<b>%T in VSP mode – Dry</b>	<b>%T in VSP mode – DI-W+TW20</b>
<b>0.5</b>	87.13	40.18
<b>1</b>	86.67	
<b>1.5</b>	85.55	
<b>2.1</b>	85.33	72.93
<b>2.4</b>	85.52	

The differences in the  $E_{trans}$  and the varying %T values (Figure 4.20-21 and Tables 4.7-10) could be related to the photothermal effects at the surface and in the bulk upon Er:YAG laser irradiation. The trends of the transmission data increase with fluence values (Chillè *et al.*, 2020), as the laser irradiated films are thinned and disrupted. As reported by Colombini *et al.* (2003), the disruption of the films, during the Er:YAG laser irradiation, is related to steam distillation, sublimation, explosion and mechanical stress (see section 4.1.3.1). In contrast to the excimer laser (Pettit *et al.*, 1994; Castillejo *et al.*, 2002, 2003; Zafiropulos, 2002; Theodorakopoulos, 2005; Fotakis *et al.*, 2006), the underlying layers coated with these varnishes may be at risks as the absorbance is not enough to reduce the transmittance, causing an increase in  $E_{trans}$  and %T as a function of fluence. The Er:YAG laser interaction with these underlying layer(s) is beyond the scope of this study.

### 4.3.3 Heat distribution on the coatings upon laser irradiation

#### 4.3.3.1 Thermal camera recordings

Tables 4.11-14 show the Average Max Temperature Variations recorded by the FLIR 620bx thermal camera on the dry and pre-wet surface of the aged varnishes (as shown in Figures 4.11-12) and the average maximum temperatures ( $\Delta T_{\text{mean}}$ ) at the fluences tested in VSP ( $\approx 100 \mu\text{s}$ ) and SP ( $\approx 300 \mu\text{s}$ ) modes.

The data show that  $\Delta T_{\text{mean}}$  are dependent on fluence and that DI-W+TW20 wetting has increased the heat impact.

The 30 Hz of the thermal camera speed of acquisition and the 7 - 12 ms of the thermal constant of the microbolometer detector seem insufficient to accurately record the true-time maximum peak temperature on the irradiated varnishes occurring at much higher pulse durations ( $\tau_L \approx 100$  and  $300 \mu\text{s}$ ) of the Er:YAG laser. Moreover, the internal temperature range settings in the IR camera (between  $-40 \text{ }^\circ\text{C}$  to  $160 \text{ }^\circ\text{C}$ ) did not allow to record temperature higher than  $160 \text{ }^\circ\text{C}$ . When this borderline temperature was reached, the data recorded were kept among the other ones, and the average data were reported in the tables highlighted in **bold**.

The highest  $\Delta T_{\text{mean}}$  has been recorded on dry and pre-wet Ketone N (Table 4.12). The highest readings of the Ketone N  $\Delta T_{\text{mean}}$  values may be related to a relatively higher absorption coefficients ( $\alpha$ ) value compared to the other coatings (Table 4.3). However, the lowest  $\Delta T_{\text{mean}}$  has been recorded on dry and pre-wet Paraloid B67 (Table 4.14). This result may be due to the lack of hydroxyl groups in Paraloid B67 (isobutyl methacrylate), showing that almost all the laser light radiation passes through the varnish film and interacts with the underlying layer.

The recordings at fluences over  $2 \text{ J/cm}^2$  have shown that there is a plateau in the heat recorded measurements (highlighted in the Tables with a \*), which requires further investigation. Nevertheless, the thermal camera enabled to demonstrate that by increasing the fluence the average temperatures were also increased.

For the same fluence ranges, higher temperatures were in general recorded in the presence of water rather than when the films were irradiated in dry conditions. This can be explained by the higher absorption of the incident laser energy in the

water film and the rapid evaporation of the liquid, resulting in a higher temperature recorded by the thermal camera.

Although the live-recorded temperatures cannot provide accurate maximum peak temperature data and could have been more accurate with a faster thermal camera, the data are, nonetheless, representative of the interaction of the varnish films with the 2940 nm laser (Chillé *et al.*, 2020).

Table 4.11 – Maximum effect of temperature variation recorded by using the FLIR thermal camera and the mean maximum heat impact ( $\Delta T_{\text{mean}}$ ) on dry and pre-wet **dammar varnish**, according to Eq. 4.11. In **bold** are highlighted the temperature at which the thermal camera reached its maximum acquisition temperature value (160 °C) and the \* indicates a plateau in the heat measurements. The beam was delivered perpendicularly to the varnish surface with a 20 cm working distance, emissivity ( $\epsilon$ ) of the varnish of 0.93 and laser  $\varnothing$  of 3 mm.

<b>Dammar</b>					
<b>Dry - VSP</b>			<b>Dry - SP</b>		
Fluence (J/cm <sup>2</sup> )	Average max temperature variation recorded $\pm \sigma$ (°C)	$\Delta T_{\text{mean}} \pm \sigma$ (°C)	Fluence (J/cm <sup>2</sup> )	Average max temperature variation recorded $\pm \sigma$ (°C)	$\Delta T_{\text{mean}} \pm \sigma$ (°C)
<b>0.6</b>	30 $\pm$ 1.3	5.9 $\pm$ 1.4	<b>0.6</b>	29.1 $\pm$ 1.0	6.2 $\pm$ 1
<b>1</b>	36.9 $\pm$ 1.8	12.7 $\pm$ 1.8	<b>1</b>	34.4 $\pm$ 1.5	11.3 $\pm$ 1.4
<b>1.6</b>	43.3 $\pm$ 1.4	18.9 $\pm$ 1.5	<b>1.6</b>	41.2 $\pm$ 2.6	17.6 $\pm$ 2.6
<b>2</b>	46.5 $\pm$ 2.5	21.6 $\pm$ 2.4*	<b>2</b>	44.1 $\pm$ 3.9	20.6 $\pm$ 3.6
<b>2.4</b>	43.5 $\pm$ 0.4	18.8 $\pm$ 0.2	<b>2.4</b>	50.1 $\pm$ 4.9	26.1 $\pm$ 4.9
<b>DI-W + TW20 - VSP</b>			<b>DI-W + TW20 - SP</b>		
<b>0.6</b>	47.2 $\pm$ 5.8	27.4 $\pm$ 5.5	<b>0.6</b>	39.5 $\pm$ 1.6	16 $\pm$ 1.6
<b>1</b>	71 $\pm$ 15.1	50.0 $\pm$ 15.4	<b>1</b>	44 $\pm$ 4.5	20.9 $\pm$ 4.6
<b>1.6</b>	71.5 $\pm$ 16.4	50.2 $\pm$ 16.4	<b>1.6</b>	70 $\pm$ 15.4	46.8 $\pm$ 15.6
<b>2</b>	91.7 $\pm$ 35.3	70.8 $\pm$ 35.7	<b>2</b>	97.5 $\pm$ 19.8	74.1 $\pm$ 19.3
<b>2.4</b>	<b>96.0 <math>\pm</math> 32.4</b>	<b>77 <math>\pm</math> 32.4</b>	<b>2.4</b>	142.9 $\pm$ 10.8	120.3 $\pm$ 10.2

Table 4.12 – Maximum effect of temperature variation recorded by using the FLIR thermal camera and the mean maximum heat impact ( $\Delta T_{\text{mean}}$ ) on dry and pre-wet **Ketone N varnish**, according to Eq. 4.11. In **bold** are highlighted the temperature at which the thermal camera reached its maximum acquisition temperature value (160 °C) and the \* indicates a plateau in the heat measurements. The beam was delivered perpendicularly to the varnish surface with a 20 cm working distance, emissivity ( $\epsilon$ ) of the varnish of 0.93 and laser  $\varnothing$  of 3 mm.

<b>Ketone N</b>					
<b>Dry - VSP</b>			<b>Dry - SP</b>		
Fluence (J/cm <sup>2</sup> )	Average max temperature variation recorded $\pm \sigma$ (°C)	$\Delta T_{\text{mean}} \pm \sigma$ (°C)	Fluence (J/cm <sup>2</sup> )	Average max temperature variation recorded $\pm \sigma$ (°C)	$\Delta T_{\text{mean}} \pm \sigma$ (°C)
<b>0.6</b>	65.4 $\pm$ 5.1	44.3 $\pm$ 5.1	<b>0.6</b>	68 $\pm$ 4	46.1 $\pm$ 4
<b>1</b>	96.1 $\pm$ 12.4	75.2 $\pm$ 12.4	<b>1</b>	92.2 $\pm$ 15.3	70.4 $\pm$ 15.3
<b>1.6</b>	140 $\pm$ 10.5	119 $\pm$ 10.5	<b>1.6</b>	126.7 $\pm$ 20	105.3 $\pm$ 20
<b>2</b>	<b>146.2 <math>\pm</math> 13.6</b>	<b>125.3 <math>\pm</math> 13.5*</b>	<b>2</b>	<b>131 <math>\pm</math> 22.6</b>	<b>110.3 <math>\pm</math> 22.6</b>
<b>2.4</b>	<b>131.8 <math>\pm</math> 16.9</b>	<b>112.3 <math>\pm</math> 16.3</b>	<b>2.4</b>	<b>144.1 <math>\pm</math> 21.1</b>	<b>121.6 <math>\pm</math> 20</b>
<b>DI-W + TW20 - VSP</b>			<b>DI-W + TW20 - SP</b>		
<b>0.6</b>	35.2 $\pm$ 3.6	13.1 $\pm$ 3.8	<b>0.6</b>	30.8 $\pm$ 1.5	10.4 $\pm$ 1.8
<b>1</b>	43.8 $\pm$ 9.3	21.2 $\pm$ 9.3	<b>1</b>	68.2 $\pm$ 19.4	47.1 $\pm$ 19.3
<b>1.6</b>	83.2 $\pm$ 20.2	60.2 $\pm$ 20.5	<b>1.6</b>	88.5 $\pm$ 26.2	67.2 $\pm$ 26.1
<b>2</b>	80.6 $\pm$ 30.2	57.9 $\pm$ 24.4	<b>2</b>	<b>106.9 <math>\pm</math> 33.1</b>	<b>85.5 <math>\pm</math> 33.1*</b>
<b>2.4</b>	<b>115.3 <math>\pm</math> 41.4</b>	<b>92.6 <math>\pm</math> 41.4</b>	<b>2.4</b>	<b>99.9 <math>\pm</math> 42.8</b>	<b>78.2 <math>\pm</math> 42.5</b>

Table 4.13 – Maximum effect of temperature variation recorded by using the FLIR thermal camera and the mean maximum heat impact ( $\Delta T_{\text{mean}}$ ) on dry and pre-wet **MS2A varnish**, according to Eq. 4.11. In **bold** are highlighted the temperature at which the thermal camera reached its maximum acquisition temperature value (160 °C). The beam was delivered perpendicularly to the varnish surface with a 20 cm working distance, emissivity ( $\epsilon$ ) of the varnish of 0.93 and laser  $\varnothing$  of 3 mm.

<b>MS2A</b>					
<b>Dry - VSP</b>			<b>Dry - SP</b>		
Fluence (J/cm <sup>2</sup> )	Average max temperature variation recorded $\pm \sigma$ (°C)	$\Delta T_{\text{mean}} \pm \sigma$ (°C)	Fluence (J/cm <sup>2</sup> )	Average max temperature variation recorded $\pm \sigma$ (°C)	$\Delta T_{\text{mean}} \pm \sigma$ (°C)
<b>0.6</b>	28.7 $\pm$ 1.1	6.3 $\pm$ 0.9	<b>0.6</b>	26.7 $\pm$ 0.8	6.1 $\pm$ 0.6
<b>1</b>	33 $\pm$ 1.3	10.6 $\pm$ 1.3	<b>1</b>	33.5 $\pm$ 1.8	12.1 $\pm$ 1.6
<b>1.6</b>	40.7 $\pm$ 2.8	17.7 $\pm$ 2.8	<b>1.6</b>	43.8 $\pm$ 2.1	22.6 $\pm$ 3.4
<b>2</b>	46.7 $\pm$ 2.8	23.5 $\pm$ 2.8	<b>2</b>	47.7 $\pm$ 2	26 $\pm$ 2.4
<b>2.4</b>	53.4 $\pm$ 1.1	30.2 $\pm$ 1	<b>2.4</b>	49.4 $\pm$ 4.8	27 $\pm$ 4.7
<b>DI-W + TW20 - VSP</b>			<b>DI-W + TW20 - SP</b>		
<b>0.6</b>	41.7 $\pm$ 6.7	22.1 $\pm$ 6.5	<b>0.6</b>	35.6 $\pm$ 3.7	16.3 $\pm$ 3.9
<b>1</b>	64.3 $\pm$ 16.3	43.9 $\pm$ 16.4	<b>1</b>	38.6 $\pm$ 6.7	18.9 $\pm$ 6.6
<b>1.6</b>	85.9 $\pm$ 33	65.8 $\pm$ 33.2	<b>1.6</b>	40.6 $\pm$ 2.3	21.3 $\pm$ 2.3
<b>2</b>	<b>103.8 <math>\pm</math> 40.2</b>	<b>84 <math>\pm</math> 40.4</b>	<b>2</b>	<b>80 <math>\pm</math> 46.1</b>	<b>60.6 <math>\pm</math> 46.2</b>
<b>2.4</b>	<b>139.8 <math>\pm</math> 35.4</b>	<b>120.2 <math>\pm</math> 35.8</b>	<b>2.4</b>	<b>105 <math>\pm</math> 44.9</b>	<b>85.5 <math>\pm</math> 45</b>

Table 4.14 – Maximum effect of temperature variation recorded by using the FLIR thermal camera and the mean maximum heat impact ( $\Delta T_{\text{mean}}$ ) on dry and pre-wet **Paraloid B67 varnish**, according to Eq. 4.11. The \* indicates a plateau in the heat measurements. The beam was delivered perpendicularly to the varnish surface with a 20 cm working distance, emissivity ( $\epsilon$ ) of the varnish of 0.93 and laser  $\varnothing$  of 3 mm.

<b>Paraloid B67</b>					
<b>Dry - VSP</b>			<b>Dry - SP</b>		
<b>Fluence (J/cm<sup>2</sup>)</b>	<b>Average max temperature variation recorded <math>\pm \sigma</math> (°C)</b>	<b><math>\Delta T_{\text{mean}} \pm \sigma</math> (°C)</b>	<b>Fluence (J/cm<sup>2</sup>)</b>	<b>Average max temperature variation recorded <math>\pm \sigma</math> (°C)</b>	<b><math>\Delta T_{\text{mean}} \pm \sigma</math> (°C)</b>
<b>0.6</b>	22.6 $\pm$ 0.7	3.3 $\pm$ 0.8	<b>0.6</b>	22.3 $\pm$ 0.9	3.5 $\pm$ 0.7
<b>1</b>	24.6 $\pm$ 0.4	5.1 $\pm$ 0.4	<b>1</b>	25.8 $\pm$ 0.9	6.9 $\pm$ 0.9
<b>1.6</b>	27.9 $\pm$ 0.6	8.3 $\pm$ 0.8	<b>1.6</b>	29.5 $\pm$ 1.6	10.4 $\pm$ 1.6
<b>2</b>	33.1 $\pm$ 4.1	14 $\pm$ 4.2	<b>2</b>	32.6 $\pm$ 1.4	13.6 $\pm$ 1.3
<b>2.4</b>	40.1 $\pm$ 3	21 $\pm$ 3	<b>2.4</b>	35.6 $\pm$ 2.3	16.5 $\pm$ 2.3
<b>DI-W + TW20 - VSP</b>			<b>DI-W + TW20 - SP</b>		
<b>0.6</b>	31.4 $\pm$ 1.8	9.2 $\pm$ 1.9	<b>0.6</b>	35.5 $\pm$ 3.4	14.6 $\pm$ 2.7
<b>1</b>	35.8 $\pm$ 2.5	13.2 $\pm$ 2.3	<b>1</b>	38.4 $\pm$ 4.4	16.6 $\pm$ 4.7
<b>1.6</b>	40.2 $\pm$ 1.9	18.0 $\pm$ 1.6	<b>1.6</b>	39.5 $\pm$ 3.5	17.3 $\pm$ 3.4
<b>2</b>	41.5 $\pm$ 3.2	19.8 $\pm$ 3.3*	<b>2</b>	41.7 $\pm$ 3.4	18.8 $\pm$ 3.4
<b>2.4</b>	39.1 $\pm$ 2.5	17 $\pm$ 2.4	<b>2.4</b>	44 $\pm$ 2.8	21.3 $\pm$ 3

Because of these experimental limitations, the heat distribution inside the irradiated coatings were determined mathematically and with a 2D simulation model.

### 4.3.3.2 Heat distribution modelling

To estimate the maximum surface heating obtained inside each class of resins upon a Er:YAG laser irradiation, the thermal diffusion length ( $l_{th}$ ), at different laser pulse duration and using the published thermal diffusivity values (D) (Fotakis *et al.*, 2006, p. 36), has been calculated by using the Eq. 4.12 (Figure 4.22).

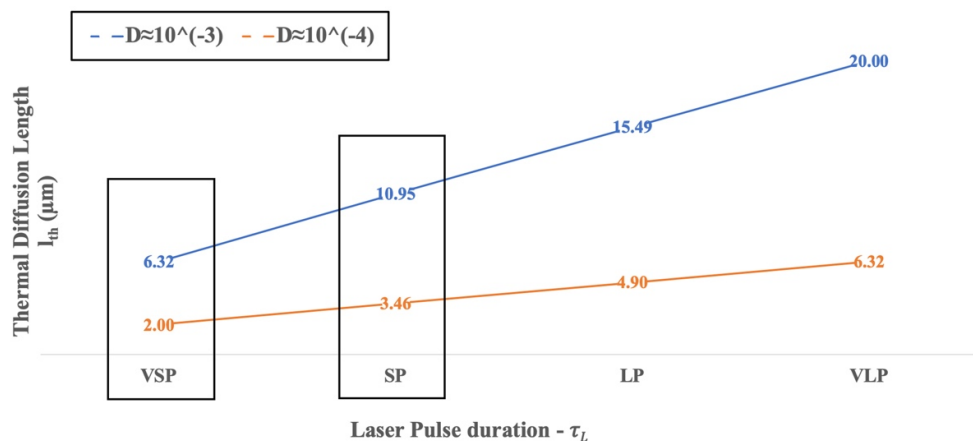


Figure 4.22 – The dependence of the thermal diffusion length ( $l_{th}$ ) of the varnishes as a function of laser pulse duration  $\tau_L$  for the Fotona Fidelis<sup>XS</sup> Er:YAG laser. VSP mode:  $\tau_L \approx 100 \mu\text{s}$ ; SP mode:  $\tau_L \approx 300 \mu\text{s}$ ; LP mode  $\tau_L \approx 600 \mu\text{s}$ ; VLP mode  $\tau_L \approx 1000 \mu\text{s}$ .

The range of thermal diffusivity (D) provided by Fotakis *et al.* (2007, p. 36) for organics substrate, ranges from  $10^{-3}$  to  $10^{-4} \text{ cm}^2/\text{sec}$ , and is herein used for the mathematical calculation and the simulations, to allow the author to calculate the thermal conductivity (k) of each varnish (Table 4.15).

Table 4.15 – Thermal conductivity (k) varnishes

Product	Thermal Conductivity (k)	
	(W/m·K)	
	$D \approx 10^{-3}$	$D \approx 10^{-4}$
Dammar	0.21	0.021
Ketone N	0.22	0.022
MS2A	0.19	0.019

Even though this range appears too broad, considering the thermal conductivity of atmosphere (gas) as  $0.026 \text{ W/m}\cdot\text{K}$  (Çengel, Ghajar and Kanoglu, 2014, p. 924) and therefore of the same order of magnitude as the thermal conductivity obtained from  $D \approx 10^{-4} \text{ cm}^2/\text{sec}$ ; these data were kept in the numerical computation (sections 4.3.3.2.1 and 4.3.3.2.2) and in the simulations (section 4.3.3.2.3) to provide evidence for the response of these coating upon the Er:YAG laser irradiation.

For this research, only the two laser pulse durations ( $\tau_L \approx 100$  and  $300 \mu\text{s}$ ) were employed because they are considered to be the most suitable laser pulse durations working on varnishes surfaces as evidenced in literature (De Cruz, Wolbarsht and Hauger, 2000a, 2000b; Bracco *et al.*, 2003; Andreotti *et al.*, 2007, 2016; Striova *et al.*, 2011a, 2015; Lopez *et al.*, 2019; Brunetto, Bono and Frezzato, 2020).

#### 4.3.3.2.1 Computation of the temperature rise

Dammar, Ketone N and MS2A cannot be considered high infrared absorber materials (Siano *et al.*, 2012; Ciofini, 2014). A rough estimation of the temperature distribution ( $\Delta T$ ) presented in this section, mathematically obtained using Eq. 4.13, could be considered as indicative values of the heat distribution attained at  $z = l_{th}$ . In this case the thermal diffusion length ( $l_{th}$ ), which can be considered as a measure of how far the energy spreads inside the material during the laser irradiation, was used in order to estimate the temperature changes involved upon a single Er:YAG laser pulse irradiation (see Tables 4.16-19). These results can be explained by the simplification of the multidimensional heat conduction system analysed using Eq. 4.13 and the boundary conditions which were not taken into account in this calculation. As reported by Brown and Arnold (2010), following this initial interaction, further thermal propagation can lead to an increase in temperatures at distances beyond this length.

Ketone N varnish film returns the highest  $\Delta T$  values (Table 4.17) with estimated temperatures in VSP mode ( $\tau_L \approx 100 \mu\text{s}$ ) between  $132 \text{ }^\circ\text{C}$  (for  $D \approx 10^{-3} \text{ cm}^2/\text{sec}$ ) and  $242 \text{ }^\circ\text{C}$  (for  $D \approx 10^{-4} \text{ cm}^2/\text{sec}$ ) at the minimum fluence of  $0.5 \text{ J}/\text{cm}^2$ , and between  $663 \text{ }^\circ\text{C}$  and  $1212 \text{ }^\circ\text{C}$  at the maximum fluence of  $2.5 \text{ J}/\text{cm}^2$ . The  $\Delta T$  values in SP mode ( $\tau_L \approx 300 \mu\text{s}$ ) range between  $69 \text{ }^\circ\text{C}$  and  $198 \text{ }^\circ\text{C}$  at  $0.5 \text{ J}/\text{cm}^2$  and between  $347 \text{ }^\circ\text{C}$  and  $988 \text{ }^\circ\text{C}$  at  $2.5 \text{ J}/\text{cm}^2$ .

Comparing the thermal data, it is possible to observe that the lowest  $\Delta T$  values have been obtained with the dammar film (Table 4.16) with estimated temperatures in VSP mode between  $60 \text{ }^\circ\text{C}$  (for  $D \approx 10^{-3} \text{ cm}^2/\text{sec}$ ) and  $69 \text{ }^\circ\text{C}$  (for  $D \approx 10^{-4} \text{ cm}^2/\text{sec}$ ) at  $0.5 \text{ J}/\text{cm}^2$ , and between  $302 \text{ }^\circ\text{C}$  and  $344 \text{ }^\circ\text{C}$  at  $2.5 \text{ J}/\text{cm}^2$ . The same

mathematical calculation carried out in SP mode has returned  $\Delta T$  values between 52 °C and 66 °C at 0.5 J/cm<sup>2</sup> and between 263 °C and 329 °C at 2.5 J/cm<sup>2</sup>.

Table 4.16 – Estimated temperature ( $z = l_{th}$ ) using Eq. 4.13 of the heat distribution inside the **dammar layer** following an Er:YAG laser pulse at VSP ( $\tau_L \approx 100 \mu s$ ) and SP ( $\tau_L \approx 300 \mu s$ ) modes.

<b>Dammar</b>					
VSP Mode	Fluence (J/cm <sup>2</sup> )	$\Delta T$ (°C)		Fluence (J/cm <sup>2</sup> )	$\Delta T$ (°C)
D 10 <sup>-3</sup>	0.5	60	D 10 <sup>-4</sup>	0.5	69
	0.6	72		0.6	82
	1	121		1	138
	1.5	181		1.5	206
	2.1	279		2.1	314
	2.4	290		2.4	330
	2.5	302		2.5	344
SP Mode	Fluence (J/cm <sup>2</sup> )	$\Delta T$ (°C)		Fluence (J/cm <sup>2</sup> )	$\Delta T$ (°C)
D 10 <sup>-3</sup>	0.5	52	D 10 <sup>-4</sup>	0.5	66
	0.6	63		0.6	79
	1	105		1	132
	1.5	158		1.5	197
	2.1	246		2.1	301
	2.4	252		2.4	316
	2.5	268		2.5	329

Table 4.17 – Estimated temperature ( $z = l_{th}$ ) using Eq. 4.13 of the heat distribution inside the **Ketone N layer** following an Er:YAG laser pulse at VSP ( $\tau_L \approx 100 \mu s$ ) and SP ( $\tau_L \approx 300 \mu s$ ) modes.

<b>Ketone N</b>					
VSP Mode	Fluence (J/cm <sup>2</sup> )	$\Delta T$ (°C)		Fluence (J/cm <sup>2</sup> )	$\Delta T$ (°C)
D 10 <sup>-3</sup>	0.5	132	D 10 <sup>-4</sup>	0.5	242
	0.6	159		0.6	291
	1	265		1	485
	1.5	398		1.5	727
	2.1	582		2.1	1043
	2.4	636		2.4	1164
	2.5	663		2.5	1212
SP Mode	Fluence (J/cm <sup>2</sup> )	$\Delta T$ (°C)		Fluence (J/cm <sup>2</sup> )	$\Delta T$ (°C)
D 10 <sup>-3</sup>	0.5	69	D 10 <sup>-4</sup>	0.5	198
	0.6	83		0.6	237
	1	139		1	395
	1.5	208		1.5	593
	2.1	317		2.1	855
	2.4	333		2.4	948
	2.5	347		2.5	988

Table 4.18 – Estimated temperature ( $z = l_{th}$ ) using Eq. 4.13 of the heat distribution inside the **MS2A layer** following an Er:YAG laser pulse at VSP ( $\tau_L \approx 100 \mu s$ ) and SP ( $\tau_L \approx 300 \mu s$ ) modes.

<b>MS2A</b>					
<b>VSP Mode</b>	<b>Fluence (J/cm<sup>2</sup>)</b>	<b><math>\Delta T</math> (°C)</b>		<b>Fluence (J/cm<sup>2</sup>)</b>	<b><math>\Delta T</math> (°C)</b>
D 10 <sup>-3</sup>	<b>0.5</b>	100	D 10 <sup>-4</sup>	<b>0.5</b>	126
	<b>0.6</b>	120		<b>0.6</b>	151
	<b>1</b>	201		<b>1</b>	252
	<b>1.5</b>	301		<b>1.5</b>	378
	<b>2.1</b>	421		<b>2.1</b>	530
	<b>2.4</b>	482		<b>2.4</b>	605
	<b>2.5</b>	502		<b>2.5</b>	630
<b>SP Mode</b>	<b>Fluence (J/cm<sup>2</sup>)</b>	<b><math>\Delta T</math> (°C)</b>		<b>Fluence (J/cm<sup>2</sup>)</b>	<b><math>\Delta T</math> (°C)</b>
D 10 <sup>-3</sup>	<b>0.5</b>	78	D 10 <sup>-4</sup>	<b>0.5</b>	117
	<b>0.6</b>	94		<b>0.6</b>	140
	<b>1</b>	157		<b>1</b>	233
	<b>1.5</b>	236		<b>1.5</b>	350
	<b>2.1</b>	330		<b>2.1</b>	490
	<b>2.4</b>	377		<b>2.4</b>	560
	<b>2.5</b>	393		<b>2.5</b>	583

As Paraloid B67 does not contain hydroxyl groups in its skeletal structure, the resin is practically transparent at Er:YAG laser wavelength (2940 nm). This results in the lowest temperature rise both at the surface and in the bulk of the film (Table 4.3.17), and therefore 90 % of the Er:YAG laser radiation passing through the Paraloid B67 which interacts with the underlying layer (see Table 4.19).

Table 4.19 – Estimated temperature ( $z = l_{th}$ ) using Eq. 4.13 of the heat distribution inside the **Paraloid B67 layer** following an Er:YAG laser pulse at VSP ( $\tau_L \approx 100 \mu s$ ) and SP ( $\tau_L \approx 300 \mu s$ ) modes.

<b>Paraloid B67</b>					
<b>VSP Mode</b>	<b>Fluence (J/cm<sup>2</sup>)</b>	<b><math>\Delta T</math> (°C)</b>		<b>Fluence (J/cm<sup>2</sup>)</b>	<b><math>\Delta T</math> (°C)</b>
D 10 <sup>-3</sup>	<b>0.5</b>	5	D 10 <sup>-4</sup>	<b>0.5</b>	5
	<b>0.6</b>	6		<b>0.6</b>	6
	<b>1</b>	9		<b>1</b>	9
	<b>1.5</b>	14		<b>1.5</b>	14
	<b>2.1</b>	20		<b>2.1</b>	20
	<b>2.4</b>	22		<b>2.4</b>	22
	<b>2.5</b>	23		<b>2.5</b>	23
<b>SP Mode</b>	<b>Fluence (J/cm<sup>2</sup>)</b>	<b><math>\Delta T</math> (°C)</b>		<b>Fluence (J/cm<sup>2</sup>)</b>	<b><math>\Delta T</math> (°C)</b>
D 10 <sup>-3</sup>	<b>0.5</b>	5	D 10 <sup>-4</sup>	<b>0.5</b>	5
	<b>0.6</b>	6		<b>0.6</b>	6
	<b>1</b>	9		<b>1</b>	9
	<b>1.5</b>	14		<b>1.5</b>	14
	<b>2.1</b>	19		<b>2.1</b>	20
	<b>2.4</b>	22		<b>2.4</b>	22
	<b>2.5</b>	23		<b>2.5</b>	23

4.3.3.2.2 Transient temperature profiles of varnishes regarded as semi-infinite solids

The absorbed laser power densities ( $F_0$ ) carried out to run the mathematical model, using Eq. 4.15, are presented in the table below (Table 4.20). The incident laser beam energy ( $E_{inc}$ ), presented in Table 4.5 section 4.3.2, was used to calculate  $F_0$ . However, as reported by Fotakis *et al.* (2007, p. 189), an accurate measure of the real absorbed energy returns little physical insight because of various laser-material interactions including the scattering of the laser beam.

Table 4.20 – Estimates of the surface power densities ( $F_0$ ) absorbed by the vanishes at  $z=0$ .

		Fluences	Dammar	Ketone N		MS2A	
				%R from FTIR	%R from Fresnel eq. (Eq. 4.21)	%R from FTIR	%R from Fresnel eq. (Eq. 4.21)
Surface power density absorbed (MW/m <sup>2</sup> )	VSP mode	0.5	41.2	41.7	46.4	41	46.5
		1	85.7	86.8	96.6	85.4	96.7
		1.5	131.9	133.6	148.7	131.4	148.9
		2.1	177.6	179.8	200.2	176.9	200.5
		2.4	202.2	204.7	227.9	201.4	228.3
	SP mode	0.5	13.7	13.9	15.5	13.7	15.5
		1	28.6	28.9	32.2	28.5	32.2
		1.5	44	44.5	49.6	43.8	49.6
		2.1	59.2	59.9	66.7	59	66.8
		2.4	67.4	68.2	76	67.1	76.1

The mathematical model is based on the assumption that the rate of heat production per unit of time per unit of volume is generated within the varnish layer surfaces, thus considering the absorption coefficient of each varnish. The result of Eq. 4.17 is an immediate rise of the temperature, followed by a temperature drop as heat is conducted into the material (Çengel, Ghajar and Kanoglu, 2014, p. 263). The estimated temperature at the surface after  $\tau_L$  has been summarised in Tables 4.21-23. The calculated heat-wave propagation inside the dammar, Ketone N and MS2A films, in VSP and SP modes are shown in Figures 4.23-28 and Appendix B, as a function of space (plots A and C) and time (plots B and D). For dammar, Ketone N and MS2A varnish films, the analytical solutions have been carried out in two distinct regimes, according to the laser thermal diffusivity provided by Fotakis *et al.* (2007, p. 36) ( $D \sim 10^{-3} - 10^{-4} \text{ cm}^2/\text{sec}$ ). Only for Ketone N and MS2A the mathematical process has been further diversified due to the reflectance data

obtained from the FT-IR analysis and the Fresnel Equation (Eq. 4.21). The difference in percentage between the temperature at the surface after  $\tau_L$  obtained using the FT-IR data and the ones using the Fresnel Equation are within 11% in VSP and SP modes for Ketone N (Table 4.22) and 12% in VSP and SP modes for MS2A (Table 4.23). All the temperatures described in this section are in Celsius ( $^{\circ}\text{C}$ ) and the mathematical model have been considered with an initial temperature at  $25^{\circ}\text{C}$  (room temperature - RT).

The temperature distribution inside the irradiated Paraloid B67 was not processed because its optical absorption depth ( $\delta = 497.1\ \mu\text{m}$ ) is much bigger than the thickness of the varnish film applied on the glass slide ( $51.3\ \mu\text{m}$ ) (see Table 4.2 and 4.3). This implies a direct interaction with the underlying layer, which leads to a compromised mathematical computation within the varnish film.

As already observed in Table 4.17, Ketone N film showed the highest estimated temperature at the surface after  $\tau_L$  for both VSP ( $\tau_L \approx 100\ \mu\text{s}$ ) and SP modes ( $\tau_L \approx 300\ \mu\text{s}$ ) (Table 4.22). The estimated temperatures in VSP mode are between  $222^{\circ}\text{C}$  (for  $D \approx 10^{-3}\ \text{cm}^2/\text{sec}$ ) and  $291^{\circ}\text{C}$  (for  $D \approx 10^{-4}\ \text{cm}^2/\text{sec}$ ) at the minimum fluence of  $0.5\ \text{J}/\text{cm}^2$ , and between  $993^{\circ}\text{C}$  (for  $D \approx 10^{-3}\ \text{cm}^2/\text{sec}$ ) and  $1332^{\circ}\text{C}$  (for  $D \approx 10^{-4}\ \text{cm}^2/\text{sec}$ ) at the maximum fluence of  $2.4\ \text{J}/\text{cm}^2$ . The  $\Delta T$  values in SP mode range between  $190^{\circ}\text{C}$  and  $274^{\circ}\text{C}$  at  $0.5\ \text{J}/\text{cm}^2$  and between  $835^{\circ}\text{C}$  and  $1245^{\circ}\text{C}$  at  $2.4\ \text{J}/\text{cm}^2$ . As presented in Table 4.3.19, dammar shows the lowest  $\Delta T$  values with estimated temperatures in VSP mode between  $80^{\circ}\text{C}$  (for  $D \approx 10^{-3}\ \text{cm}^2/\text{sec}$ ) and  $83^{\circ}\text{C}$  (for  $D \approx 10^{-4}\ \text{cm}^2/\text{sec}$ ) at  $0.5\ \text{J}/\text{cm}^2$ , and between  $295^{\circ}\text{C}$  and  $309^{\circ}\text{C}$  at  $2.4\ \text{J}/\text{cm}^2$ . The same mathematical calculation carried out in SP mode has provided  $\Delta T$  values between  $77^{\circ}\text{C}$  and  $82^{\circ}\text{C}$  at  $0.5\ \text{J}/\text{cm}^2$  and between  $283^{\circ}\text{C}$  and  $304^{\circ}\text{C}$  at  $2.4\ \text{J}/\text{cm}^2$ .

In particular, comparing the Ketone N thermal data with those of dammar film (Table 4.21), the estimated temperatures for the irradiated dammar film present a decrement of about 70 % (for  $D \approx 10^{-3} - 10^{-4}\ \text{cm}^2/\text{sec}$ ) in the VSP mode, and between 64 % (for  $D \approx 10^{-3}\ \text{cm}^2/\text{sec}$ ) and 70 % (for  $D \approx 10^{-4}\ \text{cm}^2/\text{sec}$ ) in SP mode. The same goes for the MS2A film (Table 4.23) with a decrease of the estimated temperature between 45 % for  $D \approx 10^{-3}$ , considering reflectance data obtained from the FT-IR data and the Fresnel Equation, and 50 % for  $D \approx 10^{-4}$  in the VSP mode.

The same is true for SP mode with a decrement of about 40 % for  $D \approx 10^{-3}$  and 50 % for  $D \approx 10^{-4}$ .

The time profiles in plots A and C (Figures 4.23-28) show the diffusion of heat inside the varnishes at set intervals of time at the end of the  $\tau_L$  (the curves  $t = \tau_L, 2 \tau_L, 4 \tau_L, 8 \tau_L,$  and  $10 \tau_L$ ) as a function of depth. These profiles are very similar and display a monotonically decreasing classic solution. For each irradiated varnish film, the maximum temperatures obtained at  $\tau_L$  in VSP and SP modes are shifting at lower temperatures moving towards the bulk of the coatings tending to decrease asymptotically to RT. In particular, it is possible to observe that the use of thermal conductivity ( $k$ ) values for  $D 10^{-4} \text{ cm}^2/\text{sec}$  show a slower heat dissipation inside the varnish films in both VSP and SP modes with a narrow distribution of the time profiles when compared with the same profiles obtained using thermal conductivity ( $k$ ) values for  $D 10^{-3} \text{ cm}^2/\text{sec}$ . As one gets further from the curve obtained at  $\tau_L$  in both VSP ( $\tau_L \approx 100 \mu\text{s}$ ) and SP modes ( $\tau_L \approx 300 \mu\text{s}$ ), the cooling curves at the end of the  $\tau_L$  exhibit three distinctive trends (Figures 4.23-28). Considering that the absorbed power densities for each varnish can be considered comparable with one another, for dammar varnish (Figures 4.23-24 A and C), the time profiles at  $2 \tau_L, 4 \tau_L, 8 \tau_L,$  and  $10 \tau_L$  show a narrow distribution of the cooling curves, which becomes narrower considering  $D \approx 10^{-4}$  value. In VSP mode at  $10\tau_L$ , there is a decrement in temperature of 15 % for  $D \approx 10^{-3}$  and 6 % for  $D \approx 10^{-4}$  compared to the temperature obtained at the surface. In SP mode at  $10 \tau_L$ , there is a decrement of 21 % for  $D \approx 10^{-3}$  and 10 % for  $D \approx 10^{-4}$  compared to the temperature obtained at the surface. The MS2A behaves as the dammar film but with a more gradual distribution of the cooling curves inside the bulk of the varnish (Figures 4.27-28 A and C). In VSP mode at  $10 \tau_L$ , it is possible to observe a decrease in temperature of 25 % for  $D \approx 10^{-3}$  and 10 % for  $D \approx 10^{-4}$  compared to the temperature obtained at the surface. In SP mode at  $10 \tau_L$ , the temperatures obtained are reduced by 35 % for  $D \approx 10^{-3}$  and 36 % for  $D \approx 10^{-4}$  when compared to the temperature obtained at the surface. However, Ketone N varnish presents the wider distribution of the time profiles in the time interval selected (Figures 4.25-26 A and C). In VSP mode at  $10 \tau_L$ , there is a decrement of 48 % for  $D \approx 10^{-3}$  and 26 % for  $D \approx 10^{-4}$  compared to the temperature obtained at the surface. In SP mode at  $10 \tau_L$ , there is a decrement of 56

% for  $D \approx 10^{-3}$  and 35 % for  $D \approx 10^{-4}$  compared to the temperature obtained at the surface.

Moreover, plots B and D, in Figures 4.23-28, compare the transient temperatures profiles at several points located along with the optical penetration depth ( $\delta$ ) of each varnish. The heat-wave propagation that gradually decays after attaining a maximum at its wavefront reflects the solution of the heat diffusion equation for semi-infinite homogeneous materials with the laser heat source distributed along with the irradiated coatings (Majaron, Plestenjak and Lukac, 1999). One can note that temperature sample points further away from the varnish surface show a more gradual temperature rise, and the peak temperature is reached at progressively later times with increasing distances ( $z$ ) from the surface. For all the varnishes, a thermal diffusivity ( $D$ )  $\approx 10^{-4}$  cm<sup>2</sup>/sec has shown a more gradual diffusion rate upon the end of the laser pulse in both VSP and SP modes. However, thermal diffusivity ( $D$ )  $\approx 10^{-3}$  cm<sup>2</sup>/sec has significantly different diffusion curves with sharp slopes. The computational results, in VSP and SP modes, show that the temperature rise evolution at various depths as a function of time for  $t > 0.03$  sec (for  $D \approx 10^{-3}$  cm<sup>2</sup>/sec) and  $t > 0.06$  sec (for  $D \approx 10^{-4}$  cm<sup>2</sup>/sec) in dammar, for  $t > 0.02$  sec (for  $D \approx 10^{-3}$  cm<sup>2</sup>/sec) and  $t > 0.05$  sec (for  $D \approx 10^{-4}$  cm<sup>2</sup>/sec) in MS2A, and  $t > 0.002$  sec (for  $D \approx 10^{-3}$  cm<sup>2</sup>/sec) and  $t > 0.003$  sec (for  $D \approx 10^{-4}$  cm<sup>2</sup>/sec) in Ketone N (Figures 4.25-26) are nearly the same implying that a quasi-steady state condition has been reached.

These temperature estimates tend to support the suggestion that most of the heat is contained within the varnish films, as will be later established in the simulations. The laser pulse durations have a significant impact on the laser-material interaction. A shorter pulse width ensures that the delivered energy is more rapidly deposited into the irradiated material. Thus, the volume of material that is directly affected by the laser beam energy has less time to transfer energy to the surrounding material, reducing the heat-affected zone. In fact, as reported by Partovi *et al.* (1987) and identified in the mathematical computation, the longer the pulse duration, and the larger the thermal diffusivity of the irradiated material, the deeper the heat distribution is expected to spread from the surface.

Table 4.21 – Estimated temperature rise using Eq. 4.17 on **dammar film** following an Er:YAG laser pulse at VSP ( $\approx 100 \mu\text{s}$ ) and SP ( $\approx 300 \mu\text{s}$ ) modes. Temperature is given relative to room temperature ( $25^\circ\text{C}$ ).

<b>Dammar</b>					
VSP Mode	Fluence (J/cm <sup>2</sup> )	$\Delta T$ (°C)		Fluence (J/cm <sup>2</sup> )	$\Delta T$ (°C)
D $10^{-3}$	0.5	80	D $10^{-4}$	0.5	83
	1	140		1	145
	1.5	201		1.5	210
	2.1	263		2.1	274
	2.4	295		2.4	309
SP Mode	Fluence (J/cm <sup>2</sup> )	$\Delta T$ (°C)		Fluence (J/cm <sup>2</sup> )	$\Delta T$ (°C)
D $10^{-3}$	0.5	77	D $10^{-4}$	0.5	82
	1	134		1	143
	1.5	193		1.5	207
	2.1	251		2.1	270
	2.4	283		2.4	304

Table 4.22 – Estimated temperature rise using Eq. 4.17 on **Ketone N film** following an Er:YAG laser pulse at VSP ( $\approx 100 \mu\text{s}$ ) and SP ( $\approx 300 \mu\text{s}$ ) modes. (\*)  $\Delta T$  (°C) has been determined by using the %R from the FTIR data. However, (\*\*)  $\Delta T$  (°C) has been obtained using the %R from the Fresnel equation (Eq. 4.21). Temperature is given relative to room temperature ( $25^\circ\text{C}$ ).

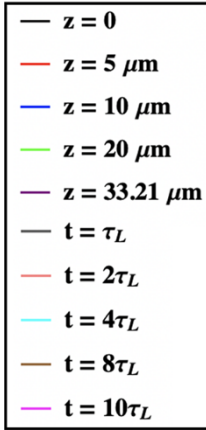
<b>Ketone N</b>							
VSP Mode	Fluence (J/cm <sup>2</sup> )	$\Delta T$ (°C)*	$\Delta T$ (°C)**		Fluence (J/cm <sup>2</sup> )	$\Delta T$ (°C)*	$\Delta T$ (°C)**
D $10^{-3}$	0.5	222	244	D $10^{-4}$	0.5	264	291
	1	435	482		1	523	579
	1.5	657	728		1.5	792	878
	2.1	875	971		2.1	1057	1173
	2.4	993	1102		2.4	1200	1332
SP Mode	Fluence (J/cm <sup>2</sup> )	$\Delta T$ (°C)*	$\Delta T$ (°C)**		Fluence (J/cm <sup>2</sup> )	$\Delta T$ (°C)*	$\Delta T$ (°C)**
D $10^{-3}$	0.5	190	209	D $10^{-4}$	0.5	248	274
	1	368	407		1	490	542
	1.5	554	613		1.5	741	821
	2.1	737	817		2.1	988	1097
	2.4	835	926		2.4	1122	1245

Table 4.23 – Estimated temperature rise using Eq. 4.17 on **MS2A film** following an Er:YAG laser pulse at VSP ( $\approx 100 \mu\text{s}$ ) and SP ( $\approx 300 \mu\text{s}$ ) modes. (\*)  $\Delta T$  ( $^{\circ}\text{C}$ ) has been determined by using the %R from the FTIR data. However, (\*\*)  $\Delta T$  ( $^{\circ}\text{C}$ ) has been obtained using the %R from the Fresnel equation (Eq. 4.21). Temperature is given relative to room temperature ( $25^{\circ}\text{C}$ ).

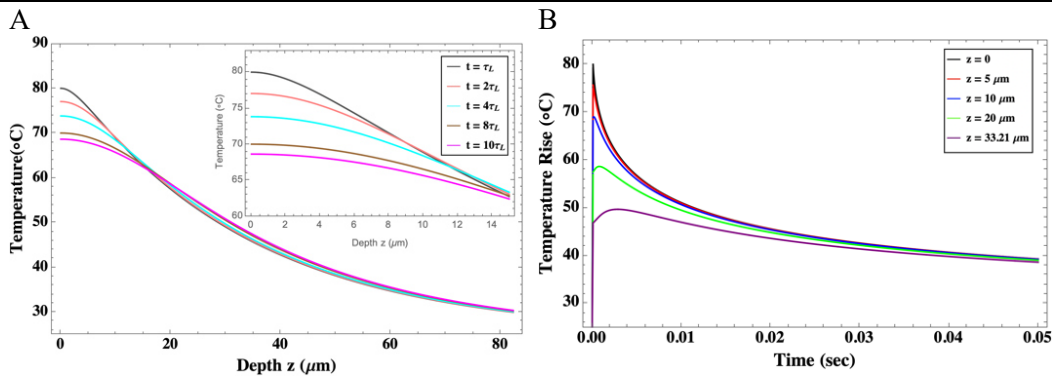
<b>MS2A</b>							
<b>VSP Mode</b>	<b>Fluence (J/cm<sup>2</sup>)</b>	<b><math>\Delta T</math> (<math>^{\circ}\text{C}</math>)*</b>	<b><math>\Delta T</math> (<math>^{\circ}\text{C}</math>)**</b>		<b>Fluence (J/cm<sup>2</sup>)</b>	<b><math>\Delta T</math> (<math>^{\circ}\text{C}</math>)*</b>	<b><math>\Delta T</math> (<math>^{\circ}\text{C}</math>)**</b>
D 10 <sup>-3</sup>	<b>0.5</b>	127	140	D 10 <sup>-4</sup>	<b>0.5</b>	135	149
	<b>1</b>	237	264		<b>1</b>	255	284
	<b>1.5</b>	351	393		<b>1.5</b>	378	423
	<b>2.1</b>	464	520		<b>2.1</b>	501	561
	<b>2.4</b>	525	588		<b>2.4</b>	567	636
<b>SP Mode</b>	<b>Fluence (J/cm<sup>2</sup>)</b>	<b><math>\Delta T</math> (<math>^{\circ}\text{C}</math>)*</b>	<b><math>\Delta T</math> (<math>^{\circ}\text{C}</math>)**</b>		<b>Fluence (J/cm<sup>2</sup>)</b>	<b><math>\Delta T</math> (<math>^{\circ}\text{C}</math>)*</b>	<b><math>\Delta T</math> (<math>^{\circ}\text{C}</math>)**</b>
D 10 <sup>-3</sup>	<b>0.5</b>	119	131	D 10 <sup>-4</sup>	<b>0.5</b>	132	146
	<b>1</b>	220	245		<b>1</b>	248	277
	<b>1.5</b>	326	364		<b>1.5</b>	369	412
	<b>2.1</b>	430	481		<b>2.1</b>	488	547
	<b>2.4</b>	486	544		<b>2.4</b>	552	619

**Dammar – VSP mode ( $\tau_L \approx 100 \mu\text{s}$ ):**

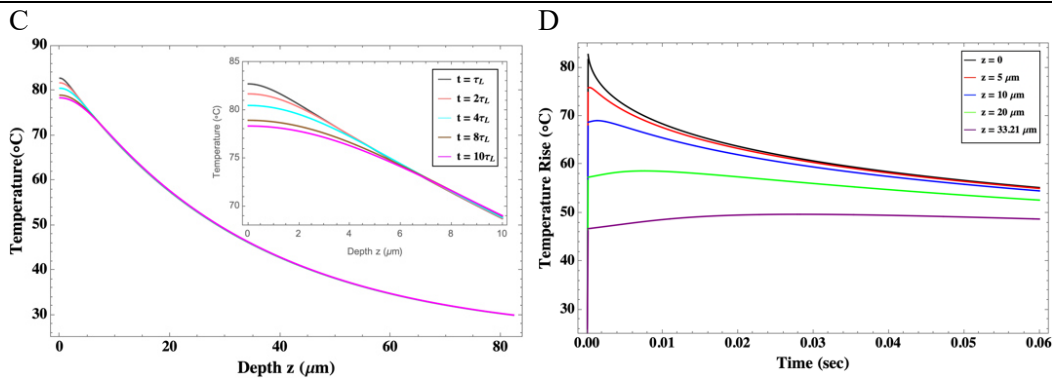
Figure 4.23 – Representation of the heat-wave propagation inside the **dammar film**, in VSP mode, at different times [100  $\mu\text{s}$  (gray), 200  $\mu\text{s}$  (pink), 400  $\mu\text{s}$  (cyan), 800  $\mu\text{s}$  (brown) and 1 ms (magenta)] as a function of depth (A and C) and the temperature rise evolution at various depth [0 (black), 5  $\mu\text{m}$  (red), 10  $\mu\text{m}$  (blue), 20  $\mu\text{m}$  (green), 33.21  $\mu\text{m}$  (purple)] as a function of time (B and D). The laser beam diameter was set at  $\varnothing = 4 \text{ mm}$ . Temperature is given relative to room temperature (25 °C).



**Dammar, VSP mode,  $F = 0.5 \text{ J/cm}^2$ ,  $k = 0.21 \text{ W/m}\cdot\text{K}$**

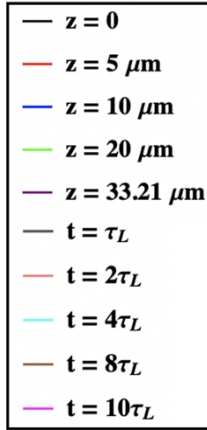


**Dammar, VSP mode,  $F = 0.5 \text{ J/cm}^2$ ,  $k = 0.021 \text{ W/m}\cdot\text{K}$**

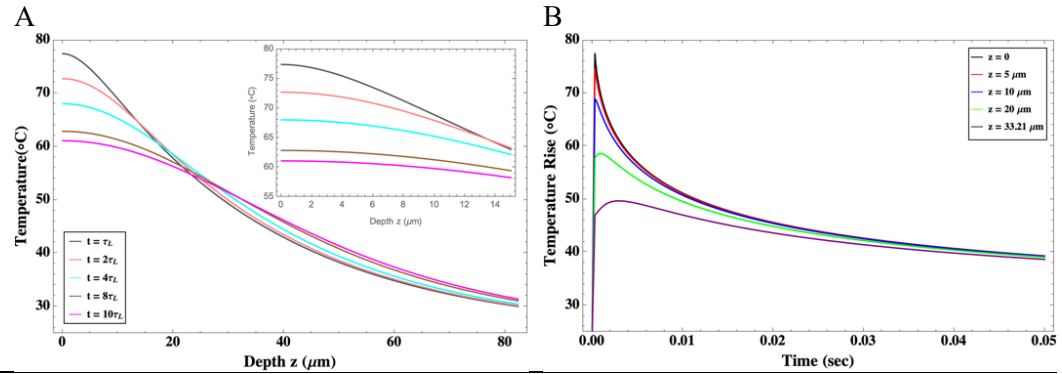


**Dammar – SP mode ( $\tau_L \approx 300 \mu\text{s}$ ):**

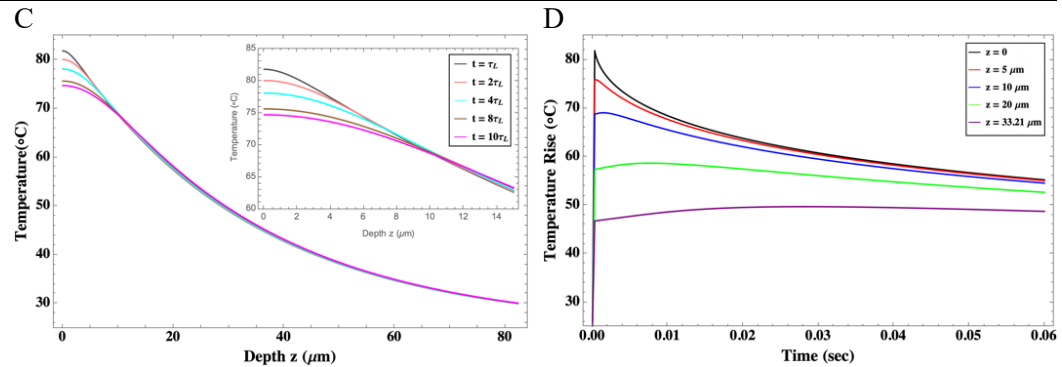
Figure 4.24 – Representation of the heat-wave propagation inside the **dammar film**, in SP mode, at different times [300  $\mu\text{s}$  (gray), 600  $\mu\text{s}$  (pink), 1.2 ms (cyan), 2.4 ms (brow) and 3 ms (magenta)] as a function of depth (A and C) and the temperature rise evolution at various depth [0 (black), 5  $\mu\text{m}$  (red), 10  $\mu\text{m}$  (blue), 20  $\mu\text{m}$  (green), 33.21  $\mu\text{m}$  (purple)] as a function of time (B and D). The laser beam diameter was set at  $\varnothing = 4 \text{ mm}$ . Temperature is given relative to room temperature (25 °C).

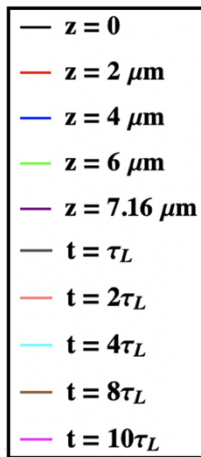


**Dammar, SP mode,  $F = 0.5 \text{ J/cm}^2$ ,  $k = 0.21 \text{ W/m}\cdot\text{K}$**



**Dammar, SP mode,  $F = 0.5 \text{ J/cm}^2$ ,  $k = 0.021 \text{ W/m}\cdot\text{K}$**



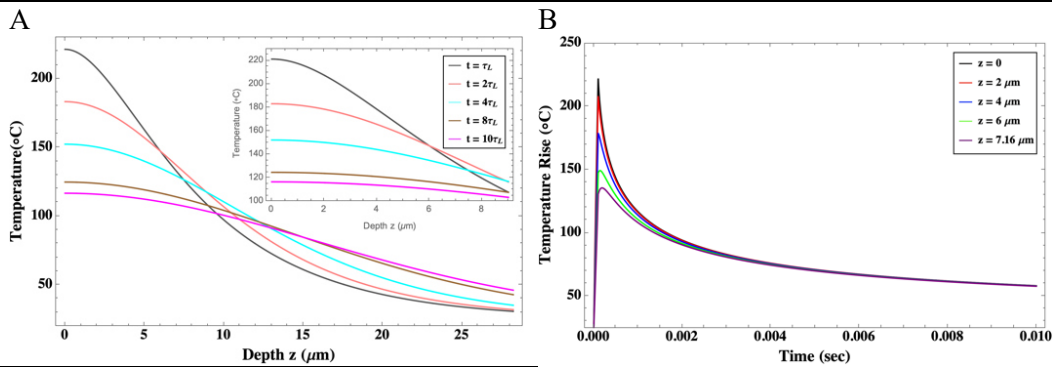


**Ketone N – VSP mode ( $\tau_L \approx 100 \mu\text{s}$ ):**

Figure 4.25 – Representation of the heat-wave propagation inside the **Ketone N film**, in VSP mode, at different times [100  $\mu\text{s}$  (gray), 200  $\mu\text{s}$  (pink), 400  $\mu\text{s}$  (cyan), 800  $\mu\text{s}$  (brow) and 1 ms (magenta)] as a function of depth (A and C) and the temperature rise evolution at various depth [0 (black), 2  $\mu\text{m}$  (red), 4  $\mu\text{m}$  (blue), 6  $\mu\text{m}$  (green), 7.16  $\mu\text{m}$  (purple)] as a function of time (B and D). The laser beam diameter was set at  $\varnothing = 4 \text{ mm}$ . Temperature is given relative to room temperature (25 °C).

Temperature evolution obtained using the %R from FTIR data

**Ketone N, VSP mode,  $F = 0.5 \text{ J/cm}^2$ ,  $k = 0.22 \text{ W/m}\cdot\text{K}$**



Temperature evolution obtained using the %R from Fresnel equation (Eq. 4.21)

**Ketone N, VSP mode,  $F = 0.5 \text{ J/cm}^2$ ,  $k = 0.22 \text{ W/m}\cdot\text{K}$**

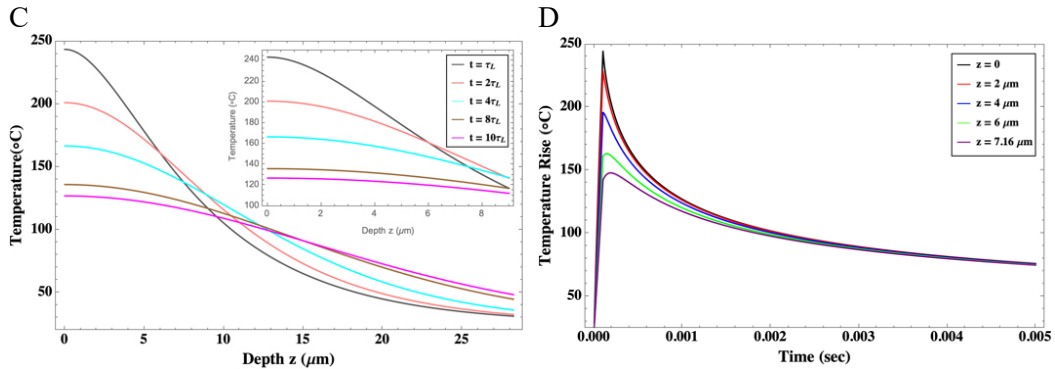
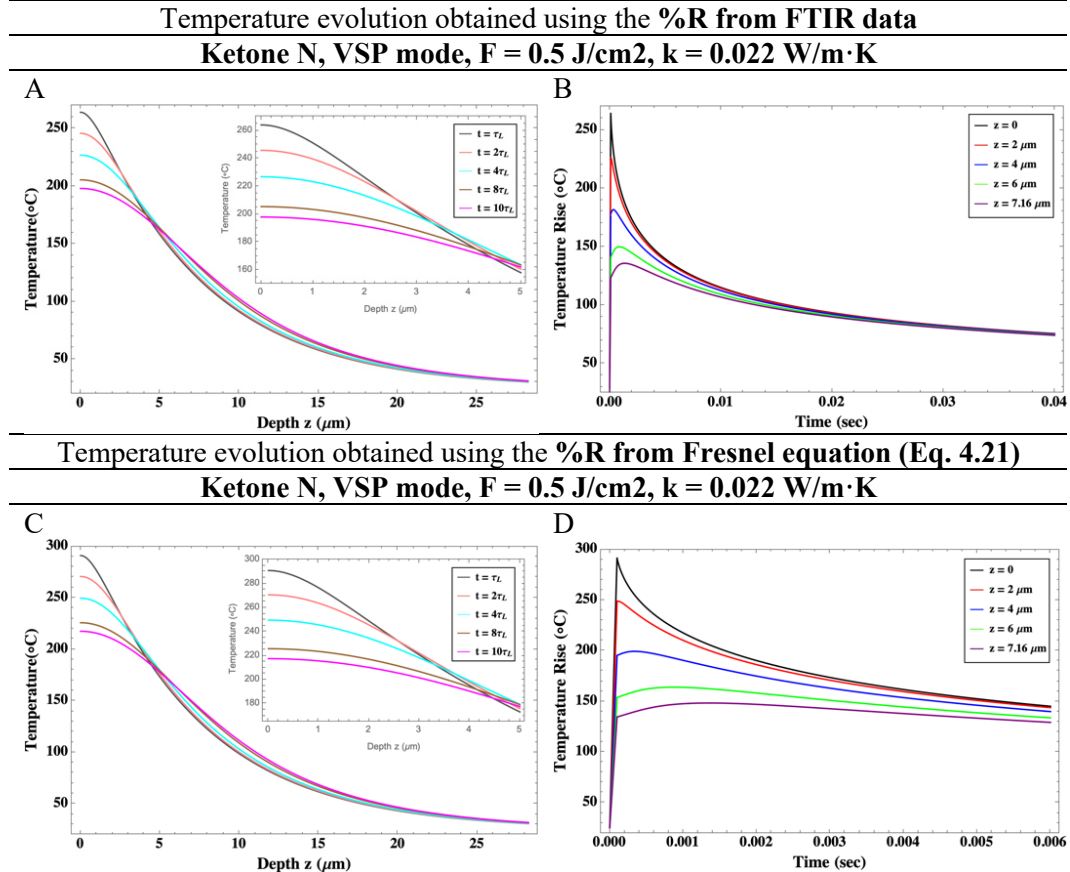
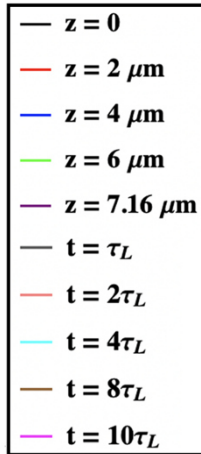


Figure 4.25 – Representation of the heat-wave propagation inside the **Ketone N film**, in VSP mode, at different times [100  $\mu\text{s}$  (gray), 200  $\mu\text{s}$  (pink), 400  $\mu\text{s}$  (cyan), 800  $\mu\text{s}$  (brow) and 1 ms (magenta)] as a function of depth (A and C) and the temperature rise evolution at various depth [0 (black), 2  $\mu\text{m}$  (red), 4  $\mu\text{m}$  (blue), 6  $\mu\text{m}$  (green), 7.16  $\mu\text{m}$  (purple)] as a function of time (B and D). The laser beam diameter was set at  $\varnothing = 4 \text{ mm}$ . Temperature is given relative to room temperature (25  $^{\circ}\text{C}$ ).



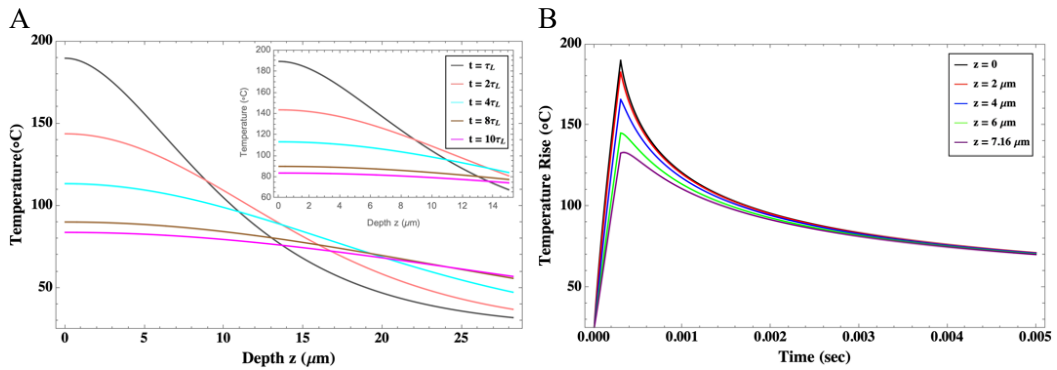


**Ketone N – SP mode ( $\tau_L \approx 300 \mu\text{s}$ ):**

Figure 4.26 – Representation of the heat-wave propagation inside the **Ketone N film**, in SP mode, at different times [300  $\mu\text{s}$  (gray), 600  $\mu\text{s}$  (pink), 1.2 ms (cyan), 2.4 ms (brown) and 3 ms (magenta)] as a function of depth (A and C) and the temperature rise evolution at various depth [0 (black), 5  $\mu\text{m}$  (red), 10  $\mu\text{m}$  (blue), 20  $\mu\text{m}$  (green), 33.21  $\mu\text{m}$  (purple)] as a function of time (B and D). The laser beam diameter was set at  $\varnothing = 4 \text{ mm}$ . Temperature is given relative to room temperature (25 °C).

Temperature evolution obtained using the %R from FTIR data

**Ketone N, SP mode,  $F = 0.5 \text{ J/cm}^2$ ,  $k = 0.22 \text{ W/m}\cdot\text{K}$**



Temperature evolution obtained using the %R from Fresnel equation (Eq. 4.21)

**Ketone N, SP mode,  $F = 0.5 \text{ J/cm}^2$ ,  $k = 0.22 \text{ W/m}\cdot\text{K}$**

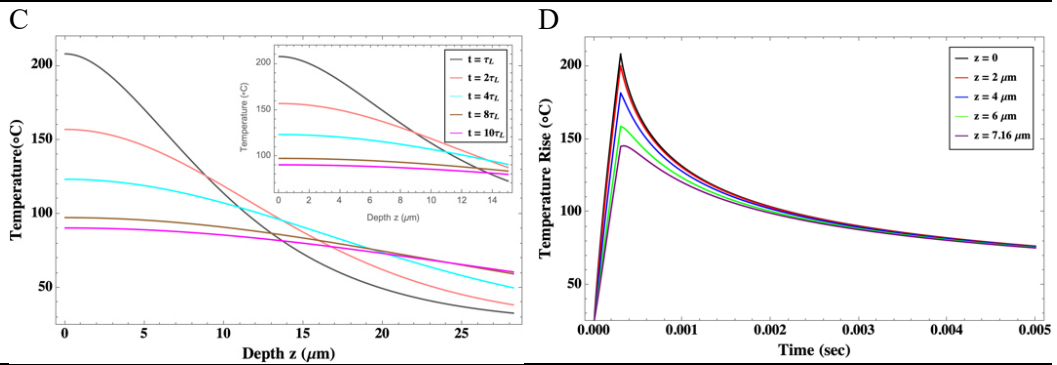
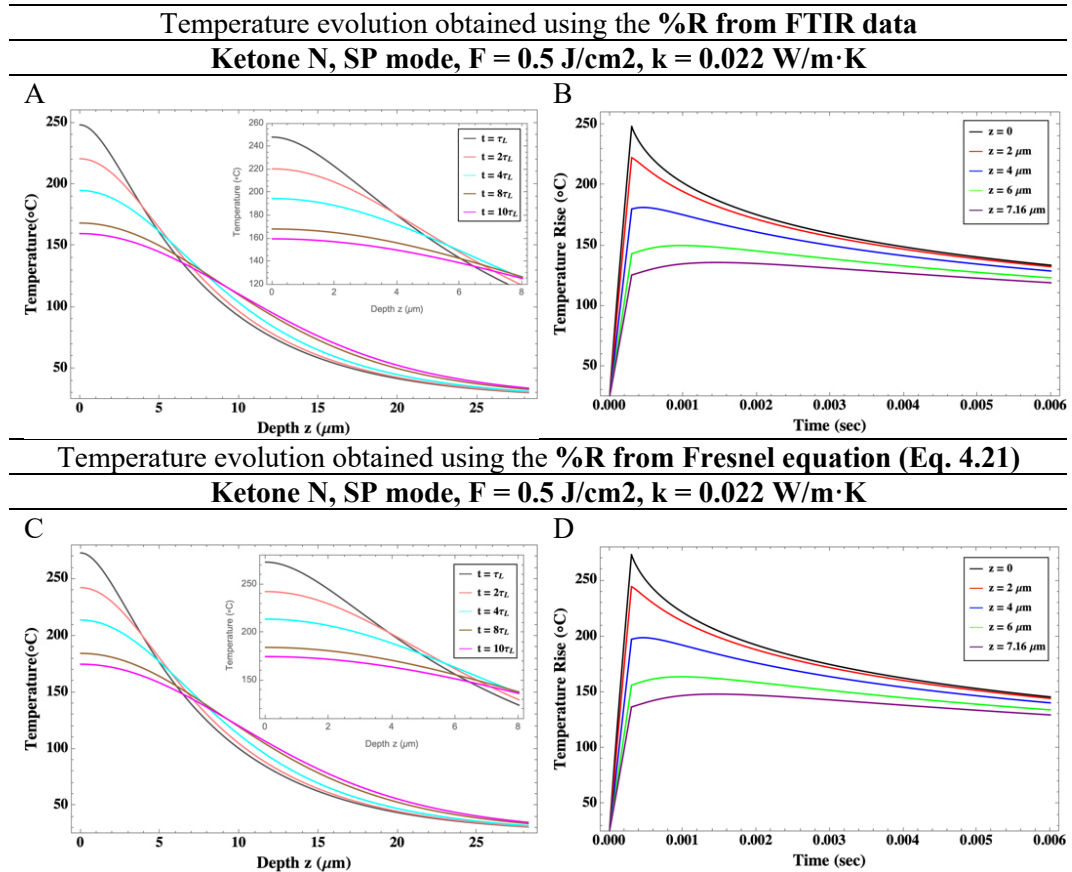
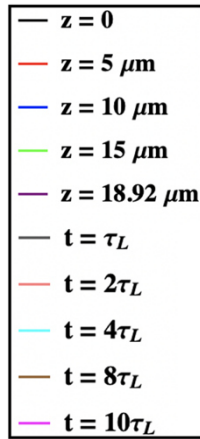


Figure 4.26 – Representation of the heat-wave propagation inside the **Ketone N film**, in SP mode, at different times [300  $\mu$ s (gray), 600  $\mu$ s (pink), 1.2 ms (cyan), 2.4 ms (brow) and 3 ms (magenta)] as a function of depth (A and C) and the temperature rise evolution at various depth [0 (black), 5  $\mu$ m (red), 10  $\mu$ m (blue), 20  $\mu$ m (green), 33.21  $\mu$ m (purple)] as a function of time (B and D). The laser beam diameter was set at  $\varnothing = 4$  mm. Temperature is given relative to room temperature (25  $^{\circ}$ C).

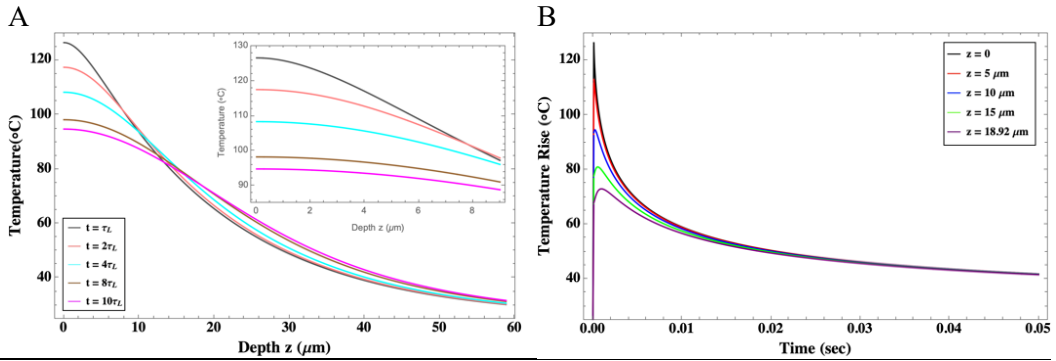




**MS2A – VSP mode ( $\tau_L \approx 100 \mu\text{s}$ ):**

Figure 4.27 – Representation of the heat-wave propagation inside the MS2A film, in VSP mode, at different times [100  $\mu\text{s}$  (gray), 200  $\mu\text{s}$  (pink), 400  $\mu\text{s}$  (cyan), 800  $\mu\text{s}$  (brown) and 1 ms (magenta)] as a function of depth (A and C) and the temperature rise evolution at various depth [0 (black), 5  $\mu\text{m}$  (red), 10  $\mu\text{m}$  (blue), 15  $\mu\text{m}$  (green), 18.92  $\mu\text{m}$  (purple)] as a function of time (B and D). The laser beam diameter was set at  $\varnothing = 4 \text{ mm}$ . Temperature is given relative to room temperature (25 °C).

Temperature evolution obtained using the %R from FTIR data  
 MS2A, VSP mode,  $F = 0.5 \text{ J/cm}^2$ ,  $k = 0.19 \text{ W/m}\cdot\text{K}$



Temperature evolution obtained using the %R from Fresnel equation (Eq. 4.21)  
 MS2A, VSP mode,  $F = 0.5 \text{ J/cm}^2$ ,  $k = 0.19 \text{ W/m}\cdot\text{K}$

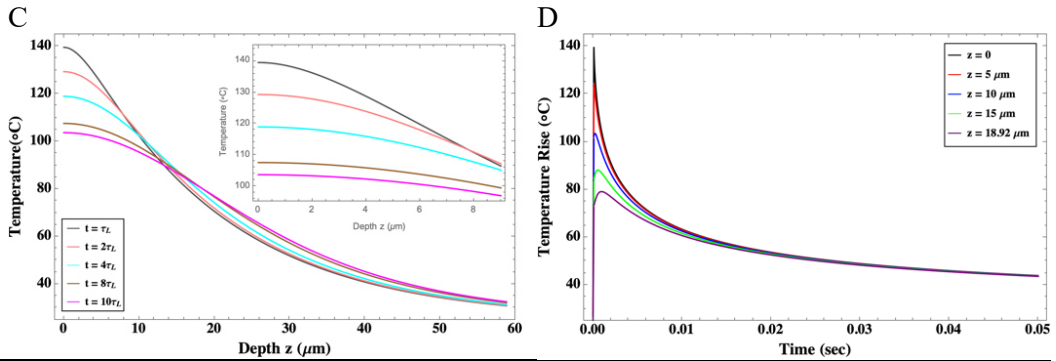
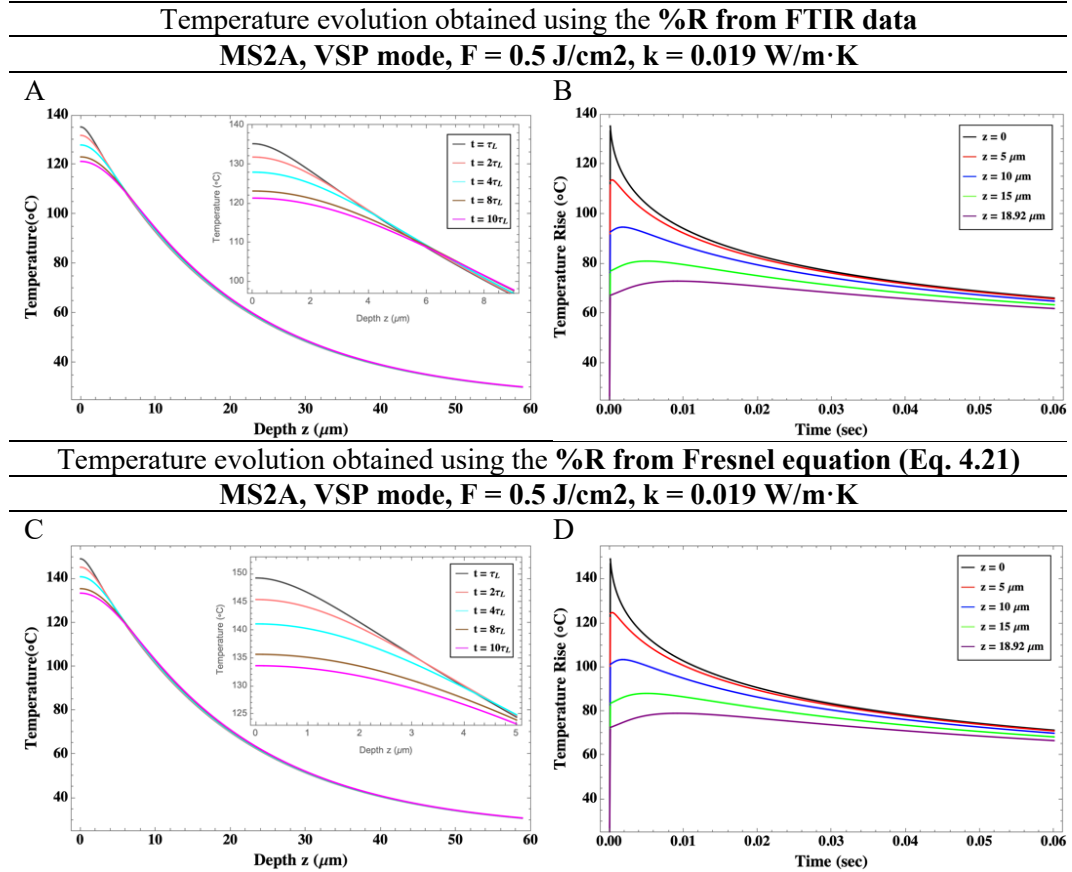
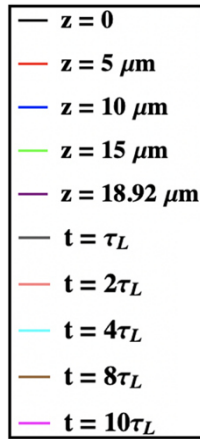


Figure 4.27 – Representation of the heat-wave propagation inside the **MS2A film**, in VSP mode, at different times [100  $\mu\text{s}$  (gray), 200  $\mu\text{s}$  (pink), 400  $\mu\text{s}$  (cyan), 800  $\mu\text{s}$  (brow) and 1 ms (magenta)] as a function of depth (A and C) and the temperature rise evolution at various depth [0 (black), 5  $\mu\text{m}$  (red), 10  $\mu\text{m}$  (blue), 15  $\mu\text{m}$  (green), 18.92  $\mu\text{m}$  (purple)] as a function of time (B and D). The laser beam diameter was set at  $\varnothing = 4$  mm. Temperature is given relative to room temperature (25  $^{\circ}\text{C}$ ).



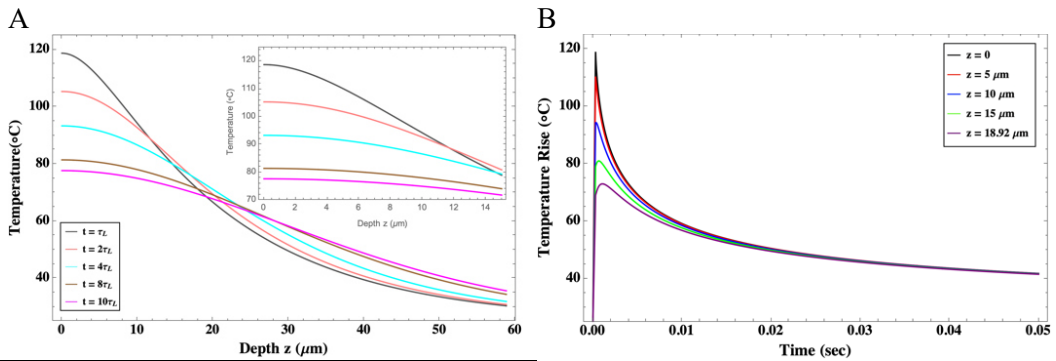


**MS2A – SP mode ( $\tau_L \approx 300 \mu\text{s}$ ):**

Figure 4.28 – Representation of the heat-wave propagation inside the MS2A film, in SP mode, at different times [300  $\mu\text{s}$  (gray), 600  $\mu\text{s}$  (pink), 1.2 ms (cyan), 2.4 ms (brown) and 3 ms (magenta)] as a function of depth (A and C) and the temperature rise evolution at various depth [0 (black), 5  $\mu\text{m}$  (red), 10  $\mu\text{m}$  (blue), 15  $\mu\text{m}$  (green), 18.92  $\mu\text{m}$  (purple)] as a function of time (B and D). The laser beam diameter was set at  $\varnothing = 4 \text{ mm}$ . Temperature is given relative to room temperature (25 °C).

Temperature evolution obtained using the %R from FTIR data

MS2A, SP mode,  $F = 0.5 \text{ J/cm}^2$ ,  $k = 0.19 \text{ W/m}\cdot\text{K}$



Temperature evolution obtained using the %R from Fresnel equation (Eq. 4.21)

MS2A, SP mode,  $F = 0.5 \text{ J/cm}^2$ ,  $k = 0.19 \text{ W/m}\cdot\text{K}$

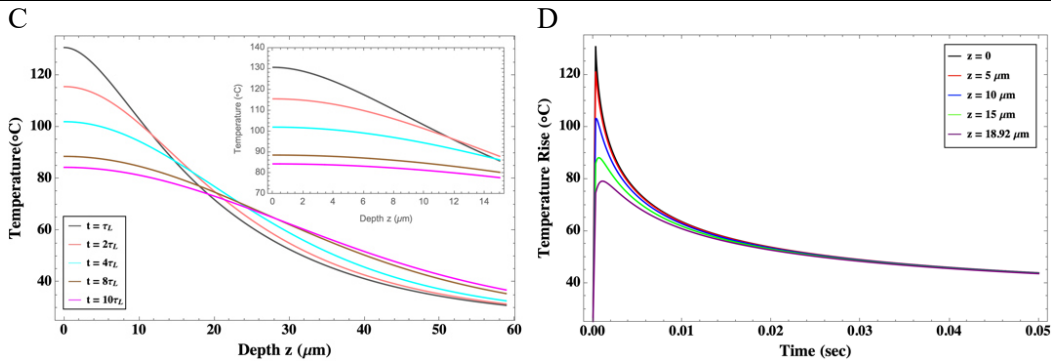
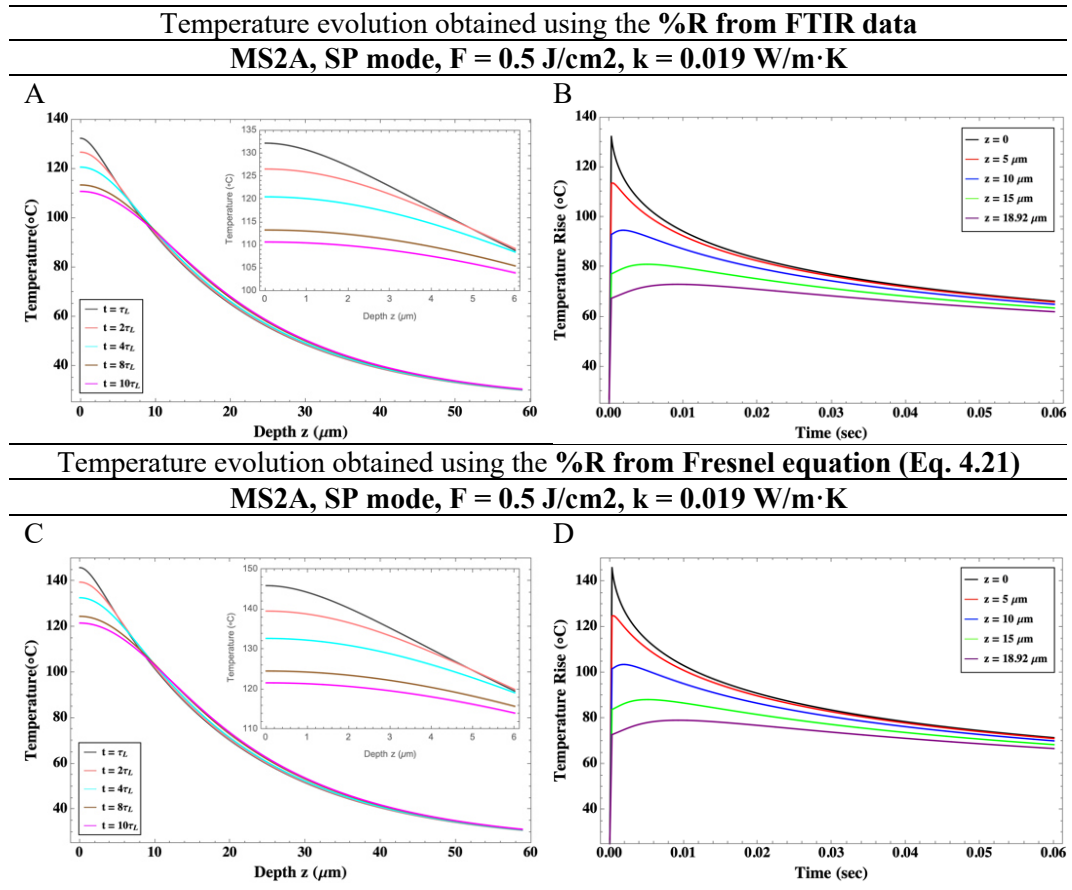


Figure 4.28 – Representation of the heat-wave propagation inside the **MS2A film**, in SP mode, at different times [300  $\mu$ s (gray), 600  $\mu$ s (pink), 1.2 ms (cyan), 2.4 ms (brow) and 3 ms (magenta)] as a function of depth (A and C) and the temperature rise evolution at various depth [0 (black), 5  $\mu$ m (red), 10  $\mu$ m (blue), 15  $\mu$ m (green), 18.92  $\mu$ m (purple)] as a function of time (B and D). The laser beam diameter was set at  $\varnothing = 4$  mm. Temperature is given relative to room temperature (25  $^{\circ}$ C).



#### 4.3.3.2.3 2 Dimensional Simulation model

The simulations reported in this study showed the final results obtained by considering only a single laser pulse fired onto the surface of the varnish films. Since these single pulses have short pulse duration (VSP  $\tau_L \approx 100 \mu\text{s}$  and SP  $\tau_L \approx 300 \mu\text{s}$ ), the boundary conditions can be assumed as adiabatic (Zuerlein *et al.*, 1998) and the convective heat is negligible. It allows to estimate the intensity of the heat spreading from the top coating surface region of the varnish films into the surrounding medium upon laser irradiation. Figures from 4.29 to 4.38 and Appendix B shows the results of the 2-dimensional (2D) simulation of the Er:YAG laser-based heat diffusion inside dammar, Ketone N and MS2A varnish films. All the temperatures that are described in this section are in degrees Celsius and the model tasks have been considered with an initial temperature of the mock-ups at 25 °C (RT).

Thanks to the simulation, it has been possible to detect a more precise heat distribution within the varnish films by increasing the fluence values from 0.5 up to 2.4 J/cm<sup>2</sup> and considering two different laser pulse durations ( $\tau_L \approx 100$  and 300  $\mu\text{s}$ ). The effect of the two distinct regimes which depend on the thermal conductivity (k) (Table 4.15) and for Ketone N and MS2A the two different reflectance data (Tables 4.3 and 4.4) have also been examined.

In particular, by using the VSP mode (Figures 4.29, 4.31-32, 4.35-36), there is a temperature increase at the surface, but lower penetration in the bulk of the coatings. On the contrary, in SP mode (Figures 4.30, 4.33-34, 4.37-38), the irradiated areas are less heated, but the average temperature of the bulk, close to the absorption of the laser energy, is higher (Chillè *et al.*, 2020). For all the varnishes, the temperature profiles presented are very similar.

The transient temperatures obtained from the 2D simulation experiments indicate that the rise in the temperature profiles along the temperature distribution by cross-section of varnish films is mainly confined within the laser absorption zone with minimal thermal tails in the remaining varnish films. This is evident in the simulations where a longer pulse width ( $\tau_L \approx 300 \mu\text{s}$ ) and a thermal diffusivity (D)  $\approx 10^{-3} \text{ cm}^2/\text{sec}$  for the varnish films analysed (Figures 4.30, 4.33, 4.37) have been used. Notwithstanding this, the results of the simulations demonstrate that most of the laser energy continues to be absorbed in the laser-absorbing part even when the

laser absorption zone is reduced due to the decreases of the optical penetration depth ( $\delta$ ) (e.g., Ketone N with the thinnest thickness – Figures 3.32-34). In all the diagrams, as already detected in section 4.3.3.2.2, it is possible to observe a narrower distribution of the isotherm lines and a higher temperature with thermal conductivity ( $k$ ) values for  $D 10^{-4} \text{ cm}^2/\text{sec}$  (see e.g., figure 4.32) compared with the same diagrams with  $k$  values for  $D 10^{-3} \text{ cm}^2/\text{sec}$  (see e.g., figure 4.31). This is due to the higher value of thermal diffusivity used in the simulations.

Moreover, comparing all the graphs in VSP and SP modes with thermal conductivity ( $k$ ) values obtained for  $D 10^{-3} \text{ cm}^2/\text{sec}$ , it is detected that the first isotherm line, at the highest temperature, is at a deeper depth in VSP mode in comparison with the SP mode (see e.g., MS2A figures 4.35 and 4.37). In general, higher power densities cause a significant temperature rise in the bulk of the varnishes due to a more considerable amount of energy delivered into the irradiated volume (Table 4.20). This results in a higher surface temperature. Nevertheless, it is important to stress that even at the highest simulated temperatures gradient (e.g. Ketone N - VSP mode, fluence  $2.4 \text{ J/cm}^2$  and peak temperature between  $1260^\circ\text{C}$  and  $1470^\circ\text{C}$  [Appendix B, Figures B32 and B33]), the interface between the glass slide and the varnish film has a temperature of  $25^\circ\text{C}$ .

As already stated, Ketone N varnish has returned the highest  $\Delta T$  values (Figures 4.31-34 and Appendix B) and dammar film the lowest (Figures 4.29-30 and Appendix B). For all the varnishes, the simulated temperatures attained upon Er:YAG laser irradiation have shown temperatures far above the  $T_g$  data presented in Chapter 3 and high enough to cause transient substrate melting<sup>11</sup>. In VSP and SP modes, the dammar varnish has shown maximum simulated temperature values, for the first isotherm line at the highest fluence of  $2.4 \text{ J/cm}^2$  (Appendix B, Figures B21 and B25), between the first degradation step ( $199^\circ\text{C}$ ) and the second one ( $349^\circ\text{C}$ ) of the thermograms obtained by the TGA analysis (Table 3.7). The first degradation step corresponds to the highest weight loss of 49.8% related to the oxidative

---

<sup>11</sup> The melting point of dammar resin ranges between  $100 - 180^\circ\text{C}$  (Merz-Le, 1998; Mills and White, 1999), the one for the cyclohexanone only (e.g., Ketone N) is  $115 - 120^\circ\text{C}$  (de la Rie and Shedrinsky, 1989). Moreover, de la Rie and Shedrinsky (1989) reported that in the case of addition of methyl cyclohexanones (e.g., MS2A) the melting point is reduced.

degradation of the dammar coating as a result of temperature increase. At the lowest fluence of  $0.5 \text{ J/cm}^2$ , the simulated temperature returned values of 40% above the  $T_g$  data for both the VSP (Figure 4.29) and SP modes (Figure 4.30). The same comparison cannot be made for the Ketone N film where the simulated temperature gradients at a fluence of  $1 \text{ J/cm}^2$ , for both VSP (Appendix B, Figures B26 and B27) and SP modes (Appendix B, Figures B34 and B35), already exceed the complete thermal decomposition temperature acquired using the TGA analysis (Table 3.7). The MS2A at a fluence of  $0.5 \text{ J/cm}^2$ , in VSP (Figures 4.35-36) and SP modes (Figures 4.37-38), has given maximum simulated temperature values, for the first isotherm line, in the range of temperature between the first stage of reaction ( $94 \text{ }^\circ\text{C}$ ) and the second one ( $254 \text{ }^\circ\text{C}$ ) of the thermogram obtained by the TGA analysis mode (Table 3.7). Instead, at the highest fluence of  $2.4 \text{ J/cm}^2$  (Appendix B), the simulated temperature returned values of 25 % above the complete decomposition of the raw MS2A for the VSP mode (Appendix B, Figures B48 and B49) and 22% for the SP mode (Appendix B, Figures B56 and B57).

In those simulations, the properties of thermal conductivity ( $k$ ) and density ( $\rho$ ) have been considered to be independent of the temperature. However, it should be emphasised that in the case of analysing cases with cumulative laser pulses, the variation of the thermal physical properties of the materials with the temperature should be hypothesised to maintain a reliable simulation result. Finally, it must be taken into account that the simulations were carried out considering two different thermal conductivity values ( $k$ ) for each varnish<sup>12</sup>, which were calculated using published thermal diffusivity values ( $D$   $10^{-3}$  to  $10^{-4} \text{ cm}^2/\text{s}$  – [Fotakis *et al.* 2007, p. 36]). It should also be noted that thermal conductivity value has a significant influence on the final results of the thermal modelling.

The simulated temperature rise can be considered apparently high (especially for the Ketone N resin) and as reported by Fotakis *et al.* (2007, p. 197) microsecond laser pulses can lead to an extensive heat diffusion and thermal degradation. In spite of that, the calculated thermal diffusion time ( $t_{th} = 1/D \cdot \alpha^2$ ) across the optical penetration depth (assuming scattering negligible [Venugopalan,

---

12 The thermal conductivities used for the simulation and mathematically calculated from the provided thermal diffusivity are dammar 0.21 and  $0.021 \text{ W/m}\cdot\text{K}$ , Ketone N 0.22 and  $0.022 \text{ W/m}\cdot\text{K}$  and MS2A 0.19 and  $0.019 \text{ W/m}\cdot\text{K}$ , respectively.

Nishioka and Mikić, 1996]) has shown to be much longer than the laser pulse durations in both regimes VSP ( $\tau_L \approx 100 \mu\text{m}$ ) and SP ( $\tau_L \approx 300 \mu\text{m}$ ) modes (Table 4.24).

<b>Laser Modes</b>	→	<b>VSP (sec)</b>	<b>SP (sec)</b>
		0.0001	0.0003

Table 4.24 – Thermal diffusion time ( $t_{th}$ ) calculated for dammar, Ketone N and MS2A and compared with the laser pulse duration in VSP and SP modes.

<b>Product</b>	<b>Thermal diffusivity (D) (cm<sup>2</sup>/s)</b>	<b>Thermal diffusion time (<math>t_{th}</math>) (sec)</b>
Dammar	$10^{-3}$	0.011
	$10^{-4}$	0.110
Ketone N	$10^{-3}$	0.00051
	$10^{-4}$	0.0051
MS2A	$10^{-3}$	0.004
	$10^{-4}$	0.04

Those results satisfy the conditions for which the laser-material interaction is considered to proceed under thermal confinement (Fotakis *et al.*, 2006, p. 197).

**Dammar – VSP mode:**

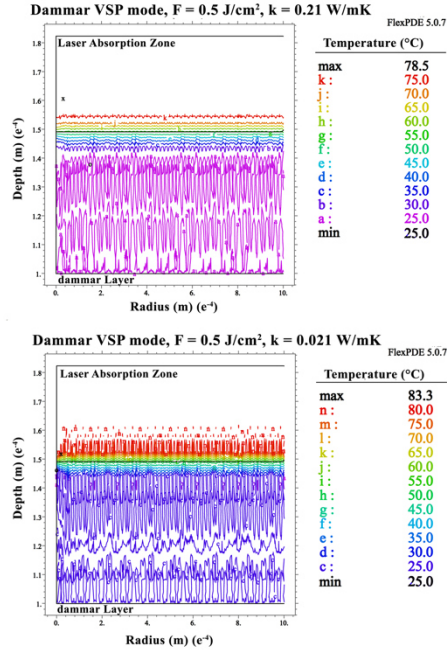


Figure 4.29 – 2D simulation of the Er:YAG laser-based heat diffusion inside the **dammar film** in VSP mode ( $\tau_L \approx 100 \mu s$ ) and temperature distribution by cross-section of varnish film + glass slide. Fluences of 0.5 J/cm<sup>2</sup>, and thermal conductivity (k) between 0.21W/m·K and 0.021W/m·K. The beam diameter was set at  $\varnothing = 4mm$ . The laser absorption zone represents the area in which the laser wavelength penetrates into the dammar film ( $\delta$ ) before releasing 63% of its energy.

**Dammar – SP mode:**

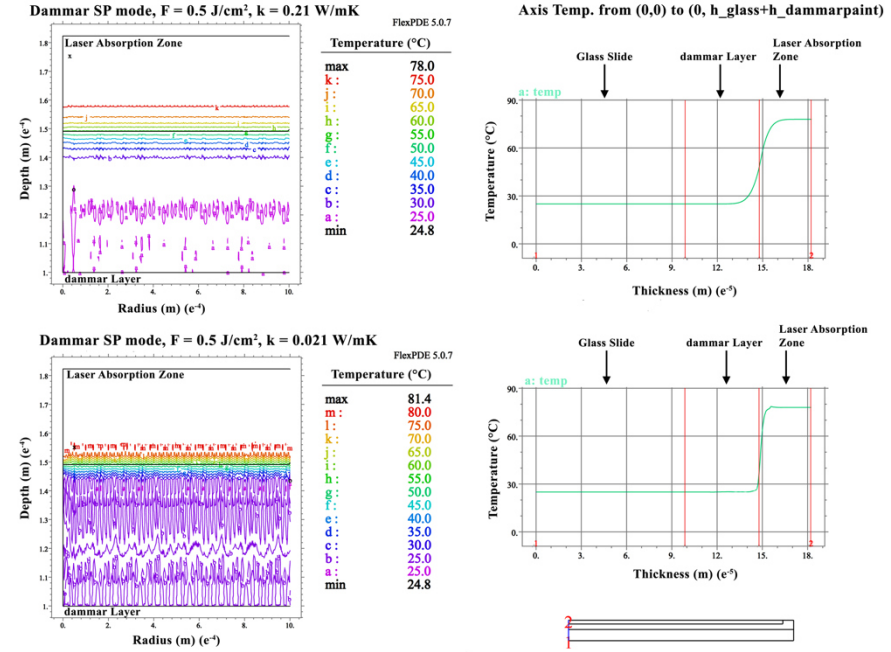


Figure 4.30 – 2D simulation of the Er:YAG laser-based heat diffusion inside the **dammar film** in SP mode ( $\tau_L \approx 300 \mu s$ ) and temperature distribution by cross-section of varnish film + glass slide. Fluences of 2.4 J/cm<sup>2</sup>, and thermal conductivity (k) between 0.21W/m·K and 0.021W/m·K. The beam diameter was set at  $\varnothing = 4mm$ . The laser absorption zone represents the area in which the laser wavelength penetrates into the dammar film ( $\delta$ ) before releasing 63% of its energy.

**Ketone N – VSP mode:**

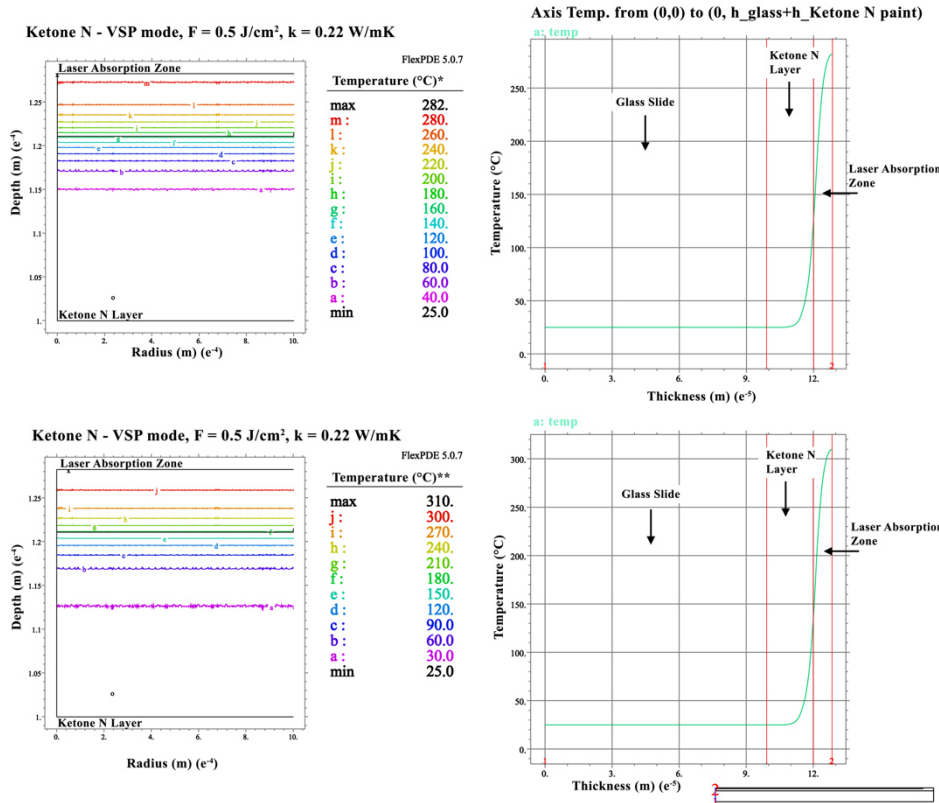


Figure 4.31 – 2D simulation of the heat diffusion inside the **Ketone N film** in VSP mode ( $\tau_L \approx 100 \mu s$ ) and temperature distribution by cross-section of varnish film + glass slide. Fluences of 0.5 J/cm<sup>2</sup> and thermal conductivity (k) of 0.22 W/m·K. One simulation was run using the %R from the FTIR (\*) the other using the %R from the Fresnel equation (\*\*). The beam diameter was set at  $\varnothing = 4mm$ . The laser absorption zone represents the area in which the laser wavelength penetrates into the Ketone N film ( $\delta$ ) before releasing 63% of its energy.

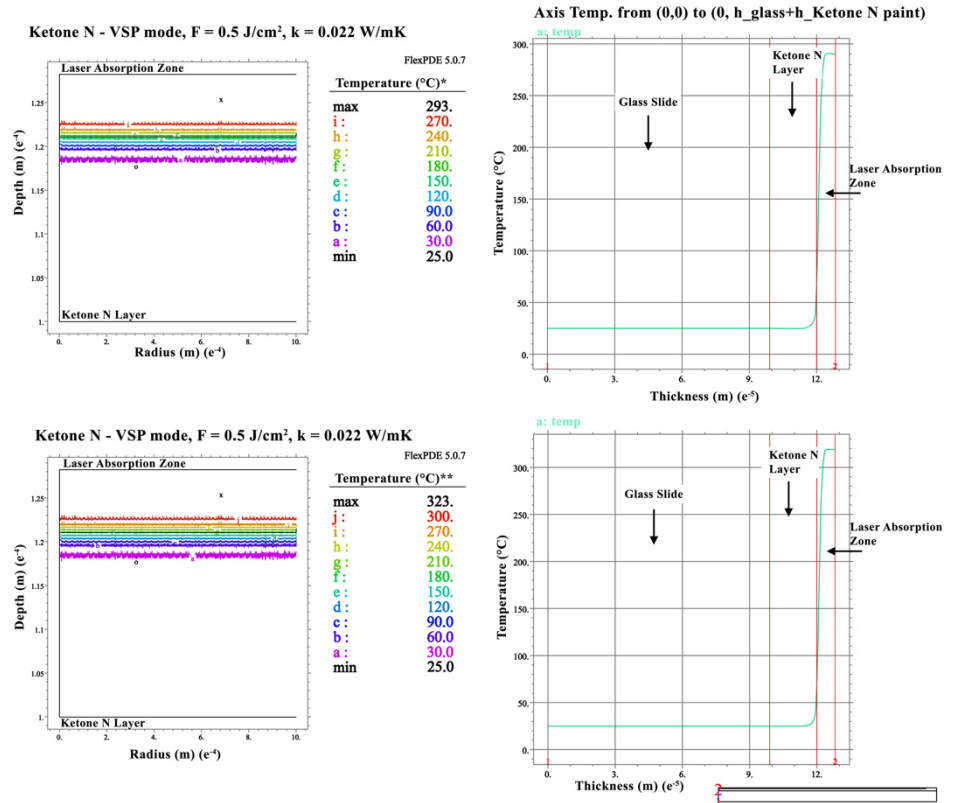


Figure 4.32 – 2D simulation of the heat diffusion inside the **Ketone N film** in VSP mode ( $\tau_L \approx 100 \mu s$ ) and temperature distribution by cross-section of varnish film + glass slide. Fluences of 0.5 J/cm<sup>2</sup> and thermal conductivity (k) of 0.022 W/m·K. One simulation was run using the %R from the FTIR (\*) the other using the %R from the Fresnel equation (\*\*). The beam diameter was set at  $\varnothing = 4mm$ . The laser absorption zone represents the area in which the laser wavelength penetrates into the Ketone N film ( $\delta$ ) before releasing 63% of its energy.

**Ketone N – SP mode:**

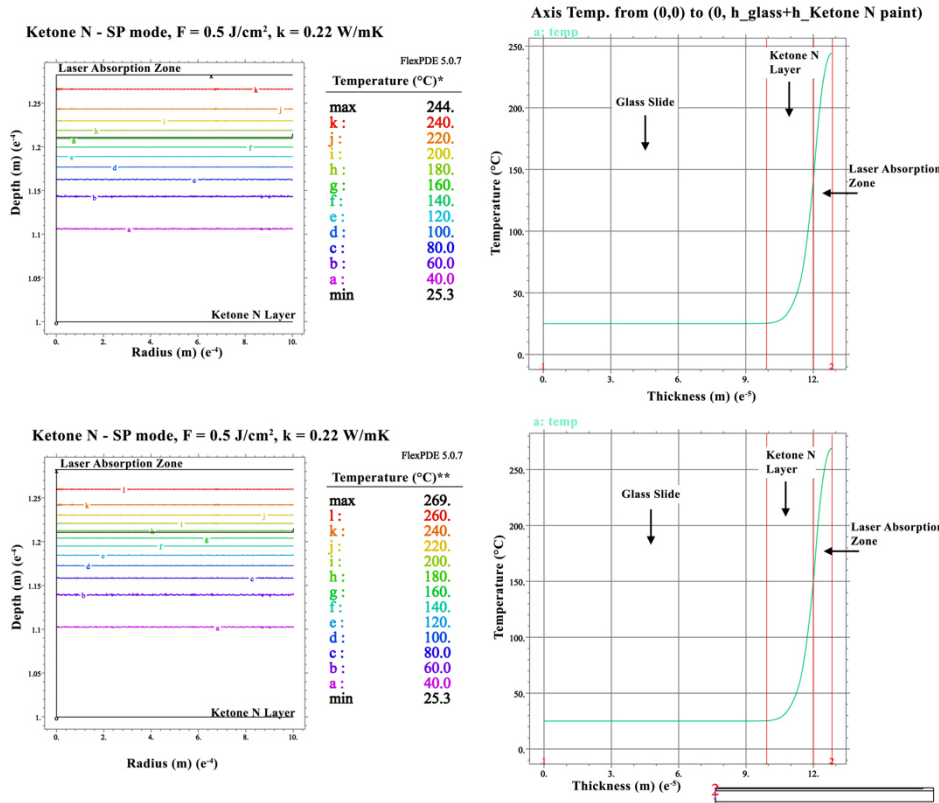


Figure 4.33 – 2D simulation of the heat diffusion inside the **Ketone N film** in SP mode ( $\tau_L \approx 300 \mu\text{s}$ ) and temperature distribution by cross-section of varnish film + glass slide. Fluences of  $0.5 \text{ J/cm}^2$  and thermal conductivity ( $k$ ) of  $0.22 \text{ W/m}\cdot\text{K}$ . One simulation was run using the %R from the FTIR (\*) the other using the %R from the Fresnel equation (\*\*). The beam diameter was set at  $\varnothing = 4\text{mm}$ . The laser absorption zone represents the area in which the laser wavelength penetrates into the Ketone N film ( $\delta$ ) before releasing 63% of its energy.

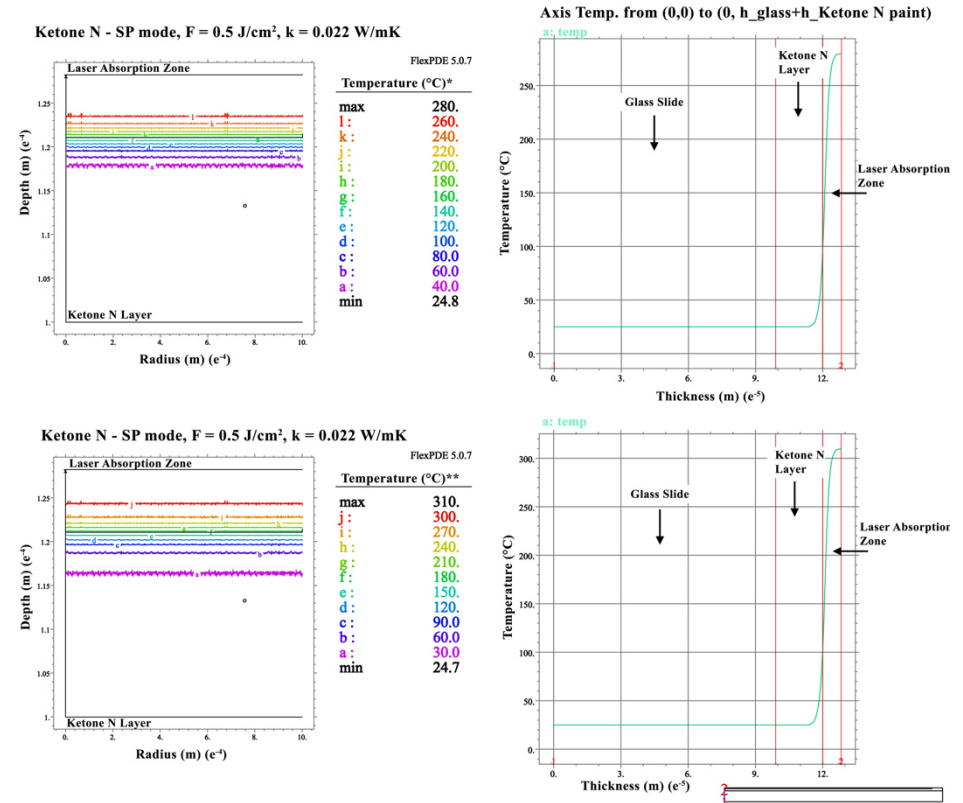


Figure 4.34 – 2D simulation of the heat diffusion inside the **Ketone N film** in SP mode ( $\tau_L \approx 300 \mu\text{s}$ ) and temperature distribution by cross-section of varnish film + glass slide. Fluences of  $0.5 \text{ J/cm}^2$  and thermal conductivity ( $k$ ) of  $0.022 \text{ W/m}\cdot\text{K}$ . One simulation was run using the %R from the FTIR (\*) the other using the %R from the Fresnel equation (\*\*). The beam diameter was set at  $\varnothing = 4\text{mm}$ . The laser absorption zone represents the area in which the laser wavelength penetrates into the Ketone N film ( $\delta$ ) before releasing 63% of its energy.

**MS2A – VSP mode:**

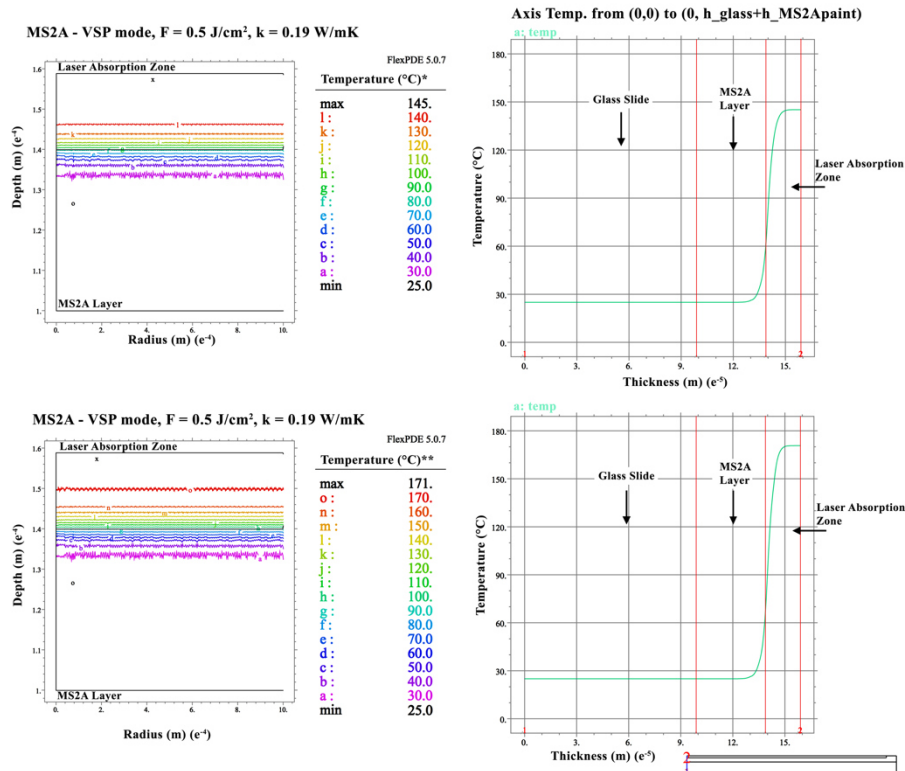


Figure 4.35 – 2D simulation of the heat diffusion inside the **MS2A film** in VSP mode ( $\tau_L \approx 100 \mu\text{s}$ ) and temperature distribution by cross-section of varnish film + glass slide. Fluences of  $0.5 \text{ J/cm}^2$  and thermal conductivity ( $k$ ) of  $0.19 \text{ W/m}\cdot\text{K}$ . One simulation was run using the %R from the FTIR (\*) the other using the %R from the Fresnel equation (\*\*). The beam diameter was set at  $\varnothing = 4\text{mm}$ . The laser absorption zone represents the area in which the laser wavelength penetrates into the MS2A film ( $\delta$ ) before releasing 63% of its energy.

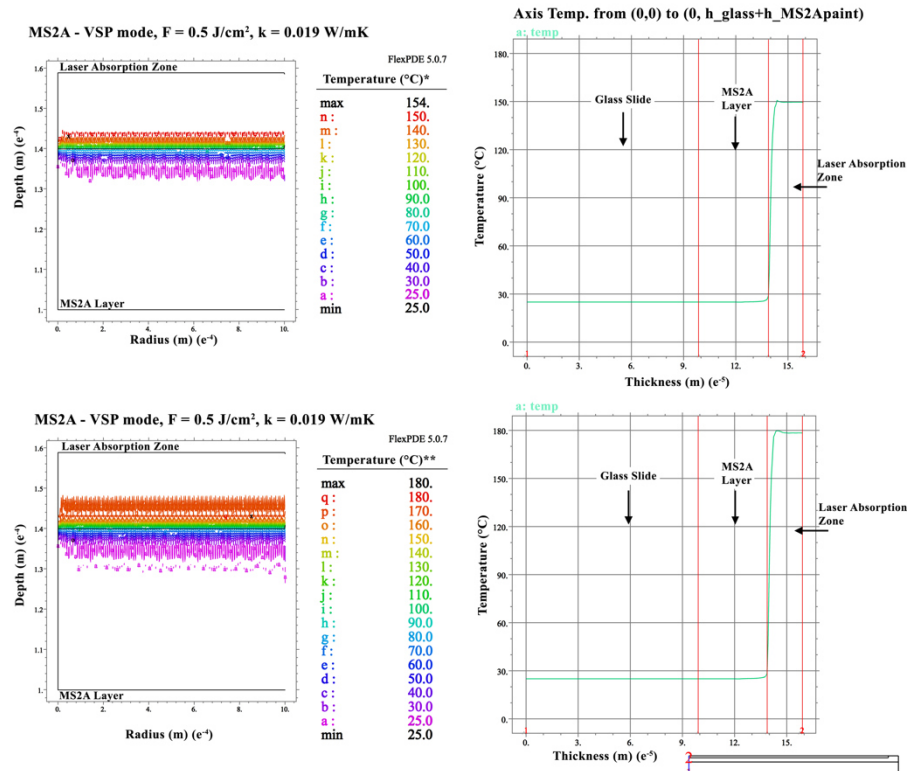


Figure 4.36 – 2D simulation of the heat diffusion inside the **MS2A film** in VSP mode ( $\tau_L \approx 100 \mu\text{s}$ ) and temperature distribution by cross-section of varnish film + glass slide. Fluences of  $0.5 \text{ J/cm}^2$  and thermal conductivity ( $k$ ) of  $0.019 \text{ W/m}\cdot\text{K}$ . One simulation was run using the %R from the FTIR (\*) the other using the %R from the Fresnel equation (\*\*). The beam diameter was set at  $\varnothing = 4\text{mm}$ . The laser absorption zone represents the area in which the laser wavelength penetrates into the MS2A film ( $\delta$ ) before releasing 63% of its energy.

**MS2A – SP mode:**

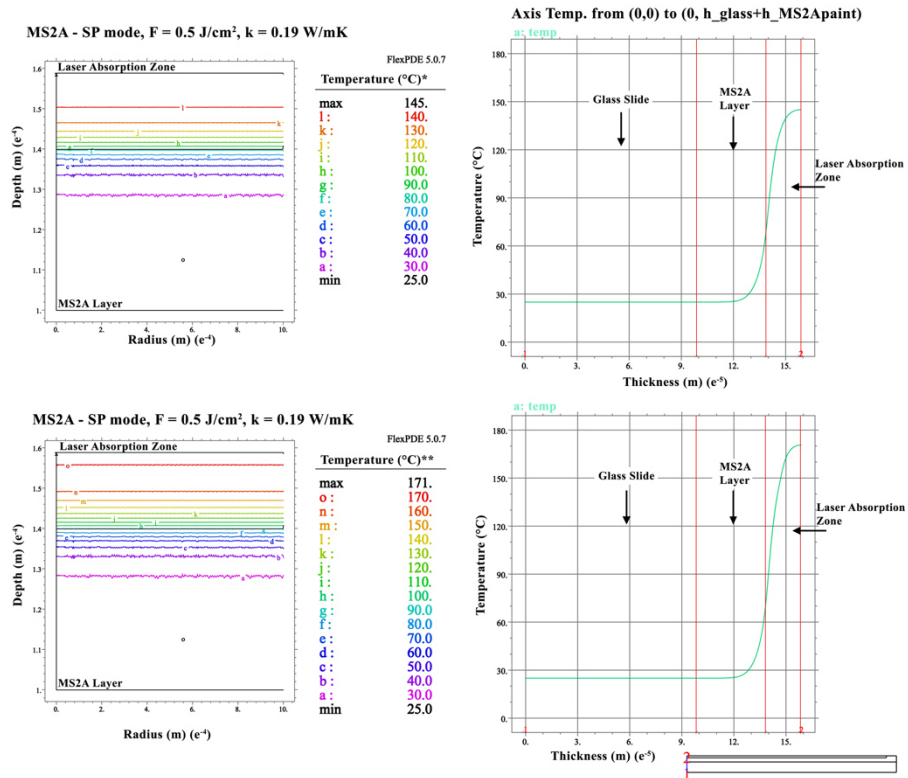


Figure 4.37 – 2D simulation of the heat diffusion inside the **MS2A film** in SP mode ( $\tau_L \approx 300 \mu\text{s}$ ) and temperature distribution by cross-section of varnish film + glass slide. Fluences of  $0.5 \text{ J/cm}^2$  and thermal conductivity ( $k$ ) of  $0.19 \text{ W/m}\cdot\text{K}$ . One simulation was run using the %R from the FTIR (\*) the other using the %R from the Fresnel equation (\*\*). The beam diameter was set at  $\varnothing = 4\text{mm}$ . The laser absorption zone represents the area in which the laser wavelength penetrates into the MS2A film ( $\delta$ ) before releasing 63% of its energy.

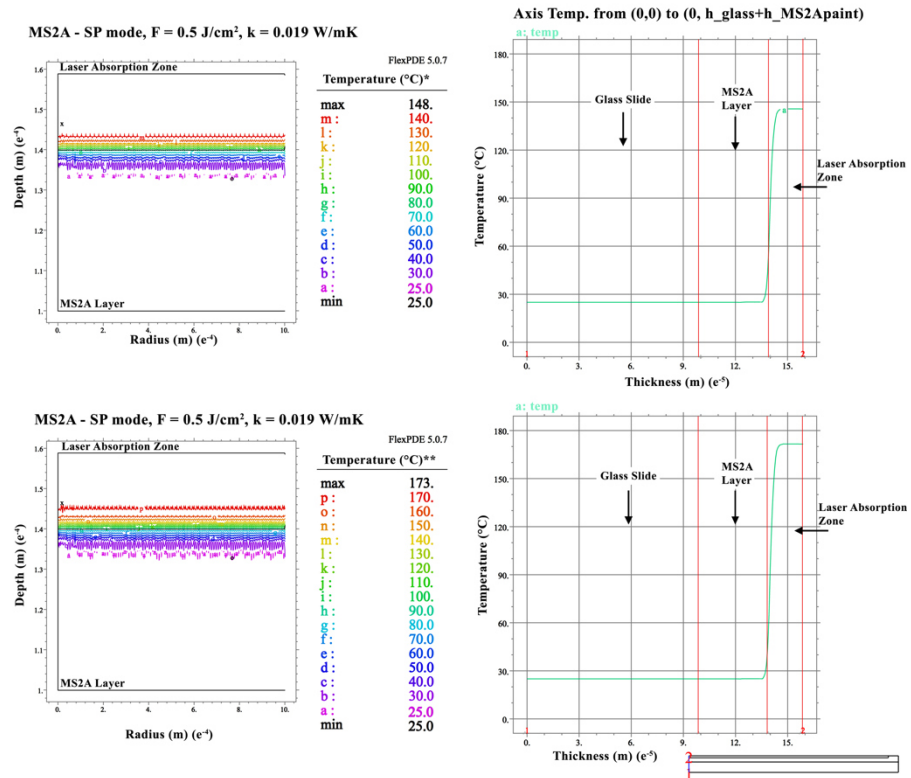


Figure 4.38– 2D simulation of the heat diffusion inside the **MS2A film** in SP mode ( $\tau_L \approx 300 \mu\text{s}$ ) and temperature distribution by cross-section of varnish film + glass slide. Fluences of  $0.5 \text{ J/cm}^2$  and thermal conductivity ( $k$ ) of  $0.019 \text{ W/m}\cdot\text{K}$ . One simulation was run using the %R from the FTIR (\*) the other using the %R from the Fresnel equation (\*\*). The beam diameter was set at  $\varnothing = 4\text{mm}$ . The laser absorption zone represents the area in which the laser wavelength penetrates into the MS2A film ( $\delta$ ) before releasing 63% of its energy.

#### 4.4 Conclusion

An Er:YAG laser was used to irradiate aged dammar, Ketone N, MS2A and Paraloid B67 varnish films.

Two procedures have been employed to examine temperature changes upon laser irradiation, addressing *objective d*. In the first procedure, the IR thermal camera recorded the maximum temperatures in real time during the laser irradiation on the varnishes with fluences ranging from 0.6 to 2.4 J/cm<sup>2</sup>, a 3 mm laser beam diameter and a pulse repetition rate of 2 Hz. The  $\Delta T_{\text{mean}}$  values, on the pre-wet irradiated varnishes with DI-W+TW20, were generally higher than on the dry varnishes, because in the former the aqueous film vaporised due to the generated heat on the surface. The use of the thermal acquisition technique highlighted that a 30 Hz thermal camera did not provide reliable temperature data due to discrepancies of the pulse durations ( $\tau_L \approx 100$  and 300  $\mu\text{s}$ ) and the camera acquisition rate (30 Hz).

The second procedure was based on the mathematical determination of the rate of heat transfer into the films while the irradiated varnishes underwent a transition from one equilibrium state to another. Infrared spectroscopy and DSC analysis allowed extrapolation of the optical properties of the varnishes with which the temperature rise associated to laser irradiation was determined. In particular, when using Eq. 4.13 (section 4.3.3.2.1), the maximum temperatures generated within the thermal diffusion lengths of the films (2–11  $\mu\text{m}$ ) were determined. Ketone N varnish, at an operational fluence of 1 J/cm<sup>2</sup>, has returned the highest  $\Delta T$  values with estimated temperatures in VSP mode ( $\tau_L \approx 100$   $\mu\text{s}$ ) between 265 °C (for  $D \approx 10^{-3}$  cm<sup>2</sup>/sec) and 485 °C (for  $D \approx 10^{-4}$  cm<sup>2</sup>/s), and between 139 °C and 395 °C in SP mode ( $\tau_L \approx 300$   $\mu\text{s}$ ). Conversely, at the same fluence, dammar film returned the lowest  $\Delta T$  values. The calculated temperatures reached in VSP mode were between 121 °C and 138 °C and between 105 °C and 132 °C in SP mode. MS2A film gave  $\Delta T$  values between these ranges, with estimated temperatures in VSP mode from 201 °C to 252 °C and in SP mode from 157 °C to 233 °C.

As poly(isobutyl methacrylate), Paraloid B67, does not contain hydroxyl groups the resin was transparent to the Er:YAG laser wavelength (2940 nm). This returned the lowest temperature rise both at the surface and in the bulk of the film, and therefore 90% of the Er:YAG laser radiation passed through the Paraloid B67 film onto the underlying layer.

By solving the equation proposed by Carslaw and Jaeger (1959, p. 80) using Eq. 4.17 (see section 4.3.3.2.2), the mathematical model assumed that the rate of heat production per unit of time per unit of volume is generated within the varnish layer surfaces, thus considering the absorption coefficient of each varnish. The mathematical model was considered with an initial temperature of the varnish surface at 25 °C (room temperature). In this case, the temperature distribution in the irradiated Paraloid B67 was not processed because its optical absorption depth ( $\delta = 497.1 \mu\text{m}$ ) was longer than the varnish film thickness (51.3  $\mu\text{m}$ ), thus implying a direct interaction with the underlying layer which would lead to a compromised mathematical computation. Also, in this case, Ketone N film returned the highest estimated temperature after  $\tau_L$  for both VSP and SP modes. Comparing the Ketone N thermal data with those of the irradiated dammar, the estimated temperatures were 70% lower than Ketone N (for  $D \approx 10^{-3} - 10^{-4} \text{ cm}^2/\text{sec}$ ) in the VSP mode, and between 64% (for  $D \approx 10^{-3} \text{ cm}^2/\text{sec}$ ) and 70% (for  $D \approx 10^{-4} \text{ cm}^2/\text{sec}$ ) in SP mode. The same process was carried out for the MS2A films. The estimated temperatures were lower than the ones mathematically obtained for Ketone N. The decrement of the MS2A temperatures ranged between 45 % for  $D \approx 10^{-3}$ , considering reflectance data obtained from the FT-IR data and the Fresnel Equation, and 50 % for  $D \approx 10^{-4}$  in the VSP mode. This also applied for the SP mode with a decrement of about 40 % for  $D \approx 10^{-3}$  and 50 % for  $D \approx 10^{-4}$ . In all presented cases (section 4.3.3.2.2), the diffusion of heat inside the varnishes, which tended to decrease asymptotically to room temperature, has been demonstrated by solving the heat diffusion equation for semi-infinite homogeneous materials (Majaron, Plestenjak and Lukac, 1999).

A 2D simulation allowed to detect a more precise heat distribution inside the varnish films as the fluence was increased from 0.5 up to 2.4  $\text{J}/\text{cm}^2$  at two different laser pulse durations,  $\tau_L \approx 100$  and 300  $\mu\text{s}$ , in VSP and SP modes, respectively. The effect of the two distinct regimes depended on the thermal conductivity ( $k$ ) (Table 4.15) and for Ketone N and MS2A, two different reflectance data were also examined. The simulation showed a defined increase in temperature confined to the laser absorption zone of the dammar, Ketone N and MS2A films. It is extremely important to highlight that all the simulations showed that the temperature at the interface between the aged coating films and the substrate (in this case glass slides) remained at the room temperature of 25 °C.

In all the thermal studies considered (including the mathematical estimation, the thermal modelling and the thermal camera recordings employing the same energy density but with two different pulse durations), it was possible to detect that in the VSP mode the maximum temperature was achieved, even though it penetrated less inside the material. Conversely, in the SP mode, all the irradiated films were less heated, but the average temperature of the area close to the absorption of the laser energy was higher.

Transmission rates were acquired for the dry and pre-wet irradiated films at a fluence of 0.5, 1, 1.5, 2.1 and 2.4 J/cm<sup>2</sup>. This study addressed *objective e*. It was shown that the energy transmitted increased almost linearly with fluence. The increasing trends in  $E_{trans}$  and therefore %T with fluence, could be related to the increase with fluence values (Chillè *et al.*, 2020), as the laser irradiated films are thinned and disrupted. In general, the application of DI-W+TW20 resulted in reduced beam propagation into the selected varnishes. The dammar film showed to have the highest  $E_{trans}$  values both in dry and pre-wet surfaces with DI-W+TW20, in VSP and SP modes. However, ketone resins presented the lowest  $E_{trans}$  values in VSP and SP modes both in dry and pre-wetting the surfaces with DI-W+TW20. Ketone N and MS2A resulted in absorbing most of the laser beam energy, thereby lowering the amount of energy interacting with the underlying paint layer.

## CHAPTER 5 Er:YAG LASER TESTS (Part II): Microscopies and Spectroscopic investigations

*The laser-material interaction of the aged triterpenoid (dammar), two ketones (Ketone N and MS2A) and an acrylic (Paraloid B67) varnishes with the Er:YAG laser in VSP and SP modes was investigated. Optical Microscopy (OM) evidenced that the laser had no impact on the Paraloid B67 films. The laser spots on the irradiated varnishes with fluences ranging from 0.6 to 2.5 J/cm<sup>2</sup> were observed with Backscattered-Electro (BSE) Scanning Electron Microscopy (SEM) addressing **objective f**. In dry irradiation and at the lowest fluence the following was observed: locally swollen areas and the formation of circular spots on dammar; lift-off phenomena upon a single pulse on MS2A; and, almost negligible response on Ketone N. By eventually increasing the fluence, BSE-SEM imaging provided evidence of deep melting and the formation of craters and bubbles into these films. The appearance of the spots at 2.5 J/cm<sup>2</sup> was almost identical in the dammar and the ketone films. Compared to the dry irradiated films, the DI-W TW20 pre-wetted dammar and ketone varnishes showed less marked spots in all fluences tested. BSE-SEM of dry irradiated varnishes after multiple-pulse in VSP and SP modes showed more swollen surfaces and more pronounced concentric rings. The DI-W+TW20 pre-wetted dammar and MS2A surfaces, at the highest laser fluence of 2.5 J/cm<sup>2</sup>, has shown a partial shrinkage and/or probable partial removal of the coatings.*

*Attenuated Total Reflection (ATR)/Fourier Transform Infrared (FT-IR) spectroscopy shed some light on compositional modifications of the irradiated varnishes within the laser spots addressing **objective g**. In dry irradiation, a significant reduction of ratios of integrated areas of hydroxide, OH, groups (2700-3700 cm<sup>-1</sup>) and carbonyl, C=O groups (1500-1900 cm<sup>-1</sup>) over carbon-hydrogen, C-H bands (2850-3000 cm<sup>-1</sup>) were observed in the dammar and Ketone N films as a function of fluence. In DI-W TW20 pre-wetted irradiation, the OH/CH and CO/CH band ratios resulted in a similar trend to the dry dammar film, but in a less evident*

trend in Ketone N. The OH/CH and CO/CH band ratios of the dry and pre-wetted irradiated MS2A film showed no significant change as a function of fluence.

## 5.1 An introduction on the use of Er:YAG laser in Conservation

The application of lasers for the removal of coatings from works of art is a challenging process due to the high sensitivity of the materials constituting these surfaces.

The highly selective absorption of the 2940 nm Er:YAG laser for hydroxyl groups, which are present in constituent materials of cultural heritage objects (e.g., varnishes, pigments and binders), can lead to diverse photo-thermal and mechanical effects on the surface of coated artworks (De Cruz *et al.*, 2014).

Andreotti *et al.* (2007) stated that the mechanism of interaction between the Er:YAG laser and the surface of the unwanted material consisted of an only slight breakage of few microns depth on the irradiated surface, enabling conservators to complete the cleaning by using ‘traditional’ cleaning methods (e.g., medium polarity organic solvents) or aqueous solutions (Wolbers, 2000; Cremonesi, 2011; Hackney, 2013; Phenix, 2013). As reported by Teppo (2020), the Er:YAG laser exposure of a dry surface leads to an increase in the surface roughness and light scatter of the targeted unwanted material. The laser-material interaction increases the surface area exposed to solvents, therefore speeding the clearing rate and improving the cleaning process (Figure 5.1).

Andreotti *et al.* (2007) also reported that in the event that the contaminated material does not contain OH groups, the application of a thin layer of hydroxylated agents before the laser irradiation can increase the efficiency of the Er:YAG laser process, decreasing the penetration of the laser beam into the underlying substrate (Andreotti *et al.*, 2007) (Figure 5.2). In fact, in order to maximise the 2940 nm beam absorption at the surface, it is a common practice to pre-wet the area with aqueous or OH-containing solutions. Moreover, the use of water is necessary as it prevents temperature build-up in the irradiated material (Diaci and Gaspirc, 2012).

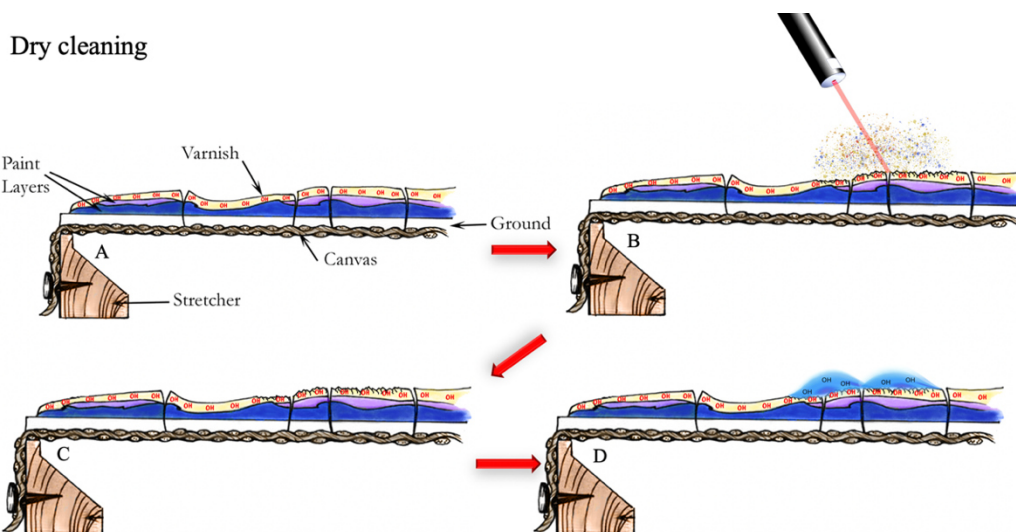


Figure 5.1 – Graphical representation of the Er:YAG laser irradiation of a dry surface: (A) if the coating contains O-H groups, the laser wavelength is strongly adsorbed by the hydroxyl groups in the unwanted layer. (B) The laser irradiation leads to heating, rapid expansion and ejection of fragments from the irradiated material. (C) The photo-thermal disaggregation causes the formation of a whitish appearance created by the light scattering. (D) The use of solvents allows to carry on with the thinning of the coating surface.

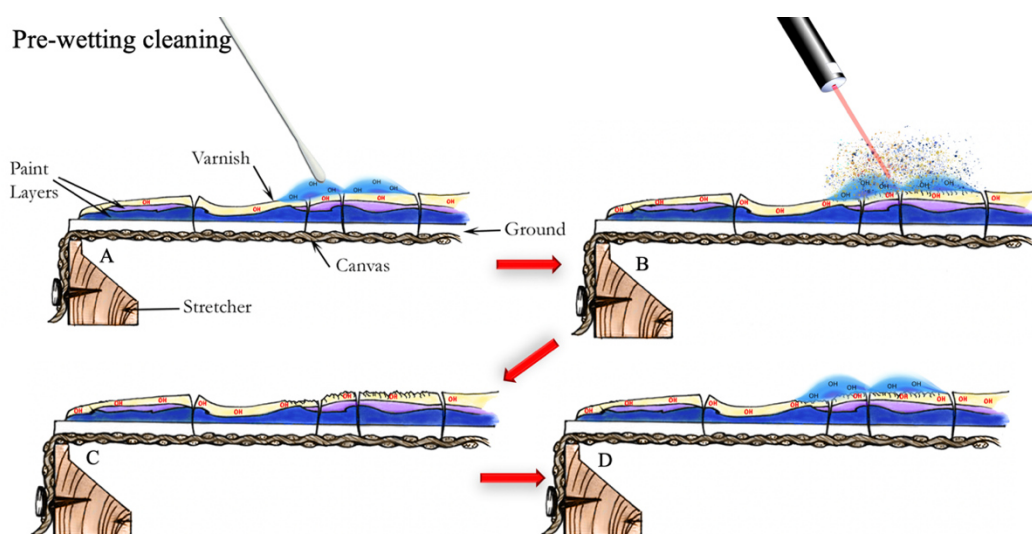


Figure 5.2 – Graphical representation of the Er:YAG laser irradiation pre-wetting the surface: (A) if the coating do not have enough O-H groups, the surface can be wetted with an OH-containing liquid. (B) The laser irradiation leads to liquid-phase expulsion, rapid expansion and ejection of liquid droplets and fragments from the irradiated material. (C) The photo-thermal disaggregation causes the formation of a whitish appearance created by the light scattering. (D) The use of solvents allows the continuation of the thinning of the coating surface.

As a rule of thumb, the ideal approach for the treatment of coated surfaces with the use of an Er:YAG laser is to thin the targeted layers first instead of attempting their full removal (De Cruz, Wolbarsht and Hauger, 2000a; Pereira-Pardo and Korenberg, 2018). This process can be obtained by setting the laser parameters such as fluence, pulse width, repetition rate and beam size in accordance with the chemical compositions of the materials in the substrates.

In this chapter the dry and pre-wet the Er:YAG laser irradiated triterpenoid (dammar), ketone (Ketone N and MS2A) and the poly(isobutyl methacrylate) (Paraloid B67) varnishes at Very Short Pulse VSP ( $\tau_L \approx 100 \mu\text{s}$ ) and Short Pulse SP ( $\tau_L \approx 300 \mu\text{s}$ ) modes are presented. The morphology of the laser spots was observed by means of Optical Microscopy (OM) and Backscattered-Electro (BSE) Scanning Electron Microscopy (SEM) and their compositional modifications were observed with Attenuated Total Reflection (ATR)/Fourier Transform Infrared (FT-IR) spectroscopy.

## **5.2 Material and methods**

### *5.2.1 Er:YAG lasers*

The Er:YAG laser tests instrumentation and parameters are detailed in section 4.2.1. The R11 handpiece was fixed and mounted on top of the samples at a 20 cm working distance between the handpiece end and the samples surface. The beam diameter was set at 4 mm, both in the handpiece and in the laser displays, and the pulse repetition rate at 2 and 5 Hz. Prior to each laser tests, the laser beam diameter was measured on a photosensitive black paper to check that the dimension of the selected diameter in the laser displays and the delivered beam were comparable. The laser irradiation tests were carried out in fluences, as shown in the laser's unit displays and single laser pulses, ranging between 0.5 and 2.5 J/cm<sup>2</sup> (depending on the laser unit selected), were fired onto dry and pre-wetted dammar, Ketone N, MS2A and Paraloid B67 varnish sample surfaces. For the water-assisted tests, an mixture of 1% (v/v) of a non-ionic surfactant (Tween 20 — Sigma Aldrich) in 50 mL of deionised water (DI-W+TW20) (Cremonesi and Signorini, 2012) was applied with a cotton swab, firstly drained on a blotting paper, and rolled onto the surface three times. The varnish surfaces were pre-wetted at the beginning of each laser scan.

### *5.2.2 Microscopies*

All the varnish films after ageing were observed using a USB microscopic camera (Dino-Lite AM313). The laser spots onto the varnish films were observed in reflected light with a Leica Stereo Zoom S6 D 6.3:1 stereomicroscope (×6.3–20 magnification) that provided a field of view up to 36.5mm. A Leica MC170 HD Microscope Camera (5 Megapixel HD) and a set of LED fibre optic lights were employed to capture the microphotographs. The laser-irradiated areas on the Paraloid B67 films were observed with a standard Olympus BX51 Metallurgical Microscope (coupled with a 100 W mercury power supply) in transmitted light and brightfield with a 5X Olympus microscope objective. A digital CCD camera (Olympus DP70 with an ultra-high resolution of 4080 x 3072 pixels) was used to acquire the images which were processed with Image ProPlus v.6.2 system.

Scanning electron microscopy (SEM) was performed using a TESCAN MIRA 3 with gigantic chamber equipped with a 4-Quadrant semiconductor (solid-state) backscattered-electro (BSE) detector. The treated surfaces were analysed in low vacuum condition at 0.2 mbar, and the system operated at 20 kV acceleration voltage and a spot size of 5.8 nm. Spots were observed at 4.37 mm, 2.49 mm, 1.55 mm fields of view.

### 5.2.3 Attenuated Total Reflection/Fourier Transform Infrared Spectroscopy (ATR/FT-IR)

ATR/FT-IR analysis aimed to assess the laser-induced modifications upon 2490 nm laser irradiation between untreated and treated dammar, MS2A and Ketone N coating. All the FT-IR spectra in this research have been performed with Attenuated Total Reflection (ATR) since the simplicity in the technique only needs the contact of the ATR crystal with the examined coating films (Pemble and Gardner, 2009). The ATR/FT-IR analysis were obtained using the same bench spectrometer as described in section 3.4.9. The non-irradiated and irradiated films, after five consecutive laser pulse released in the same place at 5 Hz of repetition rate, were placed directly on the diamond window and pressed (up to pressure gauge of 100). The ATR/FT-IR spectra were processed with the same software Perkin Elmer SpectrumTM 10.

A semi-quantitative analysis was carried out, aiming at the comparison of specific absorbance bands, conducted with the spectra obtained from the varnish mock-ups related to the states before and after the ageing and the laser irradiations. The integrated areas of the peaks corresponding to stretching vibrations of hydroxide ( $2700-3700\text{ cm}^{-1}$ ), C–H ( $2850-3000\text{ cm}^{-1}$ ) and carbonyl ( $1500-1900\text{ cm}^{-1}$ ) bands were determined (Ciofini, 2014, p. 58; Chillè *et al.*, 2020). Consequently, the ratios of the integrated areas of the selected OH/CH and the C = O/CH band were also determined. The generated data were compared to the non-irradiated samples to monitor any possible chemical changes after laser irradiation (Chillè *et al.*, 2020). The semi-quantitative analysis has been performed using OriginPro 2020 software.

### 5.3 Results and Discussion

#### 5.3.1 Laser tests on dammar, Ketone N, MS2A and Paraloid B67 films and laser-induced morphological modifications

After accelerated ageing (Section 3.4.2), the surface of dammar and Ketone N varnishes appeared cracked (Figures 5.3 and 5.5). The surface of MS2A and Paraloid B67 appeared smooth after ageing (Figures 5.4 and 5.6) as already detected with the stylus profilometer (section 3.5.1). Moreover, the aged MS2A film was fragile to the touch.

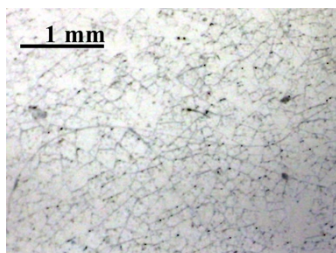


Figure 5.3 – Image taken with Dino-Lite microscope of the dammar varnish surface after ageing.

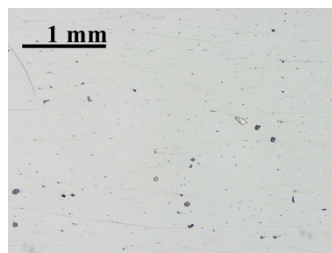


Figure 5.4 – Image taken with Dino-Lite microscope of the Paraloid B67 varnish surface after ageing.

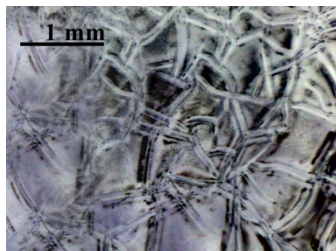


Figure 5.5 – Image taken with Dino-Lite microscope of the Ketone N varnish surface after ageing.

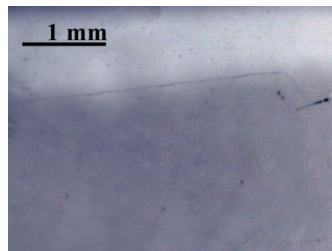


Figure 5.6 – Image taken with Dino-Lite microscope of the MS2A varnish surface after ageing.

A circular spot was identified on the dammar and both ketone varnishes upon a single laser pulse, which was gradually more defined by increasing the fluence. The spots appeared to be hazy due to increased light scattering (Figures 5.7).

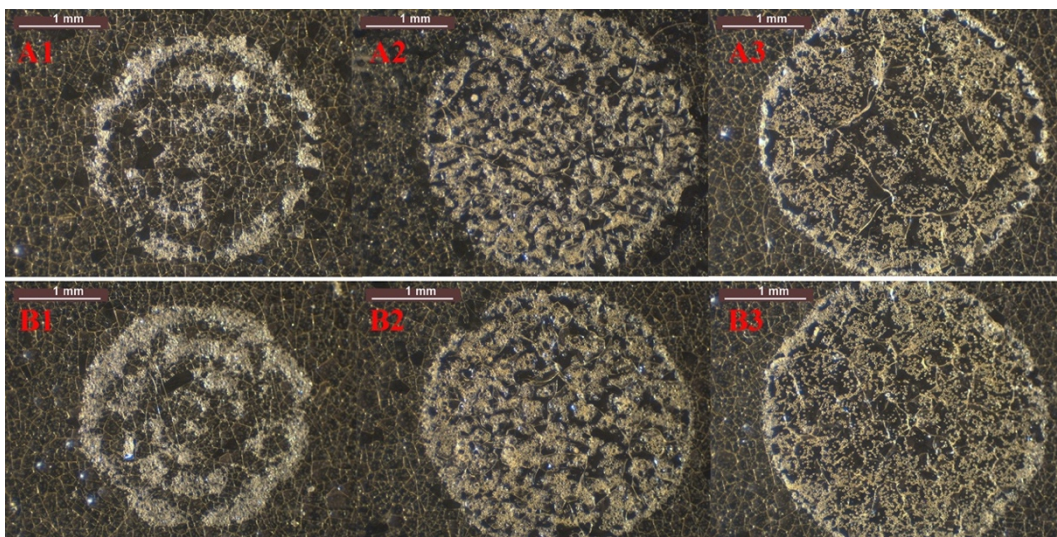


Figure 5.7 – Stereophotographs of dry irradiated dammar in VSP (A1–A3) and SP (B1–B3) modes. Spot diameter at  $\varnothing = 4\text{ mm}$ , pulse repetition rate 2Hz and spots generated by fluences of  $0.6\text{ J/cm}^2$  (A1 and B1),  $1.6\text{ J/cm}^2$  (A2 and B2) and  $2.5\text{ J/cm}^2$  (A3 and B3).

The dry and the pre-wetted Paraloid B67 films did not display any detectable spot even at the higher fluence of  $2.5\text{ J/cm}^2$  (Figure 5.8). This observation corroborated the data obtained in the transmission studies presented in sections 4.3.1 and 4.3.2.

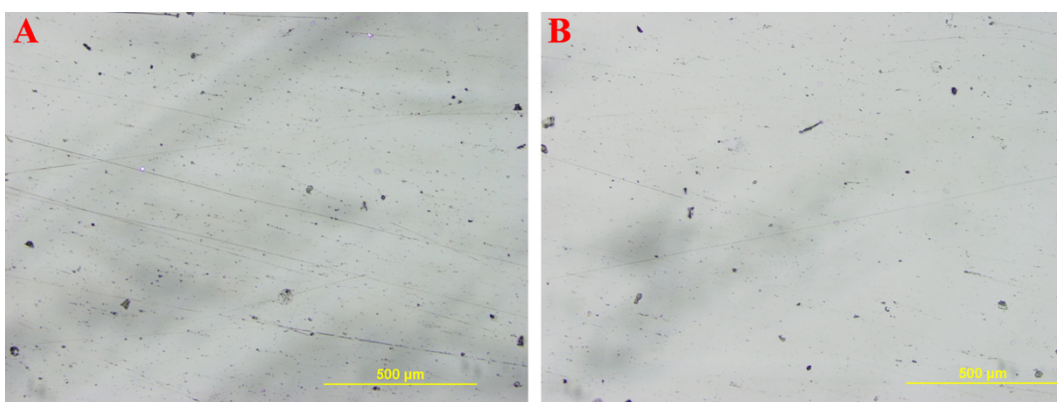


Figure 5.8 – Brightfield Optical Microscopy (OM) micrographs the dry irradiated Paraloid B67 in VSP mode ( $\tau_L \approx 100\ \mu\text{s}$ ). Spot diameter at  $\varnothing = 4\text{ mm}$ , pulse repetition rate 2Hz and fluences of  $1\text{ J/cm}^2$  (A) and  $2.5\text{ J/cm}^2$  (B). No laser spots are visible in the areas irradiated with the Er:YAG laser.

### 5.3.1.1 Single Er:YAG laser tests on dammar and ketone resin films

By comparing the BSE-SEM images of the dry irradiated dammar layer in VSP (Figure 5.9) and SP modes (Figure 5.10), it was possible to observe a circular spot even at the lowest fluence of  $0.6\text{ J/cm}^2$  as the laser wavelength (2940 nm) is absorbed by the aged coating. In particular, as regards the VSP irradiation on the dry dammar surface, the morphology of the spot at that low fluence is not

significantly marked (Figure 5.9 [A, A1]), contrary to SP mode where it shows a more noticeable imprint on the varnish (Figure 5.10 [A, A1]). At  $0.6 \text{ J/cm}^2$ , it is possible to recognise partial portions of the concentric rings of the laser spatial structure of  $\text{TEM}_{31}$  mode<sup>1</sup> (Meister *et al.*, 2003) and locally swollen dammar surface (see Figures 5.9-10 [A, A1]). This is in line with the simulated temperatures in both VSP and SP modes (Tables 4.16 and 4.21, Figures 4.23-24 and 4.29-30), which are above the  $T_g$  of the resin (as determined in section 3.5.6) but below the published value for the melting point of the dammar resin.

However, by increasing the fluence, the differences in the appearance of the spots are not readily discerned. In fact, an increase in the formation of micro-pits, craters and bubbles along with a defined molten area and a “corona” of re-solidification around the irradiated resin layer were observed (Figures 5.9-10 [B, B1, C, C1]). The increase of micro-pits and craters can be attributed to a photo-thermal disaggregation caused by the selective absorption and explosive vaporisation of hydroxide-containing species in the varnish substrates (Brown and Arnold, 2010; De Cruz *et al.*, 2014; Pereira-Pardo and Korenberg, 2018). These also relate to the simulated temperature values which showed the first isotherm line at the highest fluence of  $2.4 \text{ J/cm}^2$ , in both VSP and SP modes (see Appendix B, Figures B21 and B25), between the first degradation step ( $199 \text{ }^\circ\text{C}$ ) and the second one ( $349 \text{ }^\circ\text{C}$ ) of the thermograms obtained by the TGA analysis (section 3.5.5, Table 3.7).

---

<sup>1</sup> The mode of a resonator with the index number (i.e., the  $\text{TEM}_{mn}$  mode) (Ready, 1971a).

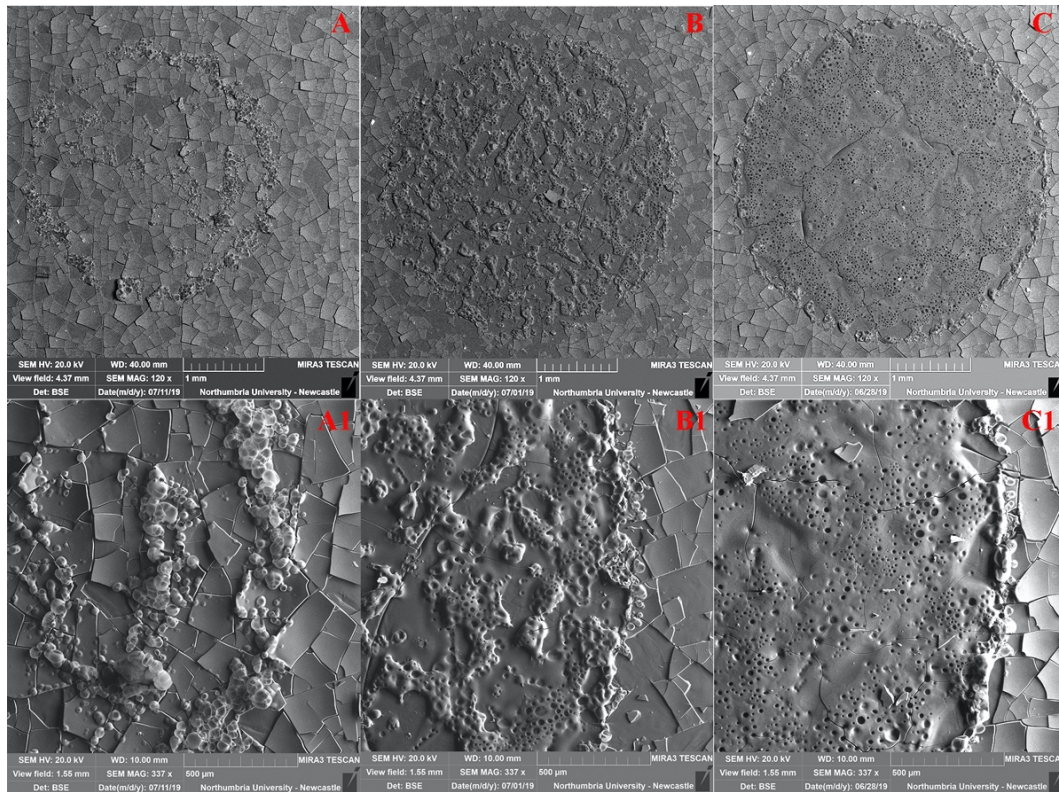


Figure 5.9 – Low vacuum BSE-SEM micrographs of the VSP single pulse dry test areas on aged **dammar films**. A and A1:  $0.6 \text{ J/cm}^2$ ; B and B1:  $1.6 \text{ J/cm}^2$ ; C and C1:  $2.5 \text{ J/cm}^2$ . Spot diameter at  $\varnothing = 4 \text{ mm}$ , pulse repetition rate 2Hz. The micro-craquelure inside the laser spots is not a result of irradiation and was observed prior to irradiation and outside the spots. In VSP, the spot diameter is increased by  $0.63 \text{ mm}$  at  $1.6 \text{ J/cm}^2$  compared to the spot at  $0.6 \text{ J/cm}^2$  and then by  $0.22 \text{ mm}$  more at  $2.5 \text{ J/cm}^2$ .

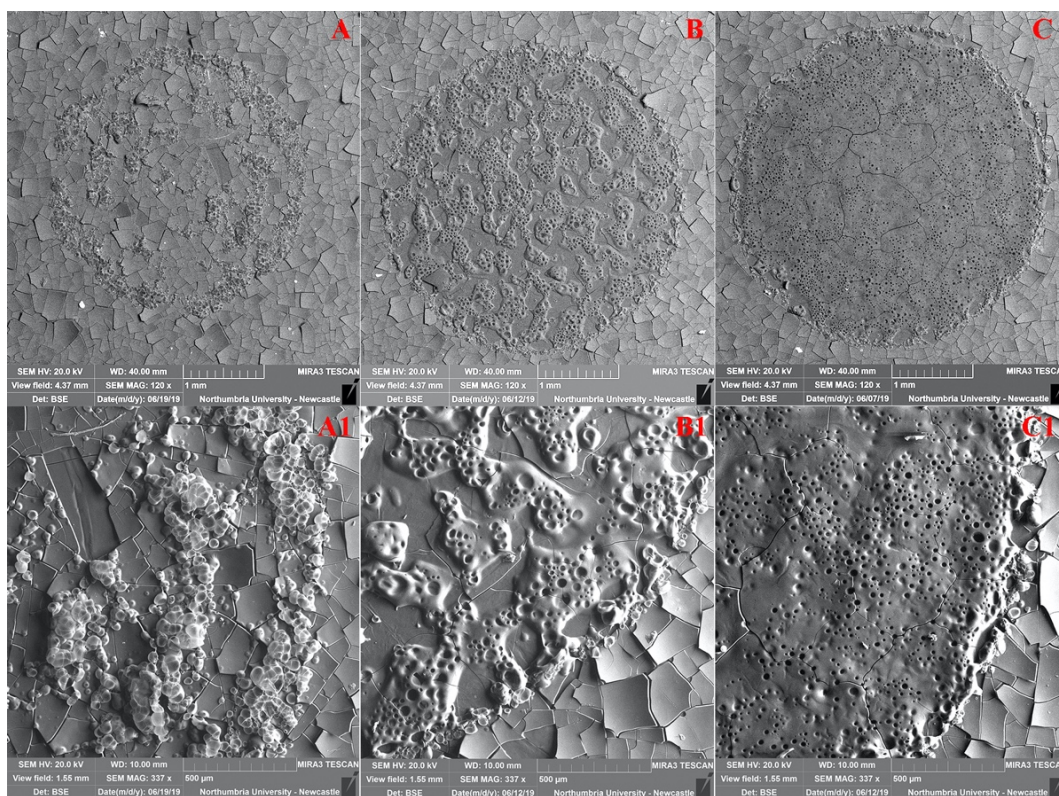


Figure 5.10 – Low vacuum BSE-SEM micrographs of the SP single pulse dry test areas on aged **dammar** films. A and A1:  $0.6 \text{ J/cm}^2$ ; B and B1:  $1.6 \text{ J/cm}^2$ ; C and C1:  $2.5 \text{ J/cm}^2$ . The micro-craquelure inside the laser spots is not a result of irradiation and was observed prior to irradiation and outside the spots. In SP, the spot diameter at  $1.6 \text{ J/cm}^2$  is  $0.54 \text{ mm}$  larger compared to the spot at  $0.6 \text{ J/cm}^2$  and by a further  $0.17 \text{ mm}$  at  $2.5 \text{ J/cm}^2$ .

The same laser tests have been carried out on the pre-wet dammar films. Upon laser irradiation, the DI-W+TW20 pre-wetted dammar surfaces show less marked laser spots when compared to the ones generated onto the dry irradiated surface (Figures 5.11-12). In this case, the single-pulse spots on the varnish at the lowest fluence is particularly difficult to detect (see Figures 5.11-12 [A, A1]). However, by increasing the fluence, the characteristic circular spots became more noticeable (see Figures 5.11-12 [B, B1, C, C1]).

Since the efficiency of the Er:YAG laser is directly proportional to the concentration of hydroxide groups in the materials, and because water is strongly absorbed at  $2940 \text{ nm}$ , the application of a thin surface layer of water with a non-ionic surfactant (DI-W+TW20) on the surface enhanced the interaction with the varnish film (Colombini *et al.*, 2003; De Cruz *et al.*, 2014; Pereira-Pardo and Korenberg, 2018). This leads to a reduction of the heat diffusion of the incident laser beam in the bulk (De Cruz, Wolbarsht and Hauger, 2000a; Andreotti *et al.*,

2016), obtaining a gentler interaction with the dammar surface. The resulting laser spots on the pre-wet dammar surface are in fact less swollen than on the dry surface and the use of the lowest fluence has resulted in a minimal interaction with the varnish surface, due to the complete absorption of laser energy in the water layer, which can only be detected at a very high magnification, such as in a view field of 1.55 mm (see Figures 5.11-12 [A1 and B1, C1]).

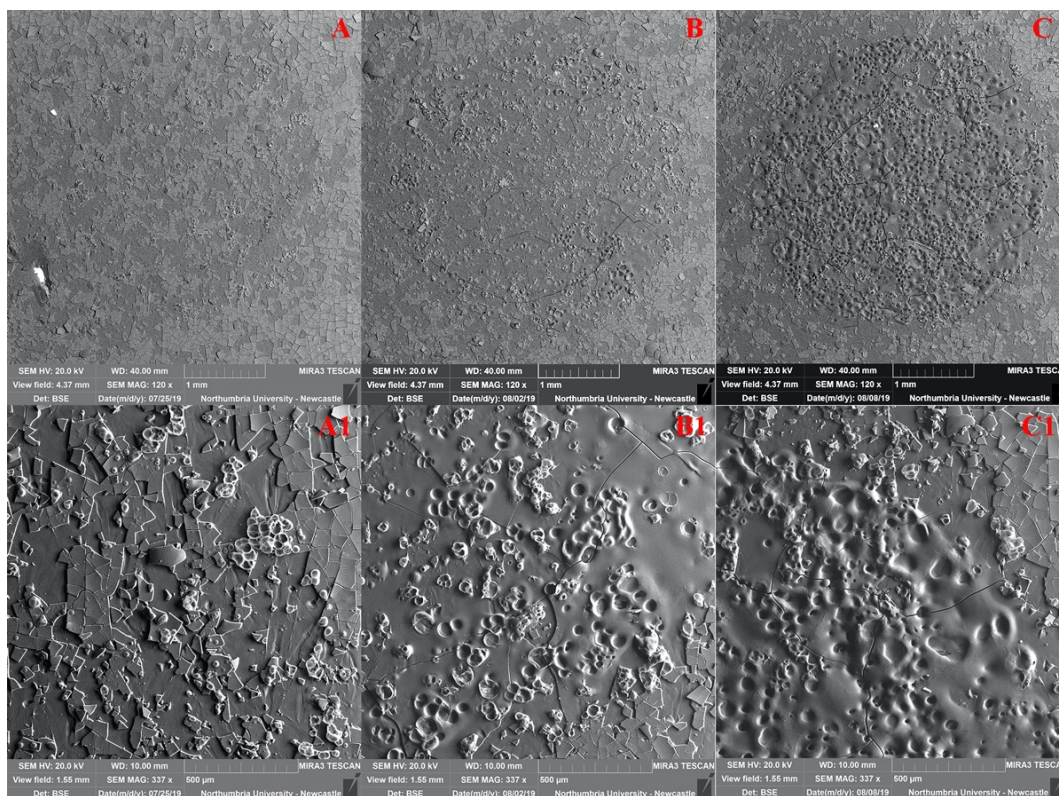


Figure 5.11 – Low vacuum BSE-SEM micrographs of the DI-W+TW20 pre-wet single pulse laser irradiated test areas in VSP mode on aged **dammar film**. A and A1: 0.6 J/cm<sup>2</sup>; B and B1: 1.6 J/cm<sup>2</sup>; C and C1: 2.5 J/cm<sup>2</sup>. The micro-craquelure inside the laser spots is not a result of irradiation and was observed prior to irradiation and outside the spots. In VSP, the spot diameter is increased by 0.37 mm at 1.6 J/cm<sup>2</sup> compared to the spot at 0.6 J/cm<sup>2</sup> and then by 0.14 mm at 2.5 J/cm<sup>2</sup>.

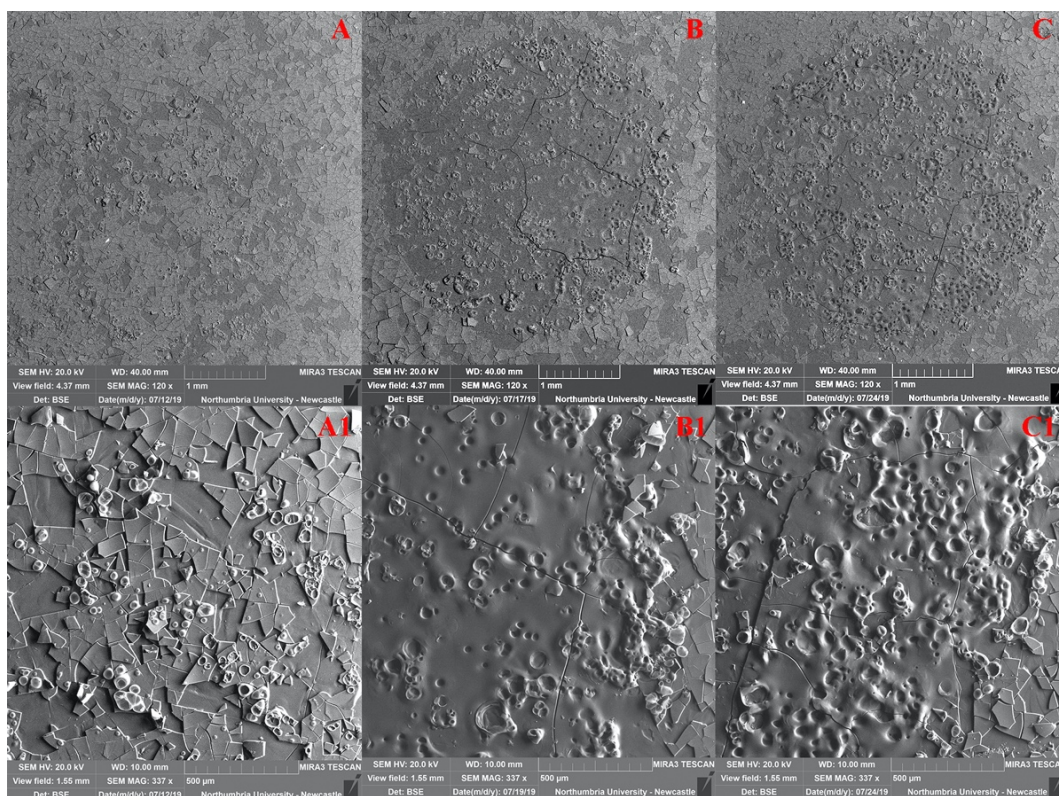


Figure 5.12 – Low vacuum BSE-SEM micrographs of the DI-W+TW20 pre-wet single pulse laser irradiated test areas in SP mode on aged **dammar** films. A and A1: 0.6 J/cm<sup>2</sup>; B and B1: 1.6 J/cm<sup>2</sup>; C and C1: 2.5 J/cm<sup>2</sup>. The micro-craquelure inside the laser spots is not a result of irradiation and was observed prior to irradiation and outside the spots. In SP, the spot diameter at 1.6 J/cm<sup>2</sup> is 0.26 mm larger compared to the spot at 0.6 J/cm<sup>2</sup> and by a further 0.17 mm at 2.5 J/cm<sup>2</sup>.

The BSE-SEM micrographs of the dry irradiated ketone resins (Ketone N and MS2A), in VSP and SP modes, (Figures 5.13-20) highlight a distinct laser-material interaction when compared to the same processed aged dammar films.

Ketone N aged films, irradiated at 0.6 J/cm<sup>2</sup> in VSP and SP modes, has resulted in a minimal interaction with the varnish surface, only detectable at high magnifications, as shown below in view fields of 1.55 and 2.49 mm (Figures 5.13-14 [A, A1]). However, lift-off phenomena have been observed on the dry irradiated MS2A films at 0.6 J/cm<sup>2</sup>, which indicate that secondary mechanical effects have been occurred possibly due to laser-induced pressure in the bulk (Figures 5.17-18 [A, A1]). Such mechanical stresses may be initiated by an increase in temperature, followed by a confined surface swelling which results in the lift-off phenomena (Bäuerle, 2011). With fluences lower than 1.6 J/cm<sup>2</sup>, the dry irradiated ketone resins showed the formation of cracking due to the drying-out of the surfaces as well as the formation of craters and bubbles (Figures 5.13-14 and 5.17-18 [B, B1]). The

craters have similar dimensions and are concentrated mainly along the perimeter of the spots on the dry irradiated Ketone N (Figures 5.13-14 [B, B1]). However, for the MS2A the craters and bubbles are spread over the whole laser spots with various diameters (Figures 5.17-18 [B, B1]). By increasing the fluence up to  $2.5 \text{ J/cm}^2$  (Figures 5.13-14 and 5.17-18 [C, C1]), single pulse irradiations resulted in a marked melting of the ketone resins with the formation of more defined craters. In these cases, the increase of craters by increasing the fluences can also be attributed to a photo-thermal disaggregation in the varnish films with the nucleation and expansion of vapour bubbles which can carry off material fragments in a solid and liquid state (Brown and Arnold, 2010; De Cruz *et al.*, 2014; Pereira-Pardo and Korenberg, 2018).

The simulated temperature values for the MS2A, determined in sections 4.3.3.2.2 and 4.3.3.2.3, has returned temperatures far above the  $T_g$  which do not appear to reflect the morphology of the spot tests obtained at  $0.6 \text{ J/cm}^2$  (Figures 5.17-18 [A, A1]). The same comment applies even more strongly regarding the aged Ketone N films where the simulated temperature gradient (Table 4.22 and Figures 4.31-34) is more of the order of the magnitude one would expect given the laser etching realised upon irradiation at the highest selected fluence of  $2.5 \text{ J/cm}^2$ , as shown in figures 5.13-14.

As already observed for the DI-W+TW20 pre-wetted dammar varnish, both Ketone N (Figures 5.15-16) and MS2A (Figures 5.19-20) films exhibit none or less marked laser spots when compared to the ones generated on the dry irradiated surfaces. The pre-wetted Ketone N irradiated areas in VSP and SP modes at  $0.6$  and  $1.6 \text{ J/cm}^2$  have shown no sign of the laser-material interaction (Figures 5.15-16). The onset of etching is displayed at  $2.5 \text{ J/cm}^2$  (Figures 5.15-16 [B, B1]). The pre-wet MS2A films have shown a more pronounced laser interaction above fluences of  $1.6 \text{ J/cm}^2$  with the formation of craters with various diameters. These craters are more visible in the VSP mode (Figure 5.19 [B, B1, C, C1]) than in the SP mode (Figure 5.20). For the pre-wetting procedure, the laser-material interaction can be explained by the formation of channel propagation followed by liquid explosion and thus the transfer of the recoil momentum to the irradiated material below the zone of water absorption (Forrer *et al.*, 1993, 1994).

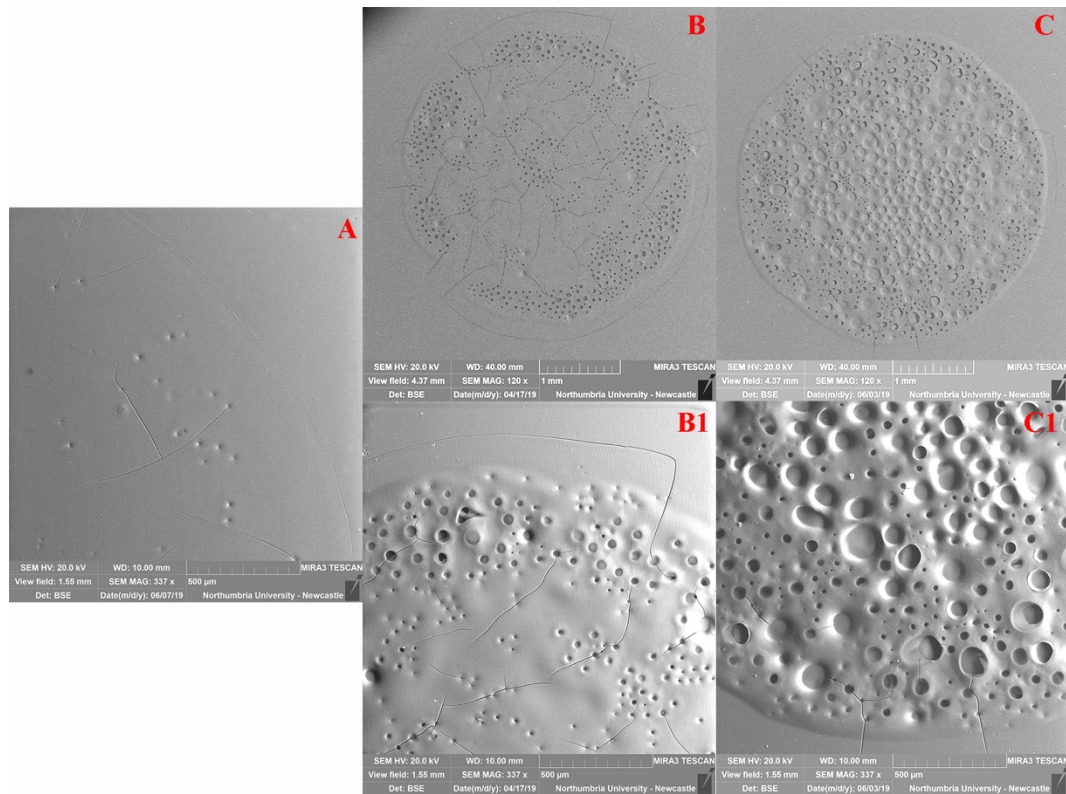


Figure 5.13 – Low vacuum BSE-SEM micrographs of the VSP single pulse dry test areas on aged **Ketone N** films. A:  $0.6 \text{ J/cm}^2$ ; B and B1:  $1.6 \text{ J/cm}^2$ ; C and C1:  $2.5 \text{ J/cm}^2$ . Spot diameter at  $\varnothing = 4\text{mm}$ , pulse repetition rate 2Hz. The micro-craquelure inside the laser spots (A and B) is a result of laser-material interaction. In VSP, the spot diameter is increased by  $0.26 \text{ mm}$  at  $2.5 \text{ J/cm}^2$  compared to the spot at  $1.6 \text{ J/cm}^2$ .

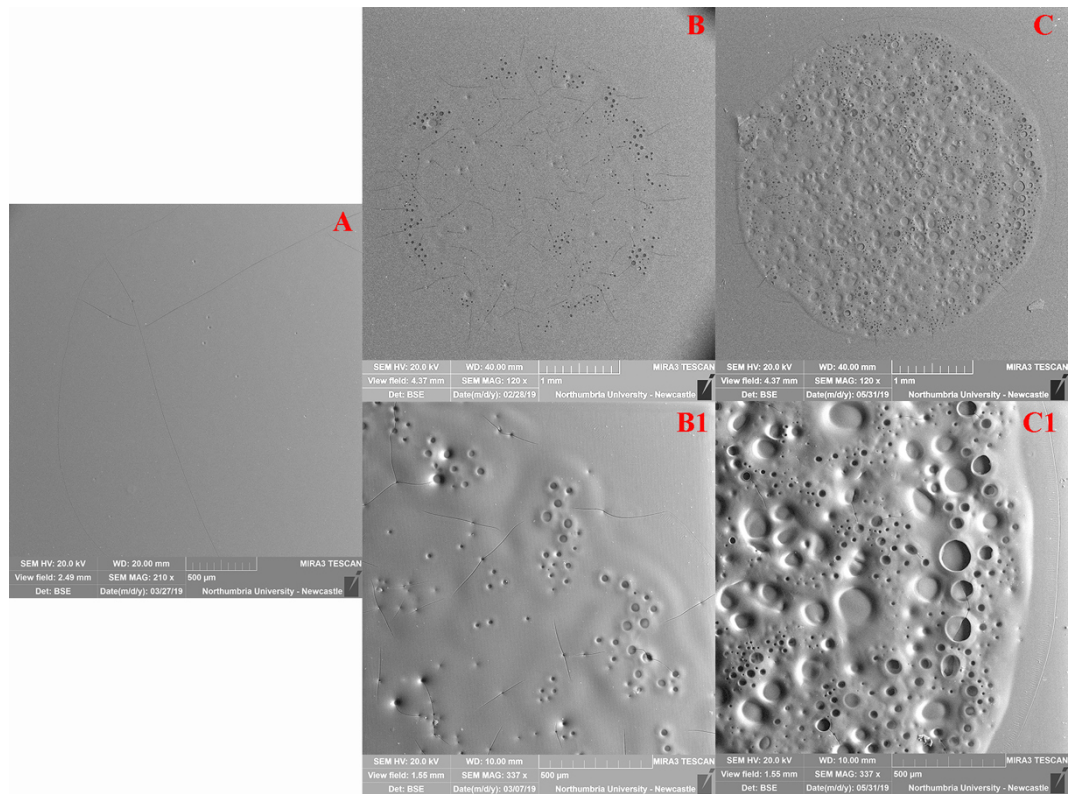


Figure 5.14 – Low vacuum BSE-SEM micrographs of the SP single pulse dry test areas on aged **Ketone N** films. A:  $0.6 \text{ J/cm}^2$ ; B and B1:  $1.6 \text{ J/cm}^2$ ; C and C1:  $2.5 \text{ J/cm}^2$ . Spot diameter at  $\varnothing = 4\text{mm}$ , pulse repetition rate 2Hz. The view field in micrograph A is 2.49 mm. The micro-craquelure inside the laser spots is a result of irradiation. In SP, the spot diameter at  $1.6 \text{ J/cm}^2$  is  $0.42 \text{ mm}$  smaller compared to the spot at  $2.5 \text{ J/cm}^2$ .

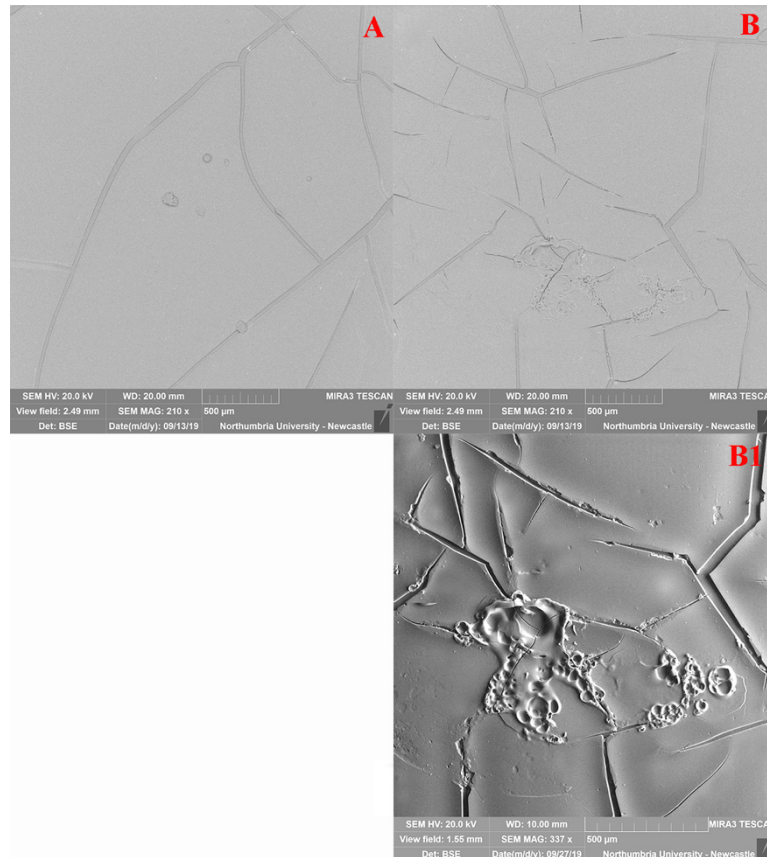


Figure 5.15 – Low vacuum BSE-SEM micrographs of the DI-W+TW20 pre-wet single pulse laser irradiated test areas in VSP mode on aged **Ketone N** films. A:  $0.6 \text{ J/cm}^2$ ; B and B1:  $2.5 \text{ J/cm}^2$ . Spot diameter at  $\varnothing = 4\text{mm}$ , pulse repetition rate 2Hz. The view field in micrographs A and B is 2.49 mm. The craquelure inside the laser spots is an intensification of the pre-existing cracking on the aged coatings not a result of irradiation and it was observed prior to irradiation and outside the spots.

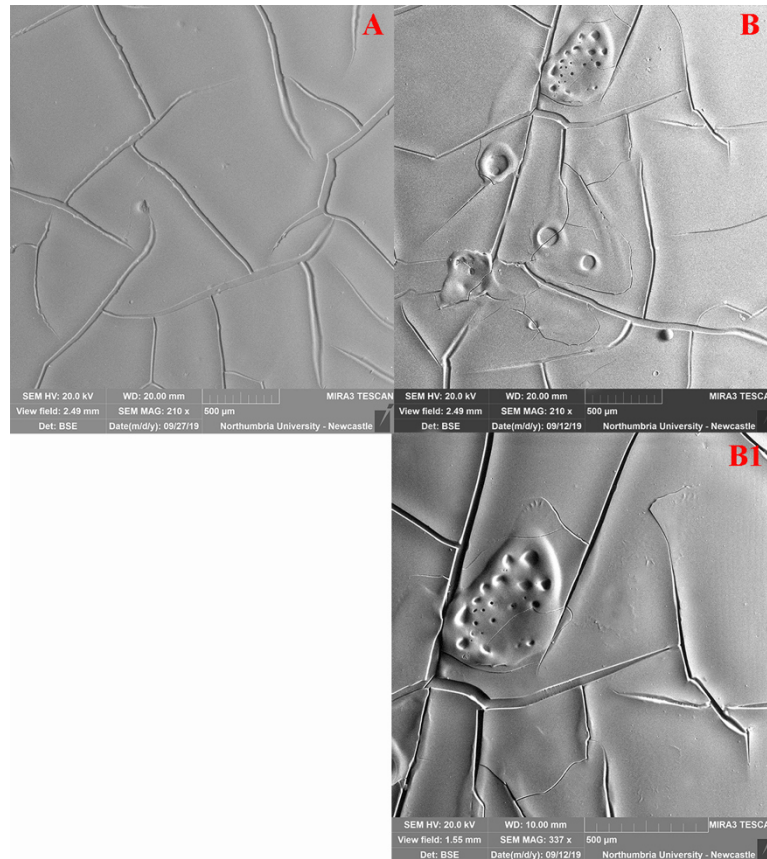


Figure 5.16 – Low vacuum BSE-SEM micrographs of the DI-W+TW20 pre-wet single pulse laser irradiated test areas in SP mode on aged **Ketone N** films. A: 1.6 J/cm<sup>2</sup>; B and B1: 2.5 J/cm<sup>2</sup>. The craquelure inside the laser spots is an intensification of the pre-existing cracking on the aged coatings not a result of irradiation and it was observed prior to irradiation and outside the spots.

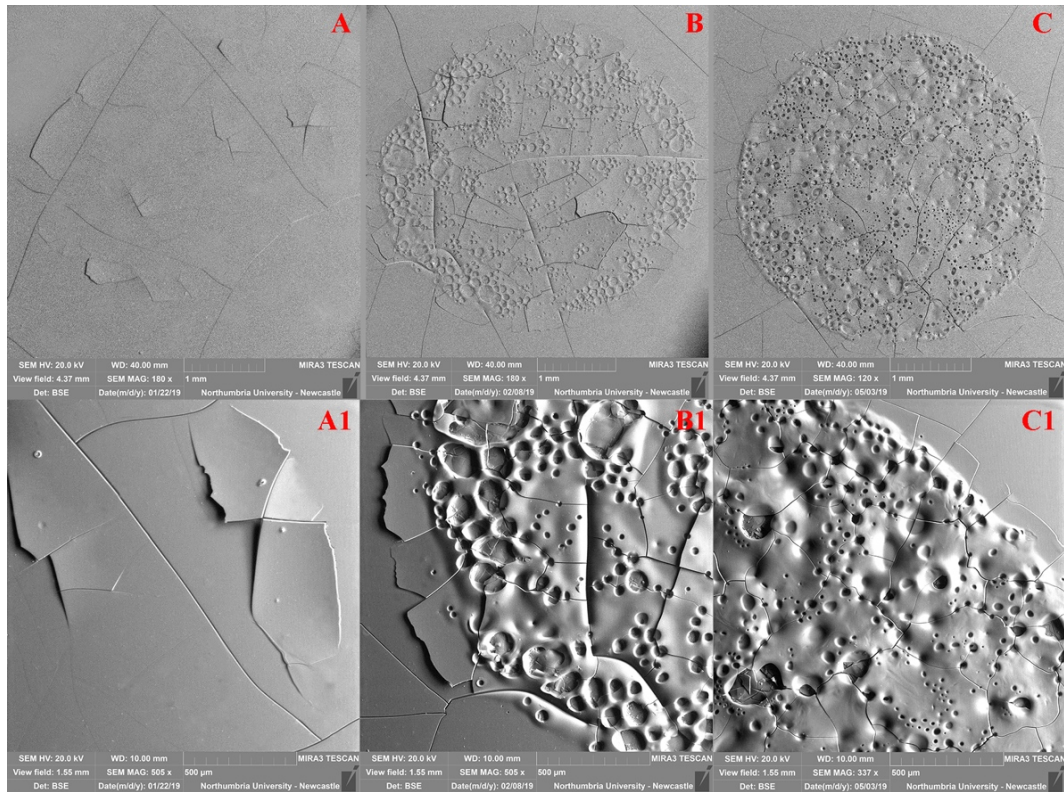


Figure 5.17 – Low vacuum BSE-SEM micrographs of the VSP single pulse dry test areas on aged MS2A films. A and A1:  $0.6 \text{ J/cm}^2$ ; B and B1:  $1.6 \text{ J/cm}^2$ ; C and C1:  $2.5 \text{ J/cm}^2$ . Spot diameter at  $\varnothing = 4 \text{ mm}$ , pulse repetition rate 2Hz. The micro-craquelure inside the laser spots is partially a result of irradiation and partially an intensification of the pre-existing cracking on the aged coatings (B, B1, C and C1). Lift-off phenomena have been observed on the dry MS2A sample irradiated at  $0.6 \text{ J/cm}^2$  (A, A1). In VSP, the spot diameter is increased by  $0.17 \text{ mm}$  at  $1.6 \text{ J/cm}^2$  compared to the spot at  $0.6 \text{ J/cm}^2$ , and the difference in diameter remains unchanged at  $2.5 \text{ J/cm}^2$ .

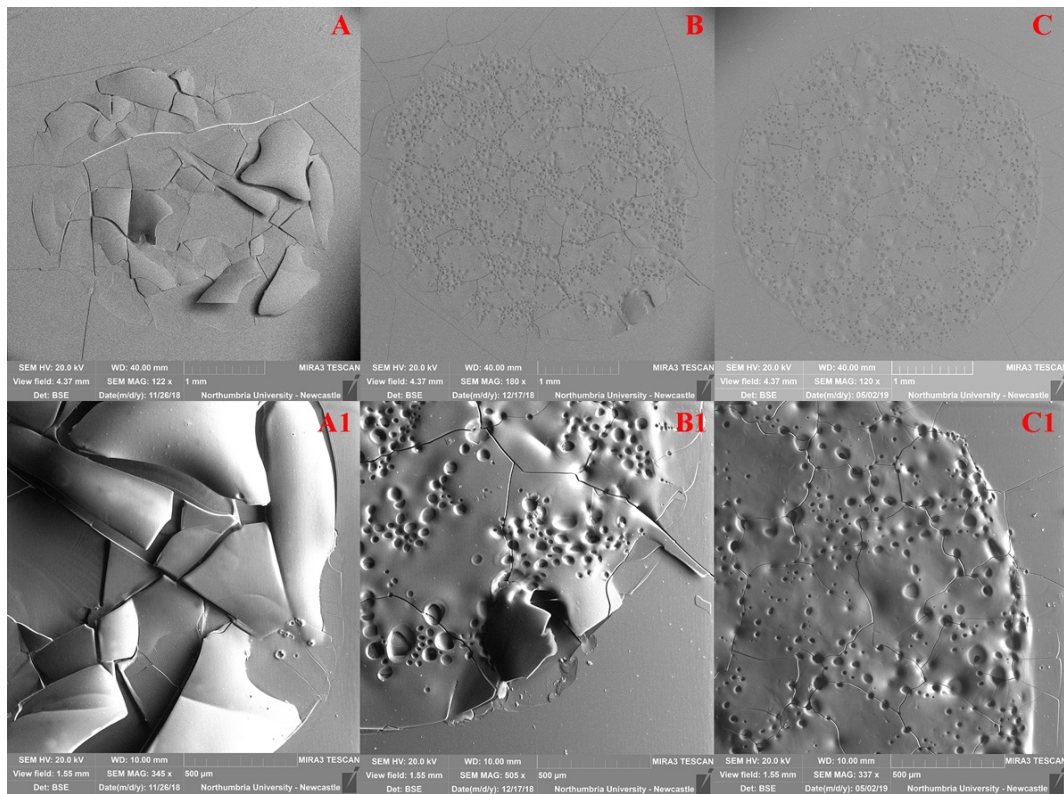


Figure 5.18 – Low vacuum BSE-SEM micrographs of the SP single pulse dry test areas on aged MS2A films. A and A1: 0.6 J/cm<sup>2</sup>; B and B1: 1.6 J/cm<sup>2</sup>; C and C1: 2.5 J/cm<sup>2</sup>. Spot diameter at  $\varnothing = 4$ mm, pulse repetition rate 2Hz. The micro-craquelure inside the laser spots is partially a result of irradiation (B, B1) and partially an intensification of the pre-existing cracking on the aged coatings (C, C1). Lift-off phenomena have been observed on the dry MS2A sample irradiated at 0.6 J/cm<sup>2</sup> (A, A1). In SP, the spot diameter at 2.5 J/cm<sup>2</sup> is 0.17 mm larger compared to the spots at 0.6 and 1.6 J/cm<sup>2</sup>.

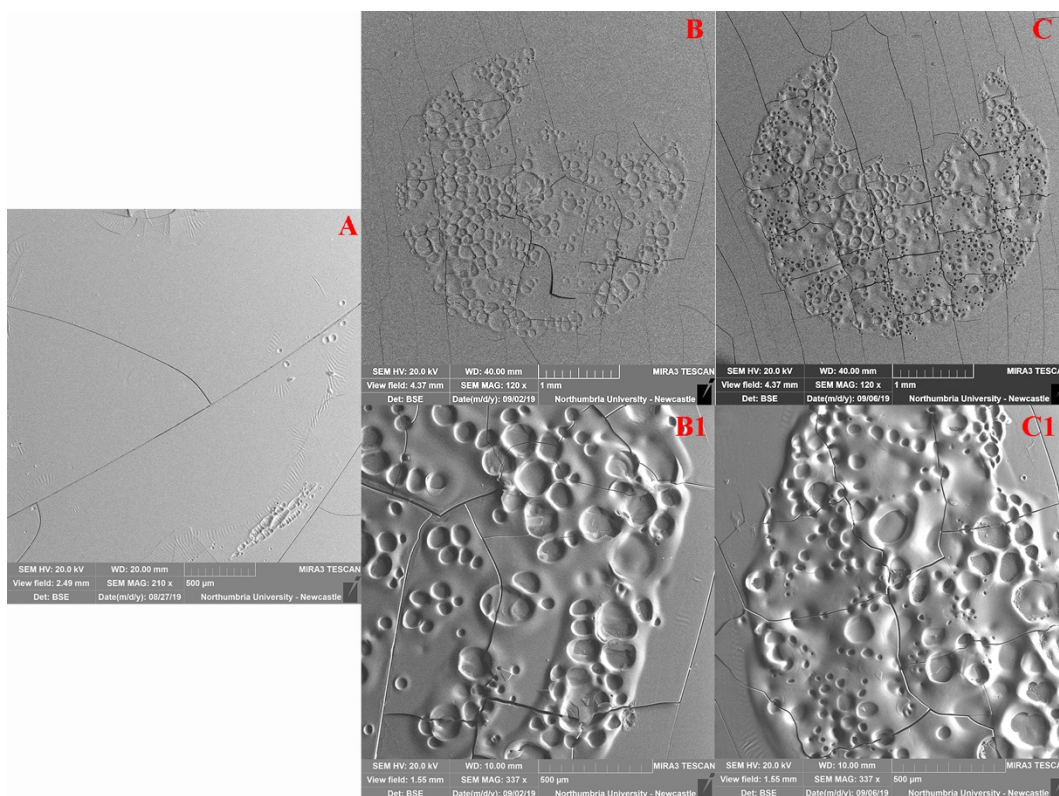


Figure 5.19 – Low vacuum BSE-SEM micrographs of the DI-W+TW20 pre-wet single pulse laser irradiated test areas in VSP mode on aged **MS2A** films. A: 0.6 J/cm<sup>2</sup>; B and B1: 1.6 J/cm<sup>2</sup>; C and C1: 2.5 J/cm<sup>2</sup>. The view field in micrograph A is 2.49 mm. The craquelure inside the laser spots is an intensification of the pre-existing cracking on the aged coatings not a result of irradiation and it was observed prior to irradiation and outside the spots. In VSP, the spot diameter at 1.6 J/cm<sup>2</sup> is 0.19 mm smaller compared to the spot at 2.5 J/cm<sup>2</sup>.

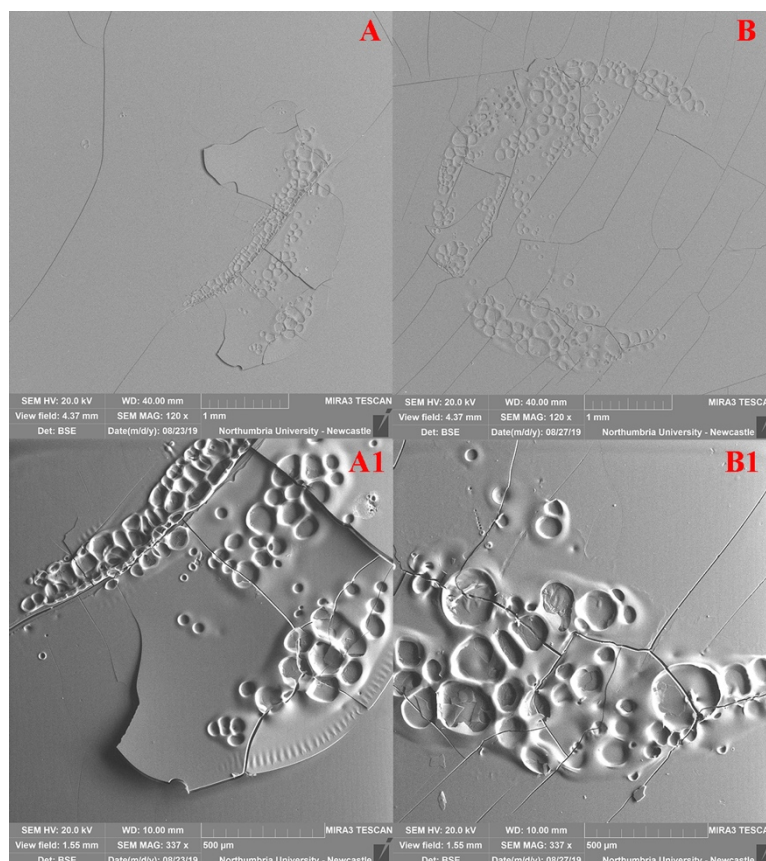


Figure 5.20 – Low vacuum BSE-SEM micrographs of the DI-W+TW20 pre-wet single pulse laser irradiated test areas in SP mode on aged **MS2A** films. A and A1: 1.6 J/cm<sup>2</sup>; B and B1: 2.5 J/cm<sup>2</sup>. The craquelure inside the laser spots is an intensification of the pre-existing cracking on the aged coatings not a result of irradiation and it was observed prior to irradiation and outside the spots.

### 5.3.1.2 3-Pulse tests on dammar and ketone resin films

The BSE-SEM micrographs of the aged dammar, Ketone N and MS2A varnish films, previously irradiated only once, are herein compared by repeating the laser-irradiation up to three times in the same area with a pulse repetition rate (PRR) of 2 Hz.

The micrographs of the dry irradiated dammar layer in VSP ( $\tau_L \approx 100 \mu\text{m}$ ) and SP ( $\tau_L \approx 300 \mu\text{m}$ ) modes have shown, also in this case, that the spots at a low fluence are not significantly marked (Figures 5.21-22 [A, A1]). Moreover, the concentric rings of the TEM<sub>31</sub> mode, easily detected with one pulse, are now less identifiable giving way to a more swollen dammar surface (Figures 5.21-22 [A, A1]). The three consecutive pulses at 2.5 J/cm<sup>2</sup> resulted in a relatively strong imprint of the concentric rings of the laser spatial structure on the dammar surface (Figures 5.21-22 [C, C1]). This indentation is more pronounced in SP mode due to

the longer pulse duration selected which slowed the laser energy transfer into the film, thereby enabling more time for the laser beam energy to spread within the varnish film according to the thermodynamics laws of heat transmission (Mazumder *et al.*, 1996, p. 176; Mayboudi, 2008, p. 8).

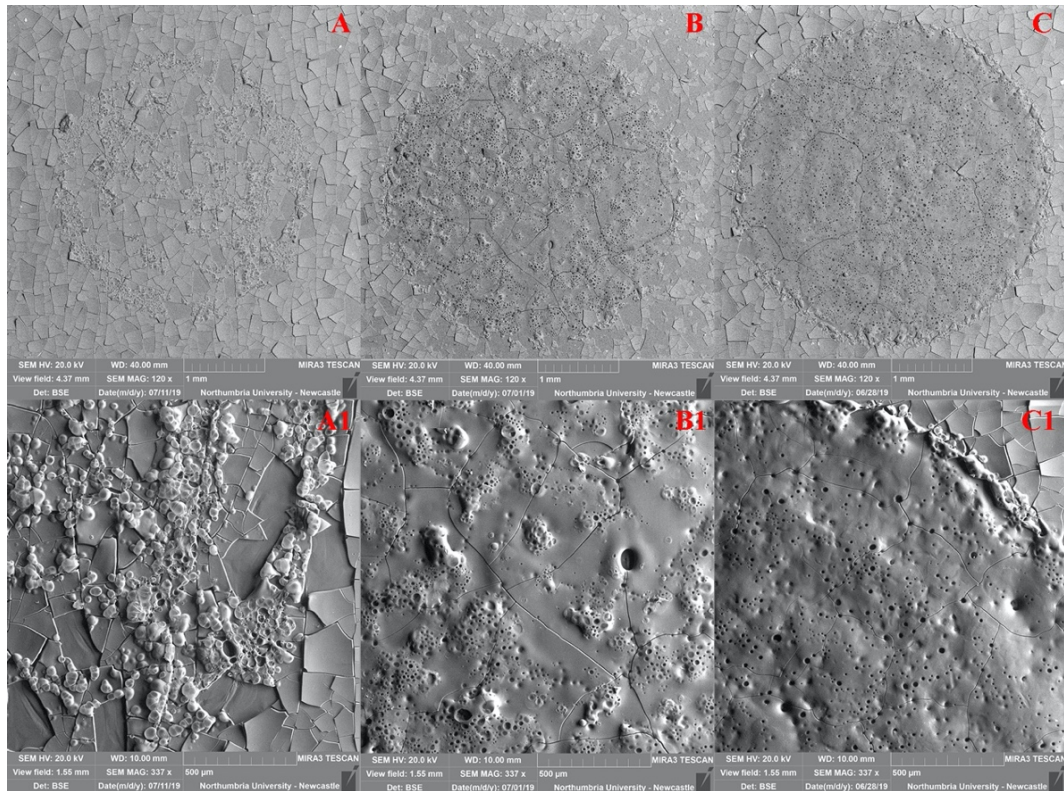


Figure 5.21 – Low vacuum BSE-SEM micrographs of the VSP dry test areas on aged **dammar films** after 3 consecutive laser pulses. A and A1:  $0.6 \text{ J/cm}^2$ ; B and B1:  $1.6 \text{ J/cm}^2$ ; C and C1:  $2.5 \text{ J/cm}^2$ . Spot diameter at  $\emptyset = 4\text{mm}$ , pulse repetition rate 2Hz. The micro-craquelure inside the laser spots at fluences above  $1.5 \text{ J/cm}^2$  is a result of the laser irradiation. In VSP, the spot diameter is increased by  $0.49 \text{ mm}$  at  $1.6 \text{ J/cm}^2$  compared to the spot at  $0.6 \text{ J/cm}^2$  and then by  $0.29 \text{ mm}$  more at  $2.5 \text{ J/cm}^2$ .

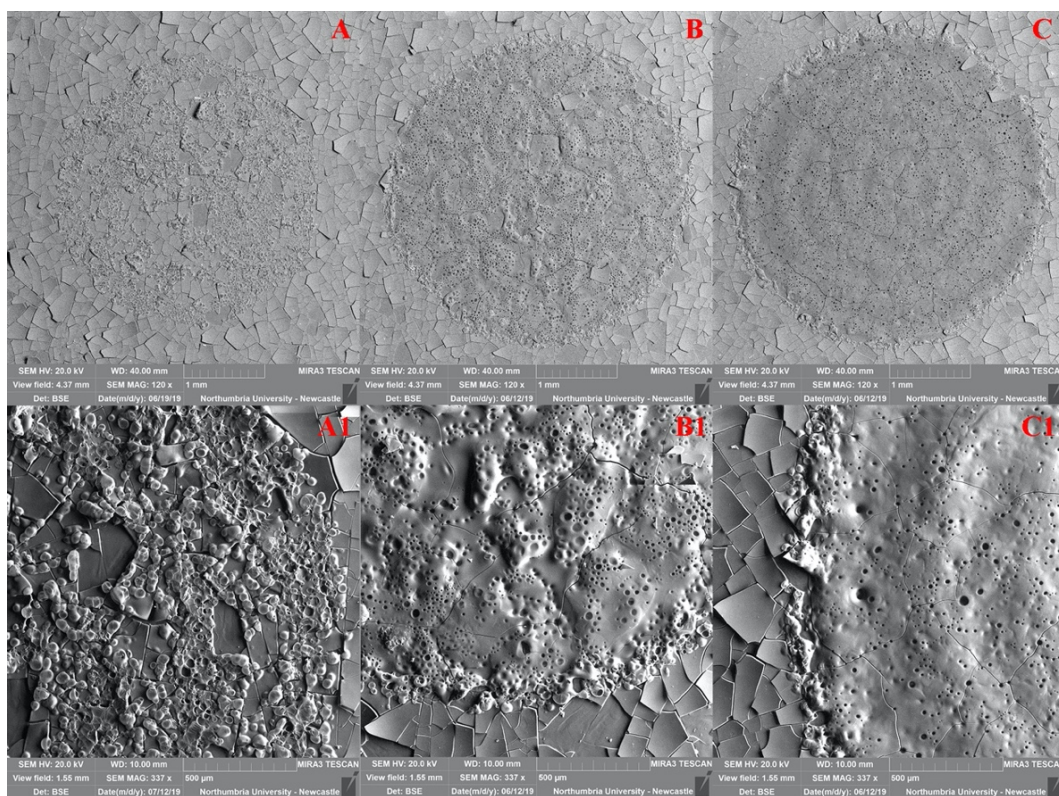


Figure 5.22 – Low vacuum BSE-SEM micrographs of the SP dry test areas on aged **dammar** films after 3 consecutive laser pulses. A and A1:  $0.6 \text{ J/cm}^2$ ; B and B1:  $1.6 \text{ J/cm}^2$ ; C and C1:  $2.5 \text{ J/cm}^2$ . Spot diameter at  $\varnothing = 4\text{mm}$ , pulse repetition rate 2Hz. The micro-craquelure inside the laser spots at fluences above  $1.5 \text{ J/cm}^2$  is a result of the laser irradiation. In SP, the spot diameter is increased by  $0.65 \text{ mm}$  at  $1.6 \text{ J/cm}^2$  compared to the spot at  $0.6 \text{ J/cm}^2$  and then by  $0.13 \text{ mm}$  more at  $2.5 \text{ J/cm}^2$ .

The spots on the pre-wetted dammar films (Figures 5.23-24) were less marked than on the dry irradiated films. The increase of micro-pits and craters can be attributed, also in this case, to a photo-thermal disaggregation caused by the selective absorption and explosive vaporisation of hydroxide-containing species in the varnish substrate (De Cruz *et al.*, 2014; Pereira-Pardo and Korenberg, 2018). A differential shrinkage and partial film removal with a fully exposed glass slide and the laser spatial structure of TEM<sub>31</sub> mode at  $2.5 \text{ J/cm}^2$  has also been observed (Meister *et al.*, 2003) (Figures 5.23-24 [C]).

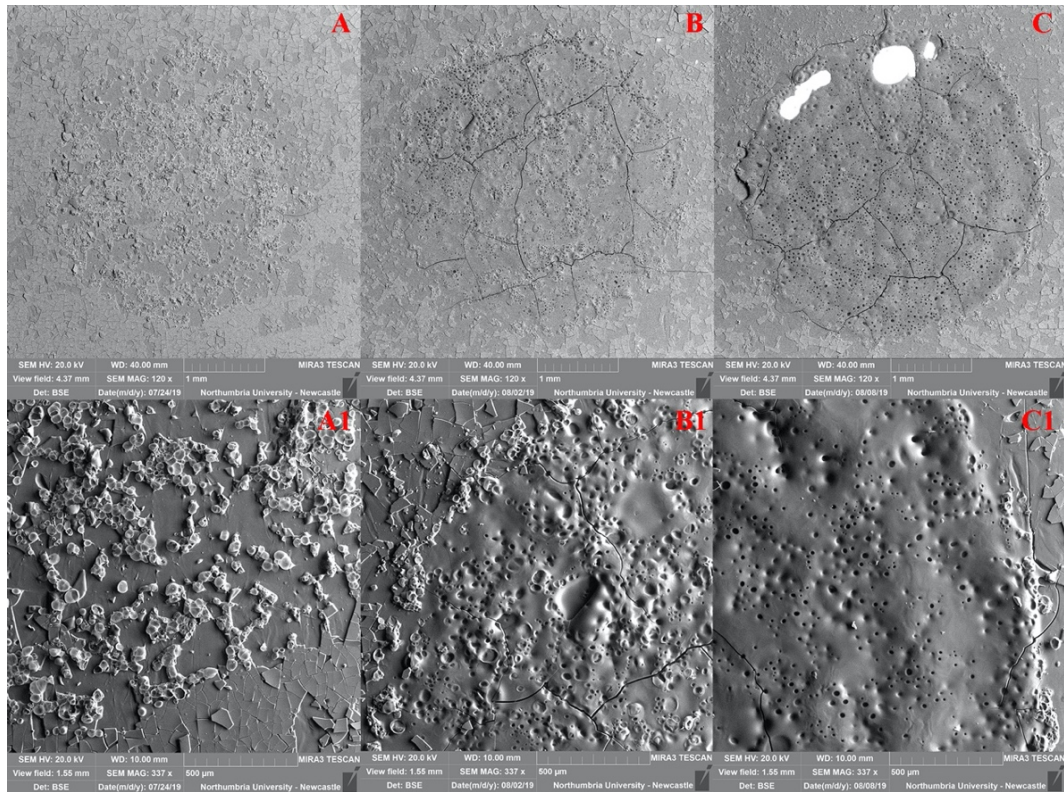


Figure 5.23 – Low vacuum BSE-SEM micrographs of the DI-W+TW20 pre-wet laser irradiated test areas in VSP mode on aged **dammar film** after 3 consecutive laser pulses. A and A1:  $0.6 \text{ J/cm}^2$ ; B and B1:  $1.6 \text{ J/cm}^2$ ; C and C1:  $2.5 \text{ J/cm}^2$ . The craquelure inside the laser spots at fluences above  $1.5 \text{ J/cm}^2$  is a result of the laser irradiation. The consecutive irradiations (three pulses at 2 Hz) have caused at  $2.5 \text{ J/cm}^2$  a partial removal or shrinkage of the dammar film (C). In VSP, the spot diameter is increased by 0.23 mm at  $1.6 \text{ J/cm}^2$  compared to the spot at  $0.6 \text{ J/cm}^2$  and then by 0.35 mm at  $2.5 \text{ J/cm}^2$ .

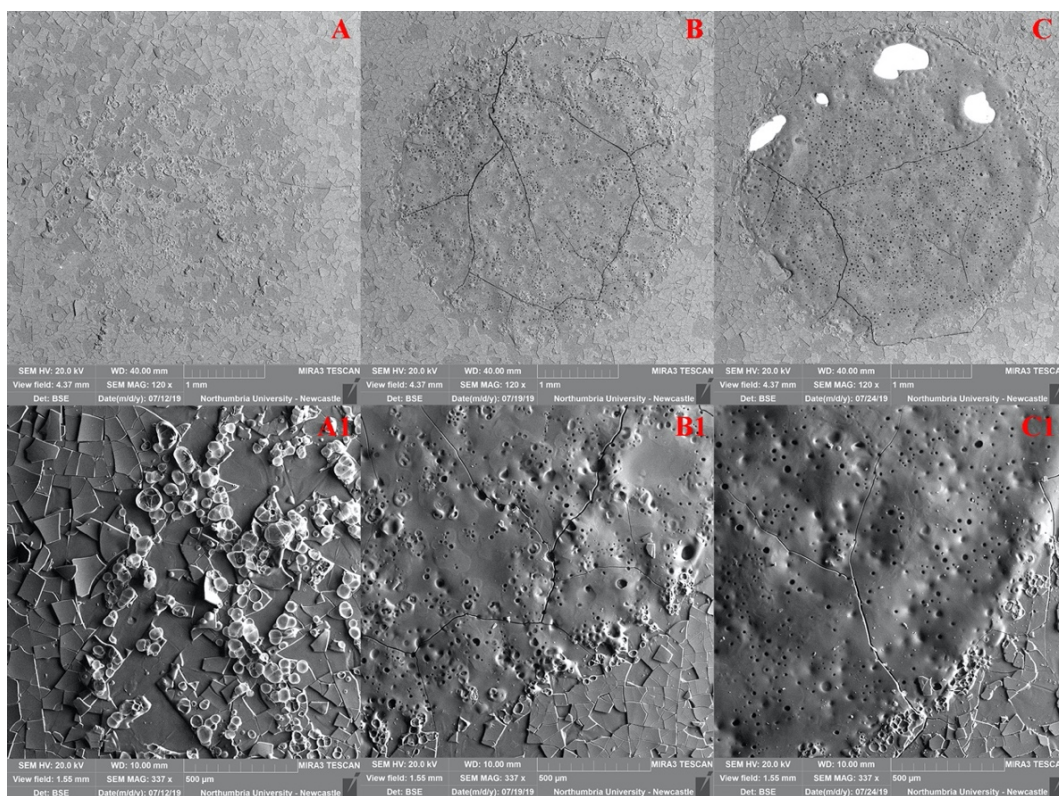


Figure 5.24 – Low vacuum BSE-SEM micrographs of the DI-W+TW20 pre-wet laser irradiated test areas in SP mode on aged **dammar film** after 3 consecutive laser pulses. A and A1: 0.6 J/cm<sup>2</sup>; B and B1: 1.6 J/cm<sup>2</sup>; C and C1: 2.5 J/cm<sup>2</sup>. The craquelure inside the laser spots at fluences above 1.5 J/cm<sup>2</sup> is a result of the laser irradiation. The consecutive irradiations (three pulses at 2 Hz) have caused at 2.5 J/cm<sup>2</sup> a partial removal or shrinkage of the dammar film (C). In SP, the spot diameter is increased by 0.65 mm at 1.6 J/cm<sup>2</sup> compared to the spot at 0.6 J/cm<sup>2</sup> and then it remains unchanged at 2.5 J/cm<sup>2</sup>.

As already detected with a single laser pulse (section 5.3.1.1), Ketone N aged films, irradiated at 0.6 J/cm<sup>2</sup>, in VSP and SP modes, resulted in almost negligible interaction with the varnish, which was detectable only at high magnifications corresponding to 1.55 mm field of view (Figures 5.25 [A] and 5.26 [A, A1]). By increasing the fluence to 1.6 J/cm<sup>2</sup>, it has been possible to observe a surface swelling together with the formation of craters particularly concentrated in the more external portion of the laser spots (Figures 5.25-26 [B, B1]) and near the concentric rings of the TEM<sub>31</sub> mode where the highest laser energy deposition occurred. This is more pronounced in the VSP ( $\tau_L \approx 300 \mu\text{s}$ ) mode than in the SP ( $\tau_L \approx 100 \mu\text{s}$ ) mode, mainly due to a higher power density delivered onto the surface as shown in Table 4.20.

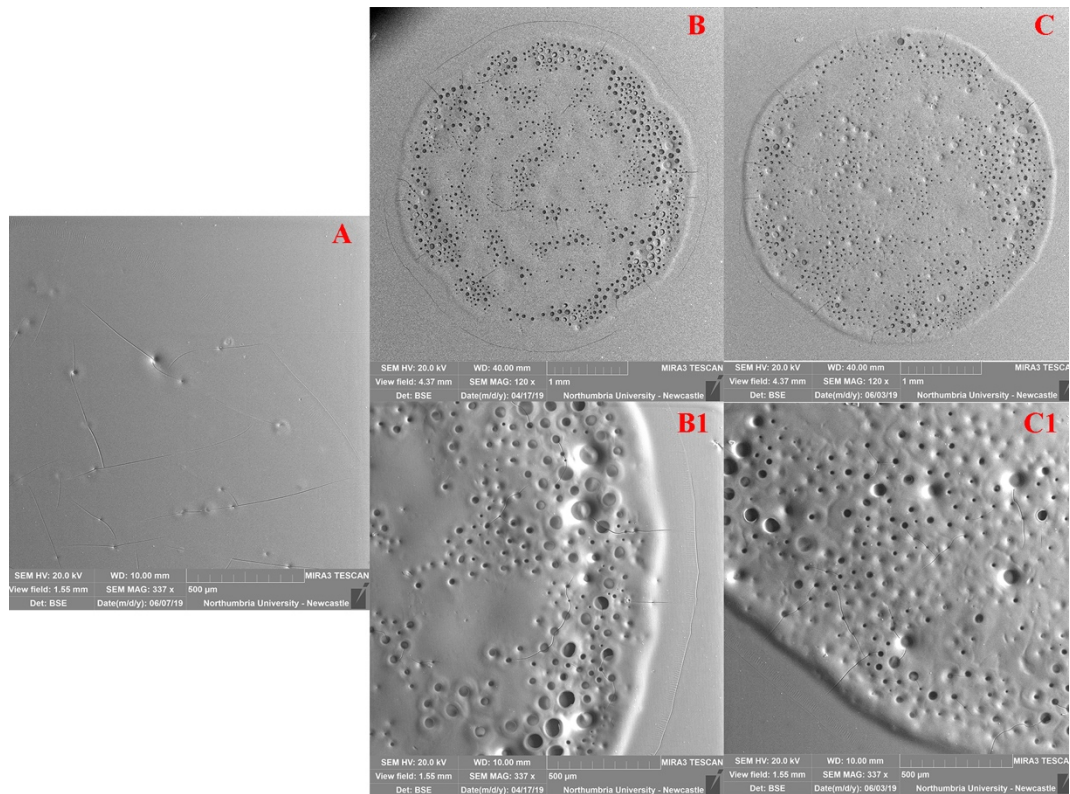


Figure 5.25 – Low vacuum BSE-SEM micrographs of the VSP dry test areas on aged **Ketone N films** after 3 consecutive laser pulses. A: 0.6 J/cm<sup>2</sup>; B and B1: 1.6 J/cm<sup>2</sup>; C and C1: 2.5 J/cm<sup>2</sup>. Spot diameter at Ø = 4mm, pulse repetition rate 2Hz. The micro-craquelure inside the laser spots at 0.6 J/cm<sup>2</sup> is a result of laser-material interaction. In VSP, the spot diameter is increased by 0.19 mm at 2.5 J/cm<sup>2</sup> compared to the spot at 1.6 J/cm<sup>2</sup>. At 0.6 J/cm<sup>2</sup>, it proved impossible to detect the external ring of the laser spot.

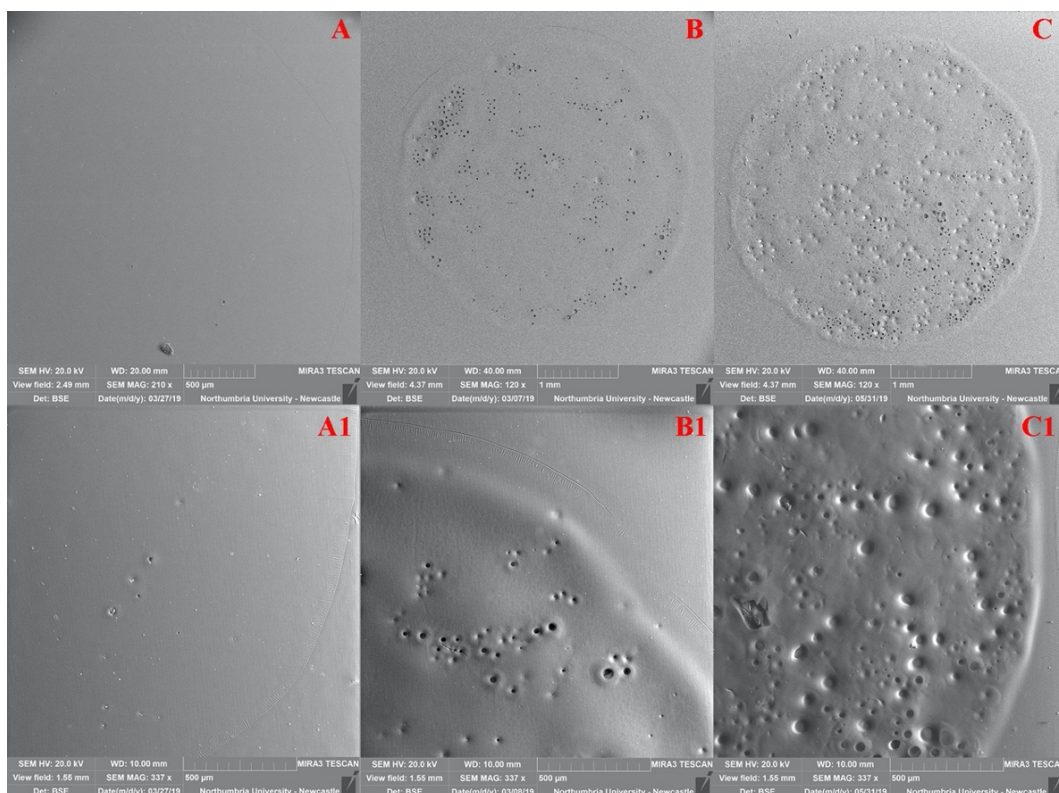


Figure 5.26 – Low vacuum BSE-SEM micrographs of the SP dry test areas on aged **Ketone N films** after 3 consecutive laser pulses. A and A1:  $0.6 \text{ J/cm}^2$ ; B and B1:  $1.6 \text{ J/cm}^2$ ; C and C1:  $2.5 \text{ J/cm}^2$ . Spot diameter at  $\varnothing = 4\text{mm}$ , pulse repetition rate 2Hz. The view field in micrograph A is 2.49 mm. In SP, the spot diameter is increased by 0.25 mm at  $2.5 \text{ J/cm}^2$  compared to the spot at  $1.6 \text{ J/cm}^2$ . At  $0.6 \text{ J/cm}^2$ , it proved impossible to detect the external ring of the laser spot.

As already observed for the DI-W+TW20 pre-wetted dammar surfaces, Ketone N films either exhibit none or very fewer marked laser spots when compared to the ones generated on the dry irradiated surfaces (Figures 5.27-28). The Ketone N films in VSP and SP modes at the lowest fluence of  $0.6 \text{ J/cm}^2$  has shown almost no sign (Figure 5.27 [A]) of the laser-material interaction and isolated craters at  $1.6 \text{ J/cm}^2$  (Figures 5.27 [B, B1] and 5.28 [A, A1]). At  $2.5 \text{ J/cm}^2$ , the characteristic circular spots became more noticeable with the formation of micro-pits and a rise in the melted area of the resin layer (Figures 5.27 [C, C1] and 5.28 [B, B1]). As discussed in section 4.1.3.1, this phenomenon can be explained by the formation of channel propagation followed by liquid explosion and therefore the transfer of the recoil momentum to the irradiated material below the zone of water absorption (Forrer *et al.*, 1993, 1994).

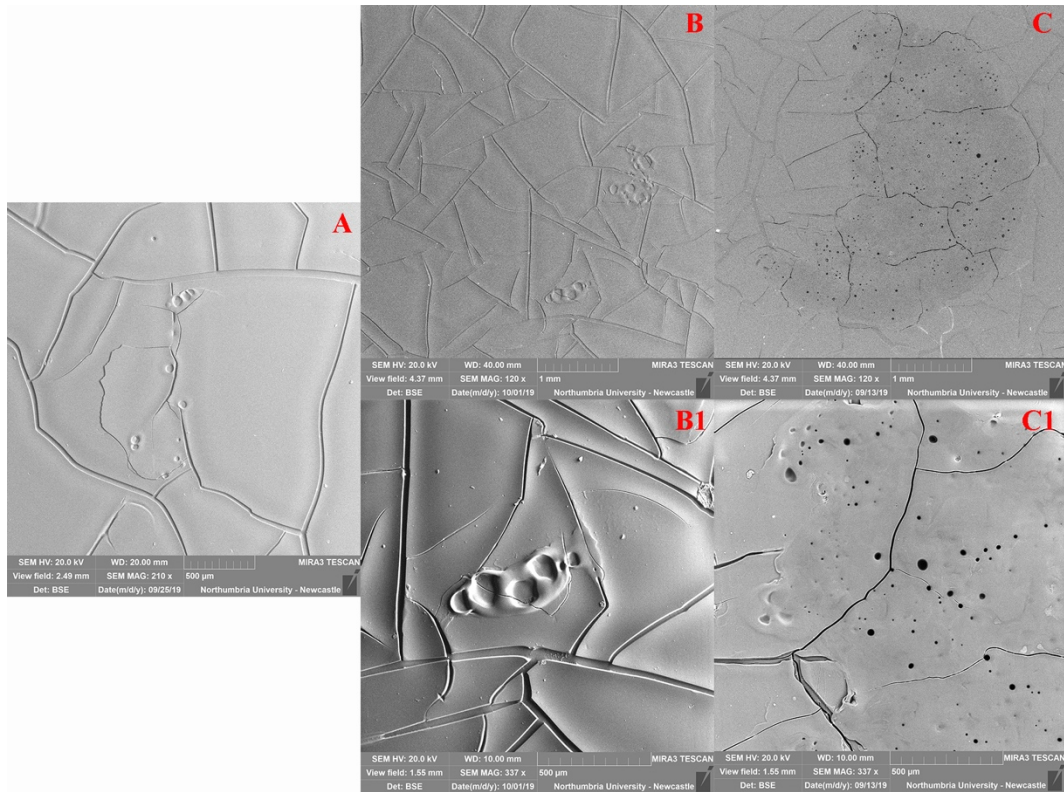


Figure 5.27 – Low vacuum BSE-SEM micrographs of the DI-W+TW20 pre-wet laser irradiated test areas in VSP mode on aged **Ketone N film** after 3 consecutive laser pulses. A:  $0.6 \text{ J/cm}^2$ ; B and B1:  $1.6 \text{ J/cm}^2$ ; C and C1:  $2.5 \text{ J/cm}^2$ . The view field in micrograph A is 2.49 mm. The craquelure inside the laser spots is an intensification of the pre-existing cracking on the aged coatings not a result of irradiation and it was observed prior to irradiation and outside the spots.

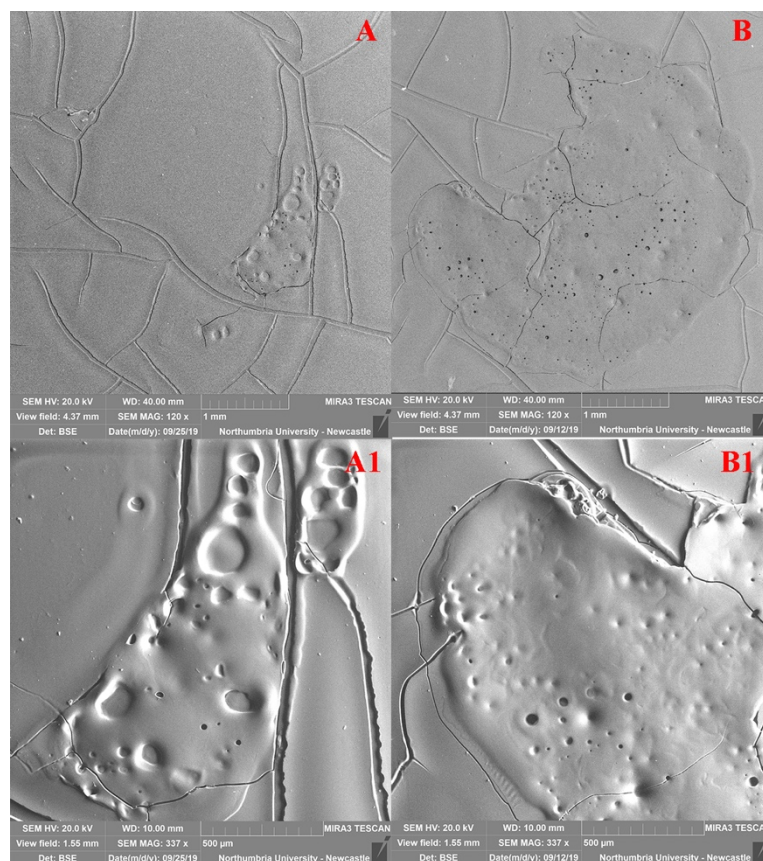


Figure 5.28 – Low vacuum BSE-SEM micrographs of the DI-W+TW20 pre-wet laser irradiated test areas in SP mode on aged **Ketone N film** after 3 consecutive laser pulses. A and A1: 1.6 J/cm<sup>2</sup>; B and B1: 2.5 J/cm<sup>2</sup>. The craquelure inside the laser spots is an intensification of the pre-existing cracking on the aged coatings not a result of irradiation and it was observed prior to irradiation and outside the spots.

The lift-off phenomena observed upon a single pulse on aged MS2A films (Figures 5.29-30 [A, A1]), are even more pronounced upon three consecutive pulses delivered on the same area. The morphology of the irradiated coating shows the flaking of the uppermost layer of the coating film (Figures 5.29-30 [A, A1]), leaving residues of the remaining varnish onto the glass slides surfaces and the formation of a visible step between the untreated surface and the irradiated one. As already observed with a single laser pulse (Figures 5.29-30 [B, B1]), when increasing the fluence the mechanism of interaction changes giving way to the formation of craters which are spread over the whole laser spots with various diameters. At 2.5 J/cm<sup>2</sup> (Figures 5.29-30 [C, C1]), multiple laser pulses resulted in marked melting of the resin layer with the formation of more defined craters. The micro-craquelure inside the laser spots is partially a result of laser irradiation (Figures 5.29-30 [B, B1]) and partially an intensification of the pre-existing cracking of the aged coatings (Figures 5.29-30 [C, C1]).

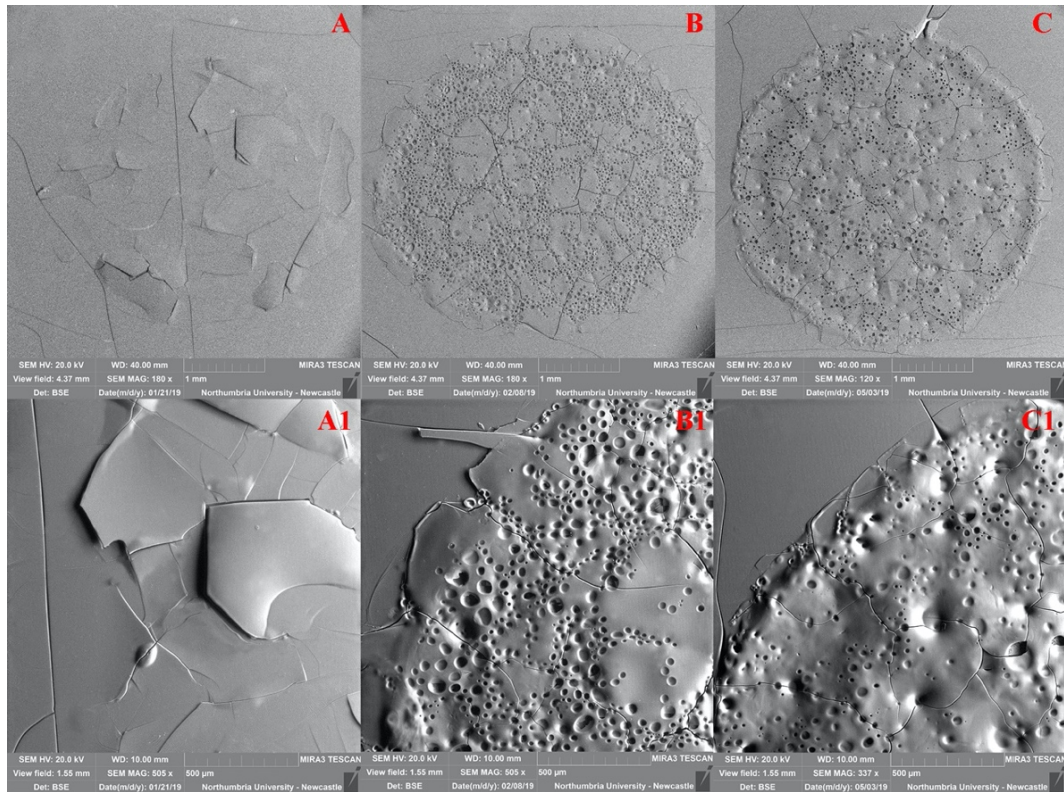


Figure 5.29 – Low vacuum BSE-SEM micrographs of the VSP dry test areas on aged **MS2A films** after 3 consecutive laser pulses. A and A1:  $0.6 \text{ J/cm}^2$ ; B and B1:  $1.6 \text{ J/cm}^2$ ; C and C1:  $2.5 \text{ J/cm}^2$ . Spot diameter at  $\varnothing = 4\text{mm}$ , pulse repetition rate 2Hz. The microcrackle inside the laser spots is a result of irradiation and lift-off phenomena have been observed on the dry MS2A sample irradiated at  $0.6 \text{ J/cm}^2$  (A, A1). In VSP, the spot diameter is increased by  $0.32 \text{ mm}$  at  $1.6 \text{ J/cm}^2$  compared to the spot at  $0.6 \text{ J/cm}^2$  and then by  $0.29 \text{ mm}$  more at  $2.5 \text{ J/cm}^2$ .

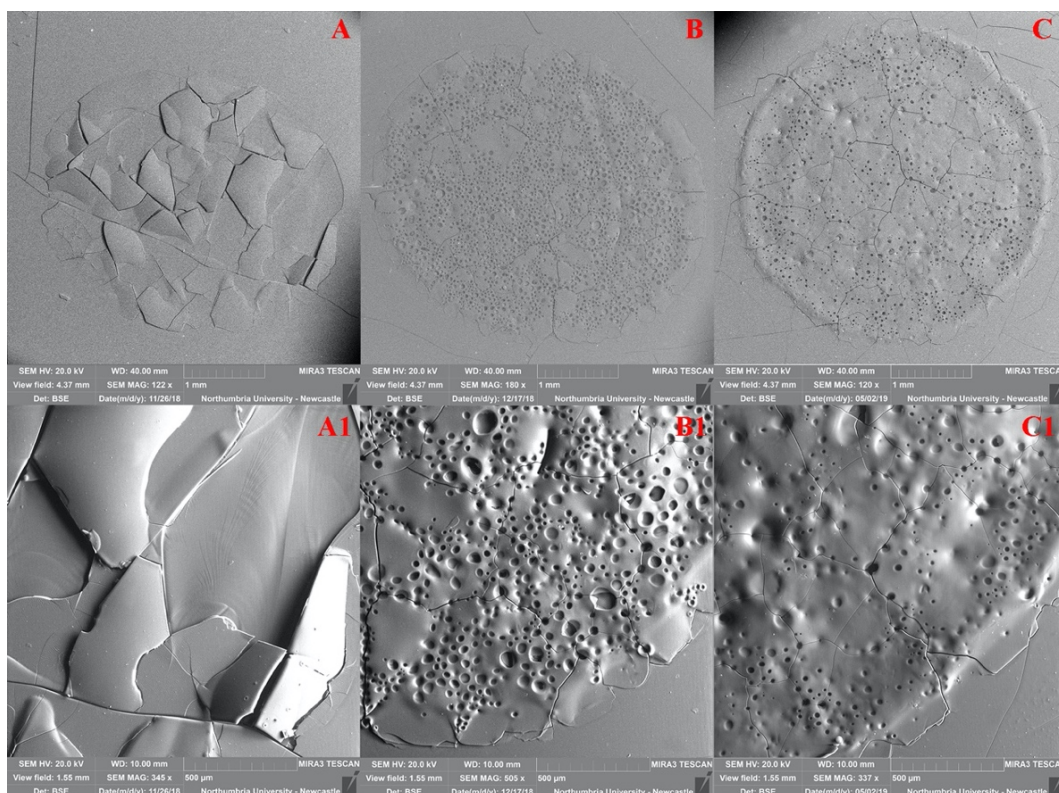


Figure 5.30 – Low vacuum BSE-SEM micrographs of the SP dry test areas on aged **MS2A films** after 3 consecutive laser pulses. A and A1: 0.6 J/ cm<sup>2</sup>; B and B1: 1.6 J/cm<sup>2</sup>; C and C1: 2.5 J/cm<sup>2</sup>. Spot diameter at Ø = 4mm, pulse repetition rate 2Hz. The micro-craquelure inside the laser spots is partially a result of irradiation (B, B1) and partially an intensification of the pre-existing cracking on the aged coatings (C, C1). Lift-off phenomena have been observed on the dry MS2A sample irradiated at 0.6 J/cm<sup>2</sup> (A, A1). In VSP, the spot diameter is increased by 0.32 mm at 1.6 J/cm<sup>2</sup> compared to the spot at 0.6 J/cm<sup>2</sup> and then by 0.16 mm more at 2.5 J/cm<sup>2</sup>.

The DI-W+TW20 pre-wetted MS2A surfaces have shown less marked laser spots when compared to the ones on the dry irradiated surfaces. This is especially noticeable when comparing the laser-material interaction at the lowest fluence of 0.6 J/cm<sup>2</sup> (Figures 5.31-32 [A, A1]). The three consecutive pulses at 2 Hz have caused partial shrinkage and warpage of the uppermost surface layer of the film at 1.6 J/cm<sup>2</sup> (Figures 5.31-32 [B, B1]) and partial removal at 2.5 J/cm<sup>2</sup> (Figures 5.31-32 [C, C1]) with a fully exposed glass slide. This increase of craters, even on the pre-wetted surface, can be attributed to the formation of channel propagations through the wetting agent by liquid explosion (Forrer *et al.*, 1993, 1994) and the subsequent photo-thermal disaggregation of the coating (De Cruz *et al.*, 2014; Pereira-Pardo and Korenberg, 2018).

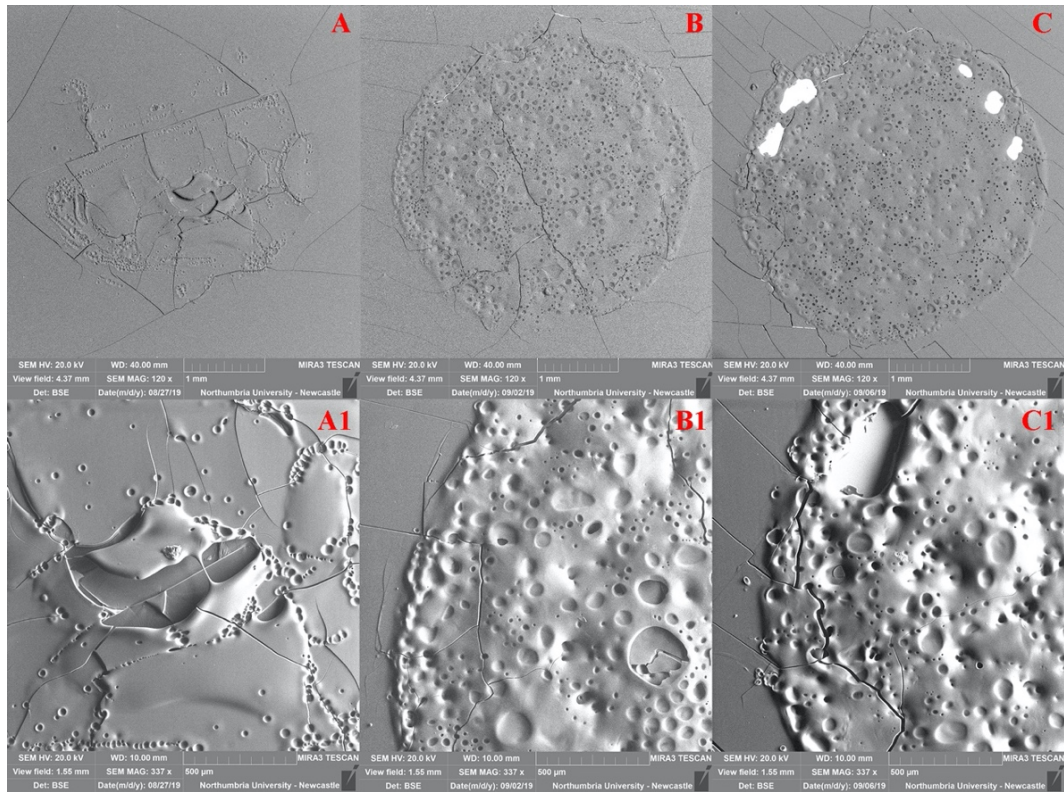


Figure 5.31 – Low vacuum BSE-SEM micrographs of the DI-W+TW20 pre-wet laser irradiated test areas in VSP mode on aged **MS2A film** after 3 consecutive laser pulses. A and A1: 0.6 J/cm<sup>2</sup>; B and B1: 1.6 J/cm<sup>2</sup>; C and C1: 2.5 J/cm<sup>2</sup>. The craquelure inside the laser spots (A and B) is an intensification of the pre-existing cracking on the aged coatings probably not a result of irradiation. Lift-off phenomena have been observed on the MS2A sample irradiated at 0.6 J/cm<sup>2</sup>. The consecutive irradiations (three pulses at 2 Hz) have caused at 2.5 J/cm<sup>2</sup> a partial removal of the MS2A film (C, C1). In VSP, the spot diameter is increased by 0.33 mm at 1.6 J/cm<sup>2</sup> compared to the spot at 0.6 J/cm<sup>2</sup> and then by 0.14 mm at 2.5 J/cm<sup>2</sup>.

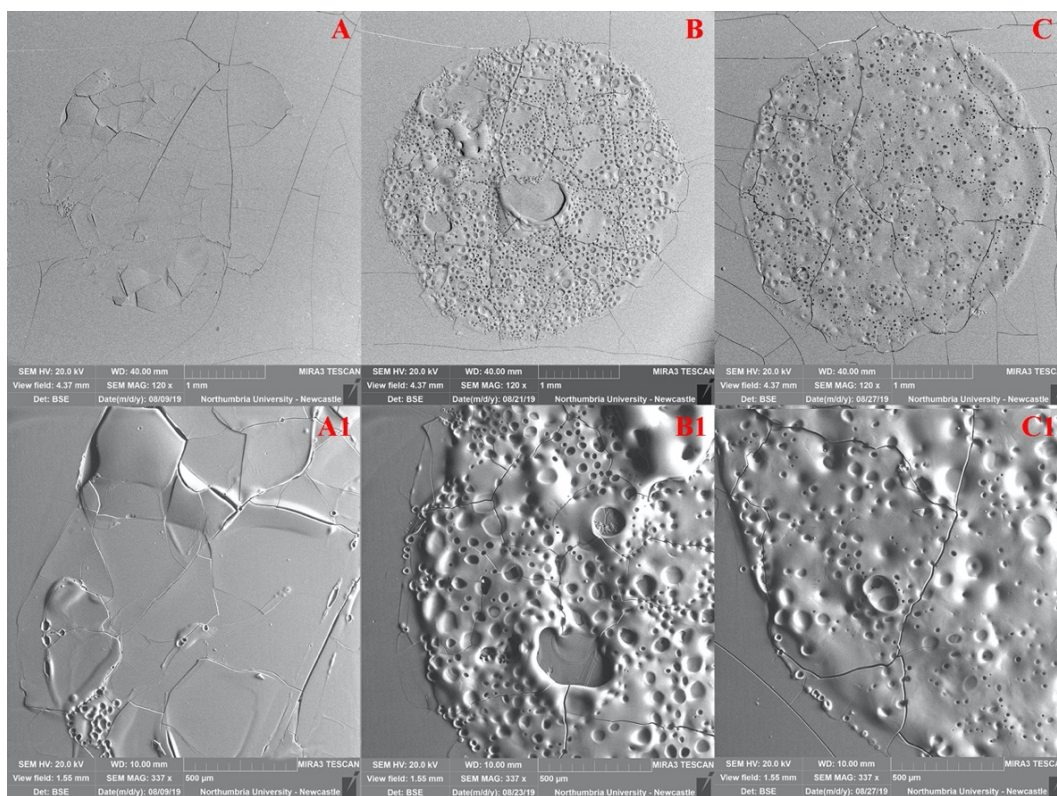


Figure 5.32 – Low vacuum BSE-SEM micrographs of the DI-W+TW20 pre-wet laser irradiated test areas in SP mode on aged MS2A film after 3 consecutive laser pulses. A and A1: 0.6 J/cm<sup>2</sup>; B and B1: 1.6 J/cm<sup>2</sup>; C and C1: 2.5 J/cm<sup>2</sup>. The craquelure inside the laser spots (A and B) is an intensification of the pre-existing cracking on the aged coatings probably not a result of irradiation. The consecutive irradiations (three pulses at 2 Hz) have caused at 1.5 J/cm<sup>2</sup> a partial shrinkage and warpage of the top layer of the MS2A film (B). In SP, the spot diameter is increased by 0.49 mm at 1.6 J/cm<sup>2</sup> compared to the spot at 0.6 J/cm<sup>2</sup> and then by 0.14 mm at 2.5 J/cm<sup>2</sup>.

Nahen and Vogel (2002) reported a phase explosion of water during the Er:YAG laser irradiation. This finding leads to the suggestion that, also in the laser tests presented herein, a phase explosion may have contributed to the disruption of the varnish surfaces. For each varnish, the differences in the laser-material interaction may be related to the matrix of the material which counterbalances the vapour expansion inside the sample until the limit tensile strength of the matrix is reached. Moreover, the identification of the special structure of TEM<sub>31</sub> (circular spot) mode on the irradiated varnish surfaces, especially when the aged varnish films were dry irradiated, highlight that the simplification in the assumption of homogeneous energy distribution in the mathematical simulation described in Chapter 4 (section 4.3.3.2) is not completely correct. In fact, the radial concentric rings are clearly visible only when a higher energy density arrives on the surface (Meister *et al.*, 2003).

Moreover, the laser spot is consistently enlarged in both dry and pre-wetted surfaces by increasing the fluences. This can be explained by the fact that the laser beam divergence gradually increases with output energy, due to the presence of a stronger thermal lens generated by the rod when the flashlamp is pumped with higher energy<sup>2</sup> (Chillè *et al.*, 2020; Chillè, Papadakis and Theodorakopoulos, 2020). This indicates that by increasing the laser energy, the beam which has been propagated through the arm and down to the handpiece has a slightly larger diameter than the one with lower energy. Another possible explanation for the observed enlargement of the spots with higher energies may be an intensified interaction of the laser beam with the material due to the increase of the fluence.

### 5.3.2 ATR/FT-IR

ATR-FTIR analysis have been used to shed some light on the micro-chemistry of the varnish films after the Er:YAG laser irradiation tests. FT-IR spectra were carried out with Attenuated Total Reflection (ATR), because of the simplicity in application, requiring only contact of the ATR crystal with the investigated films (Theodorakopoulos, 2005, p. 210; Pemble and Gardner, 2009). Figures 5.34-38 report the results of the semi-quantitative analysis carried out on the ATR/FT-IR spectra of the varnish samples before and after the laser irradiation in VSP and SP modes at fluences 0.5, 1, 1.5, 2,1 and 2.4 J/cm<sup>2</sup>. The surface was directly irradiated dry or pre-wetted with DI-W+TW20. Moreover, the spectra obtained from the unaged and aged varnishes were compared to the irradiated ones. All the spectra presented in this section have been baseline corrected. Evidence on the micro-chemistry of the varnish films after the Er:YAG laser irradiation is provided. As presented in previous research (Theodorakopoulos and Zafirooulos, 2003; Theodorakopoulos *et al.*, 2007), the ratios of the integrated areas of stretching vibration bands of hydroxide –OH (bonds at 3700-3100 cm<sup>-1</sup>) against C–H (bonds at 2850-3000 cm<sup>-1</sup>) and carbonyl –C=O (bonds at 1500-1900 cm<sup>-1</sup>) against C–H (bonds at 2850-3000 cm<sup>-1</sup>) bands increased upon ageing for all the varnish films (see Figures 5.34-38). Comparing the same ratios before and after the laser irradiation at different fluences, significant changes were observed in the dry and pre-wet treated films after five consecutive laser pulses at 5Hz (Chillè *et al.*, 2020).

---

<sup>2</sup> Personal communication with Ed Teppo (6 September 2019).

Prior to the laser irradiation, the aged dammar films showed the highest increment in intensity for both the OH/CH and the C=O/CH ratios compared to the unaged films (Figures 5.33-34), which implies a substantial oxidative degradation of the resin substrate (Theodorakopoulos and Zafirooulos, 2003; Theodorakopoulos *et al.*, 2007). Aged Ketone N films seem to have reacted similarly to the aged dammar films but with minor increment in absorption (around 51% decrease of the OH/CH ratio and 61% for the of C=O/CH ratio compared with the dammar) (Figures 5.35-36). However, the aged MS2A films exhibit the lowest increase for both ratios, indicating a less oxidative degradation of resin after ageing (Figures 5.37-38). Notwithstanding the minor absorption characteristics for the MS2A films, both Ketone N and MS2A indicate that after ageing the intensity of the absorption bands shifted gradually towards an increment in polarity as well as in an increase of  $-C=O$  groups.

Comparing the ratios of OH/CH and the C=O/CH before and after the laser irradiation at different fluences, significant changes can be observed in the dry and pre-wet dammar (Figures 5.33-34) (Chillè *et al.*, 2020) and in the dry Ketone N films (Figure 5.35) after five consecutive laser pulses at 5 Hz.

The OH stretching band shows an evident reduction in absorbance in both the dry and pre-wet irradiated dammar surfaces. This drastic reduction at the OH stretching vibrations relative to CH stretching verifies that the efficiency of the Er:YAG laser is directly proportional to the concentration of the OH groups present on the surface (De Cruz, Wolbarsht and Hauger, 2000a). The same can be said regarding the dry irradiated Ketone N areas (Figure 5.35) where the reduction in absorbance at the OH stretching vibrations has the same trend observed for the dammar films (Figures 5.33-34). These findings support the depth-dependent decreases in oxidation and polarity for both the coatings (Theodorakopoulos and Zafirooulos, 2003; Theodorakopoulos *et al.*, 2007). The DI-W+TW20 pre-wetted Ketone N films show a less marked slope suggesting a more gentle interaction with the surface even at the highest fluence tested, 2.4 J/cm<sup>2</sup> (Figure 5.36). Furthermore, decreases of OH/CH ratios in the irradiated dammar and Ketone N films with increased fluences up to 2.4 J/cm<sup>2</sup> have been determined, as also observed elsewhere (Theodorakopoulos and Zafirooulos, 2003; Theodorakopoulos, 2005, p. 223; Theodorakopoulos *et al.*, 2007). By increasing the fluence and eventually revealing deeper parts in the bulk of the dry (dammar and Ketone N films) and the

pre-wet (only dammar) irradiated films, the  $-\text{OH}/\text{C}-\text{H}$  and  $-\text{C}=\text{O}/\text{C}-\text{H}$  ratios are similar to those of the unaged films. As noted previously, the pre-wetted Ketone N has shown a less marked reduction in the  $\text{C}=\text{O}/\text{CH}$  ratios at the selected fluences of 0.5, 1, 1.5, 2.1 and 2.4  $\text{J}/\text{cm}^2$  (Figure 5.36). These observations are in line with findings that established the presence of degradation gradients formed by a reduction of the oxidised compounds as a function of depth in triterpenoid varnishes (Theodorakopoulos and Zafirooulos, 2003; Theodorakopoulos, 2005, p. 223; Theodorakopoulos *et al.*, 2007) and ketone resins treated with sodium salt-based hydrogels (Galatis, Boyatzis and Theodorakopoulos, 2012).

The results obtained from the semi-quantitative analysis carried out on the MS2A films suggested a different interaction of the aged varnish after the laser irradiation. Regardless of their dry or pre-wet irradiation and regardless the fluences, these films did not show significant changes in the  $-\text{OH}/\text{CH}$  and the  $-\text{C}=\text{O}/\text{CH}$  ratios (Figures 5.37-38). Judging by the  $-\text{OH}/\text{CH}$  and the  $-\text{C}=\text{O}/\text{CH}$  ratios of the pre-wetted MS2A films which were irradiated at different fluences one might assume that the films are not modified upon the interaction with the 2940 nm laser photons (Figure 5.38).

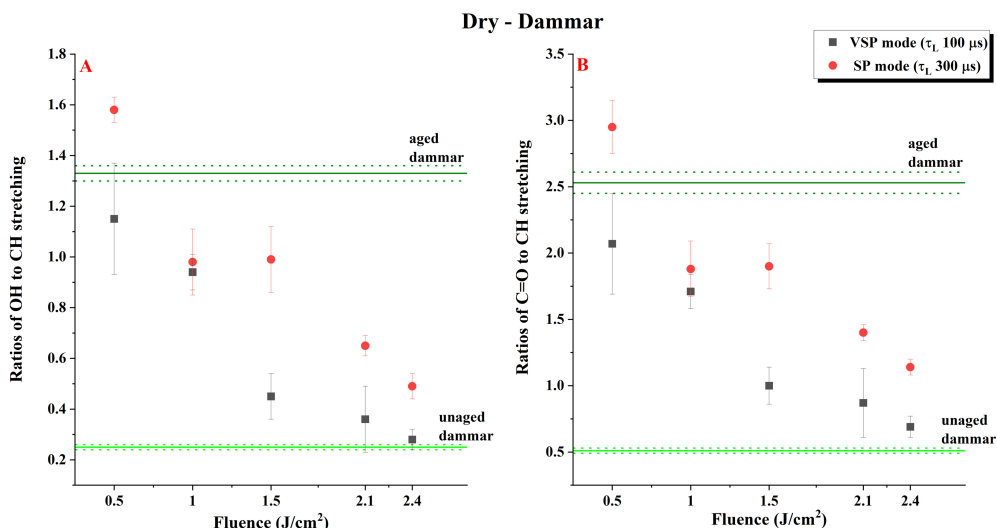


Figure 5.33 – Ratios of the integrated areas of the –OH/CH and the –C=O/CH bands as acquired by ATR/FT-IR vs fluence of the dry irradiated dammar films in VSP ( $\tau_L \approx 100 \mu s$ ) and SP ( $\tau_L \approx 300 \mu s$ ) modes after five consecutive laser pulses at 5Hz. The horizontal lines define the corresponding ratios of the dammar films before (dark green solid line) and after ageing (light green solid line). Dotted lines correspond to the experimental error (standard deviation).

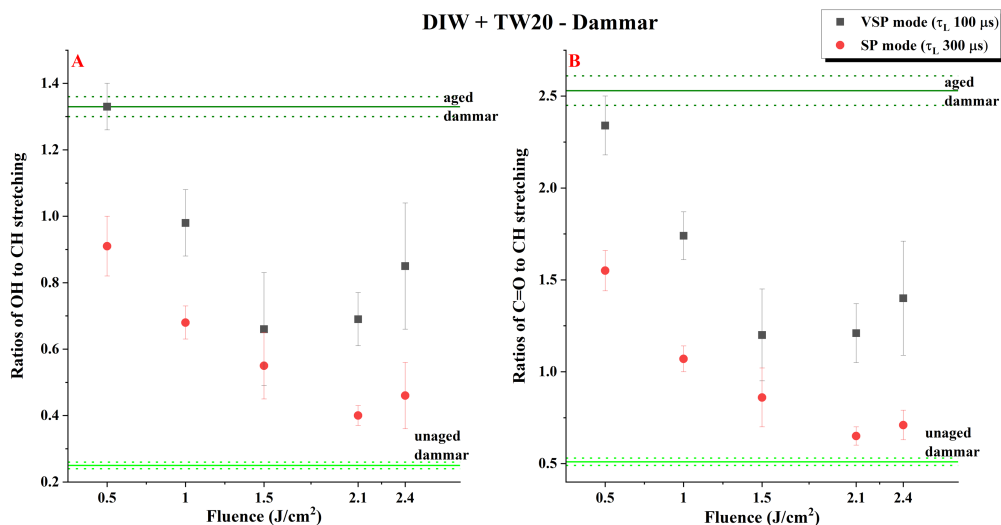


Figure 5.34 – Ratios of the integrated areas of the –OH/CH and the –C=O/CH bands as acquired by ATR/FTIR vs fluence of the DI-W+TW20 pre-wetted irradiated dammar films in VSP ( $\tau_L \approx 100 \mu s$ ) and SP ( $\tau_L \approx 300 \mu s$ ) modes after five consecutive laser pulses at 5Hz. The horizontal lines define the corresponding ratios of the dammar films before (dark green solid line) and after ageing (light green solid line). Dotted lines correspond to the experimental error (standard deviation).

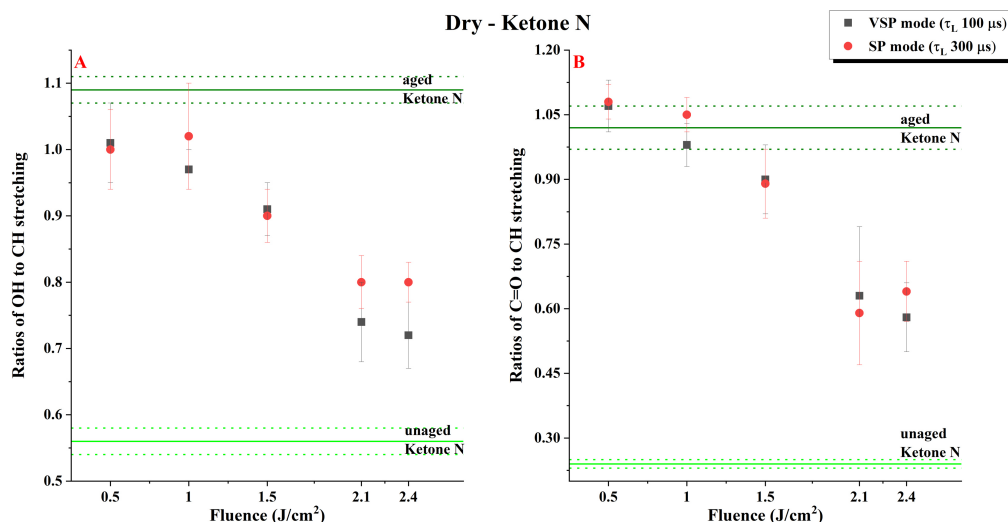


Figure 5.35 – Ratios of the integrated areas of the –OH/CH and the –C=O/CH bands as acquired by ATR/FT-IR vs fluence of the dry irradiated Ketone N films in VSP ( $\tau_L \approx 100 \mu\text{s}$ ) and SP ( $\tau_L \approx 300 \mu\text{s}$ ) modes after five consecutive laser pulses at 5Hz. The horizontal lines define the corresponding ratios of the Ketone N films before (dark green solid line) and after ageing (light green solid line). Dotted lines correspond to the experimental error (standard deviation).

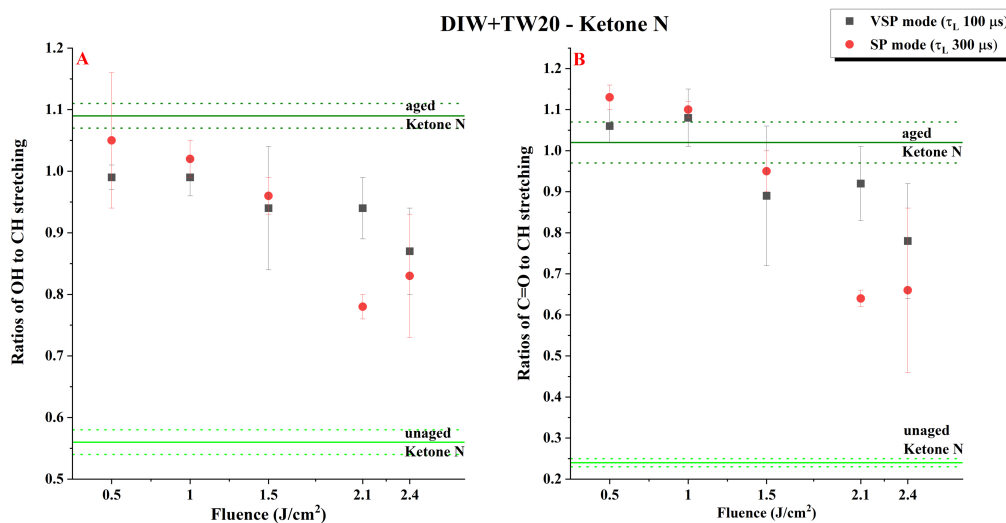


Figure 5.36 – Ratios of the integrated areas of the –OH/CH and the –C=O/CH bands as acquired by ATR/ FTIR vs fluence of the DI-W+TW20 pre-wetted irradiated Ketone N films in VSP ( $\tau_L \approx 100 \mu\text{s}$ ) and SP ( $\tau_L \approx 300 \mu\text{s}$ ) modes after five consecutive laser pulses at 5Hz. The horizontal lines define the corresponding ratios of the Ketone N films before (dark green solid line) and after ageing (light green solid line). Dotted lines correspond to the experimental error (standard deviation).

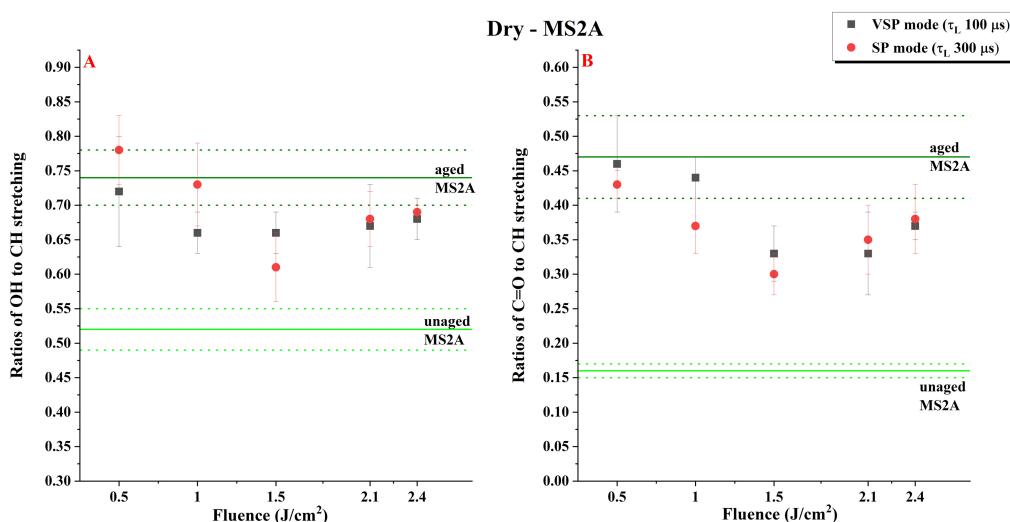


Figure 5.37 – Ratios of the integrated areas of the OH/CH and the C = O/CH bands as acquired by ATR/FT-IR vs fluence of the dry irradiated MS2A films in VSP ( $\tau_L \approx 100 \mu s$ ) and SP ( $\tau_L \approx 300 \mu s$ ) modes after five consecutive laser pulses at 5Hz. The horizontal lines define the corresponding ratios of the MS2A films before (dark green solid line) and after ageing (light green solid line). Dotted lines correspond to the experimental error (standard deviation).

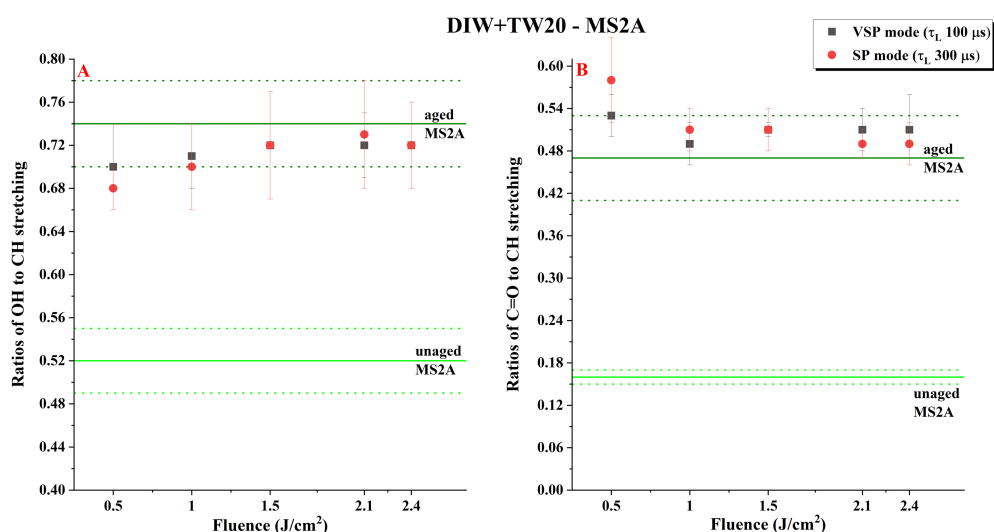


Figure 5.38 – Ratios of the integrated areas of the OH/CH and the C = O/CH bands as acquired by ATR/ FTIR vs fluence of the DI-W+TW20 pre-wetted irradiated MS2A films in VSP ( $\tau_L \approx 100 \mu s$ ) and SP ( $\tau_L \approx 300 \mu s$ ) modes after five consecutive laser pulses at 5Hz. The horizontal lines define the corresponding ratios of the MS2A films before (dark green solid line) and after ageing (light green solid line). Dotted lines correspond to the experimental error (standard deviation).

## 5.4 Conclusion

The effects of the laser-varnish interactions during the Er:YAG laser irradiation were studied and evaluated in conservation treatment scenarios where the varnishes have been either directly irradiated as a dry film or pre-wetted to enhance hydroxyl concentration on the surface.

Interaction of the Er:YAG laser with the aged dammar, Ketone N and MS2A resins as well as poly(isobutyl methacrylate) (Paraloid B67) films was studied in order to inform conservation cleaning treatments. Paraloid B67 did not absorb at 2940 nm and therefore did not interact with the Er:YAG laser, leading to the conclusion that artefacts and artworks with a Paraloid B67 coatings should never be irradiated with Er:YAG lasers at least when the film is not wetted (Striova, Camaiti, *et al.*, 2011; Striova, Castellucci, *et al.*, 2011).

BSE-SEM revealed important morphological differences between the single-pulse irradiated dammar varnish and the ketone resin (Ketone N and MS2A) varnishes. The extensive BSE-SEM study presented here addressed *objective f*. At the lowest fluence of 0.6 J/cm<sup>2</sup>, in VSP and SP modes, the aged dammar films showed locally swollen areas and the formation of circular laser spots of the TEM<sub>31</sub> mode. However, at the same fluence in VSP and SP modes, Ketone N showed minimal almost negligible interaction after laser irradiation. The lift-off phenomena were observed upon a single laser pulse irradiation on aged MS2A films. By increasing the fluence up to 2.5 J/cm<sup>2</sup>, dammar, Ketone N and MS2A showed marked melting with the formation of craters and bubbles and differences in the appearance was not readily discerned. The mathematical calculations and 2D simulations, presented in Chapter 4, were used for the interpretation of the laser-material interaction upon laser irradiation using two different laser pulse durations. Discrepancies between the BSE-images and the temperature profiles of the mathematical and two-dimensional models can be related to adopted simplifications which may lead to predictive errors (e.g., the decrease in the optical absorption coefficients with the increase in samples temperatures).

Since the efficiency of the Er:YAG laser is directly proportional to the concentration of hydroxide groups in the materials, the DI-W TW20 pre-wetted dammar, Ketone N and MS2A varnish films showed less marked laser spots when compared to the ones generated onto the dry irradiated surfaces.

BSE-SEM micrographs of the of dry irradiated varnishes after multiple-pulse

in VSP and SP modes showed more swollen surfaces and more pronounced concentric rings. Dry irradiated MS2A films displayed more pronounced lift-off phenomena, and both dammar and Ketone N showed the formation of craters. As already observed for the DI-W+TW20 pre-wetted surfaces upon a single laser pulse, at the lower fluence of  $0.6 \text{ J/cm}^2$ , dammar, Ketone N and MS2A films either exhibit none or very fewer marked laser spots when compared to the ones generated on the dry irradiated surfaces. However, at the highest laser fluence of  $2.5 \text{ J/cm}^2$ , the three consecutive irradiations at 2 Hz have caused a partial shrinkage and/or probable partial removal of the dammar and MS2A coatings.

ATR/FT-IR suggested that the use of Er:YAG laser allows the thinning of the surface layer of degraded varnishes without further modifying the overall skeletal structure of aged resins. This study addressed *objective g*. The ATR/FT-IR study confirmed that the increase in hydroxyl groups due to the ageing process of the coatings ensured increased absorption of the laser wavelength, which determines the main process of the laser-material interaction as described by Andreotti *et al.* (2007), De Cruz *et al.* (2014) and Teppo (2020). Moreover, ATR/FT-IR has been used to assess the laser cleaning efficiency process, in all the fluences tested. After having received five consecutive pulses, the dry and pre-wetted aged MS2A film was thinned but no change of hydroxides and carbonyls relative to CH bonds was monitored which is in line with the observation of the transmission studies presented in section 4.3.2. On the contrary, the five-pulse laser tests on the aged dammar and Ketone N resin films resulted in a considerable reduction of hydroxides and carbonyls relative to CH bonds compared to the films prior to irradiation. For these films, the decrease in hydroxides confirmed that the dominating mechanism of Er:YAG laser cleaning is directly related to the maximum absorption of the 2940 nm laser wavelength from the hydroxides in the irradiated surface. These gradients were not very pronounced in the wet-irradiated Ketone N film, but very pronounced in the dry irradiated films as well as in the wet-irradiated dammar varnish. The decrease in carbonyls, as deeper parts in the bulk of the films were uncovered, is in line with previous findings with UV excimer lasers indicating the presence of depth-wise oxidative gradients (Zafirooulos *et al.*, 2001; Theodorakopoulos and Zafirooulos, 2003; Theodorakopoulos *et al.*, 2007).

## CHAPTER 6      AN ANALYTICAL EVALUATION OF Er:YAG LASER CLEANING TESTS ON A NINETEENTH CENTURY VARNISHED PAINTING

*“We are dealing with complex objects and we should not expect to find easy solutions”.*

— Hedley (1989)<sup>1</sup>

*This chapter aims to evaluate the Er:YAG laser efficacy to safely thin a varnish on a nineteenth century oil painting addressing **objective h**. Tests have been carried out under single and multiple laser scans directly on the surface (dry) or after pre-wetting with deionised water (DI-W), DI-W and a non-ionic PEG(20)sorbitan monolaurate surfactant (Tween 20), Industrial Methylated Spirit (IMS) and DI-W, IMS and White Spirit (WS) and neat WS. Fluence ranged between 0.6 – 2.4 J/cm<sup>2</sup> and the Very Short Pulse (100 μs) duration mode was selected. Microscope glass coverslips were placed on the painting surface during irradiation to collect the condensed resin fragments that were extracted from the varnished surfaces. Spectral clusterisation maps of Multispectral Imaging (MSI) data of the irradiated surfaces supported the evaluation of the procedure. Further evaluation was performed by stereomicroscopy and colourimetry. Fourier Transform Infrared spectroscopy (FT-IR) and Pyrolysis Gas Chromatography/Mass Spectrometry (Py-GC/MS) analysis indicated that the varnish resin was dammar. The collected resin fragments were analysed by FT-IR. The results showed that the resin did not degrade even at the highest level of fluence employed, thereby allowing a subsequent analytical evaluation.*

---

<sup>1</sup> (Hedley, 1993)

## 6.1 Introduction

The surface cleaning of easel paintings is considered as one of the most critical, highly sensitive and complex procedure in conservation (Cremonesi and Signorini, 2012). This treatment is an irreversible process as it is impossible to reconstitute what was removed from the original painted surface (Oddy, 1999).

The interaction of the organic and inorganic paintings' constituents with laser beams and the subsequent removal mechanism of targeted materials, i.e. varnishes, patinas or/and restoration materials, is multifaceted (De Cruz *et al.*, 2014). The use of the mid-infrared wavelength Er:YAG laser (2940 nm) was successfully tested on easel paintings (Andreotti *et al.*, 2007, 2016; Brunetto, Bono and Frezzato, 2020; Chillè, Papadakis and Theodorakopoulos, 2020; Hellen, 2020), as an alternative to traditional cleaning methods, e.g. the use of solvent mixture or mechanical means.

A nineteenth century varnished oil painting depicting an “Hunting Scene” (95 × 54 cm), belonging to the collection of paintings of the Department of Arts at Northumbria University, was used to carry out laser cleaning tests (Figure 6.1).



Figure 6.1.1 – The nineteenth century oil painting “Hunting Scene” (95 × 54 cm) belonging to the collection of paintings of the Department of Arts at Northumbria University (Newcastle upon Tyne).

The aim of this chapter is to understand the effects of Er:YAG-induced thinning of a painting's varnish, scanning its surface using one laser pulse per scan and determine the fluence range for a safe varnish irradiation to avoid disruption of the underlying paint layers. In order to address this, a multi-analytical approach has been employed. Spectral clusterisation on multispectral imaging data of the treated surfaces areas was carried out to monitor the efficiency of Er:YAG laser cleaning process based on the spectral reflectivity changes across the treated areas. This enables the understanding of the treated surfaces effects including the thinning variations on the varnish layer (Papadakis, Loukaiti and Pouli, 2010). For the same reason, colourimetric analysis has been also used to determine the impact of laser irradiation to the surface gloss based on factors that were introduced elsewhere (Kun, Huimin and Shangzhong, 2014; Sanderson, 2015). Subsequently, Attenuated Total Reflectance/Fourier Transform Infra-Red (ATR/FT-IR) spectroscopy and Pyrolysis Gas Chromatography/Mass Spectroscopy (py-GC/MS) have been carried out to characterise the varnish film of the painting prior to the Er:YAG laser irradiation. Then, ATR/FT-IR was performed on the condensed fragments collected on the coverslips upon laser irradiation. Extracting minute quantities of coatings with Er:YAG lasers is a reliable sampling technique for analytical evaluation which has been established elsewhere (Bracco *et al.*, 2003; Colombini *et al.*, 2003; Andreotti *et al.*, 2007; Andreotti, Colombini and De Cruz, 2020).

## 6.2 Material and methods

### 6.2.1 Attenuated Total reflection / Fourier Transform - Infra-Red spectroscopy (ATR/FT-IR)

ATR/FT-IR spectroscopy has been carried out on the same device already described in chapters 3 and 5. Prior to laser irradiation, sampling was conducted under a stereomicroscope by scraping off minor quantities of varnish with a stainless-steel scalpel blade No10. The laser irradiated surface was sampled directly during irradiation by collecting the condensed material on glass coverslips which is an established micro-destructive sampling technique (Bracco *et al.*, 2003; Colombini *et al.*, 2003; Andreotti *et al.*, 2007; Andreotti, Colombini and De Cruz, 2020). Samples of the untreated and treated varnish were placed directly on the

diamond window and simply pressed to optimise the contact (up to pressure gauge of 100). The working wavenumber range was from 4000 to 380  $\text{cm}^{-1}$ , and the spectra were acquired at 16 scans at 4  $\text{cm}^{-1}$  resolution. The background was automatically subtracted. The ATR/FT-IR spectra were processed using PerkinElmer Spectrum™ 10 software suite.

The integrated areas of the peaks corresponding to stretching vibrations of hydroxide (2700-3700  $\text{cm}^{-1}$ ), C–H (2850-3000  $\text{cm}^{-1}$ ) and carbonyl (1500-1900  $\text{cm}^{-1}$ ) bonds were determined (Ciofini, 2014). These spectra were normalised to an identical intensity at the C–H stretching frequency of 2953  $\text{cm}^{-1}$  (Derrick, Stulik and Landry, 1999). Consequently, the ratios of the integrated areas of the selected OH/CH and the C=O/CH band were determined. The generated data were compared to the non-irradiated sample to monitor any possible chemical changes after laser irradiation (Chillè *et al.*, 2020; Chillè, Papadakis and Theodorakopoulos, 2020).

### 6.2.2 Pyrolysis–TMAH–Gas Chromatography/Mass spectroscopy (Py-TMAH-GC/MS)

Pyrolysis - Gas Chromatography / Mass Spectrometry has been carried out on a Thermo Finnigan Focus GC Gas Chromatograph with an Agilent DB5-MS UI column (ID: 0.25 mm, length: 30 m, df: 0.25  $\mu\text{m}$ , Agilent, Santa Clara, CA, USA), fitted with a Pyrola 2000 Platinum filament pyrolyser (PyroLab, Sweden).

A sample of the order of 0.5 mg was directly derivatised in an aliquot of 1  $\mu\text{l}$  of 25 wt% in methanol tetra-methylammonium hydroxide (TMAH) and placed on the Pt filament. The Pyrolyser was coupled to a DSQII Mass Spectrometer. The inlet temperature to the GC was kept at 280 °C. The helium carrier gas flow rate was 1 ml/min with a split flow of 13 ml/min. The MS transfer line was held at 280 °C and the ion source at 250 °C. The pyrolysis chamber was heated to 175 °C, and pyrolysis was carried out at 600 °C for 2 s for the majority of samples. The temperature program was set as follows: 40 °C for 2 mins followed by 26 mins of 8 °C/min to 250 °C followed by 10 mins of 3 °C/min up to 280 °C, and a final step at 280 °C held for 20 mins to a total run time of 58 mins.

Acquisition was carried out in a Total Ion Count mode, where all ions in the range 40–800 m/z were monitored. The data were examined and processed using Thermo Scientific Xcalibur™ 2.2 version.

Characterisation has been verified with previous findings (van der Doelen *et al.*, 1998; van der Doelen, van den Berg and Boon, 1998; Colombini *et al.*, 2000; Watts and de la Rie, 2002; Theodorakopoulos, Boon and Zafirooulos, 2009).

### 6.2.3 Laser cleaning tests

A Fotona Fidelis<sup>XS</sup>, VSP Er:YAG laser in Very Short Pulse (VSP) mode ( $\tau_L \approx 100 \mu\text{s}$ ) was employed. The beam was delivered perpendicularly onto the varnish surface by the R11 handpiece, held by the laser-operator like a pen. The laser beam diameter was set at 3 mm, both in the handpiece and in the Fidelis™ display, and the pulse repetition rate was set at 2 Hz.

Prior to the laser cleaning tests on the nineteenth century varnished oil painting, a Fotona XS Dynamis Er:YAG laser in the VSP mode was employed to determine the laser working distance and the laser beam diameter. The R11 handpiece was fixed at three different working distances: 2, 5 and 10 cm. The distances were measured from the lens at the end of the handpiece up to the surface of a photosensitive black paper. The laser beam was released to create a series of laser beam spots on the paper. The laser spot areas were calculated and fluences were determined by dividing the laser energy by the measured spot areas, as already presented elsewhere (Melita *et al.*, 2020). Each manually determined fluence was compared to fluence reading on the Fidelis display (Figure 6.2).

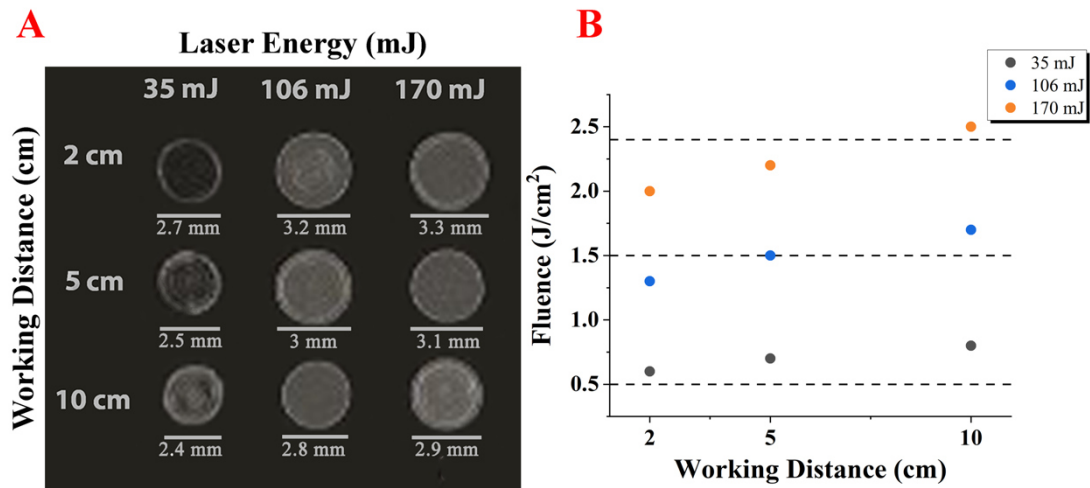


Figure 6.2 – Data collected by fixing the R11 handpiece at three different working distances (WD): 2, 5 and 10 cm from a photosensitive black paper substrate and three output laser energies: 35, 106 and 170 mJ as set in a Fotona XS Dynamis laser unit. The nominated fluences: 0.5, 1.5 and 2.4 J/cm<sup>2</sup>, and the beam diameter at 3 mm were set and shown in the laser unit display. The repetition rate was set at 5Hz to allow a single pulse to hit the paper substrate using a shutter. The spatial laser beam profiles mapped directly on the photosensitive paper (A) and demonstrate that at 5 cm WD and 106 mJ, the 1.5 J/cm<sup>2</sup> actual and nominated fluence coincides, as shown when fluence versus WD is plotted (B). Further information is provided in Chapter 5.

Therefore, the laser irradiation tests on the painting were carried out in fluences, as shown in the Fotona Fidelis<sup>XS</sup> laser unit display, with the following fluences: 0.6, 0.7, 1, 1.5, 2, 2.1, 2.3, and 2.4 J/cm<sup>2</sup>. From this point these fluences are referred to as ‘*nominated fluences*’. The working distance measured between the end of the handpiece and the painting surface was kept constant at 5 cm. Single and multiple laser pulses were fired onto the nineteenth century painting surface, creating a total of twenty-two tested areas.

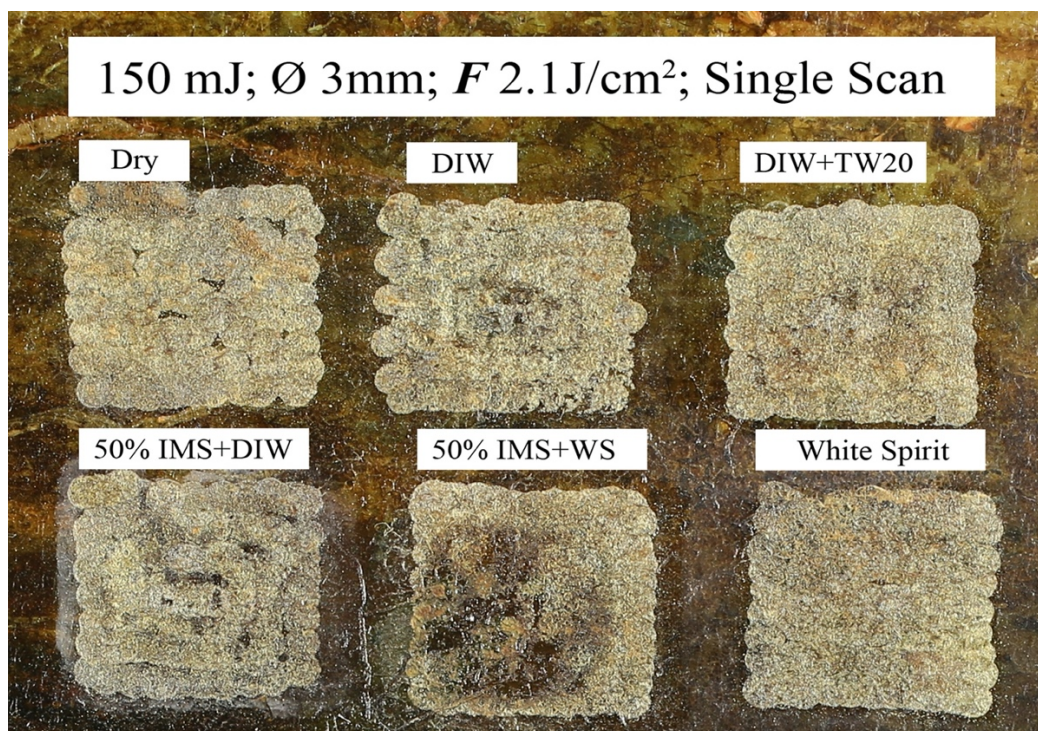


Figure 6.3 – Detail of one test (one scan, 2.1 J/cm<sup>2</sup>). At top left the dry irradiated area is shown, followed by other irradiated areas pre-wetted with the following solutions: deionised water (DI-W), 1% v/v Tween20 in DI-W, 50% v/v Industrial Methylated Spirit (IMS) in DI-W, 50% v/v IMS in White Spirit (WS) and pure White Spirit. All the laser irradiated areas were 15x15 mm.

In each of them, six different tests were run (15x15 mm squares) (Figure 6.3), at first on the dry-irradiated surface and then using five different wetting agents, which were:

- Deionised Water (D-IW);
- 1% (v/v) of non-ionic polyoxyethylenesorbitan monolaurate surfactant (Tween20, Sigma Aldrich) in 50 ml of Deionised water (DI-W+TW20) (Cremonesi and Signorini, 2012);
- 50% (v/v) Industrial Methylated Spirit (IMS: ethyl alcohol > 94% v/v; methyl alcohol 3-6% v/v; water <1% v/v, by Thermo Fisher Scientific) in deionised water (50% v/v IMS+DI-W);
- 50% (v/v) IMS and White Spirit (WS, by Sigma Aldrich) (50% v/v IMS+WS);
- White Spirit (WS).

These solvents and solutions already employed by Bracco *et al.* (2003) were herein thoughtfully selected to monitor the interaction of the laser with various surface polarities<sup>2</sup>. Cremonesi-Wolbers solubility tests (Table 6.1), binary solvent mixtures composed of iso-octane (I), acetone (A) and ethyl alcohol (E) at different concentrations (Wolbers, 2000; Cremonesi and Signorini, 2012) were carried out prior to the laser cleaning.

Table 6.1 – Cremonesi-Wolbers tests of solubility.

Solvent mixture	% Volume		
	Iso-octane	Acetone	Ethyl alcohol
I	100	-	-
IA1	90	10	-
IA2	80	20	-
IA3	70	30	-
IA4	60	40	-
IA5	50	50	-
IA6	40	60	-
IA7	30	70	-
IA8	20	80	-
IA9	10	90	-
A	-	100	-
IE1	90	-	10
IE2	80	-	20
IE3	70	-	30
IE4	60	-	40
IE5	50	-	50
IE6	40	-	60
IE7	30	-	70
IE8	20	-	80
IE9	10	-	90
E	-	-	100

The solvent blends were prepared herein using WS and acetone or WS and IMS, and they were used at various concentrations in order to monitor the polarity threshold for the efficient solubilisation of the varnish film. The Fractional Solubility Parameter (FSP) provided an indication of the surface polarity and it was calculated for each of the agents. FSPs were determined for:

- DI-W:  $F_d$  18 (non-polar dispersion force – Van der Waals or instant dipole),  $F_p$  28 (polar dipole force – permanent dipole),  $F_h$  54 (hydrogen bonding force);
- 50% (v/v) IMS+DI-W:  $F_d$  26.8,  $F_p$  23.12,  $F_h$  50.1;
- 50% (v/v) IMS+WS:  $F_d$  62.8,  $F_p$  11.12,  $F_h$  26.1;

<sup>2</sup>The interactive solvent and solubility triangle©. For the description of solubility triangle© please refer to <http://www.icr.beniculturali.it/flash/progetti/TriSolv/TriSolv.htm>

- WS:  $F_d$  90,  $F_p$  4,  $F_h$  6.

Prior to the laser irradiation of the varnish surface, all the glass coverslips (15x15 mm) were cleaned using deionised water, acetone, ethanol and then dried. For the pre-wetting procedure, the painting surface was wetted with cotton swabs. The latter loaded with wetting agents were firstly drained on a blotting paper before the swabs were rolled three times on the varnish surface. Then, the area was immediately covered with thin glass coverslips and irradiated with the laser. Considering practicalities and previous trials (Bracco *et al.*, 2003), for tests based on two laser scans, the varnish surface was pre-wetted at the beginning of each laser scan. For trials based on three laser scans, the varnish layer was pre-wetted only once prior to laser irradiations.

#### 6.2.4 Technical photography

The twenty-two test areas were photographed using a Canon digital camera Compact-Macro Lens 50 mm 1:2,5 fixed/prime. Each set was captured before and after laser irradiation in the same lighting conditions using visible (VIS) daylight and ultraviolet (UV) lamps. VIS: Bowens SL855 with 8 daylight light (approximately 5800 K) sources provided illumination in the visible and near-infrared regions. UV lamps (UV 72 W blacklight) had an emission between 315 and 400 nm (peak 365 nm). A Kodak Wratten 2E filter cutting off wavelengths below 415 nm was employed for the UV induced fluorescence imaging.

#### 6.2.5 Stereomicroscopy

Stereomicroscopic observations of the painting surface were carried out before and after laser irradiations in reflected light with a Leica Stereo Zoom S6 D 6.3:1 stereomicroscope (6.3x - 20x magnification) that provides a field of view up to 36.5 mm. A Leica MC170 HD Microscope Camera (5 Megapixel HD) and a set of LED fibre optic lights were employed to capture the micrographs.

### 6.2.6 *Colourimetry*

Colourimetric measurements were carried out with a Konica Minolta Spectrophotometer CM 2600-D covering a 360 - 740 nm spectral range at spectral resolution of 10 nm. The spot diameter was set at 3 mm, using a Target Mask CM-A147. The data were acquired in both Specular Component Included (SCI) and Specular Component Excluded (SCE) modes.

Three measurements for each examined area (inside the laser-treated tests and outside near the edge of the untreated areas) were averaged to obtain each data point.

The data used for this study were the lightness values  $L^*$  ranging between 100 (brightest white) and 0 (darkest black) acquired in SCI and SCE modes (Kun, Huimin and Shangzhong, 2014; Sanderson, 2015; Mouw, 2018). In SCE mode a glossy surface returns values closer to zero (darker) than a matte surface of the same colour (Mouw, 2018).

According to Kun, Huimin and Shangzhong (2014) and Sanderson (2015),  $SCI = SCE + GRF$  (Gloss Related Factor). Thus, the change in the painting's surface, before and after laser irradiation, was calculated by the following formulas:

$$GRF_b = L_{SCI_b}^* - L_{SCE_b}^* \quad (\text{Eq. 6.1})$$

$$GRF_a = L_{SCI_a}^* - L_{SCE_a}^* \quad (\text{Eq. 6.2})$$

where indices b and a correspond values before and after irradiation, respectively. Therefore, the irradiation impact to the surface gloss can be determined as:

$$\Delta GRF = GRF_b - GRF_a \quad (\text{Eq. 6.3})$$

Herein, the surface was not further processed with any solution after laser irradiation, which is common in art conservation procedures (Brunetto, Bono and Frezzato, 2020).

### 6.2.7 Multispectral imaging

Multispectral Imaging (MSI) was performed using an XpeCAM X01 camera (XpectralTEK) (Figure 6.4). The device, equipped with a 5 M pixels monochrome CMOS sensor, and a 35 mm / F1.3 objective lens, acquired a sequence of spectral images ranging from 350 - 400 nm every 10 nm, 400 - 700 nm every 25 nm and 700 - 1200 nm every 50 nm. The same light sources as those for studio photography were employed.



Figure 6.4 – XpeCAM X01 camera (XpectralTEK).

A white Diffuse Reflectance Target (DRT) was used for calibration purposes. The DRT was placed very close and parallel to the painting surface, enabling spectral intensity calibration and corrections for inhomogeneous illuminance of the surface. Acquisition was performed for both DRT and sample images. Each spectral image was then normalised with the corresponding DRT spectral image.

MSI data were processed with an advanced image-processing programme, Tensor Image Processing Platform (TIPP), specifically designed to analyse MSI data (Papadakis *et al.*, 2011). All the data were imported to TIPP, and the raw spectral cube was created for both the test areas images and the white reference images. Using the XpeEye acquisition software, the contribution of the dark current was removed a priori from both the test areas and DRT images. Subsequently, the sample's spectral cube was normalised by a TIPP module, correcting the spectral intensity profile and any unevenness of the light across the test areas. This was

achieved by dividing the sample's spectral images (with the relative DRT's spectral images and multiplying) with the known reflectivity of the DRT at each wavelength band investigated. Registration was conducted by a custom-made algorithm specifically designed to operate with data derived from multi-spectral imaging systems (Zacharopoulos *et al.*, 2018). The acquired spectral images were then processed by a blind clustering method (k-means clusterisation) (Ding, He and Simon, 2005), where individual pixel spectral similarities were mapped with a single colour. Spectral clustering was carried out on 11 spectral images in the 360-550 nm wavelength range, in which the aged varnish absorbed strongly. Distinct areas were classified by significant reflectance differences. The generated MSI clusterisation maps provided information related to the percentage of the varnish thinning. Quantification of the laser irradiation efficacy was performed via calculation of the clusters' surface coverage, in each scanned area.

### 6.3 Results and discussion

#### 6.3.1 Varnish Characterisation

Prior to the laser irradiation tests, the varnish of the painting was characterised by means of ATR/FT-IR and Py-TMAH-GC/MS, which showed that the varnish is a triterpenoid (TTP) dammar resin varnish.

The ATR/ FT-IR spectra are reported in Figure 6.5 and their frequency assignments are listed in Table 6.2.

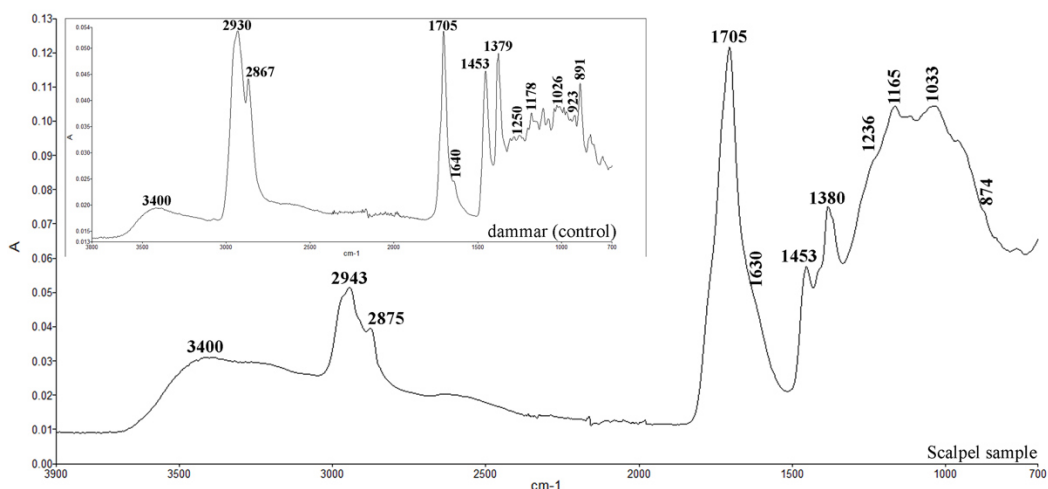


Figure 6.5 – ATR/FT-IR spectra of the triterpenoid varnish sampled on the nineteenth century painting by scalpel. The control dammar resin spectrum is shown in the inset.

Table 6.2 – Wavenumbers corresponding to the maxima of the IR absorbance bands of the control dammar and the painting varnish (Theodorakopoulos *et al.*, 2007; Ciofini *et al.*, 2016b; Invernizzi *et al.*, 2018).

dammar Wavenumbers (cm <sup>-1</sup> )	Triterpenoid varnish painting sample Wavenumbers (cm <sup>-1</sup> )	Band assignment
3400	3400	$\nu_s$ O–H
2930	2943	$\nu_{as}$ CH <sub>3</sub> /CH <sub>2</sub>
2867	2875	$\nu_s$ CH <sub>3</sub>
1705	1705	$\nu$ C=O (aldehydes, ketones and carboxylic acids)
1640	1630	$\nu$ C=C of cis –C=C–
1453	1453	$\delta$ CH <sub>3</sub> /CH <sub>2</sub>
1379	1380	$\delta$ CH <sub>3</sub>
1250	1236	$\nu$ C–C vibration, $\delta$ C–H in ring
1178	1165	$\delta$ C–H in ring, $\nu$ C–O in esters, $\nu$ C–C in alkanes
1026	1033	$\delta$ C–H in ring, $\nu$ C–O
923	-	C–H out-of-plane deformation, (one only H attached to ring)
891	874	C–H out-of-plane deformation, (two adjacent H attached to ring) <sup>2</sup>

The presence of the broad absorbance band at  $3400\text{ cm}^{-1}$  corresponding to  $2940\text{ nm}$ , attributed to stretching vibrations of O–H groups, indicates the absorption at the Er:YAG laser wavelength (Andreotti *et al.*, 2016). Methyl and methylene groups have shown two sharp absorption peaks at  $2943$  and  $2875\text{ cm}^{-1}$  due to asymmetric  $\text{CH}_3/\text{CH}_2$  and symmetric  $\text{CH}_3$  stretching, while the  $1453$  and  $1380\text{ cm}^{-1}$  peak are attributed to the C–H bending of  $\text{CH}_2$  and  $\text{CH}_3$ , respectively (Theodorakopoulos *et al.*, 2007; Russo and Avino, 2012; Invernizzi *et al.*, 2018). The triterpenoid varnish painting sample shows a characteristic IR absorbance peak at  $1705\text{ cm}^{-1}$ , due to the C=O carbonyl stretching vibration of the resinous acids (Invernizzi *et al.*, 2018). The band at  $1630\text{ cm}^{-1}$  corresponds to the C=C stretching, and  $1165\text{ cm}^{-1}$  and  $1236\text{ cm}^{-1}$  are attributed to the saturated C–C stretching vibrations. The peak at  $874\text{ cm}^{-1}$  indicates CH out-of-plane deformation of two hydrogen atoms in aromatic rings (Theodorakopoulos *et al.*, 2007).

The chromatogram of the Py-TMAH-GC/MS study has shown a series of peaks between 35 and 58 min (Figure 6.6) which correspond to a TTP resin.

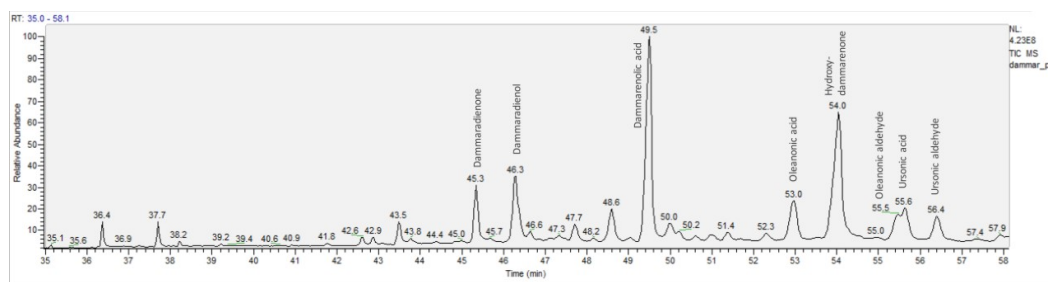
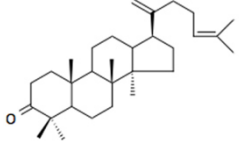
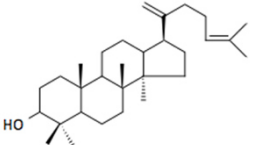
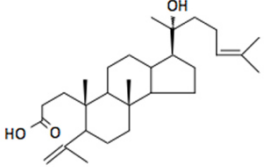
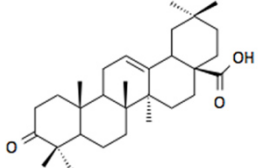
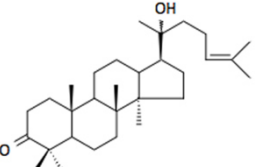
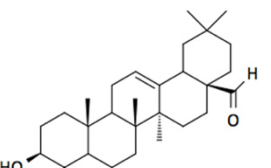
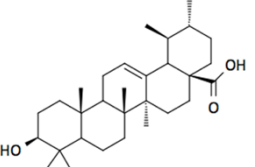
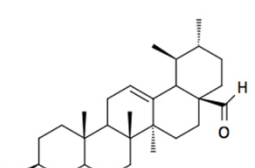


Figure 6.6 – The Py-TMAH-GC/MS chromatograph that indicates that the varnish of the painting is dammar. The MS spectra are shown in Appendix C.

The main peaks have been identified in the mass spectra as *dammaradienone*, *dammaradienol*, *dammarenolic acid*, *oleanonic acid*, *hydroxydammarenone*, *oleanonic aldehyde*, *ursonic acid* and *ursonic aldehyde* (Table 6.3 and Appendix C). The presence of *dammarenolic* and *ursonic acids* (Figures C3 and C7) indicates that the resin is dammar (van der Doelen *et al.*, 1998; Colombini *et al.*, 2000; Watts and de la Rie, 2002; Theodorakopoulos *et al.*, 2007; Dietemann *et al.*, 2009; Bonaduce *et al.*, 2016).

Table 6.3 – Molecules recorded via Py-TMAH-GC/MS. The data are in line with findings published elsewhere (van der Doelen et al., 1998; Colombini et al., 2000; Watts and de la Rie, 2002; Theodorakopoulos et al., 2007; Dietemann et al., 2009; Bonaduce et al., 2016).

Retention Time (min)	Compound	Molecular structure	MW	m/z	Figure (Appendix C)
45.3	dammaradienone		424	109, 189, 205	C1
46.3	dammaradienol		426	109, 207	C2
49.5	dammarenic acid		472	109, 454	C3
53	oleanonic acid		548	143	C4
54	hydroxydammarone (3-oxo-dammara-20,24-diene)		442	109, 205, 424	C5
55.5	oleanonic aldehyde		409	189, 203, 232	C6
55.6	ursonic acid		468	205	C7
56.4	ursonic aldehyde		438	133, 203, 232, 409	C8

### 6.3.2 Er:YAG laser tests

The procedure for the Er:YAG laser tests has been carried out on a nineteenth century oil painting to breakdown and thin the dammar varnish without removing it (Figure 6.7).



Figure 6.7 – The nineteenth century oil painting “Hunting Scene” (95 × 54 cm) with the Er:YAG laser test areas (A); Laser cleaning in progress (B) - also published in Chillè, Papadakis and Theodorakopoulos (2020).

A gradual increase in the *nominated fluence* was applied, and coverslips were placed in between the paint surface and the handpiece to collect resin fragments for further analyses. Laser irradiation was run both on dry surface and with wetting agents, ranging from auxiliary OH-containing solvents (such as DI-W and IMS) to a non-OH solvent (WS). Wetting agents have been used herein as a polarity regulator and not for varnish solubilisation.

Since the efficiency of the Er:YAG laser is directly proportional to the number of OH groups present in the surface (De Cruz, Hauger and Wolbarsht, 1999; De Cruz, Wolbarsht. and Hauger, 2000a, 2000b), hydroxides were introduced by adding hydroxylated liquids, which aided to increase the laser interaction with the varnish layer (De Cruz, Wolbarsht and Hauger, 2000a, 2000b; Colombini *et al.*, 2003; Teppo, 2020), in order to reduce the heat diffusion of the incident 2.94  $\mu\text{m}$  beam in the bulk (De Cruz, Wolbarsht and Hauger, 2000a, 2000b; Andreotti *et al.*, 2016; Chillè *et al.*, 2020).

Laser irradiation has resulted in circular spots identified on the dammar varnish surface. The spots became gradually more defined with the increase of the *nominated fluence*. This effect was clearly visible at naked eye although it was not recorded with OM and SEM techniques, mainly due to the size of the painting.

Because of this, the gloss of the varnish surface reduced progressively to a whitish appearance also due to the augmented light scattering.

The tests have shown that irradiation of the varnish had similar effects after:

- dry or pre-wetted with WS;
- pre-wetted with DI-W and DI-W+TW20;
- pre-wetted with 50% v/v IMS+WS and 50% v/v IMS+DI-W.

As reported in section 6.2.3, Cremonesi-Wolbers solubility tests (Wolbers, 2000; Cremonesi and Signorini, 2012) were carried out on the painting prior to irradiation. The presence of a natural resin varnish was determined by comparing the values of non-polar dispersion forces,  $f_d$ , polar dipole forces,  $f_p$ , and hydrogen bond forces,  $f_h$  (Cremonesi and Signorini, 2012; Phenix, 2013; Striber, Jovanović and Jovanović, 2017). A solvent-induced varnish removal was not included in the scope of this work; therefore, no comparisons have been made between the laser tests and the Cremonesi-Wolbers solubility tests.

Nominated fluences between 0.7 and 2.4 J/cm<sup>2</sup> have generated an evident breakdown of the surface after one, two and three laser scans were carried out.

The varnish thinning was verified by detecting the condensed material on the coverslips and by visually assessing the painting surface under visible and UV light (Figure 6.8).

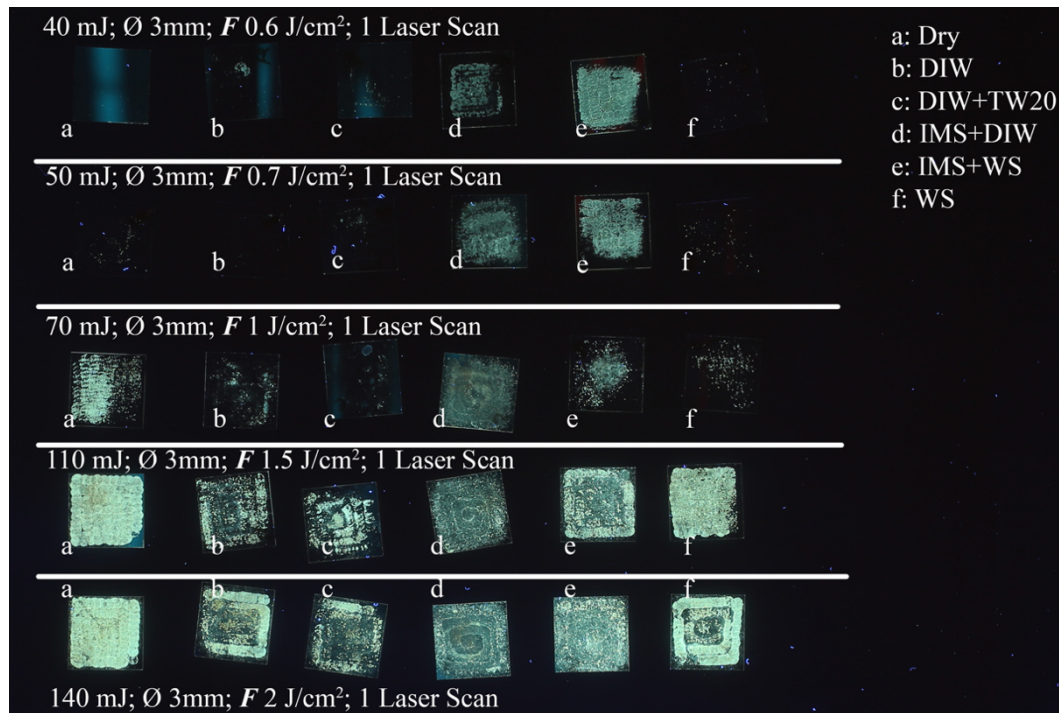


Figure 6.8 – UV induced fluorescence of resin fragments collected on glass coverslips at different fluences.

In correspondence to the dry irradiation tests, the desired outcome was obtained by one scan at  $2 \text{ J/cm}^2$  and two scans at nominated fluences ranging from  $0.7$  to  $1 \text{ J/cm}^2$  with no apparent colour variation of the varnish surface by the naked eye (Figure 6.9).

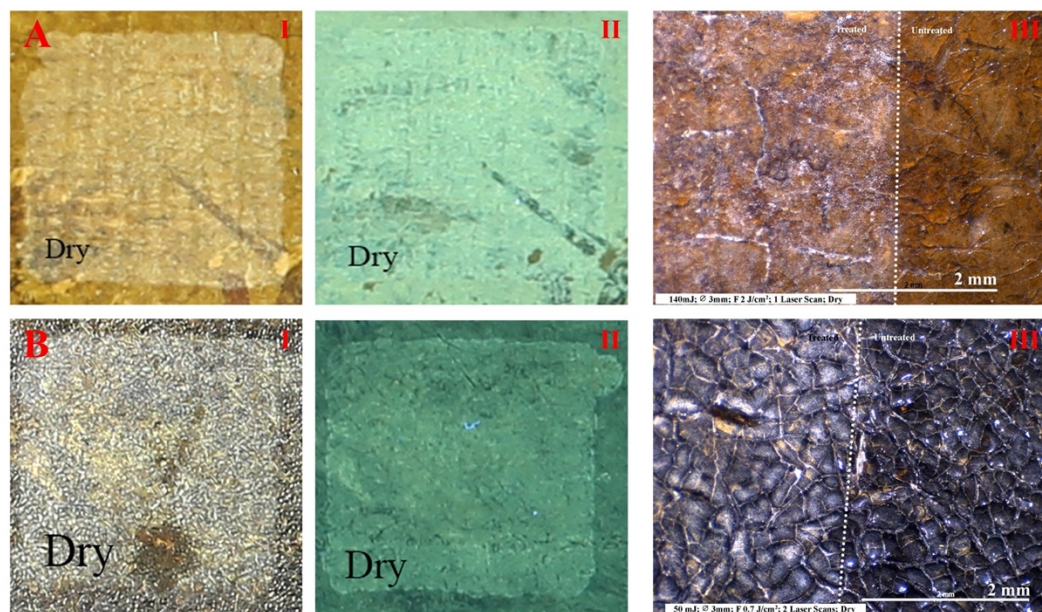


Figure 6.9 – Micrographs of the dry irradiated test areas with a satisfactory outcome. A: One laser scanned area at nominated fluence  $2 \text{ J/cm}^2$  and B: two laser scanned area at nominated fluence  $0.7 \text{ J/cm}^2$ ; I) visible light (VL); II) UV induced fluorescence; III) VL stereomicrograph. All the laser irradiated areas studied were  $15 \times 15 \text{ mm}$ .

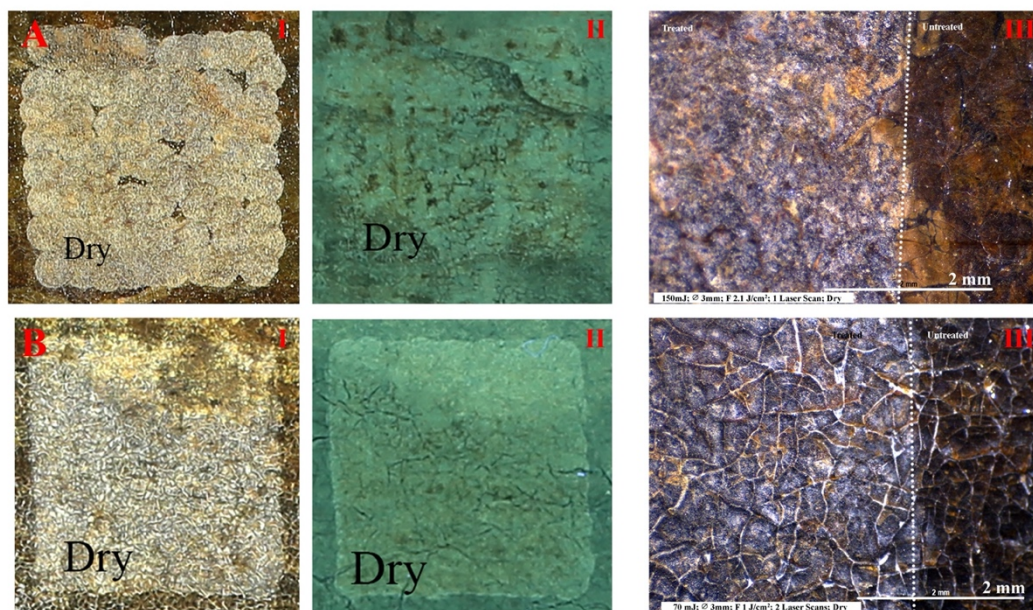


Figure 6.10 – Micrographs of the dry irradiated test areas where the brown hue was visually detected. A: One laser scanned area at nominated fluence  $2.1 \text{ J/cm}^2$  and B: two laser scanned area at nominated fluence  $1 \text{ J/cm}^2$ ; I) visible light (VL); II) UV induced fluorescence; III) VL stereomicrograph. All the laser irradiated areas studied were  $15 \times 15 \text{ mm}$ .

An over-treatment, identified as the generation of a brown hue of the irradiated area, was visually assessed after one laser scan at  $2.1 \text{ J/cm}^2$ , as well as at two laser scans of the surface at  $1 \text{ J/cm}^2$  using the stereomicroscope (Figure 6.10). The visually assessed colour variation can be related to laser-induced photothermal and photomechanical effects (Andreotti *et al.*, 2007; Pereira-Pardo and Korenberg, 2018; Lopez *et al.*, 2019; Chillè *et al.*, 2020).

Satisfying results in terms of a gradual thinning of the varnish without a brownish discolouration were obtained in the presence of DI-W+TW20 at one laser scan at  $2.4 \text{ J/cm}^2$ , two laser scans applications at  $2.3 \text{ J/cm}^2$  and three laser scans applications at  $2.1 \text{ J/cm}^2$ , respectively (Figure 6.11).

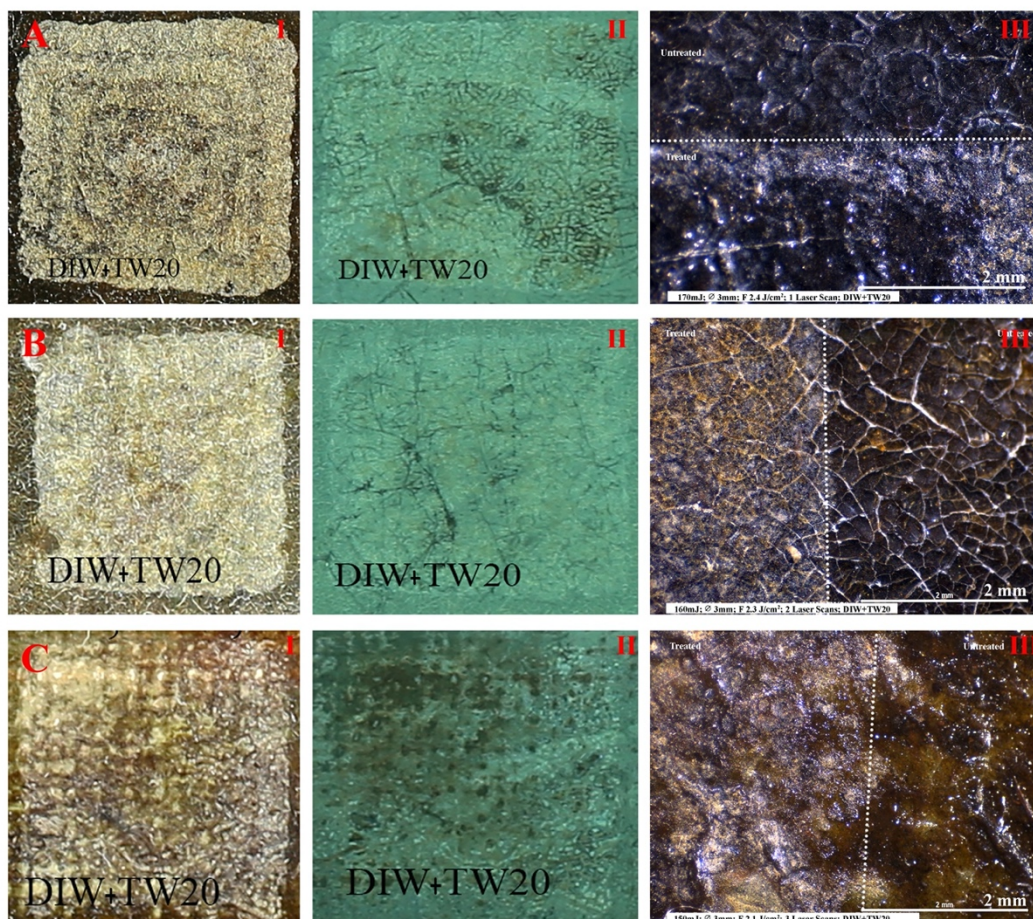


Figure 6.11 – Micrographs of the DI-W + TW20 pretweted irradiated test areas with a satisfactory outcome. A: One laser scanned area at nominated fluence  $2.4 \text{ J/cm}^2$ , B: two laser scanned area at nominated fluence  $2.3 \text{ J/cm}^2$  and C: three laser scanned area at nominated fluence  $2.1 \text{ J/cm}^2$ ; I) visible light (VL); II) UV induced fluorescence; III) VL stereomicrograph. All the laser irradiated areas studied were  $15 \times 15 \text{ mm}$ .

Prior to the laser irradiation, the tests of solubility revealed that neat IMS was able to solubilise the varnish film. Therefore, the use of 50 % v/v of IMS+WS or 50% v/v of IMS+DI-W blends may not ensure adequate evaluation of the data collected during the cleaning tests. This is due to the fact that it would not be possible to differentiate if the thinning of the final varnish had been caused by the solvent mixtures or by the laser irradiation. In fact, the visually assessed laser irradiation tests combined with 50% v/v IMS-WS were inhomogeneous in all the irradiated areas because of the uneven evaporation of the solvent mixtures around the sides of the coverslips (Figure 6.12). For this reason, the data discussed in this chapter are mainly those acquired with the dry irradiated and the DI-W+TW20 pretweted tests in order to evaluate exclusively the Er:YAG laser efficacy in safely interacting with the varnish layers.

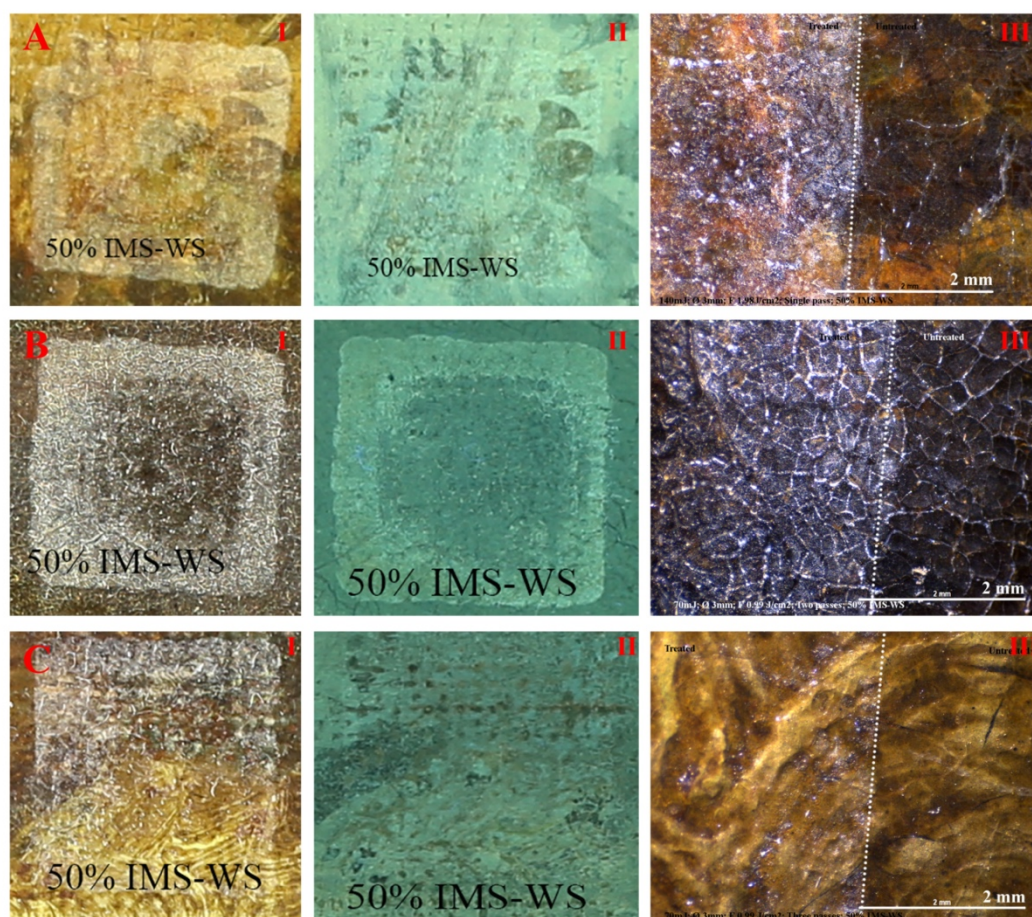


Figure 6.12 - Micrographs of the 50% IMS+WS prewetted irradiated test areas. A: One laser scanned area at nominated fluence  $2 \text{ J/cm}^2$ , B: two laser scanned area at nominated fluence  $1 \text{ J/cm}^2$  and C: three laser scanned area at nominated fluence  $1 \text{ J/cm}^2$ ; I) visible light (VL); II) UV induced fluorescence; III) VL stereomicrograph. All the laser irradiated areas studied were  $15 \times 15 \text{ mm}$ .

All the tested areas, except for those incorporating IMS, have developed a change in the surface morphology of the irradiated varnish, which has shown the formation of micro-roughness (Figures 6.9-11), as already discussed (Lopez *et al.*, 2019; Chillè *et al.*, 2020; Teppo, 2020). The surface morphology of the areas wetted with IMS-containing agents was irregularly affected. The edges of the IMS wetted test areas along the sides of the coverslips developed a similar micro-roughness to the roughness generated throughout the whole test areas with the other wetting agents. However, in the centre of the IMS-wetted test areas, a ‘reforming’<sup>3</sup> varnish was observed (Figure 6.12).

<sup>3</sup> As reported by Treacy (2006), the “reforming” procedure has been employed in the field of painting conservation as an useful method of regenerating aged and degraded varnish

The tests have shown that dry irradiation resulted in the collection of more resin fragments on the cover slips than in the case of the DIW+TW20 pre-wet tests at the same laser settings (Figures 6.8 and 6.13).

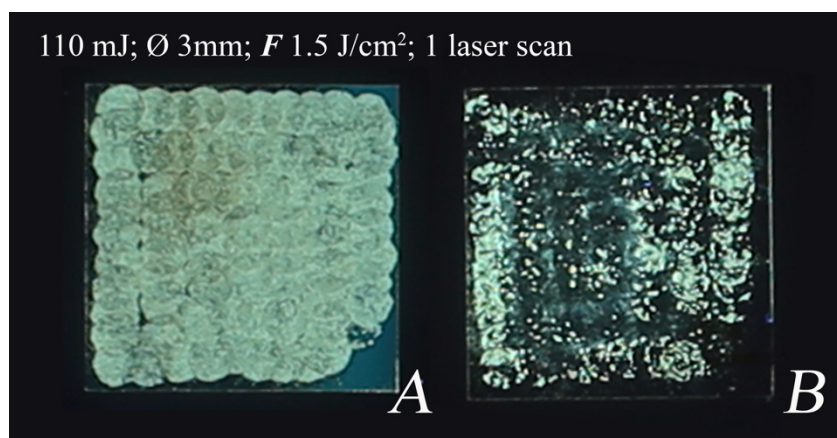


Figure 6.13 – UV induced fluorescence of resin fragments collected on glass coverslips upon dry (A) and pre-wet (B) laser irradiation at 1.5 J/cm<sup>2</sup>. The glass coverslips were 15 × 15 mm.

### 6.3.3 Colourimetric measurements

Colourimetry has allowed to assess a consistent increase in lightness  $L^*$  in SCI and SCE modes for the tested areas after laser irradiation (Table 6.4 and Appendix C). The increase in  $L^*$ , being this parameter related both to the increased light scattering and therefore to the increased brightness of the varnish, has confirmed the visually observed whitening of the irradiated varnish and its disruption induced by laser irradiation.  $L^*_{SCI}$  and  $L^*_{SCE}$  values before and after laser irradiation, have been employed to determine the gloss related factors,  $GRF_b$  and  $GRF_a$  (Eqs. 6.1 and 6.2). Thus, the  $\Delta GRF$  (Eq. 6.3) determines the impact due to laser irradiation, corresponding to the reduction in gloss of the surface (Table 6.4 and Appendix C).

---

layers. Feller *et al.* (1985) described a vapour version of this technique, commonly used for softening ‘difficult to remove’ varnishes.

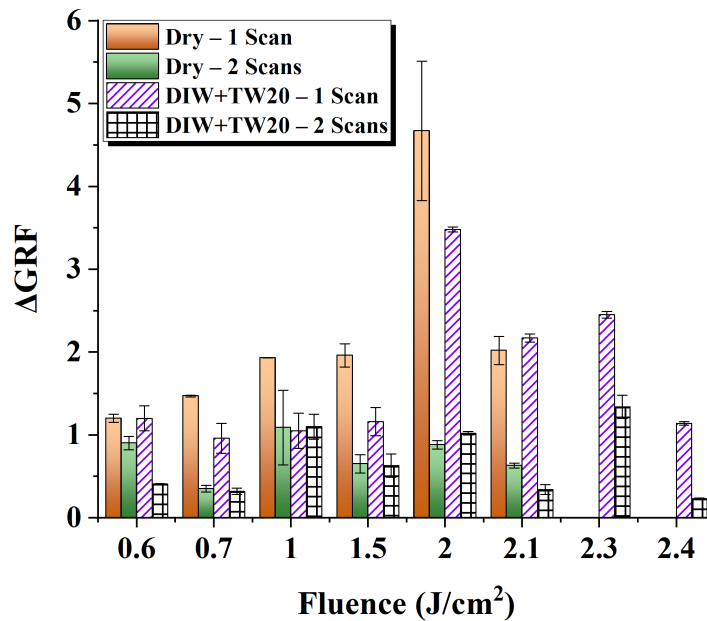


Figure 6.14 – Gloss related impact due to laser-irradiation ( $\Delta$ GRF) as a function of nominated fluences. A good correlation of this factor with the disruption of the varnish at these fluences as visually assessed for the dry irradiation tests is observed. In the case of the wet irradiation tests this correlation is less representative, perhaps due to the significantly less material that escaped the irradiated varnish.

The plot in Figure 6.14 shows that the dry irradiated areas with one laser scan have a higher  $\Delta$ GRF value compared to the two laser scanned areas. It is possible to observe a considerable gap between the area scanned once and the area scanned twice, except for the areas irradiated at 0.6 J/cm<sup>2</sup> due to the weak laser interaction with the varnish surface. By increasing the fluence, in the dry irradiated areas with one laser scan, an increasing trend in the interaction has been detected with a maximum at 2 J/cm<sup>2</sup> followed by a decrement. The same pattern has been observed in the twice scanned areas with a peak at 1 J/cm<sup>2</sup>. In this plot it is possible to identify a good correlation between the maximum  $\Delta$ GRF value with the desired outcome that has been visually assessed for the one laser scan areas at 2 J/cm<sup>2</sup> (Figure 6.14). In the case of the two laser scanned areas, the maximum  $\Delta$ GRF is obtained at about 1 J/cm<sup>2</sup>, which is in agreement with the post-irradiation visual assessment of the surface. A similar comparison is made in the  $\Delta$ GRF values of the DI-W+TW20 prewetted surfaces at one and two scans, where the values of the one scan surfaces are higher than the values for the two scans. In this case, the  $\Delta$ GRF data of the one scan areas remain almost stable up to 1.5 J/cm<sup>2</sup> and significantly increase at 2 J/cm<sup>2</sup>.  $\Delta$ GRF data of the two scanned prewetted areas are almost stable at all fluences.

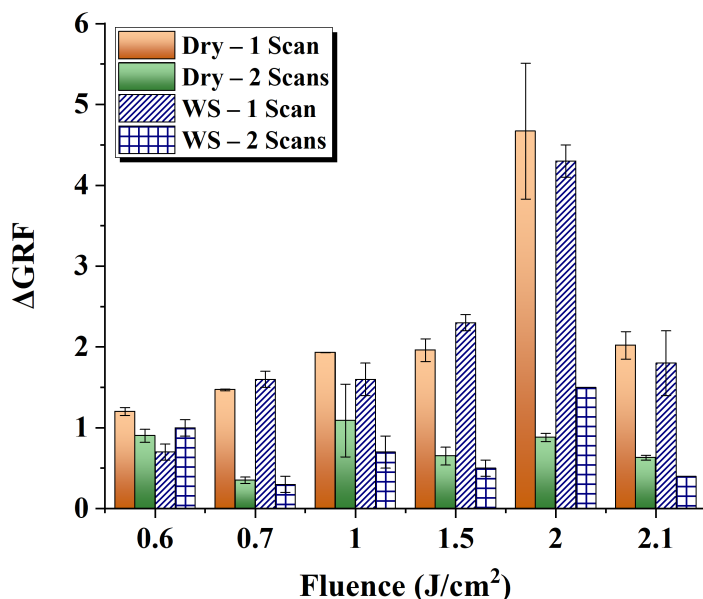


Figure 6.15 – Gloss related impact due to laser-irradiation ( $\Delta$ GRF) as a function of nominated fluences. A good correlation between the dry irradiated areas and the same areas irradiated with white spirit (WS).

The plot in Figure 6.15 shows that the dry irradiated areas with one and two laser scans have a trend similar to the one of the areas prewetted with neat White Spirit. This can be explained as the WS solvent derives from paraffin and it is mainly made of hydrocarbon compounds mixture. Therefore, owing that the WS does not contain hydroxyl groups, the laser interaction with the first substrate containing OH-bonds can be considered alike if irradiated in dry or prewetting with WS.

The three scanned prewetted areas could not be compared herein because these areas have only been pre-wetted once prior to irradiation which caused significant light scattering at the varnish surface when compared to the one- and two-scanned areas. However, the data are reported in Table 6.4.

Table 6.4 – The table provides the  $L_{SCI_{mean}}^*$  and  $L_{SCE_{mean}}^*$  and the GRF data before and after laser irradiation and the  $\Delta$ GRF values. Standard deviations ( $\sigma$ ) of all data are provided. Data in **bold** represent the least efficient visually assessed outcome. Underlined data represent an acceptable level of irradiation of the varnish with no identification of brown hue of the laser scanned area.

Energy (mJ)	Nominated Fluence (J/cm <sup>2</sup> )	Cleaning Systems	Colourimetry before laser irradiation			Colourimetry after laser irradiation			$\Delta$ GRF $\pm\sigma$		
			$L_{SCI_{mean}}^* \pm\sigma$	$L_{SCE_{mean}}^* \pm\sigma$	$GRF_b \pm\sigma$	$L_{SCI_{mean}}^* \pm\sigma$	$L_{SCE_{mean}}^* \pm\sigma$	$GRF_a \pm\sigma$			
<b>40</b>	<b>0.6</b>	Dry – 1 Scan	42±0.6	40±0.7	2±0.1	43±1.1	43±1.3	1±0.2	1±0.1		
		Dry – 2 Scans	32±0.5	31±0.1	1±0.2	36±0.9	36±1	0.3±0.1	1±0.1		
		DI-W – 1 Scan	41±0.1	39±0.2	2±0.1	43±0.8	42±0.9	1±0.1	1±0		
		DI-W – 2 Scans	33±1.5	32±1.3	1±0.2	37±1.4	36±1.5	0	1±0.1		
		DI-W – 3 Scans	35±1.7	33±2.3	2±0.5	42±0.6	41±0.7	1±0	1±0.3		
		DI-W+TW20 – 1 Scan	39±0.5	38±0.2	2±0.2	44±0.6	44±0.6	0.4±0	1±0.1		
		DI-W+TW20 – 2 Scans	32±1.3	31±1.3	1±0	37±0.7	37±0.7	0.2±0	0.4±0		
		DI-W+TW20 – 3 Scans	33±2.8	31±2.7	2±0.1	40±0.6	39±0.6	1±0	1±0		
		IMS+DI-W – 1 Scan	41±0.6	39±0.6	2±0	37±0.9	36±0.6	1±0.2	0.1±0.1		
		IMS+DI-W – 2 Scans	34±4.8	31±0.8	3±2.8	31±1.6	30±1.8	1±0.1	3±1.9		
		IMS+DI-W – 3 Scans	32±4.7	31±5	1±0.2	32±1.3	30±1.4	2±0.1	-1±0.1		
		IMS+WS – 1 Scan	38±0.7	36±0.9	2±0.2	37±0.8	36±0.8	1±0	1±0.1		
		IMS+WS – 2 Scans	32±0.8	31±0.4	1±0.3	34±2.5	33±3	1±0.4	0.4±0.1		
		IMS+WS – 3 Scans	30±1.4	30±1.7	1±0.2	31±0.2	29±0.2	3±0	-2±0.1		
		WS – 1 Scan	40±1	39±1.2	1±0.1	42±0.1	42±0.1	0±0	1±0.1		
		WS – 1 Scans	33±0.9	31±1.2	1±0.2	39±0.2	39±0.2	0±0	1±0.1		
		<b>50</b>	<b>0.7</b>	Dry – 1 Scan	32±1.3	30±1.3	2±0	38±0.1	37±0.1	0.3±0	1±0
				Dry – 2 Scans	31±0.3	31±0.4	0.5±0.1	38±0.8	37±0.8	0.1±0	0.4±0
				DI-W – 1 Scan	33±0.8	31±1.2	2±0.3	38±0.5	38±0.3	1±0.1	1±0.1
				DI-W – 2 Scans	30±0.6	30±0.7	0.4±0.1	38±1.3	38±1.3	0.1±0	0.3±0.1
DI-W – 3 Scans	31±1.7			29±1.2	2±0.4	35±0.7	34±0.7	1±0	1±0.2		
DI-W+TW20 – 1 Scan	35±1.7			33±1.3	2±0.3	43±1.2	42±1.2	1±0	1±0.2		
DI-W+TW20 – 2 Scans	31±0.5			31±0.6	0.5±0.1	37±1.1	37±1.1	0.1±0	0.3±0		
DI-W+TW20 – 3 Scans	30±1			27±1	3±0	35±0.3	34±0.3	1±0	3±0		
IMS+DI-W – 1 Scan	33±0.2			32±0.2	1±0	33±0.5	32±0.5	1±0.1	-0.3±0		
IMS+DI-W – 2 Scans	31±0.9			31±1	0.4±0	30±0.4	27±1.4	3±0.7	-3±0.5		
IMS+DI-W – 3 Scans	30±0.9			28±0.8	2±0.1	30±0.2	26±1	4±0.6	-2±0.4		
IMS+WS – 1 Scan	35±2.2			34±2.7	1±0.3	35±1.2	34±1.3	1±0.1	1±0.2		
IMS+WS – 2 Scans	32±0.3			31±0.3	0.3±0	32±1.1	32±1.3	0.4±0.2	-0.2±0.1		
IMS+WS – 3 Scans	28±1.6			26±1.3	2±0.2	31±0.2	29±0.3	2±0.1	0±0.1		
WS – 1 Scan	33±1.4			31±1.6	2±0.1	37±1	37±1.1	1±0	2±0.1		
WS – 1 Scans	30±0.8			30±0.6	0.4±0.1	36±1.3	36±1.3	0.1±0	0.3±0.1		
<b>70</b>	<b>1</b>			Dry – 1 Scan	35±1.9	33±1.9	2±0	43±0.7	42±0.6	0.2±0	2±0
				Dry – 2 Scans	34±3.4	32±2.3	1±0.8	35±0.7	35±0.9	0.2±0.2	1±0.4
				DI-W – 1 Scan	39±0.2	37±0.3	2±0	43±0.6	43±0.6	0.4±0	2±0
				DI-W – 2 Scans	35±1	34±1.3	1±0.2	36±0.5	35±0.8	0.4±0.3	1±0
		DI-W – 3 Scans	33±3.3	31±3.1	2±0.2	39±1.7	39±1.8	0.4±0.1	1±0.1		

Energy (mJ)	Nominated Fluence (J/cm <sup>2</sup> )	Cleaning Systems	Colourimetry before laser irradiation			Colourimetry after laser irradiation			$\Delta$ GRF $\pm\sigma$
			$L_{SCI_{mean}}^* \pm\sigma$	$L_{SCE_{mean}}^* \pm\sigma$	$GRF_b \pm\sigma$	$L_{SCI_{mean}}^* \pm\sigma$	$L_{SCE_{mean}}^* \pm\sigma$	$GRF_a \pm\sigma$	
110	1.5	DI-W+TW20 – 1 Scan	38±1.9	36±2.5	2±0.4	39±3.2	38±3.3	1±0.1	1±0.2
		DI-W+TW20 – 2 Scans	34±0.8	32±0.4	1±0.2	38±0.6	38±0.6	0.3±0	1±0.1
		DI-W+TW20 – 3 Scans	34±3.4	32±4.1	2±0.5	37±0.9	36±0.9	0.5±0	1±0.3
		IMS+DI-W – 1 Scan	31±1	29±1.2	2±0.2	32±1.3	29±1.6	2±0.2	-1±0
		IMS+DI-W – 2 Scans	34±0.5	33±0.8	1±0.2	31±0.6	31±0.3	1±0.2	1±0
		IMS+DI-W – 3 Scans	32±2.6	30±4.2	2±1.1	32±0.2	26±0.6	5±0.3	-3±0.6
		IMS+WS – 1 Scan	33±2.5	32±2.8	1±0.2	36±0.2	36±0.2	0.4±0	1±0.1
		IMS+WS – 2 Scans	34±1.3	23±2	1±0.5	34±1.5	33±1.6	0.3±0.1	1±0.3
		IMS+WS – 3 Scan	29±1.5	25±1.5	4±0	31±0.3	30±0.7	1±0.3	3±0.2
		WS – 1 Scan	33±0.5	31±0.9	2±0.3	42±0.8	42±0.9	0.2±0	2±0.2
		WS – 2 Scans	35±1.5	34±1.9	1±0.3	38±0.8	38±0.7	0.1±0	1±0.2
		<b>Dry – 1 Scan</b>	<b>32±1.3</b>	<b>30±1.6</b>	<b>2±0.2</b>	<b>37±0.4</b>	<b>37±0.4</b>	<b>0.2±0</b>	<b>2±0.1</b>
		<b>Dry – 2 Scans</b>	<b>32±1.1</b>	<b>32±0.9</b>	<b>1±0.2</b>	<b>38±0.2</b>	<b>38±0.2</b>	<b>0±0</b>	<b>1±0.1</b>
		DI-W – 1 Scan	31±1.1	29±1.2	2±0.1	38±1.2	38±1.3	0.3±0.1	2±0
		DI-W – 2 Scans	33±1.2	32±1	1±0.1	37±0.9	37±1	0.2±0	0.5±0.1
		DI-W – 3 Scans	31±0.3	30±0.6	2±0.2	42±1.6	42±1.6	0.3±0	1±0.1
		DI-W+TW20 – 1 Scan	32±1.2	31±1.6	1±0.2	41±1.4	41±1.4	0.2±0	1±0.2
		DI-W+TW20 – 2 Scans	34±1.8	33±1.5	1±0.2	38±0.5	38±0.5	0.1±0	1±0.1
		DI-W+TW20 – 3 Scans	32±0.7	30±0.8	1±0.1	33±1.7	33±1.7	0.5±0	1±0
		IMS+DI-W – 1 Scan	31±0.7	28±0.9	2±0.1	36±0.4	35±0.6	1±0.1	2±0
		IMS+DI-W – 2 Scans	33±0.6	33±0.5	0.4±0	31±0.5	30±2.4	2±1	-1±0.5
		IMS+DI-W – 3 Scans	32±2.7	31±3.2	2±0.4	34±1.7	32±0	2±0	-0.5±0.2
		IMS+WS – 1 Scan	32±0.6	30±1	2±0.2	42±1.3	41±1.3	0.2±0	1±0.2
		IMS+WS – 2 Scans	33±0.8	32±0.6	0.4±0.1	34±1	34±1	0.1±0	0.3±0.1
IMS+WS – 3 Scan	32±4.4	31±3.3	3±2	34±0.7	33±0.6	1±0.1	2±0.5		
<b>WS – 1 Scan</b>	<b>32±0.6</b>	<b>31±0.9</b>	<b>1±0.2</b>	<b>40±0.3</b>	<b>41±0.3</b>	<b>-1±0</b>	<b>2±0.1</b>		
<b>WS – 2 Scans</b>	<b>33±1.3</b>	<b>32±1</b>	<b>1±0.2</b>	<b>39±3.8</b>	<b>39±3.8</b>	<b>0.1±0</b>	<b>1±0.1</b>		
140	2	Dry – 1 Scan	35±4.3	30±2.6	5±1.2	40±0.2	40±0.2	0.2±0	5±0.8
		<b>Dry – 2 Scans</b>	<b>35±0.7</b>	<b>34±0.8</b>	<b>1±0.1</b>	<b>39±0.9</b>	<b>38±0.9</b>	<b>0.2±0</b>	<b>1±0.1</b>
		DI-W – 1 Scan	36±0.7	33±1.4	3±0.5	46±0.9	46±0.9	0±0	3±0.3
		DI-W – 2 Scans	35±1	34±1.2	1±0.1	38±0.4	37±0.4	0.2±0	1±0.1
		DI-W – 3 Scans	32±0.5	30±0.4	1±0.1	36±1	36±1	0.3±0	1±0.1
		DI-W+TW20 – 1 Scan	28±4.5	25±4.7	4±0.1	36±0.4	36±0.3	0.3±0.1	3±0
		DI-W+TW20 – 2 Scans	35±0.5	34±0.5	1±0	39±1.2	39±1.2	0.1±0	1±0
		DI-W+TW20 – 3 Scans	32±1.8	30±2	2±0.1	35±0.8	35±0.8	0.3±0	1±0.1
		IMS+DI-W – 1 Scan	35±2	33±2.8	1±1	34±1.4	33±1.7	2±0.2	-0.3±0.3
		IMS+DI-W – 2 Scans	35±0.3	34±0.4	2±0.1	33±0.6	33±0.6	0.2±0.1	1±0
		IMS+DI-W – 3 Scans	29±0.7	27±0.3	2±0.2	30±0.6	27±1.4	3±1	-1±0.2
		IMS+WS – 1 Scan	30±6.6	27±7.4	4±1	38±1.9	37±2	1±0.1	3±0.4
		IMS+WS – 2 Scans	35±0.8	33±0.2	1±0.4	37±1	37±1.1	0.2±0	1±0.3

Energy (mJ)	Nominated Fluence (J/cm <sup>2</sup> )	Cleaning Systems	Colourimetry before laser irradiation			Colourimetry after laser irradiation			$\Delta$ GRF $\pm\sigma$
			$L_{SCI_{mean}}^* \pm\sigma$	$L_{SCE_{mean}}^* \pm\sigma$	$GRF_b \pm\sigma$	$L_{SCI_{mean}}^* \pm\sigma$	$L_{SCE_{mean}}^* \pm\sigma$	$GRF_a \pm\sigma$	
150	2.1	IMS+WS – 3 Scan	30±0.6	27±0.9	3±0.2	32±1	30±1.6	2±0.5	1±0.2
		WS – 1 Scan	36±0.8	31±1.1	4±0.2	49±2.2	48±2.2	0.1±0	4±0.2
		<b>WS – 2 Scans</b>	<b>36±0.6</b>	<b>34±0.6</b>	<b>2±0</b>	<b>41±1</b>	<b>41±1</b>	<b>0.1±0</b>	<b>2±0</b>
		<b>Dry – 1 Scan</b>	<b>33±0.1</b>	<b>31±0.5</b>	<b>2±0.2</b>	<b>39±0.3</b>	<b>39±0.3</b>	<b>0.2±0</b>	<b>2±0.2</b>
		<b>Dry – 2 Scans</b>	<b>36±0.6</b>	<b>36±0.6</b>	<b>1±0</b>	<b>39±1.3</b>	<b>38±1.3</b>	<b>0.1±0</b>	<b>1±0</b>
		DI-W – 1 Scan	33±0.5	32±0.8	1±0.2	38±1.3	39±1.3	-1±0	2±0.2
		DI-W – 2 Scans	34±1.5	33±1.3	1±0.1	38±1	38±1	0.2±0	1±0.1
		<u>DI-W – 3 Scans</u>	<u>29±2.4</u>	<u>27±2.1</u>	<u>2±0.2</u>	<u>37±0.6</u>	<u>37±0.6</u>	<u>0.5±0</u>	<u>1±0.2</u>
		DI-W+TW20 – 1 Scan	35±2.8	33±2.7	2±0.1	39±1.1	39±1.1	0.2±0	2±0.1
		DI-W+TW20 – 2 Scans	35±1.3	34±1.4	0.5±0.1	37±1.2	37±1.2	0.1±0	0.3±0.1
		<u>DI-W+TW20 – 3 Scans</u>	<u>31±1</u>	<u>29±0.8</u>	<u>2±0.1</u>	<u>31±0.5</u>	<u>30±0.5</u>	<u>1±0</u>	<u>1±0.1</u>
		IMS+DI-W – 1 Scan	32±2.2	29±4.2	3±1	35±0.2	35±0.3	3±0	3±1
		IMS+DI-W – 2 Scans	33±0.5	32±0.5	1±0	30±0.9	29±0.7	1±0.1	-0.1±0.1
		IMS+DI-W – 3 Scans	30±1.2	27±0.8	2±0.3	31±0.2	27±1	4±1	-2±0.2
160	2.3	IMS+WS – 1 Scan	31±0.1	29±0.3	2±0.1	37±0.2	37±0.3	0.1±0	1±0.1
		IMS+WS – 2 Scans	33±0.5	33±1.5	1±0	34±0.8	34±0.8	0.2±0	1±0
		IMS+WS – 3 Scan	28±0.8	26±0.7	1±0.1	34±0.4	34±0.3	0.3±0.1	1±0
		WS – 1 Scan	31±1.1	29±2	2±1	39±0	39±0	0.2±0	2±0.5
		<b>WS – 2 Scans</b>	<b>34±0.6</b>	<b>33±0.8</b>	<b>1±0.1</b>	<b>37±0.5</b>	<b>37±0.5</b>	<b>0.1±0</b>	<b>1±0.1</b>
		<b>Dry – 1 Scan</b>	<b>31±2</b>	<b>28±2.4</b>	<b>3±0.3</b>	<b>42±0.1</b>	<b>42±0.1</b>	<b>0.1±0</b>	<b>3±0.2</b>
		DI-W – 1 Scan	30±0.6	28±0.9	2±0.2	36±1	35±1	0.2±0	1±0.1
		DI-W – 2 Scans	35±0.6	34±1	1±0.3	38±1.2	38±1.3	0.2±0	1±0.2
		DI-W+TW20 – 1 Scan	30±1.3	27±1.4	3±0.1	36±0.8	36±0.8	0.2±0	2±0
		<u>DI-W+TW20 – 2 Scans</u>	<u>35±2</u>	<u>33±2.4</u>	<u>2±0.3</u>	<u>39±0.6</u>	<u>39±0.5</u>	<u>0.2±0</u>	<u>1±0.1</u>
		IMS+DI-W – 1 Scan	32±1.3	29±0.9	3±0.3	33±1.6	32±2.6	1±1	2±0.3
		IMS+DI-W – 2 Scans	35±2	33±1.2	2±0	35±1	35±1	0.2±0	2±0
		IMS+WS – 1 Scan	32±1.3	29±1.3	3±1	38±0.7	37±0.7	0.2±0	3±0.4
		IMS+WS – 2 Scans	33±0.4	33±0.4	0.3±0	34±0.9	34±0.9	0.3±0	0±0
170	2.4	WS – 1 Scan	32±1.3	30±2.1	2±1	40±0.7	40±0.7	0.1±0	2±0.4
		<b>WS – 1 Scans</b>	<b>36±1.4</b>	<b>35±1.3</b>	<b>0.5±0.1</b>	<b>47±0.7</b>	<b>47±0.7</b>	<b>0.1±0</b>	<b>0.4±0</b>
		<b>Dry – 1 Scan</b>	<b>32±2.4</b>	<b>31±2.7</b>	<b>1±0.3</b>	<b>39±0.4</b>	<b>38±0.4</b>	<b>0.1±0</b>	<b>1±0.2</b>
		DI-W – 1 Scan	30±1	28±1.1	2±0.1	37±1.7	37±1.6	0.1±0	1±0.1
		DI-W – 2 Scans	35±0.7	34±0.6	1±0	38±1.9	38±1.9	0.1±0	0.4±0
		DI-W+TW20 – 1 Scan	30±0.6	29±0.6	1±0.02	37±0.7	38±0.7	0.1±0	1±0
		DI-W+TW20 – 2 Scans	35±0.9	35±0.9	0.3±0	39±0.5	39±0.5	0.1±0	0.2±0
		IMS+DI-W – 1 Scan	29±0.3	28±0.3	1±0	32±1.1	32±1.3	1±0.2	1±0.1
		IMS+DI-W – 2 Scans	34±3	34±2.8	0.5±0.1	34±3.1	33±3.8	1±0.5	-0.2±0.3
		IMS+WS – 1 Scan	29±0.7	27±0.6	1±0	33±0.1	33±0.1	0.2±0	1±0
		IMS+WS – 2 Scans	32±0.5	32±0.7	1±0.2	34±0.8	34±0.8	0.1±0	0.4±0.1
		<b>WS – 1 Scan</b>	<b>30±0.3</b>	<b>28±0.6</b>	<b>1±0.2</b>	<b>39±0.9</b>	<b>39±0.9</b>	<b>0.1±0</b>	<b>1±0.1</b>

### 6.3.4 *Multispectral imaging*

The colourimetric measurements along with UV fluorescence findings have been combined with multispectral imaging data to further evaluate the efficacy of the Er:YAG laser irradiation (Figure 6.16, Table 6.5 and Appendix C).

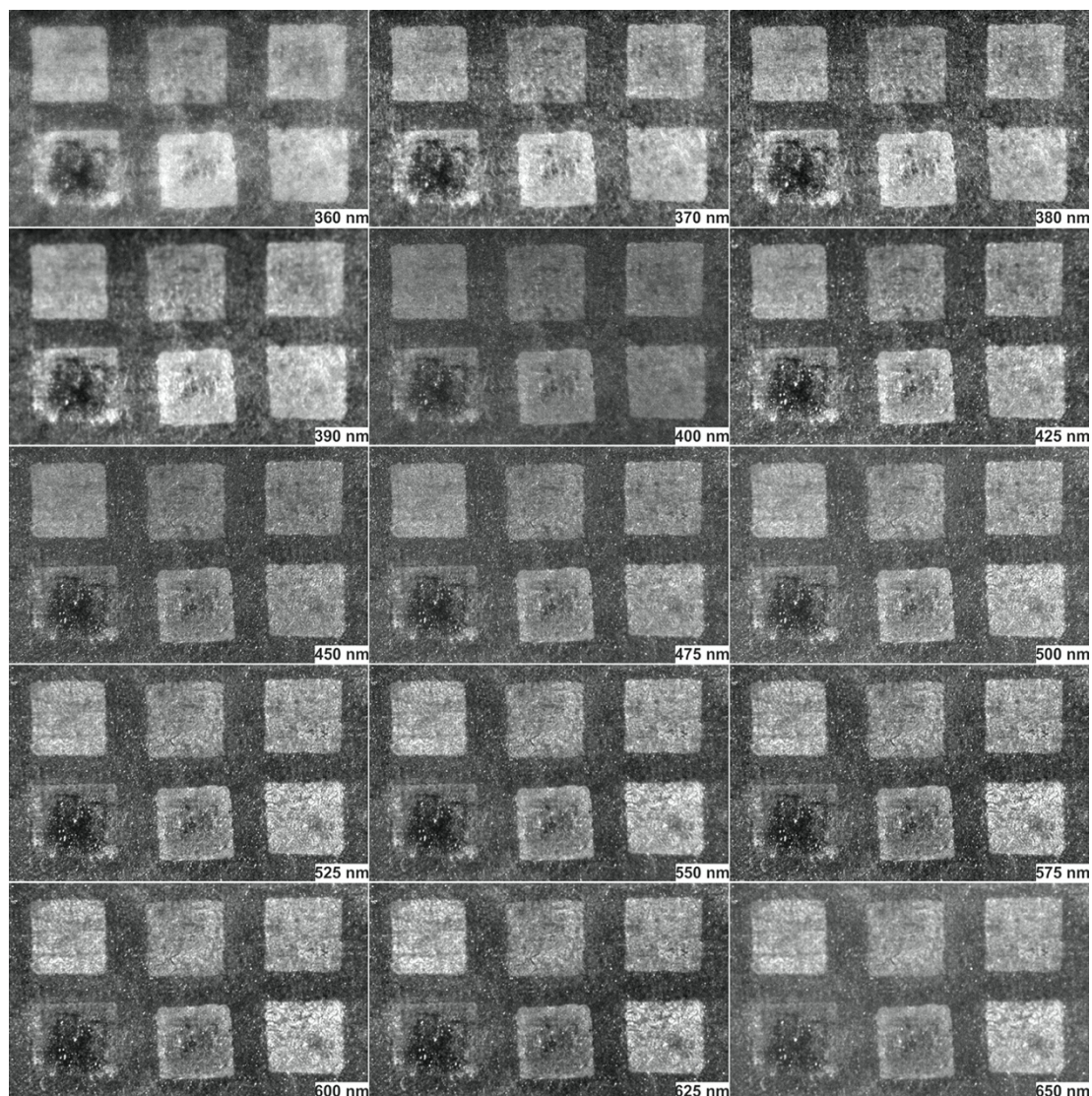


Figure 6.16 – The registered and calibrated spectral images of the Er:YAG laser scans at 1.55 J/cm<sup>2</sup> ranging from 360-650 nm. The data used are the first and the third 15x15 mm spots in the first line of each spectral image, corresponding to the dry and pre-wetted tests. Spectral clustering has been carried out inside the spots on the first 11 spectral images in the 360-550 nm range. As shown the interference of the reflectance from the underlying paint layer to the data recorded in the clusterisation maps was negligible. Even at longer wavelengths up to 650 nm the background contribution was negligible.

Figures and Tables in Appendix C provide evidence for the laser interaction run both on the dry surface and with the wetting agents, ranging from auxiliary OH-containing solvents (such as DI-W and IMS) to a non-OH solvent (WS).

Following laser irradiation, the thickness of the remaining varnish layer presented a high variability, and the laser irradiation tests displayed homogeneous results when working dry or when pre-wetting the varnish surface with DI-W, DI-W+TW20 and WS agents. Spectral clusterisation has resulted in to three clusters depicted in different colours (Figure 6.17 and Appendix C).

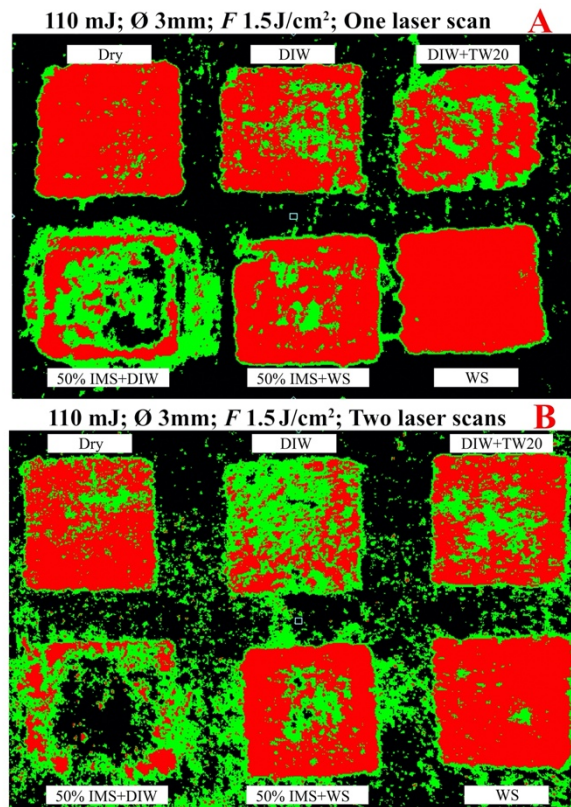


Figure 6.17 – Multispectral Imaging clusterisation maps of one (A) and two (B) laser scanned areas at nominated fluence  $1.5 \text{ J/cm}^2$ . The sequence of the cleaning test areas is the same as in Figure 6.3. All the laser irradiated areas shown are  $15 \times 15 \text{ mm}$ .

Upon ageing, dammar varnishes absorb strongly not only in the UV but also in the blue part of the visible spectrum (400-490 nm) due to the presence of unsaturated quinines (Formo, 1979; de la Rie, 1988; Theodorakopoulos *et al.*, 2007). Thus, the background reflectance is minimised due to the strong absorption of the varnish in the blue, as also has been evidenced herein (Figure 6.16).

However, in order to exclude any contribution from underlying paint layers in the scanned areas, the ratio between the average reflectance spectra of the red and green clusters was determined (Figure 6.18).

The black colour corresponds to the non-irradiated varnish, green represents an early-stage varnish thinning, while red represents a gradual deeper reduction, resulting in a thinner remaining varnish layer. The absorption of the varnish depends on its physical and chemical characteristics, such as its thickness and the concentration of compounds with light absorbing functional groups, generated in degradation products in dammar resin due to ageing (Formo, 1979; van der Doelen and Boon, 2000). The study of the spectral image sets, in the scanned areas, shows that up to 425 nm the reflectance

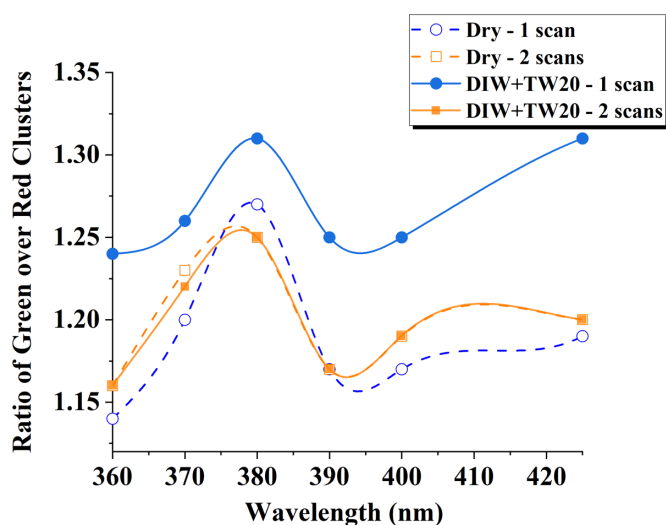


Figure 6.18 – Ratios of average reflectance spectra of red and green clusters, representing reflectance differences due to remaining varnish thickness as reported elsewhere (Papadakis *et al.*, 2011; Zacharopoulos *et al.*, 2018).

Considering that the green and red clusters represent raster of scattered points of thicker and thinner films of the remaining varnish, this ratio clearly represents the reflectance difference due to thickness. A similar approach is reported to monitor the thickness of black crust layers on marble substrates (Papadakis *et al.*, 2011). Figure 6.18 shows the similar spectral characteristics of the irradiated varnish regardless of the pre-wet or dry irradiated procedure. In the two-laser scanned pre-wetted and dry areas the ratios of the green over red clusters result in identical spectra, providing further evidence that no contribution from the background has been detected. This is also due to the fact that the two laser scanned areas, regardless of pre-wetting, has been processed with the same method as reported in section 6.2.3.

Regardless of scattering which offsets the spectra in Figure 6.18, it can be seen that the aged varnish reflects strongly at 380 nm and that by increasing the laser scans, and therefore gradually thinning the varnish layer, a stronger reflectance at 370 nm is recorded. The gradual reflectance shift from 380 nm to 370 nm is in line with previous findings on UV/VIS spectrophotometry of TTP resins thinned with excimer lasers (Theodorakopoulos *et al.*, 2007). In this spectral region, tails of the carbonyl groups of hydroperoxides, aliphatic acids, and aldehydes with peak absorption at wavelengths below 250 nm, affect the UV absorption and reflection of the films due to  $n \rightarrow \pi^*$  transitions (Silverstein, Bassler and Morrill, 1991). Moreover, absorbance in the near UV is gradually shifted towards shorter UV wavelengths as a function of depth (Theodorakopoulos *et al.*, 2007), which is verified in the presented study (Figure 6.18).

In addition to the aforementioned information, the clusterisation maps (Figure 6.19) indicate that the interactions of the dry and pre-wetted varnish with the laser have been varied and determined the progressive thinning of the varnish layer. The percentage surface coverage of the clusters of the dry and the DI-W + TW20 irradiated areas as a function of nominated fluence have shown that pre-wetting the surface has resulted in a more controlled interaction (Figure 6.19).

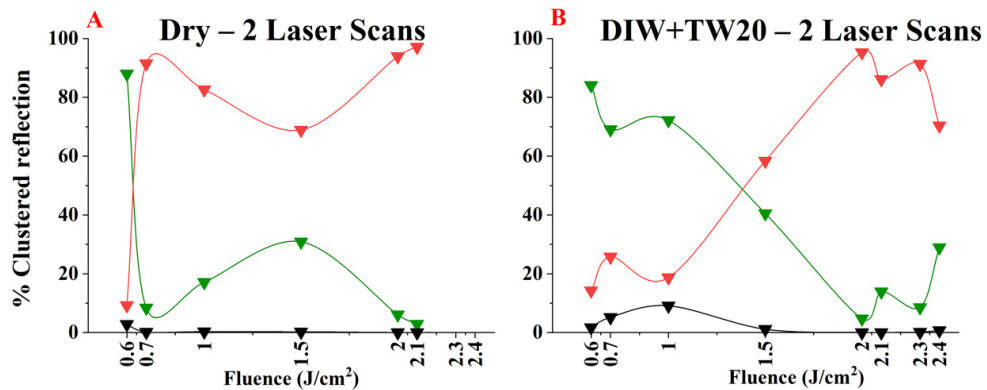


Figure 6.19 – A % clustered reflection monitored by the spectral imaging clusterisation maps as a function of fluence for the two laser scan applications in the dry and pre-wet tests. The gradual reduction of the varnish from the early stage (green line) to the deeper thinning (red line) was captured by spectral imaging. The black line corresponds to the remaining varnish within the irradiated spots.

In particular, the dry irradiated surface presents an abrupt thinning of the varnish with lower fluencies. For instance, two scans at the dry irradiation procedure maximises the varnish thinning abruptly between 0.6 and 0.7 J/cm<sup>2</sup>, contrary to the pre-wet procedure where a similar result was obtained more gradually in a higher nominated fluence range from 1 to 2 J/cm<sup>2</sup>. Thus, this study indicates that pre-wetting offers a more controlled and gentle interaction.

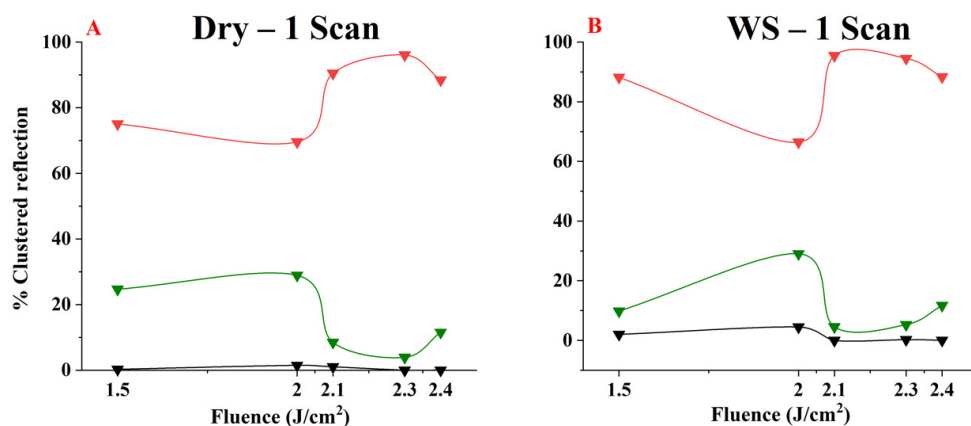


Figure 6.20 – A % clustered reflection monitored by the spectral imaging clusterisation maps as a function of fluence for a single laser scan application in the dry and pre-wet tests using WS.

Also, in this case, similarities to the dry irradiation of the varnish surface have been observed prewetting the varnish surface with neat White Spirit (Figure 6.20), confirming what had already been observed in Figure 6.16.

Table 6.5 – Multispectral Imaging (MSI) Clusterisation Analysis data of the Er:YAG laser irradiated areas. Green % corresponds to a gradual reduction of the early stage varnish thinning. Red % coincides with gradual deeper irradiation of the varnish layer. The Black % corresponds to the remaining varnish within the irradiated spots.

Energy (mJ)	Nominated Fluence (J/cm <sup>2</sup> )	Cleaning systems	Spectral Imaging Clusterisation Analysis		
			Green %	Red %	Black %
40	0.6	Dry – 2 Scans	88	9	3
		DI-W – 2 Scans	83	4	12
		DI-W – 2 Scans	5	95	0
		DI-W+TW20 – 2 Scans	84	14	2
		DI-W+TW20 – 3 Scans	23	76	1
		IMS+DI-W – 2 Scans	19	2	78
		IMS+DI-W – 3 Scans	50	3	47
		IMS+WS – 2 Scans	52	10	38
		IMS+WS – 3 Scans	34	0	66
		WS – 2 Scans	81	5	14
		50	0.7	Dry – 2 Scans	8
DI-W – 2 Scans	31			61	8
DI-W – 3 Scans	30			70	0
DI-W+TW20 – 2 Scans	69			26	5
DI-W+TW20 – 3 Scans	16			80	4
IMS+DI-W – 2 Scans	3			1	96
IMS+DI-W – 3 Scans	91			4	5
IMS+WS – 2 Scans	31			39	29
IMS+WS – 3 Scans	52			1	48
WS – 2 Scans	42			53	5
70	1			Dry – 2 Scans	17
		DI-W – 2 Scans	75	18	0
		DI-W – 3 Scans	2	98	0
		DI-W+TW20 – 2 Scans	72	19	9
		DI-W+TW20 – 3 Scan	19	81	0
		IMS+DI-W – 2 Scans	29	1	69
		IMS+DI-W – 3 Scans	16	6	77
		IMS+WS – 2 Scans	19	36	45
		IMS+WS – 3 Scans	63	10	26
		WS – 2 Scans	61	39	0
		110	1.5	Dry – 1 Scan	25
Dry – 2 Scans	31			69	0
DI-W – 1 Scan	48			48	4
DI-W – 2 Scans	67			27	6

Energy (mJ)	Nominated Fluence (J/cm <sup>2</sup> )	Cleaning systems	Spectral Imaging Clusterisation Analysis			
			Green %	Red %	Black %	
140	2	DI-W – 3 Scans	1	99	0	
		DI-W+TW20 – 1 Scan	45	45	10	
		DI-W+TW20 – 2 Scans	41	58	1	
		DI-W+TW20 – 3 Scans	66	34	0	
		IMS+DI-W – 1 Scan	43	24	33	
		IMS+DI-W – 2 Scans	27	13	59	
		IMS+DI-W – 3 Scans	52	12	36	
		IMS+WS – 1 Scan	33	65	3	
		IMS+WS – 2 Scans	17	80	3	
		IMS+WS – 3 Scans	39	59	2	
		WS – 1 Scan	10	88	2	
		WS – 2 Scans	6	94	0	
	150	2.1	Dry – 1 Scan	29	70	1
			Dry – 2 Scans	6	94	0
			DI-W – 1 Scan	29	68	3
			DI-W – 2 Scans	24	76	0
			DI-W – 3 Scans	2	98	0
			DI-W+TW20 – 1 Scan	46	52	2
			DI-W+TW20 – 2 Scans	5	95	0
			DI-W+TW20 – 3 Scans	66	34	0
			IMS+DI-W – 1 Scan	18	10	72
IMS+DI-W – 2 Scans		35	62	3		
IMS+DI-W – 3 Scans		21	3	76		
IMS+WS – 1 Scan		42	35	23		
IMS+WS – 2 Scans		13	87	0		
IMS+WS – 3 Scans		46	24	30		
WS – 1 Scan		29	66	4		
WS – 2 Scans		7	93	0		
			Dry – 1 Scan	8	91	1
			Dry – 2 Scans	3	97	0
			DI-W – 1 Scan	24	75	1
	DI-W – 2 Scans		15	84	0	
	DI-W – 3 Scans		3	97	0	
	DI-W+TW20 – 1 Scan		12	88	0	
	DI-W+TW20 – 2 Scans		14	86	0	
	DI-W+TW20 – 3 Scans		71	12	17	
	IMS+DI-W – 1 Scan		44	55	1	
	IMS+DI-W – 2 Scans		46	24	30	

Energy (mJ)	Nominated Fluence (J/cm <sup>2</sup> )	Cleaning systems	Spectral Imaging Clusterisation Analysis			
			Green %	Red %	Black %	
160	2.3	IMS+DI-W – 3 Scans	10	2	89	
		IMS+WS – 1 Scan	36	60	5	
		IMS+WS – 2 Scans	30	70	0	
		IMS+WS – 3 Scans	23	77	0	
		WS – 1 Scan	5	95	0	
		WS – 2 Scans	22	77	0	
		Dry – 1 Scan	4	96	0	
		DI-W – 1 Scan	43	56	1	
		DI-W – 2 Scans	46	54	0	
		DI-W+TW20 – 1 Scan	33	67	0	
	DI-W+TW20 – 2 Scans	9	91	0		
	IMS+DI-W – 1 Scan	58	30	12		
	IMS+DI-W – 2 Scans	18	82	0		
	IMS+WS – 1 Scan	35	65	1		
	IMS+WS – 2 Scans	35	63	2		
	WS – 1 Scan	5	95	0		
	WS – 2 Scans	0	100	0		
	170	2.4	Dry – 1 Scan	12	88	0
			DI-W – 1 Scan	60	35	6
			DI-W – 2 Scans	39	58	3
DI-W+TW20 – 1 Scan			40	60	0	
DI-W+TW20 – 2 Scans			29	71	0	
IMS+DI-W – 1 Scan			29	5	67	
IMS+DI-W – 2 Scans			40	24	36	
IMS+WS – 1 Scan			71	25	3	
IMS+WS – 2 Scans			42	49	9	
WS – 1 Scan			12	88	0	

### 6.3.5 Further spectroscopic evaluation

The ATR/FT-IR spectra obtained from the residual varnish collected on the coverslips (acquired at different nominated fluences) upon laser irradiation have been compared with the varnish samples that have been not irradiated (Figures 6.21-25 and Appendix C). Given that resin fragments were directly extracted from the glass coverslips, the results are not affected as in the case of the visual interpretation due to light scattering at the surface of the irradiated varnish, as observed on the three-scanned areas.

It is possible to detect minor differences, after one and two laser scans, when the varnish surface is irradiated in dry or pre-wetted with WS. The ratios of the integrated areas of the OH/CH bands has shown minimal reduction in absorbance with increased fluences up to 2.4 J/cm<sup>2</sup> (Figure 6.21) (Chillè *et al.*, 2020). However, the same ratios have not shown significant changes in DI-W+TW20 pre-wet mode after one, two or three laser scan irradiations (Figures 6.21 and 6.23). As presented in Figure 6.21 (B), the OH stretching vibrations show negligible changes in intensity also at the *nominated fluence* 2.1 J/cm<sup>2</sup> after three laser scans of the varnish surface. Due to the partial solubilisation of the varnish films using IMS and the ‘*reforming*’ mechanism upon Er:YAG laser irradiation in the centre of the IMS-wetted test areas, the ratios of the integrated areas of the OH/CH bands have shown negligible changes in intensity (Figure 6.25).

The varnish surface irradiated in dry or pre-wetted with WS, after one and two laser scans, shows that the intensity of the carbonyl stretching vibration band gradually decreases by increasing the *nominated fluence* (Figures 6.22 and 6.24), as was also observed in KrF excimer laser ablated triterpenoid varnishes (Silverstein, Bassler and Morrill, 1991; Theodorakopoulos *et al.*, 2007). However, the ratios of the integrated areas of the C=O/CH bands did not show significant changes in DI-W+TW20 pre-wet mode after one, two or three laser scans irradiations (Figure 6.23). Likewise, IMS-wetted test areas also displayed no significant changes in the ratios of the integrated areas of the C=O/CH bands (Figure 6.25).

Taking all these into account, there is no considerable modification in the OH/CH and C=O/CH ratios of the treated varnish fragments when increasing the nominated fluence as shown in figures 6.21-25 and Appendix C. However, the slight decrease in the carbonyl stretching vibration in the dry or pre-wetted areas with WS

has suggested the presence of degradation gradients in the triterpenoid varnish (Theodorakopoulos and Zafirooulos, 2003; Theodorakopoulos *et al.*, 2007) (Figures 6.22 and 6.24).

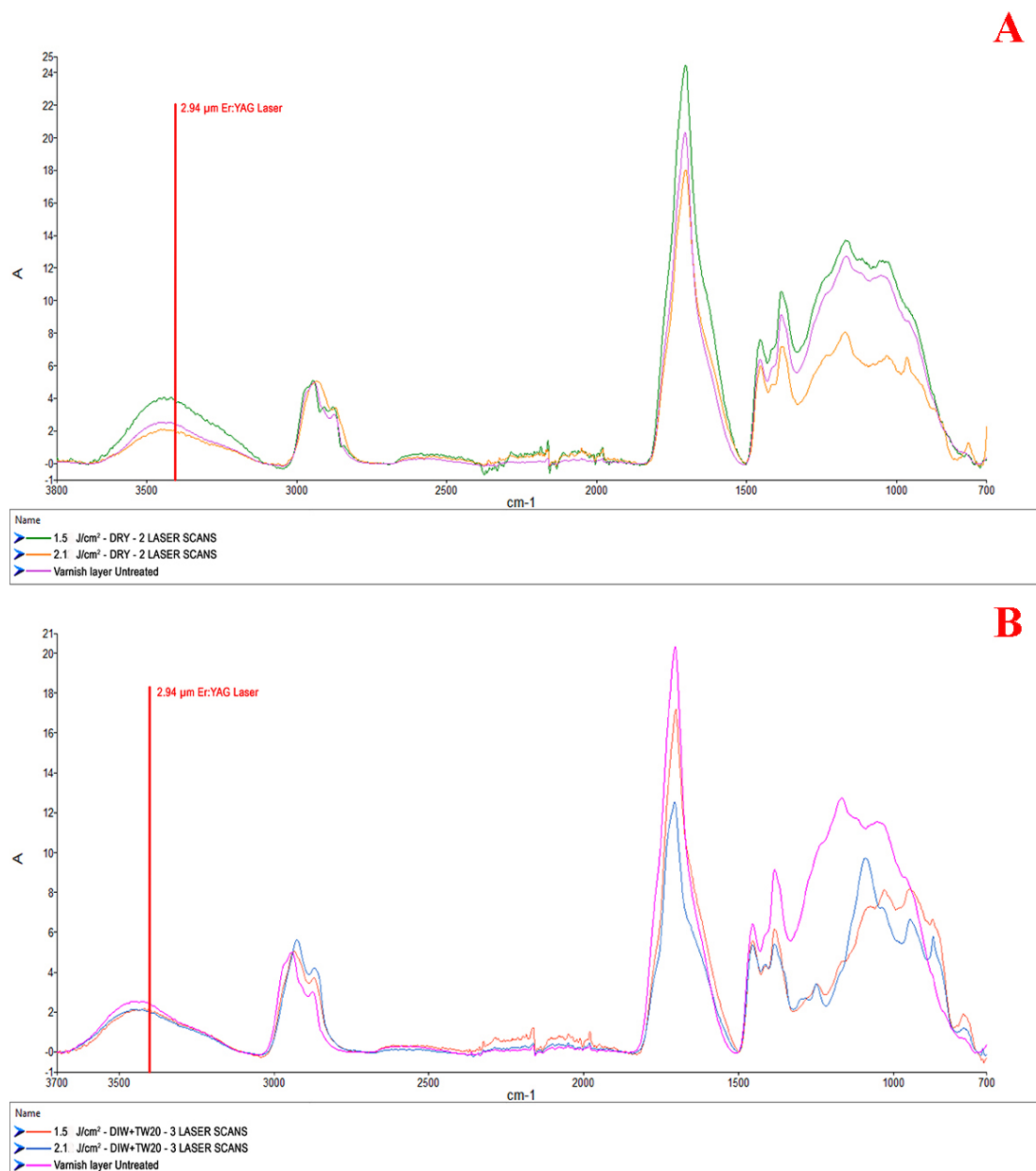


Figure 6.21 – ATR/FT-IR spectra of the resin fragments collected on the glass coverslips, acquired at nominated fluence 1.5 and 2.1 J/cm<sup>2</sup> and of the untreated varnish (control). ATR/FTIR spectra of: the dry irradiated area after two laser scans (A); and the pre-wetted area after three laser scans (B). The spectra show the gradual reduction in intensity of the C = O stretching group by increasing fluence. Baseline points ranging from 3700 to 3100, 3100-2700, and 1900-1550 cm<sup>-1</sup>.

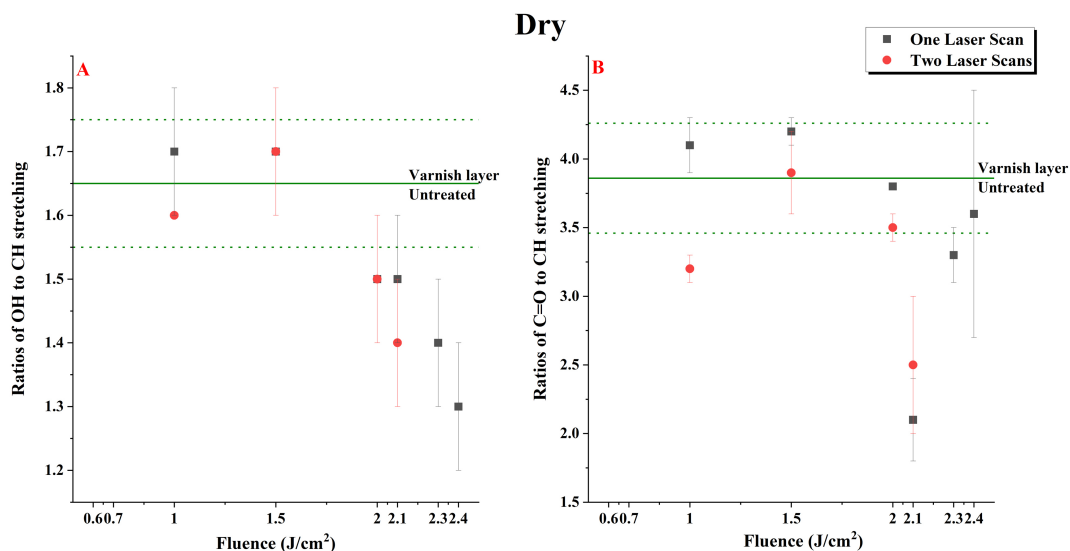


Figure 6.22 – Ratios of the integrated areas of the  $-OH/CH$  and the  $-C=O/CH$  bands as acquired by ATR/FT-IR vs fluence of the dry irradiated varnish films collected on the coverslips in VSP ( $\tau_L \approx 100 \mu s$ ) mode. The horizontal lines define the corresponding ratios of the varnish samples that have been not irradiated (dark green solid line). The dotted lines correspond with the area of the standard deviation.

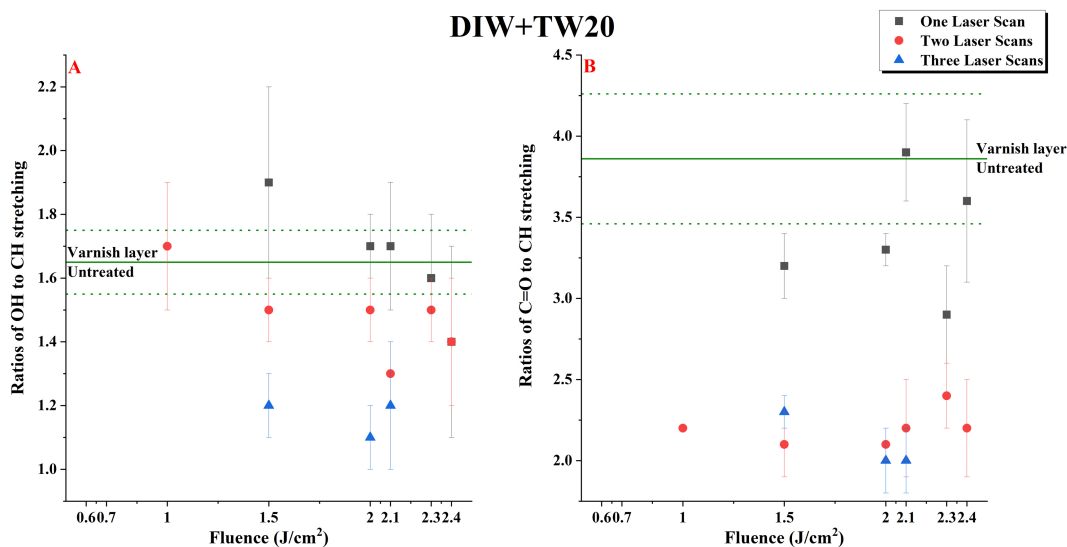


Figure 6.23 – Ratios of the integrated areas of the  $-OH/CH$  and the  $-C=O/CH$  bands as acquired by ATR/ FTIR vs fluence of the DI-W+TW20 pre-wetted irradiated varnish films collected on the coverslips in VSP ( $\tau_L \approx 100 \mu s$ ) mode. The horizontal lines define the corresponding ratios of the varnish samples that have been not irradiated (dark green solid line). The dotted lines correspond with the area of the standard deviation.

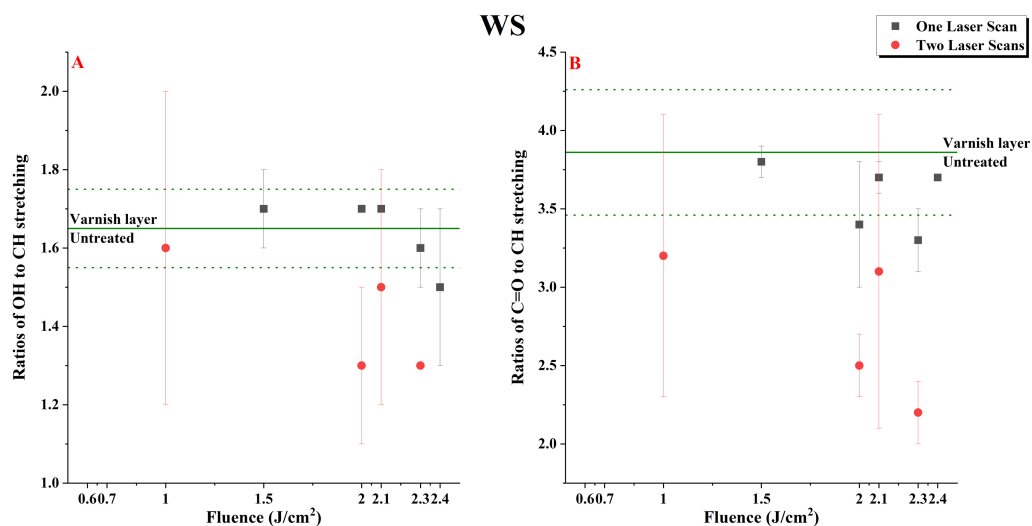


Figure 6.24 – Ratios of the integrated areas of the –OH/CH and the –C=O/CH bands as acquired by ATR/ FTIR vs fluence of the White Spirit (WS) pre-wetted irradiated varnish films collected on the coverslips in VSP ( $\tau_L \approx 100 \mu s$ ) mode. The horizontal lines define the corresponding ratios of the varnish samples that have been not irradiated (dark green solid line). The dotted lines correspond with the area of the standard deviation.

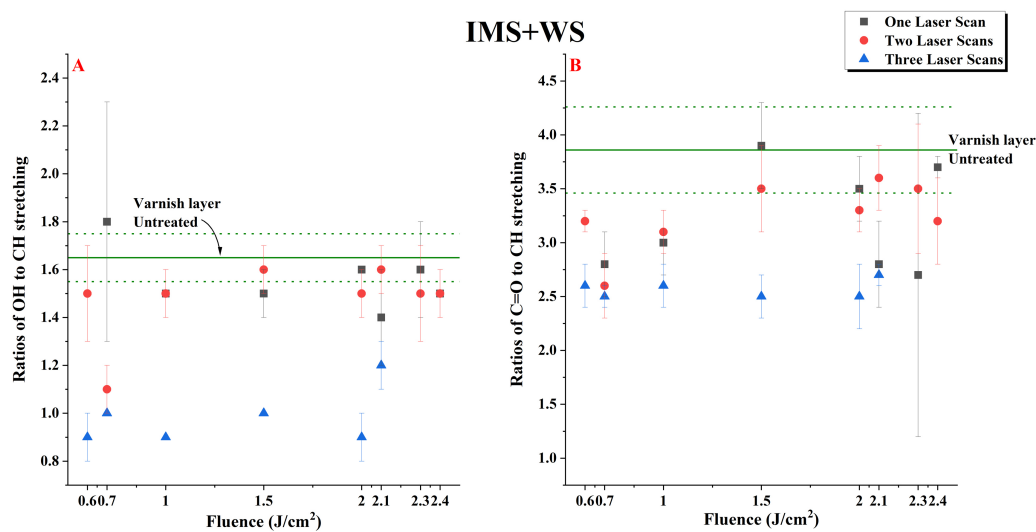


Figure 6.25 – Ratios of the integrated areas of the –OH/CH and the –C=O/CH bands as acquired by ATR/ FTIR vs fluence of the IMS+WS pre-wetted irradiated varnish films collected on the coverslips in VSP ( $\tau_L \approx 100 \mu s$ ) mode. The horizontal lines define the corresponding ratios of the varnish samples that have been not irradiated (dark green solid line). The dotted lines correspond with the area of the standard deviation.

## 6.4 Conclusion

This chapter addressed *objective h* on the Er:YAG laser cleaning tests to thin the varnish of an nineteenth century oil painting. In particular, ATR/FT-IR and py-TMAH-GC/MS analyses showed that the painting was coated with a dammar-based varnished.

Laser irradiation tests led to diverse results depending on whether the surface was directly irradiated dry or pre-wetted. The tests were effective in the nominated fluences ranging from 1 to 2.4 J/cm<sup>2</sup> in one, two and three laser scan applications, especially when irradiated in dry or pre-wetted with deionised water with a non-ionic surfactant Tween 20 (DI-W+TW20). The tests showed that irradiation of the varnish had similar results when the surface was: a) dry or pre-wetted with white spirit (WS), b) pre-wetted with DI-W and DI-W+TW20, and c) pre-wetted with 50% v/v IMS+WS and 50% v/v IMS+DI-W. Moreover, when IMS was used as pre-wetting agent, a ‘*reforming*’ varnish mechanism was observed thus affecting the reliability of the data. Multispectral imaging clusterisation maps of the tested areas were particularly useful for the evaluation and monitoring of the laser effects to the surface. A gloss related impact due to irradiation was in good agreement with the visual assessment of the post-treated surface in the dry or pre-wetted areas with DI-W+TW20. Furthermore, ATR/FT-IR spectra carried out on the resin scrapings assessed the laser cleaning efficiency process by monitoring the changes in the OH/CH and C=O/CH ratios. Laser irradiation did not show a considerable modification in the abovementioned ratios. The minor decrease in the C=O/CH ratios, however, indicated that the dammar varnish was less deteriorated in the bulk than in the surface (Theodorakopoulos and Zafirooulos, 2003).

Overall, this chapter provided an insight into the mechanism of the Er:YAG laser irradiation of varnished paintings. This alternative method can enable the conservator to address a cleaning procedure using less invasive and safer techniques when laser irradiation is used within appropriate energy levels.

# CHAPTER 7                      CONCLUSIONS & FUTURE PROSPECTS

This thesis provided a study on the 2940 nm Er:YAG laser interaction with natural and synthetic varnishes for paintings. The aim was to investigate and increase the knowledge of Er:YAG laser-induced effects in order to provide a less invasive, more selective and safe method for the cleaning of varnished paintings.

## *7.1 Conclusions*

The literature review, in **Chapter 2**, of the history of the art materials market demonstrated that in the nineteenth century a huge variety of products, produced by several companies, were made available to artists and later to conservators as finishing picture varnishes. Since the 1930s, established resins, which naturally exude from trees, have been side-lined together with the commercialisation of synthetically produced resins for the production of varnishes (Nicolaus, 1999, p. 315). The varnishes tested fall under two groups: i) dammar resin belongs to the group of natural soft resins and ii) poly-isobutyl methacrylate homopolymer (PiBMA trade name Paraloid B67), and condensation products of cyclohexanone only (Ketone N) or blended with methylcyclohexane (MS2A) which belongs to the group of synthetic resins. **Chapter 3** provided a brief review of the chemical characteristics of these varnishes. Findings on the aged varnishes were in good correspondence with the literature. The limited and fragmented pieces of information on the physicochemical features of the resinous substrates have made a systematic investigation necessary. Furthermore, the physicochemical parameters needed for interpreting later the laser-induced effects between the laser light and coatings were presented and processed in **Chapter 3**. Based on the state-of-the-art regarding the laser techniques for the cleaning of painted artworks using UV lasers and Nd:YAG lasers, and following the already published work on the use of the Er:YAG lasers, discussed in **Chapters 2 and 4**, the thesis intended to establish an initial understanding of the laser-induced effects, the side effects of the temperature rise onto the surface of selected irradiated varnishes and the heatwave propagation

in the bulk of varnishes by increasing the fluence values (**Chapter 4**). Laser transmission energies through the irradiated varnishes were performed to understand if the high-powered laser action can reach the underlying layer(s) (**Chapter 4**). Moreover, the physicochemical interaction between the Er:YAG laser and the selected varnishes had to be evaluated to provide the evidence on how these films react to laser irradiation (**Chapter 5**).

### 7.1.1 Summary of Contributions

The findings of this research addressed all the objectives outlined at the Introduction of the thesis (section 1.3). A Fotona Fidelis<sup>XS</sup> and a Fotona XS Dynamis Er:YAG (2940 nm) laser were used to irradiate aged dammar, Ketone N, MS2A and Paraloid B67 varnish films. The sum of the results presented in **Chapter 3** has given essential information of ageing impact on the varnishes selected as well as obtaining information on the thermal stability of the coatings. The varnish resins applied onto glass slides were exposed to both accelerated light- and hydrothermal-ageing. The resins and varnishes were studied by stylus profilometry, static contact angle, gas pycnometry, colourimetry, Thermogravimetric Analysis (TGA), Differential Scanning Calorimetry (DSC) and Attenuated Total Reflection - Fourier Transformed Infrared Spectroscopy (ATR/FT-IR). These analyses have allowed the characterisation of all the varnishes in terms of morphology and chemical composition. Gas pycnometry, DSC analyses and TGA were carried out only on the unaged raw resins. In particular, DSC and TAG analyses aimed to provide oxidative thermal stability data on the varnish resins tested. After the ageing processes, the PiBMA (Paraloid B67) films remained transparent and no variations were detected using colourimetric analysis. Dammar films were however found to be less stable compared to the other resins with a detected colour change towards a yellow hue. The stylus profilometer detected disruption and highly cracked surfaces, a non-contact angle was obtained by depositing a droplet of a of 1% (v/v) of a *polyethylene glycol sorbitan monolaurate* surfactant non-ionic surfactant (Tween 20) in deionised water (DI-W+TW20). Ketone N films, on the other hand, proved to be the most hydrophilic resin with the smallest static contact angle ( $32.4^\circ \pm 2.9^\circ$ ). TGA and DSC determined that the raw ketone resins (Ketone N and MS2A) were less thermally stable than dammar and Paraloid B67 resins, with oxidative

degradation processes which started at the lowest operating temperature of 105 °C (Ketone N) and 94°C (MS2A). The integrated areas of the peaks corresponding to hydroxide (2700–3700  $\text{cm}^{-1}$ ), C–H (2850–3000  $\text{cm}^{-1}$ ) and carbonyl (1500–1900  $\text{cm}^{-1}$ ) stretching vibrations, monitored by ATR/FT-IR, revealed an increase in absorbance in the carbonyl and hydroxyl frequencies for all the varnishes. However, the CH bending vibration modes (2850–3000  $\text{cm}^{-1}$ ) decreased for dammar and Ketone N and increased for MS2A and Paraloid B67.

**Chapter 3** was a starting point for interpreting the laser-induced effects on the mock-ups upon Er:YAG laser irradiation. Therefore, the main questions of this research were, whether:

- 1) the Er:YAG laser pulses induces side effects caused by the temperature rise onto the surface and the heat propagation in the bulk;
- 2) physicochemical modifications are increasing upon the laser irradiation;
- 3) the laser beam could reach the underlying layer while removing surface layers;
- 4) Er:YAG lasers can be used to safely thin varnishes applied to works of art.

The answer to the first three questions were investigated in **Chapters 4 and 5**. Two procedures were employed to examine temperature changes upon a single laser pulse test irradiation to address the first question. In the first procedure, discussed in **Chapter 4**, the IR thermal camera recorded the maximum temperatures ( $\Delta T_{\text{mean}}$ ) in real-time during the laser irradiation on the varnishes with fluences 0.6, 1, 1.6, 2 and 2.4  $\text{J}/\text{cm}^2$ . In particular, the highest  $\Delta T_{\text{mean}}$  was recorded on the dry irradiated Ketone N varnish films with values ranging from  $44.3 \pm 5.1$  at the lowest fluence tested (0.6  $\text{J}/\text{cm}^2$ ) to  $112.3 \pm 16.3$  at the highest fluence (2.4  $\text{J}/\text{cm}^2$ ) in VSP mode ( $\tau_L \approx 100 \mu\text{s}$ ) and between  $46.1 \pm 4$  at 0.6  $\text{J}/\text{cm}^2$  and  $121.6 \pm 20$  at 2.4  $\text{J}/\text{cm}^2$  in SP mode ( $\tau_L \approx 300 \mu\text{s}$ ). On the pre-wetted varnishes with DI-W+TW20, the  $\Delta T_{\text{mean}}$  values were higher than on the dry varnishes due to the superheating of the aqueous film on the surface (Nahen and Vogel, 2002). In sharp contrast, since the PiBMA does not contain hydroxyl groups, the aged varnish films returned the lowest temperature rise. The recorded  $\Delta T_{\text{mean}}$  on the dry irradiated Paraloid B67 ranged from  $3.3 \pm 0.8$  at 0.6  $\text{J}/\text{cm}^2$  to  $21 \pm 3$  at 2.4  $\text{J}/\text{cm}^2$  in VSP mode and between  $3.5 \pm 0.7$  at 0.6  $\text{J}/\text{cm}^2$  and  $16.5 \pm 2.3$  at 2.4  $\text{J}/\text{cm}^2$  in SP mode. Pre-wetting with DI-W+TW20 the recorded  $\Delta T_{\text{mean}}$  ranged between  $17 \pm 2.4$  at 2.4

$\text{J}/\text{cm}^2$  in VSP mode and  $21.3 \pm 3$  in SP mode. The use of the thermal acquisition technique highlighted that a 30 Hz thermal camera did not provide reliable temperature data due to discrepancies of the pulse durations ( $\tau_L \approx 100$  and  $300 \mu\text{s}$ ) and the camera acquisition rate (30 Hz) and the 7 - 12 ms of the thermal constant of thermal camera microbolometer detector. Although the live-recorded temperatures were unable to provide accurate maximum peak temperature data and could have been more accurate with a faster thermal camera, the data are, nonetheless, representative of the interaction of the varnish films with the 2940 nm laser (Chillè *et al.*, 2020).

The second procedure was based on the mathematical determination of the rate of heat transfer into the films upon a single laser pulse test irradiation. Two properties were required for each varnish: optical, for modelling of the heat generation by the laser beam, and thermo-physical, for thermal modelling. The optical properties of dammar, Ketone N, MS2A and Paraloid B67 varnish films were acquired by transmission infrared spectroscopy which allowed to estimate the absorption coefficient ( $\alpha$ ) at the laser wavelength (2940 nm corresponding to wavenumber  $3401 \text{ cm}^{-1}$ ) and, therefore, to obtain the optical penetration depth ( $\delta$ ). The thickness of the accelerated aged varnish films, acquired with a stylus profiler, were  $82.3 \pm 13.2 \mu\text{m}$  (dammar),  $28.2 \pm 7.5 \mu\text{m}$  (Ketone N),  $58.8 \pm 11.7 \mu\text{m}$  (MS2A) and  $51.3 \pm 12.6 \mu\text{m}$  (Paraloid B67). The laser peak power and the reflectivity of the varnishes were combined with the laser beam characteristics, such as the beam area, to determine surface power densities ( $F_0$ ) absorbed by the varnishes. However, because Paraloid B67 does not contain O-H groups in its chemical structure the transmission infrared spectroscopy showed that 90% of the Er:YAG laser radiation passed through the Paraloid B67 film reaching the underlying layer, in line with earlier observations (Striova *et al.*, 2011a). This also partially answered the third question of this research. In **Chapter 3**, the DSC analysis determined the specific heat capacity at constant pressure ( $C_p$ ) and the gas pycnometry returned the density values of the unaged raw resins. In **Chapter 4** the thermal conductivity ( $k$ ) data were presented. The thermal conductivity ( $k$ ) data ranged from  $0.0019 \text{ W}/\text{cm}\cdot\text{K}$  (for  $D \approx 10^{-3} \text{ cm}^2/\text{s}$ ) to  $0.00019 \text{ W}/\text{cm}\cdot\text{K}$  (for  $D \approx 10^{-4} \text{ cm}^2/\text{s}$ ) for MS2A; from  $0.0021 \text{ W}/\text{cm}\cdot\text{K}$  (for  $D \approx 10^{-3} \text{ cm}^2/\text{s}$ ) to  $0.00021$  (for  $D \approx 10^{-4} \text{ cm}^2/\text{s}$ ) for dammar and Paraloid B67; and from  $0.0022 \text{ W}/\text{cm}\cdot\text{K}$  (for  $D \approx 10^{-3} \text{ cm}^2/\text{s}$ ) to  $0.00022$  (for  $D \approx$

$10^{-4} \text{ cm}^2/\text{s}$ ) for Ketone N. The actual model development commenced with a simplified mathematical model of the heat distribution attained at  $z =$  thermal diffusion length ( $l_{th}$ ) of the films (2–11  $\mu\text{m}$ ). Ketone N varnish, at an operational fluence of  $1 \text{ J}/\text{cm}^2$ , has returned the highest  $\Delta T$  values with estimated temperatures in Very Short Pulse - VSP (laser pulse duration  $\tau_L \approx 100 \mu\text{s}$ ) between  $265 \text{ }^\circ\text{C}$  (for  $D \approx 10^{-3} \text{ cm}^2/\text{sec}$ ) and  $485 \text{ }^\circ\text{C}$  (for  $D \approx 10^{-4} \text{ cm}^2/\text{s}$ ), and between  $139 \text{ }^\circ\text{C}$  and  $395 \text{ }^\circ\text{C}$  in Short Pulse - SP ( $\tau_L \approx 300 \mu\text{s}$ ). However, the lowest  $\Delta T$  values were obtained with the dammar film in both VSP (between  $121 \text{ }^\circ\text{C}$  and  $138 \text{ }^\circ\text{C}$ ) and SP (between  $105 \text{ }^\circ\text{C}$  and  $132 \text{ }^\circ\text{C}$ ) modes. MS2A film gave  $\Delta T$  values between these ranges, with estimated temperatures in VSP mode from  $201 \text{ }^\circ\text{C}$  to  $252 \text{ }^\circ\text{C}$  and in SP mode from  $157 \text{ }^\circ\text{C}$  to  $233 \text{ }^\circ\text{C}$ . These data provide useful information of the estimation of the temperature upon a single pulsed Er:YAG laser irradiation. Thus, as a second step, the *volume model* was selected. This model assumed that the rate of heat production per unit of time per unit of volume was generated within the varnish layer surfaces, thus taking into consideration the absorption coefficient of each varnish. The model with an initial temperature of the varnish surface at  $25 \text{ }^\circ\text{C}$  (room temperature) was used. A software was employed to carry out the numeric computation and to minimise the possibility of human error during the manual data entry. Also, in this case, Ketone N film returned the highest estimated temperature after  $\tau_L$  for both VSP and SP modes. Comparing the Ketone N thermal data with those of the irradiated dammar, the estimated temperatures were 70% lower than Ketone N (for  $D \approx 10^{-3} - 10^{-4} \text{ cm}^2/\text{sec}$ ) in the VSP mode, and between 64% (for  $D \approx 10^{-3} \text{ cm}^2/\text{sec}$ ) and 70% (for  $D \approx 10^{-4} \text{ cm}^2/\text{sec}$ ) in SP mode. Likewise, comparing the Ketone N thermal data with the ones of MS2A, the decrement of the MS2A temperatures ranged between 45 % for  $D \approx 10^{-3}$ , considering reflectance data obtained from the FT-IR data and the Fresnel Equation, and 50 % for  $D \approx 10^{-4}$  in the VSP mode. This also applied for the SP mode with a decrement of about 40 % for  $D \approx 10^{-3}$  and 50 % for  $D \approx 10^{-4}$ . In all presented cases (**Chapter 4**), the diffusion of heat inside the varnishes, which tended to decrease asymptotically to room temperature, was demonstrated by solving the heat diffusion equation for semi-infinite homogeneous materials (Majaron, Plestenjak and Lukac, 1999). The 2-Dimensional simulation concluded the study of the laser-based heat diffusion inside each varnish. The simulation in **Chapter 4** answered the first question of this research. The 2D

simulation, carried out using a partial differential equations software, allowed the detection of a more precise heat distribution inside the varnish films upon a single laser pulse fired onto the dry surface by increasing the fluence values from 0.5 up to 2.4 J/cm<sup>2</sup> in VSP and SP modes. The simulation showed a defined increase in temperature confined to the laser absorption zone of the dammar, Ketone N and MS2A films, 33.21 μm, 7.16 μm, and 18.92 μm respectively. All the simulations showed that the temperature at the interface between the coating films and the substrate (in this case glass slides) remained at the room temperature of 25°C, thereby protecting the underlying paint surface. The temperature distribution in the irradiated Paraloid B67 was not carried out because its optical penetration depth was longer than the varnish film thickness, thus implying a direct interaction with the underlying layer, as already observed elsewhere (Striova *et al.*, 2011a). This also partially answered the third question of this research.

Transmission studies, carried out in **Chapter 4**, were acquired for the dry and pre-wet irradiated films at a fluence of 0.5, 1, 1.5, 2.1 and 2.4 J/cm<sup>2</sup>. This study answered the third question of this research. The % transmission data acquired using the pyroelectric detector, at fluences between 1.5 and 2.1 J/cm<sup>2</sup>, were comparable to the results of the FTIR transmission data. The results showed that the energy transmitted upon a single laser pulse in VSP and SP modes increased almost linearly with fluence. The beam propagation into the selected varnishes was reduced by pre-wetting the varnish surface with DI-W+TW20 because of the maximum absorption coefficient of water at the Er:YAG laser wavelength (Shori *et al.*, 2001). The dammar film showed the highest  $E_{\text{trans}}$  values both in dry ( $19.5 \pm 4$  in VSP and  $25.3 \pm 2.2$  in SP mode at 2.4 J/cm<sup>2</sup>) and pre-wet surfaces with DI-W+TW20 ( $17 \pm 6.9$  in VSP and  $18.1 \pm 5.8$  in SP mode at 2.4 J/cm<sup>2</sup>) (section 4.3.2). However, ketone resins presented the lowest  $E_{\text{trans}}$  values in dry ( $7.6 \pm 1.7$  in VSP and  $5.1 \pm 0.7$  in SP mode at 2.4 J/cm<sup>2</sup>) and pre-wetting the surfaces with DI-W+TW20 ( $4.6 \pm 5.2$  in VSP and  $9 \pm 3.1$  in SP mode at 2.4 J/cm<sup>2</sup>) (section 4.3.2). Ketone N and MS2A resulted in absorbing most of the laser beam energy, thereby lowering the amount of energy interacting with the underlying paint layer.

In **Chapter 5**, the effects of the laser-varnish interactions during the Er:YAG laser irradiation were studied and evaluated in conservation treatment scenarios where the aged varnishes were either directly irradiated or pre-wetted.

The laser spots on the irradiated varnishes with fluences ranging from 0.6 to 2.5 J/cm<sup>2</sup> were observed with Back-Scatter Electron Scanning Electron Microscopy (BSE-SEM). The extensive BSE-SEM study revealed morphological differences between the single-pulse irradiated dammar varnish and the ketone resin (Ketone N and MS2A) varnishes, therefore answering the first and second questions of this research. Paraloid B67 did not show any interaction with the laser as observed by means of Brightfield Optical Microscopy (OM), leading to the conclusion that artefacts and artworks with Paraloid B67 coatings should never be irradiated dry with Er:YAG lasers. Since the efficacy of the Er:YAG laser is directly proportional to the concentration of hydroxide groups in the materials, the pre-wetted dammar, Ketone N and MS2A varnish films showed less marked laser spots when compared to the ones generated onto the dry irradiated surfaces. In dry irradiation and at 0.6 J/cm<sup>2</sup> the following was observed: locally swollen areas and the formation of circular spots on dammar; lift-off phenomena upon a single pulse on MS2A; and almost negligible response on Ketone N. When increasing the fluence up to 2.5 J/cm<sup>2</sup>, BSE-SEM provided evidence of morphological modifications with the formation of craters and bubbles. The mathematical calculations and 2D simulations, presented in **Chapter 4**, were used to interpret the laser-material interaction upon laser irradiation. Discrepancies between the BSE-images and the temperature profiles of the models were correlated to adopted simplifications which may lead to predictive errors (e.g., the decrease in the optical absorption coefficients with the increase in samples temperatures). BSE-SEM of the dry irradiated varnishes after multiple-pulse in VSP and SP modes showed more swollen surfaces and more pronounced concentric rings. The pre-wetted dammar and MS2A films at 2.5 J/cm<sup>2</sup> showed the formation of shrinkage and warpage modifications of the uppermost surface layer with partial removal of the varnish layers and a partial exposure of the substrate.

The answer to the second question was investigated in **Chapter 5**. Attenuated Total Reflection (ATR)/Fourier Transform Infrared (FT-IR) spectroscopy was carried out directly on the irradiated aged varnish surfaces. Five consecutive laser pulses were released onto the aged varnish surfaces and ATR/FT-IR analysis was used to assess the laser cleaning efficiency at fluence of 0.5, 1, 1.5, 2, and 2.4 J/cm<sup>2</sup>. Findings suggested that the use of Er:YAG laser allowed the thinning of the surface

layer of degraded varnishes without further modifying the overall molecular structure of aged resins. The ATR/FT-IR study confirmed that the increase in hydroxyl groups due to the ageing process of the coatings ensured increased absorption of the laser wavelength, which determines the main process of the laser-material interaction as described by Andreotti *et al.* (2007), De Cruz, Wolbarsht and Hauger (2000a, 2000b), De Cruz *et al.* (2014) and Teppo (2020). The dry and pre-wetted aged MS2A film showed no change of hydroxides and carbonyls relative to CH bonds. On the contrary, the aged dammar and Ketone N resin films resulted in a considerable reduction of hydroxides and carbonyls relative to hydrocarbon bonds compared to the films prior to irradiation. For these films, the decrease in hydroxides confirmed that the dominating mechanism of Er:YAG laser cleaning is directly related to the maximum absorption of the 2940 nm laser wavelength from the hydroxides in the irradiated surface. These gradients were not very pronounced in the wet-irradiated Ketone N film. The decrease in carbonyls, as deeper parts in the bulk of the films were uncovered, is in line with previous findings with UV excimer lasers indicating the presence of depth-wise oxidative gradients (Theodorakopoulos *et al.*, 2007; Theodorakopoulos and Zafirooulos, 2009).

All the 2D simulations showed that upon a single laser pulse, the temperature at the interface between the coating films and the substrate remained at the room temperature of 25°C, protecting, therefore, the underlying paint surface. In all the thermal studies considered herein, it was shown that the maximum temperature was obtained in the VSP mode and the heat distribution was less than the one obtained with the SP mode. In the SP mode, all the dry irradiated films were less heated, but the average temperature of the area close to the absorption zone was higher than in the VSP mode. Findings of the transmission study allowed to detect that the underlying layers coated with these varnishes were not completely shielded from the Er:YAG laser interaction. It is, therefore, necessary to determine the fluence threshold parameters of the underlying layer(s) in order to carry out safe laser cleaning treatments. Moreover, the presence of the hydroxides in the irradiated surface is a crucial factor in the interaction of Er:YAG laser with organic films as indicated with the ATR/FTIR analyses. Therefore, prior to the Er:YAG laser

irradiation, the hydroxide concentration must be monitored to determine the amount of Er:YAG laser light absorbed onto the irradiated surface.

The final chapter of the thesis (**Chapter 6**) addressed the fourth question of this research on the possibility to use Er:YAG lasers to safely thin varnishes applied to works of art. A nineteenth century varnished oil painting, belonging to the Department of Arts at Northumbria University, was used to carry out laser cleaning tests. The characterisation of the final varnish applied to the nineteenth century painting was carried out by means of ATR/FT-IR and py-TMAH-GC/MS analyses. The analyses showed that the painting was coated with a dammar-based varnish. Laser irradiation tests led to diverse results depending on whether the surface was directly irradiated dry or pre-wetted. The tests showed that irradiation of the varnish had similar results when the surface was: i) dry or pre-wetted with a non-polar solvent: White Spirit (WS), ii) pre-wetted with deionised water (DI-W) and DI-W+TW20, and c) pre-wetted with 50% (v/v) blends of methylated ethanol (IMS) with WS and IMS with DI-W. Multispectral imaging clusterisation maps of the tested areas, used herein for the first time, were particularly useful in the evaluation and monitoring of the laser effects to the surface. ATR/FT-IR spectra assessed the laser cleaning efficiency process by monitoring the changes in the hydroxide and carbonyl absorbencies relative to hydrocarbon bands of the varnish. Laser irradiation did not show any considerable modification in these band ratios, indicating so that the varnish did not degrade even at the highest level of fluence employed of 2.4 J/cm<sup>2</sup>.

## **7.2 Future Prospects**

There are still several areas which have not been adequately covered by this research and which could therefore determine further study on the Er:YAG laser interaction with paintings constituent materials.

One of the most important issues during the laser cleaning on works of art is the single pulse efficacy. For each pulse, the degree of cleaning is typically controlled ex-post by observing the surface morphology using standard technologies such as micro-profilometry or optical profilometry, and measuring the depth created after

the laser irradiation. The possibility to acquire in real-time the volume of removed material (depth profile) under different operative conditions and quality of the remaining varnish layer may enable conservators to monitor the laser cleaning intervention without affecting the underlying painted layers.

Findings, based on the impact of one Er:YAG laser pulse to the surface and the bulk of aged dammar, Ketone N, MS2A films, suggest that further research is required into the interactions of the Er:YAG laser with coatings. Future models of free-running Er:YAG laser interaction with coatings and art materials should consider material ejection during the laser pulse and possible shielding effects by the generated irradiation plume using wetting agents. In particular, the laser irradiation of prewet surfaces with water may involve shielding effects, which previous publications (Nahen and Vogel, 2002) have defined as relatively weak throughout the entire laser pulse, but for which the information available for artist and conservation materials is scarce. Nonetheless, the estimations made analytically may result in predictive errors due to the simplification and approximations of mathematical modelling and simulations and because a real surface involves material layers that could be strongly heterogeneous. The possibility to acquire the real transient surface peak temperature during laser cleaning can facilitate the correct choice of laser parameters and a suitable methodology. Also, since artistic material, such as organic paints, pigments and binders, can be thermally sensitive to minor variations of temperature, these artistic materials could easily undergo a degradation process upon laser irradiation. Therefore, the development of a non-contact short time scale temperature measurement method may be crucial during laser clearing where temperature tolerance is important.

Such studies would enable the detailed design and the future implementation of more informed conservation treatments with Er:YAG lasers.

### ***7.3 Summary of the overarching findings of the thesis***

The overarching findings of this PhD thesis are summarised below, as follows:

- a) After light- and hydrothermal-ageing:

- dammar films showed colour change towards a yellow hue using colourimetric analysis and highly cracked surfaces by stylus profilometry.
  - Ketone N films proved to be the most hydrophilic resin with the smallest static contact angle.
  - MS2A films appeared smooth and extremely brittle and fragile to the touch.
  - Paraloid B67 films remained transparent, and no variations were detected using colourimetric analysis.
  - ATR/FT-IR revealed an increase in absorbance in the carbonyl and hydroxyl frequencies for all the varnishes. However, the CH bending vibration modes decreased for dammar and Ketone N and increased for MS2A and Paraloid B67.
- b) TGA and DSC determined that the raw ketone resins (Ketone N and MS2A) were less thermally stable than dammar and Paraloid B67 resins.
- c) The varnish films' optical properties were acquired by transmission infrared spectroscopy, which allowed an estimation of the absorption coefficient ( $\alpha$ ) at the laser wavelength and, therefore, to obtain the optical penetration depth ( $\delta$ ). The laser peak power and the varnishes' reflectivity were combined with the beam area to determine surface power densities ( $F_{\theta}$ ) absorbed by the varnishes. DSC analysis determined the specific heat capacity at constant pressure ( $C_p$ ) and the gas pycnometry returned the density values of the resins.
- d) The IR thermal camera recorded the maximum temperatures ( $\Delta T_{\text{mean}}$ ) in real-time during the laser irradiation. The pre-wetted varnishes showed  $\Delta T_{\text{mean}}$  values higher than on the dry varnishes due to the superheating of the aqueous film on the surface. Nonetheless, the use of the thermal acquisition technique highlighted that a 30 Hz thermal camera did not provide reliable temperature data due to discrepancies in the pulse durations ( $\tau_L \approx 100$  and  $300 \mu\text{s}$ ), the camera acquisition rate (30 Hz) and the 7 - 12 ms of the thermal constant of thermal camera microbolometer detector.
- e) The volume model, which considered the absorption coefficient and an initial surface temperature at 25 °C (room temperature - RT), was used to provide useful information of the estimation of the temperature upon a single pulsed Er:YAG laser irradiation in dry condition. For each irradiated

varnish film, the maximum temperatures obtained at  $\tau_L$  in VSP and SP modes shifted at lower temperatures moving towards the bulk of the coatings tending to decrease asymptotically to RT. The calculated heat-wave propagation returned the highest estimated temperature at the surface after  $\tau_L$  for both VSP and SP modes for Ketone N film. Conversely, dammar films showed the lowest  $\Delta T$  values in both VSP and SP modes. MS2A film gave in-between  $\Delta T$  values.

- f) The 2D simulation provided an additional possibility to study the heat propagation in the bulk of the irradiated varnishes. The simulation revealed a defined increase in temperature confined to the varnishes' laser absorption zone. The temperature at the interface between the coating films and the substrate remained at RT, thereby protecting the underlying paint surface. The maximum temperature was obtained in the VSP mode, and the heat distribution was less than the one obtained with the SP mode. In the SP mode, all the dry irradiated films were less heated, but the area's average temperature close to the absorption zone was higher than in the VSP mode.
- g) Since Paraloid B67 does not contain O-H groups in its chemical structure, the transmission infrared spectroscopy showed that 90% of the Er:YAG laser radiation passed through the film, reaching the underlying layer. The temperature distribution in the irradiated Paraloid B67 was not carried out because its optical penetration depth was longer than the varnish film thickness, thus implying a direct interaction of the laser beam with the underlying layer.
- h) The transmission study showed that the energy transmitted upon a single laser pulse in VSP and SP modes increased almost linearly with fluence. The underlying layers coated with dammar, Ketone N and MS2A were not completely shielded from the laser interaction. By pre-wetting the varnishes surface, the laser energy propagation into the selected varnishes was reduced because of the maximum absorption coefficient of water at the Er:YAG laser wavelength. The dammar film gave the highest  $E_{trans}$  values both in dry and pre-wet surfaces. However, Ketone N and MS2A resulted in absorbing most laser beam energy, thereby lowering the amount of energy interacting with the underlying paint layer. It is, therefore, necessary to

determine the fluence threshold parameters of the underlying layer(s) to carry out safe laser cleaning treatments.

- i) The extensive BSE-SEM study revealed morphological differences between the irradiated dammar varnish and the ketone resin (Ketone N and MS2A) varnishes. The pre-wetted dammar, Ketone N and MS2A varnish films showed less marked laser spots when compared to the ones generated onto the dry irradiated surfaces. Paraloid B67 did not show any interaction with the laser as observed employing Brightfield OM, leading to the conclusion that artefacts and artworks with Paraloid B67 should never be irradiated dry with Er:YAG lasers.
- j) ATR/FT-IR analysis was used to assess the laser cleaning efficiency. The dry and pre-wetted aged MS2A film showed no change of hydroxides and carbonyls relative to CH bonds. On the contrary, the aged dammar and Ketone N resin films resulted in a considerable reduction of hydroxides and carbonyls relative to hydrocarbon bonds compared to the films before irradiation. The decrease in hydroxides confirmed that the dominating mechanism of Er:YAG laser cleaning is directly related to the maximum absorption of the 2940 nm laser wavelength from the hydroxides in the irradiated surface and that the use of Er:YAG laser allowed the thinning of the degraded varnishes without further modifying their overall molecular structure.
- k) A nineteenth-century oil painting was used to evaluate the efficacy to safely thin a varnish layer(s) using the Er:YAG laser in a real case scenario. Spectral clusterisation maps of Multispectral Imaging (MSI) data were particularly useful in evaluating and monitoring the laser effects to the surface. ATR/FT-IR spectra assessed the laser cleaning efficiency process by monitoring the changes in the hydroxide and carbonyl absorbencies relative to hydrocarbon bands of the varnish acquired from the condensed resin fragments collected using microscope glass coverslips. The results showed that the resin did not degrade even at the highest level of fluence employed, thereby allowing a subsequent analytical evaluation.



## List of References

- Acherjee, B., Kuar, A. S., Mitra, S., Misra, D. (2012) ‘Modelling of laser transmission contour welding process using FEA and DoE’, *Optics and Laser Technology*. Elsevier, 44(5), pp. 1281–1289. doi: 10.1016/j.optlastec.2011.12.049.
- Al-Dharrab, A. and Shinawi, L. (2016) ‘Thermogravimetric characterization of the microstructure composition of polyamide injection molded denture base material vs conventional compression molded heat-cured denture base material’, *Journal of Contemporary Dental Practice*, 17(2), pp. 99–104. doi: 10.5005/jp-journals-10024-1810.
- Alabone, G. and Carvajal, M. S. (2020) ‘The removal of bronze paint repairs from overgilded picture frames using an Erbium:YAG laser’, *Journal of the Institute of Conservation*. Taylor & Francis, 43(1), pp. 1–15. doi: 10.1080/19455224.2019.1706595.
- Alonso Ipina, A., Lázaro Urrutia, M., Lázaro Urrutia, D., Alvear Portilla, D. (2018) ‘Thermal oxidative decomposition estimation combining TGA and DSC as optimization targets for PMMA’, *Journal of Physics: Conference Series*, 1107(3). doi: 10.1088/1742-6596/1107/3/032011.
- Althöfer, H. and Schinzel, H. (1985) ‘*Restaurierung moderner Malerei: Tendenzen, Material, Technik*/(Hrsg.) Heinz Althofer; in Zusammenarbeit mit Hiltrud Schinzel e.a.. München: Callwey. Available at: <https://lib.ugent.be/catalog/rug01:000152361>. (Accessed: 12 Jan. 21).
- Andreotti, A., Bracco, P., Colombini, M. P., De Cruz, A., Lanterna, G., Nakahara, K., Penaglia, F. (2007) ‘Novel Applications of the Er:YAG Laser Cleaning of Old Paintings’, in Nimmrichter, J., Kautek, W., and Schreiner, M. (eds.) *Lasers in the conservation of artworks, proceedings Lacona VI, Vienna, Austria, Sept 21-25, 2005*. Berlin, Heidelberg: Springer, pp. 239–247. doi: 10.1007/978-3-540-72130-7\_28.
- Andreotti, A., Brown, W. P., Camaiti, M., Colombini, M. P., De Cruz, Adele (2016)

‘Diagnosis of materials and effectiveness of Er:YAG laser cleaning as complementary treatment in a panel painting attributed to Lluís Borrassà (fifteenth century)’, *Applied Physics A*. Springer Berlin Heidelberg, 122(6), p. 572. doi: 10.1007/s00339-016-0100-1.

Andreotti, A., Colombini, M. P. and De Cruz, A. (2020) ‘Er:YAG laser cleaning of a marble Roman urn’, *Journal of the Institute of Conservation*. Taylor & Francis, 43(1), pp. 12–24. doi: 10.1080/19455224.2019.1706593.

Anglos, D., Solomidou, M., Zergioti, I., Zafiropulos, Z., Papazoglou, T. G., Fotakis C. (1996) ‘Laser-Induced Fluorescence in Artwork Diagnostics: An Application in Pigment Analysis’, *Applied Spectroscopy*. OSA, 50(10), pp. 1331–1334. Available at: <http://as.osa.org/abstract.cfm?URI=as-50-10-1331>. (Accessed: 12 Jan. 21).

Apitz, I. (2006) *Analyse von Ablationsdynamik und akustischem Signal bei der gepulsten IR-Ablation biologischer Gewebe im Hinblick auf eine Online-Ablationskontrolle*. Doctoral Thesis, Universität zu Lübeck. Available at: <https://www.zhb.uni-luebeck.de/epubs/ediss330.pdf>. (Accessed: 12 Jan. 21).

Apitz, I. and Vogel, A. (2005) ‘Material ejection in nanosecond Er:YAG laser ablation of water, liver, and skin’, *Applied Physics A: Materials Science and Processing*, 81(2), pp. 329–338. doi: 10.1007/s00339-005-3213-5.

Appala Naidu, U. and Dinda, S. (2015) ‘Development of ketonic resin by polymerization reaction: A critical review’, *Polymer*, 61, pp. 204–212. doi: 10.1016/j.polymer.2015.02.013.

Arakeri, J. H. (2000) ‘Bernoulli’s equation’, *Resonance*, 5(8), pp. 54–71. doi: 10.1007/BF02837937.

Arigoni, D., Barton, D. H. R., Bernasconi, R., Djerassi, C., Mills, J. S., Wolff, R. E. (1960) ‘The constituents of dammarenic and nyctanthic acid’, *Journal of the Chemical Society*, pp. 1900–1905.

- Armengol, V., Jean, A. and Marion, D. (2000) 'Temperature Rise During Er:YAG and Nd:YAP Laser Ablation of Dentin', *Journal of Endodontics*, 26(3), pp. 138–141. doi: 10.1097/00004770-200003000-00002.
- Armenini, G. B. (1587) *De' veri precetti della pittvra. Milano*, Italy: Dalla tipografia di Vincenzo Ferrario, contrada S. Vittore e 40 Martiri.
- Arnold, N., Luk'yanchuk, B. and Bityurin, N. (1998) 'A fast quantitative modelling of ns laser ablation based on non-stationary averaging technique', *Applied Surface Science*, 127–129, pp. 184–192. doi: 10.1016/S0169-4332(97)00630-2.
- Arvanitoyannis, I. S. (2016) *Authenticity of Foods of Animal Origin*. Portland, United States: CRC Press. doi: 10.1201/b19866.
- Asmus, J. F. (1975) 'Use of lasers in the conservation of stained glass', *Conservation in archaeology and the applied arts. Preprints of the contributions to the Stockholm Congress, 2-6 June 1975*, pp. 139–142.
- Asmus, J. F. (1986) 'More light for art conservation', *IEEE Circuits and Devices Magazine*, 2(2), pp. 6–15. doi: 10.1109/MCD.1986.6311800.
- Asmus, J. F., Guattari, G., Lazzarini, L., Musumeci, G., Wuerker, R. F. (1973) 'Holography in the Conservation of Statuary', *Studies in Conservation*, 18(2), pp. 49–63. doi: 10.1179/sic.1973.005.
- Asmus, J. F., Murphy, C. G. and Munk, W. H. (1974) 'Studies on the interaction of laser radiation with art artifacts', in Weurker, R. F. (ed.) *Proc. SPIE 0041, Developments in Laser Technology II, (1 March 1974)*, pp. 19–30. doi: 10.1117/12.953831.
- Asmus, J. F., Seracini, M. and Zetler, M. J. (1976) 'Surface Morphology of Laser Cleaned Stone', *Lithoclastia*, 1, pp. 23–46.
- Asmus, J. F., Westlake, D. L. and Newton, H. T. (1975) 'Laser technique for the divestment of a lost Leonardo da Vinci mural', *Journal of Vacuum Science and Technology*, 12 (6), pp. 1352–1355. doi: 10.1116/1.568537

- ASTM E 1269-11 (2011) ‘*Standard Test Method for Determining Specific Heat Capacity by Differential Scanning Calorimetry*’, American Society for Testing and Materials. United States: ASTM International, pp. 1–6. doi: 10.1520/E1269-11.2.
- ASTM E1356-08 (2014) ‘*Standard Test Method for Assignment of the Glass Transition Temperatures by Differential Scanning Calorimetry*’, ASTM International, pp. 1–4. doi: 10.1520/E1356-08R14.2.
- Ataie-Fashtami, L., Shirkavand, A., Sarkar, S., Alinaghizadeh, M., Hejazi, M., Fateh, M., Esmaeeli Djavid, G., Zand, N., Mohammadreza, H., (2011) ‘Simulation of heat distribution and thermal damage patterns of diode hair-removal lasers: An applicable method for optimizing treatment parameters’, *Photomedicine and Laser Surgery*, 29(7), pp. 509–515. doi: 10.1089/pho.2010.2895.
- Athanassiou, A., Hill, A. E., Fourrier, T., Burgio, L., Clark, R. J. H. (2000) ‘The effects of UV laser light radiation on artists’ pigments’, *Journal of Cultural Heritage*, pp. S209–S213. doi: 10.1016/S1296-2074(00)00180-1.
- Attrill, D. C., Davies, R. M., King, T. A., Dickinson, M. R., Blinkhorn, A. S. (2004) ‘Thermal effects of the Er:YAG laser on a simulated dental pulp: A quantitative evaluation of the effects of a water spray’, *Journal of Dentistry*, 32(1), pp. 35–40. doi: 10.1016/S0300-5712(03)00137-4.
- Azémard, C., Vieillescazes, C. and Ménager, M. (2014) ‘Effect of photodegradation on the identification of natural varnishes by FT-IR spectroscopy’, *Microchemical Journal*. Elsevier, 112, pp. 137–149. doi: 10.1016/j.microc.2013.09.020.
- Bachmann, L., Diebolder, R., Hibst, R., Zezell, D. M. (2005) ‘Changes in chemical composition and collagen structure of dentine tissue after erbium laser irradiation’, *Spectrochimica Acta - Part A: Molecular and Biomolecular Spectroscopy*, 61, pp. 2634–2639. doi: 10.1016/j.saa.2004.09.026.

- Bader, C. and Krejci, I. (2006) ‘Review Article. Indications and limitations of Er:YAG laser applications in dentistry’, *American Journal of Dentistry*, 19(3), pp. 178–186. doi: 10.1016/S0084-3717(08)70542-7.
- Baglioni, P. and Chelazzi, D. (eds.) (2013) *Nanoscience for the Conservation of Works of Art*. Cambridge: Royal Society of Chemistry (Nanoscience & Nanotechnology Series). doi: 10.1039/9781849737630.
- Baij, L., Hermans, J., Ormsby, B., Noble, P., Iedema, P., Keune, K., (2020) ‘A review of solvent action on oil paint’, *Heritage Science*. Springer International Publishing, 8(1), pp. 1–23. doi: 10.1186/s40494-020-00388-x.
- Barvinschi, P. and Bunoiu, O. M. (2017) ‘A finite element method model to simulate the thermal response of vascularized tissue to laser irradiation’, *Romanian Reports in Physics*, 69(2).
- Bäuerle, D. (2011) *Laser Processing and Chemistry*. Laser Processing and Chemistry. 3<sup>rd</sup> Ed. Heidelberg Dordrecht London New York: Springer. Available at: [https://books.google.it/books/about/Laser\\_Processing\\_and\\_Chemistry.html?id=x8ryCAAQBAJ&printsec=frontcover&source=kp\\_read\\_button&redir\\_esc=y#v=onepage&q&f=false](https://books.google.it/books/about/Laser_Processing_and_Chemistry.html?id=x8ryCAAQBAJ&printsec=frontcover&source=kp_read_button&redir_esc=y#v=onepage&q&f=false). (Accessed: 12 Jan. 21). doi: 10.1007/978-3-642-17613-5.
- Becker, F. and Potente, H. (2002) ‘A step towards understanding the heating phase of laser transmission welding in polymers’, *Polymer Engineering & Science*, 42(2), pp. 365–374. doi: 10.1002/pen.10954.
- Benson, S. W. (1976) *Thermochemical kinetics. Methods for the estimation of thermochemical data and rate parameters*. Wiley-Interscience publications. 2<sup>nd</sup> Ed. New York: Wiley.
- Bergeon, S. (1968) ‘*Resauuration des peintures, Catalogue d’exposition du Musée du Louvre (May-Dec. 1980)*’, Dossier du Département des Peintures, 21.

- Bernath, P. F. (2016) *Spectra of Atoms and Molecules*. 3<sup>rd</sup> Ed. Oxford University Press. Available at: <https://global.oup.com/academic/product/spectra-of-atoms-and-molecules-9780199382576?cc=it&lang=en&#>. . (Accessed: 12 Jan. 21).
- Berns, R. S and de la Rie, E. R. (2003c) ‘The Effect of the Refractive Index of a Varnish on the Appearance of Oil Paintings’, *Studies in Conservation*, 48(4), pp. 251–262. Available at: <https://www.jstor.org/stable/1506914>. (Accessed: 12 Jan. 21). doi: 10.1179/sic.2003.48.4.251.
- Berns, R. S. and de la Rie, E. R. (2002) ‘The relative importance of surface roughness and refractive index in the effects of varnishes on the appearance of paintings’, *Studies in Conservation. Triennial meeting (13th), Rio de Janeiro, 22-27 September 2002: preprints*. London, United Kingdom: James & James 2002, pp. 211–216. doi: 10.1179/sic.2003.48.4.251.
- Berns, R. S. and de la Rie, E. R. (2003a) ‘A methodology for analyzing the effect of varnishes on the appearance of paintings’, *Studies in Conservation*, 48, pp. 73–82.
- Berns, R. S. and de la Rie, E. R. (2003b) ‘Exploring the optical properties of picture varnishes using imaging techniques’, *Studies in Conservation*, 48(2), pp. 73–82. doi: 10.1179/sic.2003.48.2.73.
- Bird, R. B., Stewart, W. E. and Lightfoot, E. N. (1960) *Transport phenomena*. New York: John Wiley and Sons.
- Bityurin, N., Luk'yanchuk, B. S., Hong, M. H., Chong, T. C. (2003) ‘Models for laser ablation of polymers’, *Chemical Reviews*, 103(2), pp. 519–552. doi: 10.1021/cr010426b.
- Boccardi, S., Boffa, N. D., Carlomagno, G. M., Maio, L., Meola, C., Ricci, F. (2015) ‘Infrared thermography and ultrasonics to evaluate composite materials for aeronautical applications’, *Journal of Physics: Conference Series November*, 658(1). doi: 10.1088/1742-6596/658/1/012007.

- Bomford, D. and Leonard, M. (eds.) (2004) *Issues in the conservation of paintings*. Los Angeles: Getty Conservation Institute.
- Bomford, D., Dunkerton, J. and Wyld, M. (2009) *A Closer Look: Conservation of Paintings*. London, UK: National Gallery.
- Bonaduce, I., Colombini, M. P., Degano, I., Di Girolamo, F., La Nasa, J., Modugno, F., Orsini, S. (2013) 'Mass spectrometric techniques for characterizing low-molecular-weight resins used as paint varnishes', *Analytical and Bioanalytical Chemistry*, 405(2–3), pp. 1047–1065. doi: 10.1007/s00216-012-6502-9.
- Bonaduce, I., Di Girolamo, F., Corsi, I., Degano, I., Tinè, M. R., Colombini, M. P. (2016) 'Terpenoid Oligomers of Dammar Resin', *Journal of Natural Products*, 79, pp. 845–856. doi: 10.1021/acs.jnatprod.5b00916.
- Bonino, V. E. S. (2016) *Dall'olio all'acrilico, dall'impressionismo all'arte contemporanea*. Padova: Il Prato Editore.
- Boonrat, P., Dickinson, M. and Cooper, M. (2020) 'Initial investigation into the effect of varying parameters in using an Er:YAG laser for the removal of brass-based overpaint from an oil-gilded frame', *Journal of the Institute of Conservation*. Taylor & Francis, 43(1), pp. 1–13. doi: 10.1080/19455224.2019.1706592.
- Bordalo, R., Morais, P. J., Gouveia, H., Young, C. (2006) 'Laser Cleaning of Easel Paintings: An Overview', *Laser Chemistry*, 2006(90279), pp. 1–9. doi: 10.1155/2006/90279.
- Bovey, F. A. and Winslow, F. H. (eds.) (1979) *Macromolecules, an introduction to polymer science*. New York: Academic Press Inc Ltd.
- Bracco, P., Lanterna, G., Matteini, M., Nakahara, K., Sartiani, O. (2001) 'L'esperienza dell'Opificio nella sperimentazione del laser ad erbio per la pulitura dei dipinti', *OPD Restauro - Rivista dell'Opificio delle Pietre Dure e Laboratori di Restauro di Firenze*, pp. 192–202.

- Bracco, P., Lanterna, G., Matteini, M., Nakahara, K., Sartiani, O., De Cruz, A., Wolbarsht, M. L., Adamkiewicz, E., Colombini, M.P. (2003) 'Er:YAG laser: an innovative tool for controlled cleaning of old paintings: testing and evaluation', *Journal of Cultural Heritage*, 4 (1), pp. 202–208. Available at: <http://www.sciencedirect.com/science/article/pii/S1296207402012323>. (Accessed: 12 Jan. 21). doi: 10.1016/S1296-2074(02)01232-3.
- Bradford, E. (1996) III. *The History of Synthetic Resin Varnishes*, Wiki - A Collaborative Knowledge Resource. Available at: [https://www.conservation-wiki.com/wiki/III.\\_The\\_History\\_of\\_Synthetic\\_Resin\\_Varnishes](https://www.conservation-wiki.com/wiki/III._The_History_of_Synthetic_Resin_Varnishes). (Accessed: 12 Jan. 21).
- Brewis, S. and Halsall, T. G. (1961) '130. The chemistry of triterpenes and related compounds. Part XXXVIII. The acidic constituents of dammar resin', *Journal of the Chemical Society (Resumed)*, (130), p. 646. doi: 10.1039/jr9610000646.
- Brewis, S., Halsall, T. G., Harrison, H. R., Hodder, O. J. R. (1970) 'Crystallographic structure determination of a triterpene dimethyl ester epsilon-lactone from dammar resin', *Journal of Chemical Society D*, pp. 891–892.
- Brommelle, N. (1956) 'Bloom in Varnished Paintings', *The Museums Journal*, 55(10), pp. 263–266.
- Brown, M. S. and Arnold, C. B. (2010) 'Fundamentals of Laser-Material Interaction and Application to Multiscale Surface Modification - Chapter 4', in Sugioka, K., Meunier, M., and Piqué, A. (eds) *Laser Precision Microfabrication*. Berlin, Heidelberg: Springer Berlin Heidelberg (Springer Series in Materials Science), pp. 91–120. doi: 10.1007/978-3-642-10523-4.
- Brugnara, M. (2006) 'Contact Angle plugin (for ImageJ software)'. Available at: <https://imagej.nih.gov/ij/plugins/contact-angle.html>. (Accessed: 12 Jan. 21).
- Brunetto, A., Bono, G. and Frezzato, F. (2020) 'Er:YAG laser cleaning of “ San Marziale in Gloria ” by Jacopo Tintoretto in the Church of San Marziale ,

Venice', *Journal of the Institute of Conservation*. Taylor & Francis, 43(1), pp. 1–15. doi: 10.1080/19455224.2019.1706596.

Brunetto, A., Bono, G., Fiorin, E., Maida, M. C. (2019) 'Sinergie laser e emulsioni per il recupero di policrome di tre dipinti di H. Bosch della Gallerie dell'Accademia di Venezia', in Brunetto, A., Lanterna, G., and Mazzei, B. (eds.) *Proceedings of Atti del 6° Convegno APLAR, Il laser in combinazione con...*, Florence, 14th-16th Sept. 2017. Milano, Italy: Nardini Editore, pp. 247–265.

BS EN 15886:2010 (2010) '*Conservation of cultural property. Test methods. Colour measurement of surfaces*'. Standards Policy and Strategy Committee.

Buahom, P. (2018) 'Measuring the Contact Angle in ImageJ (with the plug-in Contact Angle)', pp. 3–4. Available at: [https://www.researchgate.net/publication/328733959\\_Measuring\\_the\\_Contact\\_Angle\\_using\\_ImageJ\\_with\\_Contact\\_Angle\\_plug-in](https://www.researchgate.net/publication/328733959_Measuring_the_Contact_Angle_using_ImageJ_with_Contact_Angle_plug-in). (Accessed: 12 Jan. 21).

Buder, A. (2008) 'Dammar resin degradation revisited', *Chimia*, 62(11), pp. 913–917. doi: 10.2533/chimia.2008.913.

Byrne, A. (1991) 'Wolbers Cleaning Methods: Introduction', *AICCM Bulletin*, 17(3–4), pp. 3–11. doi: 10.1179/bac.1991.17.3-4.001.

Cain, S. R., Burns, F. C., Otis, C. E., Braren, B. (1992) 'Photothermal description of polymer ablation: Absorption behaviour and degradation time scales', *Journal of Applied Physics*, 72(11), pp. 5172–5178. doi: 10.1063/1.351997.

Camaiti, M., Palmer, R., Andreotti, A., Sansonetti, A., De Cruz, A., Colombini, M. P., Matteini, M., Striová, J., Castellucci, E., (2008) 'The interaction of laser radiation at 2.94  $\mu\text{m}$  with azurite and malachite pigments', in Castillejo, M., Moreno, P., Oujja, M., Radvan, R., Ruiz, J. (eds.) *Lasers in the Conservation of Artworks, proceedings Lacona VII, Madrid, Spain, Sep. 17–21, 2007*. Boca Raton, FL: CRC Press, Taylor & Francis Group, pp. 253–258. doi: 10.1201/9780203882085.ch40.

- Cappelloni, G., Tranquilli, G., Fumelli, F., Giovagnoli, A., Priori, G., Aramini, F., Conti, L., Talarico, F., Germinario, G. (no date) 'Applicazione della radiazione laser a diversa lunghezza d'onda per la pulitura delle campiture di Azzurrite a tempera', in Brunetto, A. (ed.) *Book of Abstract of Atti del 7° Convegno APLAR, Ieri, oggi e domani, Venice, 7<sup>th</sup> - 8<sup>th</sup> Nov. 2019*.
- Carlyle, L. (1981) *Laser interactions with paintings: results and proposals for further study*. Unpublished Report, Ottawa: Canadian Conservation Institute.
- Carlyle, L. (2001) *The artist's assistant: oil painting instruction manuals and handbooks in Britain 1800-1900 with reference to selected eighteenth-century sources*. London: Archetype Publications.
- Carslaw, H. S. and Jaeger, J. C. (1959) *Conduction of heat in solids*. 2<sup>nd</sup> Ed. London, UK: Oxford University Press.
- Castelli, C., Ciatti, M., Gusmeroli, L., Parri, M., Santacesaria, A., (2011) 'Il restauro del trittico di Ambrogio Lorenzetti di Badia a Rofeno dal Museo di Asciano', *OPD Restauro 23*. Firenze: Centro Di della Edifimi s.r.l., pp. 11–41. Available at: <http://www.jstor.org/stable/24395627>.
- Castillejo, M., Martín, M., Oujja, M., Santamaría, J., Silva, D., Torres, R., Manousaki, A., Zafiropulos, V., van den Brink, O. F., Heeren, R. M. A., Teule, R., Silva, A. (2003) 'Evaluation of the chemical and physical changes induced by KrF laser irradiation of tempera paints', *Journal of Cultural Heritage*, pp. 257–263. doi: 10.1016/S1296-2074(02)01143-3.
- Castillejo, M., Martín, M., Oujja, M., Silva, D., Torres, R., Manousaki, A., Zafiropulos, V., van den Brink, O. F., Heeren, R. M. A., Teule, R., Silva, A., Gouveia, H. (2002) 'Analytical Study of the Chemical and Physical Changes Induced by KrF Laser Cleaning of Tempera Paints', *Analytical Chemistry*, 74(18), pp. 4662–4671. doi: 10.1021/ac025778c.
- Castillejo, M., Moreno, P., Oujja, M., Radvan, R., Ruiz, J. (eds.) (2008) *Lasers in the Conservation of Artworks, Lasers in the Conservation of Artworks*,

*proceedings Lacona VII, Madrid, Spain, Sep. 17–21, 2007*. Boca Raton, FL: Taylor & Francis Group, London, UK. doi: 10.1201/9780203882085.

Cavalcanti, B. N., Lage-Marques, J. L. and Rode, S. M. (2003) ‘Pulpal temperature increases with Er:YAG laser and high-speed handpieces’, *Journal of Prosthetic Dentistry*, 90(5), pp. 447–451. doi: 10.1016/j.prosdent.2003.08.022.

Caverhill, J. R. (2001) *Investigation into the use and effects of a Q-Switched Nd:YAG laser for the removal of Ink from Paper*. Doctoral Thesis, University of Northumbria at Newcastle.

Çengel, Y. A., Ghajar, A. J. and Kanoglu, M. (2014) *Heat and Mass Transfer Fundamentals & Applications*. 5<sup>th</sup> Ed. New York: McGraw-Hill.

Cennini, C. (1960) *The craftsman’s handbook: the Italian ‘Il libro dell’ arte’*. Translated by D. V. Thompson. New York: Dover Publications.

Cerny, J., Vystřcil, A. and Huneck, S. (1963) ‘Über ein neues triterpen aus dammarhartz’, *Chemische Berichte*, pp. 3021–3023.

Chappé, M., Hildenhagen, J., Dickmann, K., Bredol, M. (2003) ‘Laser irradiation of medieval pigments at IR, VIS and UV wavelengths’, *Journal of Cultural Heritage*, pp. 264–270. doi: 10.1016/s1296-2074(02)01206-2.

Cheng, X., Zhang, J., Ding, T., Wei, Z., Li, H., Wang, Z. (2013) ‘The effect of an electric field on the thermomechanical damage of nodular defects in dielectric multilayer coatings irradiated by nanosecond laser pulses’, *Light: Science & Applications*, 2(6), pp. e80–e80. doi: 10.1038/lsa.2013.36.

Chiantore, O. and Lazzari, M. (2001) ‘Photo-oxidative stability of paraloid acrylic protective polymers’, *Polymer*, 42(1), pp. 17–27 [online]. Available at: <http://www.sciencedirect.com/science/article/pii/S003238610000327X> (Accessed: 12 Jan. 21). doi: 10.1016/S0032-3861(00)00327-X.

Chiantore, O. and Rava, A. (2012) *Conserving contemporary art: issues, methods, materials, and research*. Los Angeles: Getty Conservation Institute.

- Chiantore, O., Trossarelli, L. and Lazzari, M. (2000) 'Photooxidative degradation of acrylic and methacrylic polymers', *Polymer*, 41(5), pp. 1657–1668. doi: 10.1016/S0032-3861(99)00349-3.
- Chillè, C., Papadakis, V. M. and Theodorakopoulos, C. (2020) 'An analytical evaluation of Er:YAG laser cleaning tests on a nineteenth century varnished painting', *Microchemical Journal. Elsevier*, 158(May), p. 105086. doi: 10.1016/j.microc.2020.105086.
- Chillè, C., Sala, F., Wu, Q., Theodorakopoulos, C. (2020) 'A study on the heat distribution and oxidative modification of aged dammar films upon Er:YAG laser irradiation A study on the heat distribution and oxidative irradiation', *Journal of the Institute of Conservation. Taylor & Francis*, 43(1), pp. 1–20. doi: 10.1080/19455224.2019.1707699.
- Ciofini, D. (2014) *Removal Of Varnish And Overpaint Layers From Easel Paintings Using Pulsed Nd:YAG Lasers*. Doctoral Thesis, University of Florence. Available at: <http://hdl.handle.net/2158/1003245>. (Accessed:12 Jan. 21).
- Ciofini, D., Oujja, M., Cañamares, M. V., Siano, S., Castillejo, M. (2016a) 'Spectroscopic assessment of the UV laser removal of varnishes from painted surfaces', *Microchemical Journal*, 124, pp. 792–803. doi: 10.1016/j.microc.2015.10.031.
- Ciofini, D., Oujja, M., Cañamares, M. V., Siano, S., Castillejo, M. (no date) '213 nm laser ablation as standalone approach for damage-free removal of aged varnishes: a spectroanalytical evaluation on solvent and oil terpenoid coatings', in Book of Abstract *Lasers in the conservation of artworks, proceedings Lacona XII, Paris, Sept 10-14 2018*.
- Ciofini, D., Striova, J., Camaiti, M., Siano, S. (2016b) 'Photo-oxidative kinetics of solvent and oil-based terpenoid varnishes', *Polymer Degradation and Stability*, 123, pp. 47–61. doi: 10.1016/j.polymdegradstab.2015.11.002.

- Cohen, N. S., Odlyha, M., Campana, R., Foster, G. M. (2000) 'Dosimetry of paintings: Determination of the degree of chemical change in museum exposed test paintings (smalt tempera) by thermal analysis', *Thermochimica Acta*, 365(1–2), pp. 35–44. doi: 10.1016/S0040-6031(00)00611-0.
- Coladonato, M. and Scarpitti, P. (2005) Triangolo interattivo dei solventi e delle solubilità®, iscr.beniculturali.it. Available at: <http://iscr.beniculturali.it/flash/progetti/TriSolv/TriSolv.html> (Accessed: 12 Jan. 21).
- Colombini, M. P. and Modugno, F. (eds.) (2009) *Organic Mass Spectrometry in Art and Archaeology*. Chichester, UK: John Wiley & Sons, Ltd. doi: 10.1002/9780470741917.
- Colombini, M. P., Andreotti, A., Lanterna, G., Rizzi, M. (2003) 'A novel approach for high selective micro-sampling of organic painting materials by Er:YAG laser ablation', *Journal of Cultural Heritage*, 4 (1), pp. 355s-361s. doi: 10.1016/S1296-2074(02)01218-9.
- Colombini, M. P., Modugno, F., Giannarelli, S., Fuoco, R., Matteini, M. (2000) 'GC-MS characterization of paint varnishes', *Microchemical Journal*, 67, pp. 385–396. doi: 10.1016/S0026-265X(00)00098-9.
- Comini, G. and Cortella, G. (2013) *Fondamenti di trasmissione del calore*. 4<sup>th</sup> Ed. Padova: S.G.E.
- Contente, M. M. M. G., De Lima, F. A., Galo, R., Pécora, J. D., Bachmann, L., Palma-Dibb, R. G., Borsatto, M. C. (2012) 'Temperature rise during Er:YAG cavity preparation of primary enamel', *Lasers in Medical Science*, 27, pp. 1–5. doi: 10.1007/s10103-010-0823-8.
- Conti, A. (2007) *History of the Restoration and Conservation of Works of Art*. Linacre House, Jordan Hill, Oxford: Routledge.
- Cooper, M. (ed.) (1998) *Laser cleaning in Conservation: An introduction*. Oxford, UK: Butterworth - Heinemann.

- Cooper, M. and Larson, J. (1996) 'The use of laser cleaning to preserve patina on marble sculpture', *The Conservator*. Routledge, 20(1), pp. 28–36. doi: 10.1080/01410096.1996.9995100.
- Cooper, M. I., Emmony, D. C. and Larson, J. (1995) 'Characterization of laser cleaning of limestone', *Optics & Laser Technology*, 27(1), pp. 69–73. doi: 10.1016/0030-3992(95)93962-Q.
- Coutouly, J. F., Deprez, P., Breaban, F., Longuemard, J. P. (2009) 'Optimisation of a paint coating ablation process by CO2 TEA laser: Thermal field modelling and real-time monitoring of the process', *Journal of Materials Processing Technology*, 209(17), pp. 5730–5735 [online]. Available at: <http://www.sciencedirect.com/science/article/pii/S0924013609002283>. doi: 10.1016/j.jmatprotec.2009.06.001. (Accessed:12 Jan. 21).
- Cowie, J. M. G., McEwen, I. J. and Pedram, M. Y. (1983) 'Heat Capacity Measurements on Polymers and Copolymers of Itaconic Acid Esters Exhibiting Two Glass Transitions', *Macromolecules*, 16, pp. 1151–1155. doi: 10.1021/ma00241a019.
- Cremonesi, P. (2011) *L'ambiente acquoso per la pulitura di opere policrome*. Padova: Il Prato.
- Cremonesi, P. and Signorini, E. (2012) *Un approccio alla pulitura dei dipinti mobili*. Padova: Il Prato.
- Cummings, J. P. and Walsh, J. T. (1993) 'Erbium laser ablation: The effect of dynamic optical properties', *Applied Physics Letters*, 62(16), pp. 1988–1990. doi: 10.1063/1.109512.
- D' Couto, G. C. and Babu, S. V. (1994) 'Heat transfer and material removal in pulsed excimer-laser-induced ablation: Pulse width dependence', *Journal of Applied Physics*, 76(5), pp. 3052–3058. doi: 10.1063/1.357486.
- D'Orazio, L., Gentile, G., Mancarella, C., Martuscelli, E., Massa, V. (2001) 'Water-dispersed polymers for the conservation and restoration of Cultural Heritage:

A molecular, thermal, structural and mechanical characterization', *Polymer Testing*, 20, pp. 227–240. doi: 10.1016/S0142-9418(00)00027-1.

Dąbrowski, M., Dulski, R., Żmuda, S., Zaborowski, P. (2006) 'Thermographic assessment of thermal effects during laser sterilisation of pathological periodontal pocket', *Pol Merkur Lekarski*, 116(20), pp. 192–194.

Dash, D. C. (2011) *Analytical Chemistry*. 2<sup>nd</sup> Ed. New Delhi: PHI Learning Private Limited.

Daudin-Schotte, M., Bisschoff, M., Joosten, I., van Keulen, H., van den Berg, K. J. (2013) 'Dry Cleaning Approaches for Unvarnished Paint Surfaces', in Mecklenburg, M. F., Charola, A. E., and Koestler, R. J. (eds.) *New Insights into the Cleaning of Paintings: Proceedings from the Cleaning 2010 International Conference, Universidad Politecnica de Valencia and Museum Conservation Institute. Smithsonian Contributions to Museum Conservation*. Washington, DC: Smithsonian Institution, pp. 209–219. Available at: <https://repository.si.edu/handle/10088/20512>. (Accessed:12 Jan. 21).

De Cesare, G., Izurlo, P. and Biocca, P. (2017) 'La pulitura laser di vernici sintetiche su una tavolozza acrilico-vinilica: Rimozione, resistenza e alterazioni', in Brunetto, A. (ed.) *Proceedings of Atti del 5° Convegno APLAR, Applicazioni laser nel Restauro, Musei Vaticani 18-20 Settembre 2014*. Vicenza: Nardini Editore, pp. 383–393.

De Cesare, G., Melessanaki, K., Pouli, P., Domingues, J., Rosi, F., Fotakis, C. (2013) 'Extended Abstract - Laser cleaning applied to contemporary paintings: optimization of working parameters', in Mecklenburg, M. F., Charola, A. E., and Koestler, R. J. (eds.) *New Insights into the Cleaning of Paintings: Proceedings from the Cleaning 2010 International Conference, Universidad Politecnica de Valencia and Museum Conservation Institute. Smithsonian Contributions to Museum Conservation*. Washington, DC: Smithsonian Institution, pp. 237–238. Available at: <https://repository.si.edu/bitstream/handle/10088/20517/39.DeCesare.SCMC3.Mecklenburg.Web.pdf?sequence=1&isAllowed=y>. (Accessed:12 Jan. 21).

- De Cruz, A. and Wolbarsht, M. L. (2006) ‘EP1126932 - Method for cleaning Artwork’. European Patent: England, France, Germany, Italy, Spain, Portugal, Denmark, Holland, Greece, and Egypt.
- De Cruz, A., Andreotti, A., Ceccarini, A., Colombini, M. P. (2014) ‘Laser cleaning of works of art: evaluation of the thermal stress induced by Er:YAG laser’, *Applied Physics B*, 117(2), pp. 533–541 [online]. Available at: <https://rdcu.be/cdrcI>. (Accessed:12 Jan. 21). doi: 10.1007/s00340-014-5865-3.
- De Cruz, A., Hauger, S. A. and Wolbarsht, M. L. (1999) ‘The Role of Lasers in Fine Arts Conservation and Restoration’, *Optics & Photonics News*, 10(7), p. 36. doi: 10.1364/opn.10.7.000036.
- De Cruz, A., Wolbarsht, M. L. and Hauger, S. A. (2000a) ‘Laser removal of contaminants from painted surfaces’, *Journal of Cultural Heritage*, 1(1), pp. S173–S180. doi: 10.1016/S1296-2074(00)00182-5.
- De Cruz, A., Wolbarsht., M. L. and Hauger, S. A. (2000b) ‘The Introduction of Lasers as a Tool in Removing Contaminants from Painted Surfaces’, in *Art et Chimie: La couleur Proceedings, Paris – Louvre, France*.
- de la Rie, E. R. (1982) ‘Fluorescence of paint and varnish layers (Part II)’, *Studies in Conservation*, 27(2), pp. 65–69. doi: 10.1179/sic.1982.27.2.65.
- de la Rie, E. R. (1987) ‘The Influence of Varnishes on the Appearance of Paintings’, *Studies in Conservation*, 32(1), pp. 1–13. doi: 10.2307/1506186.
- de la Rie, E. R. (1988) ‘Photochemical and thermal degradation of films of dammar resin’, *Studies in Conservation*, 33(2), pp. 53–70 [online]. Available at: [www.jstor.org/stable/1506303](http://www.jstor.org/stable/1506303). (Accessed: 12 Jan. 21). doi: 10.1179/sic.1988.33.2.53.
- de la Rie, E. R. (1988a) ‘Photochemical and thermal degradation of films of dammar resin’, *Studies in Conservation*, 33(2), pp. 53–70. doi: 10.1179/sic.1988.33.2.53.

- de la Rie, E. R. (1988b) Stable varnishes for old master paintings. Doctoral Thesis, University of Amsterdam.
- de la Rie, E. R. (1989) 'Old Master Paintings: A study of the Varnish Problem', *Analytical Chemistry*, 61(21), pp. 1228A-1240A. doi: 10.1021/ac00196a003.
- de la Rie, E. R. and Shedrinsky, A. M. (1989) 'The chemistry of ketone resins and the synthesis of a derivative with increased stability and flexibility', *Studies in Conservation*. Routledge, 34(1), pp. 9–19. doi: 10.1179/sic.1989.34.1.9.
- de la Rie, E. R., Delaney, J. K., Morales, K. M., Maines, C. A., Sung, L. P. (2010) 'Modification of surface roughness by various varnishes and effect on light reflection', *Studies in Conservation*, 55(2), pp. 134–143. doi: 10.1179/sic.2010.55.2.134.
- Debenedetti, P. G. (1996) *Metastable liquids*. Princeton, NJ: Princeton University Press.
- Demtröder, W. (2006) *Atoms, Molecules and Photons*. Berlin/Heidelberg: Springer-Verlag. doi: 10.1007/3-540-32346-5.
- Derrick, M., Stulik, D. and Landry, J. (1999) *Infrared Spectroscopy in Conservation Science. Scientific Tools for Conservation*. Los Angeles, CA: Getty Conservation Institute. Available at: [http://hdl.handle.net/10020/gci\\_pubs/infrared\\_spectroscopy](http://hdl.handle.net/10020/gci_pubs/infrared_spectroscopy). (Accessed:12 Jan. 21). doi: 10.1017/CBO9781107415324.004.
- Diaci, J. and Gaspirc, B. (2012) 'REVIEW. Comparison of Er:YAG and Er, Cr:YSGG lasers used in dentistry', *Journal of the Laser and Health Academy*, 2012(1), pp. 1–13 [online]. Available at: [https://www.laserandhealthacademy.com/media/objave/academy/priponke/1\\_13\\_laha\\_journal\\_2012\\_1a.pdf](https://www.laserandhealthacademy.com/media/objave/academy/priponke/1_13_laha_journal_2012_1a.pdf). (Accessed:12 Jan. 21).
- Dickmann, K., Fotakis, C. and Asmus, J. F. (eds) (2005) *Lasers in the Conservation of Artworks*. LACONA V Proceedings Osnabruck, Germany, Sept. 15–18,

2003, Springer Proceedings in Physics. Osnabruck, Germany: Springer Berlin Heidelberg New York Library.

Dietemann, P. (2003) *Towards more stable natural resin varnishes for paintings. The Aging of Triterpenoid Resins and Varnishes*. Doctoral Thesis, Swiss Federal Institute of Technology, ETH Zürich. doi: 10.3929/ethz-a-004621911.

Dietemann, P., Edelmann, M. J., Meisterhans, C., Pfeiffer, C., Zumbühl, S., Knochenmuss, R., Zenobi, R. (2000) 'Artificial photoaging of triterpenes studied by graphite-assisted laser desorption/ionization mass spectrometry', *Helvetica Chimica Acta*, 83(8), pp. 1766–1777. doi: 10.1002/1522-2675(20000809)83:8<1766::AID-HLCA1766>3.0.CO;2-X.

Dietemann, P., Higgitt, C., Kälin, M., Edelmann, M. J., Knochenmuss, R., Zenobi, R. (2009) 'Aging and yellowing of triterpenoid resin varnishes - Influence of aging conditions and resin composition', *Journal of Cultural Heritage*, 10(1), pp. 30–40. doi: 10.1016/j.culher.2008.04.007.

Dietemann, P., Kälin, M., Zumbühl, S., Knochenmuss, R., Wülfert, S., Zenobi, R. (2001) 'A mass spectrometry and electron paramagnetic resonance study of photochemical and thermal aging of triterpenoid varnishes', *Analytical Chemistry*, 73(9), pp. 2087–2096. doi: 10.1021/ac000754w.

Ding, C., He, X. and Simon, H. D. (2005) 'Nonnegative Lagrangian Relaxation of K-Means and Spectral Clustering'. In: Gama J., Camacho R., Brazdil P.B., Jorge A.M., Torgo L. (eds.) *Machine Learning: ECML 2005. ECML 2005. Lecture Notes in Computer Science, vol 3720*. Springer, Berlin, Heidelberg. [https://doi.org/10.1007/11564096\\_51](https://doi.org/10.1007/11564096_51).

Doménech-Carbó, M. T., Bitossi, G. Osete-Cortina, L., Yusá-Marco, D. J. (2009) 'Study of ageing of ketone resins used as picture varnishes by pyrolysis-silylation-gas chromatography-mass spectrometry', *Journal of Analytical and Applied Pyrolysis*, 85, pp. 470–479. doi: 10.1016/j.jaap.2008.11.013.

- Doménech-Carbó, M. T., Bitossi, G., Yusá-Marco, D. J., Osete-Cortina, L. (2006) ‘Characterization of Changes in the Chemical Composition of Aged Acrylic Resins Used in Contemporary Artworks’, *Arché. Publicación del instituto universitario de restauración del patrimonio de la UPV*, 7, pp. 157–162. Available at: <http://hdl.handle.net/10251/32529>. (Accessed:12 Jan. 21).
- Doménech-Carbó, M. T., Yusá-Marco, D. J., Bitossi, G., Silva, M. F., Mas-Barberá, X., Osete-Cortina, L. (2008) ‘Study of ageing of ketone resins used as picture varnishes by FTIR spectroscopy, UV-Vis spectrophotometry, atomic force microscopy and scanning electron microscopy X-ray microanalysis’, *Analytical and Bioanalytical Chemistry*, 391(4), pp. 1351–1359. doi: 10.1007/s00216-008-1864-8.
- Donato, I. D. and Lazzara, G. (2012) ‘Porosity determination with helium pycnometry as a method to characterize waterlogged woods and the efficacy of the conservation treatments’, *Archaeometry*, 54(5), pp. 906–915. doi: 10.1111/j.1475-4754.2011.00657.x.
- Eastlake, C. L. (1869) *Materials for a History of Oil Painting*. Oxford: Longman, Brown, Green, and Longmans (Materials for a History of Oil Painting).
- Elhadj, S., Matthews, M. J. and Yang, S. T. (2012) ‘Combined Infrared Thermal Imaging and Laser Heating for the Study of Materials Thermophysical and Processing Properties at High Temperatures’, *Critical Reviews in Solid State and Materials Sciences*, 39:3, 175-196, doi: 10.1080/10408436.2013.789962.
- Endo, M. and Walter, R. F. (eds.) (2018) *Gas Lasers*. CRC Press. doi: 10.1201/b13628.
- Farkas, J. P., Hoopman, J. E. and Kenkel, J. M. (2013) ‘Five parameters you must understand to master control of your laser/light-based devices’, *Aesthetic Surgery Journal*, 33(7), pp. 1059–1064. doi: 10.1177/1090820X13501174.
- Farmakalidis, H. V., Douvas, A. M., Karatasios, I., Sotiropoulou, S., Boyatzis, S. C., Argitis, P., Chryssoulakis, Y., Kilikoglou, V. (2016) ‘Accelerated thermal ageing of acrylic copolymers, cyclohexanone-based and urea-aldehyde resins

used in paintings conservation’, *Mediterranean Archaeology and Archaeometry*, 16(3), pp. 213–228. doi: 10.5281/zenodo.163773.

Farr, D., House, J., Bruce-Gardner, R., Hedley, G., Villers, C. (1987) *Impressionist and Post-Impressionist Masterpieces: The Courtauld Collection*. Edited by Courtauld Institute Galleries; International Exhibitions Foundation. New Haven: Yale University Press.

Favaro, M., Mendichi, R., Ossola, F., Russo, U., Simon, S., Tomasin, P., Vigato, P. A. (2006) ‘Evaluation of polymers for conservation treatments of outdoor exposed stone monuments. Part I: Photo-oxidative weathering’, *Polymer Degradation and Stability*, 91(12), pp. 3083–3096. doi: 10.1016/j.polymdegradstab.2006.08.012.

Felici, A., Riminesi, C., Striova, J., Bartoli, L., Zanini, A. (2019) ‘Laser induced heating during cleaning of wall painting surfaces monitored by thermal infrared imaging’, in *Proceedings of Atti del 6° Convegno APLAR, Il laser in combinazione con...*, Florence, 14th-16th Sept. 2017. Firenze: Nardini Editore, pp. 161–171.

Feller, R. L. (1958) ‘Dammar and Mastic Varnishes: Hardness, Brittleness, and Change in Weight upon Drying’, *Studies in Conservation*, 3(4), pp. 162–174. doi: 10.1097/EDE.0b013e3181.

Feller, R. L. (1961) ‘New solvent-type varnishes’, in *Thompson, G. (ed.) Recent advances in conservation: contributions to the IIC Rome Conference*. London: Butterworths, pp. 171–175. doi: 10.1179/sic.1961.s040.

Feller, R. L. (1972) ‘Problems in the investigation of picture varnishes’, in *Brommelle, N. S. and Smith, P. (eds.) Studies in Conservation. Conservation of paintings and the graphic arts: preprints of contributions to the Lisbon Congress, 9-14 October 1972*, pp. 201–209. doi: 10.1179/sic.1972.17.s1.006.

Feller, R. L. (1976) ‘The relative solvent power needed to remove various aged solvent-type coatings’, in *Brommelle, N. and Smith, P. (eds.) Conservation and Restoration of Pictorial Art*. Butterworths, pp. 158–161.

- Feller, R. L. (1994) *Accelerated Aging: Photochemical and Thermal Aspects*. Research in Conservation 4. Marina del Rey, CA: Getty Conservation Institute. Available at: [http://hdl.handle.net/10020/gci\\_pubs/accelerated\\_aging](http://hdl.handle.net/10020/gci_pubs/accelerated_aging). (Accessed:12 Jan. 21).
- Feller, R. L. (2002) 'What's in a name: Dammar or Serendipity in the Library', in Whitmore, P. M. and Feller, R. L. (eds.) *Contributions to Conservation Science: A Collection of Robert Feller's Published Studies on Artists' Paints, Paper and Varnishes*. Pittsburgh: Carnegie Mellon University Press, pp. 21–26.
- Feller, R. L. and Curran, M. (1975) 'Changes in Solubility and Removability of Varnish Resins with Age', *Bulletin of the American Institute for Conservation of Historic and Artistic Works*, 15(2), pp. 17–26. doi: 10.1179/019713675806156654
- Feller, R. L. and Whitmore, P. M. (2002) *Contributions to conservation science: a collection of Robert Feller's published studies on artists' paints, paper, and varnishes*. Pittsburgh: Carnegie Mellon University Press.
- Feller, R. L., Jones, E. H. and Stolow, N. (1985) *On picture varnishes and their solvents*. 3<sup>rd</sup> ed. Washington, D.C.: National Gallery of Art and AIC Publishers.
- Filippidis, G., Mari, M., Kelegkouri, L., Philippidis, A., Selimis, A., Melessanaki, K., Sygletou, M., Fotakis, C. (2014) 'Assessment of In-Depth Degradation of Artificially Aged Triterpenoid Paint Varnishes Using Nonlinear Microscopy Techniques', *Microscopy and Microanalysis*, 21(2), pp. 510–517. doi: 10.1017/S1431927614013580.
- Fink, J. K. (2017) 'Paintings', in *Chemicals and Methods for Conservation and Restoration*. Hoboken, NJ, USA: John Wiley & Sons, Inc., pp. 1–94. doi: 10.1002/9781119418894.ch1.

- Finn, C. B. P. (1993) *Thermal Physics*. 2<sup>nd</sup> Ed. Taylor & Francis Ltd. Available at: <https://www.routledge.com/Thermal-Physics/Finn/p/book/9780367865252>. (Accessed: 12 Jan. 21).
- Formo, M. W. (1979) 'Physical Properties of Fats and Fatty Acids', in Swern, D. (ed.) *Bailey's Industrial Oil and Fat Products*, vol. 1. 4<sup>th</sup> Ed. New York, NY, USA: John Wiley & Sons, Ltd.
- Forrer, M., Frenz, M., Romano, V., Weber, H. P., Silenok, A., Konov, V. I. (1993) 'Channel propagation in water and gelatine by a free-running erbium laser', *Journal of Applied Physics*, 74(1), pp. 720–727. doi: 10.1063/1.355238.
- Forrer, M., Ith, M., Frenz, M., Romano, V., Weber, H. P., Silenok, A. S., Konov, V. I. (1994) 'Mechanism of channel propagation in water by pulsed erbium laser radiation', *Proc. SPIE 2077, Laser Interaction with Hard and Soft Tissue*, (1 February 1994), pp. 72–77. doi: 10.1117/12.168053.
- Fotakis, C. (1995) 'LASERS FOR ART'S SAKE!', *Optics and Photonics News*, 6(5), p. 30. doi: 10.1364/OPN.6.5.000030.
- Fotakis, C., Anglos, D., Zafiropulos, V., Georgiou, S., Tornari, V. (2006) *Lasers in the Preservation of Cultural Heritage: Principles and Applications*. Boca Raton, FL: Taylor & Francis Group, LLC.
- Fotakis, C., Hontzopoulos, E. I. and Zergioti, I. (1995) 'Laser applications in paintings conservation.', in *Proceedings of the AIC Conference*, pp. 36–42.
- Fotakis, C., Zafiropulos, V., Anglos, D., Georgiou, S., Maravelaki, N., Fostiridou, A., Doulgeridis, M. (1997) 'Lasers in art conservation', in *The Interface Between Science and Conservation*, pp. 83–90.
- Fotona (no date) *Fotona Technology*. Available at: <https://www.fotona.com/en/fotona-technology/> (Accessed: 17 June 2020).
- Fourier, J. B. J. (1952) *The Analytical Theory of Heat*. Chicago: Encyclopaedia Britannica, Inc. Available at: <https://www.britannica.com/topic/The-Analytical-Theory-of-Heat>.

- Frank, P., Lang, F., Mosbacher, M., Boneberg, J., Leiderer, P. (2008) 'Infrared steam laser cleaning', *Applied Physics. A: Materials Science and Processing*, 93(1), pp. 1–4. doi: 10.1007/s00339-008-4651-7.
- Freiberg, R. J. and Cozean, C. D. (2002) 'Pulsed erbium laser ablation of hard dental tissue: the effects of atomized water spray versus water surface film', *Lasers in Dentistry VIII*, 4610, p. 74. doi: 10.1117/12.469306.
- Frick, A., Stern, C. and Muralidharan, V. (2019) *Practical testing and evaluation of plastics*. Weinheim, Germany: Wiley-VCH. Available at: <https://www.wiley.com/en-us/Practical+Testing+and+Evaluation+of+Plastics-p-9783527334117>. (Accessed: 12 Jan. 21).
- Fried, D., Ragadio, J. and Champion, A. (2001) 'Residual Heat Deposition in Dental Enamel During IR Laser Ablation at 2.79, 2.94, 9.6, and 10.6  $\mu\text{m}$ ', *Lasers in Surgery and Medicine*, 29, pp. 221–229. doi: 10.1017/S0007485300053402.
- Fried, D., Visuri, S. R., Featherstone, J. D. B., Jr., Walsh, J. T., Seka, W. D., Glens, R. E., McCormack, S. M., Wigdor, H. A. (1996) 'Infrared radiometry of dental enamel during Er:YAG and Er:YSGG laser irradiation', *Journal of Biomedical Optics*, 1(4), pp. 455–465. doi: 10.1117/12.250668.
- Fried, D., Zuerlein, M., Featherstone, J. D. B., Seka, W., Duhn, C., McCormack, Sandra M. (1998) 'IR laser ablation of dental enamel: Mechanistic dependence on the primary absorber', *Applied Surface Science*, 127–129, pp. 852–856. doi: 10.1016/S0169-4332(97)00755-1.
- Fügler, E. (2014) 'A Study on the Oxidation Behavior of Cooking Oils by Means of HP-DSC'. *NETZSCH-Gerätebau GmbH*, pp. 1–6.
- Fuster-López, L., Andersen, C. K., Bouillon, N., Fohrer, F., Rossi-Doria, M., Scharff, M., Seymour, K., Vicente-Escuder, A., Vicente-Palomino, S., Yusá-Marco, D. J. (2017) 'Glue-paste linings: An evaluation of some biological, chemical and mechanical aspects of a traditional technique', *ICOM-CC 18th*

*Triennial Conference Preprints, Copenhagen, 4-8 September 2017: preprints (ICOM Committee for Conservation)*, p. 1305.

Gaisford, S., Kett, V. and Haines, P. (2016) *Principles of Thermal Analysis and Calorimetry*. 2<sup>nd</sup> Ed. The Royal Society of Chemistry. Available at: <https://www.ebooks.com/en-ao/2596256/principles-of-thermal-analysis-and-calorimetry/edward-charsley-duncan-price-nicole-hunter/>. (Accessed:12 Jan. 21).

Galatis, P., Boyatzis, S. and Theodorakopoulos, C. (2012) ‘An Investigation of the Selective Removal of a Synthetic Soiling Mixture from Mastic, Shellac & Laropal® K80 Coatings Using Hydrogels’, *e-Preservation Science*, 9(May 2014), pp. 72–83.

Gallagher, P. K. (2002) *Handbook of Thermal Analysis and Calorimetry. Applications to polymers and plastics*. Cheng S. Z. D. (ed.). The Netherlands, Amsterdam: Elsevier B.V. doi: 10.1002/pip.2891.

Gao, X. and Masiello, C. A. (2017) ‘Analysis of biochar porosity by pycnometry’, in Singh, B., Camps-Arbestain, M., and Lehmann, J. (eds.) *Biochar: A Guide to Analytical Methods*. CRC Press Taylor & Francis Group. Available at: <https://www.routledge.com/Biochar-A-Guide-to-Analytical-Methods-1st-Edition/Singh-Arbestain-Lehmann/p/book/9781498765534>. (Accessed:12 Jan. 21).

Gates, C. H. (2018) *Estimating Wettability of Rock Fracture Surfaces from Contact Angle and Roughness Measurements*. Master’s Thesis, University of Tennessee. Available at: [https://trace.tennessee.edu/utk\\_gradthes/5109](https://trace.tennessee.edu/utk_gradthes/5109). (Accessed:12 Jan. 21).

Geary, R. C. (1943) ‘Accuracy of Boyle’s Original Observations on the Pressure and Volume of a Gas’, *Nature*, 151(3834), p. 476. doi: 10.1038/151476a0.

Geng, K., Katsumata, R., Yu, X., Ha, H., Dulaney, A. R., Ellison, C. J., Tsui, O. K. C. (2017) ‘Conflicting Confinement Effects on the T<sub>g</sub>, Diffusivity, and Effective Viscosity of Polymer Films: A Case Study with Poly(isobutyl

- methacrylate) on Silica and Possible Resolution', *Macromolecules. American Chemical Society*, 50(2), pp. 609–617. doi: 10.1021/acs.macromol.6b01354.
- Gettens, R. J. (1935) 'Polymerized vinyl acetate and related compounds in the restoration of objects of art', *Technical Studies in the Field of Fine Arts*, 4(1), pp. 15–17.
- Gettens, R. J. and Stout, G. L. (1966) *Painting Materials: A Short Encyclopaedia*. New York: Dover Publications.
- Gheno, G. (2017) *Advanced polymeric and nanostructured coatings for Cultural Heritage conservation and restoration*. Doctoral Thesis, Ca' Foscari University (Venice). Available at: [hdl.handle.net/11368/2927592](http://hdl.handle.net/11368/2927592). (Accessed:12 Jan. 21).
- Giardina, R., Santamaria, U., Morresi, F., Persegati, F. (2017) 'Rimozione selettiva di resine naturali da due dipinti su tela di Lorenzo Lotto', in *Brunetto, A. (ed.) Proceedings of Atti del 5° Convegno APLAR, Applicazioni laser nel Restauro, Musei Vaticani 18-20 Settembre 2014*. Vicenza: Nardini Editore, pp. 373–382.
- Gilson, E. (1959) *Painting and reality*. A. W. Mellon Lectures in the Fine Arts. New York: Pantheon Books.
- Giovagnoli, A. (ed.) (2009) *Il Laser. Puliture su materiali di interesse artistico. Attività sperimentale*. Kermes. Firenze: Nardini.
- Gomez, J. C., Glatzmaier, G. C. and Mehos, M. (2012) 'Heat Capacity Uncertainty Calculation for the Eutectic Mixture of Biphenyl/Diphenyl Ether Used as Heat Transfer Fluid', in *Preprint. Presented at Solar PACES 2012, Marrakech (Morocco), September 11–14, 2012*. Available at: <http://www.osti.gov/bridge>:%0Ahttp://www.osti.gov/bridge. (Accessed:12 Jan. 21).
- Gordienko, V. P. and Dmitriev, Y. A. (1996) 'The degradation and stability of polyethylene with small additions of metal oxides under UV-irradiation',

*Polymer Degradation and Stability*, 53(1), pp. 79–87. doi: 10.1016/0141-3910(96)00033-X.

Gutknecht, N. (2008) ‘State of the Art in Lasers for Dentistry’, *Journal of the Laser and Health Academy*, 2008(3/1), pp. 1–5.

Gutknecht, N., Lukač, M., Marincek, M., Perhavec, T., Kazic, M. (2011) ‘A Novel Quantum Square Pulse (QSP) Mode Erbium Dental Laser’, *Journal of the Laser and Health Academy*, 2011(1), pp. 15–21.

Hackney, S. (2013) ‘The Art and Science of Cleaning Paintings’, in Mecklenburg, M. F., Charola, A. E., and Koestler, R. J. (eds.) *New Insights into the Cleaning of Paintings: Proceedings from the Cleaning 2010 International Conference, Universidad Politecnica de Valencia and Museum Conservation Institute. Smithsonian Contributions to Museum Conservation*. Washington, DC: Smithsonian Institution, pp. 11–15.

Hahn, C., Lippert, T. and Wokaun, A. (1999) ‘Comparison of the Ablation Behavior of Polymer Films in the IR and UV with Nanosecond and Picosecond Pulses’, *The Journal of Physical Chemistry B*, 103, pp. 1287–1294. doi: 10.1021/jp983609j.

Hansen, C. M. (1967) *The three dimensional solubility parameter*. Doctoral Thesis. Available at: <https://hansen-solubility.com/contents/HSP1967-OCR.pdf>. (Accessed: 12 Jan. 21).

Hansen, C. M. (2007) *Hansen Solubility Parameters*. CRC Press. doi: 10.1201/9781420006834.

Hansen, C. M. and Beerbower, A. (1971) ‘Solubility Parameter’, in Standen, A. (ed.) *Kirk-Othmer Encyclopedia of Chemical Technology, Supplementary volume*. 2<sup>nd</sup> Ed. New York: Interscience, pp. 889–910.

Hansen, C. M. and Just, L. (2001) ‘Prediction of Environmental Stress Cracking in Plastics with Hansen Solubility Parameters’, *Industrial & Engineering*

Chemistry Research. *American Chemical Society*, 40(1), pp. 21–25. doi: 10.1021/ie9904955.

Harrison, H. R., Hodder, O. J. R., Brewis, S., Halsall, T. G. (1971) ‘Chemistry of triterpenes and related compounds XLVII. Crystal and molecular structure of “compounds B”, a triterpene dimethyl ester epsilon-lactone from dammar resin’, *Journal of Chemical Society C*, pp. 2525–2529.

Hebert, M. (2013) *Reflection and transmission of light by a flat interface, Fresnel's formulae*. Institut d' Optique, Graduate school, Paris. Available at: <http://paristech.institutoptique.fr/site.php?id=797&fileid=11468>. (Accessed:12 Jan. 21).

Hecht, J. (1986) *The Laser Guidebook*. McGraw Hill Professional. Available at: <https://www.accessengineeringlibrary.com/content/book/9780071359672>. (Accessed:12 Jan. 21).

Hedley, G. (1993) ‘Recent Developments in Cleaning. Introductory speech delivered at workshop in New Methods of Cleaning Paintings (Courtauld Institute of Art, London, 1989)’, in Hedley, G. and Villers, C. (eds.) *Measured opinions: collected papers on the conservation of paintings*. London, UK: United Kingdom Institute for Conservation, pp. 135–136.

Hellen, R. (2020) ‘Preliminary study into the reduction and removal of naturally aged varnishes from painted surfaces using an Er:YAG laser in a two-step cleaning process with solvents naturally aged varnishes from painted surfaces using solvents’, *Journal of the Institute of Conservation*. Taylor & Francis, 43(1), pp. 1–15. doi: 10.1080/19455224.2019.1706594.

Hibst, R. and Keller, U. (1996) ‘Effects of water spray and repetition rate on the temperature elevation during Er:YAG laser ablation of dentine’, in Bown, S. G., Geschwind, H. J., Hibst, R., Laffitte, F., Maira, G., Pini, R., Reidenbach, H. D., Scherer, H. H., Spinelli, P. (eds.) *Proc. SPIE 2623, Medical Applications of Lasers III, (19 January 1996)*, pp. 139–144. doi: 10.1117/12.230325.

- Hildenhausen, J. and Dickmann, K. (2003) 'Nd:YAG laser with wavelengths from IR to UV ( $\omega$ ,  $2\omega$ ,  $3\omega$ ,  $4\omega$ ) and corresponding applications in conservation of various artworks', *Journal of Cultural Heritage*, 4 (1), pp. 174–178. doi: 10.1016/S1296-2074(02)01194-9.
- Hill, A. (1948) 'Manufacture and uses of AW2 Resin', *Modern Plastics*, 25(12), pp. 119–120.
- Hilling, A. M. and Nakahara, K. (2005) 'Applicazioni sperimentali di sistemi laser per la pulitura di dipinti su tela e tavola', in Patti, M. and Siano, S. (eds.) *Dipinti modili. Applicazioni sperimentali di sistemi laser per la pulitura*. Firenze: Nardini Editore, pp. 13–24.
- Höhne, G. W. H., Hemminger, W. and Flammersheim, H. J. (1996) *Differential Scanning Calorimetry. An Introduction for Practitioners, Differential Scanning Calorimetry*. Berlin, Heidelberg: Springer Berlin Heidelberg. doi: 10.1007/978-3-662-03302-9.
- Honsberg, C. and Bowden, S. (2013) *Absorption Coefficient*, PV Education.org. Available at: <https://www.pveducation.org/pvcdrom/pn-junctions/absorption-coefficient> (Accessed: 2 June 2020).
- Hontzopoulos, E. I., Fotakis, C. and Doulgeridis, M. (1993) 'Excimer laser in art restoration', in Fotakis, C., Kalpouzos, C., and Papazoglou, T. G. (eds.) *SPIE, 9<sup>th</sup> International Symposium on Gas Flow and Chemical Lasers*. Heraklion, Greece, Vol. 1810. Bellingham, Washington, pp. 748– 751.
- Horie, V. (2010) *Materials for Conservation: Organic consolidants, adhesives and coatings*. 2<sup>nd</sup> Ed. London; New York: Routledge.
- Horsin-Déon, S. (1852) *De la conservation et de la restauration des tableaux: éléments de l'art du restaurateur*. Paris: Chez Hector Bossange.
- Incropera, F. P. and DeWitt, D. P. (1996) *Introduction to heat transfer*. 3<sup>rd</sup> Ed. John Wiley & Sons Ltd. Available at:

<https://books.google.it/books?id=vgBRAAAAMAAJ>. (Accessed: 2 June 2020).

Incropera, F. P., Dewitt, D. P., Bergman, T. L., Lavine, A. S. (2007) *Fundamentals of Heat and Mass Transfer*. 6<sup>th</sup> Ed. John Wiley & Sons Ltd. doi: 10.1007/978-3-319-15793-1\_19.

Invernizzi, C., Rovetta, T., Licchelli, M., Malagodi, M. (2018) 'Mid and near-infrared reflection spectral database of natural organic materials in the cultural heritage field', *International Journal of Analytical Chemistry*, 2018. doi: 10.1155/2018/7823248.

Irwin, W. J. (1979) 'Analytical pyrolysis - an overview', *Journal of Analytical and Applied Pyrolysis*, 1(1), pp. 3–25. doi: 10.1016/0165-2370(79)80002-9.

Izzo, F. C. (2010) *20<sup>th</sup> Century artists' oil paints: a chemical-physical survey*. Doctoral Thesis. Università Ca' Foscari Venezia Scuola. Available at: <http://hdl.handle.net/10579/1100>. (Accessed: 12 Jan. 21).

Jain, A. A., Mehra, A. and Ranade, V. V. (2016) 'Processing of TGA data: Analysis of isoconversional and model fitting methods', *Fuel*. Elsevier Ltd, 165, pp. 490–498. doi: 10.1016/j.fuel.2015.10.042.

Kane, D. M., Palmer, G., Johnston, B. F., Haefner, S., Bilicki, A. T., Fuerbach, A., Fernandes, A. J. J. (2013) 'Studies on the laser removal of consolidants and protective coatings from samples of Australian Aboriginal bark paintings', in Saunders, D., Strlič, M., Korenberg, C., Luxford, N., Birkhölzer, K. (eds.) *Lasers in the Conservation of Artworks, proceedings Lacona IX, London, UK, Sept. 7-10, 2011*. London, UK: Archetype Publications, pp. 4–11.

Karazi, S. M., Ahad, I. U. and Benyounis, K. Y. (2017) 'Laser Micromachining for Transparent Materials', in *Reference Module in Materials Science and Materials Engineering*. Dublin, Ireland: Elsevier. doi: 10.1016/B978-0-12-803581-8.04149-7.

- Kashiwagi, T., Hirata, T. and Brown, J. E. (1985) 'Thermal and oxidative degradation of poly(methyl methacrylate) molecular weight', *Macromolecules. American Chemical Society*, 18(2), pp. 131–138. doi: 10.1021/ma00144a003.
- Kautek, W., König, E., tēs Krētēs, P., Pinakothēkē, E., Soutsou, M. A. (1997) *LACONA: Lasers in the Conservation of Artworks: 4-6 October 1995, Heraklion, Crete, Greece: workshop*. Wien: Verlag Mayer & Comp.
- Kemp, J. (2020) 'Er:YAG lasers in conservation', *Journal of the Institute of Conservation*. Routledge, 43(1), p. 1. doi: 10.1080/19455224.2020.1720393.
- Khoshhesab, Z. M. (2012) 'Reflectance IR Spectroscopy', in Theophanides, T. (ed.) *Infrared Spectroscopy - Materials Science, Engineering and Technology*. IntechOpen, pp. 233–244. doi: 10.5772/37180.
- Kirsh A. and Levenson R. S. (eds.) (2002) *Seeing Through Paintings: Physical Examination in Art Historical Studies*. New Haven, London: Yale University Press, 2002. Available at: <https://yalebooks.yale.edu/book/9780300080469/seeing-through-paintings>. (Accessed:12 Jan. 21).
- Knapp, A. M. and Halloran, J. W. (2006) 'Characterization of thermoplastic blends as binders for ceramics', *Journal of the American Ceramic Society*, 89(10), pp. 3010–3018. doi: 10.1111/j.1551-2916.2006.01156.x.
- Koechner, W. (1976) *Solid-State Laser Engineering*. New York, NY: Springer New York (Springer Series in Optical Sciences). doi: 10.1007/978-1-4757-8519-7.
- Kogelnik, H. and Li, T. (1966) 'Laser Beams and Resonators', *Applied Optics. OSA*, 5(10), pp. 1550–1567. doi: 10.1364/AO.5.001550.
- Kogou, S. et al. (2011) 'The role of the substrate in the laser cleaning process: A study on the laser assisted removal of polymeric consolidation materials from various substrates', in Radvan, R., Asmus, J. F., Castillejo, M., Pouli, P.,

- Nevin, A., (eds.) *Lasers in the Conservation of Artworks, proceedings Lacona VIII, Sibiu, Romania, Sep. 21–25, 2009*. Boca Raton: CRC Press Taylor & Francis Group, pp. 23–28.
- Kokkori, M., Sutherland, K., Salvant, J., Casadio, F., Barten, J., Stringari, C. (2017) ‘More than a pure technical sensation: Twentieth-century metallic paints, their formulations, and use in paintings’, in *Bridgland, J. (ed.) ICOM-CC 18<sup>th</sup> Triennial Conference Preprints, Copenhagen, 4–8 September 2017. Paris, pp. 1–9*.
- Konica Minolta (no date) Color and gloss (SCE and SCI methods) - Part III - Precise Color Communication, Konica Minolta. Available at: <https://www.konicaminolta.com/instruments/knowledge/color/part3/02.html> (Accessed: 28 April 2020).
- Koutchoukali, O., Haloui, I. and Koutchoukali, M. S. (2013) ‘Heat capacity prediction of complex molecules by mass connectivity index’, *MATEC Web of Conferences*, 3, pp. 0–3. doi: 10.1051/mateconf/20130301080.
- Kun, Y., Huimin, Y. and Shangzhong, J. (2014) ‘A type of spectrophotometer with both SCI and SCE measurement structures’, *Optik*. Elsevier GmbH., 125(17), pp. 4672–4677. doi: 10.1016/j.ijleo.2014.04.089.
- Kuščer, L. and Diaci, J. (2013) ‘Measurements of erbium laser-ablation efficiency in hard dental tissues under different water cooling conditions’, *Journal of Biomedical Optics*, 18(10), p. 108002. doi: 10.1117/1.JBO.18.10.108002.
- Laidler, K. J. (1996) ‘A glossary of terms used in chemical kinetics, including reaction dynamics (IUPAC Recommendations 1996)’, *Pure and Applied Chemistry*, 68(1), pp. 149–192. doi: 10.1351/pac199668010149.
- Lamour, G., Hamraoui, A., Buvailo, A., Xing, Y., Keuleyan, S., Prakash, V., Eftekhari-Bafrooei, A., Borguet, E. (2010) ‘Contact angle measurements using a simplified experimental setup’, *Journal of Chemical Education*, 87(12), pp. 1403–1407. doi: 10.1021/ed100468u.

- Lank, H. (1972) 'Picture varnishes formulated with resin MS2A', in Brommelle, N. S. and Smith, P. (eds.) *Studies in Conservation. Conservation of paintings and the graphic arts: preprints of contributions to the Lisbon Congress, 9-14 October 1972*, pp. 215–216. doi: 10.1179/sic.1972.17.s1.007.
- Larson, J. (1994) 'Current development in the application of laser technology to the treatment and recording of artworks', *Conservation News*, 53, pp. 13–14.
- Larson, L. J., Shin, K. K. I. M. and Zink, J. I. (1991) 'Photoluminescence Spectroscopy of Natural Resins and Organic Binding Media of Paintings', *Journal of the American Institute for Conservation*, 30(1), pp. 89–104. Available at: <https://www.jstor.org/stable/3179519>.
- Lawman, S. J. (2011) *Optical and material properties of varnishes for paintings*. Doctoral Thesis, Nottingham Trent University. Available at: <https://core.ac.uk/download/pdf/30624382.pdf>. (Accessed:12 Jan. 21).
- Lazzari, M. and Chiantore, O. (2000) 'Thermal-ageing of paraloid acrylic protective polymers', *Polymer*, 41, pp. 6447–6455.
- Lazzarini, L. and Asmus, J. F. (1973) 'The application of laser radiation to the cleaning of statuary', *Bulletin of the American Institute for Conservation of Historic and Artistic Works*, 13(2), pp. 39–49 [online]. Available at: <https://www.jstor.org/stable/3179234>. (Accessed:12 Jan. 21). doi: 10.2307/3179234.
- Lazzarini, L., Marchesini, L. and Asmus, J. F. (1973) 'Lasers for the Cleaning of Statuary: Initial Results and Potentialities', *Journal of Vacuum Science and Technology*, 10(6), pp. 1039–1043. doi: 10.1116/1.1318462.
- League of Nations (1933) '*Les dossiers de l'Office international des musées*'. Paris: Société des nations, Institut International de Coopération Intellectuelle, Vol, 1, p. 56.
- Learner, T. J. S. (2004) *Analysis of modern paints*. Los Angeles, California: Getty Conservation Institute. Available at:

[https://www.getty.edu/conservation/publications\\_resources/books/analysis\\_modern\\_paints.html](https://www.getty.edu/conservation/publications_resources/books/analysis_modern_paints.html). (Accessed:12 Jan. 21).

Learner, T. J. S., Smithen, P., Krueger, J. W., Schilling, M. R. (eds.) (2007) *Modern Paints Uncovered: Proceedings from the Modern Paints Uncovered Symposium*. Los Angeles: Getty Conservation Institute. Los Angeles, California: The Getty Conservation Institute. Available at: [http://hdl.handle.net/10020/gci\\_pubs/paints\\_uncovered](http://hdl.handle.net/10020/gci_pubs/paints_uncovered). (Accessed:12 Jan. 21).

Leme, F. O., Godoi, Q., Kiyataka, P. H.M., Santos, D., Agnelli, J. A. M., Krug, F. J. (2012) ‘Effect of pulse repetition rate and number of pulses in the analysis of polypropylene and high density polyethylene by nanosecond infrared laser induced breakdown spectroscopy’, *Applied Surface Science*. Elsevier, 258(8), pp. 3598–3603. doi: 10.1016/j.apsusc.2011.11.122.

Li, J. and Stoliarov, S. I. (2013) ‘Measurement of kinetics and thermodynamics of the thermal degradation for non-charring polymers’, *Combustion and Flame*, 160(7), pp. 1287–1297. doi: 10.1016/j.combustflame.2013.02.012.

Lippert, T. and Dickinson, J. T. (2003) ‘Chemical and spectroscopic aspects of polymer ablation: Special features and novel directions’, *Chemical Reviews*, 103(2), pp. 453–485. doi: 10.1021/cr010460q.

Lopez, M., Bai, X., Koch-Dandolo, C., Serfaty, S., Wilkie-Chancellier, N., Detalle, V. (2019) ‘Nd:YAG vs Er:YAG: a comparative study of laser varnish removal on easel paintings’, in Targowski, P., Groves, R., and Liang, H. (eds.) *Proc. SPIE 11058, Optics for Arts, Architecture, and Archaeology VII 1105804 (8 August 2019)*, p. 3. doi: 10.1117/12.2527437.

Lopez, M., Bai, X., Serfaty, S., Wilkie-Chancellier, N., Menu, M., Datelle, V. (no date) ‘Varnish removal from easel paintings with YAG Lasers’, in Brunetto, A. (ed.) *Proceedings Book of Abstract of Atti del 7° Convegno APLAR, Ieri, oggi e domani, Venice, 7th-8th Nov. 2019*.

- Lucanus, F. G. H. (1832) *Gründliche und vollständige Anleitung zur Erhaltung, Reinigung und Wiederherstellung der Gemälde in Oel-, Tempera-, Leim-, Wasser-, Miniatur-, Pastell- und Wachsfarben, zur Bereitung der beim Malen und Ueberziehen dienlichen Firnisse, so wie auch zum Blei*. Halberstadt: Friedrich August Helm.
- Luk'yanchuk, B., Bityurin, N., Anisimov, S., Bäuerle, D. (1993) 'The role of excited species in UV-laser materials ablation - Part I: Photophysical ablation of organic polymers', *Applied Physics A Solids and Surfaces*, 57(4), pp. 367–374. doi: 10.1007/BF00332291.
- Lukač, M., Marinček, M. and Grad, L. (2004) 'Super VSP Er: YAG Pulses for Fast and Precise Cavity Preparation', *J Oral Laser Applications*, 4(3), pp. 171–173 [online]. Available at: [http://www.quintpub.com/journals/jola/abstract.php?iss2\\_id=825&article\\_id=9478&article=4&title=Super VSP Er: YAG Pulses for Fast and Precise Cavity Preparation](http://www.quintpub.com/journals/jola/abstract.php?iss2_id=825&article_id=9478&article=4&title=Super VSP Er: YAG Pulses for Fast and Precise Cavity Preparation). (Accessed:12 Jan. 21).
- Lukač, M., Marinček, M., Grad, L., Božič, Z. (2007) 'Dental Laser Drilling: State of the Art with the Latest Generation of Variable Square Pulse Erbium Dental Laser Systems', *Journal of the Laser and Health Academy*, 6(1), pp. 1–5.
- Lukač, M., Perhavec, T., Nemes, K., Ahcan, U. (2010) 'Ablation and Thermal Depths in VSP Er:YAG Laser Skin Resurfacing', *Journal of Laser Health Academy*, 2010(1), pp. 56–71 [online]. Available at: <https://www.laserandhealthacademy.com/en/journal/?id=906&type=1>. (Accessed:12 Jan. 21).
- Lukač, M., Primc, N. M. and Pirnat, S. (2012) 'Quantum Square Pulse Er:YAG Lasers for Fast and Precise Hard Dental Tissue Preparation', *Journal of the Laser and Health Academy*, 2012, pp. 1–16. doi: 10.1038/ncomms12230.
- Lukač, M., Sult, T. M. D. and Sult, R. R. N. (2007) 'New Options and Treatment Strategies with the VSP Erbium YAG Aesthetics Lasers', *Journal of the Laser and Health Academy*, 1, pp. 1–9.

- Lvovsky, A. I. (2013) 'Fresnel Equations', *Encyclopedia of Optical Engineering*, pp. 1–6. doi: 10.1081/E-EOE-120047133.
- Maclaren, N. and Werner, A. (1950) 'Some Factual Observations about Varnishes and Glazes', *The Burlington Magazine*, 92(568), pp. 189–192.
- Madden, O., Abraham, M., Scheerer, S., Werden, L. (2005) 'The Effects of Laser Radiation on Adhesives, Consolidants, and Varnishes', in Dickmann, K., Fotakis, C., and Asmus, J. F. (eds.) *Lasers in the Conservation of Artworks, proceedings Lacona V, Osnabruck, Germany, Sept. 15–18, 2003*. Berlin/Heidelberg: Springer-Verlag, pp. 247–254. doi: 10.1007/3-540-27176-7\_30.
- Madhukar, Y. K., Mullick, S. and Nath, A. K. (2013) 'Development of a water-jet assisted laser paint removal process', *Applied Surface Science*, 286, pp. 192–205. doi: 10.1016/j.apsusc.2013.09.046.
- Maines, C. A. and de la Rie, E. R. (2005) 'Size-exclusion chromatography and differential scanning calorimetry of low molecular weight resins used as varnishes for paintings', *Progress in Organic Coatings*, 52(1), pp. 39–45 [online]. Available at: <http://www.sciencedirect.com/science/article/pii/S0300944004001493>. doi: 10.1016/j.porgcoat.2004.06.006. (Accessed: 12 Jan. 21).
- Maines, C. A. and de la Rie, E. R. (2005) 'Size-exclusion chromatography and differential scanning calorimetry of low molecular weight resins used as varnishes for paintings', *Progress in Organic Coatings*, 52(1 SPEC. ISS.), pp. 39–45. doi: 10.1016/j.porgcoat.2004.06.006.
- Majaron, B., Plestenjak, P. and Lukac, M. (1999) 'Thermo-mechanical laser ablation of soft biological tissue: Modelling the micro-explosions', *Applied Physics B: Lasers and Optics*, 69(1), pp. 71–80. doi: 10.1007/s003400050772.

- Majaron, B., Sustercic, D., Lukac, M., Skaleric, U., Funduk, N (1998) ‘Heat diffusion and debris screening in Er:YAG laser ablation of hard biological tissues’, *Applied Physics B*, 66, pp. 479–487.
- Majewsky, M., Bitter, H., Eiche, E., Horn, H. (2016) ‘Determination of microplastic polyethylene (PE) and polypropylene (PP) in environmental samples using thermal analysis (TGA-DSC)’, *Science of The Total Environment*, 568, pp. 507–511. doi: 10.1016/j.scitotenv.2016.06.017.
- Maldague, X. (2002) ‘Introduction to NDT by Active Infrared Thermography’, *Materials Evaluation*, pp. 1–22.
- Marczak, J., Koss, A., Targowski, P., Góra, M., Strzelec, M., Sarzyński, A., Skrzeczanowski, W., Ostrowski, R., Rycyk, A. (2008) ‘Characterization of Laser Cleaning of Artworks’, *Sensors*, 8, pp. 6507–6548. doi: 10.3390/s8106507.
- Marczak, J., Strzelec, M., Ostrowski, R., Rycyk, A., Sarzynski, A., Skrzeczanowski, W., Koss, A., Szambelan, R., Salimbeni, R., Siano, S., Kolar, J. D., Strlič, M., Márton, Zs., Santa, I., Kisapáti, I., Gugolya, Z., Kántor, Z., Barcikowski, S., Engel, P., Pires, M. P., Guedes, J., Hipolito, A., Santos, S., Dement’ev, A. S. S., Murauskas, E., Slavinskis, N., Jasiunas, K., Trtica, M. S., (2008) ‘Advanced laser renovation of old paintings, paper, parchment and metal objects’, in Castillejo, M., Moreno, P., Oujja, M., Radvan, R., Ruiz, J. (eds.) *Lasers in the Conservation of Artworks, proceedings Lacona VII, Madrid, Spain, Sep. 17–21, 2007*. Boca Raton, FL: CRC Press, Taylor & Francis Group, pp. 263–269. doi: 10.1201/9780203882085.ch42.
- Marín, E. (2010) ‘Characteristic dimensions for heat transfer’, *Lat. Am. J. Phys. Educ*, 4(1), pp. 56–60.
- Martyniuk, M. M. (1978) ‘Phase explosion of a metastable fluid’, *Combustion, Explosion and Shock Waves*, 13(2), pp. 178–191.

- Massa, V. and Scicolone, G. C. (2004) *Le Vernici per il Restauro*. 4<sup>th</sup> Ed. Firenze: Nardini Editore. Available at: <https://www.nardinieditore.it/prodotto/le-vernici-per-il-restauro-i-leganti/>. (Accessed:12 Jan. 21).
- Masschelein-Kleiner, L. (1984) 'Die Lösungsmittel', in Banik, G. and Krist, G. (eds.) *Lösungsmittel in der Restaurierung*. Vienna, Austria: Verlag Der Apfel.
- Masschelein-Kleiner, L. (1994) *Les solvants*. Bruxelles: Institut Royal du Patrimoine Artistique.
- Mathar, R. J. (2007) 'Refractive index of humid air in the infrared: model fits', *Journal of Optics A: Pure and Applied Optics*. IOP Publishing, 9(5), pp. 470–476. doi: 10.1088/1464-4258/9/5/008.
- Matteini, M., Mazzeo, R. and Moles, A. (2016) *Chemistry for Restoration. Painting and Restoration Materials*. Florence (Italy): Nardini Editore. Available at: <https://www.nardinieditore.it/prodotto/chemistry-for-restoration-painting-and-restoration-materials/>. (Accessed:12 Jan. 21).
- Mayboudi, L. S. (2008) *Heat transfer modelling and thermal imaging experiments in laser transmission welding of thermoplastics*. Doctoral Thesis, Mechanical and Materials Engineering, Queen's University Kingston. Available at: [https://search.proquest.com/docview/288037551?accountid=10267%5Chttp://resolver.library.cornell.edu/net/openurl?ctx\\_ver=Z39.88-2004&ctx\\_enc=info:ofi/enc:UTF8&rft\\_id=info:sid/ProQuest+Dissertations+%26+Theses+Global&rft\\_val\\_fmt=info:ofi/fmt:kev:mtx:disse](https://search.proquest.com/docview/288037551?accountid=10267%5Chttp://resolver.library.cornell.edu/net/openurl?ctx_ver=Z39.88-2004&ctx_enc=info:ofi/enc:UTF8&rft_id=info:sid/ProQuest+Dissertations+%26+Theses+Global&rft_val_fmt=info:ofi/fmt:kev:mtx:disse). (Accessed:12 Jan. 21).
- Mayer, R. (1991) *The artist's handbook of materials and techniques*. 5<sup>th</sup> Ed. Sheehan S. (ed.). England: Faber & Faber.
- Mazumder, J., Mazumder, J., Conde, O., Villar, R., Steen, W. (eds.) (1996) *Laser Processing: Surface Treatment and Film Deposition*. Dordrecht / Boston / London Published: Kluwer Academic Publishers in cooperation with NATO Scientific Affairs Division. doi: 10.1007/978-94-009-0197-1.

- Mcglinchey, C. W., Stringari, C., Pratt, E., Abraham, M., Melessanaki, K., Zafirooulos, V., Anglos, D., Pouli, P., Fotakis, C. (2005) 'Evaluating the Effectiveness of Lasers for the Removal of Overpaint from a 20<sup>th</sup> Century Minimalist Painting', in Dickmann, K., Fotakis, C., and Asmus, J. F. (eds.) *Lasers in the Conservation of Artworks, proceedings Lacona V, Osnabruck, Germany, Sept. 15–18, 2003*. Berlin/Heidelberg: Springer-Verlag, pp. 209–215. doi: 10.1007/3-540-27176-7\_26.
- Mecklenburg, M. F., Charola, A. E. and Koestler, R. J. (eds.) (2013) *New Insights into the Cleaning of Paintings: Proceedings from the Cleaning 2010 International Conference, Universidad Politecnica de Valencia and Museum Conservation Institute. Smithsonian Contributions to Museum Conservation*. Washington, DC: Smithsonian Institution. doi: 10.5479/si.19492359.3.1.
- Meister, J., Apel, C., Franzen, R., Gutknecht, N. (2003) 'Influence of the spatial beam profile on hard tissue ablation. Part I: Multimode emitting Er:YAG lasers', *Lasers Med Sci*, 18(2), pp. 112–118. doi: 10.1007/s10103-003-0263-9.
- Melita, L. N., Węglowska, K., Tamburini, D., Korenberg, C. (2020) 'Investigating the Potential of the Er:YAG Laser for the Removal of Cemented Dust from Limestone and Painted Plaster', *Coatings*, 10(11), p. 1099. doi: 10.3390/coatings10111099.
- Melo, M. J., Bracci, S., Camaiti, M., Chiantore, O., Piacenti, F. (1999) 'Photodegradation of acrylic resins used in the conservation of stone', *Polymer Degradation and Stability*, 66(1), pp. 23–30. doi: 10.1016/s0141-3910(99)00048-8.
- Merz-Le, L. (1998) Natural Resin Varnishes: Damar, AIC Painting Conservation Catalog, Varnishes and Surface Coatings. Available at: [https://www.conservation-wiki.com/wiki/Varnishes\\_and\\_Surface\\_Coatings:\\_Low\\_Molecular\\_Weight\\_Varnishes#Damar1](https://www.conservation-wiki.com/wiki/Varnishes_and_Surface_Coatings:_Low_Molecular_Weight_Varnishes#Damar1). (Accessed:12 Jan. 21).

- Mestdagh, H., Rolando, C., Sablier, M., Rioux, J. P. (1992) 'Characterization of Ketone Resins by Pyrolysis/Gas Chromatography/Mass Spectrometry', *Analytical Chemistry*, 64(19), pp. 2221–2226. doi: 10.1021/ac00043a007.
- Micheli, L., Mazzuca, C., Palleschi, A., Palleschi, G. (2016) 'Development of a diagnostic and cleaning tool for paper artworks: a case of study', *Microchemical Journal*. Elsevier, 126(December), pp. 32–41. doi: 10.1016/j.microc.2015.11.052.
- Mills, J. S. (1956) 'The constitution of the natural, tetracyclic triterpenes of dammar resin', *Journal of Chemical Society*, pp. 2196–2202.
- Mills, J. S. and White, R. (1977) 'Natural Resins of Art and Archaeology Their Sources, Chemistry, and Identification', *Studies in Conservation*, 22(1), pp. 12–31.
- Mills, J. S. and White, R. (1999) *The Organic Chemistry of Museum Objects*. 2<sup>nd</sup> Ed. London; New York: Routledge. doi: 10.4324/9780080513355.
- Miotello, A. and Kelly, R. (1995) 'Critical assessment of thermal models for laser sputtering at high fluences', *Applied Physics Letters*, 67(24), pp. 3535–3537. doi: 10.1063/1.114912.
- Misra, D., Acherjee, B., Kuar, A. S., Mitra, S. (2011) 'Transmission Laser Contour Welding of Polycarbonates With a Moving Laser Beam: Process Simulation Via Fem', *FEM*, pp. 11–14. Available at: <https://pdfs.semanticscholar.org/a7ce/c00120f2995e7e11ae6d2f6555aec52bda4b.pdf>. (Accessed:12 Jan. 21).
- Morais, P. J., Bordalo, R., dos Santos, L., Marques, S. F., Salgueiredo, E., Gouveia, H. (2007) 'Excimer Laser Ablation of Egg Tempera Paints and Varnishes', in Nimmrichter, J., Kautek, W., and Schreiner, M. (eds.) *Lasers in the conservation of artworks, proceedings Lacona VI, Vienna, Austria, Sept 21-25, 2005*. Berlin, Heidelberg: Springer Berlin Heidelberg, pp. 303–311. doi: 10.1007/978-3-540-72310-7\_35.

- Morgan, N. (1993) 'Excimer lasers restore 14<sup>th</sup> century icons', *Opto & Laser Europe*, 7, pp. 36–37.
- Morîntale, E., Harabor, A., Constantinescu, C., Rotaru, P. (2013) 'Use of heat flows from DSC curve for calculation of specific heat of the solid materials', *Annals of the University of Craiova, Physics*, 23, pp. 89–94.
- Morrison, R., Bagley-Young, A., Burnstock, A., van den Berg, K. J., van Keulen, H. (2007) 'An investigation of parameters for the use of citrate solutions for surface cleaning unvarnished paintings', *Studies in Conservation*, 52(4), pp. 255–270. doi: 10.1179/sic.2007.52.4.255.
- Motherwell, R. and O'Hara, F. (1965) *Robert Motherwell: with selections from the artist's writings*. Museum of Modern Art (New York. Distributed by Doubleday & Complany, Inc., Garden City, N.Y. Available at: [https://www.moma.org/documents/moma\\_catalogue\\_2920\\_300190149.pdf](https://www.moma.org/documents/moma_catalogue_2920_300190149.pdf). (Accessed:12 Jan. 21).
- Mouw, T. (2018) Specular Included or Specular Excluded: Which is Best?, *X-Rite Blog*. Available at: [https://www.xrite.com/blog/specular-included-or-specular-excluded-which-is-best?utm\\_source=google&utm\\_medium=cpc&utm\\_campaign=03-GO-GB-EN-DSA&utm\\_content=DSA\\_Website&utm\\_term=&matchtype=b&device=c&gclid=Cj0KCQjwmpb0BRCBARIsAG7y4zbfWs3j-AaD7f03TdfLeYVibFQt](https://www.xrite.com/blog/specular-included-or-specular-excluded-which-is-best?utm_source=google&utm_medium=cpc&utm_campaign=03-GO-GB-EN-DSA&utm_content=DSA_Website&utm_term=&matchtype=b&device=c&gclid=Cj0KCQjwmpb0BRCBARIsAG7y4zbfWs3j-AaD7f03TdfLeYVibFQt) (Accessed: 14 April 2020).
- Nahen, K. and Vogel, A. (2002) 'Plume dynamics and shielding by the ablation plume during Er:YAG laser ablation', *Journal of Biomedical Optics*, 7(2), p. 165. doi: 10.1117/1.1463047.
- Nath, A. K., Gupta, A. and Benny, F. (2012) 'Theoretical and experimental study on laser surface hardening by repetitive laser pulses', *Surface and Coatings Technology*. Elsevier, 206(8–9), pp. 2602–2615. doi: 10.1016/j.surfcoat.2011.11.019.

- Neher, H. T. (1936) 'Acrylic Resins', *Industrial & Engineering Chemistry. American Chemical Society*, 28(3), pp. 267–271. doi: 10.1021/ie50315a002.
- Nemeš, K., Lukač, M. and Možina, J. (2012) 'Variable square pulse vs conventional PFN pumping of Er:YAG laser', *Optics and Laser Technology*, 44(3), pp. 664–668. doi: 10.1016/j.optlastec.2011.09.020.
- Nevin, A., Comelli, D., Osticioli, I., Toniolo, L., Valentini, G., Cubeddu, R. (2009) 'Assessment of the ageing of triterpenoid paint varnishes using fluorescence, Raman and FTIR spectroscopy', *Analytical and Bioanalytical Chemistry*, 395(7), pp. 2139–2149. doi: 10.1007/s00216-009-3005-4.
- Nicolaus, K. (1999) *The restoration of paintings*. Westphal, C. (ed.). Cologne: Cologne: Könemann.
- Nielsen, L. E. and Landel, R. F. (1993) *Mechanical properties of polymers and composites*. Bosa Roca, United States: Taylor & Francis Inc.
- Niku-Lari, A. and Mordike, B. L. (eds.) (1989) *High Power Lasers*. Pergamon. Available at: <https://www.elsevier.com/books/high-power-lasers/niku-lari/978-0-08-035918-2>. (Accessed:12 Jan. 21).
- Nimmrichter, J., Kautek, W. and Schreiner, M. (eds.) (2007) *Lasers in the Conservation of Artworks XI. LACONA XI Proceedings*. Vienna, Austria: Springer Berlin Heidelberg. doi: 10.1007/978-3-540-72310-7.
- Ocon, N. and Findley, D. (no date) 'A Primer for the Materials, Methods and Techniques of Conservation', *North Carolina Museum of Art*, pp. 1–10. Available at: <https://ncartmuseum.org/images/uploads/conservation-primer.pdf>. (Accessed:12 Jan. 21).
- Oddy, A. (1999) 'Does reversibility exist in conservation?', in Oddy, A. and Carroll, S. (eds.) *Reversibility - does it exist?*. London: British Museum, pp. 1–5.
- Oddy, A. and Carroll, S. (eds.) (1999) 'Reversibility: does it exist?', in *British Museum Occasional Papers Nr. 135*. London: British Museum Press.

Available at: <http://catalog.hathitrust.org/api/volumes/oclc/45153605.html>.  
(Accessed:12 Jan. 21).

- Odlyha, M. (1988) 'Characterisation of aged paint films by Differential Scanning Calorimetry', *Thermochimica Acta*, 134, pp. 85–90.
- Odlyha, M. (1991) 'A novel approach to the problem of characterizing the binding media in early Italian paintings (13<sup>th</sup>/16<sup>th</sup> century)', *Journal of Thermal Analysis*, 37(7), pp. 1431–1440. doi: 10.1007/BF01913479.
- Odlyha, M. (1995) 'Investigation of the binding media of paintings by thermoanalytical and spectroscopic techniques', *Thermochimica Acta*, 269–270(C), pp. 705–727. doi: 10.1016/0040-6031(95)02674-6.
- Odlyha, M. and Burmester, A. (1988) 'Preliminary investigations of the binding media of paintings by differential thermal analysis', *Journal of Thermal Analysis*, 33(4), pp. 1041–1052. doi: 10.1007/BF01912728.
- Odlyha, M. and Scott, R. P. W. (1994) 'The "enthalpic" value of paintings', *Thermochimica Acta*, 234(C), pp. 165–178. doi: 10.1016/0040-6031(94)85142-5.
- Olivi, G. and Olivi, M. (eds) (2010) *Lasers in Restorative Dentistry. A Practical Guide, Principles and Practice of Laser Dentistry*. London: Springer-Verlag Berlin Heidelberg. doi: 10.1016/B978-0-323-06206-0.00011-4.
- Opeña, M. and Jägers, E. (2013) 'Extended Abstract—Effects of Solvents on the Physical Properties of Polymeric Films', in Mecklenburg, M. F., Charola, A. E., and Koestler, R. J. (eds.) *New Insights into the Cleaning of Paintings: Proceedings from the Cleaning 2010 International Conference, Universidad Politecnica de Valencia and Museum Conservation Institute. Smithsonian Contributions to Museum Conservation*. Washington, DC: Smithsonian Institution, pp. 165–167.
- Oujja, M., García, A., Romero, C., Vázquez De Aldana, J. R., Moreno, P., Castillejo, M. (2011) 'UV laser removal of varnish on tempera paints with

nanosecond and femtosecond pulses’, *Physical Chemistry Chemical Physics*, 13, pp. 4625–4631. doi: 10.1039/c0cp02147d.

Oxford English Dictionary on Compact Disc. 2<sup>nd</sup> Ed. (1995). Oxford, UK: Oxford University Press. doi: 10.1093/acref/9780199571123.001.0001.

Papadakis, V. M., Orphanos, Y., Kogou, S., Melessanaki, K., Pouli, P., Fotakis, C. (2011) ‘IRIS: a novel spectral imaging system for the analysis of cultural heritage objects’, *Proc. SPIE 8084, O3A: Optics for Arts, Architecture, and Archaeology III, 80840W (6 June 2011)*. doi: <https://doi.org/10.1117/12.889510>. **Tensor Image Processing Platform (TIPP) at <http://www.tipp.gr>, latest access on 3 June 2020.**

Papadakis, V., Loukaiti, A. and Pouli, P. (2010) ‘A spectral imaging methodology for determining on-line the optimum cleaning level of stonework’, *Journal of Cultural Heritage*. Elsevier, 11(3), pp. 325–328. doi: 10.1016/j.culher.2009.10.007.

Partovi, F., Izatt, J. A., Cothren, R. M., Kittrell, C., Thomas, J. E., Strikwerda, S., Kramer, J. R., Feld, M. S. (1987) ‘A model for thermal ablation of biological tissue using laser radiation’, *Lasers in Surgery and Medicine*. John Wiley & Sons, Ltd, 7(2), pp. 141–154. doi: 10.1002/lsm.1900070202.

Patti, M. and Siano, S. (eds.) (2015) *I dipinti mobili. Applicazioni sperimentali di sistemi laser per la pulitura*. Firenze: Nardini Editore.

Pavić, M. (2014) ‘Non-traditionally Painted oil Painting: How to Treat it Properly? Josip Vaništa’s Cake (1955)’, in van den Berg, K.J., Burnstock, A., de Keijzer, M., Krueger, J., Learner, T., de Tagle, A., Heydenreich, G. (eds.) (2014) *Issues in Contemporary Oil Paint*. Cham, Switzerland: Springer International Publishing, pp. 159–166.

Pemble, M. E. and Gardner, P. (2009) ‘Vibrational Spectroscopy from Surfaces’, in Vickerman, J. C. and Gilmore, I. S. (eds.) *Surface Analysis – The Principal Techniques*. Chichester, UK: John Wiley & Sons, Ltd, pp. 333–390. doi: 10.1002/9780470721582.ch7.

- Pereira-Pardo, L. and Korenberg, C. (2018) ‘The use of erbium lasers for the conservation of cultural heritage. A review’, *Journal of Cultural Heritage*. Elsevier, 31, pp. 236–247. Available at: <http://www.sciencedirect.com/science/article/pii/S129620741730287X>. (Accessed:12 Jan. 21). doi: 10.1016/j.culher.2017.10.007.
- Pereira-Pardo, L., Melita, L. N. and Korenberg, C. (2020) ‘Tackling conservation challenges using erbium lasers: case studies at the British Museum’, *Journal of the Institute of Conservation*. Taylor & Francis, 43(1), pp. 25–43. doi: 10.1080/19455224.2019.1706591.
- Perhavec, T. and Diaci, J. (2009) ‘Comparison of heat deposition of Er:YAG and Er,Cr:YSGG lasers in hard dental tissues’, *Journal of the Laser and Health Academy*, 2(1), pp. 1–6. Available at: [http://www.fotona.com/media/objave/academy/priponke/85475\\_2\\_1\\_erbium\\_heatdeposition\\_dentistry.pdf](http://www.fotona.com/media/objave/academy/priponke/85475_2_1_erbium_heatdeposition_dentistry.pdf). (Accessed:12 Jan. 21).
- Perhavec, T., Lukac, M., Diaci, J., Marincek, M. (2009) ‘Heat Deposition of Erbium Lasers in Hard Dental Tissues’, *J Oral Laser Applications*, 9, pp. 205–212.
- PerkinElmer (no date) *Differential Scanning Calorimetry (DSC)*, PerkinElmer. Available at: [https://www.perkinelmer.com/CMSResources/Images/46-74542GDE\\_DSCBeginnersGuide.pdf](https://www.perkinelmer.com/CMSResources/Images/46-74542GDE_DSCBeginnersGuide.pdf). (Accessed:12 Jan. 21).
- Pettit, G. H., Ediger, M. N., Hahn, D. W., Brinson, B. E., Sauerbrey, R. (1994) ‘Transmission of polyimide during pulsed ultraviolet laser irradiation’, *Applied Physics A Solids and Surfaces*, 58(6), pp. 573–579. doi: 10.1007/BF00348168.
- Pham, D. K., Wright, J. P., Ivanova, E. P., Nicolau, D. V. (2003) ‘AFM analysis of the polymer microstructures used for novel multianalyte protein micro assay’, in Nicolau, D. V and Raghavachari, R. (eds.) *Microarrays and Combinatorial Technologies for Biomedical Applications: Design, Fabrication, and Analysis*. SPIE, pp. 83–91. doi: 10.1117/12.483471.

- Phenix, A. (2013) 'Effects of Organic Solvents on Artists' Oil Paint Films: Swelling', in Mecklenburg, M. F., Charola, A. E., and Koestler, R. J. (eds.) *New Insights into the Cleaning of Paintings: Proceedings from the Cleaning 2010 International Conference, Universidad Politecnica de Valencia and Museum Conservation Institute. Smithsonian Contributions to Museum Conservation*. Washington, DC: Smithsonian Institution, pp. 69–76.
- Phenix, A. and Sutherland, K. (2001) 'The cleaning of paintings: effects of organic solvents on oil paint films', *Studies in Conservation*, 46(1), pp. 47–60. doi: 10.1179/sic.2001.46.supplement-1.47.
- Pich, O., Franzen, R., Gutknecht, N., Wolfart, S. (2015) 'Laser treatment of dental ceramic/cement layers: transmitted energy, temperature effects and surface characterisation', *Lasers in Medical Science*, 30(2), pp. 591–597. doi: 10.1007/s10103-013-1340-3.
- Piena, H. (2001) 'Regalrez in Furniture Conservation', *Journal of the American Institute for Conservation*, 40(1), pp. 59–68.
- Ploeger, R., Musso, S. and Chiantore, O. (2009) 'Contact angle measurements to determine the rate of surface oxidation of artists' alkyd paints during accelerated photo-ageing', *Progress in Organic Coatings*, 65(1), pp. 77–83. doi: 10.1016/j.porgcoat.2008.09.018.
- Poon, C. Y. and Bhushan, B. (1995) 'Comparison of surface roughness measurements by stylus profiler, AFM and non-contact optical profiler', *Wear*, 190(1), pp. 76–88. doi: 10.1016/0043-1648(95)06697-7.
- Pouli, P. and Emmony, D. C. (2000) 'The effect of Nd:YAG laser radiation on medieval pigments', *Journal of Cultural Heritage*, 1(2), pp. 181–188. doi: 10.1016/S1296-2074(00)00143-6.
- Pouli, P., Bounos, G., Georgiou, S. K., Fotakis, C. (2007) 'Femtosecond Laser Cleaning of Painted Artefacts; Is this the Way Forward?', in Nimmrichter, J., Kautek, W., and Schreiner, M. (eds.) *Lasers in the conservation of artworks, proceedings Lacona VI, Vienna, Austria, Sept. 21-25, 2005*. Berlin,

Heidelberg: Springer Berlin Heidelberg, pp. 287–293. doi: 10.1007/978-3-540-72310-7\_33.

Pouli, P., Emmony, D. C., Madden, C. E., Sutherland, I. (2003) ‘Studies towards a thorough understanding of the laser-induced discoloration mechanisms of medieval pigments’, in *Journal of Cultural Heritage*, pp. 271–275. doi: 10.1016/S1296-2074(02)01207-4.

Pouli, P., Nevin, A., Andreotti, A., Colombini, M. P., Georgiou, S. K., Fotakis, C. (2009) ‘Laser assisted removal of synthetic painting-conservation materials using UV radiation of ns and fs pulse duration: Morphological studies on model samples’, *Applied Surface Science*, 255(9), pp. 4955–4960. doi: 10.1016/j.apsusc.2008.12.049.

Prati, S., Chiavari, G. and Cam, D. (2001) ‘DSC application in the conservation field’, *Journal of Thermal Analysis and Calorimetry*, 66, pp. 315–327. doi: 10.1023/A:1012472606631.

Prati, S., Sciutto, G., Mazzeo, R., Torri, C., Fabbri, D. (2011) ‘Application of ATR-far-infrared spectroscopy to the analysis of natural resins’, *Analytical and Bioanalytical Chemistry*, 399(9), pp. 3081–3091. doi: 10.1007/s00216-010-4388-y.

Q-Lab Corporation (2014) ‘A Choice of Filters for Q-SUN Xenon Test Chambers’, pp. 1–4. Available at: <https://www.q-lab.com/documents/public/41b5935b-d41d-4368-a53e-98a3d528baf1.pdf>. (Accessed: 12 Jan. 21).

Radvan, R., Asmus, J. F., Castillejo, M., Pouli, P., Nevin, A. (eds.) (2011) *Laser in the Conservation of Artworks VIII, Proceedings of the International Conference on Lasers in Conservation of Artwork (LACONA VIII), 21-25 Sept. 2009, Sibiu, Romania*. London, UK: CRC Press Taylor & Francis Group. doi: 10.1017/CBO9781107415324.004.

Raimondi, V., Andreotti, A., Colombini, M. P., Cucci, C., Cuzman, O., Galeotti, M., Lognoli, D., Palombi, L., Picollo, M., Tiano, P. (2015) ‘Test measurements on a secco white-lead containing model samples to assess the

- effects of exposure to low-fluence UV laser radiation’, *Applied Surface Science*. Elsevier, 337, pp. 45–57. doi: 10.1016/j.apsusc.2015.02.062.
- Rasband, W. (2009) ‘ImageJ’. *National Institute of Health*. Available at: <https://imagej.nih.gov/ij/index.html> (Accessed: 29 April 2020).
- Rasi, S., Ricart, S., Obradors, X., Puig, T., Roura, P., Farjas, J. (2018) ‘Thermal decomposition of yttrium propionate: film and powder’, *Journal of Analytical and Applied Pyrolysis*. Elsevier, 133(March), pp. 225–233. doi: 10.1016/j.jaap.2018.03.021.
- Razab, M. K. A. A., Mohamed Noor, A., Suhaimi Jaafar, M., Abdullah, N. H., Suhaimi, F. M., Mohamed, M., Adam, N., Auli Nik Yusuf, N. A. (2018) ‘A review of incorporating Nd:YAG laser cleaning principal in automotive industry’, *Journal of Radiation Research and Applied Sciences*. Elsevier, 11(4), pp. 393–402. doi: 10.1016/j.jrras.2018.08.002.
- Ready, J. F. (1971a) *Effects of High-Power Laser Radiation*. London: Academic Press Inc Ltd. doi: 10.1016/B978-0-12-583950-1.X5001-6.
- Ready, J. F. (1971b) ‘Properties of Lasers’, in *Effects of High-Power Laser Radiation*. London: Academic Press Inc Ltd., pp. 1–31. doi: 10.1016/B978-0-12-583950-1.50006-4.
- Ready, J. F. (1978) ‘Interaction of high-power laser radiation with materials’, in *Industrial Applications of Lasers*. Academic Press, pp. 336–357. doi: <https://doi.org/10.1016/B978-0-12-583960-0.50019-8>.
- Redtenbacher, J. (1843) ‘On the degradation products of glyceryl oxide by dry distillation (in German)’, *Ann. Chem. Pharm.*, 47, pp. 113–148.
- Röhm, O. (1901) *Über Polymerisationsprodukte der Acrylsäure*. Doctoral Thesis. Universität Tübingen, Tübingen, DE.
- Routledge, V. (2000) ‘The development and application of MS2A reduced ketone resin in painting conservation’, *WAAC Newsletter*, 22(2), pp. 16–17.

Available at: <https://cool.culturalheritage.org/waac/wn/wn22/wn22-2/wn22-206.html>. (Accessed:12 Jan. 21).

- Ruhemann, H. M. (1931) 'La technique de la conservation des tableaux', *Mouseion*, XV(3), p. 14—23.
- Ruhemann, H. M. (1968) *The Cleaning of Pictures. Problems and Potentialities*. London, UK: Faber and Faber. doi: 10.2307/429442.
- Russo, M. V. and Avino, P. (2012) 'Characterization and Identification of Natural Terpenic Resins employed in "Madonna con Bambino e Angeli" by Antonello da Messina using Gas Chromatography-Mass Spectrometry', *Chemistry Central Journal*, 6(1), p. 59. doi: 10.1186/1752-153X-6-59.
- Saba, N., Jawaïd, M. and Sultan, M. T. H. (2017) 'Thermal properties of oil palm biomass based composites', *Lignocellulosic Fibre and Biomass-Based Composite Materials*. Elsevier, pp. 95–122. doi: 10.1016/B978-0-08-100959-8.00006-8.
- Saito, M., Gojo, T., Kato, Y., Miyagi, M. (1995) 'Optical constants of polymer coatings in the infrared', *Infrared Physics and Technology*, 36(7), pp. 1125–1129. doi: 10.1016/1350-4495(95)00042-9.
- Sanderson, K. (2015) 'A Comparative Study of Handheld Reflectance Spectrophotometers', *Topics in Photographic Preservation, AIC Annual Meeting in San Francisco 2014*, 16, pp. 47–62.
- Sanderson, K. (2015) 'A Comparative Study of Handheld Reflectance Spectrophotometers', *Topics in Photographic Preservation, AIC Annual Meeting in San Francisco 2014*, 16, pp. 47–62.
- Sansonetti, A. and Realini, M. (2000) 'Nd:YAG laser effects on inorganic pigments', *Journal of Cultural Heritage*, 1(2), pp. 189–198. doi: 10.1016/S1296-2074(00)00181-3.
- Santos, J. C. O., Santos, M. G. O., Dantas, J. P., Conceição, M. M., Athaide-Filho, P. F., Souza, A. G. (2005) 'Comparative study of specific heat capacities of

- some vegetable oils obtained by DSC and microwave oven', *Journal of Thermal Analysis and Calorimetry*, 79, pp. 283–287. doi: 10.1007/s10973-005-0050-x.
- Sato, H. and Nishio, S. (2001) 'Polymer laser photochemistry, ablation, reconstruction, and polymerization', *Journal of Photochemistry and Photobiology C: Photochemistry Reviews*, 2(2), pp. 139–152. doi: 10.1016/S1389-5567(01)00015-6.
- Sato, T. and Okaya, T. (1992) 'Characterization and Physical Properties of Low Molecular Weight Poly(vinyl acetate) and Poly(vinyl alcohol)', *Polymer Journal*, 24(9), pp. 849–856. doi: 10.1295/polymj.24.849.
- Saulick, Y., Lourenço, S. D. N. and Baudet, B. A. (2017) 'A Semi-Automated Technique for Repeatable and Reproducible Contact Angle Measurements in Granular Materials using the Sessile Drop Method', *Soil Science Society of America Journal*, 81(2), pp. 241–249. doi: 10.2136/sssaj2016.04.0131.
- Saunders, D. (1995) 'Photographic flash: threat or nuisance?', *The National Gallery Technical Bulletin*, pp. 64–75.
- Scalarone, D. van der Horst, J., Boon, J. J., Chiantore, O. (2003) 'Direct-temperature mass spectrometric detection of volatile terpenoids and natural terpenoid polymers in fresh and artificially aged resins', *Journal of Mass Spectrometry*, 38(6), pp. 607–617. doi: 10.1002/jms.470.
- Scalarone, D., Duursma, M. C., Boon, J. J., Chiantore, O. (2005) 'MALDI-TOF mass spectrometry on cellulosic surfaces of fresh and photo-aged di- and triterpenoid varnish resins', *Journal of Mass Spectrometry*, 40(12), pp. 1527–1535. doi: 10.1002/jms.893.
- Schanda, D. J. (ed.) (2007) *Colorimetry. Understanding the CIE System*. Hoboken, NJ, USA: John Wiley & Sons, Inc.
- Schanda, D. J. (ed.) (2007) *Colorimetry. Understanding the CIE System*. Hoboken, NJ, USA: John Wiley & Sons, Inc.

- Schawlow, A. L. (1965) 'Lasers', *Science*, 149(3679), pp. 13–21.
- Schawlow, A. L. and Townes, C. H. (1958) 'Infrared and Optical Masers', *Physical Review*, 112(6), pp. 1940–1949. doi: 10.1103/PhysRev.112.1940.
- Schawlow, A. L. and Townes, C. H. (1958) 'Infrared and Optical Masers', *Physical Review*, 112(6), pp. 1940–1949. doi: 10.1103/PhysRev.112.1940.
- Scheerer, S., Abraham, M. and Madden, O. (2003) 'Study of the effects of laser radiation on epoxy resins and epoxy systems on stone, ceramic, and glass surfaces', *Journal of Cultural Heritage*, 4, pp. 223–229. doi: 10.1016/S1296-2074(02)01201-3.
- Schilling, M. R. (1989) 'The Glass Transition of Materials Used in Conservation', *Studies in Conservation*, 34(3), pp. 110–116.
- Schnell, A., Goretzki, L. and Kaps, C. (2005) 'IR-Laser Effects on Pigments and Paint Layers', in Dickmann, K., Fotakis, C., and Asmus, J. F. (eds.) *Lasers in the Conservation of Artworks, proceedings Lacona V, Osnabruck, Germany, Sept. 15–18, 2003*. Berlin/Heidelberg: Springer-Verlag, pp. 291–296. doi: 10.1007/3-540-27176-7\_35.
- Scholten, H. and Schipper, D. A. (2001) 'Advanced workstation for controlled laser cleaning of paintings', *Proc. SPIE 4402, Laser Techniques and Systems in Art Conservation, (22 October 2001)*, p. 121. doi: 10.1117/12.445653.
- Scholten, H., Teule, J. M., Zafirooulos, V., Heeren, R. M. A. (2000) 'Controlled laser cleaning of painted artworks using accurate beam manipulation and on-line LIBS-detection', in *Journal of Cultural Heritage*, pp. S215–S220. doi: 10.1016/S1296-2074(00)00142-4.
- Scholten, H., Teule, J. M., Zafirooulos, V., Heeren, R. M. A. (2005) 'Controlled laser cleaning of fire-damaged paintings', in *Postprints (American Institute for Conservation of Historic and Artistic Works. Paintings Specialty Group)*, 17, pp. 30–31.

- Schorbach, S. (2009) 'Reinigungsschwämme in der Restaurierung—Vergleichende Untersuchung zu Material, Wirkung und Rückständen. [Cleaning Sponges in Restoration—A Comparative Study with Regards to Material, Effectiveness and Conditions.]', *Zeitschrift für Kunsttechnologie und Konservierung*, 23(1), pp. 41–54.
- Serafetinides, A. A., Makropoulou, M. I., Skordoulis, C. D., Kar, A. K. (2001) 'Ultra-short pulsed laser ablation of polymers', *Applied Surface Science*, 180(1–2), pp. 42–56. doi: 10.1016/S0169-4332(01)00324-5.
- Shang, J., Shang, J., Flury, M., Harsh, J. B., Zollars, R. L. (2008) 'Comparison of different methods to measure contact angles of soil colloids', *Journal of Colloid and Interface Science*, 328(2), pp. 299–307. doi: 10.1016/j.jcis.2008.09.039.
- Shirtcliffe, N. J. et al. (2010) 'An introduction to superhydrophobicity', *Advances in Colloid and Interface Science*, 161(1–2), pp. 124–138. doi: 10.1016/j.cis.2009.11.001.
- Shori, R. K., Walston, A. A., Stafsudd, O. M., Fried, D., Walsh, J. T. (2001) 'Quantification and modelling of the dynamic changes in the absorption coefficient of water at  $\lambda = 2.94 \mu\text{m}$ ', *IEEE Journal of Selected Topics in Quantum Electronics*, 7(6), pp. 959–970. doi: 10.1109/2944.983300.
- Siano, S. (2008) 'Principles of Laser Cleaning in Conservation', in Schreiner, M., Strlič, M., and Salimbeni, R. (eds) *Handbook of the Use of Lasers in Conservation and Conservation Science*. Brussels, Belgium: COST Office. pp. 1–16. Available at: <http://www.science4heritage.org/COSTG7/booklet/>. (Accessed:12 Jan. 21).
- Siano, S., Agresti, J., Cacciari, I., Ciofini, D., Mascalchi, M., Osticioli, I., Mencaglia, A. A. (2012) 'Laser cleaning in conservation of stone, metal, and painted artifacts: state of the art and new insights on the use of the Nd:YAG lasers', *Applied Physics A*, 106(2), pp. 419–446. doi: 10.1007/s00339-011-6690-8.

- Siano, S., Fabiani, F., Pini, R., Salimbeni, R., Giamello, M., Sabatini, G. (2000) ‘Determination of damage thresholds to prevent side effects in laser cleaning of Pliocene sandstone of Siena’, *Journal of Cultural Heritage*, 1(2), pp. 47–53. doi: 10.1016/S1296-2074(00)00194-1.
- Siano, S., Osticioli, I., Pavia, A., Ciofini, D. (2015) ‘Overpaint removal from easel paintings using an LQS Nd:YAG laser: The first validation study’, in Elnaggar, A., Nevin, A., Castillejo, M., Strlič, M. (eds.) *Studies in Conservation, Proceedings from the Tenth Conference on Laser in the conservation of Artworks, Lacona X, Sharjah, United Arab Emirates, June 9-13, 2014*. Maney Publishing, pp. S49–S57. doi: 10.1179/0039363015Z.0000000000207.
- Siano, S., Pini, R. and Salimbeni, R. (2000) *Aspetti fisici della pulitura laser, Tecniche e sistemi laser per il restauro dei Beni Culturali*. Kermes quaderni; Supplementi of Kermes. Firenze.
- Siano, S., Salimbeni, R., Pini, R., Giusti, A., Matteini, M. (2003) ‘Laser cleaning methodology for the preservation of the Porta del Paradiso by Lorenzo Ghiberti’, *Journal of Cultural Heritage*, 4(SUPPL. 1), pp. 140–146. doi: 10.1016/S1296-2074(02)01138-X.
- Siano, S., Zanini, A., Gioè, L., Modi, S., Agresti, J., Mencaglia, A. (2011) ‘Sviluppo e Trasferimento di tecnologie laser progetto TEMART’, in Brunetto, A. (ed.) *Aplar 3. Il Laser e I Laser (Conference Proceedings ‘Applicazioni Laser nel Restauro’, Bari 18-19 June 2010)*. Saonara, Italy: Il Prato Editore, pp. 239–244.
- Silverstein, R. M., Bassler, G. C. and Morrill, T. C. (1991) *Spectrometric identification of organic compounds*. Journal of Chemical Education. 5<sup>th</sup> Ed. New York: John Wiley & Sons, Ltd.
- Slough, C. G. and Hesse, N. D. (2007) High Precision Heat Capacity Measurements of Metals by Modulated, *TA 339*. New Castle, DE, USA. Available at: <http://www.tainstruments.com/pdf/literature/TA339%20High%20Precision>

%20Cp%20Measurements%20of%20Metals%20by%20MDSC.pdf.

(Accessed:12 Jan. 21).

Steen, W. M. and Mazumder, J. (2010) *Laser Material Processing*. 4<sup>th</sup> Ed. London: Springer London. doi: 10.1007/978-1-84996-062-5.

Steyn, L., Stols-Witlox, M. J. N., Hendriks, E., van den Berg, K. J. (2017) ‘Cleaning modern oil paints: The removal of imbibed surface dirt. Towards an integrated conservation methodology for the assessment, contextualization and treatment of imbibed surface dirt on unvarnished modern oil paintings’, *ICOM-CC 18th Triennial Conference Preprints, Copenhagen, 4–8 September 2017: preprints (ICOM Committee for Conservation)*, p. 2017. Available at: <https://hdl.handle.net/11245.1/2f751deb-e2f7-4072-93f5-9b0361e78f73>. (Accessed:12 Jan. 21).

Steyn, L., Stols-Witlox, M., Hendriks, E., van den Berg, K. J. (2017) ‘Cleaning modern oil paints: The removal of imbibed surface dirt. Towards an integrated conservation methodology for the assessment, contextualization and treatment of imbibed surface dirt on unvarnished modern oil paintings’, *ICOM-CC 18th Triennial Conference Preprints, Copenhagen, 4–8 September 2017: preprints (ICOM Committee for Conservation)*, p. 2017. Available at: <http://icom-cc-publications-online.org/PublicationDetail.aspx?cid=532b337e-c2f6-4067-95af-e852ee259169>. (Accessed:12 Jan. 21).

Stols-Witlox, M. (2017) *A perfect ground: preparatory layers for oil paintings, 1550-1900*. London, UK: Archetype Publications Ltd.

Stoner, J. H. and Rushfield, R. (eds.) (2012) *Conservation of easel paintings*. Abingdon, Oxon [England]; New York, NY: Routledge.

Stout, G. L. (1948) *The Care of Pictures*. New York: Columbia Univ. Press.

Stout, G. L. and Cross, H. F. (1937) ‘Properties of surface films’, *Technical studies in the field of fine arts*, 5, pp. 241–249.

- Striber, J., Jovanović, V. and Jovanović, M. (2017) 'Easel paintings on canvas and panel: application of Nd:YAG laser at 355 nm, 1064 nm and UV, IR and visible light for the development of new methodologies in conservation', in Targowski, P., Walczak, M., and Pouli, P. (eds.) *Proceedings of the International Conference LACONA XI. Toruń: Nicolaus Copernicus University Press*, pp. 279–292. doi: 10.12775/3875-4.20.
- Stringari, C., McGlinchey, C. W., Melessanaki, K., Postma, S., D'Augustine, C. (2007) 'Laser Cleaning of a Study Painting by Ad Reinhardt and the Analysis/Assessment of the Surface after Treatment', in Learner, T. J. S., Smithen, P., Krueger, J. W., Schilling, M. R. (eds.) *Modern Paints Uncovered: Proceedings from the Modern Paints Uncovered Symposium*. Los Angeles: Getty Conservation Institute. Los Angeles, California: The Getty Conservation Institute, pp. 208–217.
- Striova, J. Camaiti, M., Castellucci, E. M., Sansonetti, A. (2011a) 'Chemical, morphological and chromatic behaviour of mural paintings under Er:YAG laser irradiation', *Applied Physics A: Materials Science and Processing*, 104(2), pp. 649–660. doi: 10.1007/s00339-011-6303-6.
- Striova, J., Castellucci, E., Sansonetti, A., Camaiti, M., Matteini, M., De Cruz, A., Andreotti, A., Colombini, M. P. (2011b) 'Free-running Er:YAG laser cleaning of mural painting specimens treated with linseed oil, "beverone" and Paraloid B72', in Radvan, R., Asmus, J. F., Castillejo, M., Pouli, P., Nevin, A. (eds.) *Lasers in the Conservation of Artworks, proceedings Lacona VIII, Sibiu, Romania, Sep. 21–25, 2009. Boca Raton: CRC Press Taylor & Francis Group*, pp. 85–91. Available at: <http://hdl.handle.net/2158/550266>. (Accessed:12 Jan. 21).
- Striova, J., Salvadori, B., Fontana, R., Sansonetti, A., Barucci, M., Pampaloni, E., Marconi, E., Pezzati, L., Colombini, M. P. (2015) 'Optical and spectroscopic tools for evaluating Er:YAG laser removal of shellac varnish', in Elnaggar, A., Nevin, A., Castillejo, M., Strlič, M. (eds.) *Studies in Conservation, Proceedings from the Tenth Conference on Laser in the conservation of*

- Artworks, Lacona X, Sharjah, United Arab Emirates, June 9-13, 2014*. Maney Publishing, pp. S91–S96. doi: 10.1179/0039363015Z.000000000213.
- Talarico, F. and Coladonato, M. (1997) *Impiego dei parametri di solubilità nel restauro – Materiali e strutture*. Roma.
- Tam, A. C., Leung, W. P., Zapka, W., Ziemlich, W. (1992) ‘Laser-cleaning techniques for removal of surface particulates’, *Journal of Applied Physics*. American Institute of Physics, 71(7), pp. 3515–3523. doi: 10.1063/1.350906.
- Tamari, S. (2004) ‘Optimum design of the constant-volume gas pycnometer for determining the volume of solid particles’, *Measurement Science and Technology*. IOP Publishing, 15(3), pp. 549–558. doi: 10.1088/0957-0233/15/3/007.
- Tanaka, S. (1992) ‘Theory of power-compensated DSC’, *Thermochimica Acta*, 210(C), pp. 67–76. doi: 10.1016/0040-6031(92)80277-4.
- Teas, J. P. (1968) ‘Graphic analysis of resin solubilities’, *Journal of paint technology*, 40(516), pp. 19–25.
- Tempest, H., Burnstock, A., Saltmarsh, P., van den Berg, K. J. (2013) ‘Sensitivity of Oil Paint Surfaces to Aqueous and Other Solvents’, in Mecklenburg, M. F., Charola, A. E., and Koestler, R. J. (eds.) *New Insights into the Cleaning of Paintings: Proceedings from the Cleaning 2010 International Conference, Universidad Politecnica de Valencia and Museum Conservation Institute. Smithsonian Contributions to Museum Conservation*. Washington, DC: Smithsonian Institution, pp. 107–114. Available at: <https://repository.si.edu/handle/10088/20496>. (Accessed:12 Jan. 21).
- Teppo, E. (2020) ‘Introduction: Er:YAG lasers in the conservation of artworks’, *Journal of the Institute of Conservation*. Taylor & Francis, 43(1), pp. 1–10. doi: 10.1080/19455224.2019.1706597.

- Teppo, E. (2020) 'Introduction: Er:YAG lasers in the conservation of artworks', *Journal of the Institute of Conservation*. Taylor & Francis, 43(1), pp. 1–10. doi: 10.1080/19455224.2019.1706597.
- Teppo, E. and Calcagno, G. (1995) 'Restoration with lasers halts decay of ancient artefacts', *Laser Focus World*, pp. 55–59.
- Teule, R., Scholten, H., van den Brink, O. F., Heeren, R. M. A., Zafirooulos, V., Hesterman, R., Castillejo, M., Martín, M., Ullenius, U., Larsson, I., Guerra-Librero, F., Silva, A., Gouveia, H., Albuquerque, M. B. (2003) 'Controlled UV laser cleaning of painted artworks: a systematic effect study on egg tempera paint samples', in *Journal of Cultural Heritage*, pp. 209–215. doi: 10.1016/S1296-2074(02)01137-8.
- The Corporate Archives of Evonik (no date) Otto Röhm - Das Evonik Geschichtsportal - Die Geschichte von Evonik Industries, history.evonik.com. Available at: <https://history.evonik.com/sites/geschichte/en/personalities/roehm-otto/>. (Accessed:12 Jan. 21).
- Theodorakopoulos, C. (2005) *The Excimer Laser Ablation of Picture Varnishes. An evaluation with reference to light-induced deterioration*. Doctoral Thesis, Royal college of art London. Available at: <https://amolf.nl/publications/the-excimer-laser-ablation-of-picture-varnishes-an-evaluation-with-reference-to-light-induced-deterioration>. (Accessed:12 Jan. 21).
- Theodorakopoulos, C. and Boon, J. J. (2011) 'A high performance size exclusion chromatographic study on the depth-dependent gradient in the molecular weight of aged triterpenoid varnish films', *Progress in Organic Coatings*. Elsevier, 72(4), pp. 778–783. Available at: <http://www.sciencedirect.com/science/article/pii/S0300944011002414>. (Accessed:12 Jan. 21). doi: 10.1016/j.porgcoat.2011.08.010.
- Theodorakopoulos, C. and Zafirooulos, V. (2003) 'Uncovering of scalar oxidation within naturally aged varnish layers', *Journal of Cultural Heritage*, 4, pp. 216–222. doi: 10.1016/S1296-2074(02)01200-1.

- Theodorakopoulos, C. and Zafiropulos, V. (2005) 'Laser Cleaning Applications for religious objects', *European Journal of Science and Theology*, 1(1), pp. 63–76.
- Theodorakopoulos, C. and Zafiropulos, V. (2009) 'Depth-profile investigations of triterpenoid varnishes by KrF excimer laser ablation and laser-induced breakdown spectroscopy', *Applied Surface Science*, 255(20), pp. 8520–8526. doi: 10.1016/j.apsusc.2009.06.012.
- Theodorakopoulos, C., Boon, J. J. and Zafiropulos, V. (2009) 'Direct temperature mass spectrometric study on the depth-dependent compositional gradients of aged triterpenoid varnishes', *International Journal of Mass Spectrometry*, 284(1–3), pp. 98–107. doi: 10.1016/j.ijms.2008.11.004.
- Theodorakopoulos, C., Zafiropulos, V., Boon, J. J., Boyatzis, S. C. (2007) 'Spectroscopic investigations on the depth-dependent degradation gradients of aged triterpenoid varnishes', *Applied Spectroscopy*, 61(10), pp. 1045–1051. doi: 10.1366/000370207782217833.
- Theodorakopoulos, C., Zafiropulos, V., Fotakis, C., Boon, J. J., Horst, J., Dickmann, K., Knapp, D. (2005) 'A Study on the Oxidative Gradient of Aged Traditional Triterpenoid Resins Using "Optimum" Photoablation Parameters', in Dickmann, K., Fotakis, C., and Asmus, J. F. (eds.) *Lasers in the Conservation of Artworks, proceedings Lacona V, Osnabruck, Germany, Sept. 15–18, 2003*. Berlin/Heidelberg: Springer-Verlag, pp. 255–262. doi: 10.1007/3-540-27176-7\_31.
- Thomson, G. (1957) 'Some Picture Varnishes', *Studies in Conservation*, 3(2), pp. 64–79. doi: 10.1097/EDE.0b013e3181.
- Thomson, G. (1986) *The Museum Environment*. 2<sup>nd</sup> Ed. Oddy, A. and Lintrum, D. (eds.). Elsevier. doi: 10.1016/C2013-0-01226-1.
- Thomson, G. (ed.) (1961) 'New picture varnishes', *Studies in Conservation. Abstracts of the Rome Conference Contributions 1961*. London: Butterworths, pp. 143–144.

- Toch, M. (1934) 'Dammar as a Picture Varnish', *Technical Studies in the Field of the Fine Arts* 2, 3(January), pp. 149–151.
- Treacy, A. (2006) 'Reforming varnish on varnished works of art on paper. A case study', in *AICCM Symposium 2006, Conservation of Paper, Books and Photographic Materials. Post-prints and Posters. 19-21 April 2006*, Wellington, New Zealand, pp. 117–136. Available at: <https://aiccm.org.au/conference-proceedings/reforming-varnish-on-varnished-works-of-art-on-paper/>. (Accessed:12 Jan. 21).
- Tsang, J. S. and Erhardt, D. (2018) 'Current Research on the Effects of Solvents and Gelled and Aqueous Cleaning Systems on Oil Paint Films', *Journal of the American Institute for Conservation*, 31(1), pp. 87–94. doi: 10.1179/019713692806156457.
- Usamentiaga, R., Venegas, P., Guerediaga, J., Vega, L., Molleda, J., Bulnes, F. G. (2014) 'Infrared thermography for temperature measurement and non-destructive testing', *Sensors*, 14(7), pp. 12305–12348. doi: 10.3390/s140712305.
- Uttaravalli, A. N. (2018) Polymerization and Kinetic Studies of Ketonic Resin Synthesized by Environment-Friendly Method. Doctoral Thesis, Birla Institute of Technology and Science. Available at: <http://hdl.handle.net/10603/251972>. (Accessed:12 Jan. 21).
- van Aarssen, B. G. K., Cox, H. C., Hoogendoorn, P., De Leeuw, J.W. (1990) 'A cadinene biopolymer in fossil and extant dammar resins as a source for cadinanes and bicadinanes in crude oils from South East Asia', *Geochimica et Cosmochimica Acta*, 54(11), pp. 3021–3031. doi: 10.1016/0016-7037(90)90119-6.
- van Aarssen, B. G. K., de Leeuw, J. W. and Horsfield, B. (1991) 'A comparative study of three different pyrolysis methods used to characterise a biopolymer isolated from fossil and extant dammar resins', *Journal of Analytical and Applied Pyrolysis*, 20, pp. 125–139. doi: 10.1016/0165-2370(91)80067-I.

- van den Berg, K. J., Boon, J. J., Pastorova, I., Spetter, L. F. M. (2000) 'Mass spectrometric methodology for the analysis of highly oxidized diterpenoid acids in Old Master paintings', *Journal of Mass Spectrometry*, 35(4), pp. 512–533. doi: 10.1002/(SICI)1096-9888(200004)35:4<512::AID-JMS963>3.0.CO;2-3.
- van den Berg, K.J., Burnstock, A., de Keijzer, M., Krueger, J., Learner, T., de Tagle, A., Heydenreich, G. (eds.) (2014) *Issues in Contemporary Oil Paint*. Cham, Switzerland: Springer International Publishing. doi: 10.1007/978-3-319-10100-2.
- van der Doelen, G. A. (1999) *Molecular studies of fresh and aged triterpenoid varnishes*, Doctoral Thesis. University of Amsterdam. Available at: <https://hdl.handle.net/11245/1.180090>. (Accessed:12 Jan. 21). doi: 10.2307/1506734.
- van der Doelen, G. A. and Boon, J. J. (2000) 'Artificial ageing of varnish triterpenoids in solution', *Journal of Photochemistry and Photobiology A: Chemistry*, 134, pp. 45–57. doi: 10.1016/S1010-6030(00)00245-8.
- van der Doelen, G. A., van den Berg, K. J. and Boon, J. J. (1998) 'Comparative chromatographic and mass-spectrometric studies of triterpenoid varnishes: fresh material and aged samples from paintings', *Studies in Conservation*, 43(4), pp. 249–264. doi: 10.1179/sic.1998.43.4.249.
- van der Doelen, G. A., van den Berg, K. J., Boon, J. J., Shibayama, N., de la Rie, E. R., Genuit, W. J. L. (1998) 'Analysis of fresh triterpenoid resins and aged triterpenoid varnishes by high-performance liquid chromatography-atmospheric pressure chemical ionisation (tandem) mass spectrometry', *Journal of Chromatography A*, 809, pp. 21–37. doi: 10.1016/S0021-9673(98)00186-1.
- Vandenabeele, P., Wehling, B., Moens, L., Edwards, H., De Reu, M., Van Hooydonk, G. (2000) 'Analysis with micro-Raman spectroscopy of natural organic binding media and varnishes used in art', *Analytica Chimica Acta*, 407(1–2), pp. 261–274. doi: 10.1016/S0003-2670(99)00827-2.

- Venugopalan, V., Nishioka, N. S. and Mikić, B. B. (1996) 'Thermodynamic response of soft biological tissues to pulsed infrared-laser irradiation', *Biophysical Journal*, 70(6), pp. 2981–2993. doi: 10.1016/S0006-3495(96)79868-5.
- Verdu, J. (1994) 'Effect of Aging on the Mechanical Properties of Polymeric Materials', *Journal of Macromolecular Science, Part A*, 31(10), pp. 1383–1398. doi: 10.1080/10601329409350099.
- Verges-Belmin, V. (1997) 'Comparison of three cleaning methods - microsandblasting, chemical pads and Q-switched YAG laser - on a portal of the Cathedral Notre-Dame in Paris, France', in *Lasers in the Conservation of Artworks, workshop, 4-6 October 1995, Heraklion, Crete, Greece proceedings*. Wien, Austria: Mayer & Comp 1997. pp. 17-24.
- Verges-Belmin, V., Pichot, C. and Oriol, G. (1993) 'Elimination de croûtes noires sur marbre et craie: à quel niveau arrêter le nettoyage?', in *Conservation of stone and other materials: proceedings of the international RILEM/UNESCO congress held at the UNESCO headquarters, Paris, June 29-July 1, 1993*. London: E. & F.N. Spon Ltd., pp. 534–541.
- Vitkus, J. R. and Asmus, J. F. (1976) 'Treatment of leather and vellum with transient heating', *AIC preprints, 4<sup>th</sup> Annual Meeting, American Institute for Conservation*, Washington, D.C., pp. 111–17.
- Vogel, A. and Venugopalan, V. (2003a) 'Kinetics of phase transitions in pulsed IR laser ablation of biological tissues', in *Proc. SPIE 4961, Laser Tissue Interaction XIV*, pp. 66–74. doi: 10.1117/12.519895.
- Vogel, A. and Venugopalan, V. (2003b) 'Mechanisms of Pulsed Laser Ablation of Biological Tissues', *Chemical Reviews*, 103(2), pp. 577–644. doi: 10.1021/cr010379n.
- Vogel, A. and Venugopalan, V. (2010) 'Pulsed Laser Ablation of Soft Biological Tissues', in Welch A., van Gemert M. (eds.) *Optical-Thermal Response of*

*Laser-Irradiated Tissue*. Dordrecht: Springer Netherlands, pp. 551–615. doi: 10.1007/978-90-481-8831-4\_14.

Vogel, A., Apitz, I. and Venugopalan, V. (2007) ‘Phase transitions, material ejection, and plume dynamics in pulsed laser ablation of soft biological tissues’, in Kurz, T., Parlitz, U., and Kaatz, U. (eds) *Oscillations, waves and interactions*, pp. 217–258. Available at: [http://www.ncbi.nlm.nih.gov/entrez/query.fcgi?db=pubmed&cmd=Retrieve&dopt=AbstractPlus&list\\_uids=wVA2BbEc9qgC%5Cnpapers://3417802c-d225-4431-ae35-ca17933cab09/Paper/p124](http://www.ncbi.nlm.nih.gov/entrez/query.fcgi?db=pubmed&cmd=Retrieve&dopt=AbstractPlus&list_uids=wVA2BbEc9qgC%5Cnpapers://3417802c-d225-4431-ae35-ca17933cab09/Paper/p124). (Accessed:12 Jan. 21).

von Pettenkofer, M. (1902) *Über Ölfarbe und Konservierung der Gemäldegalerien durch das Regenerations-Verfahren*. Braunschweig, Vieweg.

Wallert, A., Hermens, E. and Peek, M. (eds.) (1995) ‘Historical painting techniques, materials, and studio practice’, in *Preprints of a Symposium Held at the University of Leiden, the Netherlands, 26-29 June 1995*. Marina Del Rey, CA: Getty Conservation Institute. Available at: [http://hdl.handle.net/10020/gci\\_pubs/historical\\_painting](http://hdl.handle.net/10020/gci_pubs/historical_painting). (Accessed:12 Jan. 21).

Walsh, J. T. and Cummings, J. P. (1994) ‘Effect of the dynamic optical properties of water on midinfrared laser ablation’, *Lasers in Surgery and Medicine*, 15(3), pp. 295–305. doi: 10.1002/lsm.1900150310.

Walsh, J. T. and Deutsch, T. F. (1991) ‘Measurement of Er:YAG laser ablation plume dynamics’, *Applied Physics B Photophysics and Laser Chemistry*, 52(3), pp. 217–224. doi: 10.1007/BF00750954.

Wang, Y., Abe, Y., Matsuura, Y., Miyagi, M., Uyama, H. (1998) ‘Refractive indices and extinction coefficients of polymers for the mid-infrared region’, *Applied Optics*, 37(30), p. 7091. doi: 10.1364/ao.37.007091.

Watkins, K. G. (1997) ‘A review of materials interaction during laser cleaning in art restoration’, in Kautek, W. and König, E. (eds.) *Lasers in the Conservation*

*of Artworks, proceedings Lacona I, Crete, Greece, 4-6 October 1995*. Wein: Verlag Mayer & Comp., pp. 7–15.

Watson, M. and Burnstock, A. (2013) ‘An Evaluation of Color Change in Nineteenth-Century Grounds on Canvas upon Varnishing and Varnish Removal’, in Mecklenburg, M. F., Charola, A. E., and Koestler, R. J. (eds.) *New Insights into the Cleaning of Paintings: Proceedings from the Cleaning 2010 International Conference, Universidad Politecnica de Valencia and Museum Conservation Institute. Smithsonian Contributions to Museum Conservation*. Washington, DC: Smithsonian Institution, pp. 77–84.

Watts, S. and de la Rie, E. R. (2002) ‘GCMS Analysis of Triterpenoid Resins: In Situ Derivatization Procedures Using Quaternary Ammonium Hydroxides’, *Studies in Conservation*, 47(4), pp. 257–272. doi: 10.1179/sic.2002.47.4.257.

Weber, J. and Bastick, M. (1968) ‘Influence de la température sur la détermination de la masse volumique de divers carbones par pycnométrie dans l’helium’, *Bulletin de la Société Chimique de France*, 7, pp. 2702–2706.

Weber, R., Graf, T., Berger, P., Onuseit, V., Wiedenmann, M., Freitag, C., Feuer, A. (2014) ‘Heat accumulation during pulsed laser materials processing’, *Optics Express*, 22(9), pp. 11312–11324. doi: 10.1364/oe.22.011312.

Wehlte, K. (1971) ‘Trockenreiniger für Tafelgemälde und Wandmalereien [A Dry Cleaning Material for Panel and Wall Paintings.]’, *Maltechnik Nr.1*, pp. 10–13.

Wellen, R. M. R., Canedo, E. and Rabello, M. S. (2011) ‘Nonisothermal cold crystallization of poly(ethylene terephthalate)’, *Journal of Materials Research*, 26(9), pp. 1107–1115. doi: 10.1557/jmr.2011.44.

Werner, A. (1952) ‘Plastics aid in conservation of old paintings’, *British plastics and moulded products trader*, 25, pp. 363–366.

- Williams, D. L., Kuhn, A. T., Amann, M. A., Hausinger, M. B., Konarik, M. M., Nesselrode, E. I. (2010) ‘Computerised measurement of contact angles’, *Galvanotechnik*, 101(11), pp. 2502–2512.
- Wolbarsht, M. L. and De Cruz, A. (1999) ‘#5,951,778 - Method for cleaning Artwork’. U.S. Patent.
- Wolbers, R. (2000) *Cleaning painted surfaces: aqueous methods*. London: Archetype Publications.
- Wolbers, R. C., Sterman, N. T. and Stavroudis, C. (1990) *Notes for workshop on new methods in the cleaning of paintings*, in Marina del Rey: Getty Conservation Institute.
- Wunderlich, B. (2005) *Thermal Analysis of Polymeric Materials*. Berlin/Heidelberg: Springer-Verlag. doi: 10.1007/b137476.
- Yaneva, B. K., Zagorchev, P.I., Firkova, E.I., Glavinkov, I.T. (2016) ‘In Vitro Study of Temperature Changes in Pulp Chamber During Root Planing Procedure Using Er:YAG Laser’, *Folia medica*, 58(3), pp. 206–210. doi: 10.1515/folmed-2016-0022.
- Yao, Y. L., Chen, H. and Zhang, W. (2005) ‘Time scale effects in laser material removal: A review’, *International Journal of Advanced Manufacturing Technology*, 26, pp. 598–608. doi: 10.1007/s00170-003-2026-y.
- Yoder, J. (2000) ‘Thermocouple technology, a matter of resistance and metal’, *InTech*. Available at: [http://www.flowresearch.com/articles/InTech\\_3\\_17\\_00.PDF](http://www.flowresearch.com/articles/InTech_3_17_00.PDF). (Accessed:12 Jan. 21).
- Zacharopoulos, A., Hatzigiannakis, K., Karamaoynas, P., Papadakis, V. M., Andrianakis, M., Melessanaki, K., Zabulis, X. (2018) ‘A method for the registration of spectral images of paintings and its evaluation’, *Journal of Cultural Heritage*. Elsevier, 29, pp. 10–18. doi: 10.1016/J.CULHER.2017.07.004.

- Zafirooulos, V. (2002) 'Laser ablation in cleaning of artworks', in Luk'yanchuk, B. (ed.) *Laser Cleaning: Optical Physics, Applied Physics and Materials Science*. London; New York: WORLD SCIENTIFIC, pp. 343–392. doi: 10.1142/9789812777515\_0008.
- Zafirooulos, V. and Fotakis, C. (1997) 'Laser Cleaning in Conservation: an Introduction', in Cooper, M. (ed.) *Lasers in the Conservation of Painted Artworks*. Butterworth Heinemann, Oxford.
- Zafirooulos, V. and Fotakis, C. (1998) 'Laser in the conservation of painted artworks', in Cooper, M. (ed.) *Laser Cleaning in Conservation: An Introduction*. Oxford, UK: Butterworth-Heinemann, pp. 79–90.
- Zafirooulos, V., Manousaki, A., Kaminari, A., Boyatzis, S. (2001) 'Laser ablation of aged resin layers: a means of uncovering the scalar degree of aging', *Proc. SPIE 4430, ROMOPTO 2000: Sixth Conference on Optics, (29 June 2001)*, p. 181. doi: 10.1117/12.432839.
- Zapka, W., Ziemlich, W. and Tam, A. C. (1991) 'Efficient pulsed laser removal of 0.2  $\mu\text{m}$  sized particles from a solid surface', *Applied Physics Letters*. American Institute of Physics, 58(20), pp. 2217–2219. doi: 10.1063/1.104931.
- Zergioti, I., Petrakis, A., Zafirooulos, V., Fotakis, C., Fostiridou, A., Doulgeridis, M. (1997) 'Laser Applications in Painting Conservation', in *Restauratorenblätter*.
- Zgavec, B. and Stopajnik, N. (2014) 'Clinical and Histological Evaluation of Er : YAG Ablative Fractional Skin Resurfacing', *Journal of the Laser and Health Academy*, 1(1), pp. 1–6. Available at: [https://www.laserandhealthacademy.com/media/objave/academy/priponke/01\\_06\\_zgavec\\_laha\\_2014\\_1.pdf](https://www.laserandhealthacademy.com/media/objave/academy/priponke/01_06_zgavec_laha_2014_1.pdf). (Accessed:12 Jan. 21).
- Zuccari, F. (2003) 'The Conservation of Early Italian Paintings at the Art Institute of Chicago', in Garland, P. S. (ed.) *Early Italian Paintings: Approaches to Conservation*. New Haven, Conn.: Yale University Press, pp. 251–257.

Zuerlein, M. J., Fried, D., Seka, W., Featherstone, J. D. B. (1998) 'Modelling thermal emission in dental enamel induced by 9-11  $\mu\text{m}$  laser light', *Applied Surface Science*, 127-129, pp. 863-868. doi: 10.1016/S0169-4332(97)00757-5.

Zumbühl, S., Knochenmuss, R. D. and Wülfert, S. (1998) 'Rissig und blind werden in relativ kurzer Zeit alle Harzessenzfirnisse', *Zeitschrift für Kunsttechnologien und Konservierung*, 12, pp. 205-219.

Zumbühl, S., Knochenmuss, R., Wülfert, S., Dubois, F., Dale, M. J., Zenobi, R. (1998) 'A Graphite-Assisted Laser Desorption/Ionization Study of Light-Induced Aging in Triterpene Dammar and Mastic Varnishes', *Analytical Chemistry*, 70(4), pp. 707-715. doi: 10.1021/ac970574v.



## **Appendix A VARNISHES DATA**

Appendix A contains the data acquired for the characterisation of the varnishes:

A1) Stylus Profilometry:

*A.1.1. Dammar*

*A.1.2. Ketone N*

*A.1.3. MS2A*

*A.1.4. Paraloid B67*

A2) Colourimetry;

A3) Determination of Specific heat at constant pressure ( $C_p$ ) using Differential Scanning Calorimetry (DSC) analysis.

## A1 Stylus Profilometry

A Bruker Dektak XT™2D stylus profiler was employed to describe and measure the thickness of all the varnish films after the accelerated ageing.

### A.1.1 Dammar

Table A1 – The thicknesses of dammar varnish casted on glass slides were acquired using Vision64 application software.

<b>Profile</b>	Hills And Valleys
<b>Scan Duration</b>	40 s
<b>Scan Length</b>	24920 $\mu\text{m}$
<b>Scan Resolution</b>	2.07632 $\mu\text{m}$
<b>Scan Type</b>	Standard Scan
<b>Stylus Force</b>	10 mg
<b>Stylus Scan Range</b>	1 mm
<b>Stylus Type</b>	Radius: 12.5 $\mu\text{m}$

Analytical Results			
Height ( $\mu\text{m}$ )	Starting point cursor position	Ending point cursor position	Width scanned area
72.86	0.15 mm	3.53 mm	18.44 mm
75.50	0.25 mm	0.25 mm	24.57 mm
69.41	0.25 mm	3.45 mm	18.44 mm
79.28	0.20 mm	0.25 mm	24.56 mm
73.32	0.20 mm	3.70 mm	18.25 mm
75.93	0.08 mm	4.37 mm	16.72 mm
106.56	0.11 mm	0.15 mm	24.37 mm
102.42	0.11 mm	4.98 mm	16.40 mm
96.25	0.19 mm	5.84 mm	15.11 mm
71.54	0.16 mm	4.79 mm	16.35 mm
82.31	0.16 mm	0.16 mm	24.58 mm

## A.1.2 Ketone N

Table A2 – The thicknesses of the Ketone N casted on glass slides were acquired using Vision64 application software.

<b>Profile</b>	Hills And Valleys
<b>Scan Duration</b>	40 s
<b>Scan Length</b>	24826.2 $\mu\text{m}$
<b>Scan Resolution</b>	2.06851 $\mu\text{m}$
<b>Scan Type</b>	Standard Scan
<b>Stylus Force</b>	10 mg
<b>Stylus Scan Range</b>	524 $\mu\text{m}$
<b>Stylus Type</b>	Radius: 12.5 $\mu\text{m}$

<b>Analytical Results</b>			
<b>Height (<math>\mu\text{m}</math>)</b>	<b>Starting point cursor position</b>	<b>Ending point cursor position</b>	<b>Width scanned area</b>
25.36	0.08 mm	1.41 mm	22.35 mm
38.25	0.1 mm	2.09 mm	20.90 mm
39.80	0.1 mm	0.15 mm	24.37 mm
23.29	0.1 mm	1.54 mm	21.89 mm
22.99	0.03 mm	1.25 mm	22.43 mm
22.09	0 mm	1.40 mm	48.91 mm
25.81	0 mm	1.40 mm	48.91 mm

## A.1.3 MS2A

Table A3 – The thicknesses of the MS2A casted on glass slides were acquired using Vision64 application software.

<b>Profile</b>	Hills And Valleys
<b>Scan Duration</b>	40 s
<b>Scan Length</b>	24814.3 $\mu\text{m}$
<b>Scan Resolution</b>	2.06751 $\mu\text{m}$
<b>Scan Type</b>	Standard Scan
<b>Stylus Force</b>	10 mg
<b>Stylus Scan Range</b>	524 $\mu\text{m}$
<b>Stylus Type</b>	Radius: 12.5 $\mu\text{m}$

<b>Analytical Results</b>			
<b>Height (<math>\mu\text{m}</math>)</b>	<b>Starting point cursor position</b>	<b>Ending point cursor position</b>	<b>Width scanned area</b>
46.96	0.19 mm	1.665 mm	20.577 mm
60.99	0.197 mm	1.991 mm	18.857 mm
78.66	0.067 mm	2.674 mm	16.729 mm
59.77	0.041 mm	2.115 mm	18.946 mm
59.77	0.041 mm	2.115 mm	18.946 mm
46.82	0.161 mm	1.62 mm	20.107 mm

## A.1.4 Paraloid B67

Table A4 - The thicknesses of the Paraloid B67 casted on glass slides were acquired using Vision64 application software.

<b>Profile</b>	HillsAndValleys
<b>Scan Duration</b>	40 s
<b>Scan Length</b>	24322.3 $\mu\text{m}$
<b>Scan Resolution</b>	2.02652 $\mu\text{m}$
<b>Scan Type</b>	Standard Scan
<b>Stylus Force</b>	10 mg
<b>Stylus Scan Range</b>	1 mm
<b>Stylus Type</b>	Radius: 12.5 $\mu\text{m}$

<b>Analytical Results</b>			
<b>Height (<math>\mu\text{m}</math>)</b>	<b>Starting point cursor position</b>	<b>Ending point cursor position</b>	<b>Width scanned area</b>
41.68	0.74 mm	1.124 mm	22.077 mm
61.18	0.548 mm	0.98 mm	23.253 mm
35.43	0.247 mm	0.868 mm	22.272 mm
53.46	0.253 mm	0.715 mm	22.117 mm
64.88	0.354 mm	0.841 mm	22.169 mm

## A2 Colourimetry

Colourimetric measurements were carried out with a Konica Minolta portable Spectrophotometer CM 2600-D with a diameter spot set at 3 mm. The data were acquired with CM-S 100w Spectra Magic™ NX software in SCI and SCE modes.

Table A5 – White paper and Glass slide + white paper colourimetric results.

Product	SCI			SCE		
	L* ± σ	a* ± σ	b* ± σ	L* ± σ	a* ± σ	b* ± σ
White Paper	94.3 ± 0.1	3.2 ± 0.03	-13.7 ± 0.1	94.2 ± 0.1	3.3 ± 0.03	-13.8 ± 0.1
Glass Slide + White Paper	94.1 ± 0.01	2.8 ± 0.02	-12.5 ± 0.1	90.2 ± 0.02	3.0 ± 0.03	-13.4 ± 0.1

Table A6 – Colorimetric coordinates (L\*, a\* and b\*) before and after ageing. Dammar was the resin with the highest variation in the chromatic coordinates after ageing. A different behaviour was detected for Paraloid B67 with good resistance in terms of colour changes.

Product	Unaged Varnishes						Aged Varnishes					
	SCI			SCE			SCI			SCE		
	L* ± σ	a* ± σ	b* ± σ	L* ± σ	a* ± σ	b* ± σ	L* ± σ	a* ± σ	b* ± σ	L* ± σ	a* ± σ	b* ± σ
Dammar	93.2 ± 0.1	1.3 ± 0.1	-7.9 ± 0.3	89.4 ± 0.1	1.4 ± 0.1	-8.5 ± 0.3	88.1 ± 0.4	-0.3 ± 0.1	-0.1 ± 0.4	85.3 ± 0.2	-0.2 ± 0.1	-0.4 ± 0.5
Ketone N	93.7 ± 0.1	2.2 ± 0.1	-10.8 ± 0.3	89.7 ± 0.1	2.4 ± 0.1	-11.5 ± 0.4	91.2 ± 0.3	0.9 ± 0.1	-5.9 ± 0.2	88.1 ± 0.3	1 ± 0.1	-6.4 ± 0.3
MS2A	93.3 ± 0.3	1.4 ± 0.1	-8.4 ± 0.5	89.5 ± 0.2	1.6 ± 0.1	-9.0 ± 0.5	91.6 ± 0.7	0.2 ± 0.4	-4.1 ± 1.1	87.7 ± 0.9	0.3 ± 0.4	-4.6 ± 1.2
Paraloid B67	93.8 ± 0.1	2.7 ± 0.03	-12.3 ± 0.1	90.1 ± 0.1	3 ± 0.03	-13.1 ± 0.1	93.1 ± 0.3	2.6 ± 0.1	-11.2 ± 0.5	89.6 ± 0.4	2.8 ± 0.1	-12.1 ± 0.5

Table A7 – Colorimetric measurements of the resins selected for this research in SCI and SCE modes.

Product	SCI				SCE			
	$\Delta L \pm \sigma$	$\Delta a \pm \sigma$	$\Delta b \pm \sigma$	$\Delta E$	$\Delta L^* \pm \sigma$	$\Delta a^* \pm \sigma$	$\Delta b^* \pm \sigma$	$\Delta E$
Dammar	$-5.1 \pm 0.4$	$-1.6 \pm 0.1$	$7.9 \pm 0.5$	9.5	$-4.1 \pm 0.2$	$-1.7 \pm 0.1$	$8.1 \pm 0.5$	9.3
Ketone N	$-2.5 \pm 0.3$	$-1.3 \pm 0.1$	$4.9 \pm 0.4$	5.6	$-1.7 \pm 0.3$	$-1.4 \pm 0.1$	$5.2 \pm 0.5$	5.6
MS2A	$-1.7 \pm 0.7$	$-1.2 \pm 0.4$	$4.2 \pm 1.2$	4.7	$-1.8 \pm 0.9$	$-1.3 \pm 0.4$	$4.4 \pm 1.3$	4.9
Paraloid B67	$-0.7 \pm 0.3$	$-0.2 \pm 0.1$	$1.0 \pm 0.5$	1.2	$-0.5 \pm 0.4$	$-0.2 \pm 0.1$	$1.0 \pm 0.5$	1.2

### A3 Differential Scanning Calorimetry (DSC) analysis

A Double-furnace LAB SYS-DSC 8500 Perkin Elmer was used to determine the specific heat at constant pressure ( $C_p$ ) of all the varnishes. This technique reveals qualitative and quantitative information about temperature-dependent physical and chemical changes concerning endothermic and exothermic processes that occur during heating. Perkin Elmer DSC is based on power compensated principle (Tanaka, 1992; Höhne, Hemminger and Flammersheim, 2003).

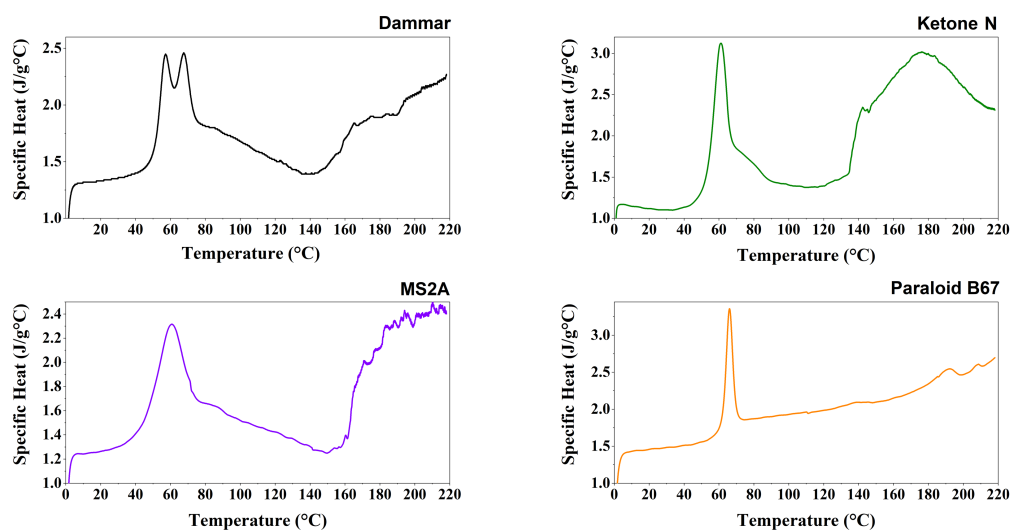


Figure A1 – Specific heat capacity ( $C_p$ ) ( $J/g \cdot ^\circ C$ ) vs temperature ( $^\circ C$ ) obtained from DSC (LAB SYS-DSC 8500 Perkin Elmer) for all the raw unaged resins. The  $C_p$  values and the temperature are listed in Table 3.9 (see section 3.5.7).

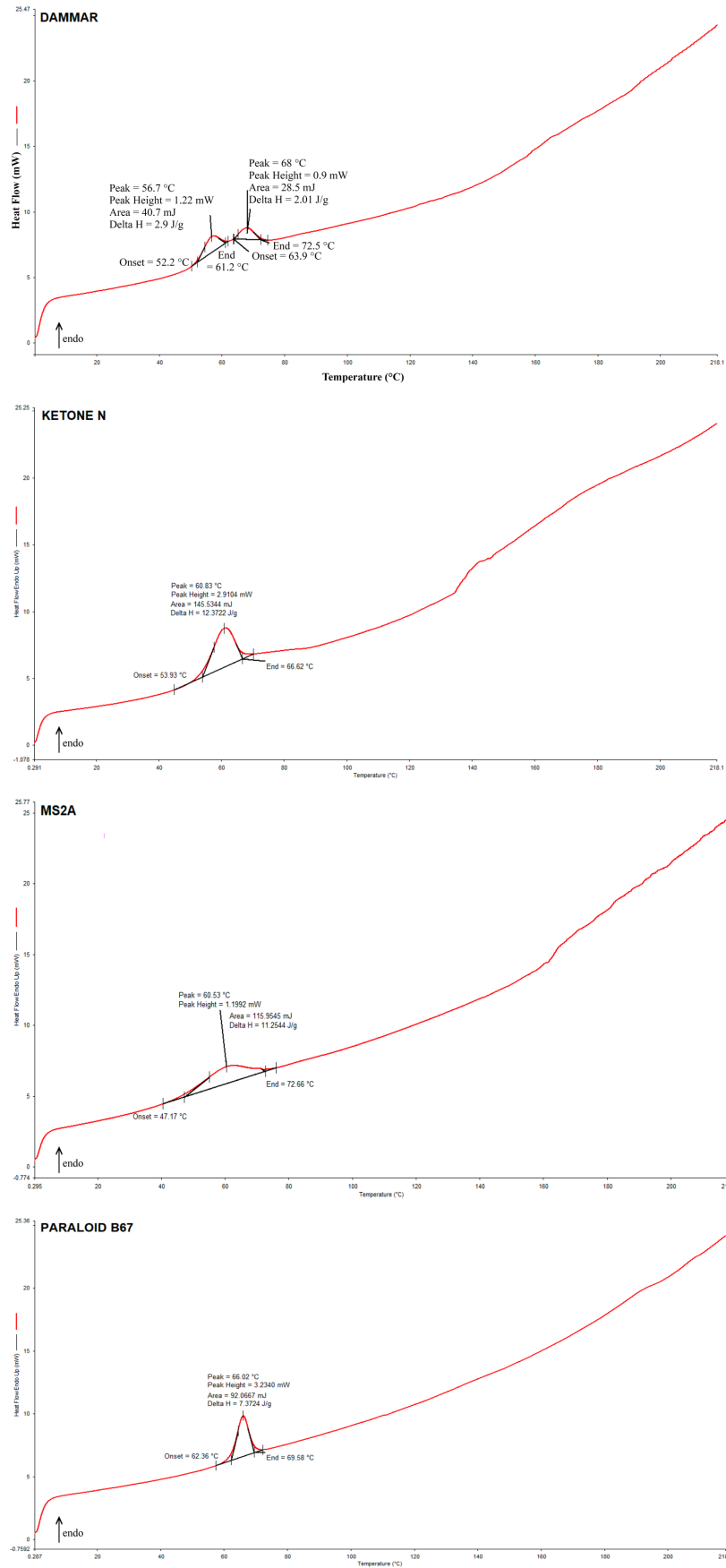


Figure A2 – DSC curve (LAB SYS-DSC 8500 Perkin Elmer) of raw unaged dammar, Ketone N, MS2A and Paraloid B67 resins.

## Appendix B Er:YAG LASER TESTS & EXPERIMENTAL RESULTS

Appendix B contains the following topics:

- B1) Transmission FT-IR spectra;
- B2) Mid-IR integrating sphere measurement;
- B3) Fotona Fidelis Er:YAG lasers system specifications;
- B4) FLIR T620bx IR thermal camera;
- B5) FLIR with K type thermocouple;
- B6) FLIR thermal camera: thermal data acquired on the uncoated glass slide;
- B7) Transient temperature profiles of varnishes regarded as semi-infinite solids:

*B7.1 Dammar – VSP mode ( $\tau_L \approx 100 \mu\text{s}$ );*

*B7.2 Dammar – SP mode ( $\tau_L \approx 300 \mu\text{s}$ );*

*B7.3 Ketone N – VSP mode ( $\tau_L \approx 100 \mu\text{s}$ );*

*B7.4 Ketone N – SP mode ( $\tau_L \approx 300 \mu\text{s}$ );*

*B7.5 MS2A – VSP mode ( $\tau_L \approx 100 \mu\text{s}$ );*

*B7.6 MS2A – SP mode ( $\tau_L \approx 300 \mu\text{s}$ ).*

- B8) An example of FlexPDE script for the 2D simulation

- B9) 2D Simulations:

*B9.1 Dammar – VSP mode ( $\tau_L \approx 100 \mu\text{s}$ );*

*B9.2 Dammar – SP mode ( $\tau_L \approx 300 \mu\text{s}$ );*

*B9.3 Ketone N – VSP mode ( $\tau_L \approx 100 \mu\text{s}$ );*

*B9.4 Ketone N – SP mode ( $\tau_L \approx 300 \mu\text{s}$ );*

*B9.5 MS2A – VSP mode ( $\tau_L \approx 100 \mu\text{s}$ );*

*B9.6 Ketone N – SP mode ( $\tau_L \approx 300 \mu\text{s}$ ).*

- B10) Varnish parameters:

*B10.1 Dammar;*

*B10.2 Ketone N;*

*B10.3 MS2A;*

*B10.4 Paraloid B67.*

### B1) Transmission FT-IR spectra

Transmission spectra of all the aged varnish films acquired using the Perkin Elmer Frontier bench, Spectrum 400TM FT-IR. The working wave-number range was from 4000 to 2000  $\text{cm}^{-1}$ , and the spectra were over 16 scans at 4  $\text{cm}^{-1}$  resolution.

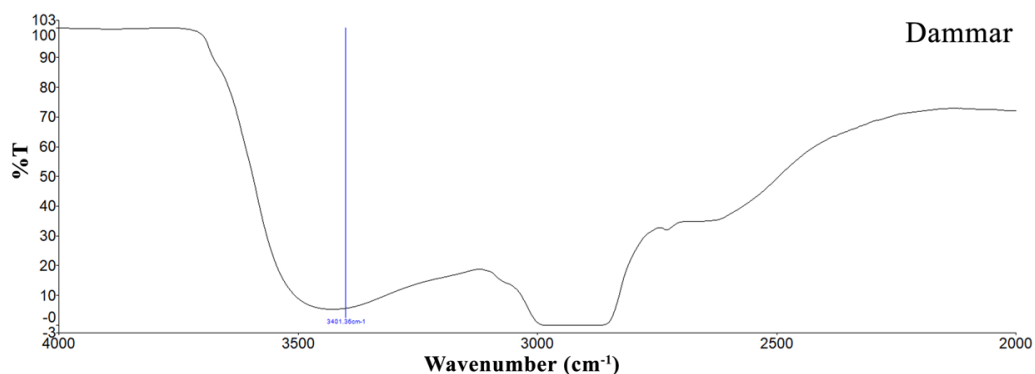


Figure B1 – Transmission spectra of dammar film. The transmission spectrum of the glass was subtracted from the spectra of the aged film on glass slide to obtain the percentage transmission component (% T) of the varnish film at the Er:YAG laser wavelength (2940 nm).

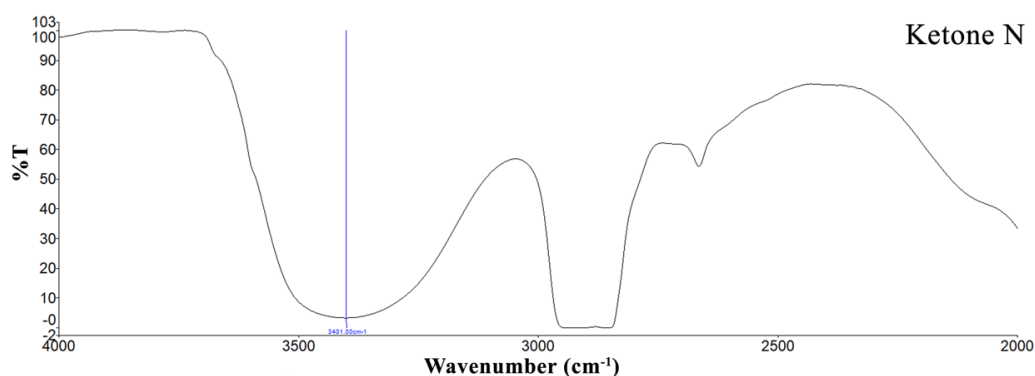


Figure B2 – Transmission spectra of Ketone N film. The transmission spectrum of the glass was subtracted from the spectra of the aged film on glass slide to obtain the percentage transmission component (% T) of the varnish film at the Er:YAG laser wavelength (2940 nm).

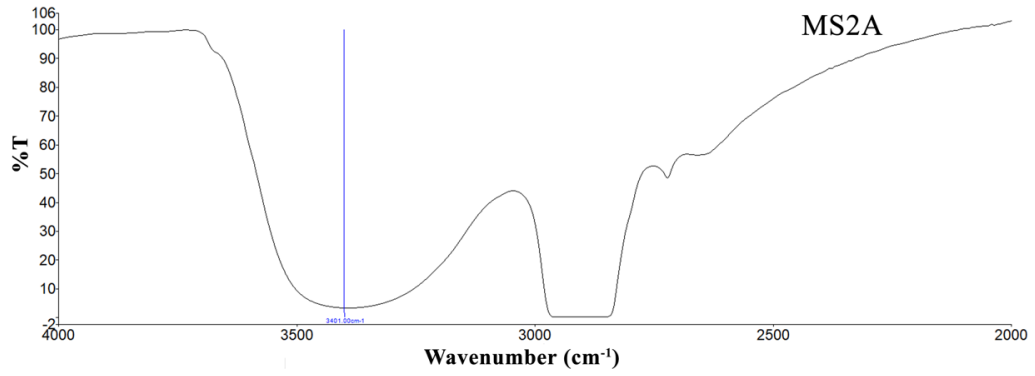


Figure B3 – Transmission spectra of MS2A film. The transmission spectrum of the glass was subtracted from the spectra of the aged film on glass slide to obtain the percentage transmission component (% T) of the varnish film at the Er:YAG laser wavelength (2940 nm).

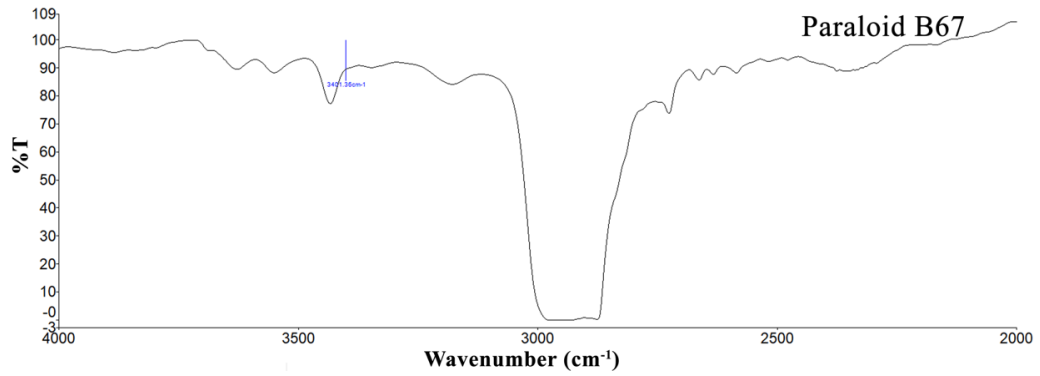


Figure B4 – Transmission spectra of Paraloid B67 film. The transmission spectrum of the glass was subtracted from the spectra of the aged films on glass slides to obtain the percentage transmission component (% T) of the varnish films at the Er:YAG laser wavelength (2940 nm).

## B2) Mid-IR integrating sphere measurement

Reflectance spectra of all the aged coating films acquired using the Perkin Elmer Frontier bench, Spectrum 400TM FT-IR equipped with a PIKE IntegratIR™ sphere. The working wave-number range was from 4000 to 2000  $\text{cm}^{-1}$  and the spectra were recorded at 32 scans and 8  $\text{cm}^{-1}$  resolution.

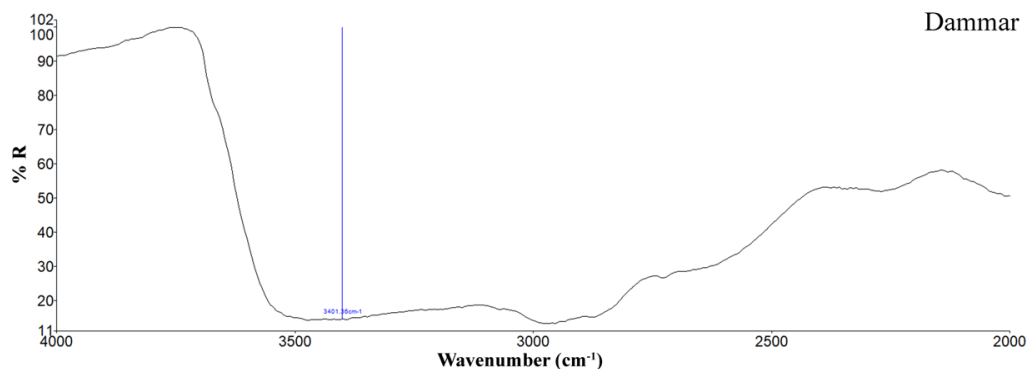


Figure B5 – Reflectance spectra of the aged dammar varnish applied on glass slides. The reflectance spectra of the glass slide was subtracted from the spectra of the aged film to obtain only component %R of the resins at the Er:YAG laser wavelength (2940 nm).

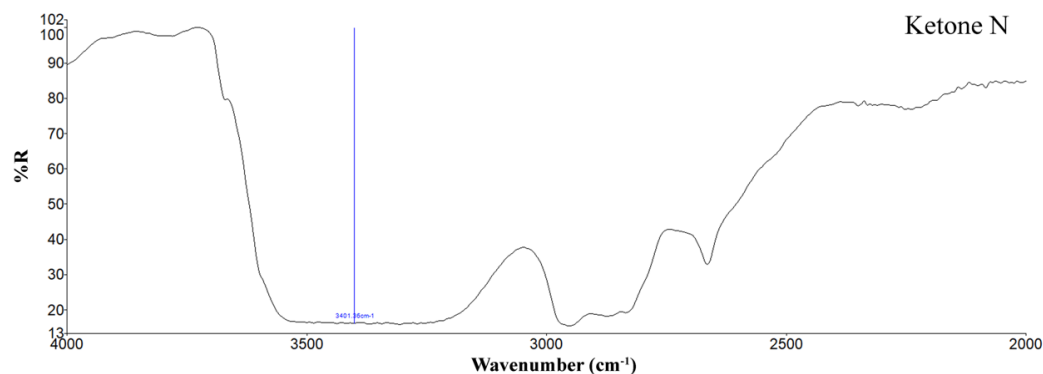


Figure B6 – Reflectance spectra of the aged Ketone N varnish applied on glass slides. The reflectance spectra of the glass slide was subtracted from the spectra of the aged film to obtain only component %R of the resins at the Er:YAG laser wavelength (2940 nm).

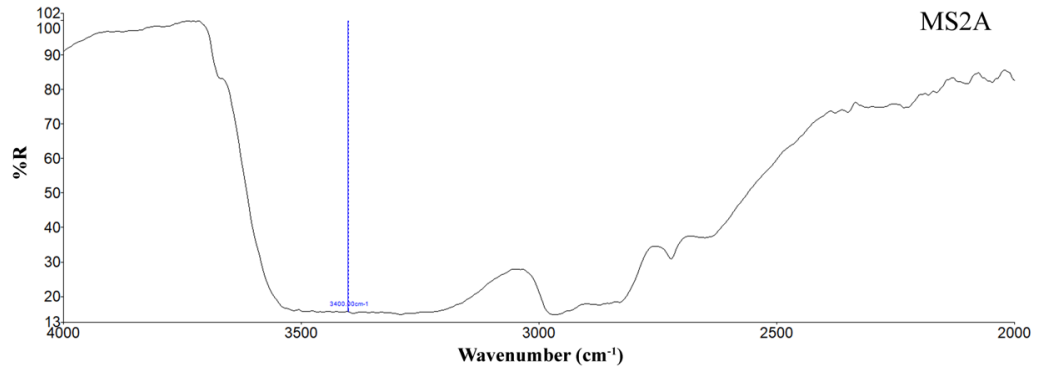


Figure B7 – Reflectance spectra of the aged MS2A varnish applied on glass slides. The reflectance spectra of the glass slide was subtracted from the spectra of the aged film to obtain only component %R of the resins at the Er:YAG laser wavelength (2940 nm).

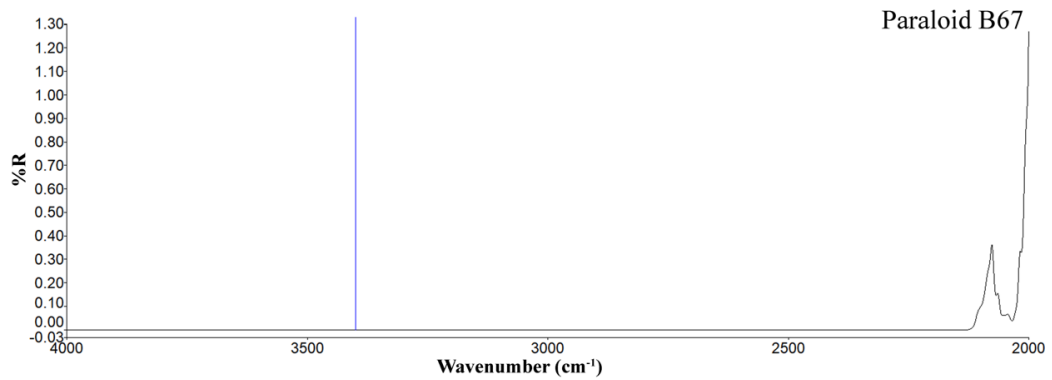


Figure B8 – Reflectance spectra of the aged Paraloid B67 varnish applied on glass slides. The reflectance spectra of the glass slide was subtracted from the spectra of the aged film to obtain only component %R of the resins at the Er:YAG laser wavelength (2940 nm).

### B3) Fotona Fidelis Er:YAG lasers system specifications

The lasers employed for this research are two Fotona Fidelis Er:YAG lasers. Table B1 presents the two laser system specifications.

Table B1 – Fotona laser specifications.

<b>Laser Type</b>	<b>Fotona Fidelis<sup>XS</sup></b>	<b>Fotona XS Dynamis</b>
Wavelength	2940 nm	2940 nm
Max Fluence	Up to 15 J/cm <sup>2</sup>	Up to 48 J/cm <sup>2</sup>
Max. power	15 W	20 W
Pulse duration	VSP ( $\tau_L \approx 100 \mu\text{s}$ ); SP ( $\tau_L \approx 300 \mu\text{s}$ ); LP ( $\tau_L \approx 600 \mu\text{s}$ ); VLP ( $\tau_L \approx 1000 \mu\text{s}$ )	SSP ( $\tau_L \approx 50 \mu\text{s}$ ); MSP ( $\tau_L \approx 100 \mu\text{s}$ ); SP ( $\tau_L \approx 300 \mu\text{s}$ ), LP ( $\tau_L \approx 600 \mu\text{s}$ ); VLP ( $\tau_L \approx 1000 \mu\text{s}$ )
Max. Frequency	50 Hz	50 Hz
Typology of laser beam delivery	7-mirror articulated arm	FeatherLight arm

### B4) FLIR T620bx IR thermal camera

An FLIR T620bx IR thermal camera has been employed for this PhD research. The camera was able to observe changes in temperatures up to 160°C.



Figure B9 – FLIR T620bx IR thermal camera.

Table B2 – FLIR thermal camera specifications.

<b>Imaging Performance</b>	
Field of view / min focus distance	15° x 11°/ 0.5 m
Spatial resolution	1.23 mrad for 45° lens
Thermal sensitivity	0.08 °C at 30 °C
<b>Detector</b>	
Resolution	640x480 pixels
Spectral range	7.8 to 14 μm
Image frequency	30 Hz
Focus	Manual/autofocus
Detector cooling	Uncooled micro-bolometer
<b>Measurement</b>	
Accuracy	± 2 °C or ± 2% of readings
Temperature range	-40 °C to 160 °C,
Atmospheric correlation	atmospheric temperature, and relative humidity
Emissivity correction	Variable from 0.01 to 1.0 or selected from materials list
<b>Image storage</b>	
Type	IR/visual images; simultaneous storage of visual and IR images
Format	Standard JPEG
<b>Environmental specifications</b>	
Operating temperature range	-15 to +50 °C
Storage temperature range	-40 °C to +70 °C
Humidity	IEC 60068-2-30/24h, 95% relative humidity +25 °C to +40 °C, non-condensing
Encapsulation	IP 54, IEC 60529

### B5) FLIR with K type thermocouple

An experiment was configured to verify the accuracy of the FLIR T620bx IR thermal camera (Figure B10).

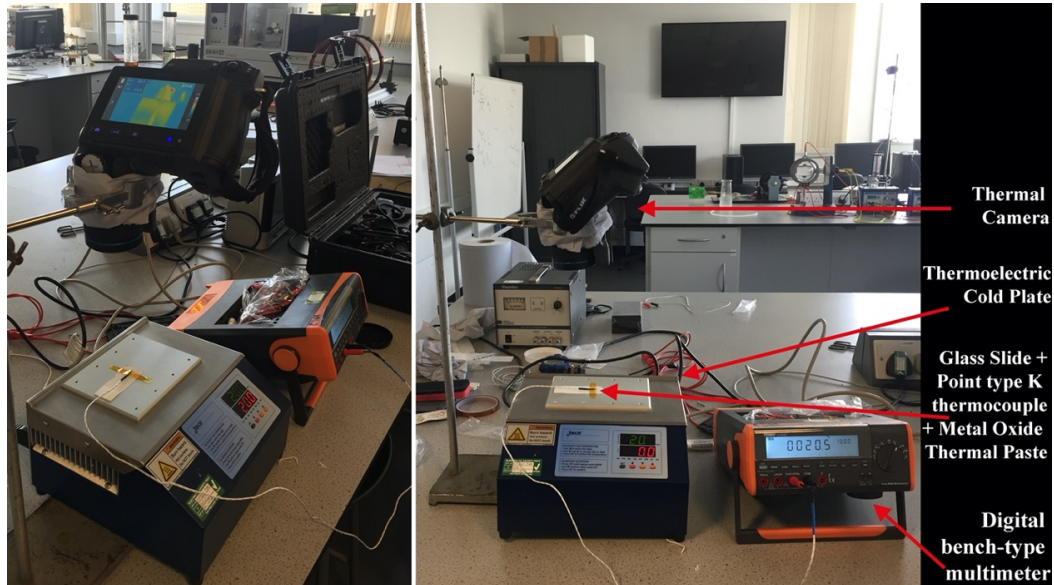


Figure B10 – Experimental set-up using the FLIR T620bx IR thermal camera, a point type K thermocouple and a thermoelectric solid-state Heat/Cool plate to check the reliability of the thermal camera in pre-set temperature values.

An uncoated glass slide was placed onto a thermoelectric solid-state Heat/Cool plate (AHP-301CPV 240V, 1.5A by Teca) and a thermal oxide thermal paste (554-311, 0.65W/m·K by RS PRO) was spread over the lower face of the glass slide in contact with the plate. Thus, a point type K thermocouple (Ulysses UTT10K Universal Meter K thermocouple) was put on top of the glass slide to record the increase in temperatures. The camera was set with the glass emissivity ( $\epsilon = 0.93$ ).

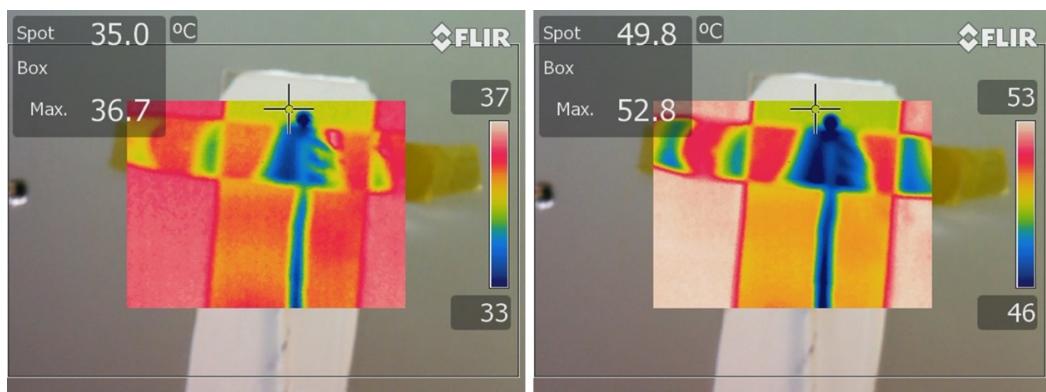


Figure B11 - Visual and IR images showing the recorded temperature registered by the thermal camera during the tests.

As the temperature on the Heat/Cool plate was changed from room temperature 20 °C to 60 °C, the temperature readings of the IR thermal camera and those obtained using the K thermocouple were recorded as soon as the temperatures shown in the digital multimeter were stable. The acquired temperatures are reported in Table C5.1.

Table B3 – Temperature data acquired using a Type K thermocouple and IR thermal camera vs. temperature from the Hot Plate.

Hot Plate	Type K thermocouple	FLIR Thermal Camera
20	20.5	20.6
25	25.2	25.6
30	29.6	30.3
35	34.0	35.2
40	38.7	40.1
45	43.1	45.0
50	47.7	49.8
52	50.6	52.8
57	53.8	56.8
60	56.7	59.6

The data recorded by using the IR thermal camera has proven that the camera temperature readings differ from the set-temperature of the hot plate heat source of  $\pm 0.6^{\circ}\text{C}$ , over the range of the temperature selected for the test. Thus, the data acquired with the device returns a satisfying reliability considering the accuracy of  $\pm 2^{\circ}\text{C}$  specified by the manufacturer.

**B6) FLIR thermal camera: thermal data acquired on an uncoated glass slide**

Prior to the acquisition of the heat impact on the varnishes selected for this study, the FLIR thermal camera was used to calculate the heat impact on an uncoated glass slide in a range of fluences, as shown in the laser's unit displays, between 0.6 and 2.4 J/cm<sup>2</sup>.

The methodology used for this initial test was the same as the one already discussed in section 4.2.4.1. The room temperature recorded together with the Relative Humidity (RH) were 23.3°C and 48.6%, respectively.

Table B4 - Maximum effect of temperature variation recorded by using the FLIR thermal camera and the mean maximum heat impact ( $\Delta T_{\text{mean}}$ ) on a dry glass slide, according to Eq. 4.11.

Dry - VSP			Dry - SP		
Fluence (J/cm <sup>2</sup> )	Average max temperature variation recorded $\pm \sigma$ (°C)	$\Delta T_{\text{mean}} \pm \sigma$ (°C)	Fluence (J/cm <sup>2</sup> )	Average max temperature variation recorded $\pm \sigma$ (°C)	$\Delta T_{\text{mean}} \pm \sigma$ (°C)
<b>0.6</b>	25 $\pm$ 0.1	0.5 $\pm$ 0.1	<b>0.6</b>	25 $\pm$ 0.1	0.5 $\pm$ 0.2
<b>1</b>	26 $\pm$ 0.1	1 $\pm$ 0	<b>1</b>	26 $\pm$ 0	1 $\pm$ 0.1
<b>1.5</b>	27 $\pm$ 0.1	2 $\pm$ 0	<b>1.5</b>	26 $\pm$ 0.1	1 $\pm$ 0.8
<b>2</b>	27 $\pm$ 0.2	2 $\pm$ 0	<b>2</b>	27 $\pm$ 0.1	2 $\pm$ 0.1
<b>2.4</b>	28 $\pm$ 0.0	3 $\pm$ 0.1	<b>2.4</b>	27 $\pm$ 0.1	2 $\pm$ 0.1

The average max temperature variation recorded and presented in table B4 shows a linear increase in temperature for both the VSP and SP modes, which differs only 4.3 °C in VSP mode and 4.1 °C in SP mode from the room temperature.

**B7) Transient temperature profiles of varnishes regarded as semi-infinite solids**

*B7.1 Dammar – VSP mode ( $\tau_L \approx 100 \mu\text{s}$ ):*

Figure B12 – Representation of the heat-wave propagation inside the **dammar film**, in VSP mode, at different times [100  $\mu\text{s}$  (gray), 200  $\mu\text{s}$  (pink), 400  $\mu\text{s}$  (cyan), 800  $\mu\text{s}$  (brown) and 1 ms (magenta)] as a function of depth (A and C) and the temperature rise evolution at various depth [0 (black), 5  $\mu\text{m}$  (red), 10  $\mu\text{m}$  (blue), 20  $\mu\text{m}$  (green), 33.21  $\mu\text{m}$  (purple)] as a function of time (B and D). The laser beam diameter was set at  $\varnothing = 4 \text{ mm}$ . Temperature is given relative to room temperature (25 °C).

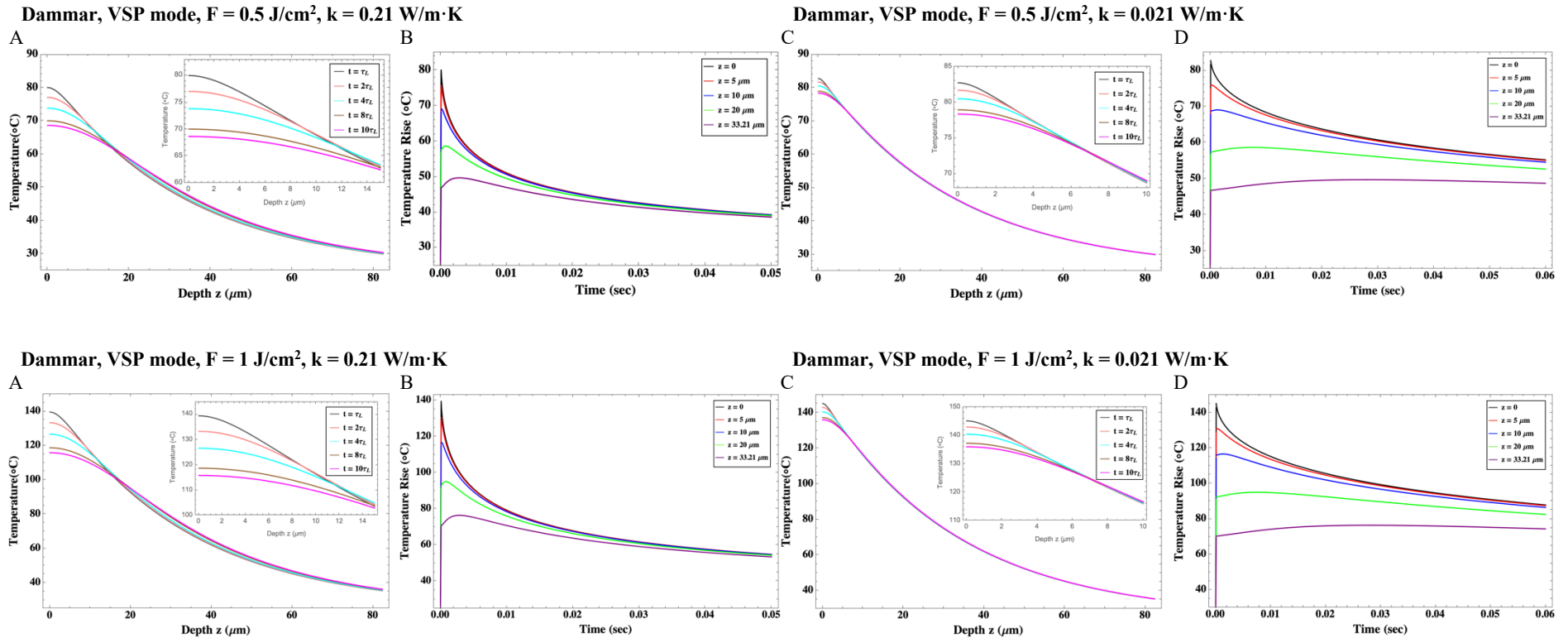


Figure B12 – Representation of the heat-wave propagation inside the **dammar film**, in VSP mode, at different times [100  $\mu\text{s}$  (gray), 200  $\mu\text{s}$  (pink), 400  $\mu\text{s}$  (cyan), 800  $\mu\text{s}$  (brown) and 1 ms (magenta)] as a function of depth (A and C) and the temperature rise evolution at various depth [0 (black), 5  $\mu\text{m}$  (red), 10  $\mu\text{m}$  (blue), 20  $\mu\text{m}$  (green), 33.21  $\mu\text{m}$  (purple)] as a function of time (B and D). The laser beam diameter was set at  $\varnothing = 4$  mm. Temperature is given relative to room temperature (25  $^{\circ}\text{C}$ ), (continued).

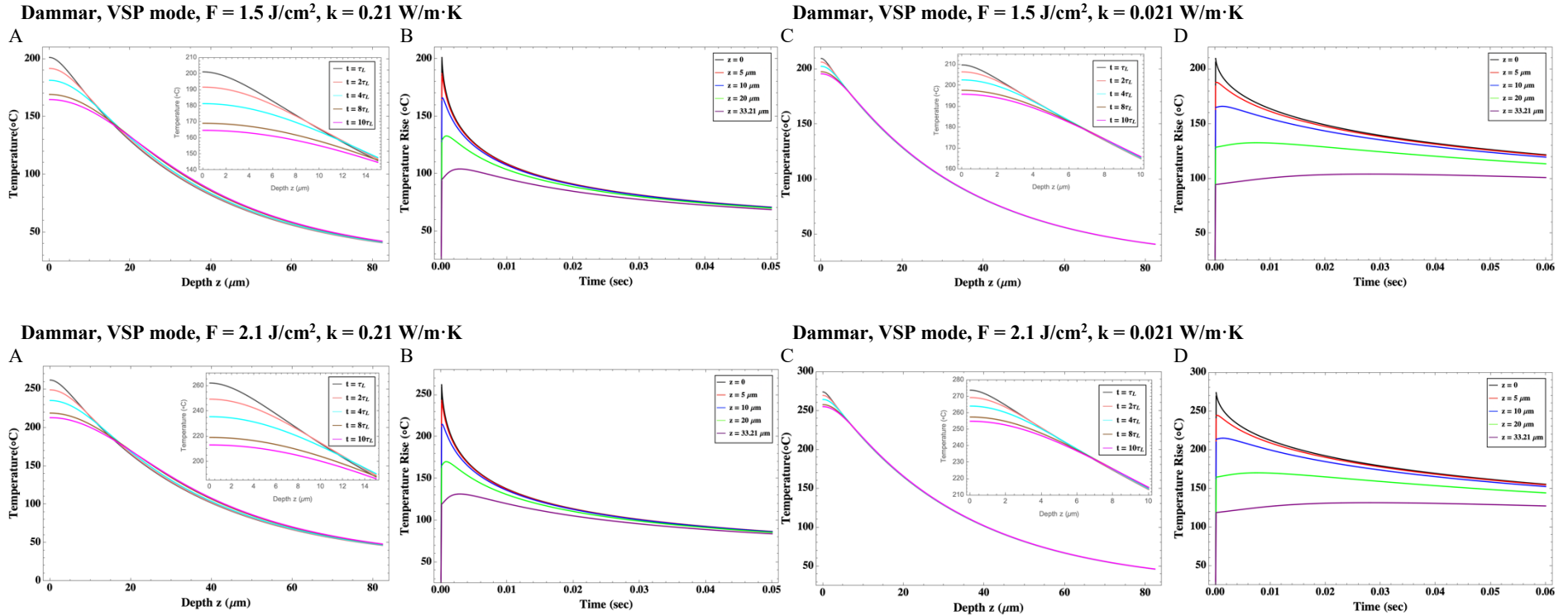
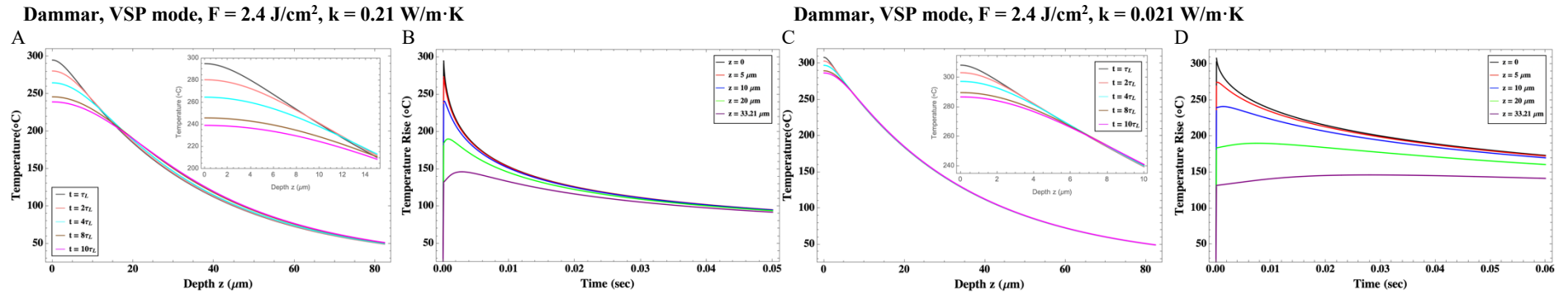


Figure B12 – Representation of the heat-wave propagation inside the **dammar film**, in VSP mode, at different times [100  $\mu\text{s}$  (gray), 200  $\mu\text{s}$  (pink), 400  $\mu\text{s}$  (cyan), 800  $\mu\text{s}$  (brow) and 1 ms (magenta)] as a function of depth (A and C) and the temperature rise evolution at various depth [0 (black), 5  $\mu\text{m}$  (red), 10  $\mu\text{m}$  (blue), 20  $\mu\text{m}$  (green), 33.21  $\mu\text{m}$  (purple)] as a function of time (B and D). The laser beam diameter was set at  $\varnothing = 4$  mm. Temperature is given relative to room temperature (25  $^{\circ}\text{C}$ ).



B7.2 Dammar – SP mode ( $\tau_L \approx 300 \mu s$ ):

Figure B13 – Representation of the heat-wave propagation inside the **dammar film**, in SP mode, at different times [300  $\mu s$  (gray), 600  $\mu s$  (pink), 1.2 ms (cyan), 2.4 ms (brow) and 3 ms (magenta)] as a function of depth (A and C) and the temperature rise evolution at various depth [0 (black), 5  $\mu m$  (red), 10  $\mu m$  (blue), 20  $\mu m$  (green), 33.21  $\mu m$  (purple)] as a function of time (B and D). The laser beam diameter was set at  $\varnothing = 4 \text{ mm}$ . Temperature is given relative to room temperature (25 °C).

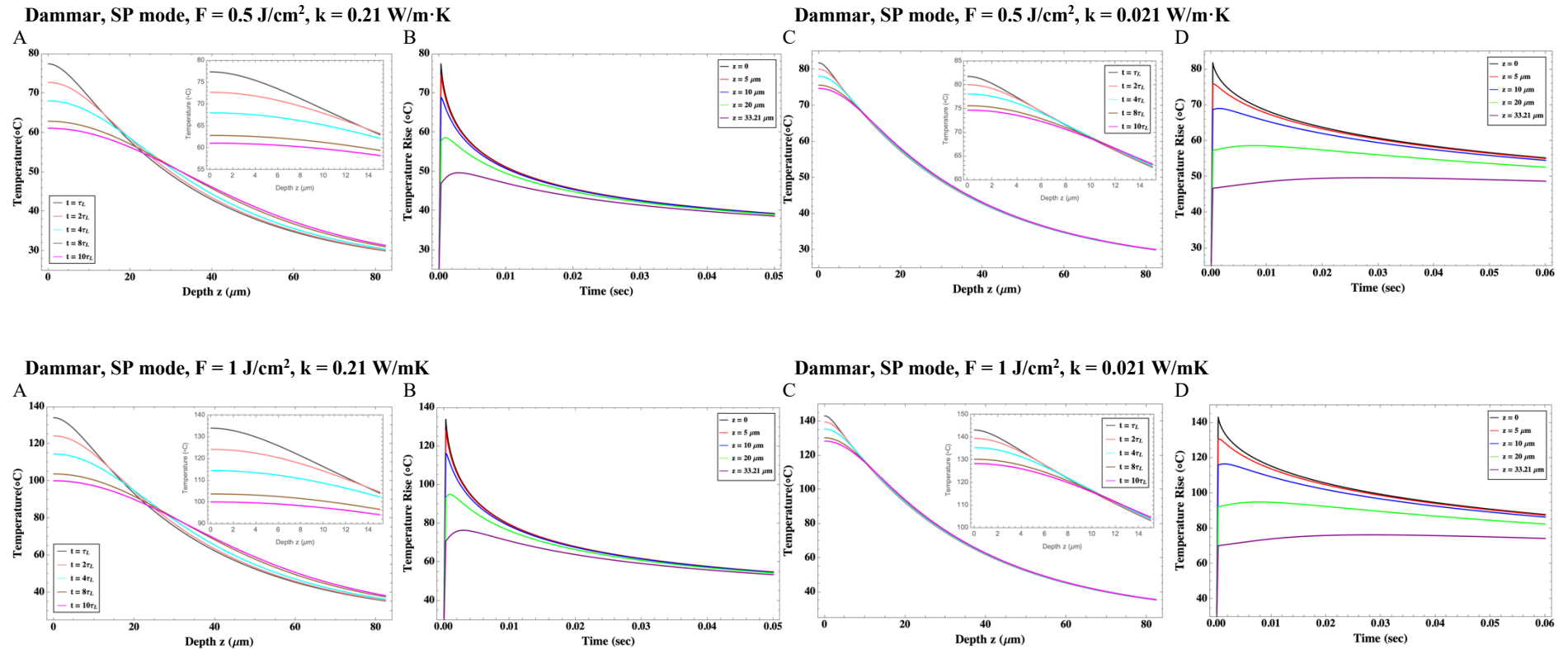


Figure B13 – Representation of the heat-wave propagation inside the **dammar film**, in SP mode, at different times [300  $\mu$ s (gray), 600  $\mu$ s (pink), 1.2 ms (cyan), 2.4 ms (brow) and 3 ms (magenta)] as a function of depth (A and C) and the temperature rise evolution at various depth [0 (black), 5  $\mu$ m (red), 10  $\mu$ m (blue), 20  $\mu$ m (green), 33.21  $\mu$ m (purple)] as a function of time (B and D). The laser beam diameter was set at  $\varnothing = 4$  mm. Temperature is given relative to room temperature (25  $^{\circ}$ C), (continued).

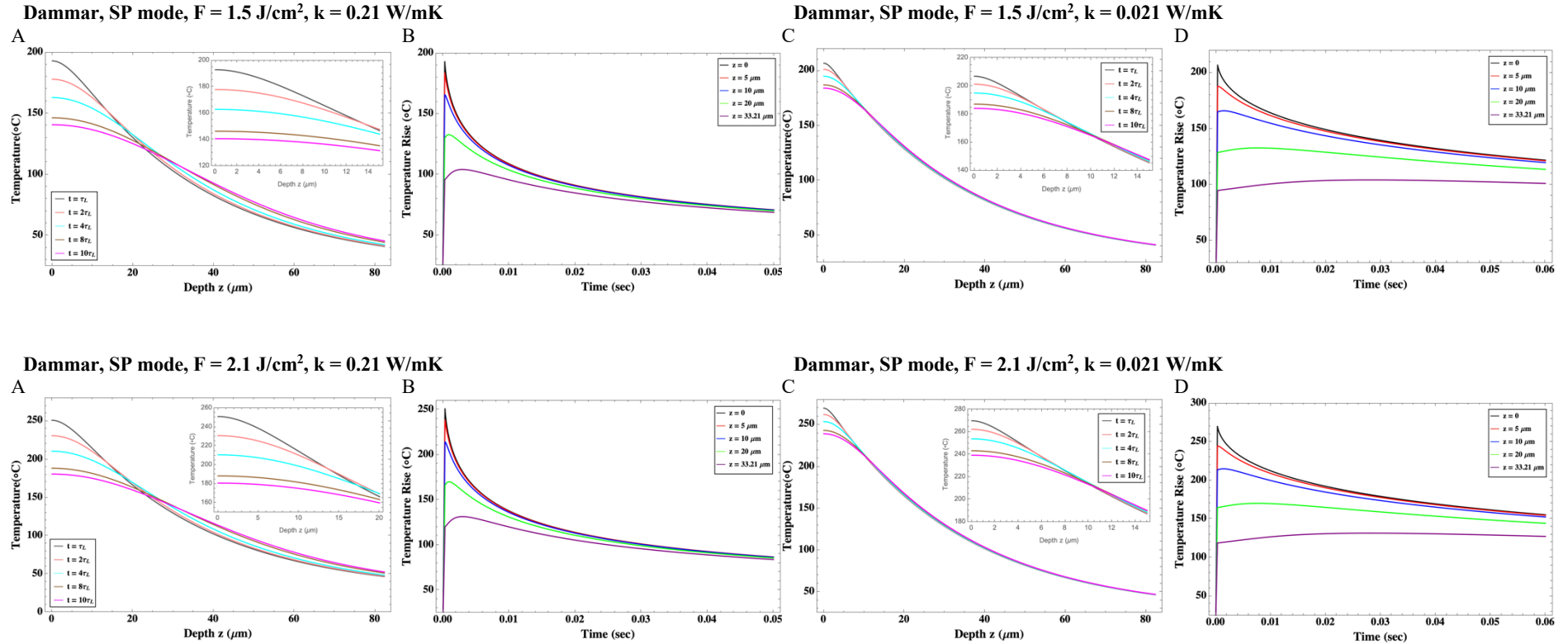
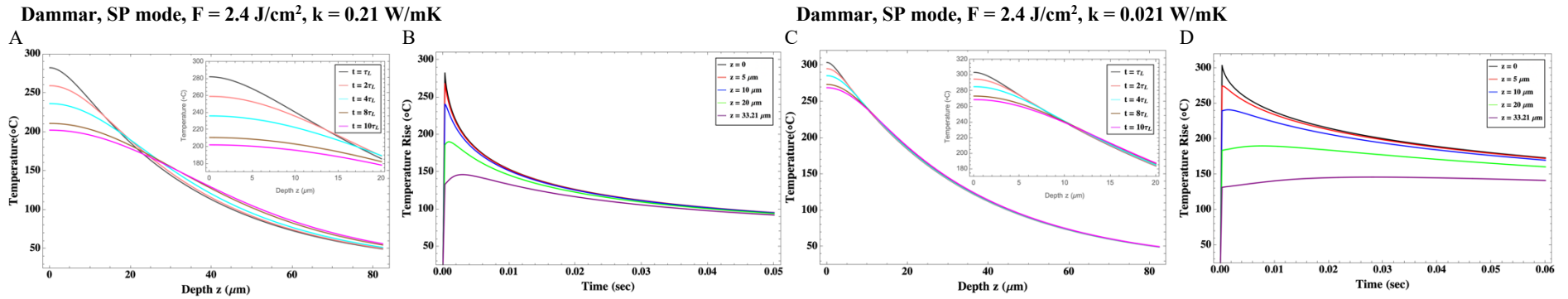


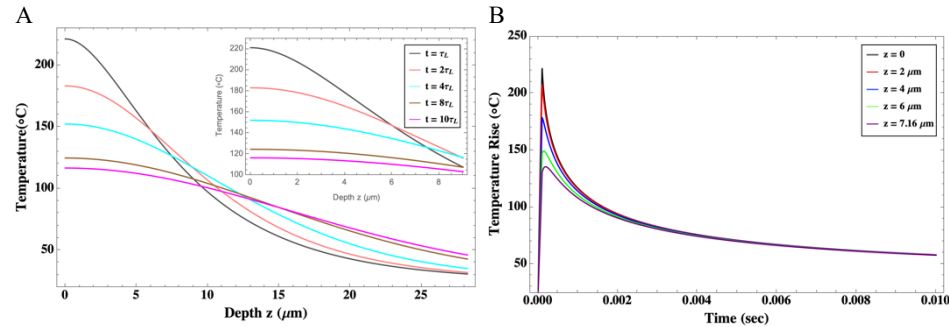
Figure B13 – Representation of the heat-wave propagation inside the **dammar film**, in SP mode, at different times [300  $\mu$ s (gray), 600  $\mu$ s (pink), 1.2 ms (cyan), 2.4 ms (brow) and 3 ms (magenta)] as a function of depth (A and C) and the temperature rise evolution at various depth [0 (black), 5  $\mu$ m (red), 10  $\mu$ m (blue), 20  $\mu$ m (green), 33.21  $\mu$ m (purple)] as a function of time (B and D). The laser beam diameter was set at  $\varnothing = 4$  mm. Temperature is given relative to room temperature (25  $^{\circ}$ C).



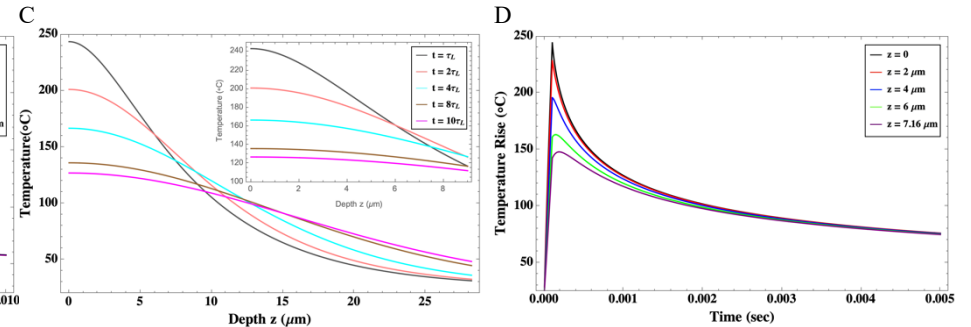
B7.3 Ketone N – VSP mode ( $\tau_L \approx 100 \mu s$ ):

Figure B14 – Representation of the heat-wave propagation inside the **Ketone N film**, in VSP mode, at different times [100  $\mu s$  (gray), 200  $\mu s$  (pink), 400  $\mu s$  (cyan), 800  $\mu s$  (brown) and 1 ms (magenta)] as a function of depth (A and C) and the temperature rise evolution at various depth [0 (black), 2  $\mu m$  (red), 4  $\mu m$  (blue), 6  $\mu m$  (green), 7.16  $\mu m$  (purple)] as a function of time (B and D). The laser beam diameter was set at  $\varnothing = 4 \text{ mm}$ . Temperature is given relative to room temperature (25 °C).

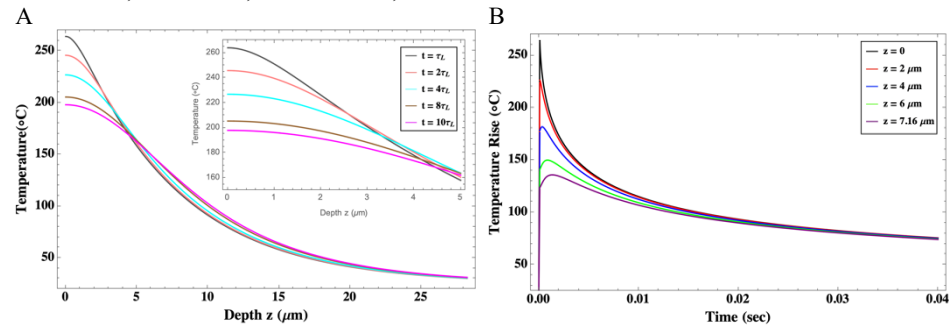
Temperature evolution obtained using the %R from FTIR data  
Ketone N, VSP mode,  $F = 0.5 \text{ J/cm}^2$ ,  $k = 0.22 \text{ W/mK}$



Temperature evolution obtained using the %R from Fresnel equation (Eq. 4.21)



Temperature evolution obtained using the %R from FTIR data  
Ketone N, VSP mode,  $F = 0.5 \text{ J/cm}^2$ ,  $k = 0.022 \text{ W/mK}$



Temperature evolution obtained using the %R from Fresnel equation (Eq. 4.21)

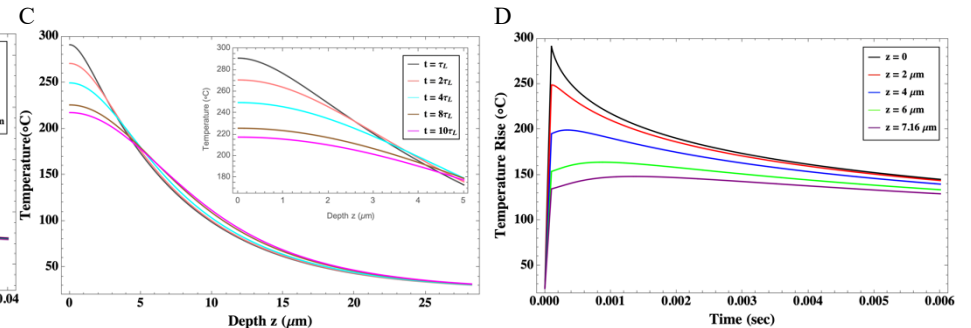
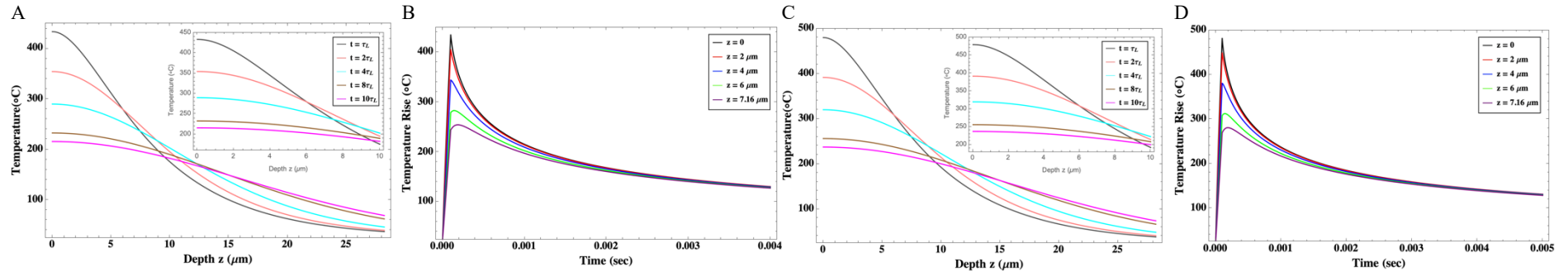


Figure B14 – Representation of the heat-wave propagation inside the **Ketone N film**, in VSP mode, at different times [100  $\mu\text{s}$  (gray), 200  $\mu\text{s}$  (pink), 400  $\mu\text{s}$  (cyan), 800  $\mu\text{s}$  (brown) and 1 ms (magenta)] as a function of depth (A and C) and the temperature rise evolution at various depth [0 (black), 2  $\mu\text{m}$  (red), 4  $\mu\text{m}$  (blue), 6  $\mu\text{m}$  (green), 7.16  $\mu\text{m}$  (purple)] as a function of time (B and D). The laser beam diameter was set at  $\varnothing = 4$  mm. Temperature is given relative to room temperature (25  $^{\circ}\text{C}$ ), (continued).

Temperature evolution obtained using the %R from FTIR data  
**Ketone N, VSP mode,  $F = 1 \text{ J/cm}^2$ ,  $k = 0.22 \text{ W/mK}$**

Temperature evolution obtained using the %R from Fresnel equation (Eq. 4.21)



Temperature evolution obtained using the %R from FTIR data  
**Ketone N, VSP mode,  $F = 1 \text{ J/cm}^2$ ,  $k = 0.022 \text{ W/mK}$**

Temperature evolution obtained using the %R from Fresnel equation (Eq. 4.21)

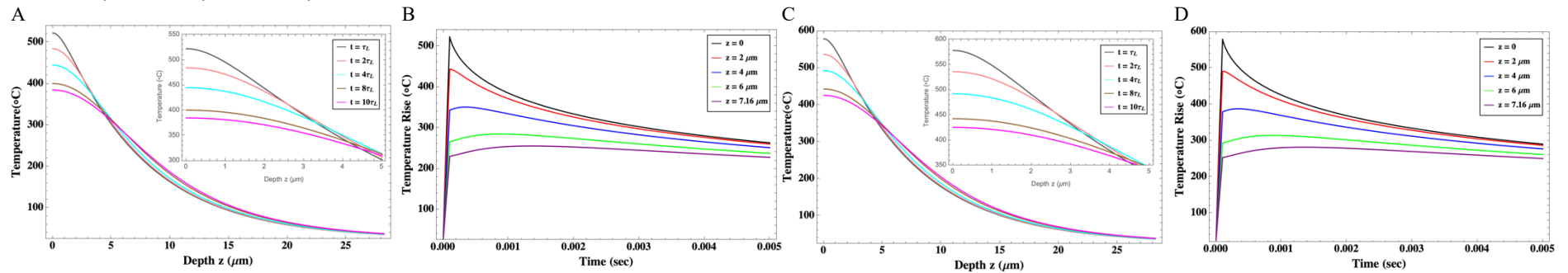
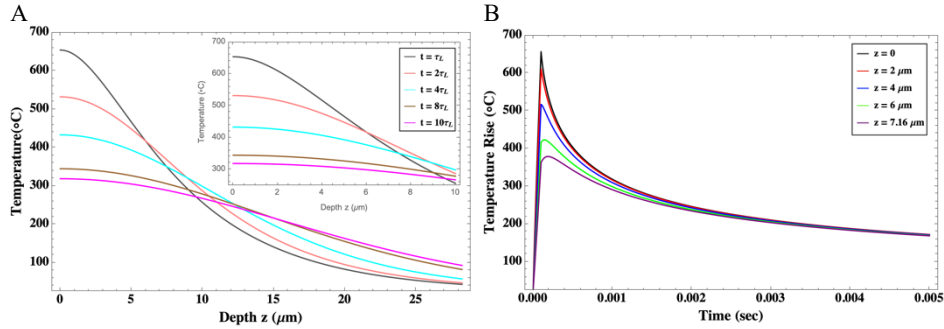
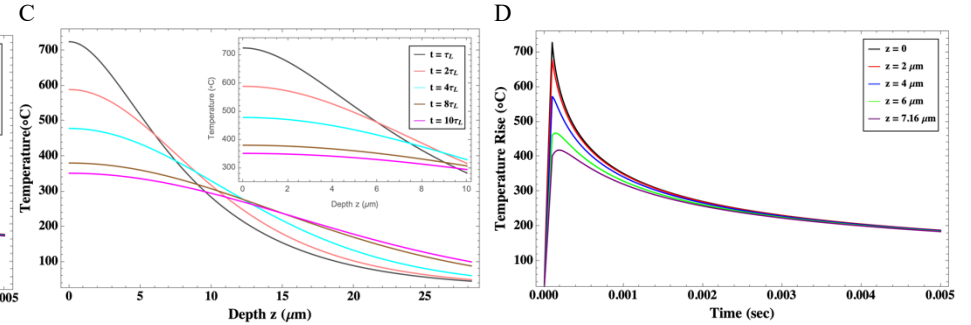


Figure B14 – Representation of the heat-wave propagation inside the **Ketone N film**, in VSP mode, at different times [100  $\mu\text{s}$  (gray), 200  $\mu\text{s}$  (pink), 400  $\mu\text{s}$  (cyan), 800  $\mu\text{s}$  (brown) and 1 ms (magenta)] as a function of depth (A and C) and the temperature rise evolution at various depth [0 (black), 2  $\mu\text{m}$  (red), 4  $\mu\text{m}$  (blue), 6  $\mu\text{m}$  (green), 7.16  $\mu\text{m}$  (purple)] as a function of time (B and D). The laser beam diameter was set at  $\varnothing = 4$  mm. Temperature is given relative to room temperature (25  $^{\circ}\text{C}$ ), (continued).

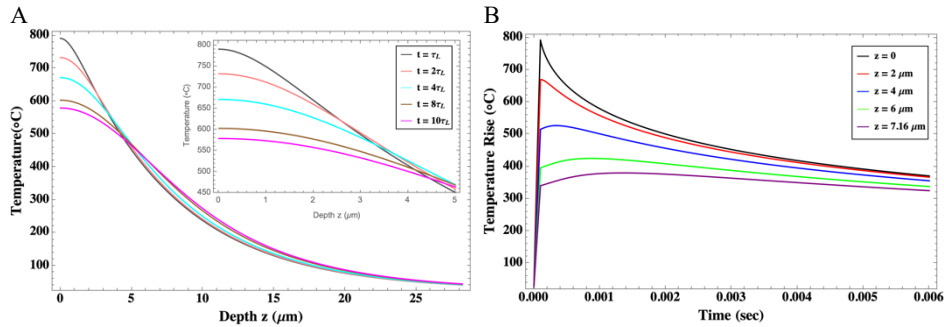
Temperature evolution obtained using the %R from FTIR data  
**Ketone N, VSP mode,  $F = 1.5 \text{ J/cm}^2$ ,  $k = 0.22 \text{ W/mK}$**



Temperature evolution obtained using the %R from Fresnel equation (Eq. 4.21)



Temperature evolution obtained using the %R from FTIR data  
**Ketone N, VSP mode,  $F = 1.5 \text{ J/cm}^2$ ,  $k = 0.022 \text{ W/mK}$**



Temperature evolution obtained using the %R from Fresnel equation (Eq. 4.21)

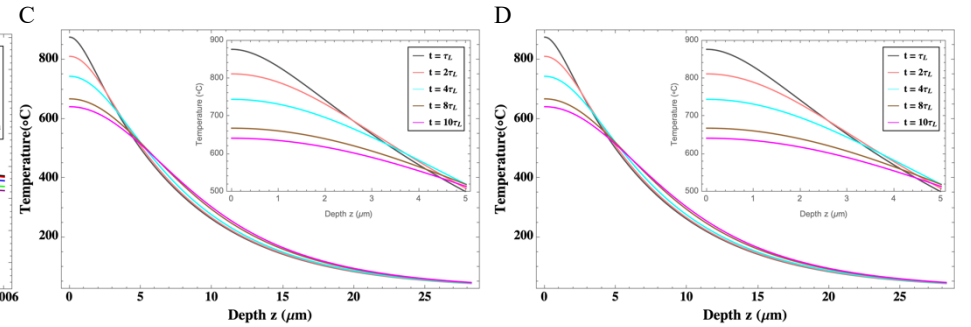
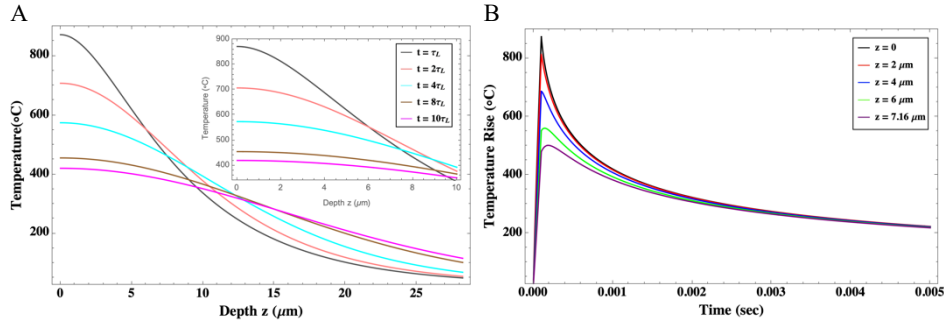
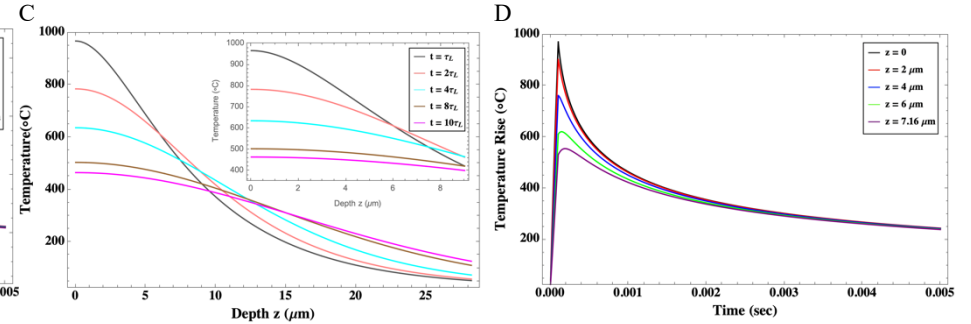


Figure B14 – Representation of the heat-wave propagation inside the **Ketone N film**, in VSP mode, at different times [100  $\mu\text{s}$  (gray), 200  $\mu\text{s}$  (pink), 400  $\mu\text{s}$  (cyan), 800  $\mu\text{s}$  (brown) and 1 ms (magenta)] as a function of depth (A and C) and the temperature rise evolution at various depth [0 (black), 2  $\mu\text{m}$  (red), 4  $\mu\text{m}$  (blue), 6  $\mu\text{m}$  (green), 7.16  $\mu\text{m}$  (purple)] as a function of time (B and D). The laser beam diameter was set at  $\varnothing = 4$  mm. Temperature is given relative to room temperature (25  $^{\circ}\text{C}$ ), (continued).

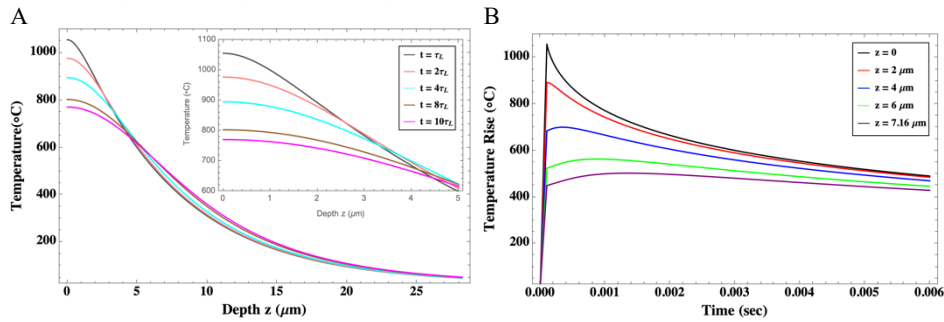
Temperature evolution obtained using the %R from FTIR data  
**Ketone N, VSP mode,  $F = 2.1 \text{ J/cm}^2$ ,  $k = 0.022 \text{ W/mK}$**



Temperature evolution obtained using the %R from Fresnel equation (Eq. 4.21)



Temperature evolution obtained using the %R from FTIR data  
**Ketone N, VSP mode,  $F = 2.1 \text{ J/cm}^2$ ,  $k = 0.022 \text{ W/mK}$**



Temperature evolution obtained using the %R from Fresnel equation (Eq. 4.21)

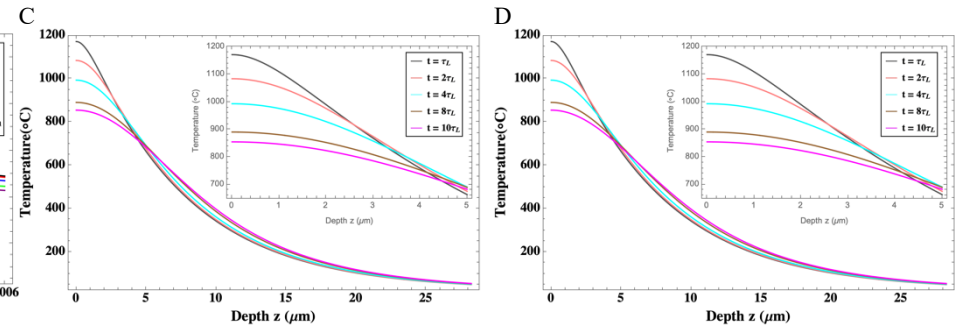
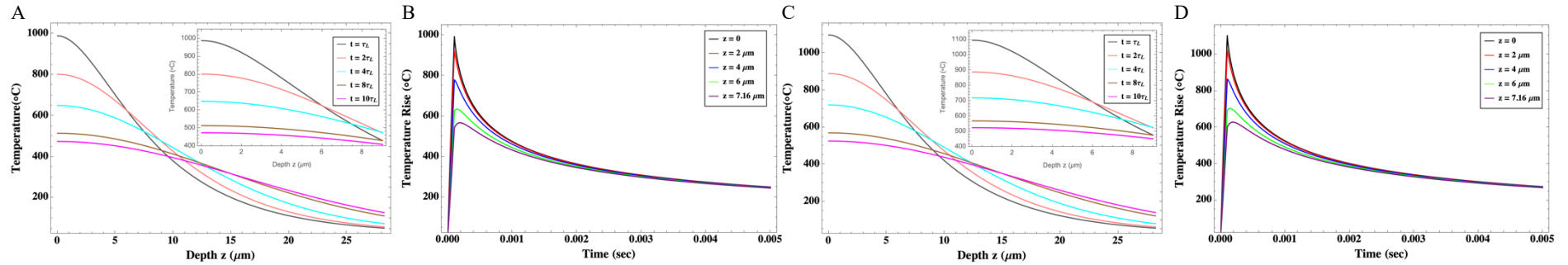


Figure B14 – Representation of the heat-wave propagation inside the **Ketone N film**, in VSP mode, at different times [100  $\mu\text{s}$  (gray), 200  $\mu\text{s}$  (pink), 400  $\mu\text{s}$  (cyan), 800  $\mu\text{s}$  (brown) and 1 ms (magenta)] as a function of depth (A and C) and the temperature rise evolution at various depth [0 (black), 2  $\mu\text{m}$  (red), 4  $\mu\text{m}$  (blue), 6  $\mu\text{m}$  (green), 7.16  $\mu\text{m}$  (purple)] as a function of time (B and D). The laser beam diameter was set at  $\varnothing = 4$  mm. Temperature is given relative to room temperature (25  $^{\circ}\text{C}$ ).

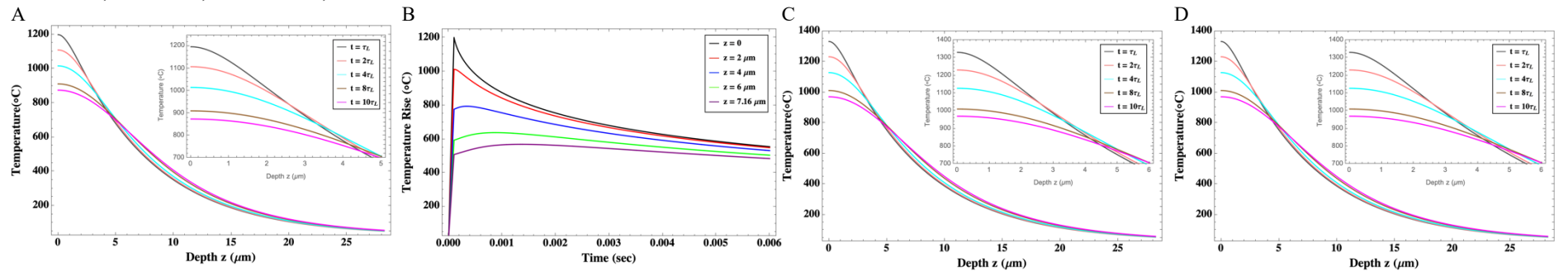
Temperature evolution obtained using the %R from FTIR data  
**Ketone N, VSP mode,  $F = 2.4 \text{ J/cm}^2$ ,  $k = 0.22 \text{ W/mK}$**

Temperature evolution obtained using the %R from Fresnel equation (Eq. 4.21)



Temperature evolution obtained using the %R from FTIR data  
**Ketone N, VSP mode,  $F = 2.4 \text{ J/cm}^2$ ,  $k = 0.022 \text{ W/mK}$**

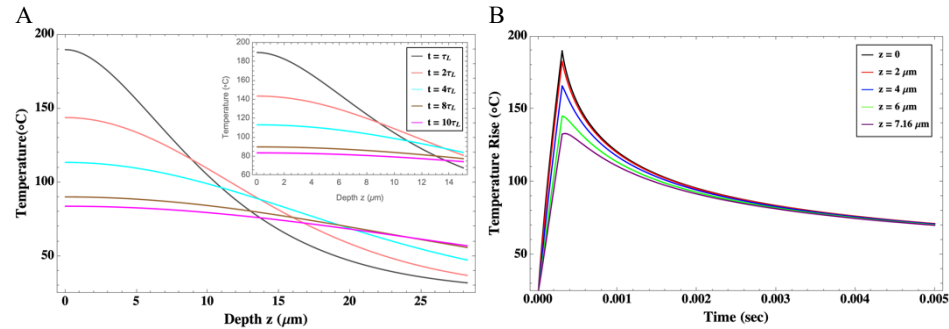
Temperature evolution obtained using the %R from Fresnel equation (Eq. 4.21)



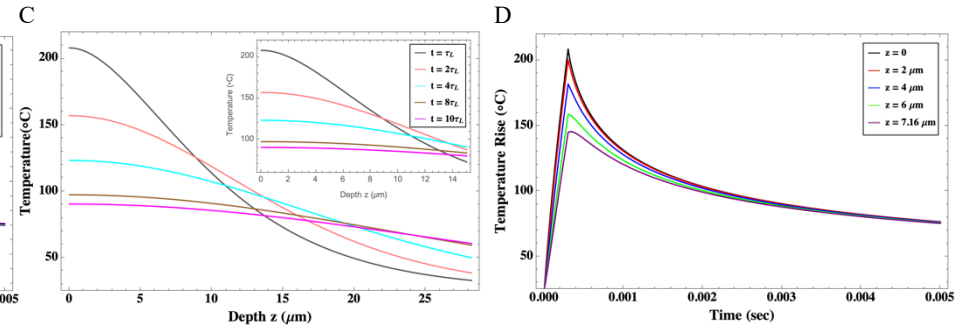
B7.4 Ketone N – SP mode ( $\tau_L \approx 300 \mu\text{s}$ ):

Figure B15 – Representation of the heat-wave propagation inside the **Ketone N film**, in SP mode, at different times [300  $\mu\text{s}$  (gray), 600  $\mu\text{s}$  (pink), 1.2 ms (cyan), 2.4 ms (brow) and 3 ms (magenta)] as a function of depth (A and C) and the temperature rise evolution at various depth [0 (black), 2  $\mu\text{m}$  (red), 4  $\mu\text{m}$  (blue), 6  $\mu\text{m}$  (green), 7.16  $\mu\text{m}$  (purple)] as a function of time (B and D). The laser beam diameter was set at  $\varnothing = 4 \text{ mm}$ . Temperature is given relative to room temperature (25 °C).

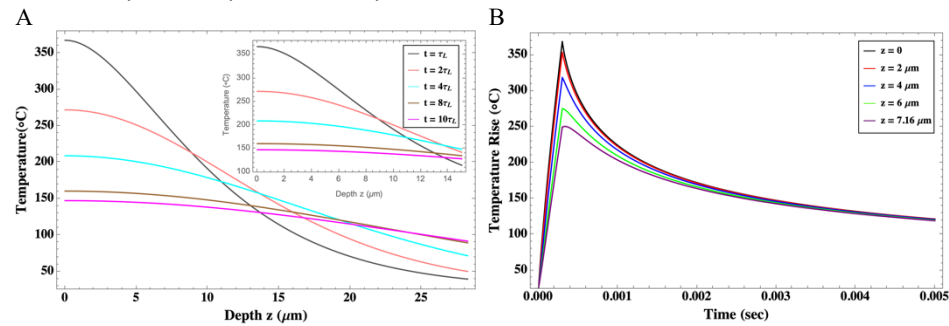
Temperature evolution obtained using the %R from FTIR data  
Ketone N, SP mode,  $F = 0.5 \text{ J/cm}^2$ ,  $k = 0.22 \text{ W/mK}$



Temperature evolution obtained using the %R from Fresnel equation (Eq. 4.21)



Temperature evolution obtained using the %R from FTIR data  
Ketone N, SP mode,  $F = 0.5 \text{ J/cm}^2$ ,  $k = 0.022 \text{ W/mK}$



Temperature evolution obtained using the %R from Fresnel equation (Eq. 4.21)

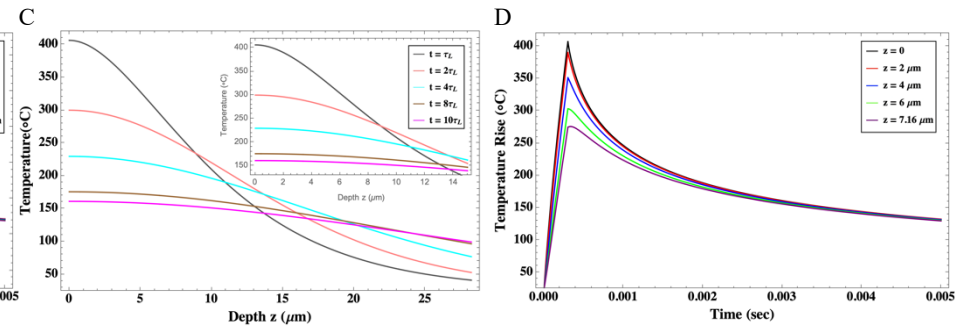
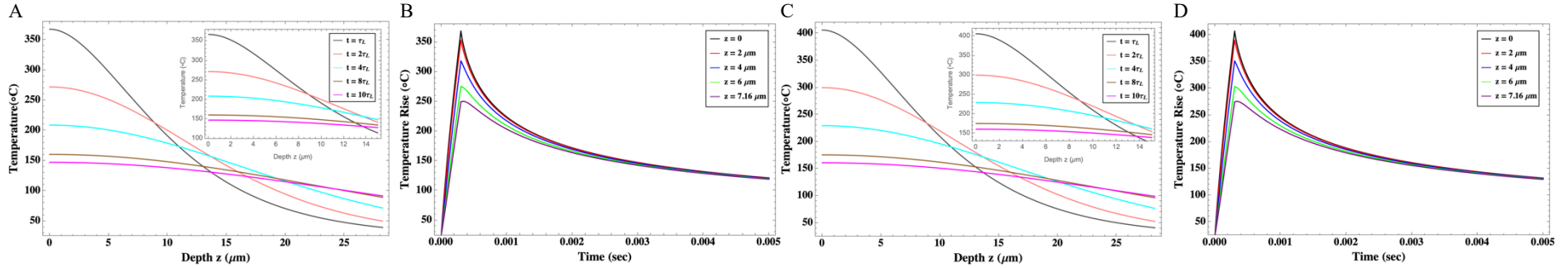


Figure B15 – Representation of the heat-wave propagation inside the **Ketone N film**, in SP mode, at different times [300  $\mu\text{s}$  (gray), 600  $\mu\text{s}$  (pink), 1.2 ms (cyan), 2.4 ms (brow) and 3 ms (magenta)] as a function of depth (A and C) and the temperature rise evolution at various depth [0 (black), 2  $\mu\text{m}$  (red), 4  $\mu\text{m}$  (blue), 6  $\mu\text{m}$  (green), 7.16  $\mu\text{m}$  (purple)] as a function of time (B and D). The laser beam diameter was set at  $\varnothing = 4$  mm. Temperature is given relative to room temperature (25  $^{\circ}\text{C}$ ), (continued).

Temperature evolution obtained using the %R from FTIR data  
**Ketone N, SP mode,  $F = 1 \text{ J/cm}^2$ ,  $k = 0.22 \text{ W/mK}$**

Temperature evolution obtained using the %R from Fresnel equation (Eq. 4.21)



Temperature evolution obtained using the %R from FTIR data  
**Ketone N, SP mode,  $F = 1 \text{ J/cm}^2$ ,  $k = 0.022 \text{ W/mK}$**

Temperature evolution obtained using the %R from Fresnel equation (Eq. 4.21)

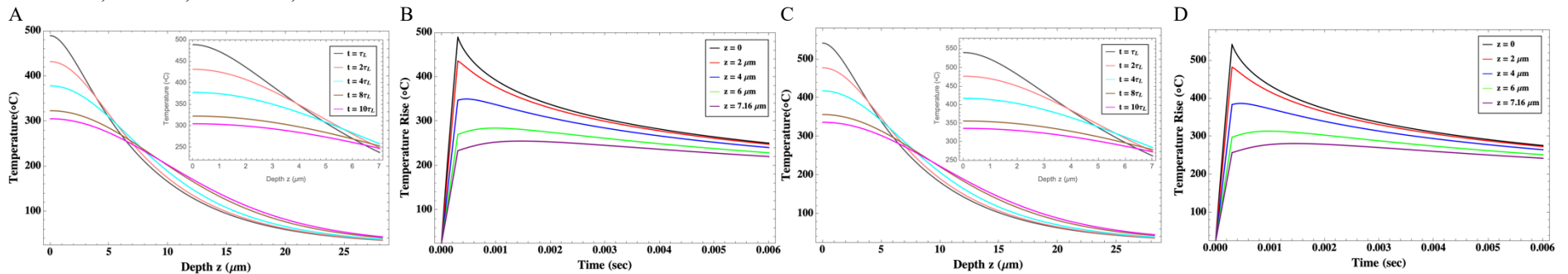
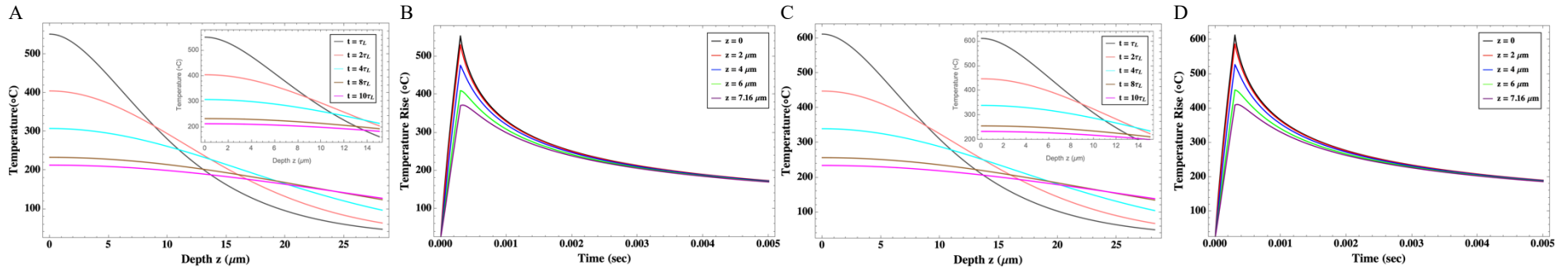


Figure B15 – Representation of the heat-wave propagation inside the **Ketone N film**, in SP mode, at different times [300  $\mu$ s (gray), 600  $\mu$ s (pink), 1.2 ms (cyan), 2.4 ms (brow) and 3 ms (magenta)] as a function of depth (A and C) and the temperature rise evolution at various depth [0 (black), 2  $\mu$ m (red), 4  $\mu$ m (blue), 6  $\mu$ m (green), 7.16  $\mu$ m (purple)] as a function of time (B and D). The laser beam diameter was set at  $\varnothing = 4$  mm. Temperature is given relative to room temperature (25 °C), (continued).

Temperature evolution obtained using the %R from FTIR data  
**Ketone N, SP mode,  $F = 1.5 \text{ J/cm}^2$ ,  $k = 0.22 \text{ W/mK}$**

Temperature evolution obtained using the %R from Fresnel equation (Eq. 4.21)



Temperature evolution obtained using the %R from FTIR data  
**Ketone N, SP mode,  $F = 1.5 \text{ J/cm}^2$ ,  $k = 0.022 \text{ W/mK}$**

Temperature evolution obtained using the %R from Fresnel equation (Eq. 4.21)

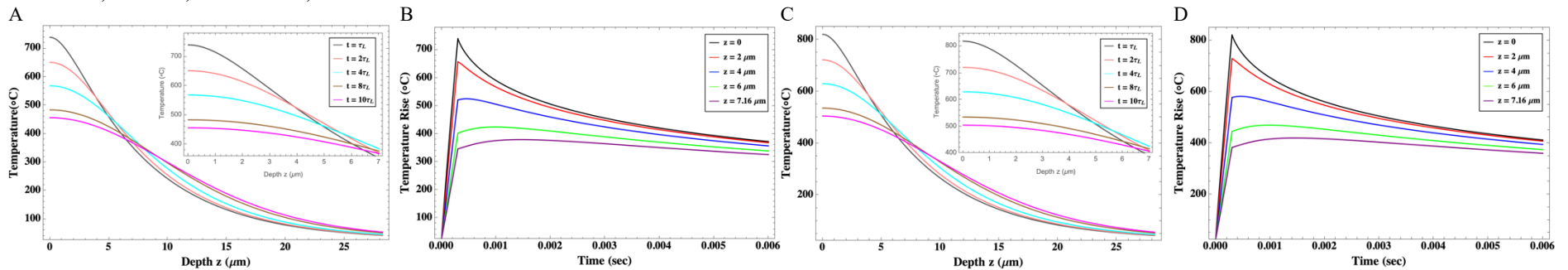
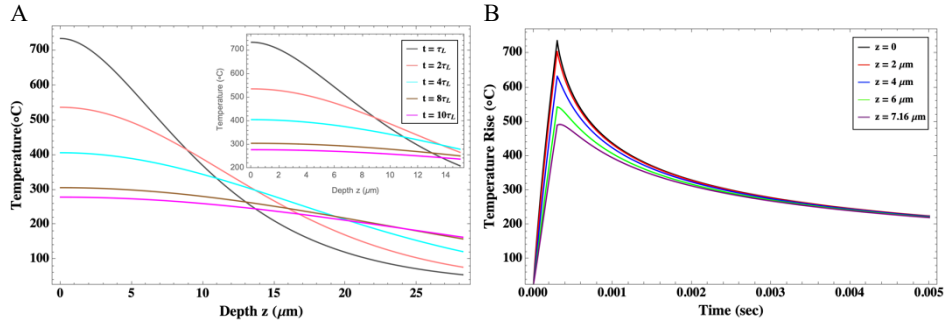
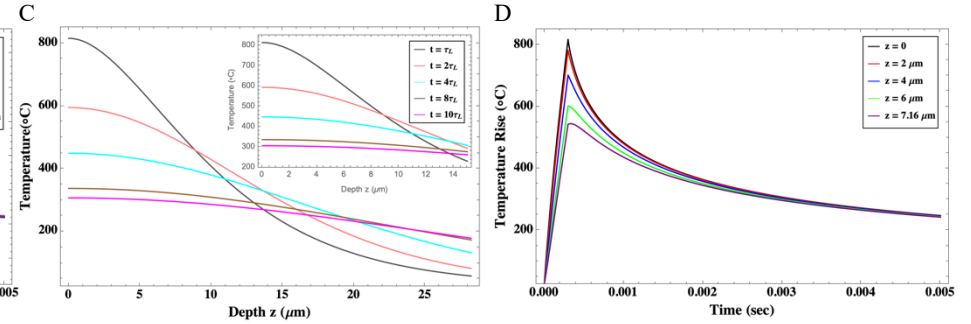


Figure B15 – Representation of the heat-wave propagation inside the **Ketone N film**, in SP mode, at different times [300  $\mu\text{s}$  (gray), 600  $\mu\text{s}$  (pink), 1.2 ms (cyan), 2.4 ms (brow) and 3 ms (magenta)] as a function of depth (A and C) and the temperature rise evolution at various depth [0 (black), 2  $\mu\text{m}$  (red), 4  $\mu\text{m}$  (blue), 6  $\mu\text{m}$  (green), 7.16  $\mu\text{m}$  (purple)] as a function of time (B and D). The laser beam diameter was set at  $\varnothing = 4$  mm. Temperature is given relative to room temperature (25  $^{\circ}\text{C}$ ), (continued).

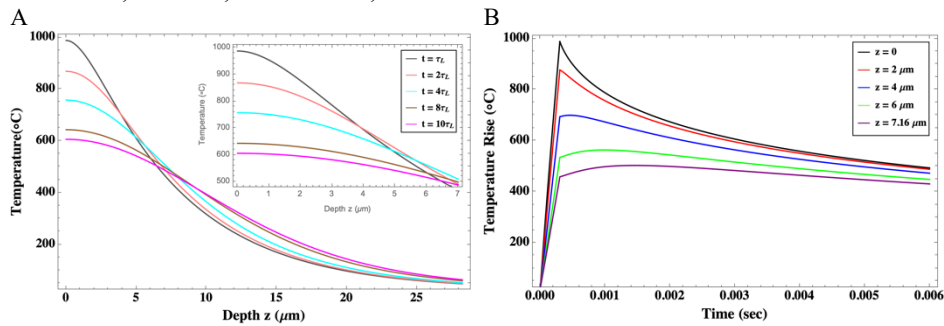
Temperature evolution obtained using the %R from FTIR data  
**Ketone N, SP mode,  $F = 2.1 \text{ J/cm}^2$ ,  $k = 0.22 \text{ W/mK}$**



Temperature evolution obtained using the %R from Fresnel equation (Eq. 4.21)



Temperature evolution obtained using the %R from FTIR data  
**Ketone N, SP mode,  $F = 2.1 \text{ J/cm}^2$ ,  $k = 0.022 \text{ W/mK}$**



Temperature evolution obtained using the %R from Fresnel equation (Eq. 4.21)

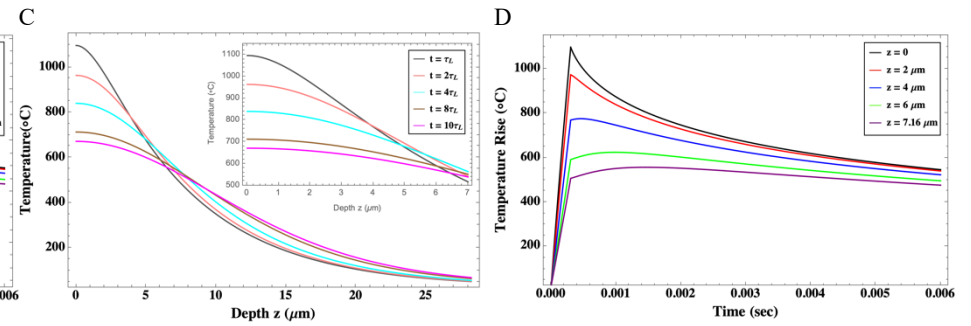
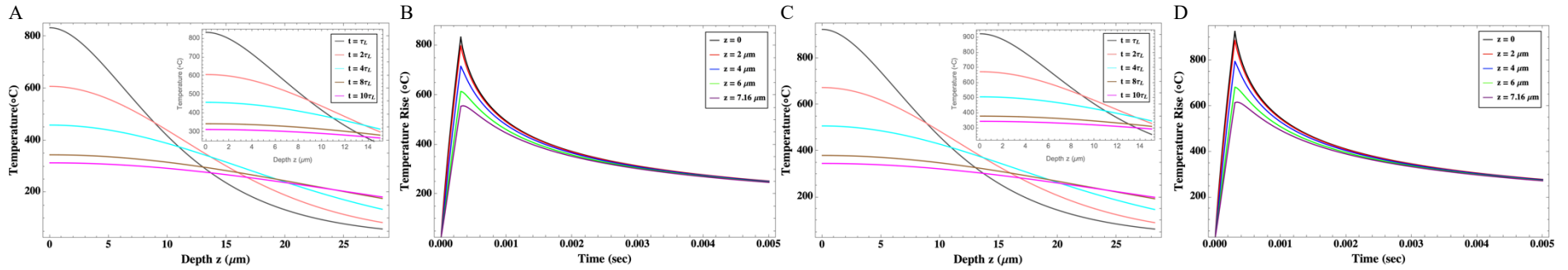


Figure B15 – Representation of the heat-wave propagation inside the **Ketone N film**, in SP mode, at different times [300  $\mu$ s (gray), 600  $\mu$ s (pink), 1.2 ms (cyan), 2.4 ms (brow) and 3 ms (magenta)] as a function of depth (A and C) and the temperature rise evolution at various depth [0 (black), 2  $\mu$ m (red), 4  $\mu$ m (blue), 6  $\mu$ m (green), 7.16  $\mu$ m (purple)] as a function of time (B and D). The laser beam diameter was set at  $\varnothing = 4$  mm. Temperature is given relative to room temperature (25  $^{\circ}$ C).

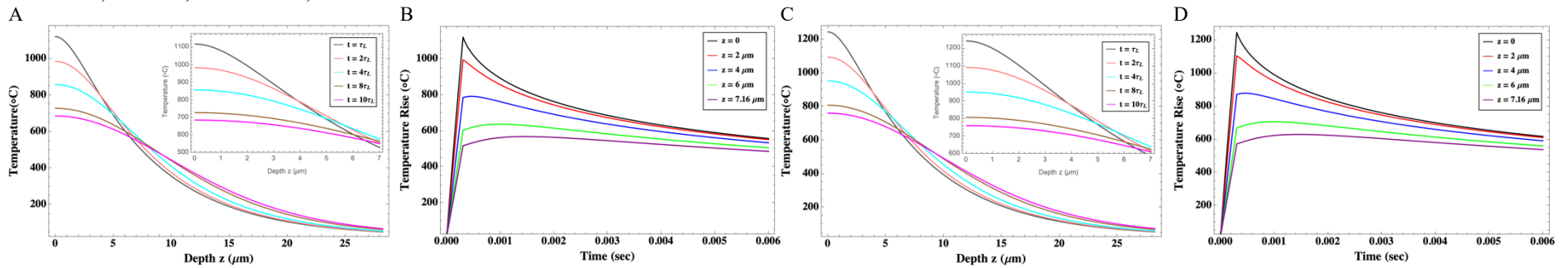
Temperature evolution obtained using the %R from FTIR data  
**Ketone N, SP mode,  $F = 2.4 \text{ J/cm}^2$ ,  $k = 0.22 \text{ W/mK}$**

Temperature evolution obtained using the %R from Fresnel equation (Eq. 4.21)



Temperature evolution obtained using the %R from FTIR data  
**Ketone N, SP mode,  $F = 2.4 \text{ J/cm}^2$ ,  $k = 0.022 \text{ W/mK}$**

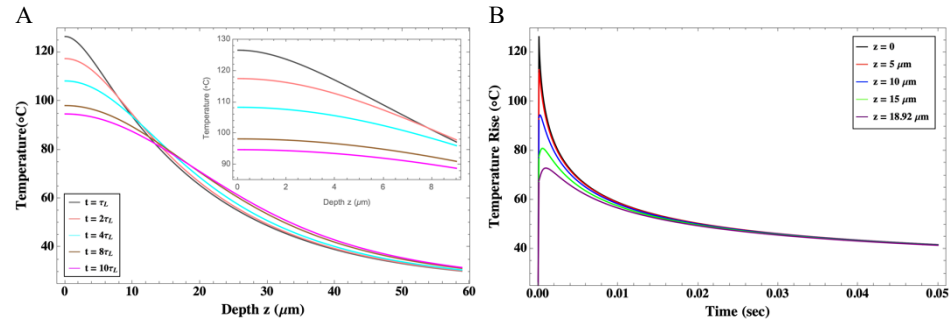
Temperature evolution obtained using the %R from Fresnel equation (Eq. 4.21)



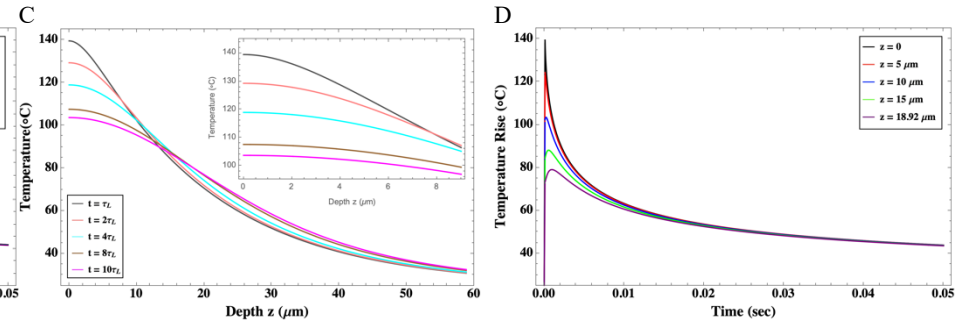
B7.5 MS2A – VSP mode ( $\tau_L \approx 100 \mu s$ ):

Figure B16 – Representation of the heat-wave propagation inside the **MS2A film**, in VSP mode, at different times [100  $\mu s$  (gray), 200  $\mu s$  (pink), 400  $\mu s$  (cyan), 800  $\mu s$  (brow) and 1 ms (magenta)] as a function of depth (A and C) and the temperature rise evolution at various depth [0 (black), 5  $\mu m$  (red), 10  $\mu m$  (blue), 15  $\mu m$  (green), 18.92  $\mu m$  (purple)] as a function of time (B and D). The laser beam diameter was set at  $\varnothing = 4 \text{ mm}$ . Temperature is given relative to room temperature (25 °C).

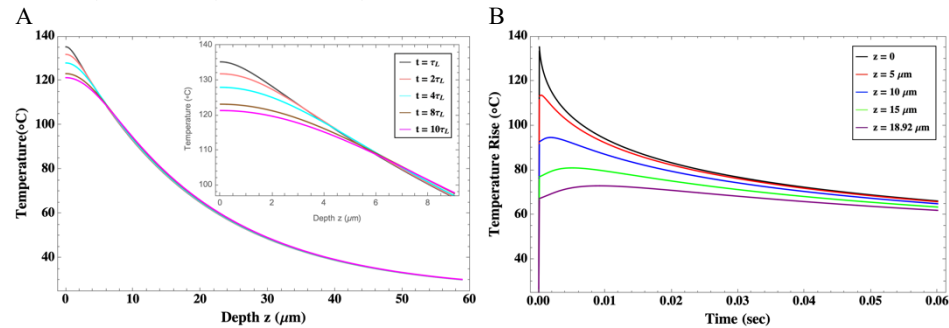
Temperature evolution obtained using the %R from FTIR data  
MS2A, VSP mode,  $F = 0.5 \text{ J/cm}^2$ ,  $k = 0.19 \text{ W/mK}$



Temperature evolution obtained using the %R from Fresnel equation (Eq. 4.21)



Temperature evolution obtained using the %R from FTIR data  
MS2A, VSP mode,  $F = 0.5 \text{ J/cm}^2$ ,  $k = 0.019 \text{ W/mK}$



Temperature evolution obtained using the %R from Fresnel equation (Eq. 4.21)

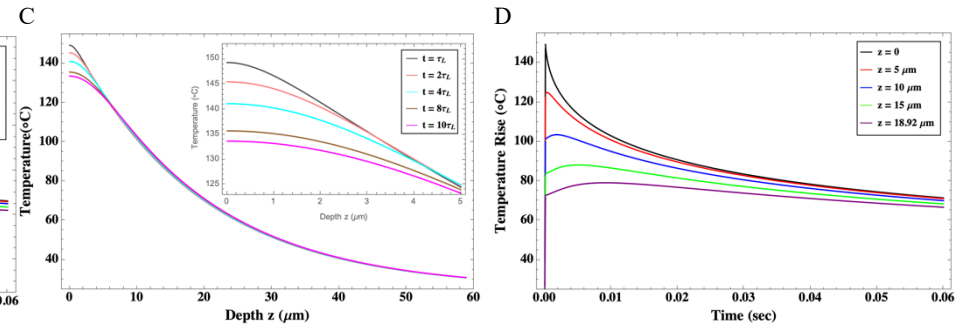
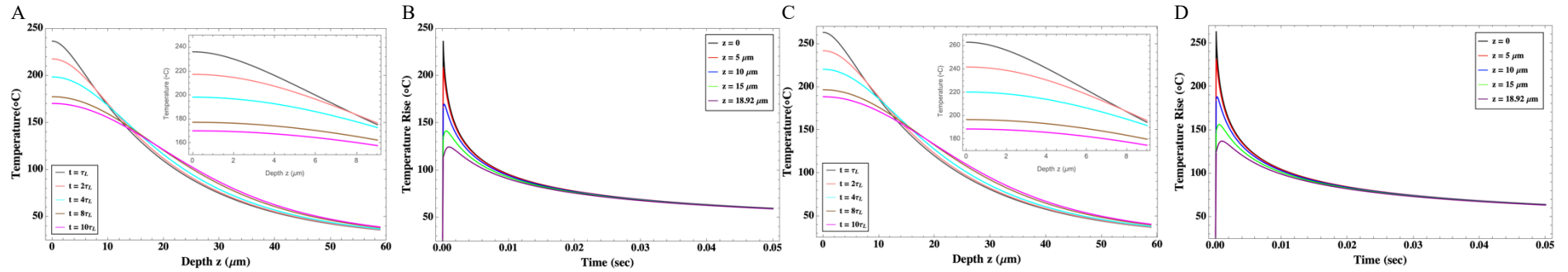


Figure B16 – Representation of the heat-wave propagation inside the **MS2A film**, in VSP mode, at different times [100  $\mu\text{s}$  (gray), 200  $\mu\text{s}$  (pink), 400  $\mu\text{s}$  (cyan), 800  $\mu\text{s}$  (brow) and 1 ms (magenta)] as a function of depth (A and C) and the temperature rise evolution at various depth [0 (black), 5  $\mu\text{m}$  (red), 10  $\mu\text{m}$  (blue), 15  $\mu\text{m}$  (green), 18.92  $\mu\text{m}$  (purple)] as a function of time (B and D). The laser beam diameter was set at  $\varnothing = 4$  mm. Temperature is given relative to room temperature (25  $^{\circ}\text{C}$ ), (continued).

Temperature evolution obtained using the %R from FTIR data  
**MS2A, VSP mode,  $F = 1 \text{ J/cm}^2$ ,  $k = 0.19 \text{ W/mK}$**

Temperature evolution obtained using the %R from Fresnel equation (Eq. 4.21)



Temperature evolution obtained using the %R from FTIR data  
**MS2A, VSP mode,  $F = 1 \text{ J/cm}^2$ ,  $k = 0.019 \text{ W/mK}$**

Temperature evolution obtained using the %R from Fresnel equation (Eq. 4.21)

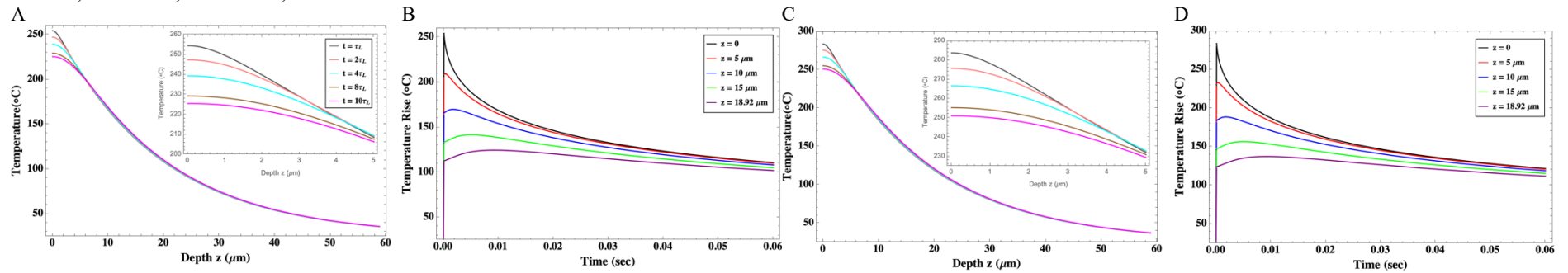
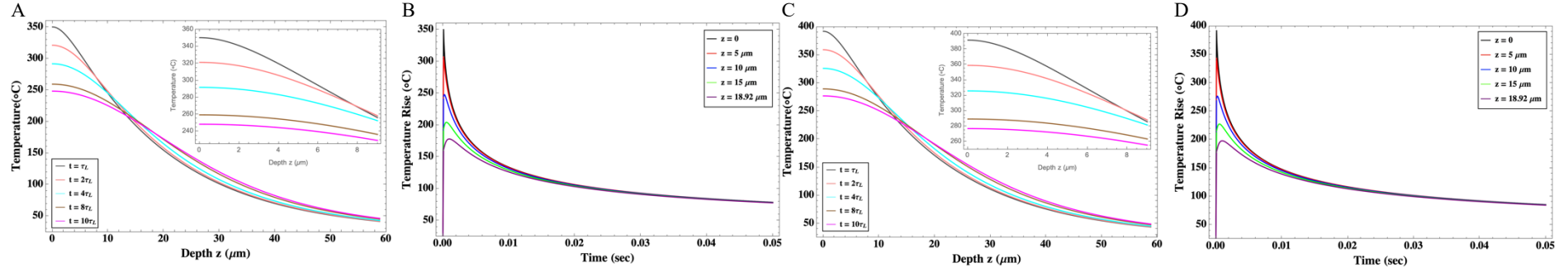


Figure B16 – Representation of the heat-wave propagation inside the **MS2A film**, in VSP mode, at different times [100  $\mu$ s (gray), 200  $\mu$ s (pink), 400  $\mu$ s (cyan), 800  $\mu$ s (brow) and 1 ms (magenta)] as a function of depth (A and C) and the temperature rise evolution at various depth [0 (black), 5  $\mu$ m (red), 10  $\mu$ m (blue), 15  $\mu$ m (green), 18.92  $\mu$ m (purple)] as a function of time (B and D). The laser beam diameter was set at  $\varnothing = 4$  mm. Temperature is given relative to room temperature (25  $^{\circ}$ C), (continued).

Temperature evolution obtained using the %R from FTIR data  
**MS2A, VSP mode,  $F = 1.5 \text{ J/cm}^2$ ,  $k = 0.19 \text{ W/mK}$**

Temperature evolution obtained using the %R from Fresnel equation (Eq. 4.21)



Temperature evolution obtained using the %R from FTIR data  
**MS2A, VSP mode,  $F = 1.5 \text{ J/cm}^2$ ,  $k = 0.019 \text{ W/mK}$**

Temperature evolution obtained using the %R from Fresnel equation (Eq. 4.21)

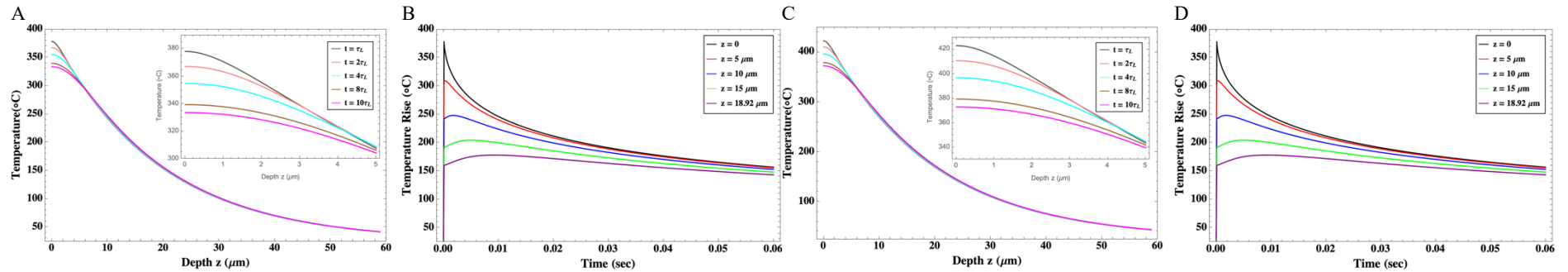
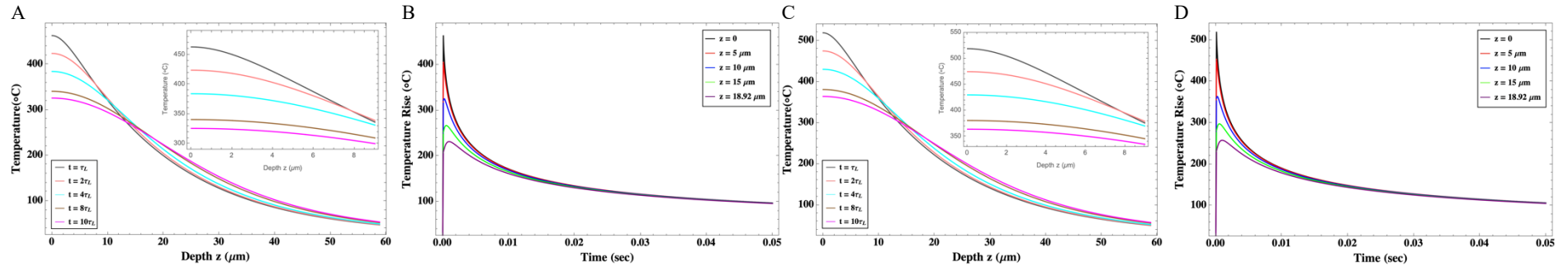


Figure B16 – Representation of the heat-wave propagation inside the **MS2A film**, in VSP mode, at different times [100  $\mu$ s (gray), 200  $\mu$ s (pink), 400  $\mu$ s (cyan), 800  $\mu$ s (brow) and 1 ms (magenta)] as a function of depth (A and C) and the temperature rise evolution at various depth [0 (black), 5  $\mu$ m (red), 10  $\mu$ m (blue), 15  $\mu$ m (green), 18.92  $\mu$ m (purple)] as a function of time (B and D). The laser beam diameter was set at  $\varnothing = 4$  mm. Temperature is given relative to room temperature (25  $^{\circ}$ C), (continued).

Temperature evolution obtained using the %R from FTIR data  
**MS2A, VSP mode,  $F = 2.1 \text{ J/cm}^2$ ,  $k = 0.19 \text{ W/mK}$**

Temperature evolution obtained using the %R from Fresnel equation (Eq. 4.21)



Temperature evolution obtained using the %R from FTIR data  
**MS2A, VSP mode,  $F = 2.1 \text{ J/cm}^2$ ,  $k = 0.019 \text{ W/mK}$**

Temperature evolution obtained using the %R from Fresnel equation (Eq. 4.21)

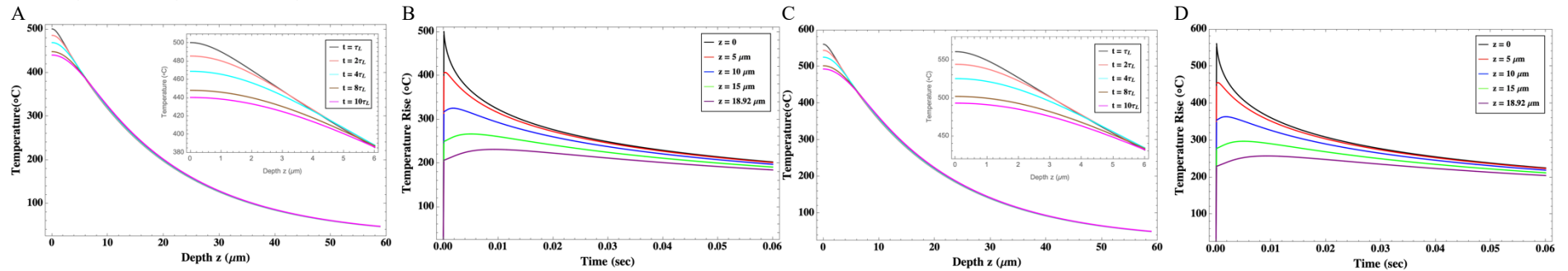
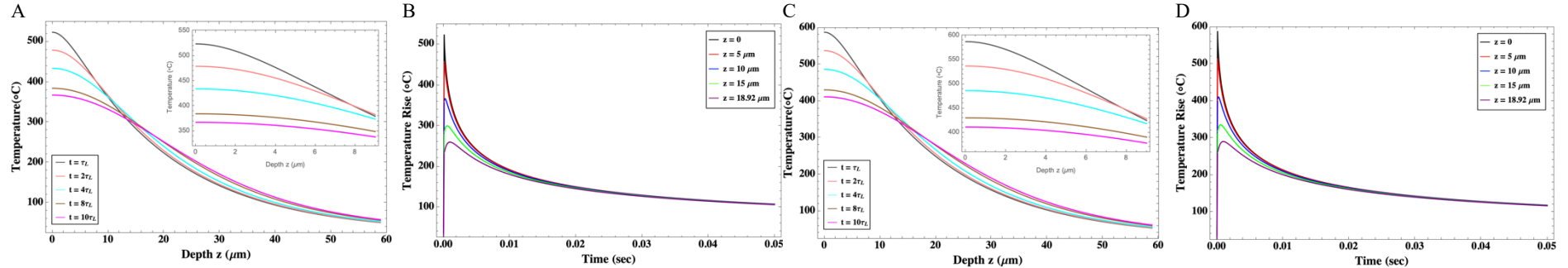


Figure B16 – Representation of the heat-wave propagation inside the **MS2A film**, in VSP mode, at different times [100  $\mu\text{s}$  (gray), 200  $\mu\text{s}$  (pink), 400  $\mu\text{s}$  (cyan), 800  $\mu\text{s}$  (brown) and 1 ms (magenta)] as a function of depth (A and C) and the temperature rise evolution at various depth [0 (black), 5  $\mu\text{m}$  (red), 10  $\mu\text{m}$  (blue), 15  $\mu\text{m}$  (green), 18.92  $\mu\text{m}$  (purple)] as a function of time (B and D). The laser beam diameter was set at  $\varnothing = 4$  mm. Temperature is given relative to room temperature (25  $^{\circ}\text{C}$ ).

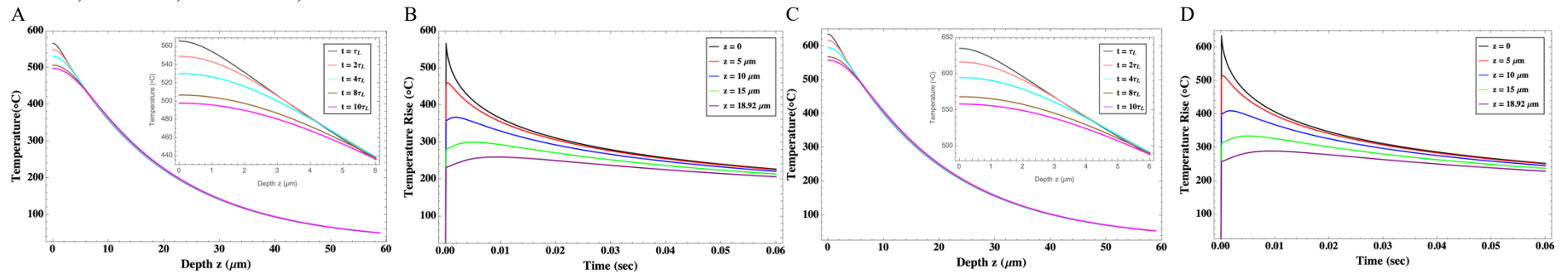
Temperature evolution obtained using the %R from FTIR data  
**MS2A, VSP mode,  $F = 2.4 \text{ J/cm}^2$ ,  $k = 0.19 \text{ W/mK}$**

Temperature evolution obtained using the %R from Fresnel equation (Eq. 4.21)



Temperature evolution obtained using the %R from FTIR data  
**MS2A, VSP mode,  $F = 2.4 \text{ J/cm}^2$ ,  $k = 0.019 \text{ W/mK}$**

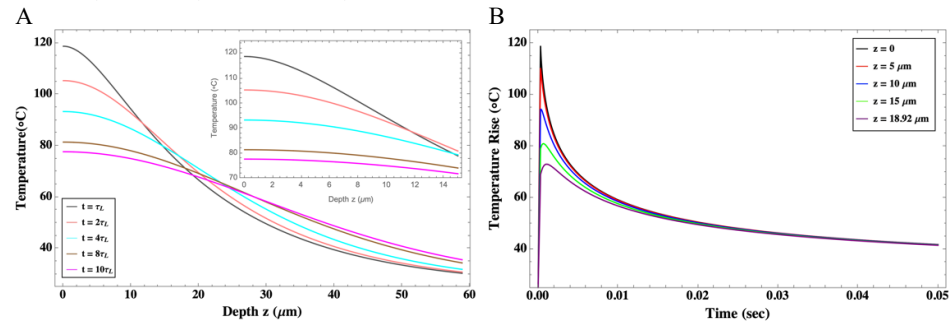
Temperature evolution obtained using the %R from Fresnel equation (Eq. 4.21)



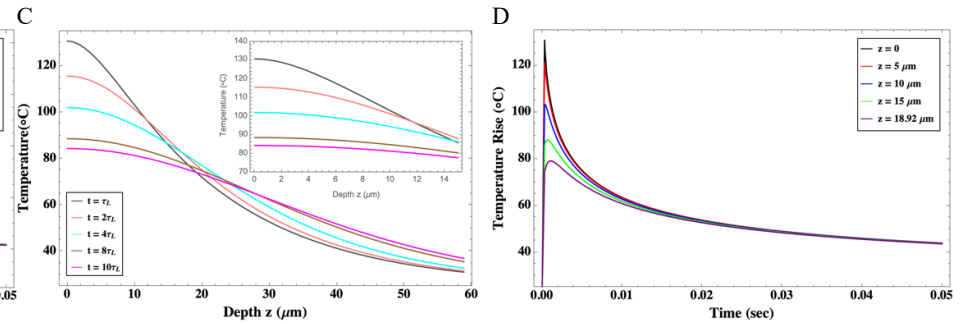
B7.6 MS2A – SP mode ( $\tau_L \approx 300 \mu s$ ):

Figure B17 - Representation of the heat-wave propagation inside the **MS2A film**, in SP mode, at different times [300  $\mu s$  (gray), 600  $\mu s$  (pink), 1.2 ms (cyan), 2.4 ms (brow) and 3 ms (magenta)] as a function of depth (A and C) and the temperature rise evolution at various depth [0 (black), 5  $\mu m$  (red), 10  $\mu m$  (blue), 15  $\mu m$  (green), 18.92  $\mu m$  (purple)] as a function of time (B and D). The laser beam diameter was set at  $\varnothing = 4 \text{ mm}$ . Temperature is given relative to room temperature (25 °C).

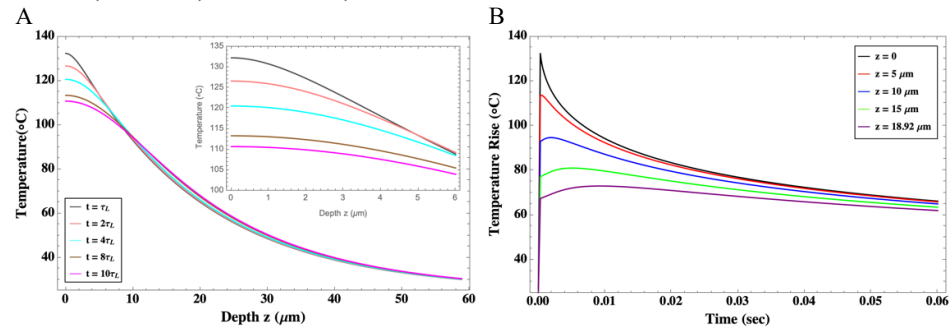
Temperature evolution obtained using the %R from FTIR data  
MS2A, SP mode,  $F = 0.5 \text{ J/cm}^2$ ,  $k = 0.19 \text{ W/mK}$



Temperature evolution obtained using the %R from Fresnel equation (Eq. 4.21)



Temperature evolution obtained using the %R from FTIR data  
MS2A, SP mode,  $F = 0.5 \text{ J/cm}^2$ ,  $k = 0.019 \text{ W/mK}$



Temperature evolution obtained using the %R from Fresnel equation (Eq. 4.21)

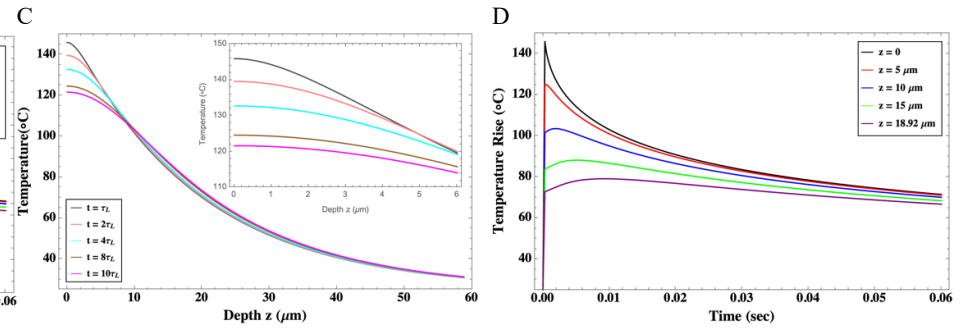
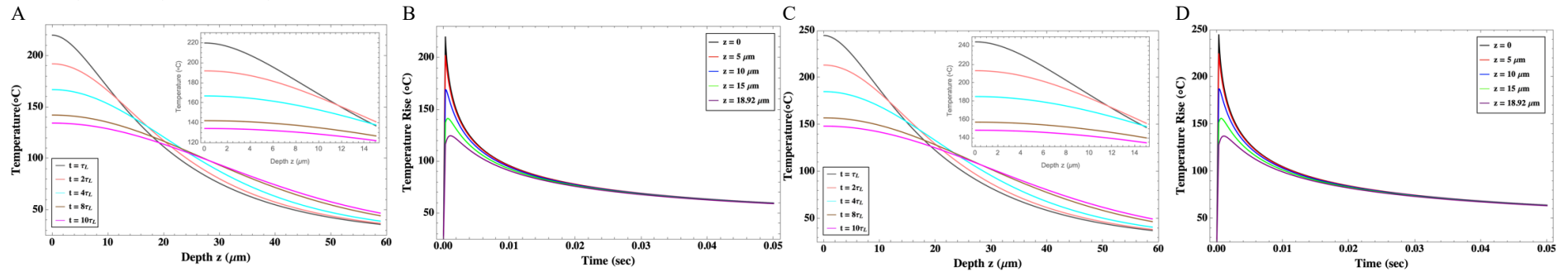


Figure B17 - Representation of the heat-wave propagation inside the **MS2A film**, in SP mode, at different times [300  $\mu$ s (gray), 600  $\mu$ s (pink), 1.2 ms (cyan), 2.4 ms (brow) and 3 ms (magenta)] as a function of depth (A and C) and the temperature rise evolution at various depth [0 (black), 5  $\mu$ m (red), 10  $\mu$ m (blue), 15  $\mu$ m (green), 18.92  $\mu$ m (purple)] as a function of time (B and D). The laser beam diameter was set at  $\varnothing = 4$  mm. Temperature is given relative to room temperature (25  $^{\circ}$ C), (continued).

Temperature evolution obtained using the %R from FTIR data  
MS2A, SP mode,  $F = 1 \text{ J/cm}^2$ ,  $k = 0.19 \text{ W/mK}$

Temperature evolution obtained using the %R from Fresnel equation (Eq. 4.21)



Temperature evolution obtained using the %R from FTIR data  
MS2A, SP mode,  $F = 1 \text{ J/cm}^2$ ,  $k = 0.019 \text{ W/mK}$

Temperature evolution obtained using the %R from Fresnel equation (Eq. 4.21)

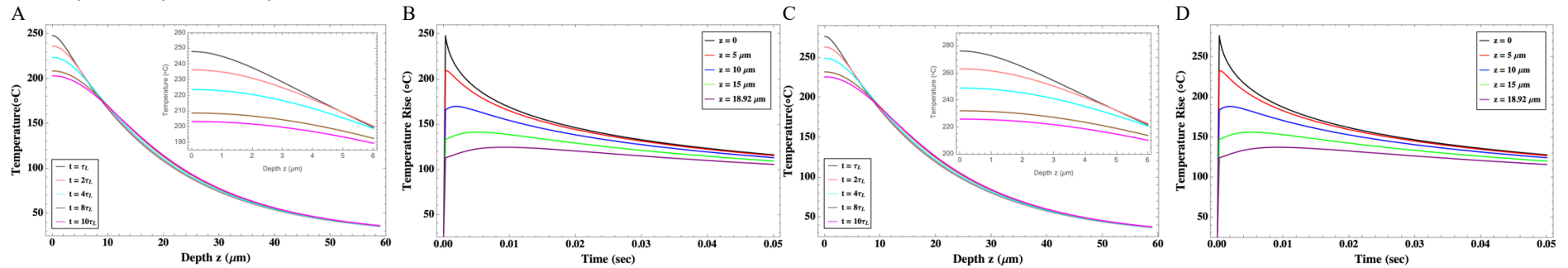
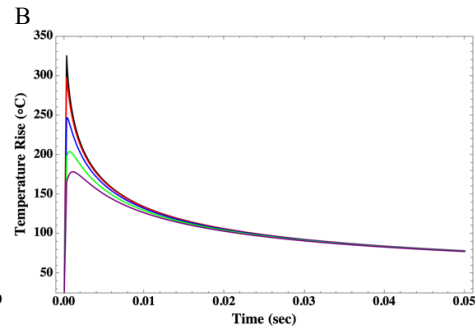
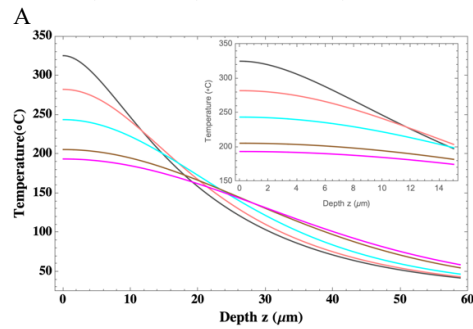
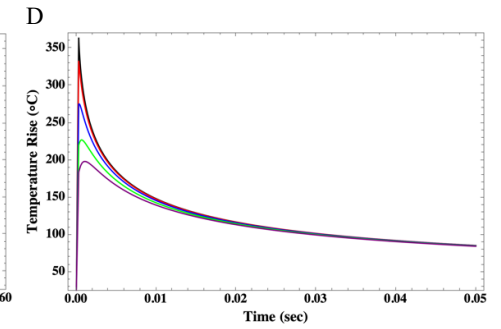
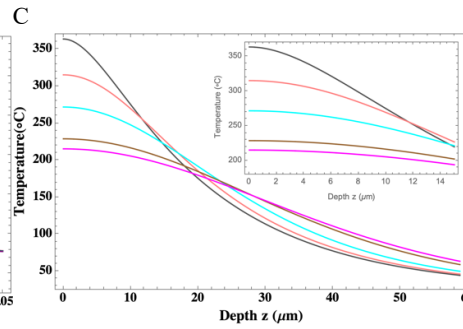


Figure B17 - Representation of the heat-wave propagation inside the **MS2A film**, in SP mode, at different times [300  $\mu\text{s}$  (gray), 600  $\mu\text{s}$  (pink), 1.2 ms (cyan), 2.4 ms (brown) and 3 ms (magenta)] as a function of depth (A and C) and the temperature rise evolution at various depth [0 ( $\mu\text{m}$ ) (black), 5  $\mu\text{m}$  (red), 10  $\mu\text{m}$  (blue), 15  $\mu\text{m}$  (green), 18.92  $\mu\text{m}$  (purple)] as a function of time (B and D). The laser beam diameter was set at  $\varnothing = 4$  mm. Temperature is given relative to room temperature (25  $^{\circ}\text{C}$ ), (continued).

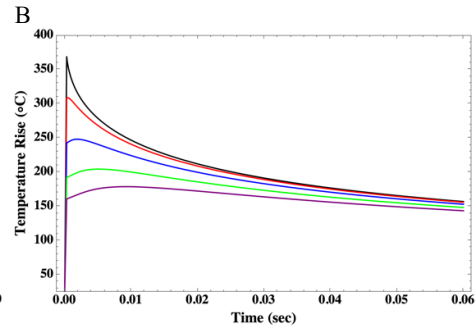
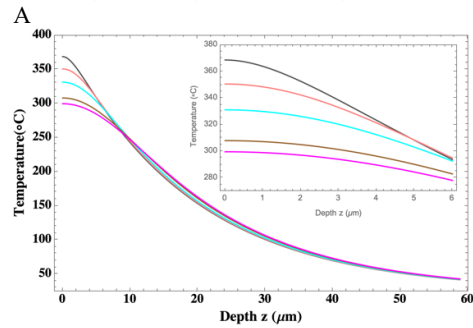
Temperature evolution obtained using the %R from FTIR data  
MS2A, SP mode,  $F = 1.5 \text{ J/cm}^2$ ,  $k = 0.19 \text{ W/mK}$



Temperature evolution obtained using the %R from Fresnel equation (Eq. 4.21)



Temperature evolution obtained using the %R from FTIR data  
MS2A, SP mode,  $F = 1.5 \text{ J/cm}^2$ ,  $k = 0.019 \text{ W/mK}$



Temperature evolution obtained using the %R from Fresnel equation (Eq. 4.21)

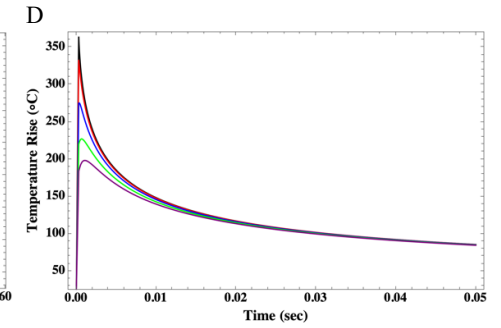
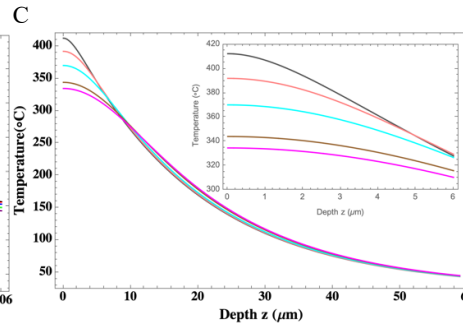
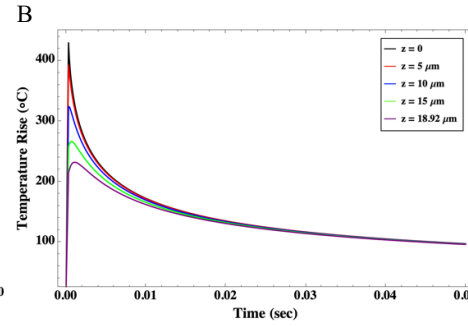
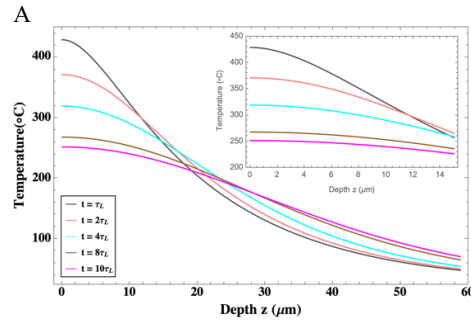
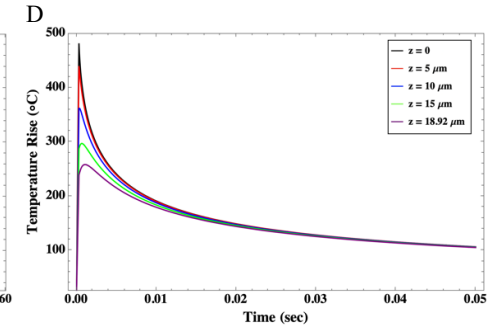
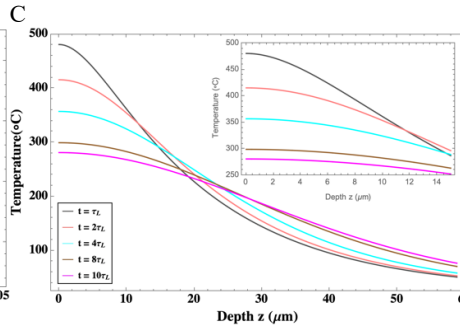


Figure B17 - Representation of the heat-wave propagation inside the **MS2A film**, in SP mode, at different times [300  $\mu\text{s}$  (gray), 600  $\mu\text{s}$  (pink), 1.2 ms (cyan), 2.4 ms (brow) and 3 ms (magenta)] as a function of depth (A and C) and the temperature rise evolution at various depth [0 (black), 5  $\mu\text{m}$  (red), 10  $\mu\text{m}$  (blue), 15  $\mu\text{m}$  (green), 18.92  $\mu\text{m}$  (purple)] as a function of time (B and D). The laser beam diameter was set at  $\varnothing = 4 \text{ mm}$ . Temperature is given relative to room temperature (25  $^{\circ}\text{C}$ ), (continued).

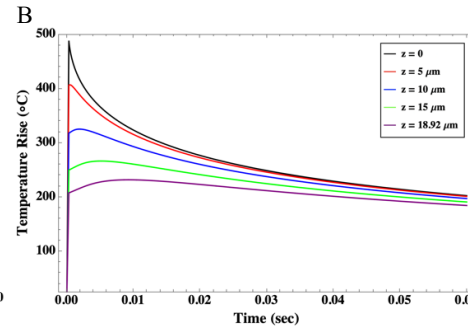
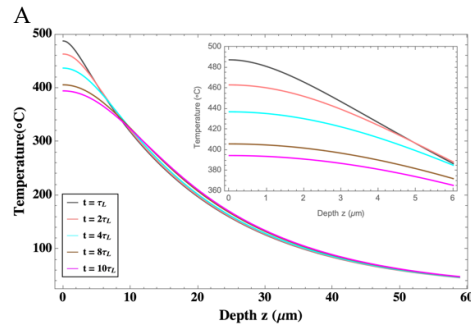
Temperature evolution obtained using the %R from FTIR data  
MS2A, SP mode,  $F = 2.1 \text{ J/cm}^2$ ,  $k = 0.19 \text{ W/mK}$



Temperature evolution obtained using the %R from Fresnel equation (Eq. 4.21)



Temperature evolution obtained using the %R from FTIR data  
MS2A, SP mode,  $F = 2.1 \text{ J/cm}^2$ ,  $k = 0.019 \text{ W/mK}$



Temperature evolution obtained using the %R from Fresnel equation (Eq. 4.21)

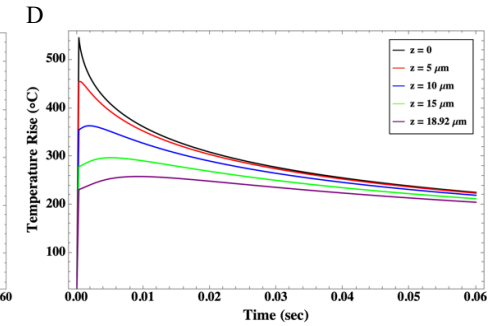
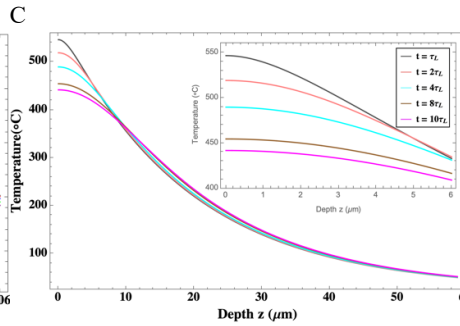
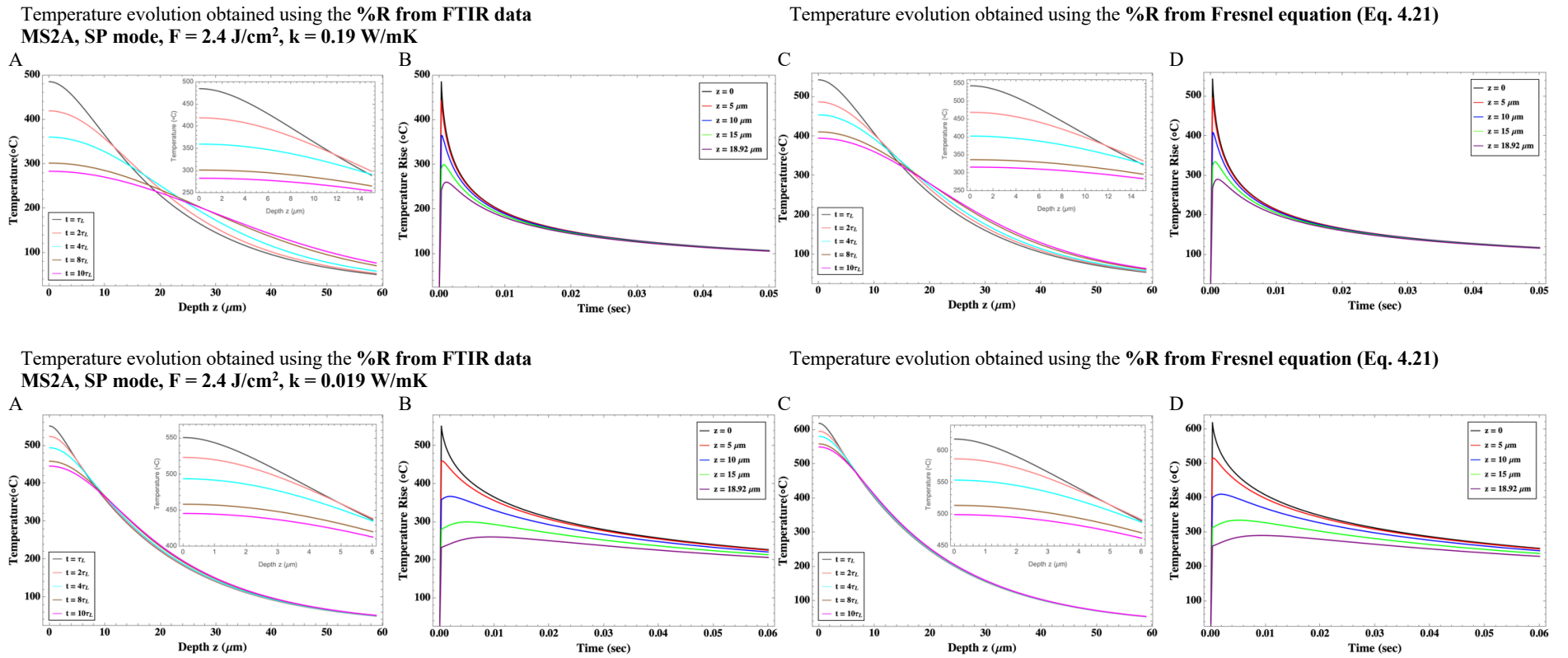


Figure B17 - Representation of the heat-wave propagation inside the **MS2A film**, in SP mode, at different times [300  $\mu$ s (gray), 600  $\mu$ s (pink), 1.2 ms (cyan), 2.4 ms (brow) and 3 ms (magenta)] as a function of depth (A and C) and the temperature rise evolution at various depth [0 (black), 5  $\mu$ m (red), 10  $\mu$ m (blue), 15  $\mu$ m (green), 18.92  $\mu$ m (purple)] as a function of time (B and D). The laser beam diameter was set at  $\varnothing = 4$  mm. Temperature is given relative to room temperature (25  $^{\circ}$ C).



### B8) An example of FlexPDE script for the 2D simulation

Below is reported an example of the computer program used in Flex PDE platform simulator software to run the computation for dammar in VSP mode ( $\approx 100 \mu\text{s}$ ).

```

Title "Dammar VSP mode, 0.5 J/cm2 [k = 0.21 (W/mK)]"
Beamsource = IF t < mu then 0 ELSE IF t >= mu
and t <= mu+Laserpulse then PowerVoldensity
ELSE 0 {W}

Coordinates: cylinder('radius (m)',depth (m)')
Select cubic { Use Cubic Basis }
Variables temp(threshold=1000)
Definitions:
source {heat source}
k {thermal conductivity}
Cp {heat capacity}
rho {density}
H = 5 {free convection boundary coupling
(W/m2·K)}
Ta = 25 {ambient temperature (°C)}

rglass = {radius glass slide (m)}
hglass = {height glass slide (m)}
rpaint = rglass
hpaint = {thickness of the varnish film (m)}
rbeam = {radius beam (m)}
hbeam = {Optical penetration depth (m)}

Trans = {Transmittance varnish film}
Refl = {Reflectance varnish film}

kglass = {(W/m·K)} 1
Cpglass = {(J/kg·K)} 2
kpaint = {(W/m·K)}
Cppaint = {(W/m·K)}

Energysource = {Energy selected (J)}
rhopaint= {Density varnish (kg/m3)}
rhoglass = {Density glass (kg/m3)} 3
Laserpulse = {Laser pulse duration (s)}
Vbeam = 3.14*(rbeam2)*hbeam

PowerVoldensity = Energysource / (Laserpulse *
Vbeam) {W/m3}

mu = 50*(10-6) {time before the release of the
laser pulse (s)}
timemax = 10*Laserpulse {the overall time
considered for the
simulation (s)}
timeintervall = 10-6 {s}

initial value temp = Ta

equations
div(k*grad(temp))+ source = rho*Cp*dt(temp)

boundaries
region 1 {glass}
k = kglass: Cp = cpglass: rho = rhoglass
source = 0
start (0,0)
natural(temp) = -H*(temp-Ta) line to (rglass,0)
natural(temp) = -H*(temp-Ta) line to
(rglass,hglass)
line to (0,hglass)
natural(temp) = -H*(temp-Ta) line to close

region 2 {paint}
source = 0
start(0,hglass)
line to (rpaint,hglass)
natural(temp) = -H*(temp-Ta) line to
(rpaint,hglass+hpaint)
natural(temp) = -H*(temp-Ta) line to
(rbeam,hglass+hpaint)
line to (rbeam,hglass+hpaint-hbeam)
line to (0,hglass+hpaint-hbeam)
natural(temp) = -H*(temp-Ta) line to close

region 3 {beam}
source = beamsource*(1-Trans-Refl)
start(0,hglass+hpaint-hbeam)
mesh_spacing = rbeam/50
line to (rbeam,hglass+hpaint-hbeam)
mesh_spacing = hbeam/5
line to (rbeam,hglass+hpaint)
natural(temp) = -H*(temp-Ta) line to
(0,hglass+hpaint)
line to close

time 0 to timemax by timeintervall

histories

```

1 For the thermal conductivity (k) of the glass please refer to Karazi, Ahad and Benyounis (2017);

2 For the Cp of the glass please refer to Karazi, Ahad and Benyounis (2017);

3 For the density of the glass please refer to Karazi, Ahad and Benyounis (2017).

```
history(temp)          at          (0,hpaint+hglass) "Surface Temp" contour(temp) zoom(0,hglass,
(rbeam/2,hpaint+hglass) (rbeam,hpaint+hglass) rbeam/2, hpaint) contours = 10
history(beamsource)    at          (0,hpaint+hglass)
(rbeam/2,hpaint+hglass) (rbeam,hpaint+hglass) plots
monitors               for t = 0 by timeintervall to (mu+laserpulse )
for t = 0 by timeintervall to (mu+laserpulse ) elevation(temp) from (0,0) to (0,hglass+hpaint)
elevation(temp)        from (0,hpaint+hglass) to range=(0,180) as "Axis Temp"
(rpaint,hpaint+hglass) range=(0,180) as end
```

## B9) 2D Simulations

### B9.1 Dammar – VSP mode ( $\tau_L \approx 100 \mu s$ ):

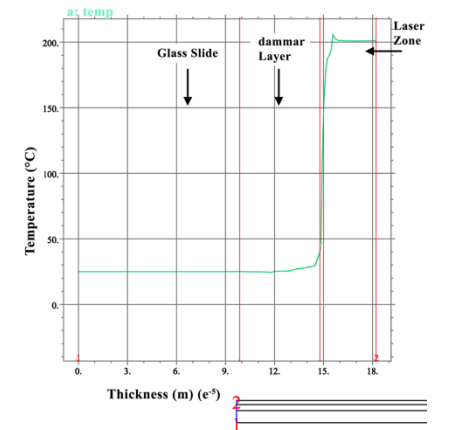
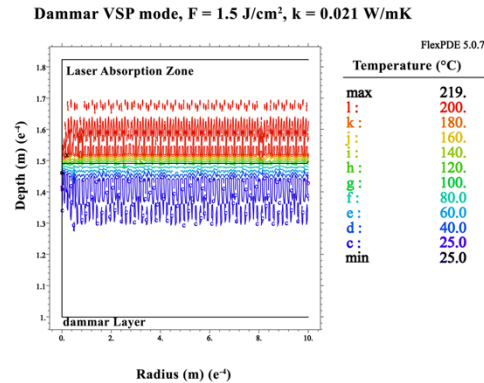
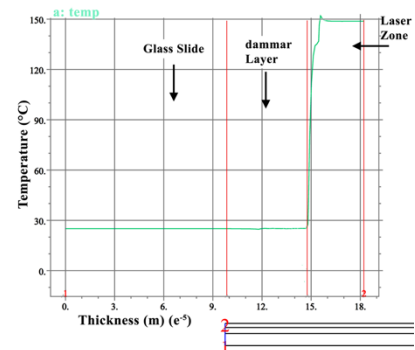
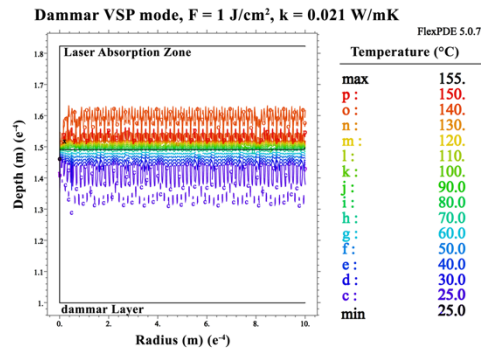
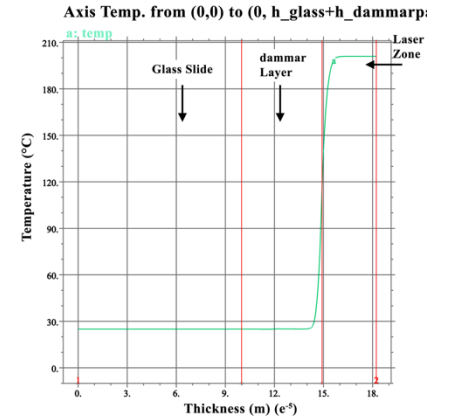
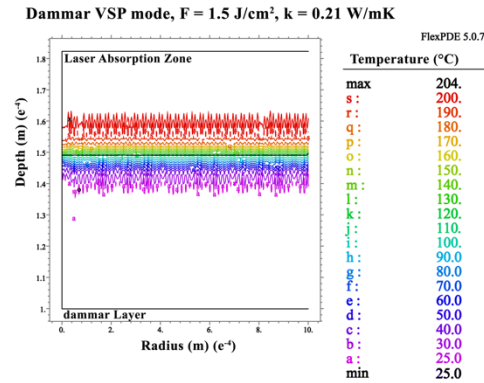
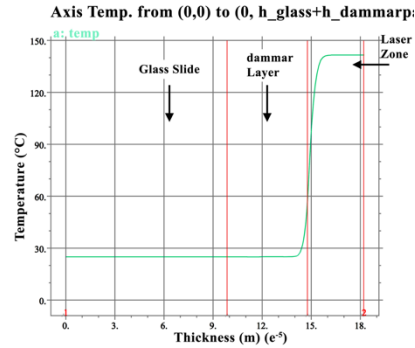
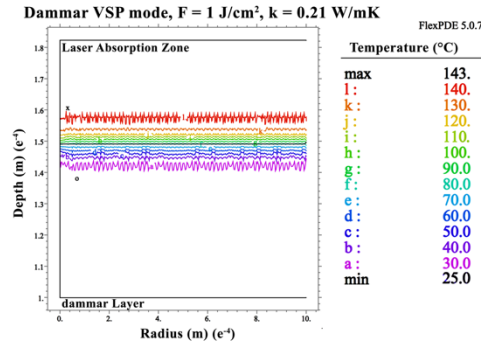
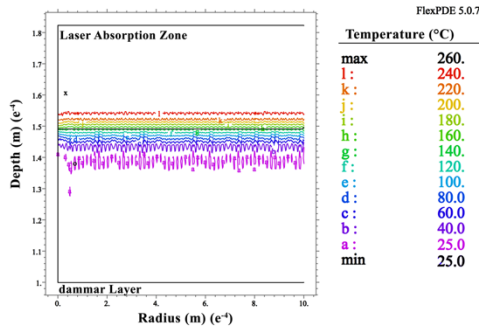


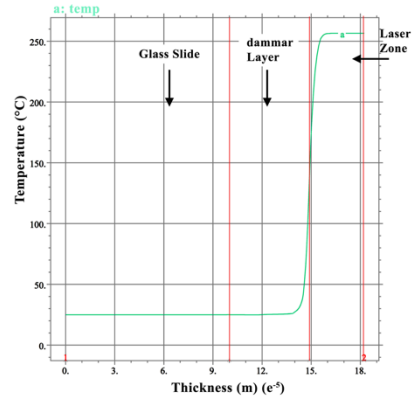
Figure B18 – 2D simulation of the heat diffusion inside the dammar film in VSP mode ( $\tau_L \approx 100 \mu s$ ) and temperature distribution by cross-section of varnish film + glass slide. Fluences of  $1 \text{ J/cm}^2$ , and thermal conductivity ( $k$ ) between  $0.21 \text{ W/m}\cdot\text{K}$  and  $0.021 \text{ W/m}\cdot\text{K}$ . The beam diameter was set at  $\varnothing = 4 \text{ mm}$ . The laser absorption zone represents the area in which the laser wavelength penetrates into the dammar film ( $\delta$ ) before releasing 63% of its energy.

Figure B19 – 2D simulation of the heat diffusion inside the dammar film in VSP mode ( $\tau_L \approx 100 \mu s$ ) and temperature distribution by cross-section of varnish film + glass slide. Fluences of  $1.5 \text{ J/cm}^2$ , and thermal conductivity ( $k$ ) between  $0.21 \text{ W/m}\cdot\text{K}$  and  $0.021 \text{ W/m}\cdot\text{K}$ . The beam diameter was set at  $\varnothing = 4 \text{ mm}$ . The laser absorption zone represents the area in which the laser wavelength penetrates into the dammar film ( $\delta$ ) before releasing 63% of its energy.

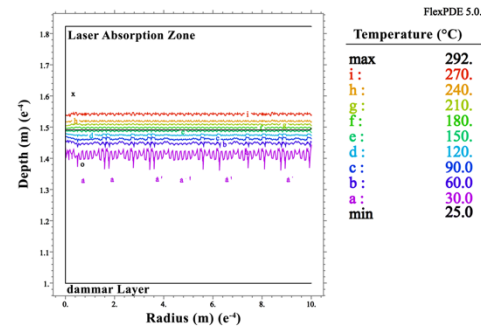
Dammar VSP mode,  $F = 2.1 \text{ J/cm}^2$ ,  $k = 0.21 \text{ W/mK}$



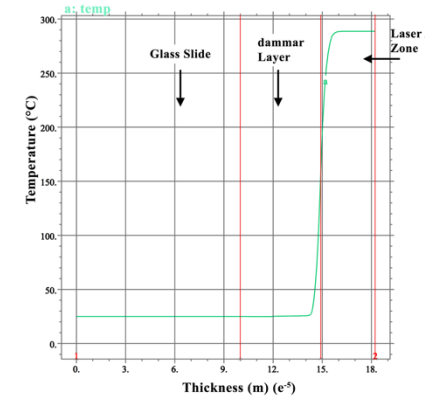
Axis Temp. from (0,0) to (0, h\_glass+h\_dammar):



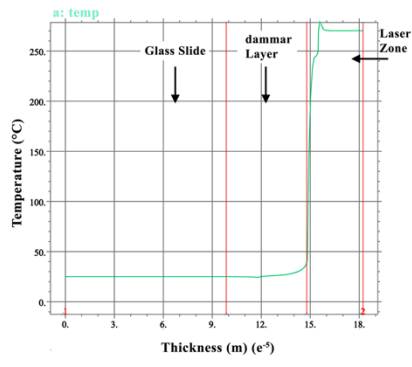
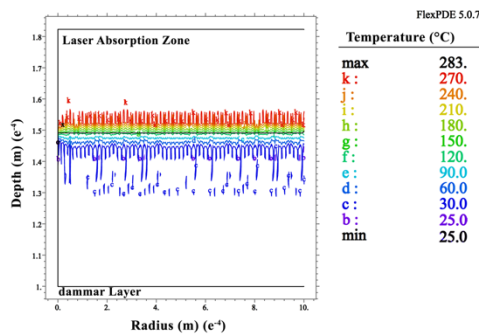
Dammar VSP mode,  $F = 2.4 \text{ J/cm}^2$ ,  $k = 0.21 \text{ W/mK}$



Axis Temp. from (0,0) to (0, h\_glass+h\_dammar):



Dammar VSP mode,  $F = 2.1 \text{ J/cm}^2$ ,  $k = 0.021 \text{ W/mK}$



Dammar VSP mode,  $F = 2.4 \text{ J/cm}^2$ ,  $k = 0.021 \text{ W/mK}$

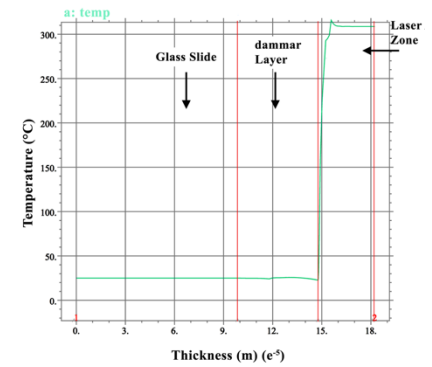
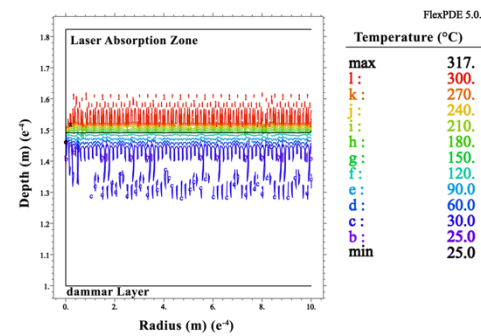


Figure B20 – 2D simulation of the heat diffusion inside the dammar film in VSP mode ( $\tau_L \approx 100 \mu\text{s}$ ) and temperature distribution by cross-section of varnish film + glass slide. Fluences of  $2.1 \text{ J/cm}^2$ , and thermal conductivity ( $k$ ) between  $0.21 \text{ W/m}\cdot\text{K}$  and  $0.021 \text{ W/m}\cdot\text{K}$ . The beam diameter was set at  $\varnothing = 4 \text{ mm}$ . The laser absorption zone represents the area in which the laser wavelength penetrates into the dammar film ( $\delta$ ) before releasing 63% of its energy.

Figure B21 – 2D simulation of the heat diffusion inside the dammar film in VSP mode ( $\tau_L \approx 100 \mu\text{s}$ ) and temperature distribution by cross-section of varnish film + glass slide. Fluences of  $2.4 \text{ J/cm}^2$ , and thermal conductivity ( $k$ ) between  $0.21 \text{ W/m}\cdot\text{K}$  and  $0.021 \text{ W/m}\cdot\text{K}$ . The beam diameter was set at  $\varnothing = 4 \text{ mm}$ . The laser absorption zone represents the area in which the laser wavelength penetrates into the dammar film ( $\delta$ ) before releasing 63% of its energy.

B9.2 Dammar – SP mode ( $\tau_L \approx 300 \mu s$ ):

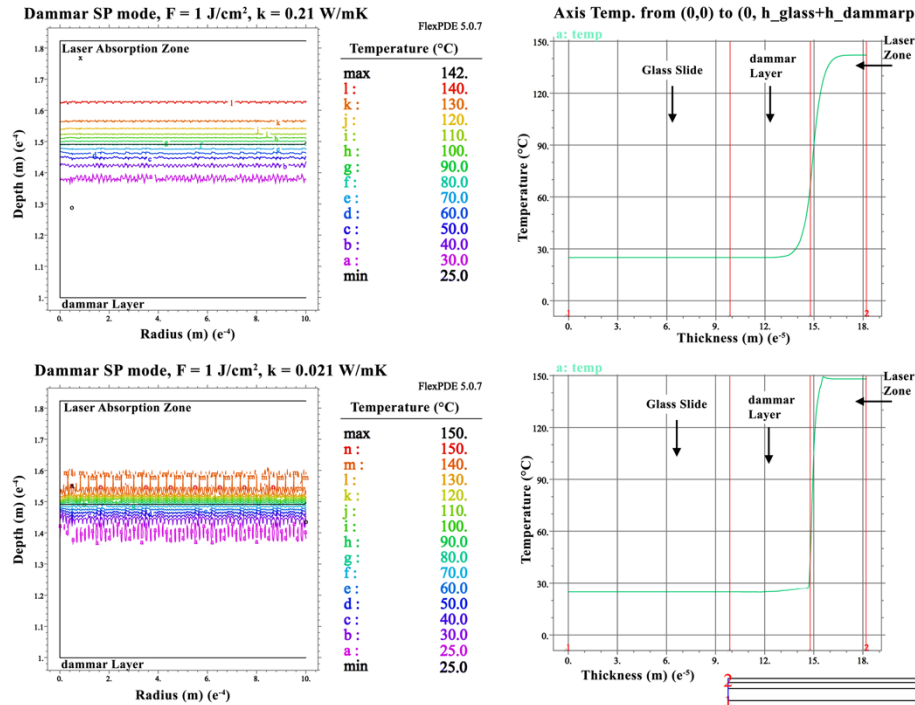


Figure B22 – 2D simulation of the heat diffusion inside the dammar film in SP mode ( $\tau_L \approx 300 \mu s$ ) and temperature distribution by cross-section of varnish film + glass slide. Fluences of 1 J/cm<sup>2</sup>, and thermal conductivity (k) between 0.21 W/m·K and 0.021 W/m·K. The beam diameter was set at  $\varnothing = 4$  mm. The laser absorption zone represents the area in which the laser wavelength penetrates into the dammar film ( $\delta$ ) before releasing 63% of its energy.

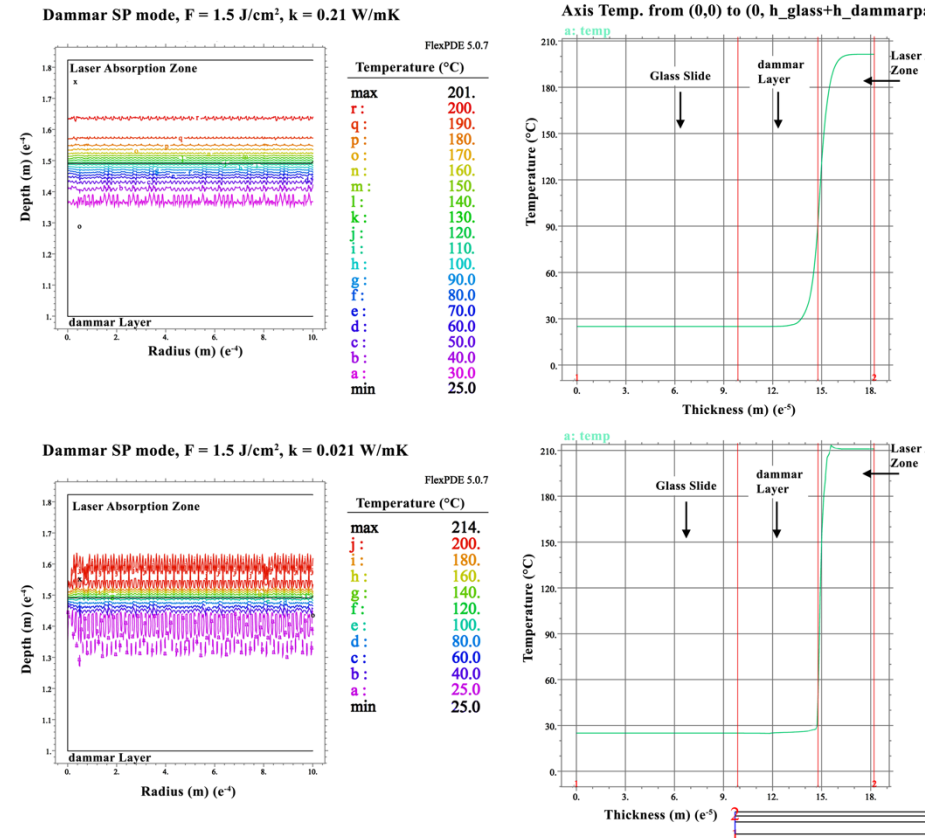


Figure B23 – 2D simulation of the heat diffusion inside the dammar film in SP mode ( $\tau_L \approx 300 \mu s$ ) and temperature distribution by cross-section of varnish film + glass slide. Fluences of 1.5 J/cm<sup>2</sup>, and thermal conductivity (k) between 0.21 W/m·K and 0.021 W/m·K. The beam diameter was set at  $\varnothing = 4$  mm. The laser absorption zone represents the area in which the laser wavelength penetrates into the dammar film ( $\delta$ ) before releasing 63% of its energy.

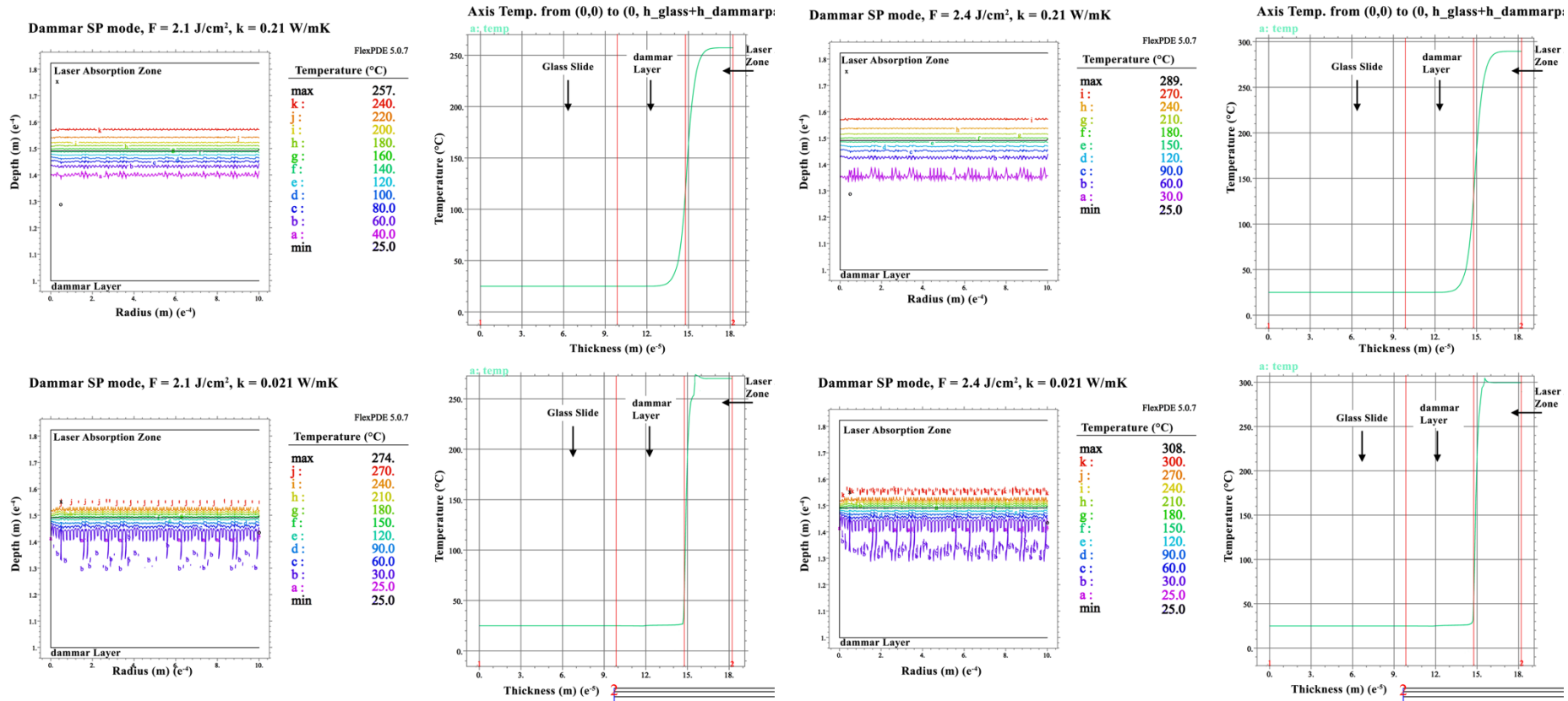


Figure B24 – 2D simulation of the heat diffusion inside the dammar film in SP mode ( $\tau_L \approx 300 \mu\text{s}$ ) and temperature distribution by cross-section of varnish film + glass slide. Fluences of  $2.1 \text{ J/cm}^2$ , and thermal conductivity ( $k$ ) between  $0.21 \text{ W/m}\cdot\text{K}$  and  $0.021 \text{ W/m}\cdot\text{K}$ . The beam diameter was set at  $\varnothing = 4 \text{ mm}$ . The laser absorption zone represents the area in which the laser wavelength penetrates into the dammar film ( $\delta$ ) before releasing 63% of its energy.

Figure B25 – 2D simulation of the heat diffusion inside the dammar film in SP mode ( $\tau_L \approx 300 \mu\text{s}$ ) and temperature distribution by cross-section of varnish film + glass slide. Fluences of  $2.4 \text{ J/cm}^2$ , and thermal conductivity ( $k$ ) between  $0.21 \text{ W/m}\cdot\text{K}$  and  $0.021 \text{ W/m}\cdot\text{K}$ . The beam diameter was set at  $\varnothing = 4 \text{ mm}$ . The laser absorption zone represents the area in which the laser wavelength penetrates into the dammar film ( $\delta$ ) before releasing 63% of its energy.

B9.3 Ketone N – VSP mode ( $\tau_L \approx 100 \mu s$ ):

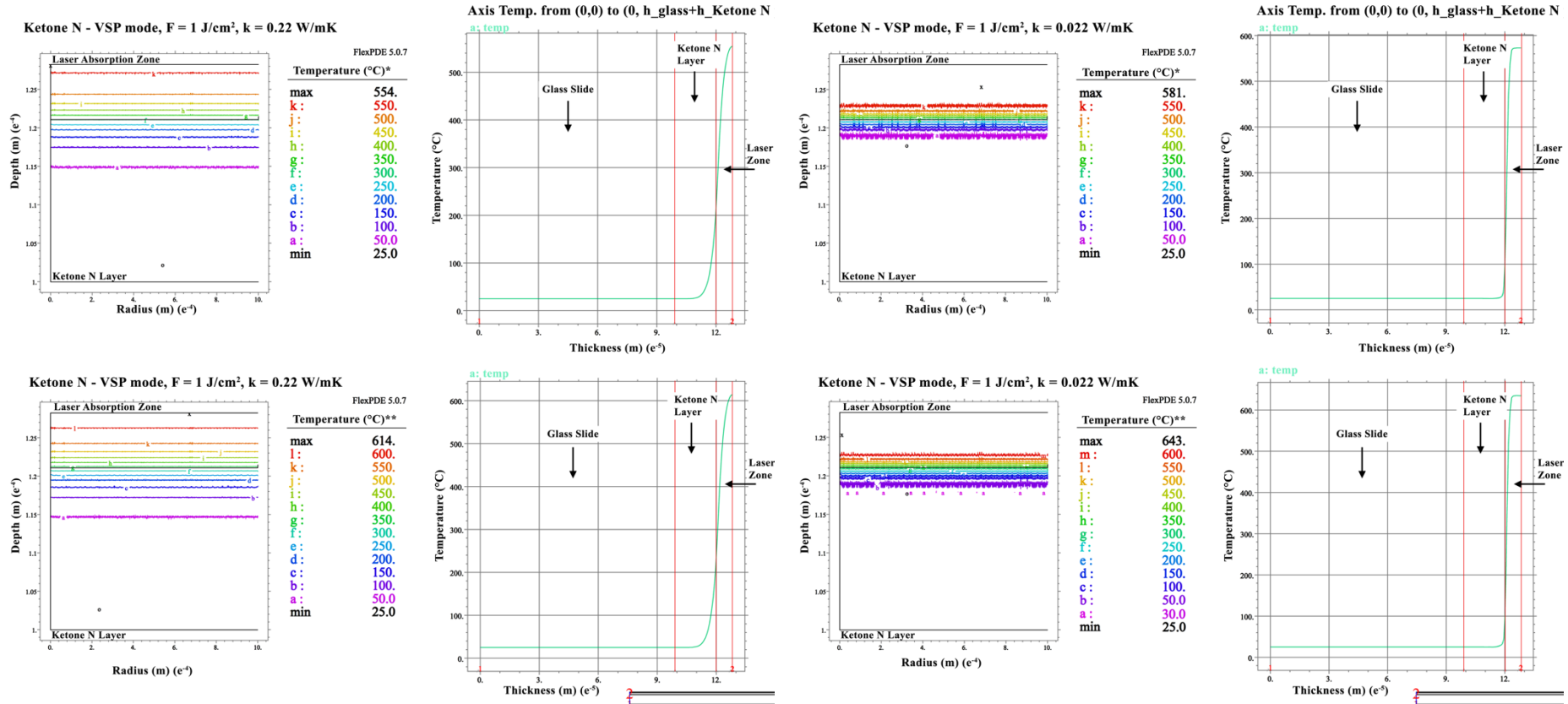


Figure B26 – 2D simulation of the heat diffusion inside the Ketone N film in VSP mode ( $\tau_L \approx 100 \mu s$ ) and temperature distribution by cross-section of varnish film + glass slide. Fluences of  $1 J/cm^2$  and thermal conductivity (k) of  $0.22 W/m \cdot K$ . One simulation was run using the %R from the FTIR (\*) the other using the %R from the Fresnel equation (\*\*). The beam diameter was set at  $\varnothing = 4mm$ . The laser absorption zone represents the area in which the laser wavelength penetrates into the Ketone N film ( $\delta$ ) before releasing 63% of its energy.

Figure B27 – 2D simulation of the heat diffusion inside the Ketone N film in VSP mode ( $\tau_L \approx 100 \mu s$ ) and temperature distribution by cross-section of varnish film + glass slide. Fluences of  $1 J/cm^2$  and thermal conductivity (k) of  $0.022 W/m \cdot K$ . One simulation was run using the %R from the FTIR (\*) the other using the %R from the Fresnel equation (\*\*). The beam diameter was set at  $\varnothing = 4mm$ . The laser absorption zone represents the area in which the laser wavelength penetrates into the Ketone N film ( $\delta$ ) before releasing 63% of its energy.

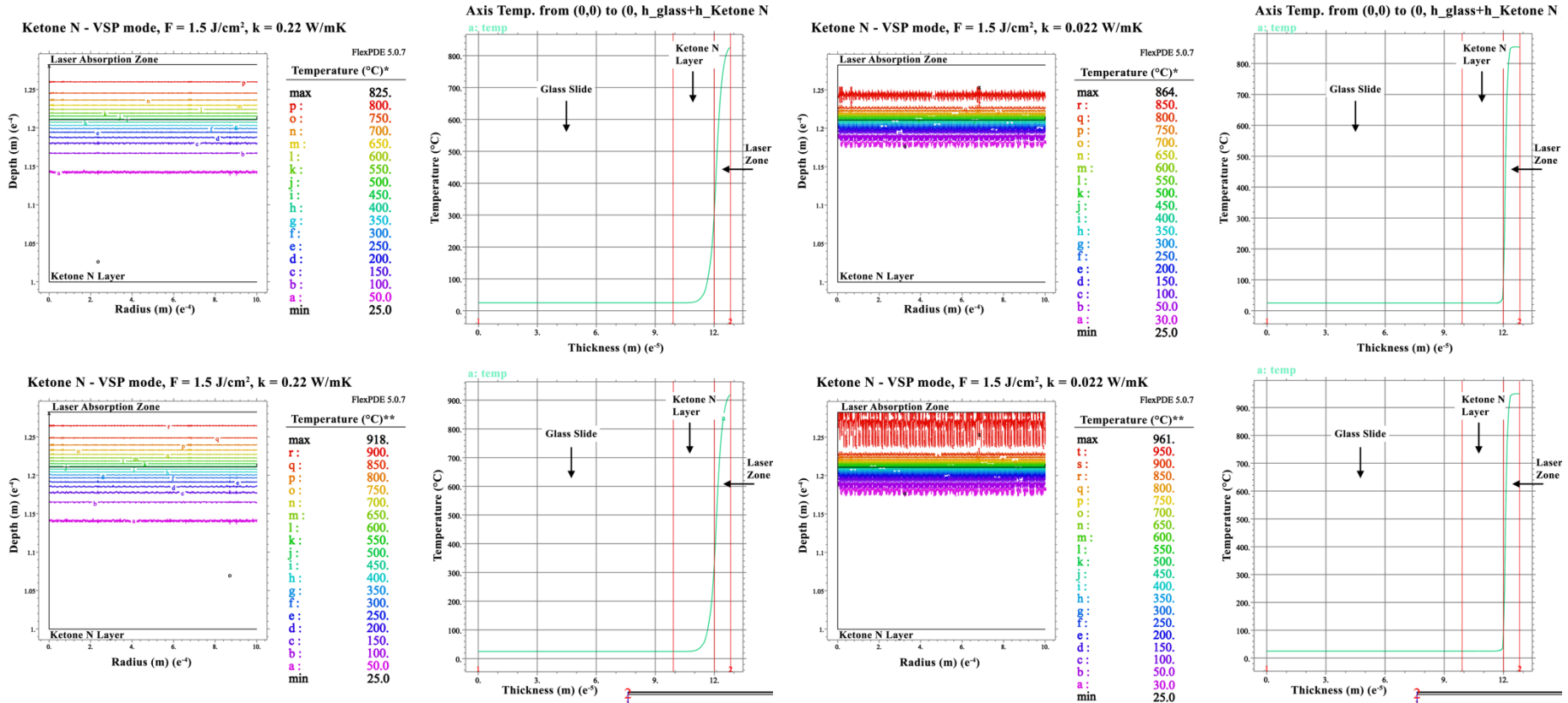


Figure B28 – 2D simulation of the heat diffusion inside the Ketone N film in VSP mode ( $\tau_L \approx 100 \mu\text{s}$ ) and temperature distribution by cross-section of varnish film + glass slide. Fluences of  $1.5 \text{ J/cm}^2$  and thermal conductivity ( $k$ ) of  $0.22 \text{ W/m}\cdot\text{K}$ . One simulation was run using the %R from the FTIR (\*) the other using the %R from the Fresnel equation (\*\*). The beam diameter was set at  $\varnothing = 4\text{mm}$ . The laser absorption zone represents the area in which the laser wavelength penetrates into the Ketone N film ( $\delta$ ) before releasing 63% of its energy.

Figure B29 – 2D simulation of the heat diffusion inside the Ketone N film in VSP mode ( $\tau_L \approx 100 \mu\text{s}$ ) and temperature distribution by cross-section of varnish film + glass slide. Fluences of  $1.5 \text{ J/cm}^2$  and thermal conductivity ( $k$ ) of  $0.022 \text{ W/m}\cdot\text{K}$ . One simulation was run using the %R from the FTIR (\*) the other using the %R from the Fresnel equation (\*\*). The beam diameter was set at  $\varnothing = 4\text{mm}$ . The laser absorption zone represents the area in which the laser wavelength penetrates into the Ketone N film ( $\delta$ ) before releasing 63% of its energy.

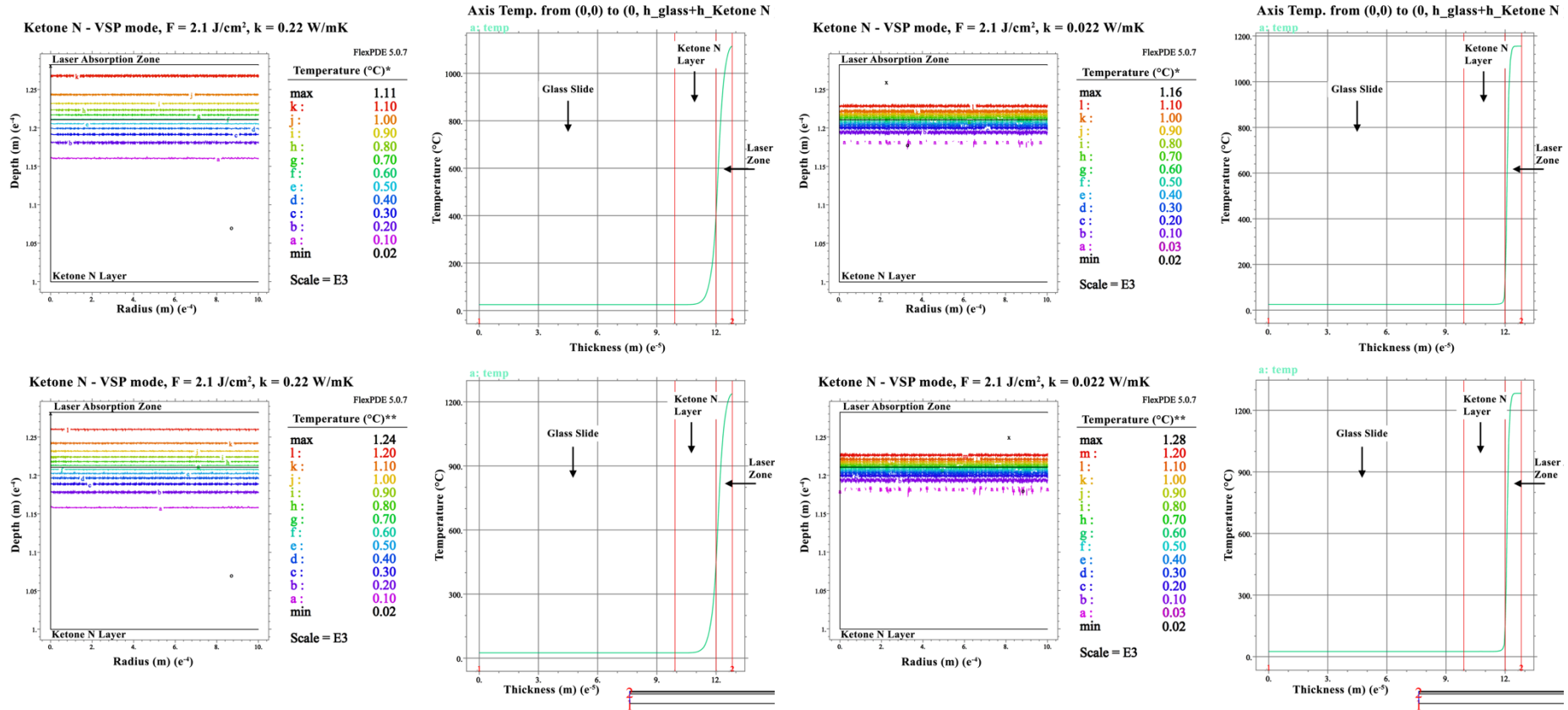


Figure B30 – 2D simulation of the heat diffusion inside the Ketone N film in VSP mode ( $\tau_L \approx 100 \mu s$ ) and temperature distribution by cross-section of varnish film + glass slide. Fluences of 2.1 J/cm<sup>2</sup> and thermal conductivity (k) of 0.22 W/m·K. One simulation was run using the %R from the FTIR (\*) the other using the %R from the Fresnel equation (\*\*). The beam diameter was set at  $\varnothing = 4mm$ . The laser absorption zone represents the area in which the laser wavelength penetrates into the Ketone N film ( $\delta$ ) before releasing 63% of its energy.

Figure B31 – 2D simulation of the heat diffusion inside the Ketone N film in VSP mode ( $\tau_L \approx 100 \mu s$ ) and temperature distribution by cross-section of varnish film + glass slide. Fluences of 2.1 J/cm<sup>2</sup> and thermal conductivity (k) of 0.022 W/m·K. One simulation was run using the %R from the FTIR (\*) the other using the %R from the Fresnel equation (\*\*). The beam diameter was set at  $\varnothing = 4mm$ . The laser absorption zone represents the area in which the laser wavelength penetrates into the Ketone N film ( $\delta$ ) before releasing 63% of its energy.

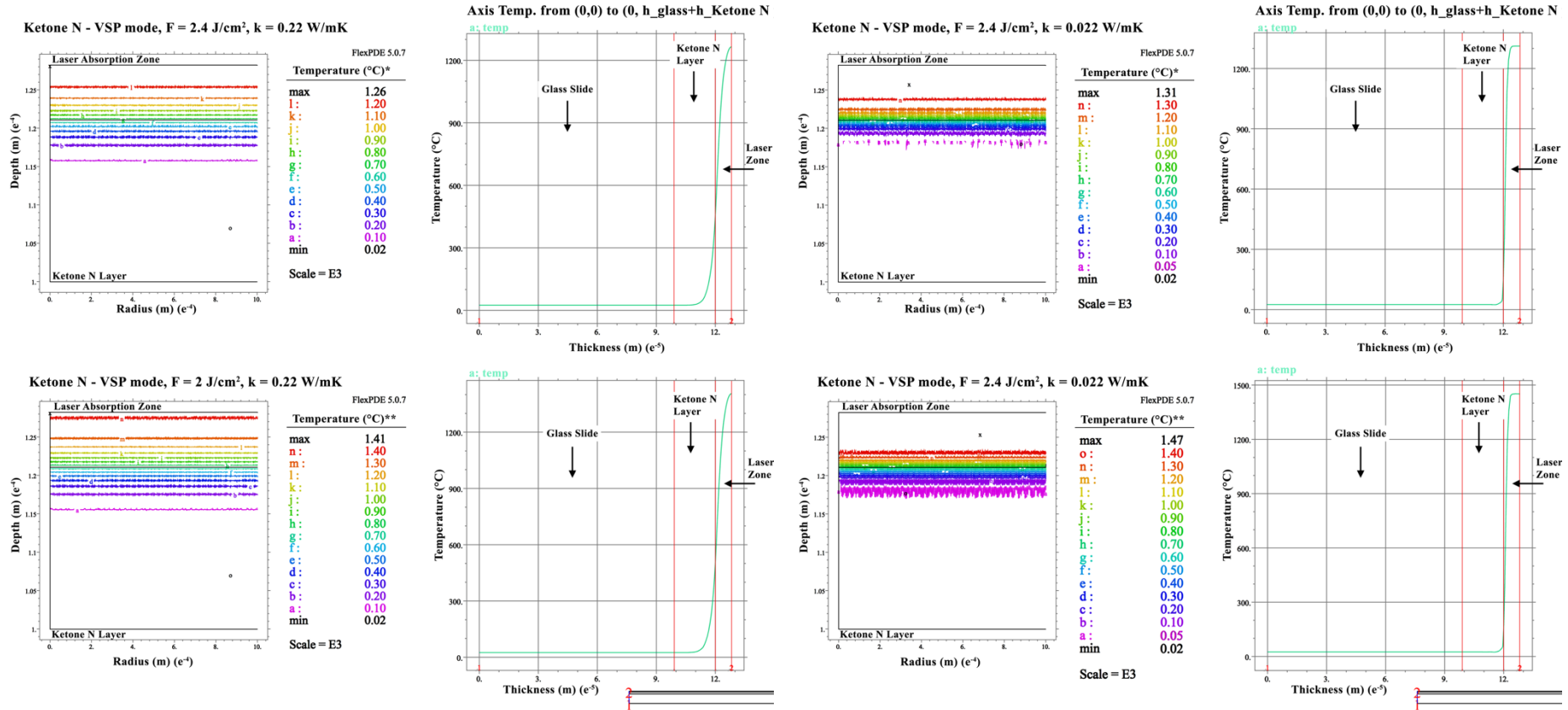


Figure B32 – 2D simulation of the heat diffusion inside the Ketone N film in VSP mode ( $\tau_L \approx 100 \mu\text{s}$ ) and temperature distribution by cross-section of varnish film + glass slide. Fluences of  $2.4 \text{ J/cm}^2$  and thermal conductivity ( $k$ ) of  $0.22 \text{ W/m}\cdot\text{K}$ . One simulation was run using the %R from the FTIR (\*) the other using the %R from the Fresnel equation (\*\*). The beam diameter was set at  $\varnothing = 4\text{mm}$ . The laser absorption zone represents the area in which the laser wavelength penetrates into the Ketone N film ( $\delta$ ) before releasing 63% of its energy.

Figure B33 – 2D simulation of the heat diffusion inside the Ketone N film in VSP mode ( $\tau_L \approx 100 \mu\text{s}$ ) and temperature distribution by cross-section of varnish film + glass slide. Fluences of  $2.4 \text{ J/cm}^2$  and thermal conductivity ( $k$ ) of  $0.022 \text{ W/m}\cdot\text{K}$ . One simulation was run using the %R from the FTIR (\*) the other using the %R from the Fresnel equation (\*\*). The beam diameter was set at  $\varnothing = 4\text{mm}$ . The laser absorption zone represents the area in which the laser wavelength penetrates into the Ketone N film ( $\delta$ ) before releasing 63% of its energy.

B9.4 Ketone N – SP mode ( $\tau_L \approx 300 \mu s$ ):

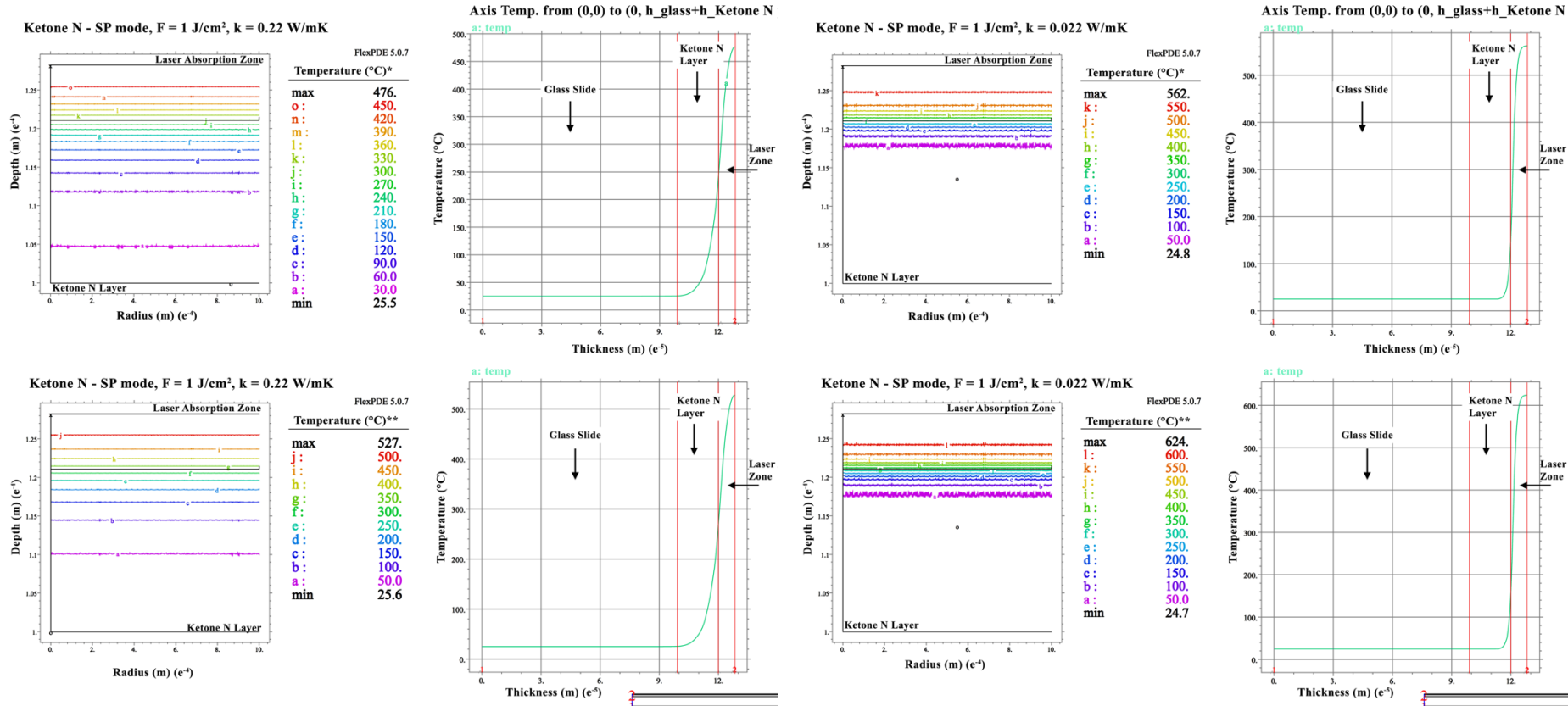


Figure B34 – 2D simulation of the heat diffusion inside the Ketone N film in SP mode ( $\tau_L \approx 300 \mu s$ ) and temperature distribution by cross-section of varnish film + glass slide. Fluences of  $1 J/cm^2$  and thermal conductivity ( $k$ ) of  $0.22 W/m \cdot K$ . One simulation was run using the %R from the FTIR (\*) the other using the %R from the Fresnel equation (\*\*). The beam diameter was set at  $\varnothing = 4mm$ . The laser absorption zone represents the area in which the laser wavelength penetrates into the Ketone N film ( $\delta$ ) before releasing 63% of its energy.

Figure B35 – 2D simulation of the heat diffusion inside the Ketone N film in SP mode ( $\tau_L \approx 300 \mu s$ ) and temperature distribution by cross-section of varnish film + glass slide. Fluences of  $1 J/cm^2$  and thermal conductivity ( $k$ ) of  $0.022 W/m \cdot K$ . One simulation was run using the %R from the FTIR (\*) the other using the %R from the Fresnel equation (\*\*). The beam diameter was set at  $\varnothing = 4mm$ . The laser absorption zone represents the area in which the laser wavelength penetrates into the Ketone N film ( $\delta$ ) before releasing 63% of its energy.

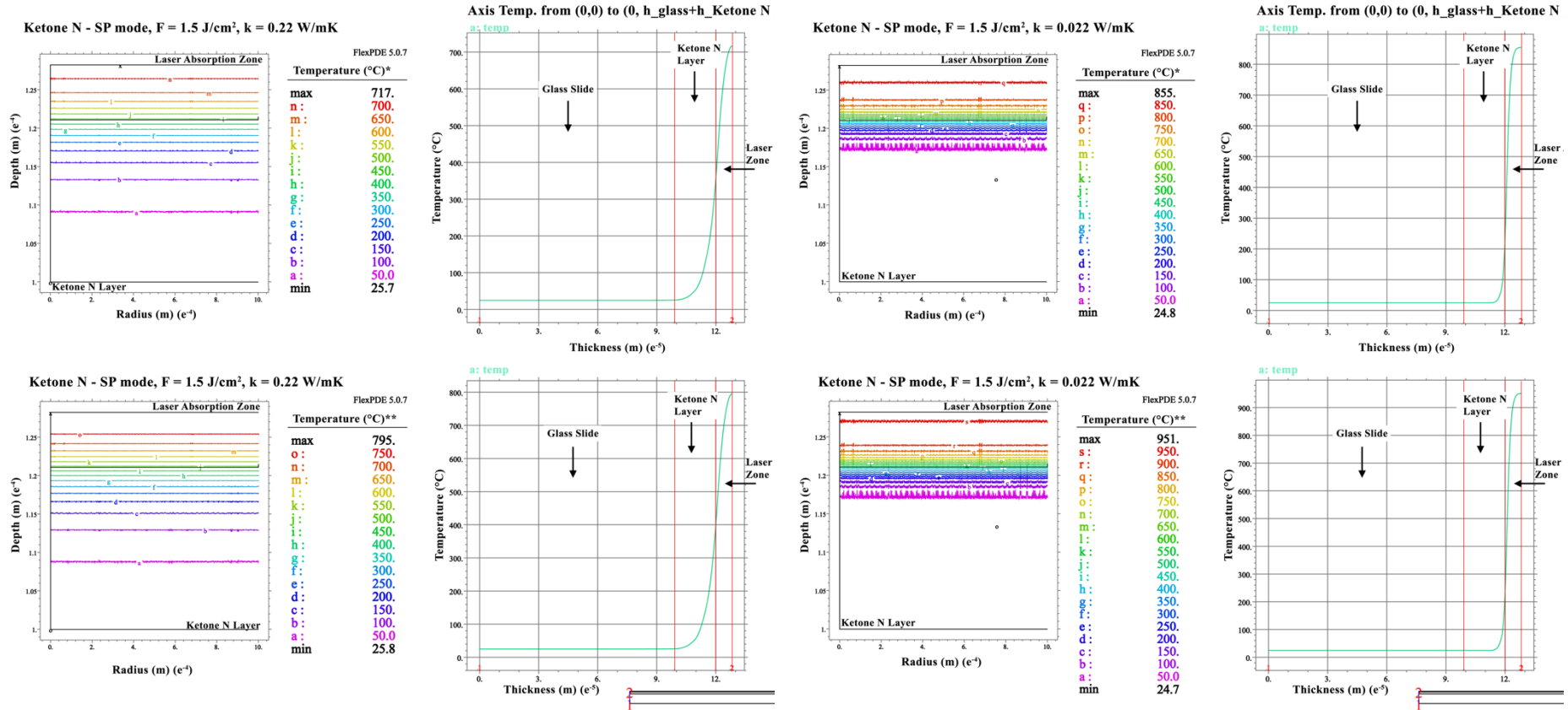


Figure B36 – 2D simulation of the heat diffusion inside the Ketone N film in SP mode ( $\tau_L \approx 300 \mu s$ ) and temperature distribution by cross-section of varnish film + glass slide. Fluences of  $1.5 J/cm^2$  and thermal conductivity (k) of  $0.22 W/m \cdot K$ . One simulation was run using the %R from the FTIR (\*) the other using the %R from the Fresnel equation (\*\*). The beam diameter was set at  $\varnothing = 4mm$ . The laser absorption zone represents the area in which the laser wavelength penetrates into the Ketone N film ( $\delta$ ) before releasing 63% of its energy.

Figure B37 – 2D simulation of the heat diffusion inside the Ketone N film in SP mode ( $\tau_L \approx 300 \mu s$ ) and temperature distribution by cross-section of varnish film + glass slide. Fluences of  $1.5 J/cm^2$  and thermal conductivity (k) of  $0.22 W/m \cdot K$ . One simulation was run using the %R from the FTIR (\*) the other using the %R from the Fresnel equation (\*\*). The beam diameter was set at  $\varnothing = 4mm$ . The laser absorption zone represents the area in which the laser wavelength penetrates into the Ketone N film ( $\delta$ ) before releasing 63% of its energy.

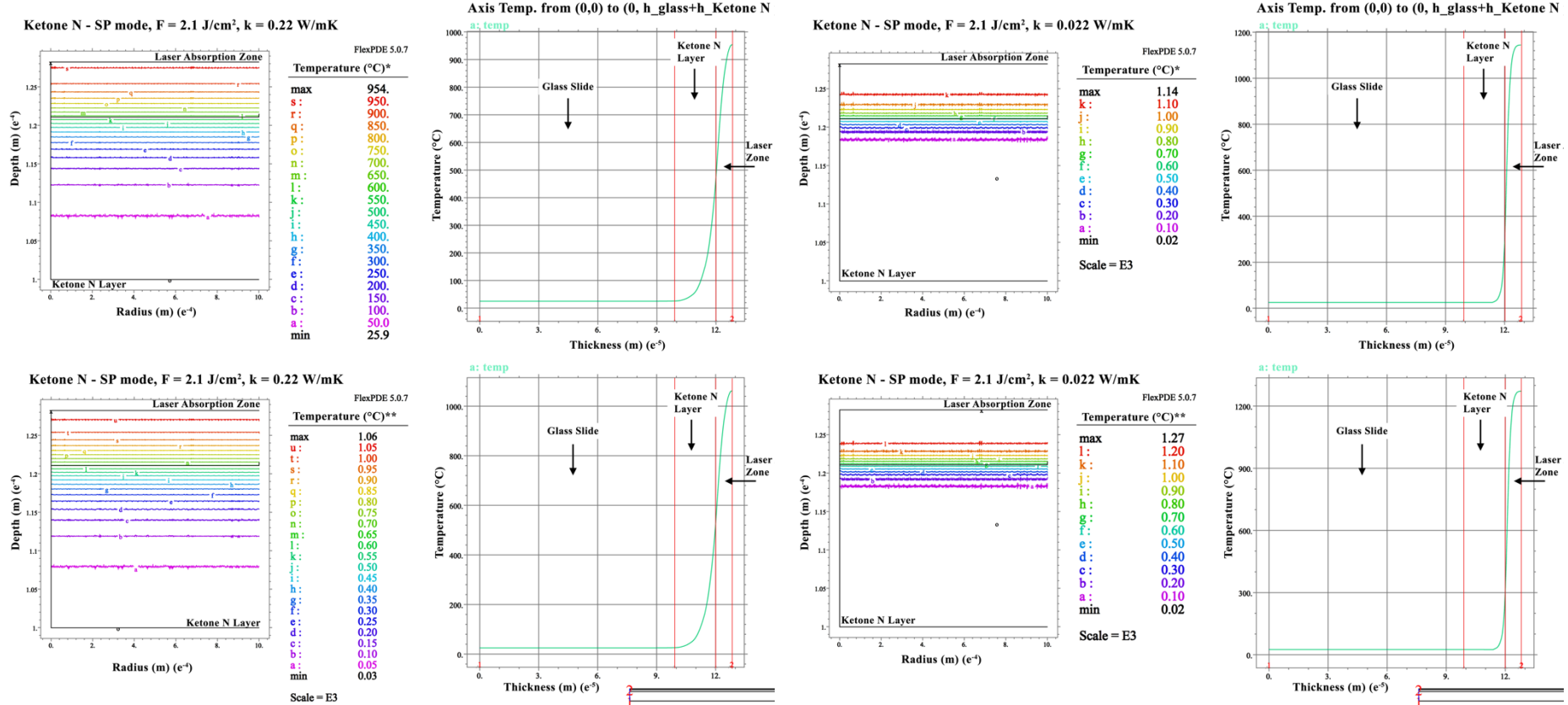


Figure B38 – 2D simulation of the heat diffusion inside the Ketone N film in SP mode ( $\tau_L \approx 300 \mu\text{s}$ ) and temperature distribution by cross-section of varnish film + glass slide. Fluences of  $2.1 \text{ J/cm}^2$  and thermal conductivity ( $k$ ) of  $0.22 \text{ W/m}\cdot\text{K}$ . One simulation was run using the %R from the FTIR (\*) the other using the %R from the Fresnel equation (\*\*). The beam diameter was set at  $\varnothing = 4\text{mm}$ . The laser absorption zone represents the area in which the laser wavelength penetrates into the Ketone N film ( $\delta$ ) before releasing 63% of its energy.

Figure B39 – 2D simulation of the heat diffusion inside the Ketone N film in SP mode ( $\tau_L \approx 300 \mu\text{s}$ ) and temperature distribution by cross-section of varnish film + glass slide. Fluences of  $2.1 \text{ J/cm}^2$  and thermal conductivity ( $k$ ) of  $0.022 \text{ W/m}\cdot\text{K}$ . One simulation was run using the %R from the FTIR (\*) the other using the %R from the Fresnel equation (\*\*). The beam diameter was set at  $\varnothing = 4\text{mm}$ . The laser absorption zone represents the area in which the laser wavelength penetrates into the Ketone N film ( $\delta$ ) before releasing 63% of its energy.

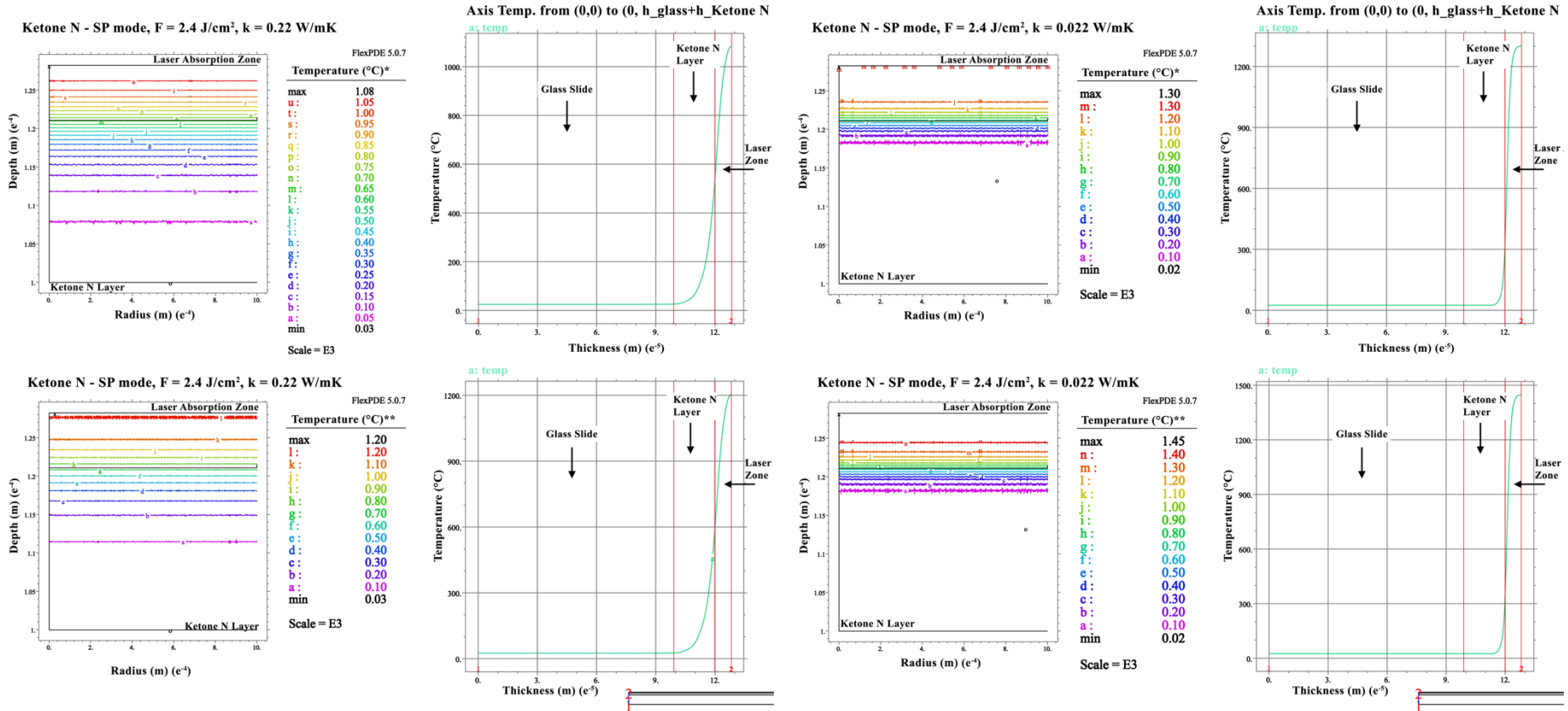


Figure B40 – 2D simulation of the heat diffusion inside the Ketone N film in SP mode ( $\tau_L \approx 300 \mu s$ ) and temperature distribution by cross-section of varnish film + glass slide. Fluences of  $2.4 J/cm^2$  and thermal conductivity ( $k$ ) of  $0.22 W/m \cdot K$ . One simulation was run using the %R from the FTIR (\*) the other using the %R from the Fresnel equation (\*\*). The beam diameter was set at  $\varnothing = 4mm$ . The laser absorption zone represents the area in which the laser wavelength penetrates into the Ketone N film ( $\delta$ ) before releasing 63% of its energy.

Figure B41 – 2D simulation of the heat diffusion inside the Ketone N film in SP mode ( $\tau_L \approx 300 \mu s$ ) and temperature distribution by cross-section of varnish film + glass slide. Fluences of  $2.4 J/cm^2$  and thermal conductivity ( $k$ ) of  $0.22 W/m \cdot K$ . One simulation was run using the %R from the FTIR (\*) the other using the %R from the Fresnel equation (\*\*). The beam diameter was set at  $\varnothing = 4mm$ . The laser absorption zone represents the area in which the laser wavelength penetrates into the Ketone N film ( $\delta$ ) before releasing 63% of its energy.

B9.5 MS2A – VSP mode ( $\tau_L \approx 100 \mu s$ ):

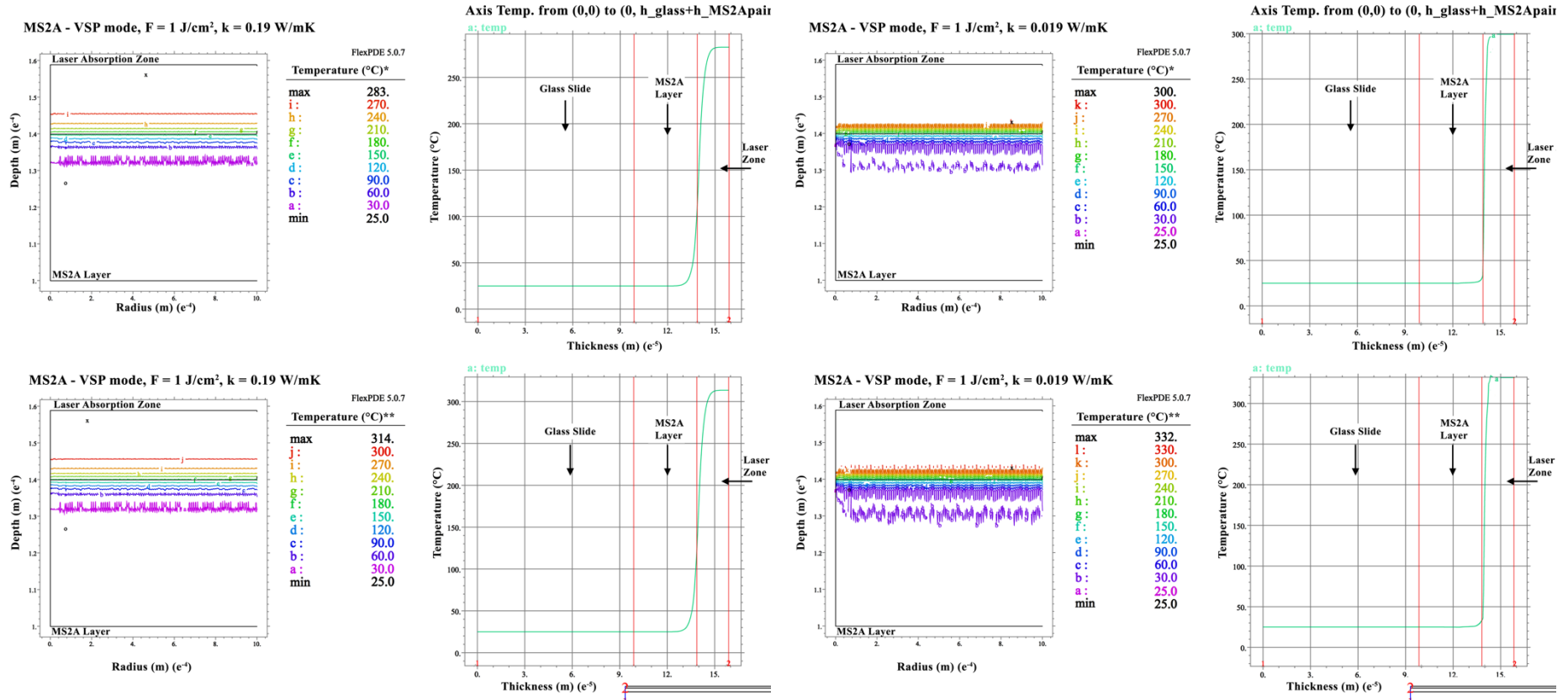


Figure B42 – 2D simulation of the heat diffusion inside the MS2A film in VSP mode ( $\tau_L \approx 100 \mu s$ ) and temperature distribution by cross-section of varnish film + glass slide. Fluences of  $1 J/cm^2$  and thermal conductivity (k) of  $0.19 W/m \cdot K$ . One simulation was run using the %R from the FTIR (\*) the other using the %R from the Fresnel equation (\*\*). The beam diameter was set at  $\varnothing = 4mm$ . The laser absorption zone represents the area in which the laser wavelength penetrates into the MS2A film ( $\delta$ ) before releasing 63% of its energy.

Figure B43 – 2D simulation of the heat diffusion inside the MS2A film in VSP mode ( $\tau_L \approx 100 \mu s$ ) and temperature distribution by cross-section of varnish film + glass slide. Fluences of  $1 J/cm^2$  and thermal conductivity (k) of  $0.019 W/m \cdot K$ . One simulation was run using the %R from the FTIR (\*) the other using the %R from the Fresnel equation (\*\*). The beam diameter was set at  $\varnothing = 4mm$ . The laser absorption zone represents the area in which the laser wavelength penetrates into the MS2A film ( $\delta$ ) before releasing 63% of its energy.

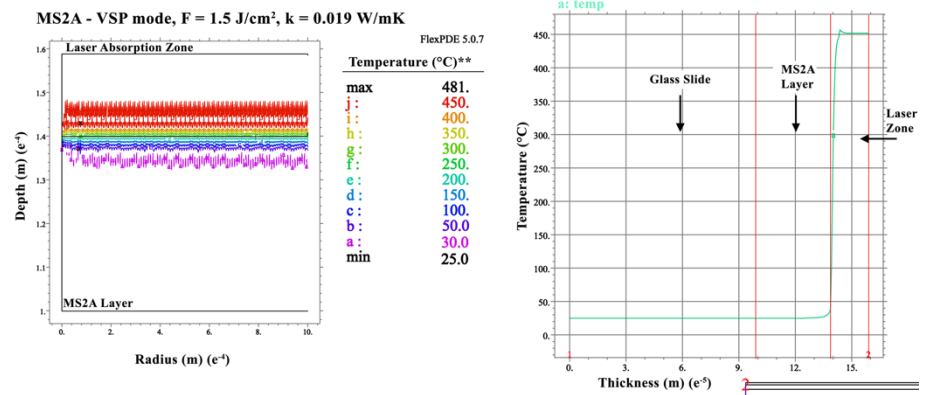
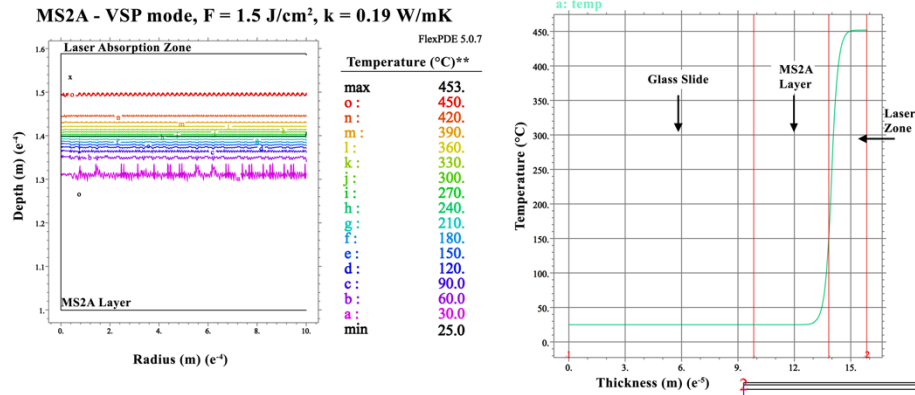
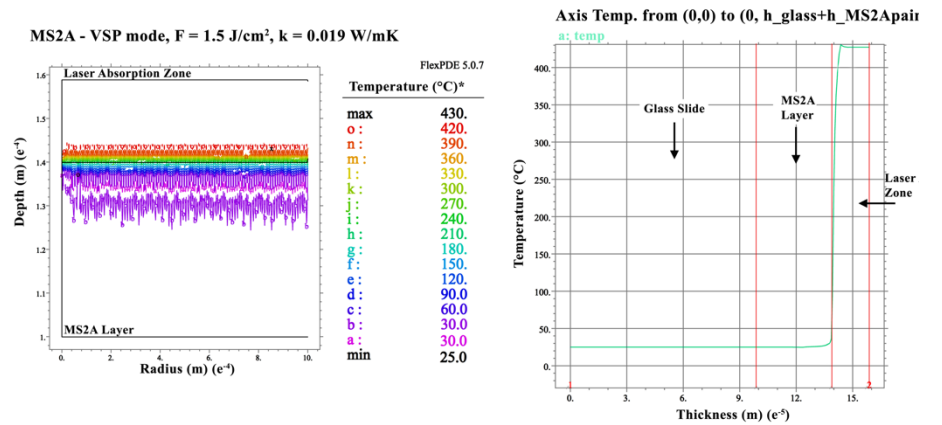
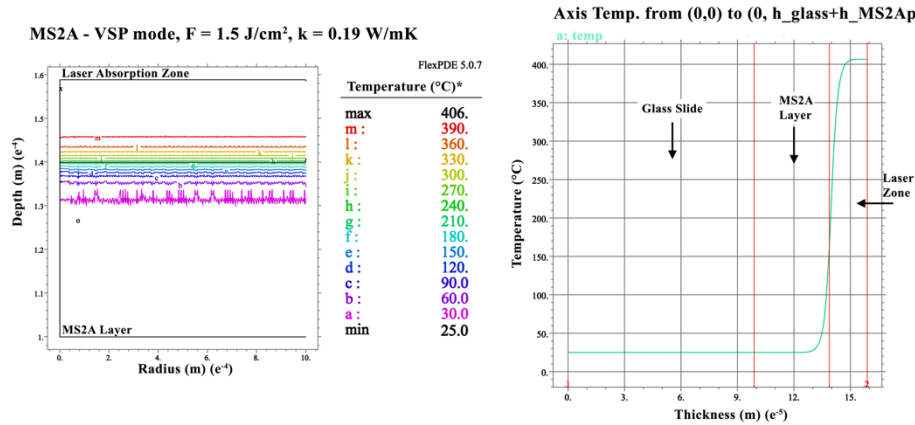


Figure B44 – 2D simulation of the heat diffusion inside the MS2A film in VSP mode ( $\tau_L \approx 100 \mu\text{s}$ ) and temperature distribution by cross-section of varnish film + glass slide. Fluences of  $1.5 \text{ J/cm}^2$  and thermal conductivity ( $k$ ) of  $0.19 \text{ W/m}\cdot\text{K}$ . One simulation was run using the %R from the FTIR (\*) the other using the %R from the Fresnel equation (\*\*). The beam diameter was set at  $\varnothing = 4\text{mm}$ . The laser absorption zone represents the area in which the laser wavelength penetrates into the MS2A film ( $\delta$ ) before releasing 63% of its energy.

Figure B45 – 2D simulation of the heat diffusion inside the MS2A film in VSP mode ( $\tau_L \approx 100 \mu\text{s}$ ) and temperature distribution by cross-section of varnish film + glass slide. Fluences of  $1.5 \text{ J/cm}^2$  and thermal conductivity ( $k$ ) of  $0.019 \text{ W/m}\cdot\text{K}$ . One simulation was run using the %R from the FTIR (\*) the other using the %R from the Fresnel equation (\*\*). The beam diameter was set at  $\varnothing = 4\text{mm}$ . The laser absorption zone represents the area in which the laser wavelength penetrates into the MS2A film ( $\delta$ ) before releasing 63% of its energy.

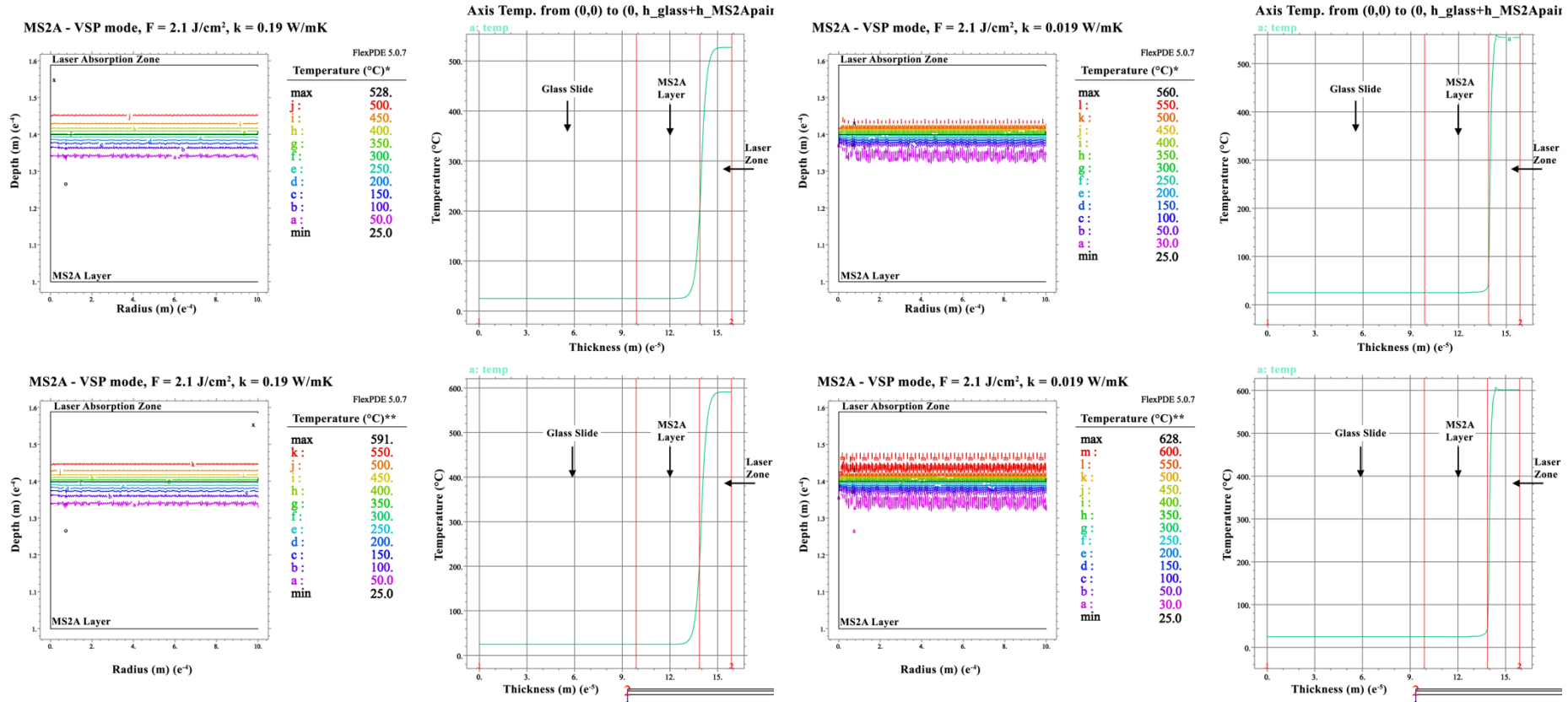


Figure B46 – 2D simulation of the heat diffusion inside the MS2A film in VSP mode ( $\tau_L \approx 100 \mu s$ ) and temperature distribution by cross-section of varnish film + glass slide. Fluences of 2.1 J/cm<sup>2</sup> and thermal conductivity (k) of 0.19 W/m·K. One simulation was run using the %R from the FTIR (\*) the other using the %R from the Fresnel equation (\*\*). The beam diameter was set at  $\varnothing = 4mm$ . The laser absorption zone represents the area in which the laser wavelength penetrates into the MS2A film ( $\delta$ ) before releasing 63% of its energy.

Figure B47 – 2D simulation of the heat diffusion inside the MS2A film in VSP mode ( $\tau_L \approx 100 \mu s$ ) and temperature distribution by cross-section of varnish film + glass slide. Fluences of 2.1 J/cm<sup>2</sup> and thermal conductivity (k) of 0.019 W/m·K. One simulation was run using the %R from the FTIR (\*) the other using the %R from the Fresnel equation (\*\*). The beam diameter was set at  $\varnothing = 4mm$ . The laser absorption zone represents the area in which the laser wavelength penetrates into the MS2A film ( $\delta$ ) before releasing 63% of its energy.

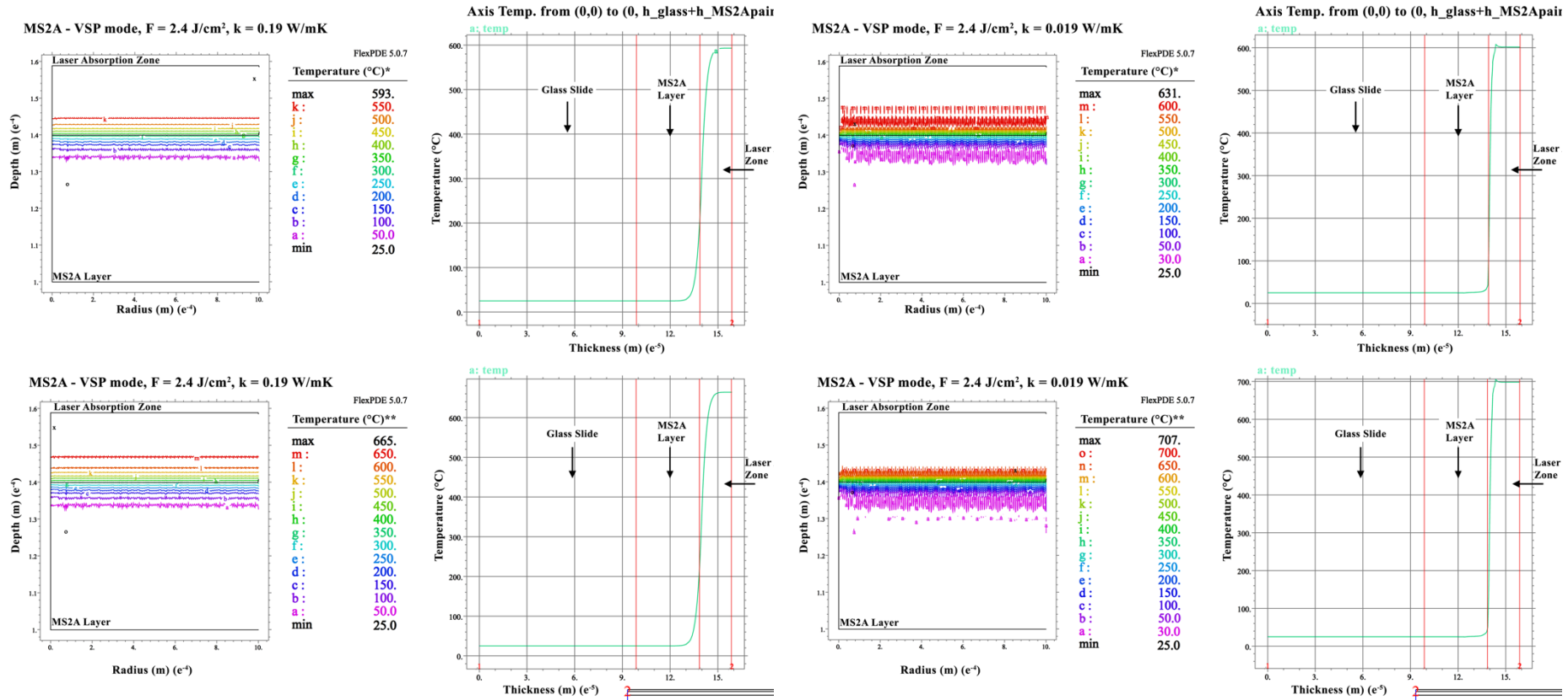


Figure B48 – 2D simulation of the heat diffusion inside the MS2A film in VSP mode ( $\tau_L \approx 100 \mu s$ ) and temperature distribution by cross-section of varnish film + glass slide. Fluences of 2.4 J/cm<sup>2</sup> and thermal conductivity (k) of 0.19 W/m·K. One simulation was run using the %R from the FTIR (\*) the other using the %R from the Fresnel equation (\*\*). The beam diameter was set at  $\varnothing = 4mm$ . The laser absorption zone represents the area in which the laser wavelength penetrates into the MS2A film ( $\delta$ ) before releasing 63% of its energy.

Figure B49 – 2D simulation of the heat diffusion inside the MS2A film in VSP mode ( $\tau_L \approx 100 \mu s$ ) and temperature distribution by cross-section of varnish film + glass slide. Fluences of 2.4 J/cm<sup>2</sup> and thermal conductivity (k) of 0.019 W/m·K. One simulation was run using the %R from the FTIR (\*) the other using the %R from the Fresnel equation (\*\*). The beam diameter was set at  $\varnothing = 4mm$ . The laser absorption zone represents the area in which the laser wavelength penetrates into the MS2A film ( $\delta$ ) before releasing 63% of its energy.

B9.6 MS2A – SP mode ( $\tau_L \approx 300 \mu s$ ):

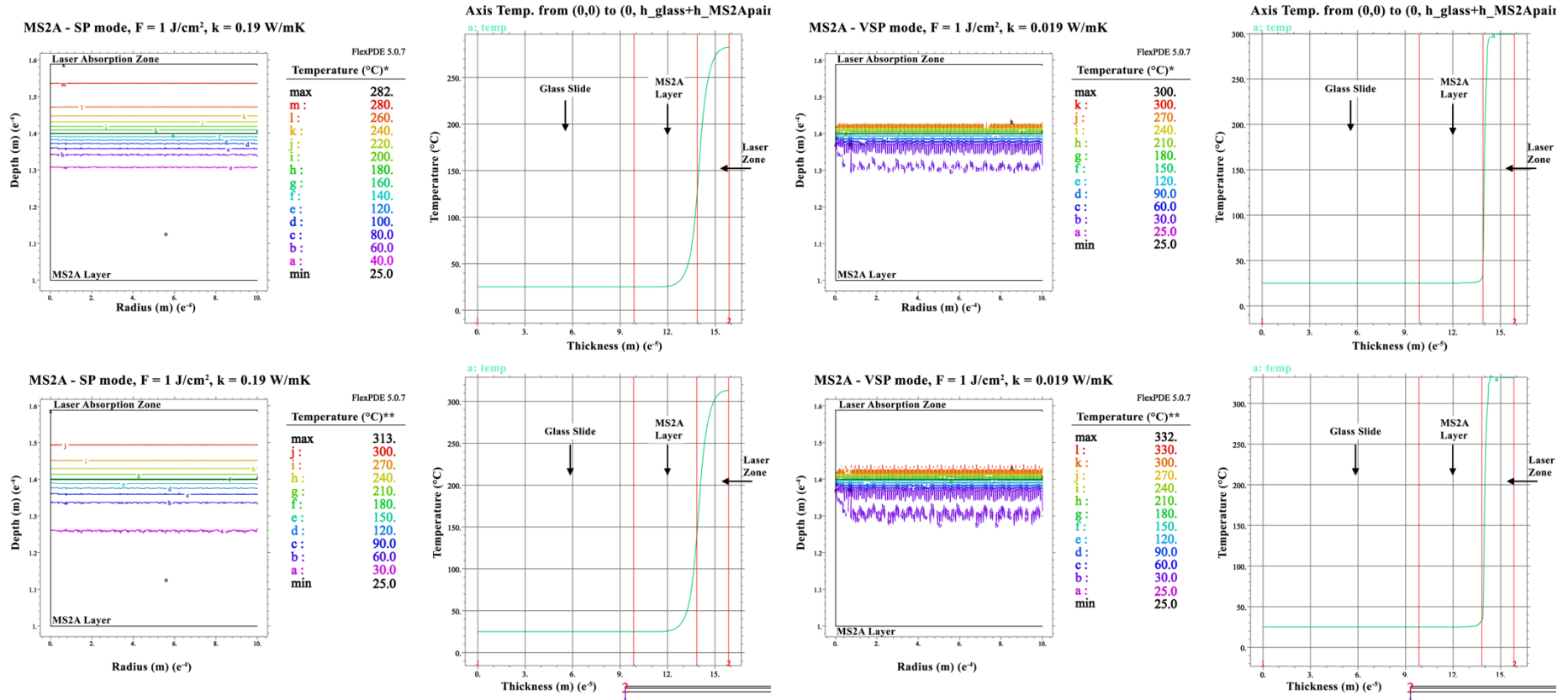


Figure B50 – 2D simulation of the heat diffusion inside the MS2A film in SP mode ( $\tau_L \approx 300 \mu s$ ) and temperature distribution by cross-section of varnish film + glass slide. Fluences of  $1 \text{ J/cm}^2$  and thermal conductivity ( $k$ ) of  $0.19 \text{ W/m}\cdot\text{K}$ . One simulation was run using the %R from the FTIR (\*) the other using the %R from the Fresnel equation (\*\*). The beam diameter was set at  $\varnothing = 4\text{mm}$ . The laser absorption zone represents the area in which the laser wavelength penetrates into the MS2A film ( $\delta$ ) before releasing 63% of its energy.

Figure B51 – 2D simulation of the heat diffusion inside the MS2A film in SP mode ( $\tau_L \approx 300 \mu s$ ) and temperature distribution by cross-section of varnish film + glass slide. Fluences of  $1 \text{ J/cm}^2$  and thermal conductivity ( $k$ ) of  $0.019 \text{ W/m}\cdot\text{K}$ . One simulation was run using the %R from the FTIR (\*) the other using the %R from the Fresnel equation (\*\*). The beam diameter was set at  $\varnothing = 4\text{mm}$ . The laser absorption zone represents the area in which the laser wavelength penetrates into the MS2A film ( $\delta$ ) before releasing 63% of its energy.

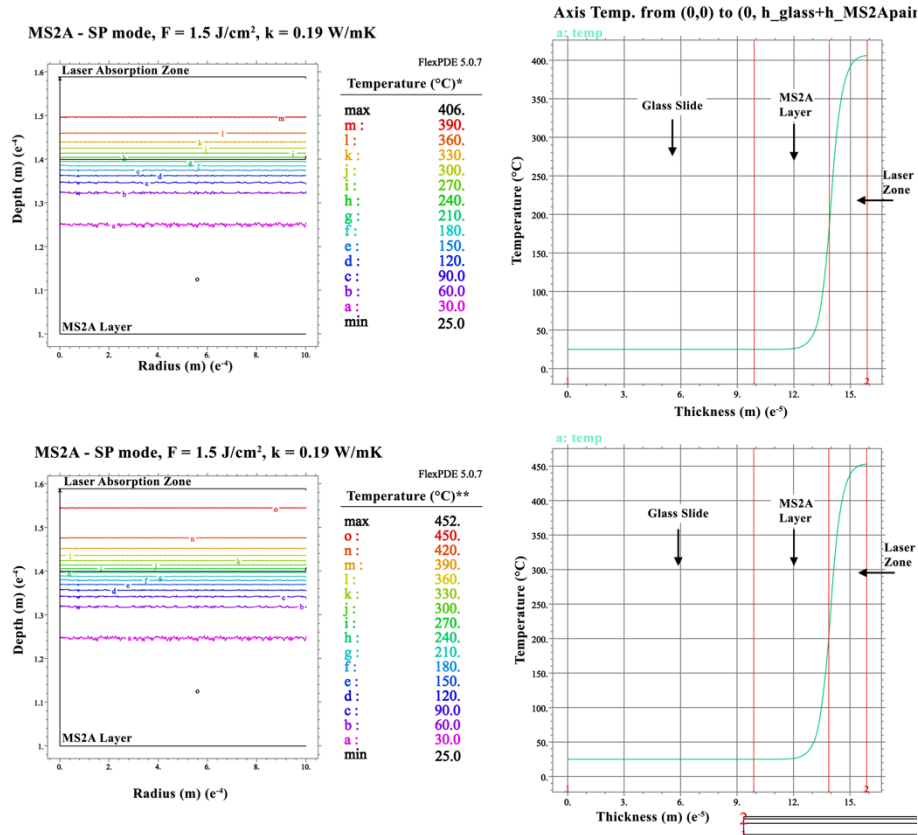


Figure B52 – 2D simulation of the heat diffusion inside the MS2A film in SP mode ( $\tau_L \approx 300 \mu\text{s}$ ) and temperature distribution by cross-section of varnish film + glass slide. Fluences of  $1.5 \text{ J/cm}^2$  and thermal conductivity ( $k$ ) of  $0.19 \text{ W/m}\cdot\text{K}$ . One simulation was run using the %R from the FTIR (\*) the other using the %R from the Fresnel equation (\*\*). The beam diameter was set at  $\varnothing = 4\text{mm}$ . The laser absorption zone represents the area in which the laser wavelength penetrates into the MS2A film ( $\delta$ ) before releasing 63% of its energy.

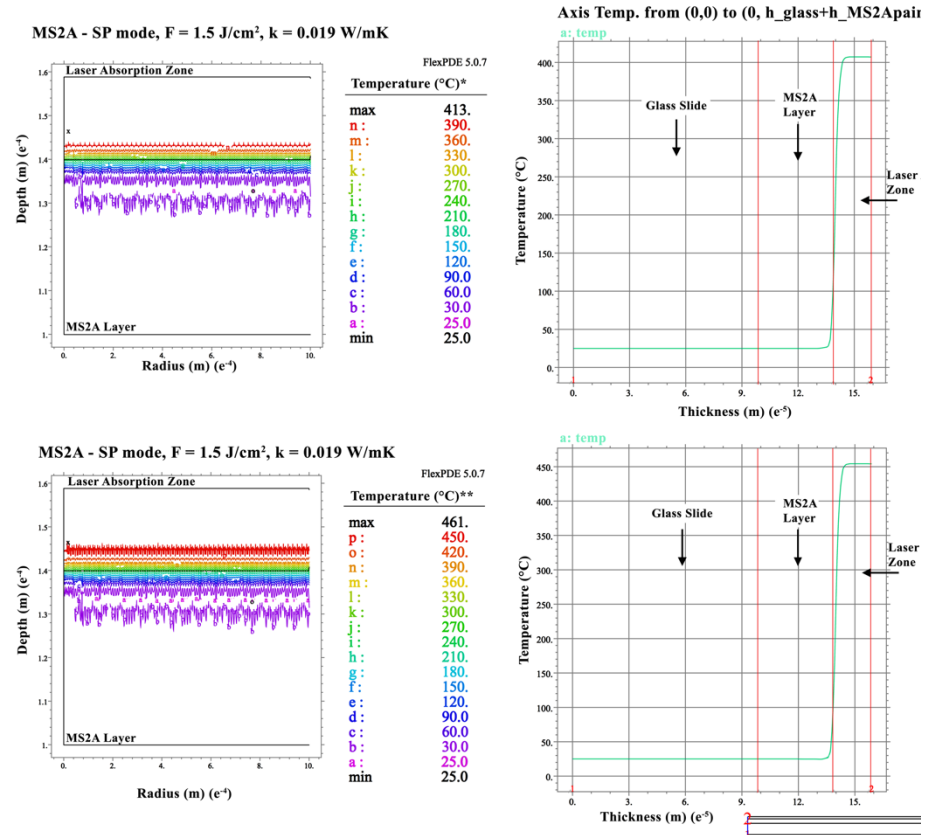


Figure B53 – 2D simulation of the heat diffusion inside the MS2A film in SP mode ( $\tau_L \approx 300 \mu\text{s}$ ) and temperature distribution by cross-section of varnish film + glass slide. Fluences of  $1.5 \text{ J/cm}^2$  and thermal conductivity ( $k$ ) of  $0.019 \text{ W/m}\cdot\text{K}$ . One simulation was run using the %R from the FTIR (\*) the other using the %R from the Fresnel equation (\*\*). The beam diameter was set at  $\varnothing = 4\text{mm}$ . The laser absorption zone represents the area in which the laser wavelength penetrates into the MS2A film ( $\delta$ ) before releasing 63% of its energy.

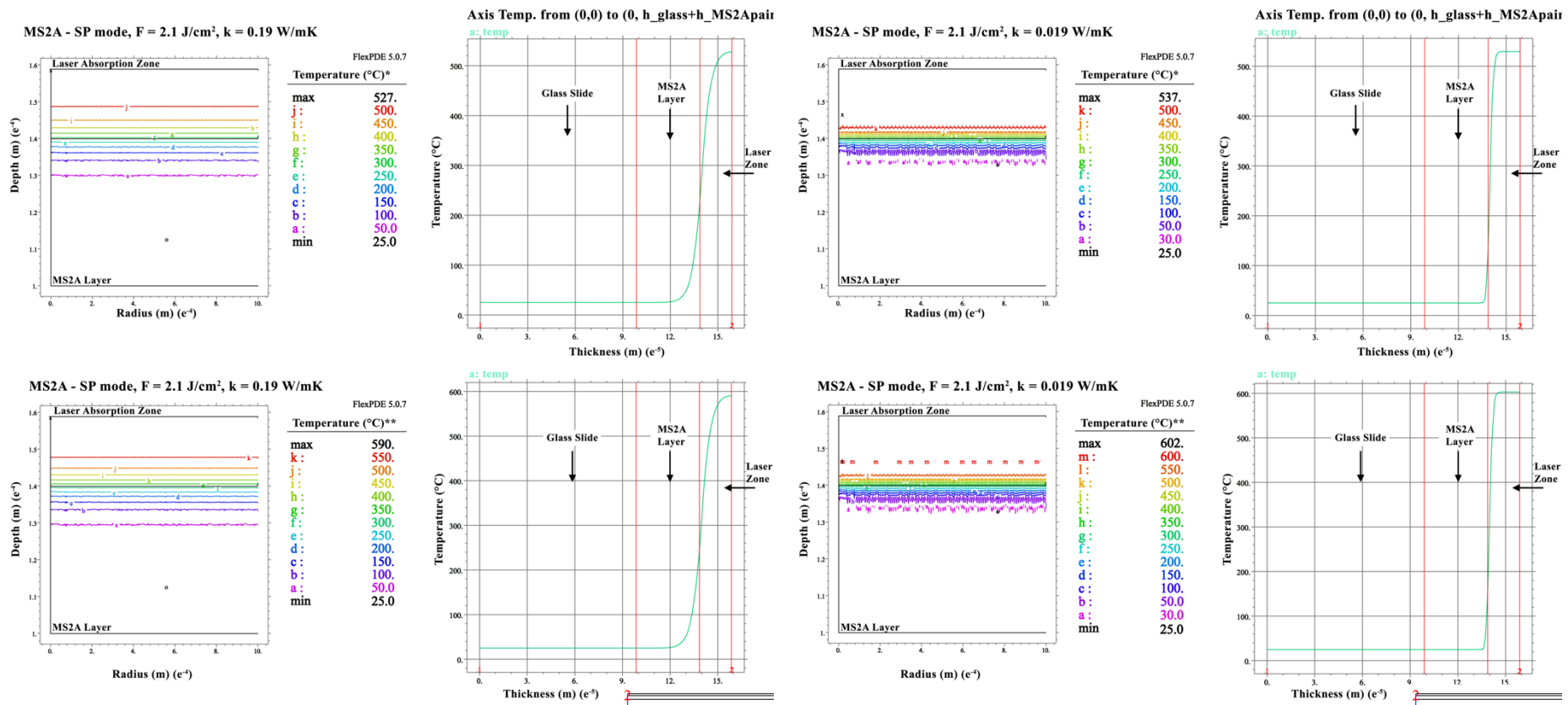


Figure B54 – 2D simulation of the heat diffusion inside the MS2A film in SP mode ( $\tau_L \approx 300 \mu s$ ) and temperature distribution by cross-section of varnish film + glass slide. Fluences of  $2.1 \text{ J/cm}^2$  and thermal conductivity ( $k$ ) of  $0.19 \text{ W/m}\cdot\text{K}$ . One simulation was run using the %R from the FTIR (\*) the other using the %R from the Fresnel equation (\*\*). The beam diameter was set at  $\varnothing = 4\text{mm}$ . The laser absorption zone represents the area in which the laser wavelength penetrates into the MS2A film ( $\delta$ ) before releasing 63% of its energy.

Figure B55 – 2D simulation of the heat diffusion inside the MS2A film in SP mode ( $\tau_L \approx 300 \mu s$ ) and temperature distribution by cross-section of varnish film + glass slide. Fluences of  $2.1 \text{ J/cm}^2$  and thermal conductivity ( $k$ ) of  $0.019 \text{ W/m}\cdot\text{K}$ . One simulation was run using the %R from the FTIR (\*) the other using the %R from the Fresnel equation (\*\*). The beam diameter was set at  $\varnothing = 4\text{mm}$ . The laser absorption zone represents the area in which the laser wavelength penetrates into the MS2A film ( $\delta$ ) before releasing 63% of its energy.

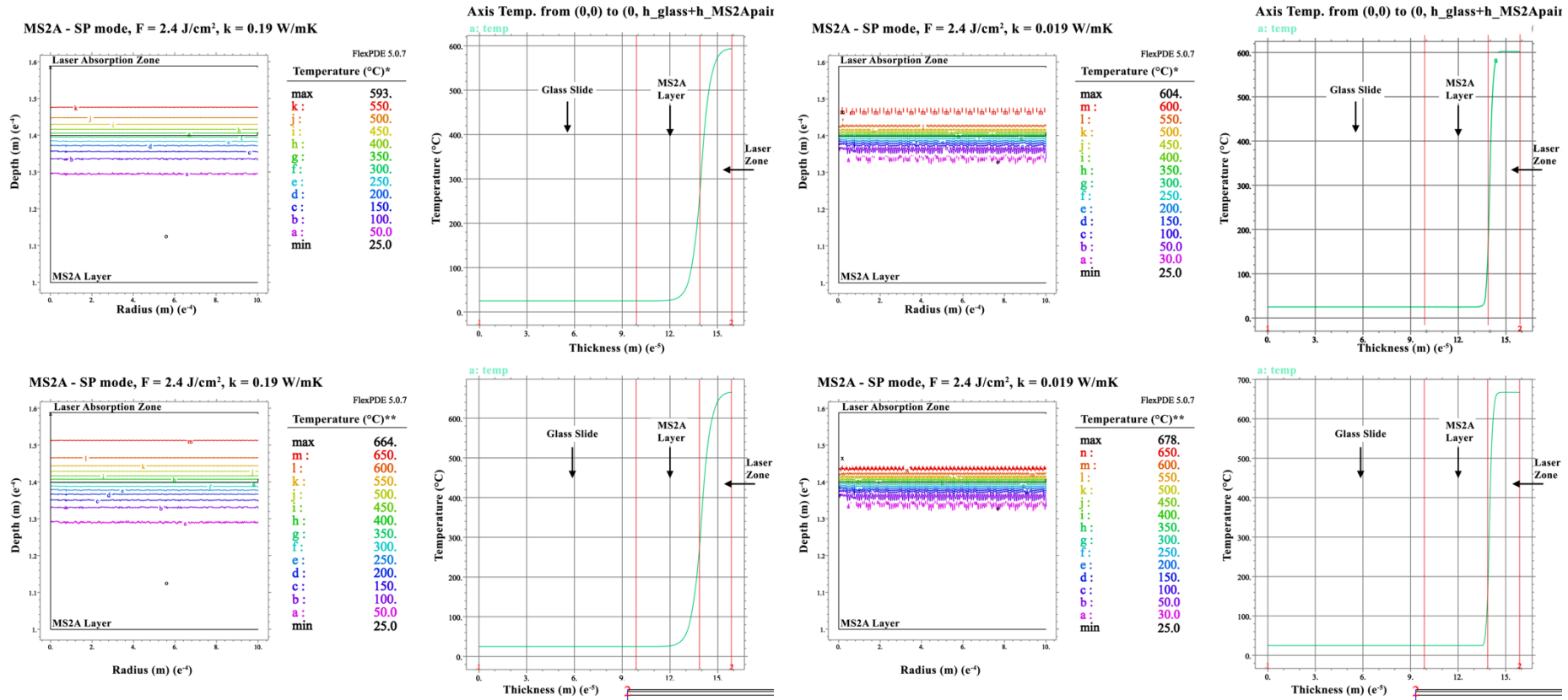


Figure B56 – 2D simulation of the heat diffusion inside the MS2A film in SP mode ( $\tau_L \approx 300 \mu\text{s}$ ) and temperature distribution by cross-section of varnish film + glass slide. Fluences of  $2.4 \text{ J/cm}^2$  and thermal conductivity ( $k$ ) of  $0.19 \text{ W/m}\cdot\text{K}$ . One simulation was run using the %R from the FTIR (\*) the other using the %R from the Fresnel equation (\*\*). The beam diameter was set at  $\varnothing = 4\text{mm}$ . The laser absorption zone represents the area in which the laser wavelength penetrates into the MS2A film ( $\delta$ ) before releasing 63% of its energy.

Figure B57 – 2D simulation of the heat diffusion inside the MS2A film in SP mode ( $\tau_L \approx 300 \mu\text{s}$ ) and temperature distribution by cross-section of varnish film + glass slide. Fluences of  $2.4 \text{ J/cm}^2$  and thermal conductivity ( $k$ ) of  $0.019 \text{ W/m}\cdot\text{K}$ . One simulation was run using the %R from the FTIR (\*) the other using the %R from the Fresnel equation (\*\*). The beam diameter was set at  $\varnothing = 4\text{mm}$ . The laser absorption zone represents the area in which the laser wavelength penetrates into the MS2A film ( $\delta$ ) before releasing 63% of its energy.

## B10) Varnish parameters

### B10.1 Dammar

Table B5 – Parametric table for the dammar resin required to define the thermal modelling of varnish film.

<b>Chemical classification</b>	Triterpenoid resin
<b>Initial Thickness</b>	200 $\mu\text{m}$
<b>Thickness after ageing</b>	$82.3 \pm 13.2 \mu\text{m}$
<b>Density</b>	$1.2 \text{ g/cm}^3$
<b>FT-IR %T</b>	$8.4 \pm 2.3$
<b>%R (integrated sphere)</b>	$15.1 \pm 0.6$
<b>Absorption coefficient (<math>\alpha</math>)</b>	$301.1 \text{ cm}^{-1}$
<b>Optical penetration depth (<math>\delta</math>)</b>	$33.2 \mu\text{m}$
<b>Specific heat capacity (Cp)</b>	$1.8 \text{ J/g}\cdot^\circ\text{C}$ (mean)
<b>Thermal diffusivity (D)</b>	$10^{-3} \text{ cm}^2/\text{sec}$
<b>(Fotakis <i>et al.</i>, 2007, p. 36)</b>	$10^{-4} \text{ cm}^2/\text{sec}$
	$0.0021 \text{ W/cm}\cdot^\circ\text{C}$
<b>Thermal conductivity (k)</b>	$0.02 \text{ W/cm}\cdot^\circ\text{C}$

### B10.2 Ketone N

Table B6 – Parametric table for the Ketone N resin required to define the thermal modelling of varnish film.

<b>Chemical classification</b>	Ketone resin
<b>Initial Thickness</b>	200 $\mu\text{m}$
<b>Thickness after ageing</b>	$28.2 \pm 7.5 \mu\text{m}$
<b>Density</b>	$1.1 \text{ g/cm}^3$
<b>FT-IR %T</b>	$1.9 \pm 1.4$
<b>%R (integrated sphere)</b>	$14.1 \pm 4.1$
<b>%R (Fresnel's Eq.)</b>	4.3
<b>Absorption coefficient (<math>\alpha</math>)</b>	$1396.1 \text{ cm}^{-1}$
<b>Optical penetration depth (<math>\delta</math>)</b>	$7.2 \mu\text{m}$
<b>Specific heat capacity (Cp)</b>	$1.98 \text{ J/g}\cdot^\circ\text{C}$ (mean)
<b>Thermal diffusivity (D)</b>	$10^{-3} \text{ cm}^2/\text{sec}$
<b>(Fotakis <i>et al.</i>, 2007, p. 36)</b>	$10^{-4} \text{ cm}^2/\text{sec}$
	$0.0022 \text{ W/cm}\cdot^\circ\text{C}$
<b>Thermal conductivity (k)</b>	$0.22 \text{ W/cm}\cdot^\circ\text{C}$

## B10.3 MS2A

Table B7 – Parametric table for the MS2A resin required to define the thermal modelling of varnish film.

<b>Chemical classification</b>	Ketone resin
<b>Initial Thickness</b>	200 $\mu\text{m}$
<b>Thickness after ageing</b>	$58.8 \pm 11.7 \mu\text{m}$
<b>Density</b>	1.1 $\text{g}/\text{cm}^3$
<b>FT-IR %T</b>	$4.5 \pm 1.1$
<b>%R (integrated sphere)</b>	$15.6 \pm 0.1$
<b>%R (Fresnel's Eq.)</b>	4.2
<b>Absorption coefficient (<math>\alpha</math>)</b>	$528.7 \text{ cm}^{-1}$
<b>Optical penetration depth (<math>\delta</math>)</b>	18.9 $\mu\text{m}$
<b>Specific heat capacity (<math>C_p</math>)</b>	1.7 $\text{J}/\text{g}\cdot^\circ\text{C}$ (mean)
<b>Thermal diffusivity (<math>D</math>)</b>	$10^{-3} \text{ cm}^2/\text{sec}$
<b>(Fotakis <i>et al.</i>, 2007, p. 36)</b>	$10^{-4} \text{ cm}^2/\text{sec}$
	0.0019 $\text{W}/\text{cm}\cdot^\circ\text{C}$
<b>Thermal conductivity (<math>k</math>)</b>	0.19 $\text{W}/\text{cm}\cdot^\circ\text{C}$

## B10.4 Paraloid B67

Table B8 – Parametric table for the Paraloid B67 resin required to define the thermal modelling of varnish film.

<b>Chemical classification</b>	Acrylic resin
<b>Initial Thickness</b>	200 $\mu\text{m}$
<b>Thickness after ageing</b>	$28.2 \pm 7.5 \mu\text{m}$
<b>Density</b>	1.0 $\text{g}/\text{cm}^3$
<b>FT-IR %T</b>	$90.19 \pm 0.6$
<b>%R (integrated sphere)</b>	$0 \pm 0$
<b>Absorption coefficient (<math>\alpha</math>)</b>	$20.1 \text{ cm}^{-1}$
<b>Optical penetration depth (<math>\delta</math>)</b>	497.1 $\mu\text{m}$
<b>Specific heat capacity (<math>C_p</math>)</b>	2.1 $\text{J}/\text{g}\cdot^\circ\text{C}$ (mean)
<b>Thermal diffusivity (<math>D</math>)</b>	$10^{-3} \text{ cm}^2/\text{sec}$
<b>(Fotakis <i>et al.</i>, 2007, p. 36)</b>	$10^{-4} \text{ cm}^2/\text{sec}$
	0.0021 $\text{W}/\text{cm}\cdot^\circ\text{C}$
<b>Thermal conductivity (<math>k</math>)</b>	0.00021 $\text{W}/\text{cm}\cdot^\circ\text{C}$

## **Appendix C Er:YAG LASER CLEANING TESTS ON A NINETEENTH CENTURY VARNISHED PAINTING**

Appendix C contains the following topics:

C1) Py-TMAH-GC/MS acquired from the nineteenth century varnished painting;

C2) Er:YAG laser tests:

- UV induced fluorescence micrographs of the irradiated test areas (A, B, C) and Multispectral Imaging clusterisation maps;
- the  $L_{SCI_{mean}}^*$  and  $L_{SCE_{mean}}^*$  and the GRF data before and after laser irradiation and the  $\Delta GRF$  values;
- Multispectral Imaging (MSI) Clusterisation Analysis data.

C3) ATR/FT-IR.

### C1 Py-TMAH-GC/MS acquired from the nineteenth century varnished painting

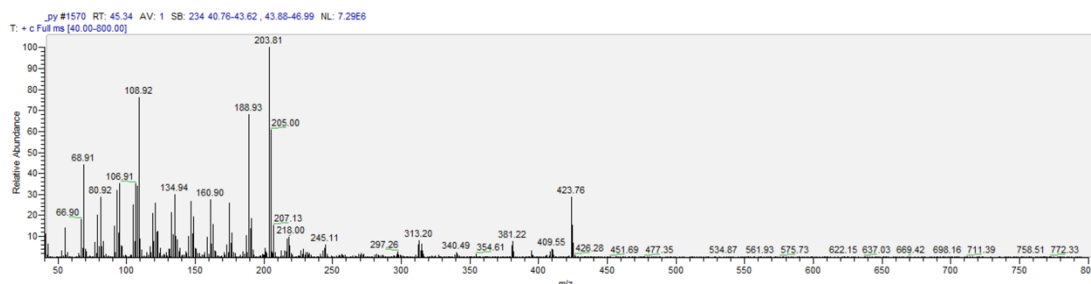


Figure C1 – Py-TMAH-GC/MS of the varnish painting at 45.3 min. Characteristic m/z 109, 205 and 424 due to methylated dammaradienone and its derivatisation products.

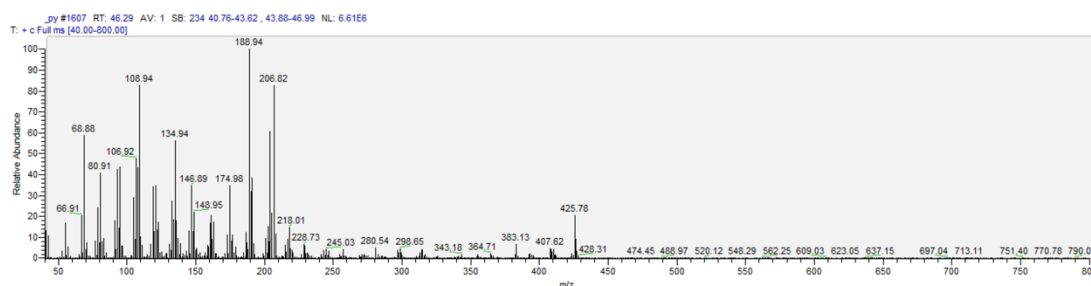


Figure C2 – Py-TMAH-GC/MS of the varnish painting at 46.3 min. Characteristic m/z 109, 207 and 426 due to methylated dammaradienol and its derivatisation products.

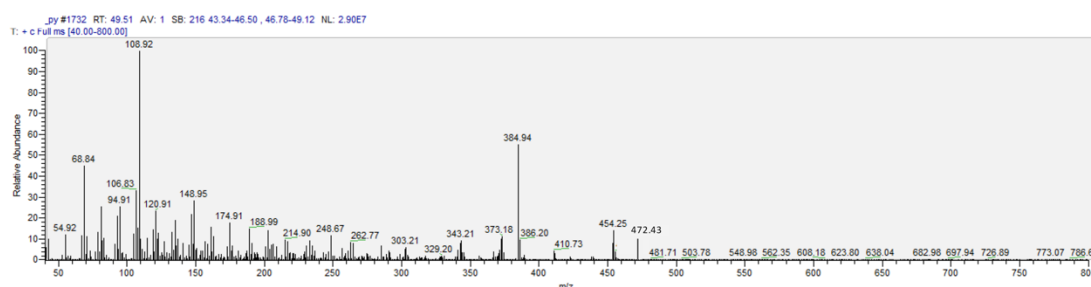


Figure C3 – Py-TMAH-GC/MS of the varnish painting at 49.5 min. Characteristic m/z 109, 454 and 472 due to methylated dammarenolic acid and its derivatisation products.

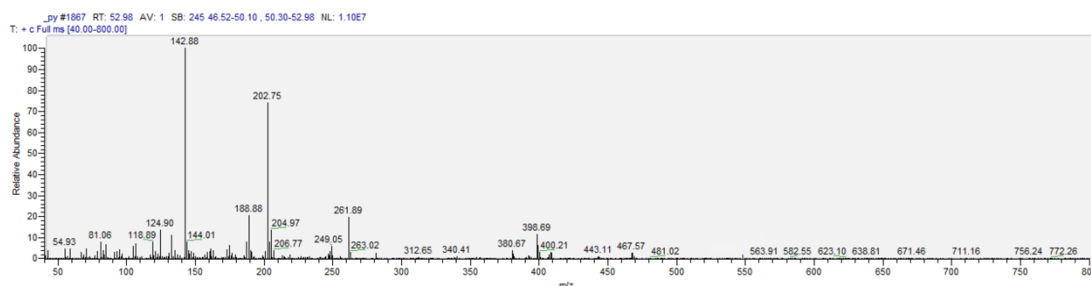


Figure C4 – Py-TMAH-GC/MS of the varnish painting at 53 min. Characteristic m/z 133, 189, 203, 262, 408, and 468 due to methylated oleanonic acid and its derivatisation products.

Appendix C – Er:YAG laser cleaning tests on a nineteenth century varnished painting

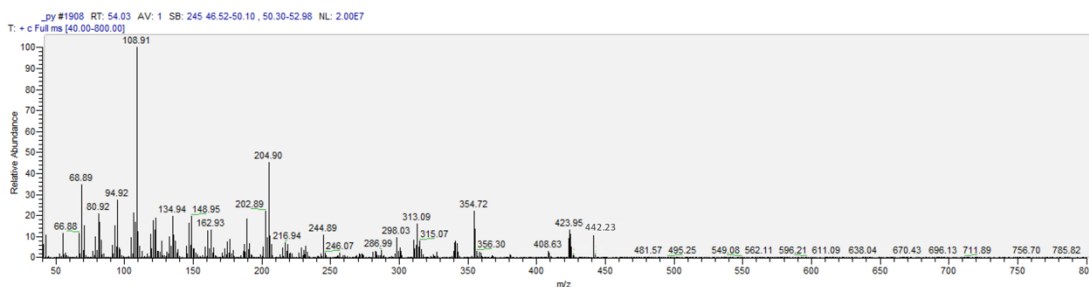


Figure C5 – Py-TMAH-GC/MS of the varnish painting at 54 min. Characteristic m/z 109, 205, 424 and 442 due to methylated hydroxydammarenone (3-oxo-dammara-20,24-diene) and its derivatisation products.

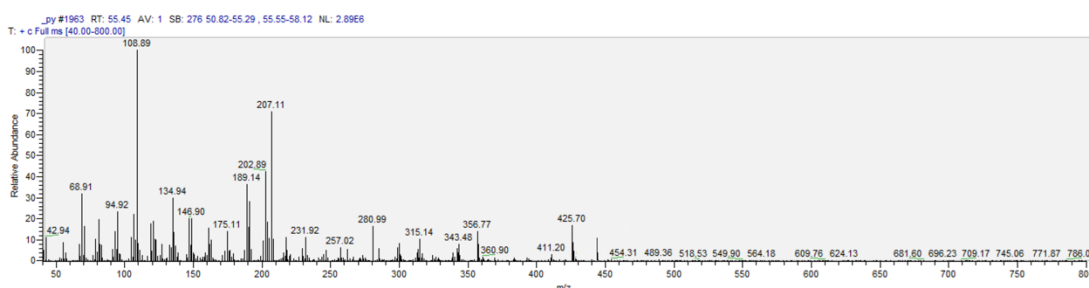


Figure C6 – Py-TMAH-GC/MS of the varnish painting at 55.5 min. Characteristic m/z 189, 203, 232 and 409 due to methylated oleanonic aldehyde and its derivatisation products.

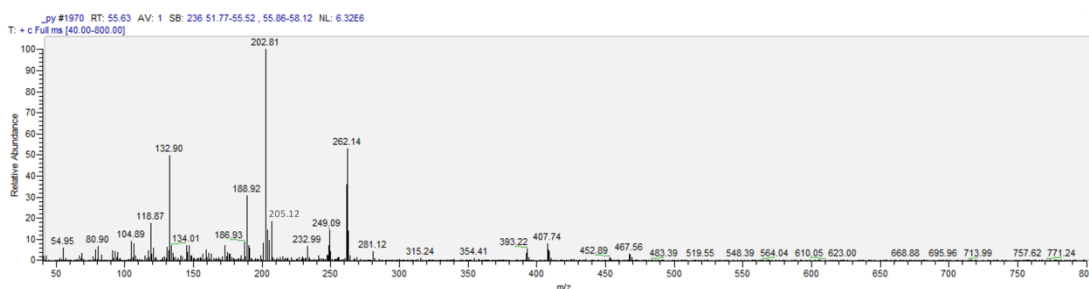


Figure C7 – Py-TMAH-GC/MS of the varnish painting at 55.6 min. Characteristic m/z 133, 203, 262, 409 and 468 due to methylated ursonic acid and its derivatisation products.

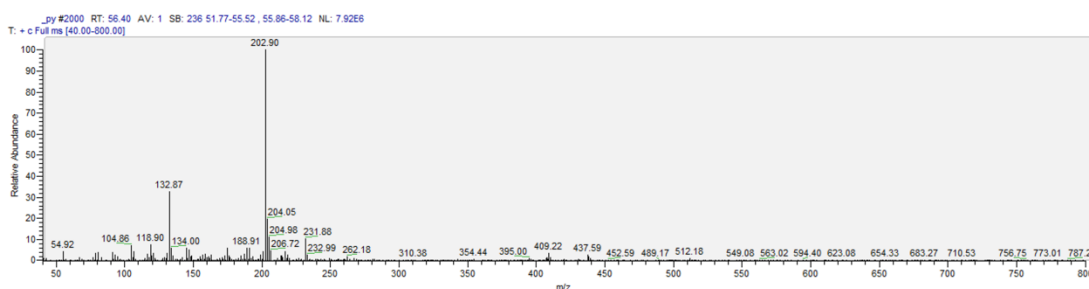


Figure C8 – Py-TMAH-GC/MS of the varnish painting at 56.4 min. Characteristic m/z 133, 189, 203, 232, 409 and 438 due to methylated ursonic aldehyde and its derivatization products.

## D2 Er:YAG laser tests

Figure C9 – UV induced fluorescence micrographs of the irradiated test areas (A, B, C) and Multispectral Imaging clusterisation maps (B1 and C1) of one (A), two (B and B1) and three (C and C1) laser scanned areas at ‘nominated fluence’  $0.6 \text{ J/cm}^2$ . At the top left the dry irradiated area is shown, followed by other irradiated areas pre-wetted with the following solutions: deionised water (DI-W), 1% v/v Tween20 in DI-W, 50% v/v Industrial Methylated Spirit (IMS) in DI-W, 50% v/v IMS in White Spirit (WS) and pure White Spirit. All the laser-irradiated areas were  $15 \times 15 \text{ mm}$ .

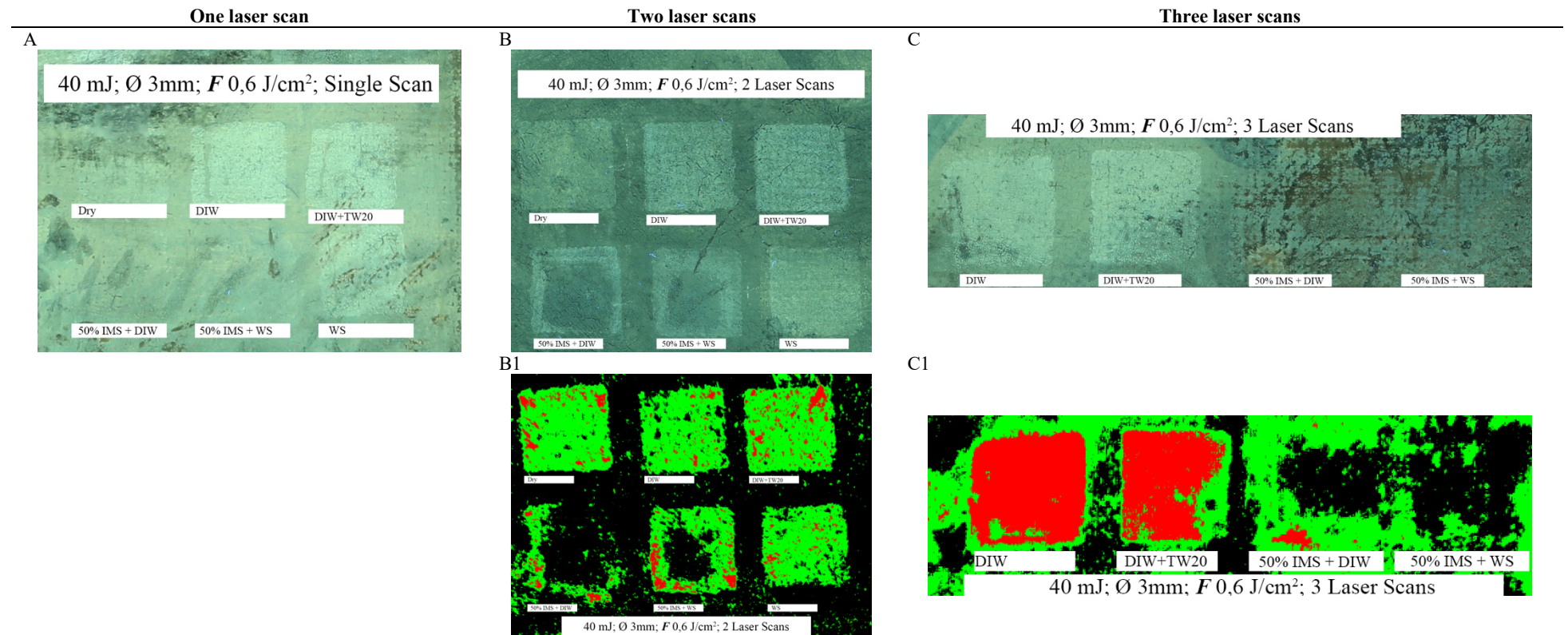


Table C1 – The table provides the  $L_{SCI_{mean}}^*$  and  $L_{SCE_{mean}}^*$  and the GRF data before and after laser irradiation  $0.6 \text{ J/cm}^2$  and the  $\Delta\text{GRF}$  values. Standard deviations ( $\sigma$ ) of all data are provided.

Energy (mJ)	Nominated Fluence ( $\text{J/cm}^2$ )	Cleaning Systems	Colourimetry before laser irradiation			Colourimetry after laser irradiation			$\Delta\text{GRF} \pm \sigma$
			$L_{SCI_{mean}}^* \pm \sigma$	$L_{SCE_{mean}}^* \pm \sigma$	$\text{GRF}_b \pm \sigma$	$L_{SCI_{mean}}^* \pm \sigma$	$L_{SCE_{mean}}^* \pm \sigma$	$\text{GRF}_a \pm \sigma$	
40	0.6	Dry – 1 Scan	$41.8 \pm 0.6$	$39.8 \pm 0.7$	$2.0 \pm 0.1$	$43.5 \pm 1.1$	$42.7 \pm 1.3$	$0.8 \pm 0.2$	$1.2 \pm 0.1$
		Dry – 2 Scans	$32.2 \pm 0.5$	$31.1 \pm 0.1$	$1.2 \pm 0.2$	$36.3 \pm 0.9$	$36.0 \pm 1.0$	$0.3 \pm 0.1$	$0.9 \pm 0.1$
		DI-W – 1 Scan	$41.0 \pm 0.1$	$39.1 \pm 0.2$	$1.9 \pm 0.1$	$43.3 \pm 0.8$	$42.4 \pm 0.9$	$0.9 \pm 0.1$	$1 \pm 0$
		DI-W – 2 Scans	$32.6 \pm 1.5$	$31.6 \pm 1.3$	$1.0 \pm 0.2$	$36.7 \pm 1.4$	$36.4 \pm 1.5$	$0.3 \pm 0$	$0.7 \pm 0.1$
		DI-W – 3 Scans	$34.7 \pm 1.7$	$32.5 \pm 2.3$	$2.2 \pm 0.5$	$41.6 \pm 0.6$	$40.9 \pm 0.7$	$0.7 \pm 0$	$1.5 \pm 0.3$
		DI-W+TW20 – 1 Scan	$39.2 \pm 0.5$	$37.6 \pm 0.2$	$1.6 \pm 0.2$	$44.3 \pm 0.6$	$43.9 \pm 0.6$	$0.4 \pm 0$	$1.2 \pm 0.1$
		DI-W+TW20 – 2 Scans	$32.1 \pm 1.3$	$31.4 \pm 1.3$	$0.6 \pm 0.0$	$36.9 \pm 0.7$	$36.6 \pm 0.7$	$0.2 \pm 0$	$0.4 \pm 0$
		DI-W+TW20 – 3 Scans	$33.0 \pm 2.8$	$31.2 \pm 2.7$	$1.8 \pm 0.1$	$40.4 \pm 0.6$	$39.3 \pm 0.6$	$1.1 \pm 0$	$0.7 \pm 0$
		50% IMS+DI-W – 1 Scan	$40.8 \pm 0.6$	$39.1 \pm 0.6$	$1.6 \pm 0.0$	$37.5 \pm 0.9$	$36 \pm 0.6$	$1.5 \pm 0.2$	$0.1 \pm 0.1$
		50% IMS+DI-W – 2 Scans	$34.5 \pm 4.8$	$31.0 \pm 0.8$	$3.4 \pm 2.8$	$30.8 \pm 1.6$	$30 \pm 1.8$	$0.8 \pm 0.1$	$2.6 \pm 1.9$
		50% IMS+DI-W – 3 Scans	$31.9 \pm 4.7$	$30.5 \pm 5.0$	$1.4 \pm 0.2$	$32.1 \pm 1.3$	$29.6 \pm 1.4$	$2.5 \pm 0.1$	$-1 \pm 0.1$
		50% IMS+WS – 1 Scan	$37.6 \pm 0.7$	$35.8 \pm 0.9$	$1.9 \pm 0.2$	$37.4 \pm 0.8$	$36.5 \pm 0.8$	$0.9 \pm 0$	$1 \pm 0.1$
		50% IMS+WS – 2 Scans	$32.2 \pm 0.8$	$31.2 \pm 0.4$	$1.1 \pm 0.3$	$33.5 \pm 2.5$	$32.9 \pm 3.0$	$0.7 \pm 0.4$	$0.4 \pm 0.1$
		50% IMS+WS – 3 Scans	$30.4 \pm 1.4$	$29.5 \pm 1.7$	$0.9 \pm 0.2$	$31.3 \pm 0.2$	$28.7 \pm 0.2$	$2.6 \pm 0$	$-1.7 \pm 0.1$
		WS – 1 Scan	$39.6 \pm 1.0$	$38.5 \pm 1.2$	$1.1 \pm 0.1$	$42.1 \pm 0.1$	$41.7 \pm 0.1$	$0.4 \pm 0$	$0.7 \pm 0.1$
		WS – 2 Scans	$32.6 \pm 0.9$	$31.4 \pm 1.2$	$1.2 \pm 0.2$	$39.1 \pm 0.2$	$38.9 \pm 0.2$	$0.2 \pm 0$	$1 \pm 0.1$

Table C2 – Multispectral Imaging (MSI) Clusterisation Analysis data of the Er:YAG laser irradiated areas 0.6 J/cm<sup>2</sup>. Green % corresponds to a gradual reduction of the early-stage varnish thinning. Red % coincides with gradual deeper irradiation of the varnish layer. The Black % corresponds to the remaining varnish within the irradiated spots.

Energy (mJ)	Nominated Fluence (J/cm <sup>2</sup> )	Cleaning systems	Spectral Imaging Clusterisation Analysis		
			Green %	Red %	Black %
40	0.6	Dry – 2 Scans	88	9	3
		DI-W – 2 Scans	83	1	12
		DI-W – 3 Scans	5	95	0
		DI-W+TW20 – 2 Scans	84	14	2
		DI-W+TW20 – 3 Scans	23	76	1
		50% IMS+DI-W – 2 Scans	19	2	78
		50% IMS+DI-W – 3 Scans	50	3	47
		50% IMS+WS – 2 Scans	52	10	38
		50% IMS+WS – 3 Scans	34	0	66
		WS – 2 Scans	81	5	19

Figure C10 – UV induced fluorescence micrographs of the irradiated test areas (A, B, C) and Multispectral Imaging clusterisation maps (B1 and C1) of one (A), two (B and B1) and three (C and C1) laser scanned areas at ‘nominated fluence’  $0.7 \text{ J/cm}^2$ . At the top left the dry irradiated area is shown, followed by other irradiated areas pre-wetted with the following solutions: deionised water (DI-W), 1% v/v Tween20 in DI-W, 50% v/v Industrial Methylated Spirit (IMS) in DI-W, 50% v/v IMS in White Spirit (WS) and pure White Spirit. All the laser-irradiated areas were  $15 \times 15 \text{ mm}$ .

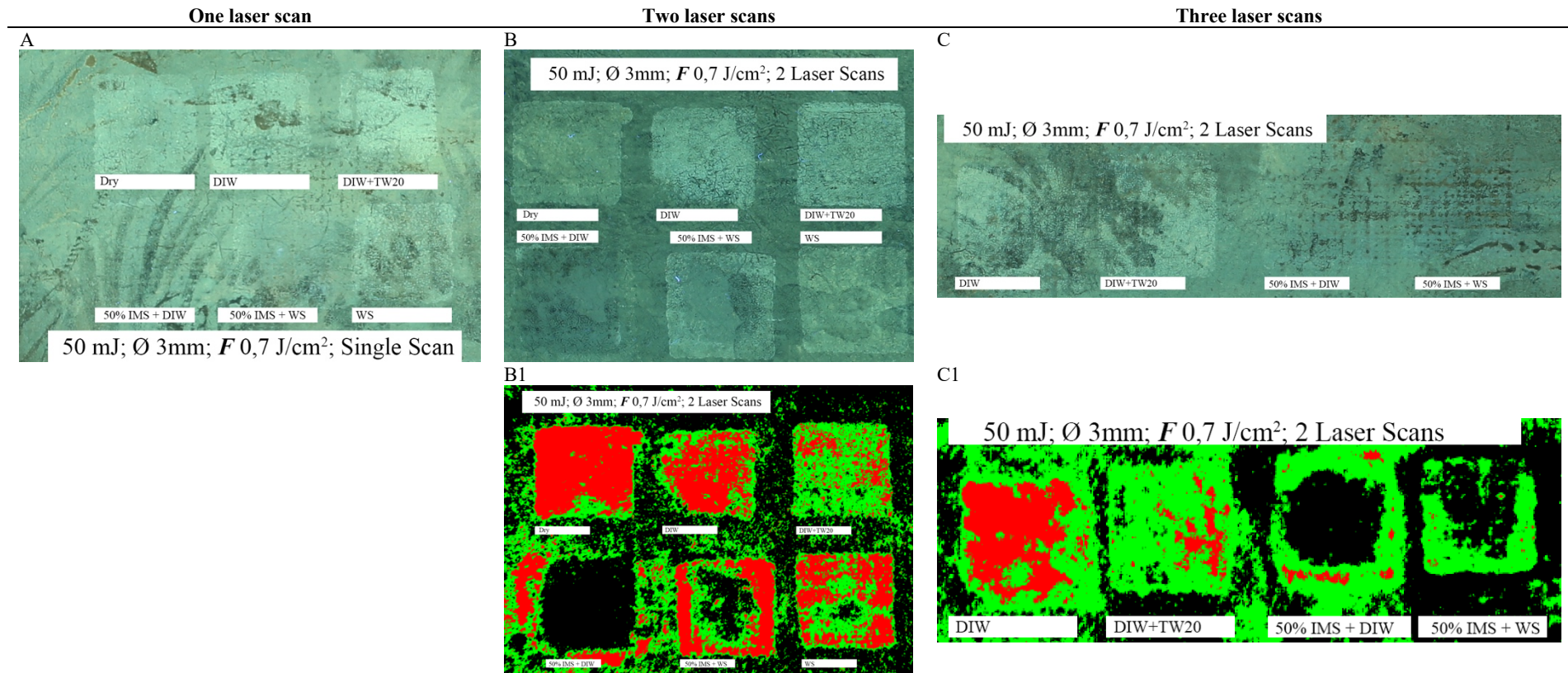


Table C3 – The table provides the  $L_{SCI_{mean}}^*$  and  $L_{SCE_{mean}}^*$  and the GRF data before and after laser irradiation at  $0.7 \text{ J/cm}^2$  and the  $\Delta\text{GRF}$  values. Standard deviations ( $\sigma$ ) of all data are provided.

Energy (mJ)	Nominated Fluence ( $\text{J/cm}^2$ )	Cleaning Systems	Colourimetry before laser irradiation			Colourimetry after laser irradiation			$\Delta\text{GRF} \pm \sigma$
			$L_{SCI_{mean}}^* \pm \sigma$	$L_{SCE_{mean}}^* \pm \sigma$	$\text{GRF}_b \pm \sigma$	$L_{SCI_{mean}}^* \pm \sigma$	$L_{SCE_{mean}}^* \pm \sigma$	$\text{GRF}_a \pm \sigma$	
50	0.7	Dry – 1 Scan	$32.3 \pm 1.3$	$30.5 \pm 1.3$	$1.8 \pm 0$	$37.7 \pm 0.1$	$37.4 \pm 0.1$	$0.3 \pm 0$	$1.5 \pm 0$
		Dry – 2 Scans	$31.2 \pm 0.3$	$30.8 \pm 0.4$	$0.5 \pm 0.1$	$37.5 \pm 0.8$	$37.4 \pm 0.8$	$0.1 \pm 0$	$0.4 \pm 0$
		DI-W – 1 Scan	$32.6 \pm 0.8$	$31 \pm 1.2$	$1.6 \pm 0.3$	$38.4 \pm 0.5$	$37.8 \pm 0.3$	$0.6 \pm 0.1$	$1 \pm 0.1$
		DI-W – 2 Scans	$30.1 \pm 0.6$	$29.7 \pm 0.7$	$0.4 \pm 0.1$	$38.0 \pm 1.3$	$37.9 \pm 1.3$	$0.1 \pm 0$	$0.3 \pm 0.1$
		DI-W – 3 Scans	$31.0 \pm 1.7$	$28.8 \pm 1.2$	$2.2 \pm 0.4$	$34.9 \pm 0.7$	$34.1 \pm 0.7$	$0.8 \pm 0$	$1.4 \pm 0.2$
		DI-W+TW20 – 1 Scan	$34.5 \pm 1.7$	$33 \pm 1.3$	$1.5 \pm 0.3$	$42.6 \pm 1.2$	$42.1 \pm 1.2$	$0.6 \pm 0$	$1 \pm 0.2$
		DI-W+TW20 – 2 Scans	$31.2 \pm 0.5$	$30.7 \pm 0.6$	$0.5 \pm 0.1$	$37.3 \pm 1.1$	$37.1 \pm 1.1$	$0.1 \pm 0$	$0.3 \pm 0$
		DI-W+TW20 – 3 Scans	$30.1 \pm 1.0$	$26.7 \pm 1$	$3.4 \pm 0$	$35.1 \pm 0.3$	$34.4 \pm 0.3$	$0.7 \pm 0$	$2.7 \pm 0$
		50% IMS+DI-W – 1 Scan	$32.8 \pm 0.2$	$31.9 \pm 0.2$	$0.9 \pm 0$	$33.1 \pm 0.5$	$32 \pm 0.5$	$1.2 \pm 0.1$	$-0.3 \pm 0$
		50% IMS+DI-W – 2 Scans	$31.2 \pm 0.9$	$30.8 \pm 1$	$0.4 \pm 0$	$29.8 \pm 0.4$	$26.8 \pm 1.4$	$3 \pm 0.7$	$-2.6 \pm 0.5$
		50% IMS+DI-W – 3 Scans	$29.9 \pm 0.9$	$28.0 \pm 0.8$	$1.9 \pm 0.1$	$29.6 \pm 0.2$	$26.1 \pm 1$	$3.6 \pm 0.6$	$-1.6 \pm 0.4$
		50% IMS+WS – 1 Scan	$35.1 \pm 2.2$	$33.8 \pm 2.7$	$1.2 \pm 0.3$	$35.0 \pm 1.2$	$34.4 \pm 1.3$	$0.6 \pm 0.1$	$0.6 \pm 0.2$
		50% IMS+WS – 2 Scans	$31.5 \pm 0.3$	$31.3 \pm 0.3$	$0.3 \pm 0$	$32 \pm 1.1$	$31.5 \pm 1.3$	$0.4 \pm 0.2$	$-0.2 \pm 0.1$
		50% IMS+WS – 3 Scans	$28.2 \pm 1.6$	$26.4 \pm 1.3$	$1.8 \pm 0.2$	$30.5 \pm 0.2$	$28.7 \pm 0.3$	$1.9 \pm 0.1$	$0 \pm 0.1$
		WS – 1 Scan	$32.9 \pm 1.4$	$30.8 \pm 1.6$	$2.2 \pm 0.1$	$37.4 \pm 1$	$36.8 \pm 1.1$	$0.5 \pm 0$	$1.6 \pm 0.1$
		WS – 2 Scans	$30.2 \pm 0.8$	$29.8 \pm 0.6$	$0.4 \pm 0.1$	$36.5 \pm 1.3$	$36.4 \pm 1.3$	$0.1 \pm 0$	$0.3 \pm 0.1$

Table C4 – Multispectral Imaging (MSI) Clusterisation Analysis data of the Er:YAG laser irradiated areas 0.7 J/cm<sup>2</sup>. Green % corresponds to a gradual reduction of the early-stage varnish thinning. Red % coincides with gradual deeper irradiation of the varnish layer. The Black % corresponds to the remaining varnish within the irradiated spots.

Energy (mJ)	Nominated Fluence (J/cm <sup>2</sup> )	Cleaning systems	Spectral Imaging Clusterisation Analysis		
			Green %	Red %	Black %
50	0.7	Dry – 2 Scans	8	91	0
		DI-W – 2 Scans	31	61	8
		DI-W – 3 Scans	30	70	0
		DI-W+TW20 – 2 Scans	69	26	5
		DI-W+TW20 – 3 Scans	80	16	4
		50% IMS+DI-W – 2 Scans	3	1	96
		50% IMS+DI-W – 3 Scans	91	4	5
		50% IMS+WS – 2 Scans	31	39	29
		50% IMS+WS – 3 Scans	51	1	48
		WS – 2 Scans	42	53	5

Figure C11 – UV induced fluorescence micrographs of the irradiated test areas (A, B, C) and Multispectral Imaging clusterisation maps (B1 and C1) of one (A), two (B and B1) and three (C and C1) laser scanned areas at ‘*nominated fluence*’ 1 J/cm<sup>2</sup>. At the top left the dry irradiated area is shown, followed by other irradiated areas pre-wetted with the following solutions: deionised water (DI-W), 1% v/v Tween20 in DI-W, 50% v/v Industrial Methylated Spirit (IMS) in DI-W, 50% v/v IMS in White Spirit (WS) and pure White Spirit. All the laser-irradiated areas were 15x15 mm.

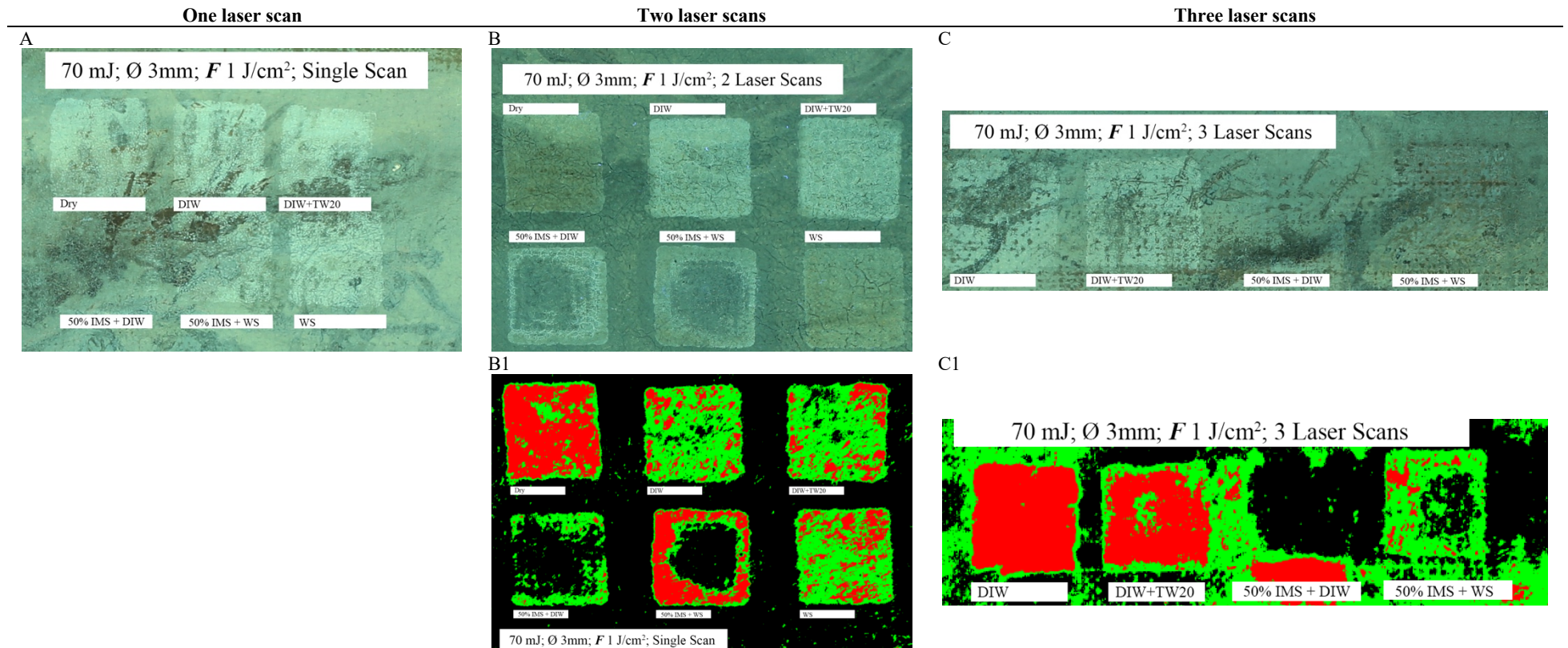


Table C5 - The table provides the  $L_{SCI_{mean}}^*$  and  $L_{SCE_{mean}}^*$  and the GRF data before and after laser irradiation at 1 J/cm<sup>2</sup> and the  $\Delta$ GRF values. Standard deviations ( $\sigma$ ) of all data are provided.

Energy (mJ)	Nominated Fluence (J/cm <sup>2</sup> )	Cleaning Systems	Colourimetry before laser irradiation			Colourimetry after laser irradiation			$\Delta$ GRF $\pm\sigma$
			$L_{SCI_{mean}}^* \pm\sigma$	$L_{SCE_{mean}}^* \pm\sigma$	$GRF_b \pm\sigma$	$L_{SCI_{mean}}^* \pm\sigma$	$L_{SCE_{mean}}^* \pm\sigma$	$GRF_a \pm\sigma$	
70	1	Dry – 1 Scan	35.2 $\pm$ 1.9	33.1 $\pm$ 1.9	2.1 $\pm$ 0	42.6 $\pm$ 0.7	42.4 $\pm$ 0.6	0.2 $\pm$ 0	1.9 $\pm$ 0
		Dry – 2 Scans	33.8 $\pm$ 3.4	32.5 $\pm$ 2.3	1.3 $\pm$ 0.8	35.3 $\pm$ 0.7	35.1 $\pm$ 0.9	0.2 $\pm$ 0.2	1.1 $\pm$ 0.4
		DI-W – 1 Scan	38.6 $\pm$ 0.2	36.7 $\pm$ 0.3	2 $\pm$ 0	43.0 $\pm$ 0.6	42.7 $\pm$ 0.6	0.4 $\pm$ 0	1.6 $\pm$ 0
		DI-W – 2 Scans	35.2 $\pm$ 1	34.3 $\pm$ 1.3	0.9 $\pm$ 0.2	35.5 $\pm$ 0.5	35.1 $\pm$ 0.8	0.4 $\pm$ 0.3	0.5 $\pm$ 0
		DI-W – 3 Scans	32.7 $\pm$ 3.3	30.9 $\pm$ 3.1	1.9 $\pm$ 0.2	38.9 $\pm$ 1.7	38.5 $\pm$ 1.8	0.4 $\pm$ 0.1	1.4 $\pm$ 0.1
		DI-W+TW20 – 1 Scan	37.6 $\pm$ 1.9	35.9 $\pm$ 2.5	1.7 $\pm$ 0.4	38.6 $\pm$ 3.2	38 $\pm$ 3.3	0.7 $\pm$ 0.1	1.1 $\pm$ 0.2
		DI-W+TW20 – 2 Scans	33.8 $\pm$ 0.8	32.4 $\pm$ 0.4	1.4 $\pm$ 0.2	37.8 $\pm$ 0.6	37.5 $\pm$ 0.6	0.3 $\pm$ 0	1.1 $\pm$ 0.1
		DI-W+TW20 – 3 Scans	33.6 $\pm$ 3.4	32.0 $\pm$ 4.1	1.6 $\pm$ 0.5	36.7 $\pm$ 0.9	36.2 $\pm$ 0.9	0.5 $\pm$ 0	1.1 $\pm$ 0.3
		50% IMS+DI-W – 1 Scan	31 $\pm$ 1	29.3 $\pm$ 1.2	1.7 $\pm$ 0.2	31.6 $\pm$ 1.3	29.1 $\pm$ 1.6	2.5 $\pm$ 0.2	-0.8 $\pm$ 0
		50% IMS+DI-W – 2 Scans	33.9 $\pm$ 0.5	32.8 $\pm$ 0.8	1.2 $\pm$ 0.2	31.2 $\pm$ 0.6	30.7 $\pm$ 0.3	0.6 $\pm$ 0.2	0.6 $\pm$ 0
		50% IMS+DI-W – 3 Scans	32.0 $\pm$ 2.6	29.5 $\pm$ 4.2	2.5 $\pm$ 1.1	31.7 $\pm$ 0.2	26.4 $\pm$ 0.6	5.3 $\pm$ 0.3	-2.8 $\pm$ 0.6
		50% IMS+WS – 1 Scan	33.2 $\pm$ 2.5	32.1 $\pm$ 2.8	1.1 $\pm$ 0.2	36.4 $\pm$ 0.2	36.0 $\pm$ 0.2	0.4 $\pm$ 0	0.8 $\pm$ 0.1
		50% IMS+WS – 2 Scans	34.3 $\pm$ 1.3	33.1 $\pm$ 2	1.2 $\pm$ 0.5	33.6 $\pm$ 1.5	33.2 $\pm$ 1.6	0.3 $\pm$ 0.1	0.9 $\pm$ 0.3
		50% IMS+WS – 3 Scans	29.3 $\pm$ 1.5	24.9 $\pm$ 1.5	4.4 $\pm$ 0	31 $\pm$ 0.3	29.5 $\pm$ 0.7	1.5 $\pm$ 0.3	3 $\pm$ 0.2
		WS – 1 Scan	33.0 $\pm$ 0.5	31.2 $\pm$ 0.9	1.8 $\pm$ 0.3	42 $\pm$ 0.8	41.8 $\pm$ 0.9	0.2 $\pm$ 0	1.6 $\pm$ 0.2
		WS – 2 Scans	34.7 $\pm$ 1.5	33.9 $\pm$ 1.9	0.8 $\pm$ 0.3	37.8 $\pm$ 0.7	37.7 $\pm$ 0.7	0.1 $\pm$ 0	0.7 $\pm$ 0.2

Table C6 – Multispectral Imaging (MSI) Clusterisation Analysis data of the Er:YAG laser irradiated areas at 1 J/cm<sup>2</sup>. Green % corresponds to a gradual reduction of the early-stage varnish thinning. Red % coincides with gradual deeper irradiation of the varnish layer. The Black % corresponds to the remaining varnish within the irradiated spots.

Energy (mJ)	Nominated Fluence (J/cm <sup>2</sup> )	Cleaning systems	Spectral Imaging Clusterisation Analysis		
			Green %	Red %	Black %
70	1	Dry – 2 Scans	17	83	0
		DI-W – 2 Scans	75	18	7
		DI-W – 3 Scans	2	98	0
		DI-W+TW20 – 2 Scans	72	19	9
		DI-W+TW20 – 3 Scans	19	81	0
		50% IMS+DI-W – 2 Scans	29	1	69
		50% IMS+DI-W – 3 Scans	16	6	77
		50% IMS+WS – 2 Scans	19	36	45
		50% IMS+WS – 3 Scans	63	10	26
		WS – 2 Scans	68	33	7

Figure C12 – UV induced fluorescence micrographs of the irradiated test areas (A, B, C) and Multispectral Imaging clusterisation maps (A1 and C1) of one (A and A1), two (B and B1) and three (C and C1) laser scanned areas at ‘nominated fluence’ 1.5 J/cm<sup>2</sup>. At the top left the dry irradiated area is shown, followed by other irradiated areas pre-wetted with the following solutions: deionised water (DI-W), 1% v/v Tween20 in DI-W, 50% v/v Industrial Methylated Spirit (IMS) in DI-W, 50% v/v IMS in White Spirit (WS) and pure White Spirit. All the laser-irradiated areas were 15x15 mm.

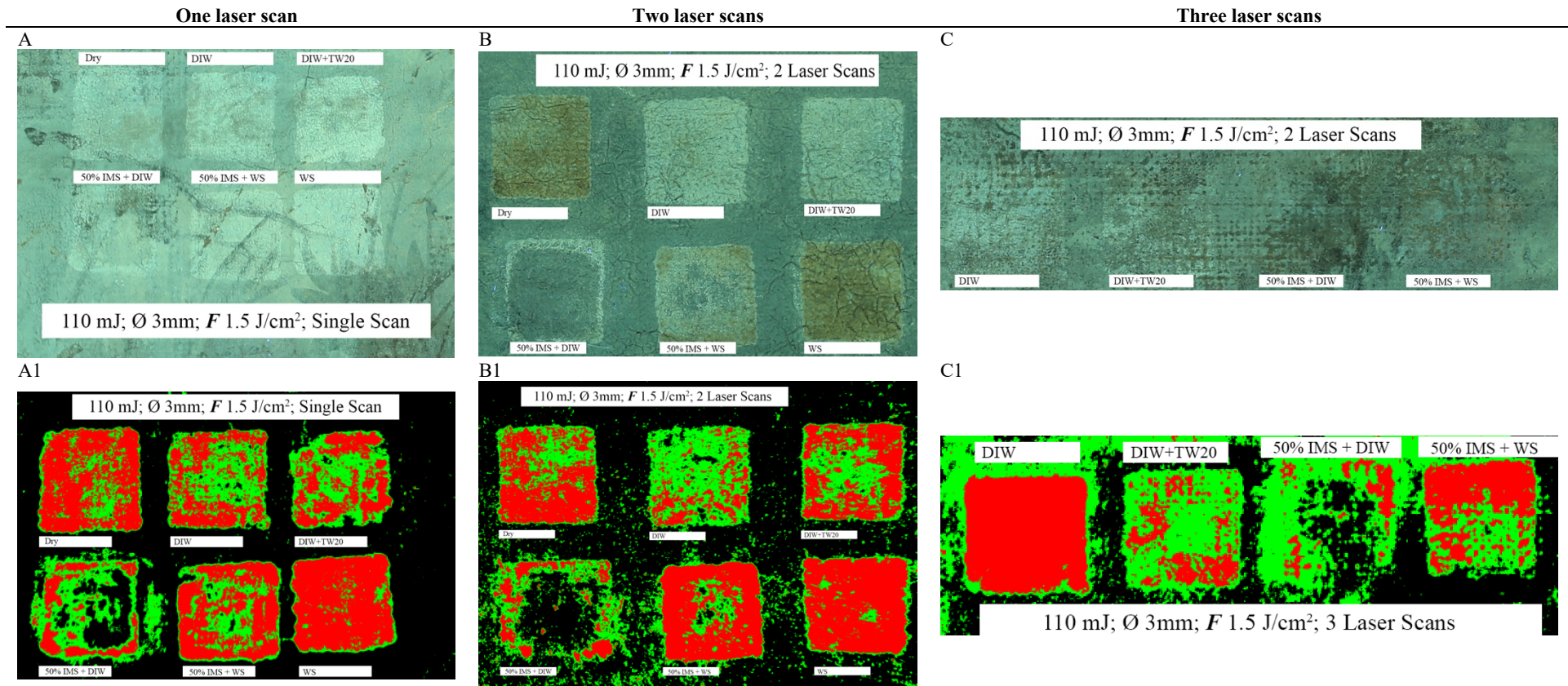


Table C7 – The table provides the  $L_{SCI_{mean}}^*$  and  $L_{SCE_{mean}}^*$  and the GRF data before and after laser irradiation at 1.5 J/cm<sup>2</sup> and the  $\Delta$ GRF values. Standard deviations ( $\sigma$ ) of all data are provided.

Energy (mJ)	Nominated Fluence (J/cm <sup>2</sup> )	Cleaning Systems	Colourimetry before laser irradiation			Colourimetry after laser irradiation			$\Delta$ GRF $\pm\sigma$
			$L_{SCI_{mean}}^* \pm\sigma$	$L_{SCE_{mean}}^* \pm\sigma$	$GRF_b \pm\sigma$	$L_{SCI_{mean}}^* \pm\sigma$	$L_{SCE_{mean}}^* \pm\sigma$	$GRF_a \pm\sigma$	
110	1.5	Dry – 1 Scan	31.7 $\pm$ 1.3	29.6 $\pm$ 1.6	2.2 $\pm$ 0.2	37.2 $\pm$ 0.4	37.0 $\pm$ 0.4	0.2 $\pm$ 0	2 $\pm$ 0.1
		Dry – 2 Scans	32.1 $\pm$ 1.1	31.5 $\pm$ 0.9	0.6 $\pm$ 0.2	38.3 $\pm$ 0.2	38.4 $\pm$ 0.2	0 $\pm$ 0	0.7 $\pm$ 0.1
		DI-W – 1 Scan	30.8 $\pm$ 1.1	28.8 $\pm$ 1.2	2 $\pm$ 0.1	37.9 $\pm$ 1.2	37.6 $\pm$ 1.3	0.3 $\pm$ 0.1	1.7 $\pm$ 0
		DI-W – 2 Scans	32.9 $\pm$ 1.2	32.2 $\pm$ 1	0.6 $\pm$ 0.1	36.7 $\pm$ 0.9	36.5 $\pm$ 1	0.2 $\pm$ 0	0.5 $\pm$ 0.1
		DI-W – 3 Scans	31.4 $\pm$ 0.3	29.8 $\pm$ 0.6	1.6 $\pm$ 0.2	42.5 $\pm$ 1.6	42.2 $\pm$ 1.6	0.3 $\pm$ 0	1.3 $\pm$ 0.1
		DI-W+TW20 – 1 Scan	32.2 $\pm$ 1.2	30.8 $\pm$ 1.6	1.3 $\pm$ 0.2	41.2 $\pm$ 1.4	41.0 $\pm$ 1.4	0.2 $\pm$ 0	1.2 $\pm$ 0.2
		DI-W+TW20 – 2 Scans	33.6 $\pm$ 1.8	32.9 $\pm$ 1.5	0.8 $\pm$ 0.2	38.2 $\pm$ 0.5	38.1 $\pm$ 0.5	0.1 $\pm$ 0	0.6 $\pm$ 0.1
		DI-W+TW20 – 3 Scans	31.7 $\pm$ 0.7	30.4 $\pm$ 0.8	1.3 $\pm$ 0.1	33.5 $\pm$ 1.7	33.0 $\pm$ 1.7	0.5 $\pm$ 0	0.8 $\pm$ 0
		50% IMS+DI-W – 1 Scan	30.8 $\pm$ 0.7	28.4 $\pm$ 0.9	2.5 $\pm$ 0.1	35.7 $\pm$ 0.4	35 $\pm$ 0.6	0.7 $\pm$ 0.1	1.7 $\pm$ 0
		50% IMS+DI-W – 2 Scans	33.3 $\pm$ 0.6	32.8 $\pm$ 0.5	0.4 $\pm$ 0	31.4 $\pm$ 1.4	29.8 $\pm$ 2.4	1.5 $\pm$ 0.7	-1.1 $\pm$ 0.5
		50% IMS+DI-W – 3 Scans	32.3 $\pm$ 2.7	30.7 $\pm$ 3.2	1.6 $\pm$ 0.4	33.8 $\pm$ 0.1	31.7 $\pm$ 0	2.1 $\pm$ 0	-0.5 $\pm$ 0.2
		50% IMS+WS – 1 Scan	31.8 $\pm$ 0.6	30.3 $\pm$ 1	1.5 $\pm$ 0.2	41.5 $\pm$ 1.3	41.3 $\pm$ 1.3	0.2 $\pm$ 0	1.3 $\pm$ 0.2
		50% IMS+WS – 2 Scans	32.6 $\pm$ 0.8	32.2 $\pm$ 0.6	0.4 $\pm$ 0.1	33.9 $\pm$ 1	33.8 $\pm$ 1	0.1 $\pm$ 0	0.3 $\pm$ 0.1
		50% IMS+WS – 3 Scans	33.4 $\pm$ 4.4	30.5 $\pm$ 3.3	2.8 $\pm$ 0.7	34.0 $\pm$ 0.7	33.2 $\pm$ 0.6	0.8 $\pm$ 0.1	2.1 $\pm$ 0.5
		WS – 1 Scan	31.8 $\pm$ 0.6	30.5 $\pm$ 0.9	1.3 $\pm$ 0.2	40.4 $\pm$ 0.3	41.4 $\pm$ 0.3	-1 $\pm$ 0	2.3 $\pm$ 0.1
		WS – 2 Scans	33.0 $\pm$ 1.3	32.4 $\pm$ 1	0.6 $\pm$ 0.2	38.7 $\pm$ 3.8	38.6 $\pm$ 3.8	0.1 $\pm$ 0	0.5 $\pm$ 0.1

Table C8 – Multispectral Imaging (MSI) Clusterisation Analysis data of the Er:YAG laser irradiated areas at 1.5 J/cm<sup>2</sup>. Green % corresponds to a gradual reduction of the early-stage varnish thinning. Red % coincides with gradual deeper irradiation of the varnish layer. The Black % corresponds to the remaining varnish within the irradiated spots.

Energy (mJ)	Nominated Fluence (J/cm <sup>2</sup> )	Cleaning systems	Spectral Imaging Clusterisation Analysis		
			Green %	Red %	Black %
110	1.5	Dry – 1 Scan	25	75	0
		Dry – 2 Scans	31	69	0
		DI-W – 1 Scan	48	48	4
		DI-W – 2 Scans	67	27	6
		DI-W – 3 Scans	1	99	0
		DI-W+TW20 – 1 Scan	45	45	10
		DI-W+TW20 – 2 Scans	41	58	1
		DI-W+TW20 – 3 Scans	66	34	0
		50% IMS+DI-W – 1 Scan	43	24	33
		50% IMS+DI-W – 2 Scans	27	13	59
		50% IMS+DI-W – 3 Scans	52	12	36
		50% IMS+WS – 1 Scan	33	65	3
		50% IMS+WS – 2 Scans	17	80	3
		50% IMS+WS – 3 Scans	39	59	2
		WS – 1 Scan	10	88	2
WS – 2 Scans	6	94	0		

Figure C13 – UV induced fluorescence micrographs of the irradiated test areas (A, B, C) and Multispectral Imaging clusterisation maps (A1 and C1) of one (A and A1), two (B and B1) and three (C and C1) laser scanned areas at ‘nominated fluence’  $2 \text{ J/cm}^2$ . At the top left the dry irradiated area is shown, followed by other irradiated areas pre-wetted with the following solutions: deionised water (DI-W), 1% v/v Tween20 in DI-W, 50% v/v Industrial Methylated Spirit (IMS) in DI-W, 50% v/v IMS in White Spirit (WS) and pure White Spirit. All the laser-irradiated areas were  $15 \times 15 \text{ mm}$ .

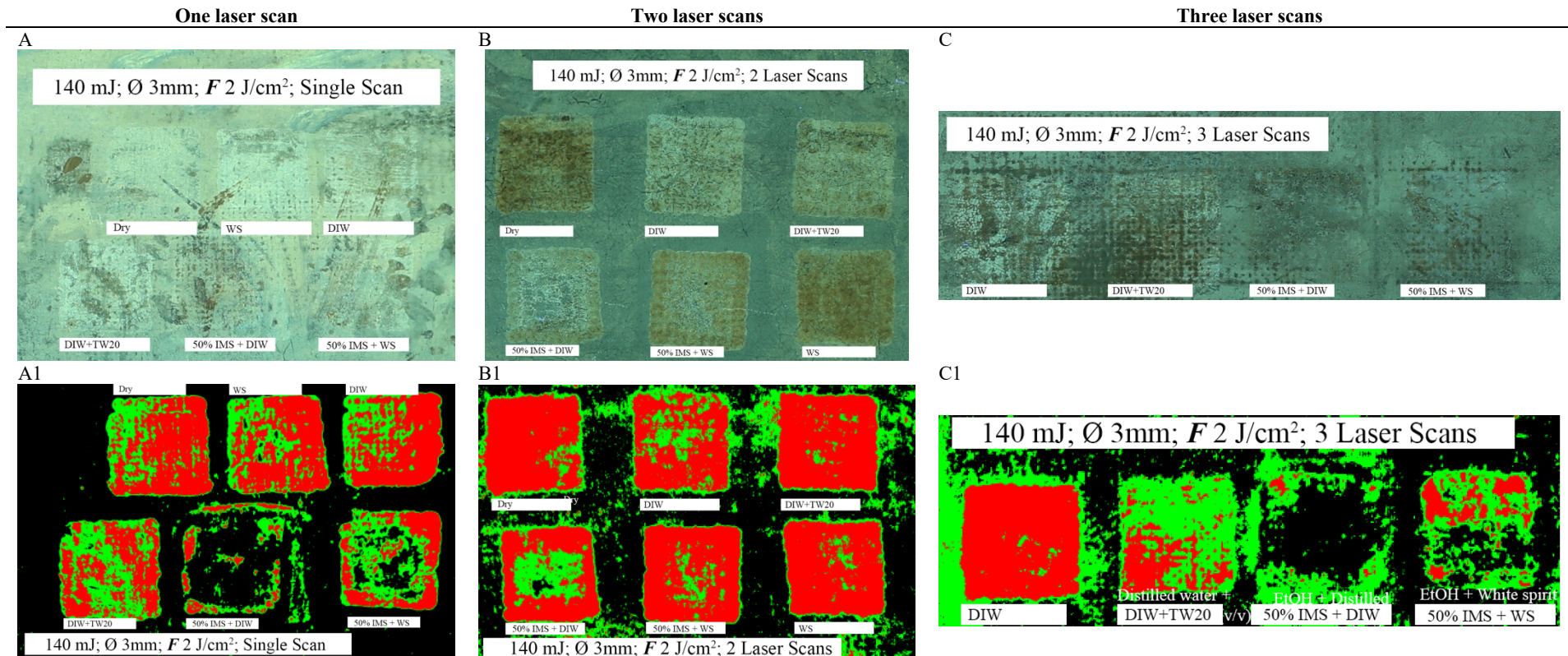


Table C9 – The table provides the  $L_{SCI_{mean}}^*$  and  $L_{SCE_{mean}}^*$  and the GRF data before and after laser irradiation at 2 J/cm<sup>2</sup> and the  $\Delta$ GRF values. Standard deviations ( $\sigma$ ) of all data are provided.

Energy (mJ)	Nominated Fluence (J/cm <sup>2</sup> )	Cleaning Systems	Colourimetry before laser irradiation			Colourimetry after laser irradiation			$\Delta$ GRF $\pm\sigma$
			$L_{SCI_{mean}}^* \pm\sigma$	$L_{SCE_{mean}}^* \pm\sigma$	$GRF_b \pm\sigma$	$L_{SCI_{mean}}^* \pm\sigma$	$L_{SCE_{mean}}^* \pm\sigma$	$GRF_a \pm\sigma$	
140	2	Dry – 1 Scan	35.1 $\pm$ 4.3	30.2 $\pm$ 2.6	4.8 $\pm$ 1.2	40.2 $\pm$ 0.2	40.0 $\pm$ 0.2	0.2 $\pm$ 0	4.7 $\pm$ 0.8
		Dry – 2 Scans	34.9 $\pm$ 0.7	33.8 $\pm$ 0.8	1.1 $\pm$ 0.1	38.7 $\pm$ 0.9	38.5 $\pm$ 0.9	0.2 $\pm$ 0	0.9 $\pm$ 0.1
		DI-W – 1 Scan	36.0 $\pm$ 0.7	33.1 $\pm$ 1.4	2.9 $\pm$ 0.5	45.7 $\pm$ 0.9	45.7 $\pm$ 0.9	0.0 $\pm$ 0	3.0 $\pm$ 0.3
		DI-W – 2 Scans	34.8 $\pm$ 1	33.8 $\pm$ 1.2	1 $\pm$ 0.1	37.6 $\pm$ 0.4	37.5 $\pm$ 0.4	0.2 $\pm$ 0	0.9 $\pm$ 0.1
		DI-W – 3 Scans	31.7 $\pm$ 0.5	30.4 $\pm$ 0.4	1.3 $\pm$ 0.1	36.5 $\pm$ 1	36.2 $\pm$ 1	0.3 $\pm$ 0	1 $\pm$ 0.1
		DI-W+TW20 – 1 Scan	28.3 $\pm$ 4.5	24.5 $\pm$ 4.7	3.8 $\pm$ 0.1	36.2 $\pm$ 0.4	35.8 $\pm$ 0.3	0.3 $\pm$ 0.1	3.5 $\pm$ 0
		DI-W+TW20 – 2 Scans	35.3 $\pm$ 0.5	34.2 $\pm$ 0.5	1.1 $\pm$ 0	39 $\pm$ 1.2	38.9 $\pm$ 1.2	0.1 $\pm$ 0	1 $\pm$ 0
		DI-W+TW20 – 3 Scans	31.9 $\pm$ 1.8	30.4 $\pm$ 2	1.5 $\pm$ 0.1	35.1 $\pm$ 0.8	34.8 $\pm$ 0.8	0.3 $\pm$ 0	1.2 $\pm$ 0.1
		50% IMS+DI-W – 1 Scan	34.6 $\pm$ 2	33.4 $\pm$ 2.8	1.2 $\pm$ 0.6	34.1 $\pm$ 1.4	32.6 $\pm$ 1.7	1.5 $\pm$ 0.2	-0.3 $\pm$ 0.3
		50% IMS+DI-W – 2 Scans	35.4 $\pm$ 0.3	33.9 $\pm$ 0.4	1.5 $\pm$ 0.1	33.4 $\pm$ 0.6	33.2 $\pm$ 0.6	0.2 $\pm$ 0.1	1.3 $\pm$ 0
		50% IMS+DI-W – 3 Scans	29.3 $\pm$ 0.7	27.2 $\pm$ 0.3	2.1 $\pm$ 0.2	29.6 $\pm$ 0.6	26.8 $\pm$ 1.4	2.8 $\pm$ 0.6	-0.7 $\pm$ 0.2
		50% IMS+WS – 1 Scan	30.2 $\pm$ 6.6	26.5 $\pm$ 7.4	3.7 $\pm$ 0.6	37.6 $\pm$ 1.9	36.7 $\pm$ 2	0.9 $\pm$ 0.1	2.8 $\pm$ 0.4
		50% IMS+WS – 2 Scans	34.7 $\pm$ 0.8	33.5 $\pm$ 0.2	1.2 $\pm$ 0.4	36.7 $\pm$ 1	36.6 $\pm$ 1.1	0.2 $\pm$ 0	1 $\pm$ 0.3
		50% IMS+WS – 3 Scans	29.7 $\pm$ 0.6	26.8 $\pm$ 0.9	2.9 $\pm$ 0.2	31.9 $\pm$ 1	30.1 $\pm$ 1.6	1.7 $\pm$ 0.5	1.2 $\pm$ 0.2
		WS – 1 Scan	39.8 $\pm$ 0.8	37.4 $\pm$ 1.1	2.4 $\pm$ 0.2	48.6 $\pm$ 2.2	48.5 $\pm$ 2.2	0.1 $\pm$ 0	2.3 $\pm$ 0.2
WS – 2 Scans	35.8 $\pm$ 0.6	34.1 $\pm$ 0.6	1.6 $\pm$ 0	40.6 $\pm$ 1	40.5 $\pm$ 1	0.1 $\pm$ 0	1.5 $\pm$ 0		

Table C10 – Multispectral Imaging (MSI) Clusterisation Analysis data of the Er:YAG laser irradiated areas at 2 J/cm<sup>2</sup>. Green % corresponds to a gradual reduction of the early-stage varnish thinning. Red % coincides with gradual deeper irradiation of the varnish layer. The Black % corresponds to the remaining varnish within the irradiated spots.

Energy (mJ)	Nominated Fluence (J/cm <sup>2</sup> )	Cleaning systems	Spectral Imaging Clusterisation Analysis		
			Green %	Red %	Black %
140	2	Dry – 1 Scan	29	70	2
		Dry – 2 Scans	6	94	0
		DI-W – 1 Scan	29	71	0
		DI-W – 2 Scans	24	76	0
		DI-W – 3 Scans	2	98	0
		DI-W+TW20 – 1 Scan	46	52	2
		DI-W+TW20 – 2 Scans	5	95	0
		DI-W+TW20 – 3 Scans	66	34	0
		50% IMS+DI-W – 1 Scan	18	10	72
		50% IMS+DI-W – 2 Scans	35	62	3
		50% IMS+DI-W – 3 Scans	21	3	76
		50% IMS+WS – 1 Scan	42	35	23
		50% IMS+WS – 2 Scans	13	87	0
		50% IMS+WS – 3 Scans	46	24	30
		WS – 1 Scan	29	66	4
		WS – 2 Scans	7	93	0

Figure C14 – UV induced fluorescence micrographs of the irradiated test areas (A, B, C) and Multispectral Imaging clusterisation maps (A1 and C1) of one (A and A1), two (B and B1) and three (C and C1) laser scanned areas at ‘nominated fluence’ 2.1 J/cm<sup>2</sup>. At the top left the dry irradiated area is shown, followed by other irradiated areas pre-wetted with the following solutions: deionised water (DI-W), 1% v/v Tween20 in DI-W, 50% v/v Industrial Methylated Spirit (IMS) in DI-W, 50% v/v IMS in White Spirit (WS) and pure White Spirit. All the laser-irradiated areas were 15x15 mm.

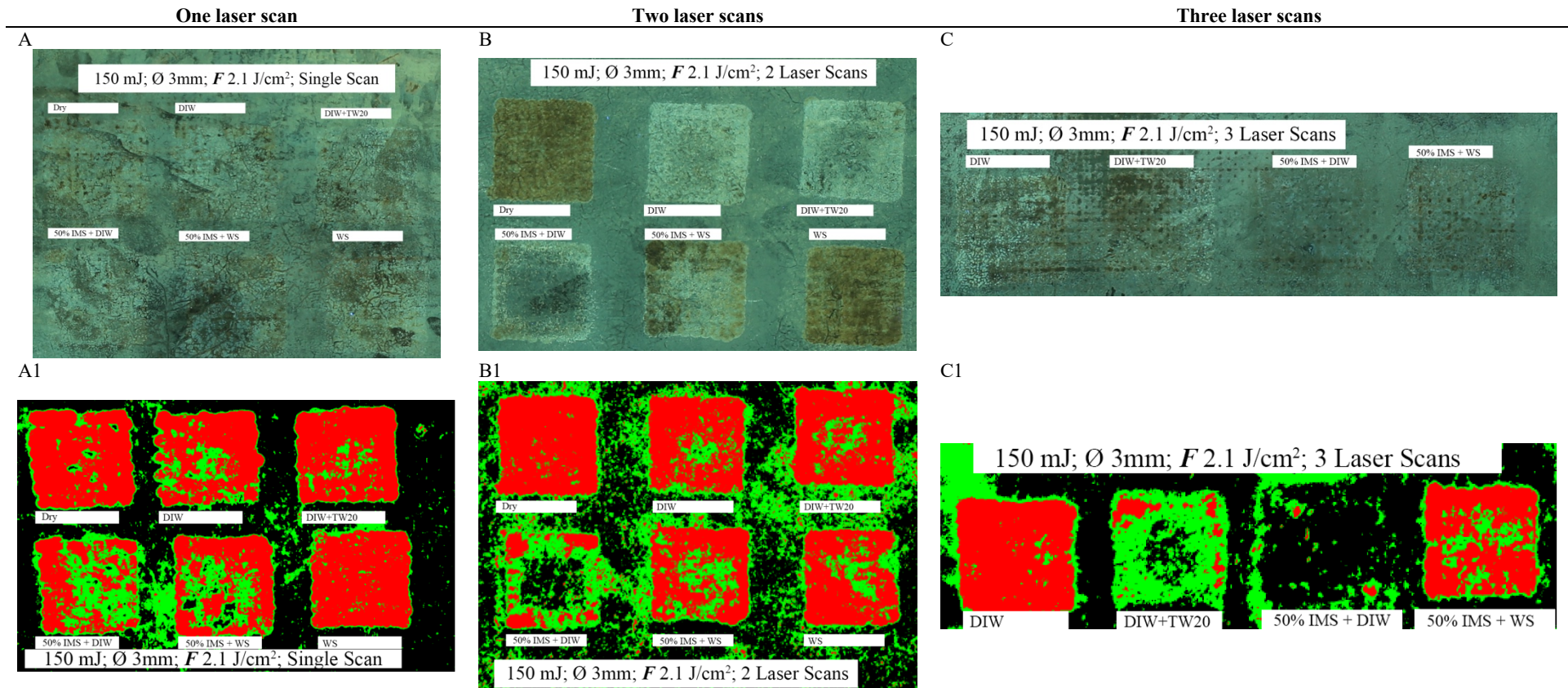


Table C11 – The table provides the  $L_{SCI_{mean}}^*$  and  $L_{SCE_{mean}}^*$  and the GRF data before and after laser irradiation at 2.1 J/cm<sup>2</sup> and the  $\Delta$ GRF values. Standard deviations ( $\sigma$ ) of all data are provided.

Energy (mJ)	Nominated Fluence (J/cm <sup>2</sup> )	Cleaning Systems	Colourimetry before laser irradiation			Colourimetry after laser irradiation			$\Delta$ GRF $\pm\sigma$
			$L_{SCI_{mean}}^* \pm\sigma$	$L_{SCE_{mean}}^* \pm\sigma$	$GRF_b \pm\sigma$	$L_{SCI_{mean}}^* \pm\sigma$	$L_{SCE_{mean}}^* \pm\sigma$	$GRF_a \pm\sigma$	
150	2.1	Dry – 1 Scan	32.7 $\pm$ 0.1	30.5 $\pm$ 0.5	2.2 $\pm$ 0.2	39.3 $\pm$ 0.3	39.1 $\pm$ 0.3	0.2 $\pm$ 0	2 $\pm$ 0.2
		Dry – 2 Scans	36.4 $\pm$ 0.6	35.7 $\pm$ 0.6	0.7 $\pm$ 0	38.6 $\pm$ 1.3	38.5 $\pm$ 1.3	0.1 $\pm$ 0	0.6 $\pm$ 0
		DI-W – 1 Scan	33.2 $\pm$ 0.5	31.9 $\pm$ 0.8	1.3 $\pm$ 0.2	38.3 $\pm$ 1.3	38.9 $\pm$ 1.3	-0.6 $\pm$ 0	2.0 $\pm$ 0.2
		DI-W – 2 Scans	34.2 $\pm$ 1.5	33.4 $\pm$ 1.3	0.8 $\pm$ 0.1	38 $\pm$ 1	37.8 $\pm$ 1	0.2 $\pm$ 0	0.6 $\pm$ 0.1
		DI-W – 3 Scans	29.0 $\pm$ 2.4	27.2 $\pm$ 2.1	1.8 $\pm$ 0.2	37.5 $\pm$ 0.6	37 $\pm$ 0.6	0.5 $\pm$ 0	1.4 $\pm$ 0.2
		DI-W+TW20 – 1 Scan	35.3 $\pm$ 2.8	33 $\pm$ 2.7	2.3 $\pm$ 0.1	38.8 $\pm$ 1.1	38.6 $\pm$ 1.1	0.2 $\pm$ 0	2.2 $\pm$ 0.1
		DI-W+TW20 – 2 Scans	34.8 $\pm$ 1.3	34.3 $\pm$ 1.4	0.5 $\pm$ 0.1	37.3 $\pm$ 1.2	37.2 $\pm$ 1.2	0.1 $\pm$ 0	0.3 $\pm$ 0.1
		DI-W+TW20 – 3 Scans	30.5 $\pm$ 1	28.5 $\pm$ 0.8	2 $\pm$ 0.1	31.1 $\pm$ 0.5	30.3 $\pm$ 0.5	0.8 $\pm$ 0	1.2 $\pm$ 0.1
		50% IMS+DI-W – 1 Scan	32.2 $\pm$ 2.2	29.3 $\pm$ 4.2	2.9 $\pm$ 1.4	35.4 $\pm$ 0.2	35.2 $\pm$ 0.3	0.3 $\pm$ 0	2.6 $\pm$ 1
		50% IMS+DI-W – 2 Scans	32.9 $\pm$ 0.5	32.1 $\pm$ 0.5	0.9 $\pm$ 0	30.2 $\pm$ 0.9	29.2 $\pm$ 0.7	0.9 $\pm$ 0.1	-0.1 $\pm$ 0.1
		50% IMS+DI-W – 3 Scans	29.6 $\pm$ 1.2	27.4 $\pm$ 0.8	2.2 $\pm$ 0.3	30.6 $\pm$ 0.2	26.6 $\pm$ 1	4.1 $\pm$ 0.6	-1.9 $\pm$ 0.2
		50% IMS+WS – 1 Scan	31 $\pm$ 0.1	29.5 $\pm$ 0.3	1.5 $\pm$ 0.1	36.8 $\pm$ 0.2	36.6 $\pm$ 0.3	0.1 $\pm$ 0	1.4 $\pm$ 0.1
		50% IMS+WS – 2 Scans	33.4 $\pm$ 1.5	32.6 $\pm$ 1.5	0.8 $\pm$ 0	34.4 $\pm$ 0.8	34.3 $\pm$ 0.8	0.2 $\pm$ 0	0.6 $\pm$ 0
		50% IMS+WS – 3 Scans	27.8 $\pm$ 0.8	26.3 $\pm$ 0.7	1.5 $\pm$ 0.1	34.3 $\pm$ 0.4	34 $\pm$ 0.3	0.3 $\pm$ 0.1	1.2 $\pm$ 0
		WS – 1 Scan	31.2 $\pm$ 1.1	29.1 $\pm$ 2	2.1 $\pm$ 0.7	39.5 $\pm$ 0	39.3 $\pm$ 0	0.2 $\pm$ 0	2 $\pm$ 0.5
WS – 2 Scans	34.1 $\pm$ 0.6	33.5 $\pm$ 0.8	0.6 $\pm$ 0.2	37.4 $\pm$ 0.5	37.3 $\pm$ 0.5	0.1 $\pm$ 0	0.5 $\pm$ 0.1		

Table C12 - Multispectral Imaging (MSI) Clusterisation Analysis data of the Er:YAG laser irradiated areas at 2.1 J/cm<sup>2</sup>. Green % corresponds to a gradual reduction of the early-stage varnish thinning. Red % coincides with gradual deeper irradiation of the varnish layer. The Black % corresponds to the remaining varnish within the irradiated spots.

Energy (mJ)	Nominated Fluence (J/cm <sup>2</sup> )	Cleaning systems	Spectral Imaging Clusterisation Analysis		
			Green %	Red %	Black %
150	2.1	Dry – 1 Scan	8	90	1
		Dry – 2 Scans	3	97	0
		DI-W – 1 Scan	24	75	1
		DI-W – 2 Scans	15	84	0
		DI-W – 3 Scans	3	97	0
		DI-W+TW20 – 1 Scan	12	88	0
		DI-W+TW20 – 2 Scans	14	86	0
		DI-W+TW20 – 3 Scans	71	12	17
		50% IMS+DI-W – 1 Scan	44	55	1
		50% IMS+DI-W – 2 Scans	46	24	30
		50% IMS+DI-W – 3 Scans	10	2	89
		50% IMS+WS – 1 Scan	30	60	5
		50% IMS+WS – 2 Scans	30	70	0
		50% IMS+WS – 3 Scans	23	70	0
		WS – 1 Scan	5	95	0
		WS – 2 Scans	22	77	0

Figure C15 – UV induced fluorescence micrographs of the irradiated test areas (A, B) and Multispectral Imaging clusterisation maps (A1 and B1) of one (A and A1) and two (B and B1) laser scanned areas at ‘nominated fluence’  $2.3 \text{ J/cm}^2$ . At the top left the dry irradiated area is shown, followed by other irradiated areas pre-wetted with the following solutions: deionised water (DI-W), 1% v/v Tween20 in DI-W, 50% v/v Industrial Methylated Spirit (IMS) in DI-W, 50% v/v IMS in White Spirit (WS) and pure White Spirit. All the laser-irradiated areas were  $15 \times 15 \text{ mm}$ .

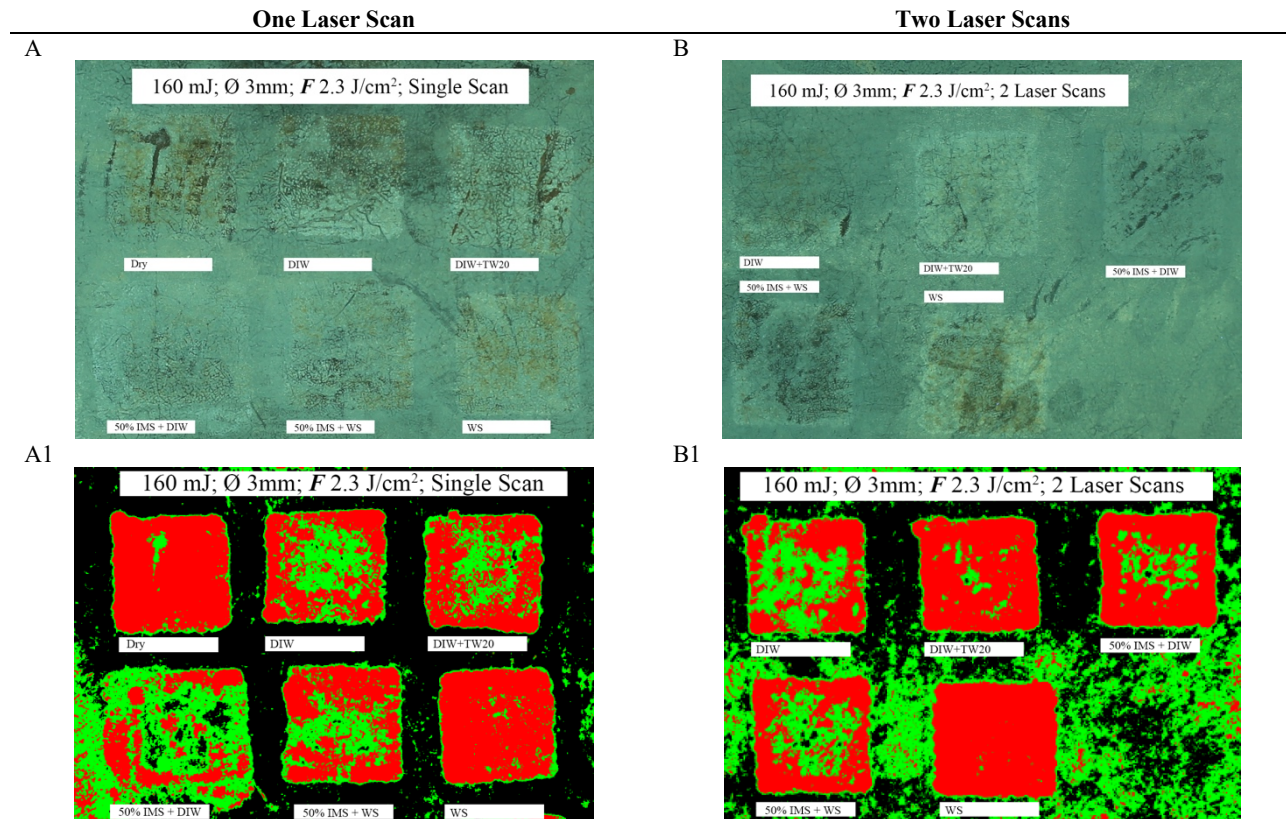


Table C13 – The table provides the  $L_{SCI_{mean}}^*$  and  $L_{SCE_{mean}}^*$  and the GRF data before and after laser irradiation at 2.3 J/cm<sup>2</sup> and the  $\Delta$ GRF values. Standard deviations ( $\sigma$ ) of all data are provided.

Energy (mJ)	Nominated Fluence (J/cm <sup>2</sup> )	Cleaning Systems	Colourimetry before laser irradiation			Colourimetry after laser irradiation			$\Delta$ GRF $\pm\sigma$
			$L_{SCI_{mean}}^* \pm\sigma$	$L_{SCE_{mean}}^* \pm\sigma$	$GRF_b \pm\sigma$	$L_{SCI_{mean}}^* \pm\sigma$	$L_{SCE_{mean}}^* \pm\sigma$	$GRF_a \pm\sigma$	
160	2.3	Dry – 1 Scan	31.1 $\pm$ 2	28 $\pm$ 2.4	3.1 $\pm$ 0.3	42.3 $\pm$ 0.1	42.2 $\pm$ 0.1	0.1 $\pm$ 0	3 $\pm$ 0.2
		DI-W – 1 Scan	29.6 $\pm$ 0.6	28.1 $\pm$ 0.9	1.5 $\pm$ 0.2	35.7 $\pm$ 1	35.4 $\pm$ 1	0.2 $\pm$ 0	1.3 $\pm$ 0.1
		DI-W – 2 Scans	35.4 $\pm$ 0.6	34.1 $\pm$ 1	1.3 $\pm$ 0.3	38 $\pm$ 1.2	37.8 $\pm$ 1.3	0.2 $\pm$ 0	1.1 $\pm$ 0.2
		DI-W+TW20 – 1 Scan	29.6 $\pm$ 1.3	26.9 $\pm$ 1.4	2.7 $\pm$ 0.1	36.2 $\pm$ 0.8	36.0 $\pm$ 0.8	0.2 $\pm$ 0	2.4 $\pm$ 0
		DI-W+TW20 – 2 Scans	35.0 $\pm$ 2	33.5 $\pm$ 2.4	1.5 $\pm$ 0.3	39.4 $\pm$ 0.6	39.2 $\pm$ 0.5	0.2 $\pm$ 0.1	1.3 $\pm$ 0.1
		50% IMS+DI-W – 1 Scan	31.9 $\pm$ 1.3	29 $\pm$ 0.9	2.9 $\pm$ 0.3	33.3 $\pm$ 1.6	32.2 $\pm$ 2.6	1.1 $\pm$ 0.7	1.8 $\pm$ 0.3
		50% IMS+DI-W – 2 Scans	34.7 $\pm$ 1.2	32.7 $\pm$ 1.2	2 $\pm$ 0	35.4 $\pm$ 1	35.2 $\pm$ 1	0.2 $\pm$ 0	1.8 $\pm$ 0
		50% IMS+WS – 1 Scan	31.7 $\pm$ 0.4	28.9 $\pm$ 1.3	2.8 $\pm$ 0.6	37.6 $\pm$ 0.7	37.5 $\pm$ 0.7	0.2 $\pm$ 0	2.6 $\pm$ 0.4
		50% IMS+WS – 2 Scans	33.2 $\pm$ 0.4	33 $\pm$ 0.4	0.3 $\pm$ 0	34 $\pm$ 0.9	33.6 $\pm$ 0.9	0.3 $\pm$ 0	0 $\pm$ 0
		WS – 1 Scan	31.9 $\pm$ 1.3	3 $\pm$ 2.1	1.9 $\pm$ 0.6	40.0 $\pm$ 0.7	39.9 $\pm$ 0.7	0.1 $\pm$ 0	1.8 $\pm$ 0.4
		WS – 2 Scans	35.8 $\pm$ 1.4	35.3 $\pm$ 1.3	0.5 $\pm$ 0.1	46.6 $\pm$ 0.7	46.6 $\pm$ 0.7	0.1 $\pm$ 0	0.4 $\pm$ 0

Table C14 – Multispectral Imaging (MSI) Clusterisation Analysis data of the Er:YAG laser irradiated areas at 2.3 J/cm<sup>2</sup>. Green % corresponds to a gradual reduction of the early-stage varnish thinning. Red % coincides with gradual deeper irradiation of the varnish layer. The Black % corresponds to the remaining varnish within the irradiated spots.

Energy (mJ)	Nominated Fluence (J/cm <sup>2</sup> )	Cleaning systems	Spectral Imaging Clusterisation Analysis		
			Green %	Red %	Black %
160	2.3	Dry – 1 Scan	4	96	0
		DI-W – 1 Scan	43	56	1
		DI-W – 2 Scans	46	54	0
		DI-W+TW20 – 1 Scan	33	67	0
		DI-W+TW20 – 2 Scans	9	91	0
		50% IMS+DI-W – 1 Scan	58	30	12
		50% IMS+DI-W – 2 Scans	18	82	0
		50% IMS+WS – 1 Scan	35	65	1
		50% IMS+WS – 2 Scans	35	63	2
		WS – 1 Scan	5	95	0
		WS – 2 Scans	0	100	0

Figure C16 – UV induced fluorescence micrographs of the irradiated test areas (A, B) and Multispectral Imaging clusterisation maps (A1 and B1) of one (A and A1) and two (B and B1) laser scanned areas at ‘nominated fluence’ 2.4 J/cm<sup>2</sup>. At the top left the dry irradiated area is shown, followed by other irradiated areas pre-wetted with the following solutions: deionised water (DI-W), 1% v/v Tween20 in DI-W, 50% v/v Industrial Methylated Spirit (IMS) in DI-W, 50% v/v IMS in White Spirit (WS) and pure White Spirit. All the laser-irradiated areas were 15x15 mm.

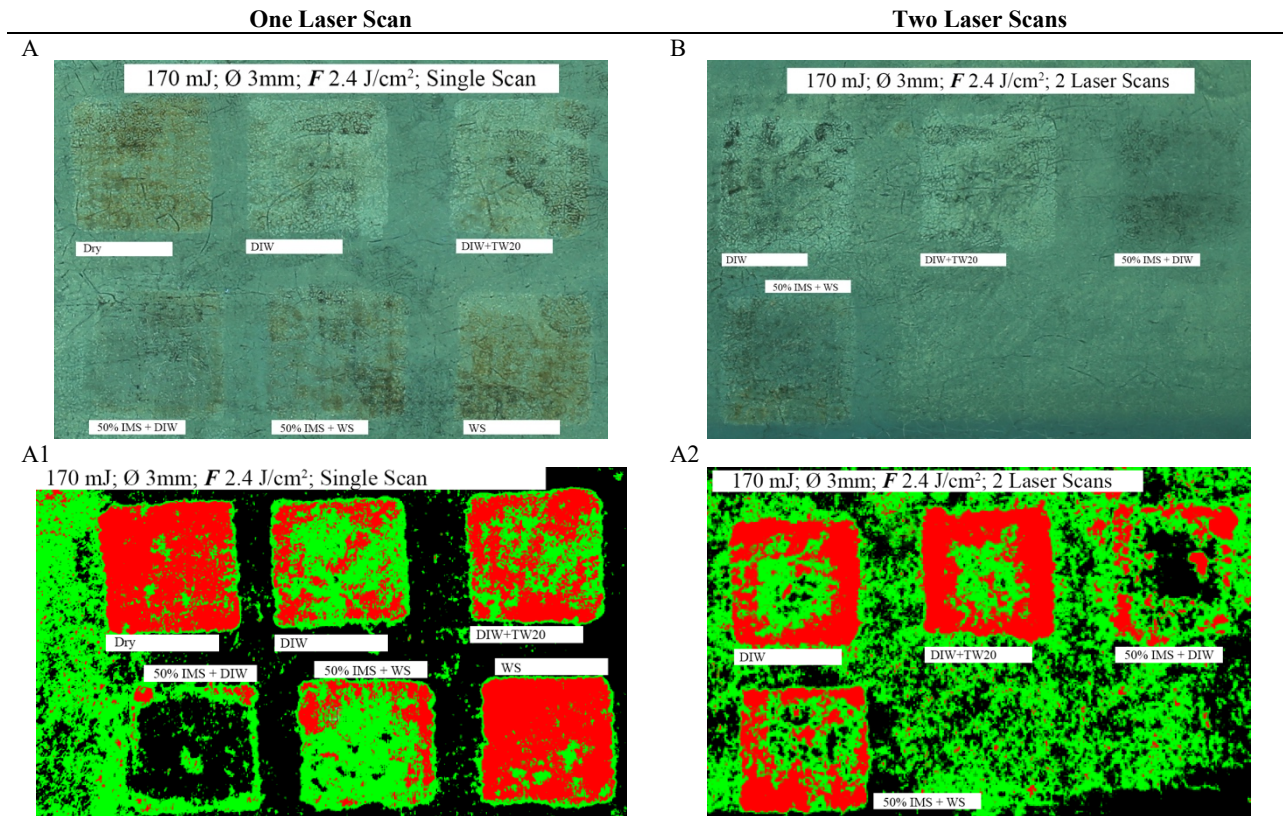


Table C15 – The table provides the  $L_{SCI_{mean}}^*$  and  $L_{SCE_{mean}}^*$  and the GRF data before and after laser irradiation at 2.4 J/cm<sup>2</sup> and the  $\Delta$ GRF values. Standard deviations ( $\sigma$ ) of all data are provided.

Energy (mJ)	Nominated Fluence (J/cm <sup>2</sup> )	Cleaning Systems	Colourimetry before laser irradiation			Colourimetry after laser irradiation			$\Delta$ GRF $\pm\sigma$
			$L_{SCI_{mean}}^* \pm\sigma$	$L_{SCE_{mean}}^* \pm\sigma$	$GRF_b \pm\sigma$	$L_{SCI_{mean}}^* \pm\sigma$	$L_{SCE_{mean}}^* \pm\sigma$	$GRF_a \pm\sigma$	
170	2.4	Dry – 1 Scan	32.3 $\pm$ 2.4	31.1 $\pm$ 2.7	1.2 $\pm$ 0.3	38.5 $\pm$ 0.4	38.4 $\pm$ 0.4	0.1 $\pm$ 0	1.1 $\pm$ 0.2
		DI-W – 1 Scan	29.9 $\pm$ 1	28.4 $\pm$ 1.1	1.5 $\pm$ 0.1	37.1 $\pm$ 1.7	37 $\pm$ 1.6	0.1 $\pm$ 0	1.4 $\pm$ 0.1
		DI-W – 2 Scans	34.7 $\pm$ 0.7	34.2 $\pm$ 0.6	0.5 $\pm$ 0	37.9 $\pm$ 1.9	37.7 $\pm$ 1.9	0.1 $\pm$ 0	0.4 $\pm$ 0
		DI-W+TW20 – 1 Scan	30 $\pm$ 0.6	28.7 $\pm$ 0.6	1.3 $\pm$ 0	37.2 $\pm$ 0.7	37.1 $\pm$ 0.7	0.1 $\pm$ 0	1.1 $\pm$ 0
		DI-W+TW20 – 2 Scans	35.3 $\pm$ 0.9	35 $\pm$ 0.9	0.3 $\pm$ 0	39.3 $\pm$ 0.5	39.2 $\pm$ 0.5	0.1 $\pm$ 0	0.2 $\pm$ 0
		50% IMS+DI-W – 1 Scan	29.5 $\pm$ 0.3	28.4 $\pm$ 0.3	1.2 $\pm$ 0	32.1 $\pm$ 1.1	31.5 $\pm$ 1.3	0.6 $\pm$ 0.2	0.5 $\pm$ 0.1
		50% IMS+DI-W – 2 Scans	34.0 $\pm$ 3	33.6 $\pm$ 2.8	0.5 $\pm$ 0.1	34.0 $\pm$ 3.1	33.3 $\pm$ 3.8	0.7 $\pm$ 0.5	-0.2 $\pm$ 0.3
		50% IMS+WS – 1 Scan	28.5 $\pm$ 0.7	27.1 $\pm$ 0.6	1.5 $\pm$ 0	33.4 $\pm$ 0.1	33.2 $\pm$ 0.1	0.2 $\pm$ 0	1.3 $\pm$ 0
		50% IMS+WS – 2 Scans	32.5 $\pm$ 0.5	31.9 $\pm$ 0.7	0.5 $\pm$ 0.2	34.1 $\pm$ 0.8	33.9 $\pm$ 0.8	0.1 $\pm$ 0	0.4 $\pm$ 0.1
		WS – 1 Scan	29.7 $\pm$ 0.3	28.4 $\pm$ 0.6	1.3 $\pm$ 0.2	39.2 $\pm$ 0.9	39.1 $\pm$ 0.9	0.1 $\pm$ 0	1.2 $\pm$ 0.1

Table C16 – Multispectral Imaging (MSI) Clusterisation Analysis data of the Er:YAG laser irradiated areas at 2.4 J/cm<sup>2</sup>. Green % corresponds to a gradual reduction of the early-stage varnish thinning. Red % coincides with gradual deeper irradiation of the varnish layer. The Black % corresponds to the remaining varnish within the irradiated spots.

Energy (mJ)	Nominated Fluence (J/cm <sup>2</sup> )	Cleaning systems	Spectral Imaging Clusterisation Analysis		
			Green %	Red %	Black %
170	2.4	Dry – 1 Scan	12	88	0
		DI-W – 1 Scan	60	35	6
		DI-W – 2 Scans	39	58	3
		DI-W+TW20 – 1 Scan	40	60	0
		DI-W+TW20 – 2 Scans	29	70	1
		50% IMS+DI-W – 1 Scan	29	5	67
		50% IMS+DI-W – 2 Scans	40	24	36
		50% IMS+WS – 1 Scan	71	25	3
		50% IMS+WS – 2 Scans	42	49	9
		WS – 1 Scan	12	88	0

### C3 ATR/FT-IR

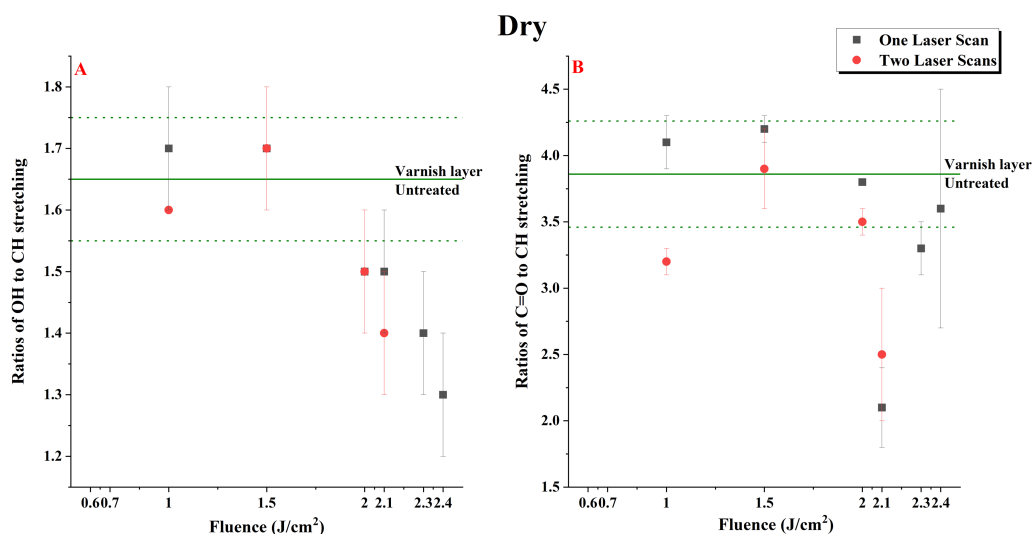


Figure C17 – Ratios of the integrated areas of the –OH/CH and the –C=O/CH bands as acquired by ATR/FT-IR vs fluence of the dry irradiated varnish films collected on the coverslips in VSP ( $\tau_L \approx 100 \mu s$ ) mode. The horizontal lines define the corresponding ratios of the varnish samples that have been not irradiated (dark green solid line). The dotted lines correspond with the area of the standard deviation.

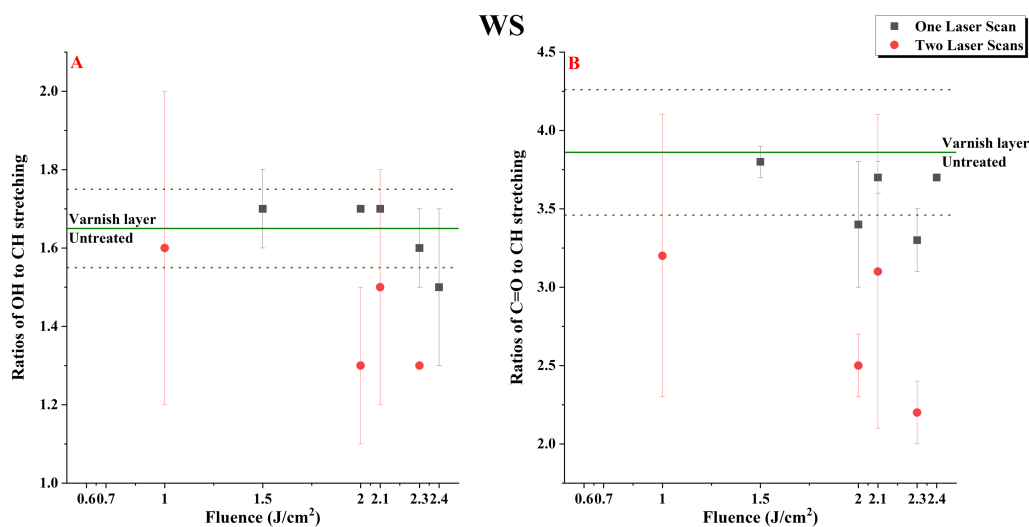


Figure C18 – Ratios of the integrated areas of the –OH/CH and the –C=O/CH bands as acquired by ATR/ FTIR vs fluence of the White Spirit (WS) pre-wetted irradiated varnish films collected on the coverslips in VSP ( $\tau_L \approx 100 \mu s$ ) mode. The horizontal lines define the corresponding ratios of the varnish samples that have been not irradiated (dark green solid line). The dotted lines correspond with the area of the standard deviation.

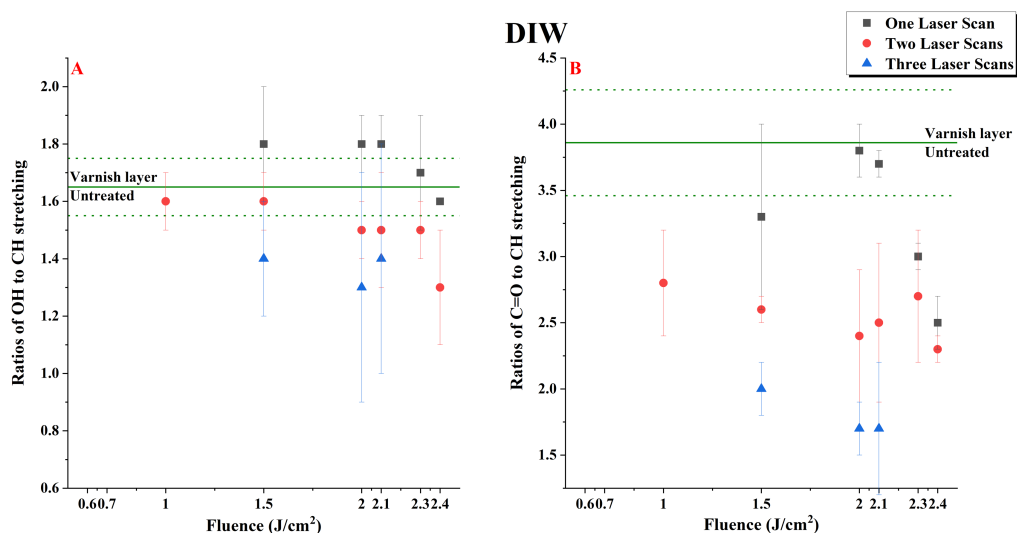


Figure C19 – Ratios of the integrated areas of the –OH/CH and the –C=O/CH bands as acquired by ATR/ FTIR vs fluence of the DI-W pre-wetted irradiated varnish films collected on the coverslips in VSP ( $\tau_L \approx 100 \mu s$ ) mode. The horizontal lines define the corresponding ratios of the varnish samples that have been not irradiated (dark green solid line). The dotted lines correspond with the area of the standard deviation.

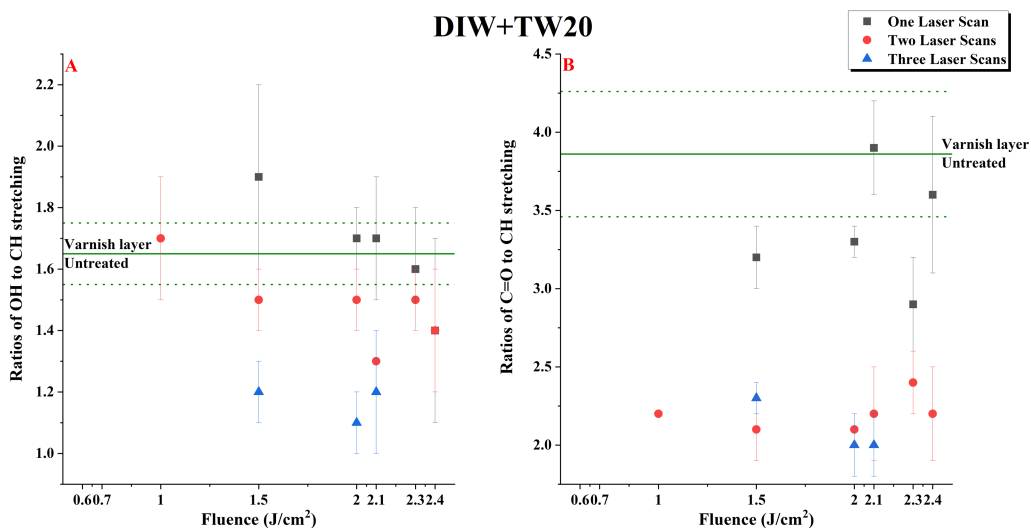


Figure C20 – Ratios of the integrated areas of the –OH/CH and the –C=O/CH bands as acquired by ATR/ FTIR vs fluence of the DI-W+TW20 pre-wetted irradiated varnish films collected on the coverslips in VSP ( $\tau_L \approx 100 \mu s$ ) mode. The horizontal lines define the corresponding ratios of the varnish samples that have been not irradiated (dark green solid line). The dotted lines correspond with the area of the standard deviation.

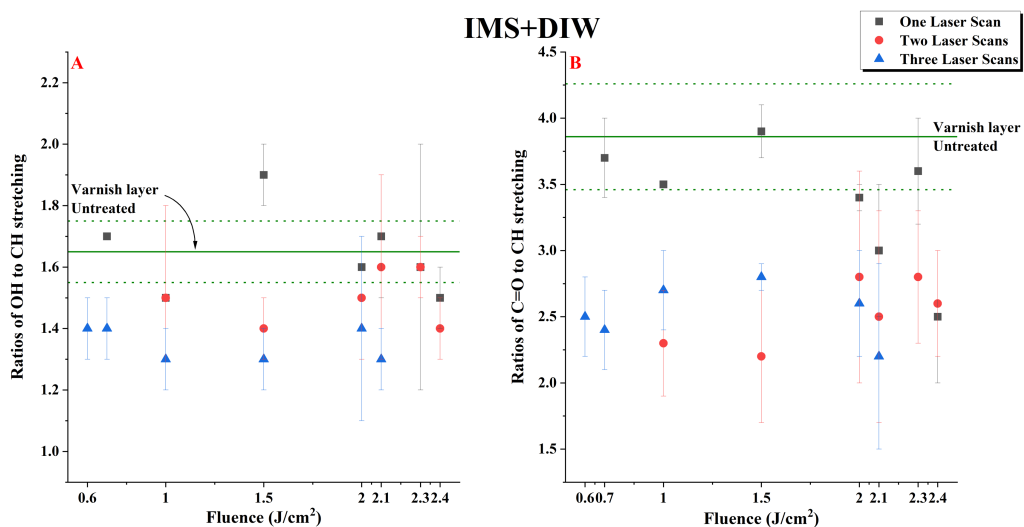


Figure C21 – Ratios of the integrated areas of the  $-OH/CH$  and the  $-C=O/CH$  bands as acquired by ATR/ FTIR vs fluence of the IMS+DI-W pre-wetted irradiated varnish films collected on the coverslips in VSP ( $\tau_L \approx 100 \mu s$ ) mode. The horizontal lines define the corresponding ratios of the varnish samples that have been not irradiated (dark green solid line). The dotted lines correspond with the area of the standard deviation.

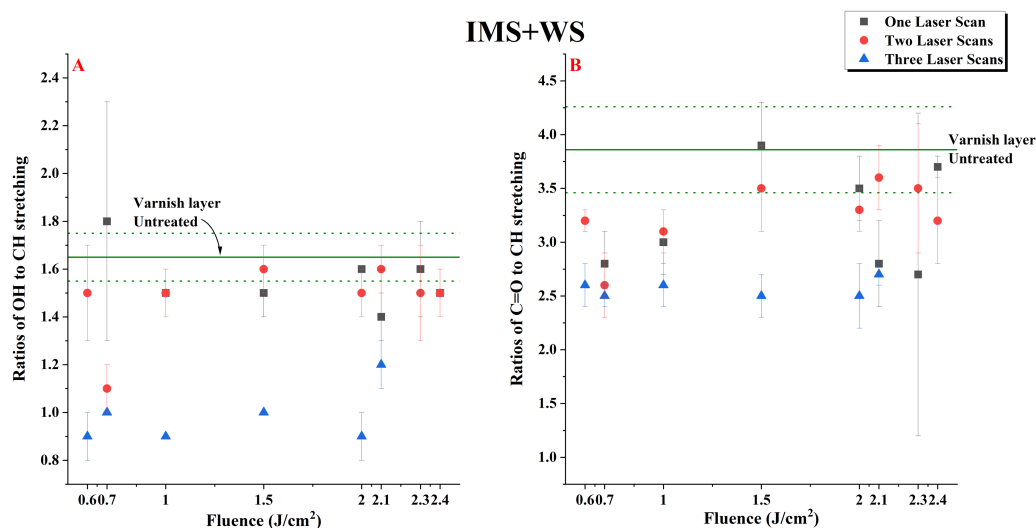


Figure C22 – Ratios of the integrated areas of the  $-OH/CH$  and the  $-C=O/CH$  bands as acquired by ATR/ FTIR vs fluence of the IMS+WS pre-wetted irradiated varnish films collected on the coverslips in VSP ( $\tau_L \approx 100 \mu s$ ) mode. The horizontal lines define the corresponding ratios of the varnish samples that have been not irradiated (dark green solid line). The dotted lines correspond with the area of the standard deviation.